Physics of the Solid State, Vol. 42, No. 8, 2000, pp. 1381–1386. Translated from Fizika Tverdogo Tela, Vol. 42, No. 8, 2000, pp. 1345–1349.

METALS AND SUPERCONDUCTORS

Magnetothermo-emf and Wiedemann–Franz Law for Tungsten Single Crystals under the Conditions of Static Skin Effect

A. B. Batdalov, Sh. B. Abdulvagidov, and A. M. Aliev

Institute of Physics, Dagestan Scientific Center, Russian Academy of Sciences, ul. 26 Bakinskikh Komissarov 94, Makhachkala, Dagestan, 367003 Russia

e-mail: kamilov@datacom.ru

Received November 2, 1999; in final form, December 28, 1999

Abstract—Results of the experimental investigation of the thermal conductivity, the thermo-emf, the Nernst effect, and the magnetoresistance of thin monocrystalline tungsten films under conditions of static skin effect in the temperature range $T = 2$–18 K in magnetic fields of up to 28 kOe are presented. It is shown that the field dependence of the magnetothermo-emf follows the predictions of the theory of galvano- and thermomagnetic phenomena in strong fields and exhibits anisotropy associated with both the shape of the sample and reflecting properties of the crystal surface. The temperature dependence of the magnetothermo-emf is investigated and a contribution from the phonon drag is detected. The surface contribution to the electrical and thermal conductivity under conditions of the static skin effect is singled out, and the temperature dependence of the Lorentz number for surface scattering is traced. © *2000 MAIK "Nauka/Interperiodica".*

It is well known [1] that, in strong transverse magnetic fields, compensated metals with a closed Fermi surface exhibit the static skin effect, i.e., the displacement of a direct current to the sample surface. The concentration of the current near the sample surface is due to the electrons moving in the surface layer and colliding with the surface actually being more mobile than electrons in the bulk of the sample.

In a magnetic field parallel to the sample surface, almost all the electrons moving in the surface layer of a thickness of the order of the Larmor radius collide with the boundary, which leads to the rupture of the orbits and to a translational motion of electrons along the sample boundary; the reflectivity of the surface in this case is an important factor in determining its electronic properties.

The behavior of galvanomagnetic coefficients for compensated metals under such conditions has been studied in detail both experimentally [2] and theoretically [1]. It is clear, however, that the skin effect also affects, to a certain extent, the behavior of other kinetic coefficients associated with the heat flux transferred by conduction electrons, including thermal conductivity, thermo-emf, and thermomagnetic effects.

The localization of the heat flux transferred by electrons in the surface layer of a monocrystalline tungsten film was first observed in [3]. A complex radial distribution of the heat flux density is induced in a sample with a temperature gradient $\nabla_x T$, which is placed in a transverse magnetic field H_z, due to the skin effect with corresponding consequences for the kinetic coefficients.

In this paper, we report on the results of the experimental investigation of magnetothermo-emf, the Nernst effect, and the Wiedemann-Franz law for tungsten single crystals under the static skin effect conditions $r \ll l < d$ (r is the Larmor radius, l is the electron mean free path, and d is the transverse dimension of the crystal) as functions of the magnetic field, temperature, and reflecting properties of the crystal surface. We investigated two thin monocrystalline tungsten plates cut from the same bulk single crystal with the resistivity ratio $\rho_{300\,K}/\rho_{4.2\,K} \sim 10^5$ in such a way that the planes of the plates coincided with the crystallographic faces (100) and (110), reflecting electrons diffusely and specularly, respectively [4]. We will henceforth denote by W-1 the sample with a wide diffusely reflecting surface and by W-2 the sample with a specularly reflecting surface. The characteristic size of the samples was $40 \times 4.0 \times 0.4$ mm, with the longer axis of the plates coinciding with the crystallographic direction $\langle 110 \rangle$.

The field and temperature dependences of the thermal conductivity, the thermo-emf, and the Nernst effect were measured by the method of steady-state heat flow, while the magnetoresistance was measured using the conventional dc four-probe technique. The temperature gauges were Allen–Bradley carbon resistance thermometers calibrated from the saturated pressure of helium vapor over the liquid (1.8–4.2 K) and with the help of a calibrated resistance thermometer TSU-2 (4–18 K). The temperature drop across the sample was 0.3–1.0 K. The potential probes were thin superconducting wires of diameter 0.08 mm, which enabled us to measure the absolute values of thermo-emf. The error in the measurements of the absolute values of the kinetic coefficients did not exceed 5–8%.

1063-7834/00/4208-1381$20.00

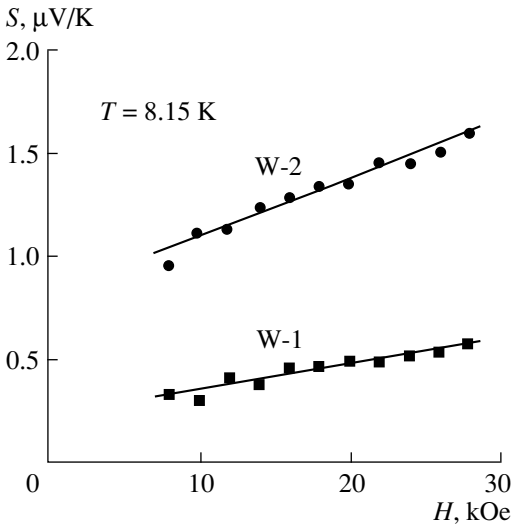

Fig. 1. Field dependence of the magnetothermo-emf in the case when the magnetic field is parallel to the plane of the sample.

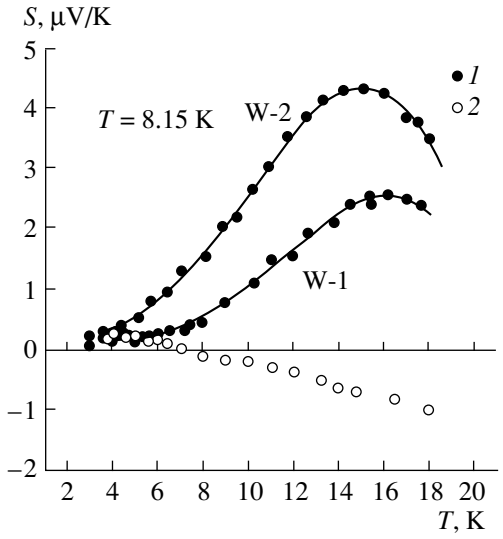

Fig. 2. Temperature dependence of thermo-emf in a magnetic field of 28 kOe (curve *1*) and in zero magnetic field (curve *2*). The magnetic field is parallel to the plane of the sample.

1. DISCUSSION OF EXPERIMENTAL RESULTS

1.1. Magnetothermo-emf and Nernst Effect

The thermo-emf of metals is quite sensitive to the peculiarities of the energy spectrum of quasiparticles and the type of their scattering; for this reason, it is an interesting subject for investigations. As a rule, the thermo-emf of metals has a complex temperature dependence at low temperatures and can be presented as the sum of two terms, one of which ($S_d \sim T$) is responsible for the diffusion thermo-emf, while the other ($S_{\text{drag}} \sim T^3$) is due to the effect of electron drag by phonons, which emerges due to the nonequilibrium nature of the phonon distribution function:

$$S = S_d + S_{\text{drag}} = aT + bT^3. \quad (1)$$

The thermo-emf of tungsten also possesses these features: the value of S for tungsten changes its sign twice upon cooling, attaining a negative peak at $T = 80$ K, and then a small positive peak at $T = 5$–10 K, the sign-inversion temperature for S and the low-temperature peak being displaced towards lower values upon a decrease in the amount of impurities in the sample. It is generally accepted [5] that the low-temperature positive peak of $S(T)$ for tungsten is a consequence of the combined operation of two mechanisms: the positive diffusion thermo-emf increasing linearly with temperature, and a negative phonon-drag thermo-emf increasing rapidly with temperature and having a peak at $T \approx 70$ K.

The thermo-emf measurements for metals in a magnetic field revealed [6] that, as in the case of zero magnetic field, S can be presented as the sum of a term depending linearly on T and a term proportional to T^3. A common feature of the thermo-emf of metals is that the value of S increases in a magnetic field irrespective of the sign of the thermo-emf, both S_d and S_{drag} increasing simultaneously. It should be noted that the experiments on the thermo-emf of compensated metals involve considerable difficulties due to peculiarities of these metals. Equal numbers of electrons and holes participate in the conduction of compensated metals; for this reason, their thermoelectric contributions are subtracted, and the experimentally measured S^m appears as the small difference between approximately equal quantities, which hampers its theoretical analysis and exact measurement at helium temperatures.

At the same time, an asymmetric arrangement of measuring probes relative to the direction of the heat flux can lead to the superposition of a relatively strong stray signal due to the Nernst effect (the field E_y transverse to the magnetic field H_z and the heat flux q_x) on the small value of S^m being measured. The Nernst effect reverses its sign depending on the direction of the magnetic field. For this reason, the experimentally measured values of $S^m(+H)$ and $S^m(-H)$ are often different; moreover, they may have opposite signs, while $S(H)$ is an even function of the magnetic field, and the equality $S^m(+H) = S^m(-H)$ must be observed. This circumstance was first noted by Blumenstock and Schroeder [7], who proved that, in this case, the thermo-emf should be defined as

$$S = \frac{1}{2}[S^m(+H) + S^m(-H)]. \quad (2)$$

Consequently, a reliable measurement of $S(H, T)$ requires a meticulous mounting of the sample, and all measurements must be made for two directions of the

magnetic field, while calculations must be made on the basis of formula (2). The temperature and magnetic-field dependences of the thermo-emf of the investigated samples are shown in Figs. 1 and 2.

The effect of magnetic field on the adiabatic thermo-emf coefficient of compensated metals was theoretically considered in [8, 9], while the measurements of magnetothermo-emf of a bulk tungsten sample in a narrow range of helium temperatures were made by Blumenstock and Schroeder [7]. According to Fletcher *et al.* [8], the thermo-emf coefficient defined as $E_x/\dfrac{\Delta T}{\Delta x}$ is given by

$$S = -\rho_{xx}\varepsilon_{xx}\left(1-\frac{\gamma_{yx}\rho_{yx}}{\gamma_{xx}\rho_{xx}}\right)+\rho_{yx}\varepsilon_{yx}\left(1+\frac{\gamma_{yx}\rho_{xx}}{\rho_{yx}\gamma_{xx}}\right), \quad (3)$$

where ρ and γ with subscripts are the corresponding components of the magnetoresistance and electron thermoresistance tensors, respectively, while ε_{xx} and ε_{yx} are the thermoelectric tensor components.

It can be seen from (3) that S is a complex function not only of thermoelectric coefficients, but also other kinetic coefficients. The problem of determining S is simplified if the measurements are made in strong magnetic fields $\omega\tau \gg 1$ (ω is the cyclotron frequency and τ is the relaxation time), which is the case under our experimental conditions at $T < 18$ K and $H = 28$ kOe. Even for the largest orbits (for charge carriers with the lowest mobility), $\omega\tau > 10$ for $T = 18$ K and $H = 28$ kOe. In such a case, the relations $\rho_{xx} \gg \rho_{yx}$ and $\gamma_{xx} \gg \gamma_{yx}$ are valid for compensated metals in a strong magnetic field [9], and the second term in the first parentheses in (3) can thus be neglected, and we also have $\left(\dfrac{\gamma_{yx}}{\rho_{yx}}\right)\left(\dfrac{\rho_{xx}}{\gamma_{xx}}\right) \approx 1$. Consequently, expression (3) can be written in the form

$$S = -\rho_{xx}\varepsilon_{xx} + 2\rho_{yx}\varepsilon_{yx}. \quad (4)$$

Let us consider the field dependence of the magneto-thermo-emf. Our measurements show that, to a high degree of accuracy, $\rho_{xx} \sim H^2$ for any mutual orientation of the magnetic field and the sample plane. It was also established that the off-diagonal component ρ_{yx} of the magnetoresistivity tensor under the skin effect increases quadratically with the field for both the diffusion- and the specularly reflecting faces [2]. At the same time, in accordance with the theory of thermomagnetic phenomena in a strong magnetic field, $\varepsilon_{xx} \sim H^{-2}$, while $\varepsilon_{yx} \sim H^{-1}$ [9]. Thus, the first term in formula (4) is independent of H, while the second must increase linearly with the field.

Taking into account the above arguments and the experimentally observed linear (although rather weak) magnetic-field dependence of S (Fig. 1), we can state that the theory is in reasonable agreement with the experimental results.

It is well known that the effect of the sample shape, i.e., the emergence of an additional anisotropy associated with the shape, is an experimental confirmation of the existence of the static skin effect: the conductivity of a plate in the field parallel to the plane of the sample is higher than its value for the transverse orientation. The reflectivity of the surface is quite significant: the surface conductivity for the diffusive boundary turns out to be smaller than for the specularly reflecting boundary by a factor of l/r [1], which must lead to an additional anisotropy.

Since the well-known Mott formula for the diffusion-induced thermoelectromotive force $S_d = L_0 eT(\partial \ln\sigma/\partial\varepsilon)_\eta$, where L_0 is the Lorentz number, σ is the electrical conductivity, and ε is the electron energy at the Fermi level η, includes, like formula (4), the terms depending on the sample shape and the reflectivity of the crystal surface, we can also expect a manifestation of the corresponding anisotropy in the behavior of the magnetothermo-emf. It should also be noted that the diffusion component of magnetothermo-emf has the same field dependence as the magnetothermo-emf of phonon drag [10].

It can be seen from Fig. 1, showing the magnetic-field dependence of S for both samples in the same experimental geometry in which the magnetic field is in the plane of the sample, that such an anisotropy is indeed observed: the absolute value of magnetothermo-emf for the face (110) is much larger than its value for the specularly reflecting face (100), which agrees with the theoretical concepts and our results for $\rho_{xx}(H, T)$.

The temperature dependence of the magneto-thermo-emf for $H = 28$ kOe for both samples is presented in Fig. 2. As expected, the values of S for the specularly reflecting face exceed the magnetothermo-emf for the diffusely reflecting face, while the form of the $S(T)$ dependence is not the same in the two cases: the $S(T)$ curve for the specularly reflecting face passes through the peak at $T \approx 14$ K, while for the diffusely reflecting face the peak is manifested less clearly and is shifted towards higher temperatures. The same figure shows the $S(T)$ dependence in zero field, in which no significant difference in the behavior of the thermo-emf is observed for the two samples. It can be seen that the temperature dependences of the thermo-emf in a field and in zero field differ radically. Carter *et al.* [11] believe that the sign inversion of the thermo-emf is a direct consequence of the participation of positive, as well as negative, charges (whose relative role changes with temperature) in the formation of the temperature dependence of the thermo-emf for tungsten.

The conventional procedure of separating the diffusion component and the phonon contribution to the thermo-emf lies in presenting the $S(T)$ dependence in the form $S/T = a + bT^2$, where a corresponds to the diffusion contribution and bT^2 is the contribution of the electron drag by phonons. Using this method, Blumenstock and Schroeder [7] unsuccessfully tried to determine the phonon contribution to the thermo-emf of a tungsten single crystal of considerably lower purity ($\rho_{300\,K}/\rho_{4.2\,K} \approx 30000$) in the range of helium tempera-

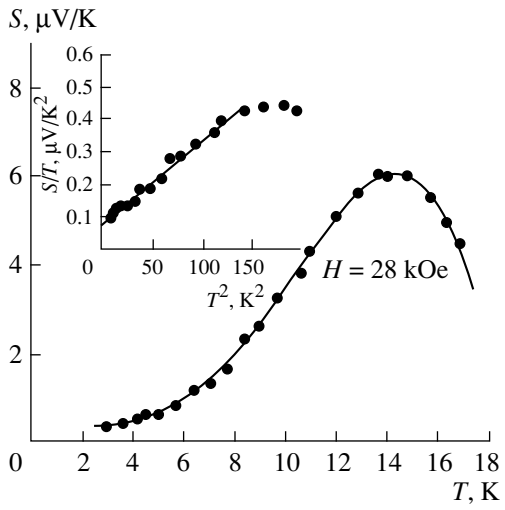

Fig. 3. Temperature dependence of magnetothermo-emf of the W-1 sample. The magnetic field is perpendicular to the plane of the sample. The inset shows the dependence $S/T = f(T^2)$.

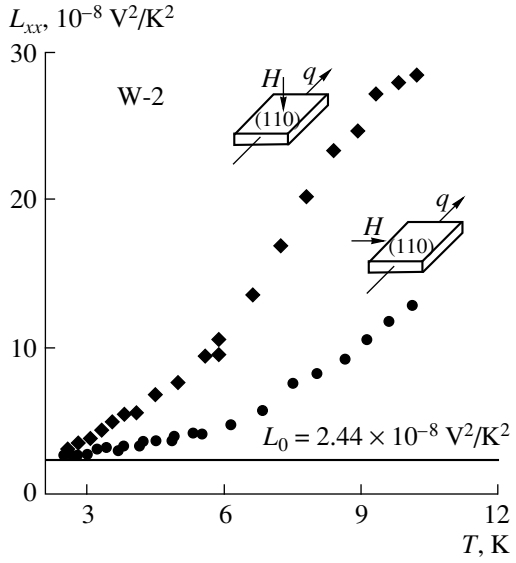

Fig. 4. Temperature dependence of the Lorentz number for a "specularly reflecting" sample; H = 28 kOe.

tures (1.5–4.2 K). This is probably due to the measurements having been made in a very narrow range of low temperatures, in which the phonon spectrum is still weakly excited, and all the processes are determined by the electron–impurity interaction.

In order to separate S_d and S_{drag}, the $S(H, T)$ dependence was measured for the W-1 sample in a wider temperature range T = 2.5–18 K in the geometry in which the magnetic field is perpendicular to the plane of the sample. For such a geometry, the effect of surface scattering is minimal. In the same experiment, we also investigated the Nernst effect. Figure 3 shows the $S(T)$ dependence, while the inset shows a plot of $S/T = f(T^2)$. It can be seen from the figure that the $S(T)$ curve for $T < 12$ K is correctly described by the equation $S/T = a + bT^2$ ($a = 0.075$, $b = 2.40 \times 10^{-3}$ μV/K⁴, which agrees with the analogous available data [6]), which leads to the conclusion that the effect of electron drag by phonons makes a noticeable contribution to the magnetothermo-emf for tungsten at low temperatures. An analysis of the Nernst effect also confirms the result obtained earlier [12] on the effect of the electron–phonon drag in tungsten. As expected, the measurements for a magnetic field parallel to the plane of a crystal plate, when the surface scattering prevails, did not reveal a phonon contribution to $S(H, T)$.

Figure 4 shows the experimental curves obtained during investigation of the Wiedemann–Franz law for the W-2 sample in different experimental geometries. The Wiedemann–Franz law establishes a relation between the electronic thermal conductivity κ^e and the electrical conductivity σ of a solid:

$$L = \frac{\kappa^e}{\sigma T} = \frac{\pi}{3}\left(\frac{K_B}{e}\right)^2 \frac{\tau_\kappa}{\tau_\sigma} = \frac{\tau_\kappa}{\tau_\sigma} L_0, \qquad (5)$$

where τ_σ and τ_κ are the electron relaxation times for electrical and thermal processes, respectively, K_B is the Boltzmann constant, and L is the Lorentz number equal to its Sommerfeld value $L_0 = 2.44 \times 10^{-8}$ V²/K² if the electron scattering is elastic, i.e., if $\tau_\sigma = \tau_\kappa$, which is observed for pure metals at extremely low temperatures, when electron–impurity collisions dominate, or at high temperatures $T \geq \Theta$ (Θ is the Debye temperature).

The value of κ^e can be determined experimentally as the difference between the measured value of κ^m_{xx} and the phonon thermal conductivity κ_{ph} determined by the method of κ^e suppression by a strong magnetic field [13]. The experiments also proved that the nature of electron scattering from the surface does not affect the result of separating κ_{ph} by an extrapolation procedure: $\kappa_{ph} \approx 0.5 \times 10^{-3} T^2$ W/cm K for both specularly and diffusely reflecting faces.

In a strong magnetic field ($\omega\tau \gg 1$) directed along a high-order symmetry axis, each of the scattering mechanisms makes a strictly additive contribution to the electrical conductivity σ_{xx} and not to ρ_{xx} [13], and the Wiedemann–Franz law has the form

$$L_{xx}(H \longrightarrow \infty) = \frac{\kappa^e_{xx}}{\sigma_{xx} T} = \frac{\tau_\sigma}{\tau_\kappa} L_0, \qquad (6)$$

where κ^e_{xx} and σ_{xx} are the transverse components of the electron thermal conductivity and electrical conductiv-

ity tensors, respectively. In the case of elastic scattering of electrons, the Lorentz number in a strong magnetic field is $L_{xx}(H \longrightarrow \infty) = L_0$ [14], i.e., an analysis of $L_{xx}(T)$ in a strong magnetic field can actually be used for estimating the elasticity of electron collisions. Figure 4, presenting the $L_{xx}(T)$ dependence for the W-2 sample in a field 28 kOe, shows that the values of $L_{xx}(\mathbf{H} \parallel \square)$ and $L_{xx}(\mathbf{H} \perp \square)$ differ considerably: for a parallel orientation of the magnetic field, the conditions for the emergence of the skin effect are created, electrons interact predominantly with the crystal surface, collisions that are regarded as purely elastic [15], and $L_{xx}(\mathbf{H} \parallel \square)$ is much closer to L_0 ($L_{xx}(\mathbf{H} \parallel \square) = L_0$ in the case of purely elastic scattering from the boundary) than $L_{xx}(\mathbf{H} \perp \square)$, for which the scattering from the boundary is extremely weak, and bulk processes of inelastic electron–phonon collisions prevail (scattering from impurities is manifested identically in both cases and does not affect the line of reasoning). It should also be noted that the anisotropy $L_{xx}(\mathbf{H} \parallel \square)/L_{xx}(\mathbf{H} \perp \square)$ associated with the sample shape and the state of the crystal surface is much higher for a specularly reflecting sample than for a diffusely reflecting one. The latter statement has a simple explanation: the "physical" anisotropy associated with the topology of the Fermi surface of tungsten (with the magnetoresistance minimum for $\mathbf{H} \parallel \langle 100 \rangle$ [16]) is superimposed on the "geometrical" anisotropy associated with the skin effect. The anisotropies enhance each other in one case (W-2 sample) and suppress in the other (W-1 sample).

The simultaneous measurement of the thermal and electrical conductivities under conditions of the static skin effect makes it possible to use the Wiedemann–Franz law to experimentally verify the statement concerning the elastic nature of conduction electron collisions with the crystal surface. To our knowledge, such measurements have not yet been made.

If we attribute the experimentally observed difference in the conductivity (σ_{xx}, κ_{xx}) for the orientation of the plane of a crystal plate parallel and perpendicular to the magnetic field (the magnetic field in both cases must be directed along equivalent crystallographic axes in order to eliminate the effect of "physical" anisotropy) only to the surface conduction and assume that the scattering from the surface is elastic,[1] we can write

$$L_{xx}^{\text{surf}} = \frac{\kappa_{xx}^{\text{surf}}}{\sigma_{xx}^{\text{surf}} T} = \frac{\Delta\kappa_{xx}}{\Delta\sigma_{xx} T} = L_0. \qquad (7)$$

Such a procedure should rather be made on the same sample, but for this purpose we need a plate of a single crystal whose geometrical axis coincides with the fourfold symmetry axis $\langle 100 \rangle$. In our case, we can use the results of measurements of κ_{xx} and σ_{xx} for different samples (W-2 for a parallel orientation of the magnetic field and W-1 for the perpendicular orientation), as both samples are cut from the same single crystal; however, the error in determining L_{xx}^{surf} may increase to a certain extent in this case. Taking into account what has been said above, we can write expression (7) in the form

$$L_{xx}^{\text{surf}} = \frac{\Delta\kappa_{xx}}{\Delta\sigma_{xx} T},$$

where (for $\mathbf{H} \parallel \langle 100 \rangle$)

$$\Delta\kappa_{xx} = \kappa_{xx}(\mathbf{H} \parallel \square) - \kappa_{xx}(\mathbf{H} \perp \square),$$

$$\Delta\sigma_{xx} = \sigma_{xx}(\mathbf{H} \parallel \square) - \sigma_{xx}(\mathbf{H} \perp \square).$$

Such a method of analysis is also convenient, since it allows us to get rid of the effect of the quantity κ_{ph}, which is always a part of the κ_{xx}^{m} being measured and is independent of the magnetic field.

The results of such a processing of experimental data prove that, in a limited temperature range (2.5–7 K) in which the values of $\Delta\kappa_{xx}$ and $\Delta\sigma_{xx}$ can be determined with a reasonable accuracy, the value of L_{xx}^{surf} remains unchanged and equal to $(2.7 \pm 0.3) \times 10^{-8}\ \text{V}^2/\text{K}^2$, which is slightly larger than the theoretical value of L_0. However, taking into account the method of determining L_{xx}^{surf}, the result can be regarded as successfully matching the theory [15], which is an additional experimental argument confirming the conclusion about the elastic nature of electron scattering from the surface.

Thus, we have investigated the magnetic-field and temperature dependences of magnetothermo-emf and the Lorentz number for thin tungsten plates under conditions of the static skin effect. It is shown that the behavior of magnetothermo-emf follows the predictions of the theory of galvano- and thermomagnetic phenomena in strong magnetic fields and exhibits anisotropy associated with the sample shape and the reflectivity of the crystal surface.

The temperature dependence of the magnetothermo-emf exhibits the electron–phonon drag effect in the case of the minimum scattering from the boundary.

An analysis of the Wiedemann–Franz relation under the conditions of the static skin effect led to an experimental confirmation of the elastic nature of electron collisions with the crystal surface.

ACKNOWLEDGMENTS

The authors are grateful to A. N. Cherepanov for supplying single crystals for investigation.

This research was partly supported in part by the Russian Foundation for Basic Research (project no. 96-02-17736a).

[1] According to Gantmakher and Levinson [17], scattering from the surface can sometimes also be inelastic: electrons colliding with the surface can exchange energy with surface vibrations and impurity atoms. However, most experiments can be described in terms of elastic scattering.

REFERENCES

1. V. T. Peschanskiĭ and M. Ya. Azbel', Zh. Éksp. Teor. Fiz. **55**, 1980 (1968) [Sov. Phys. JETP **28**, 1045 (1969)].
2. N. N. Volkenshteĭn, M. Glinski, V. V. Marchenkov, *et al.*, Zh. Éksp. Teor. Fiz. **95**, 2103 (1989) [Sov. Phys. JETP **68**, 1216 (1989)].
3. A. B. Batdalov, A. N. Cherepanov, V. E. Startsev, and V. V. Marchenkov, Fiz. Met. Metalloved. **75** (6), 85 (1993).
4. O. A. Panchenko, P. P. Lutsishin, and Yu. G. Ptushinskiĭ, Zh. Éksp. Teor. Fiz. **66**, 2191 (1974) [Sov. Phys. JETP **39**, 1079 (1974)].
5. J. C. Garland and D. J. van Harlinger, Phys. Rev. B **10**, 4825 (1974).
6. F. J. Blatt, P. A. Schroeder, C. L. Foiles, and P. Greig, *Thermoelectric Power of Metals* (Plenum, New York, 1976; Metallurgiya, Moscow, 1980).
7. B. J. Blumenstock and P. A. Schroeder, J. Low Temp. Phys. **38**, 605 (1980).
8. R. Fletcher, J. L. Opsal, and B. J. Thaler, J. Phys. F **7**, 1489 (1980).
9. I. M. Lifshits, M. Ya. Azbel', and M. I. Kaganov, *Electron Theory of Metals* (Nauka, Moscow, 1971; Consultants Bureau, New York, 1973).
10. J. L. Opsal, J. Phys. F **7**, 2349 (1977).
11. R. Carter, A. Davidson, and P. A. Schroeder, J. Phys. Chem. Solids **31**, 2374 (1970).
12. A. B. Batdalov, N. P. Katrich, N. A. Red'ko, *et al.*, Fiz. Tverd. Tela (Leningrad) **19**, 672 (1977) [Sov. Phys. Solid State **19**, 389 (1977)].
13. A. B. Batdalov and N. A. Red'ko, Fiz. Tverd. Tela (Leningrad) **22**, 1141 (1980) [Sov. Phys. Solid State **22**, 664 (1980)].
14. D. K. Wagner, Phys. Rev. B **5**, 336 (1972).
15. A. F. Andreev, Usp. Fiz. Nauk **105** (1), 113 (1971) [Sov. Phys. Usp. **14**, 609 (1972)].
16. E. Wawcett, Phys. Rev. **128**, 154 (1962).
17. V. F. Gantmakher and I. B. Levinson, *Carrier Scattering in Metals and Semiconductors* (Nauka, Moscow, 1984), p. 219.

Translated by N. Wadhwa

Physics of the Solid State, Vol. 42, No. 8, 2000, pp. 1387–1393. Translated from Fizika Tverdogo Tela, Vol. 42, No. 8, 2000, pp. 1350–1356.

METALS AND SUPERCONDUCTORS

Raman and IR Spectra of New Organic Metals $(ET)_8[Hg_4X_{12}(C_6H_5Y)_2]$ (X, Y = Cl, Br)

R. M. Vlasova*, I. I. Reshina*, N. V. Drichko*, and R. N. Lyubovskaya**

** Ioffe Physicotechnical Institute, Russian Academy of Sciences, Politekhnicheskaya ul. 26, St. Petersburg, 194021 Russia*
e-mail: Rema.Vlasova@shuvpop.ioffe.rssi.ru

*** Institute for Problems of Chemical Physics, Russian Academy of Sciences, Chernogolovka, Moscow oblast, 142432 Russia*

Received January 20, 2000

Abstract—The Raman and IR reflectivity spectra of the new organic metals $(ET)_8[Hg_4X_{12}(C_6H_5Y)_2]$ (X, Y = Cl, Br) based on the molecule bis(ethylenedithio)tetrathiafulvalene (BEDT-TTF or ET in abbreviated form) have been investigated. These metals differ from the previously studied compounds, particularly, in the type of ET molecular packing in the quasi-two-dimensional conducting layers. A high reflectivity and a plasma minimum observed in the IR reflectivity spectrum indicate the presence of quasi-free charge carriers (holes), as in other conducting ET salts. However, the A_g vibrational modes in the Raman spectrum are not activated in the IR spectrum, as is the case of conducting ET salts with other packing types. The Raman lines are assigned to the normal vibrations in the ET molecule, and their ionization shifts are determined. It is demonstrated that the frequencies of the most intense line $\nu_3(A_g)$ show a linear dependence on the cation charge, which is characteristic of different ET salts. No correlations are revealed between the $\nu_3(A_g)$ frequencies and the packing type. The strong background with a broad maximum at a Raman shift of about 3000 cm^{-1} is observed in the Raman spectra upon excitation with the 2.54- and 2.41-eV lines of an Ar^+ laser. The assumption is made that such a background can be associated with the scattering by one-particle and collective electronic excitations. © *2000 MAIK "Nauka/Interperiodica".*

1. INTRODUCTION

The discovery of superconductivity in radical ion salts based on the molecule bis(ethylenedithio)tetrathiafulvalene (BEDTTTF or ET in abbreviated form) [1] lent impetus to an extensive investigation into their structural and physical properties with the aim of elucidating the mechanism of superconductivity and stimulated the synthesis of new materials based on this molecule. A large number of similar compounds have been synthesized to date [2]. Among these are superconductors (with the highest superconducting transition temperature observed in organic compounds T_c = 11.6 K for κ-$(ET)_2CuN(CN)_2Br$ [3]) and metals with the transitions to the dielectric state at different temperatures [2, 4]. Opinions regarding the mechanism of superconductivity remain contradictory to the present day. The majority of these compounds are characterized by a strong interaction between quasi-free charge carriers in layers of the ET molecules and the intramolecular totally symmetric vibrations (A_g) of this molecule. Owing to this interaction, the normally Raman-forbidden A_g vibrations are activated in the IR reflectivity spectrum, even though their frequencies substantially differ from those observed in the Raman spectrum [5, 6].

Compounds of the $(ET)_8[Hg_4X_{12}(C_6H_5Y)_2]$ (where X, Y = Cl, Br) type have been synthesized recently [7]. In the reflectivity spectrum of these compounds, only a weak smeared maximum, rather than pronounced intense vibrational bands, was observed in the frequency range of intramolecular vibrations (800–1300 cm^{-1}) [8]. At the same time, a high reflectivity and a plasma minimum in the IR reflectivity spectrum for at least one polarization direction indicated the presence of quasi-free charge carriers (holes), as in other conducting ET salts. Kaplunov and Lyubovskaya [8] related the absence of vibronic bands in the IR reflectivity spectrum to the structural features of these compounds. In the majority of the ET-based conducting salts, the molecules in quasi-two-dimensional conducting layers are packed face-to-face to form mutually perpendicular dimers (κ phase) or parallel stacks (β phase). By contrast, in the new family of compounds, the ET molecules located in conducting layers form "ribbons" in which they are linked by the short S–S contacts in a side-by-side fashion [9]. The authors of [8] assumed that, for a ribbon configuration, the vibronic interactions can occur only with nontotally symmetric, optically active vibrational modes and demonstrated using the model calculations that the intense vibrational bands in the IR spectrum are absent in this case.

It was of interest to investigate the Raman spectra of these compounds, which were not measured earlier, in order to reveal both the possible effect of the unusual type of molecular packing on the spectral behavior and the influence of the anion on the Raman frequencies. As is known, the frequencies of the most intense Raman

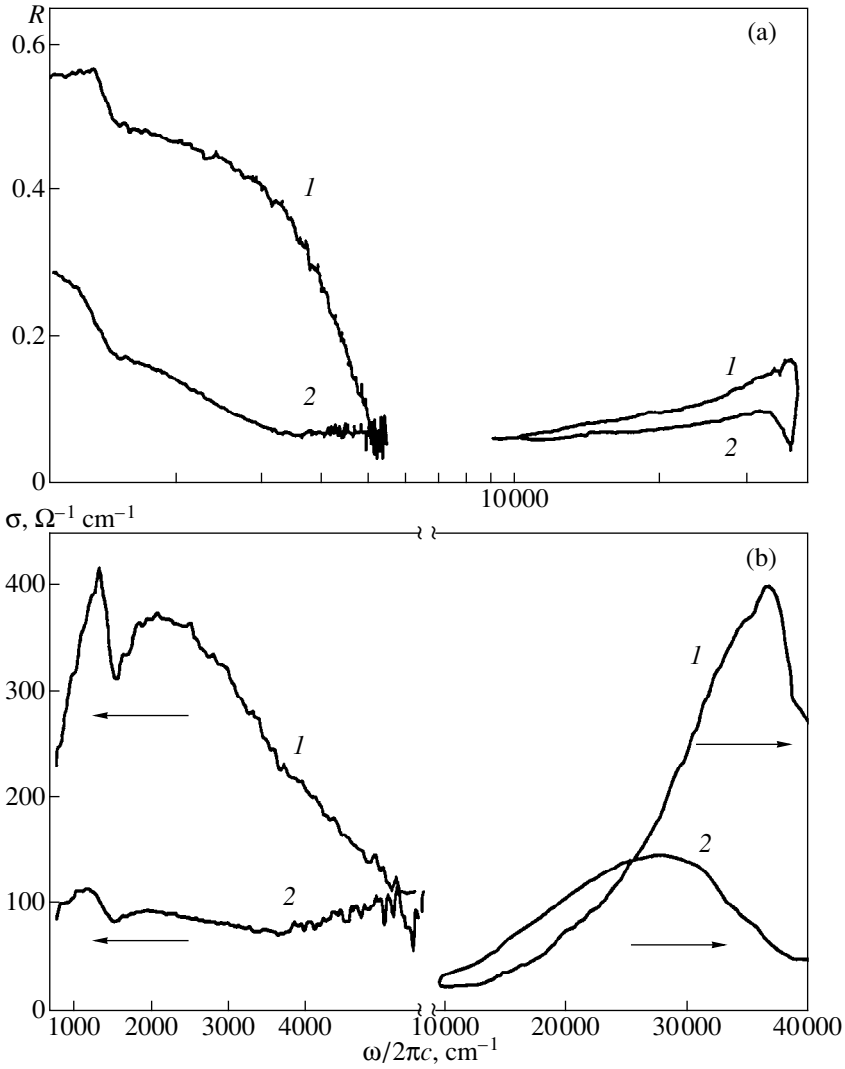

Fig. 1. (a) Polarized reflectivity spectra $R(\omega)$ and (b) optical conductivity spectra $\sigma(\omega)$ of the $(ET)_8[Hg_4Br_{12}(C_6H_5Br)_2]$ (no. 9) organic metal for the (100) face at (*1*) **E** || **x** and (*2*) **E** || **y** polarizations. T = 293 K.

lines ν_2 and ν_3 (for the D_{2h} symmetry of the ET molecule), which correspond to the stretching A_g vibrations of the central and ring C=C bonds, exhibit an approximately linear dependence on the cation charge [10]. The mean cation charge is governed by the stoichiometric ratio between the ET and anion. An increase in the positive cation charge leads to a decrease in the electron population of the highest-occupied molecular orbital, which results in a weakening of the C=C bonds and, hence, in a decrease in the vibrational frequencies. However, considerable (as large as 20 cm^{-1}) deviations from the mean linear dependence are observed for a number of different compounds. These deviations can be caused by the intermolecular interactions (dependent on the ET molecular packing in the crystal) and the influence of anions. It could be assumed that the frequency of the most intense line ν_3 in the spectra of the studied salts with a ribbon molecular packing would deviate from the mean linear dependence.

Moreover, it was also instructive to measure the Raman spectra and IR reflectivity spectra of the samples obtained in the same cycle of synthesis.

2. SAMPLES AND EXPERIMENTAL TECHNIQUE

The Raman spectra were taken for the following samples: (i) the $(ET)_8[Hg_4Cl_{12}(C_6H_5Cl)_2]$ (no. 8), $(ET)_8[Hg_4Br_{12}(C_6H_5Cl)_2]$ (no. 7), and $(ET)_8[Hg_4Br_{12}(C_6H_5Br)_2]$ (no. 9) salts, which are the organic metals with transitions to the dielectric state at 1.5, 90, and 130 K, respectively [11]; (ii) the $(ET)_2[Hg(SCN)Cl_2]$ (no. 2) metal and the $(ET)_4Hg_{2.89}Br_8$ (no. 1) superconductor (T_c = 4.2 K) with an ET molecular packing of the type κ phase in

both compounds; and (iii) the crystal formed by the neutral molecules BEDT-TTF (ET^0).

The polarized reflectivity spectra were measured for the $(ET)_8[Hg_4Br_{12}(C_6H_5Br)_2]$ (no. 9) crystal in a wider spectral range as compared to the range covered in [8]. The reflectivity spectra of the $(ET)_4Hg_{2.89}Br_8$ (no. 1) and $(ET)_2[Hg(SCN)Cl_2]$ (no. 2) crystals were described in our earlier works [12] and [13], respectively.

The Raman spectra were recorded on a spectrometer with a Jobin Ivon U-1000 double monochromator in a backscattering or a 90° geometry. In the latter case, the sample was placed at the focus of a short-distance objective lens collecting the scattering light at a large solid angle, which provided a fivefold increase in the sensitivity as compared to the backscattering configuration. Usually, the experiments were carried out in a 90° geometry, because the intensity of the Raman scattering by all the ET salts was very low. Excitation was achieved with the 488-nm (2.54-eV) line of an Ar^+ laser in resonance with the absorption band in this range. The laser radiation power at the sample was no more than 6 mW; moreover, a laser spot was slightly defocused in order to prevent sample damage. The exciting beam was polarized in the incidence plane (*H* polarization). Both polarizations (*H* and *V*) were usually observed in the scattering light. The spectra were recorded at room temperature with a step of 1 cm^{-1}. The measurement time at each point was 10 s. As a rule, several replicate measurements were made for a 200-cm^{-1} portion of the spectrum, followed by their averaging and joining. The spectrum of the crystal formed by neutral ET^0 molecules was obtained in the backscattering geometry upon excitation with a He–Ne laser (632.8 nm).

The polarized reflectivity spectra $R(\omega)$ of the $(ET)_8[Hg_4Br_{12}(C_6H_5Br)_2]$ crystal (no. 9) in the range 700–5500 cm^{-1} were measured at room temperature on a Bruker-IFS-88 IR Fourier spectrometer equipped with an IR microscope (light beam diameter, 75 μm; KRS-5 polarizer). In the range 9000–40000 cm^{-1}, the spectra were taken on a microspectroreflectometer devised at the State Optical Institute (beam diameter, 25 μm; Glan–Thompson prism as a polarizer). The measurements were performed at an almost normal light incidence to the naturally grown (100) crystal face (parallel to the conducting layers of the ET molecules) for two mutually perpendicular polarization directions for which the maximum (**E** || **x**) and minimum (**E** || **y**) reflectivities were observed in the range 700–5500 cm^{-1}. (**E** is the electric vector of a light wave, and **x** and **y** are the principal crystal optic axes found in such a way.) The most perfect surface region was chosen for the measurements. The absolute reflectivities were determined with respect to an aluminum mirror and references samples (silicon carbide and quartz). The optical conductivity spectra $\sigma(\omega)$ were obtained from the reflectivity spectra by the Kramers–Kronig method using the procedures described in [12] for the extrapolations to the low-frequency and high-frequency ranges.

3. RESULTS AND DISCUSSION

The reflectivity spectra $R(\omega)$ and the optical conductivity spectra $\sigma(\omega)$ of the $(ET)_8[Hg_4Br_{12}(C_6H_5Br)_2]$ crystal for the above two polarization directions **E** || **x** and **E** || **y** are displayed in Fig. 1a and 1b, respectively. According to [8], **x** and **y** are close to the crystallographic directions $[02\bar{1}]$ and [011]. As can be seen from Fig. 1a, the $R(\omega)$ spectrum in the IR range at the polarization **E** || **x** shows a high reflectivity (0.4–0.5) with a smeared vibrational structure in the range 1000–1500 cm^{-1}, a sharp plasma edge at 3500–5000 cm^{-1}, and the related plasma minimum at about 5200 cm^{-1} due to a system of quasi-free charge carriers (holes) in the ET conducting layers. Reasoning from the data obtained in [9], it can be concluded that the **x** direction slightly deviates from the direction of the ribbons formed by the ET molecules in the crystal (the angle between these directions is equal to approximately 13°). The electronic effects mentioned above are substantially less pronounced in the reflectivity spectrum at the **E** || **y** polarization. In the $\sigma(\omega)$ spectrum at **E** || **x** (Fig. 1b), a broad electron band with a maximum (σ_m = 350 Ω^{-1} cm^{-1}) near 2000 cm^{-1} and a broad vibrational structure in the range 1000–1500 cm^{-1} is observed over the entire IR range. Our spectra and their anisotropy virtually coincide with those obtained in [8] in the overlapping spectral range (700–5500 cm^{-1}). A small difference resides at somewhat larger values of *R* and σ for both polarizations in the IR range and a sharper vibrational feature at 1000–1500 cm^{-1} (**E** || **x**) in our spectra. In the high-frequency range (above the plasma minimum), a broad band (20000–40000 cm^{-1}) with a maximum at about 34 000 cm^{-1} for the **E** || **x** polarization and 27000 cm^{-1} for the **E** || **y** polarization is observed against the low "Drude" background. The band is associated with the intramolecular electron transition (polarized along the long molecular axis) in the ET molecule [13].

The Raman spectrum of the ET^0 crystal is depicted in Fig. 2. The frequencies of the lines in this spectrum (Table 1) coincide to within 1 cm^{-1} with the data obtained by Eldridge *et al.* [5]. The Raman spectra of samples nos. 7, 9, and 2 were measured in the range 200–1600 cm^{-1}. Figure 3 displays the spectrum of sample no. 7. Raman lines for ET^0 and the no. 7, 9, and 2 samples, as well as their assignment to the normal vibrations of the ET^0 molecule, are presented in Table 1. The assignment of Raman lines was performed on the basis of their intensities and the assignment of the Raman lines for the κ-$(ET)_2Cu[N(CN)_2]Br$ superconductor studied in [5]. The ionization shifts of the lines (i.e., the shifts with respect to the lines of ET^0) are also listed in Table 1. Since the lines at 1051 and 1056 cm^{-1} (observed in the spectra of samples nos. 7 and 2, respectively) are not revealed in the spectrum of ET^0, we assign them to the vibrations of the

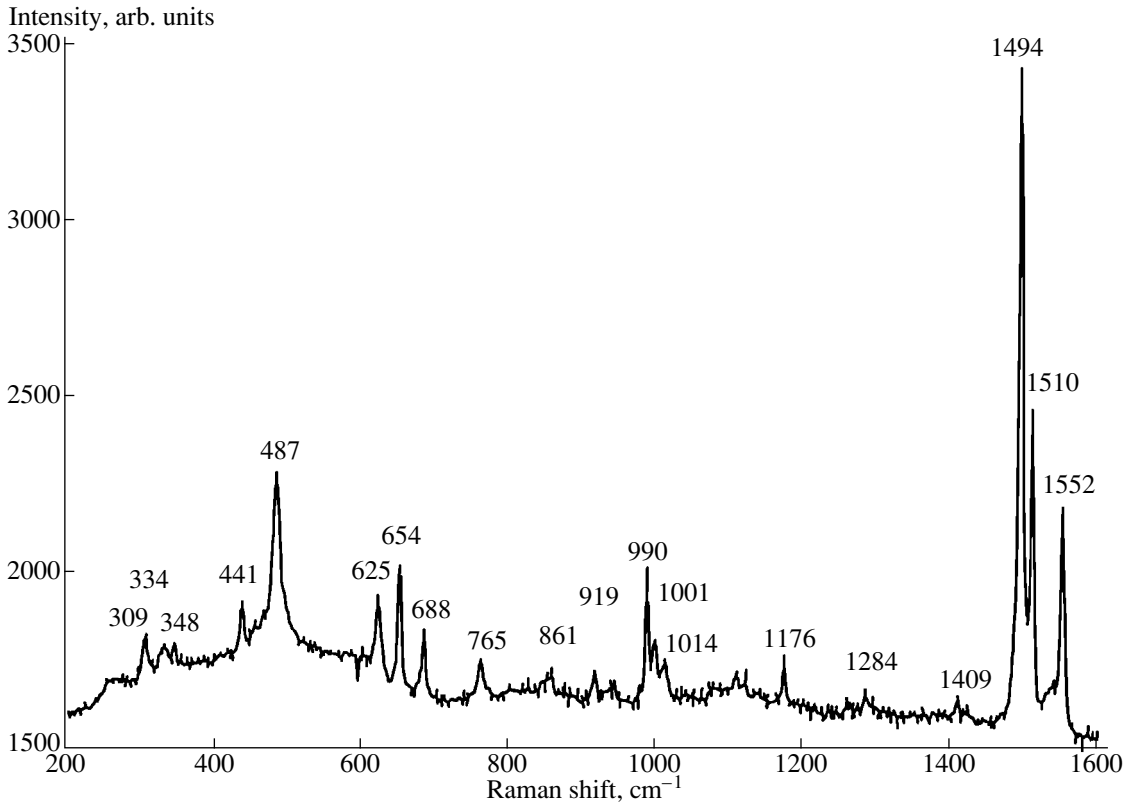

Fig. 2. Raman spectrum of the ET^0 crystal. E_{exc} = 1.96 eV, T = 293 K.

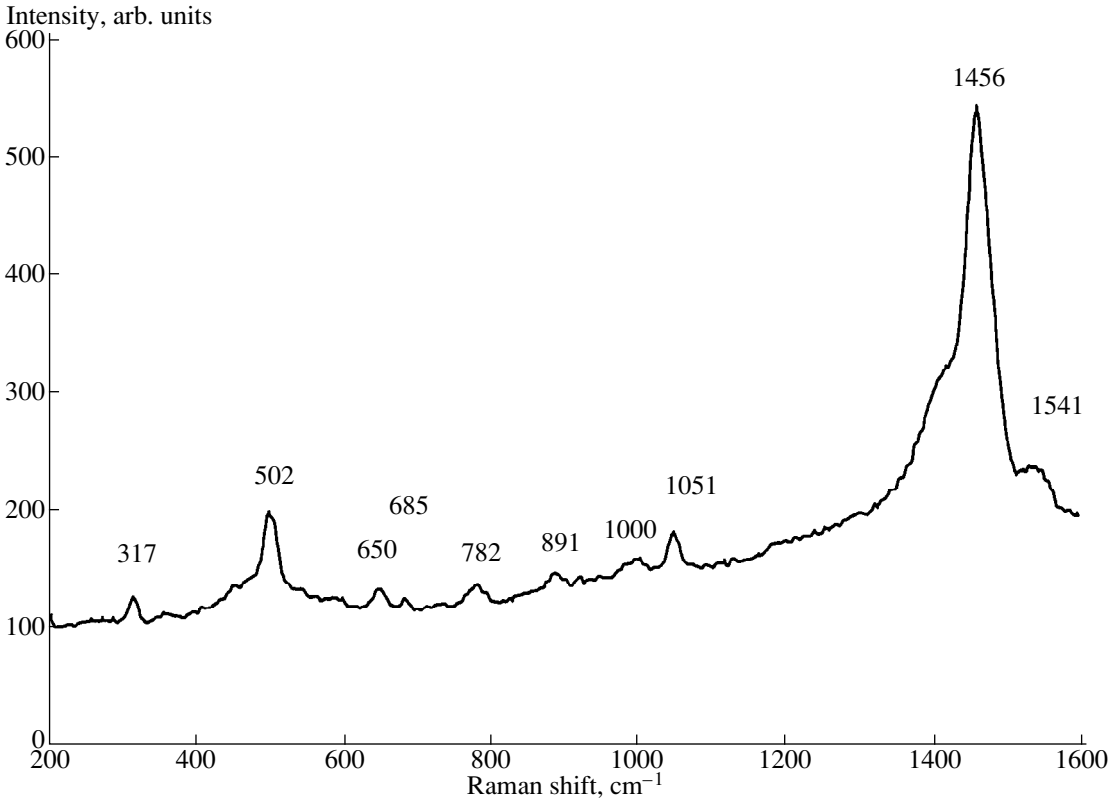

Fig. 3. Raman spectrum of the $(ET)_8[Hg_4Br_{12}(C_6H_5Cl)_2]$ (no. 7) organic metal in the frequency range 200–1600 cm^{-1}. E_{exc} = 2.54 eV, T = 293 K.

Table 1. Raman lines for the ET_0, $(ET)_8[Hg_4Br_{12}(C_6H_5Cl)_2]$ (no. 7), $(ET)_8[Hg_4Br_{12}(C_6H_5Br)_2]$ (no. 9), and $(ET)_2[Hg(SCN)Cl_2]$ (no. 2) compounds and their assignment

$\nu_i(ET^0)$, cm^{-1}	Normal vibration	ν_i(no. 7), cm^{-1}	ν_i(no. 9), cm^{-1}	ν_i(no. 2), cm^{-1}	Ionization shift, cm^{-1}		
					no. 7	no. 9	no. 2
1552	$\nu_2(A_g)$	1541		1547	–11		–5
1510	$\nu_{27}(B_{1u})$						
1494	$\nu_3(A_g)$	1456	1474	1455	–38	–20	–39
1442[a]	$\nu_{56}(B_{3g})$						
1409	$\nu_4(A_g)$	1396 Shoulder					
1284	$\nu_5(A_g)$						
1257[a]	$\nu_{57}(B_{3g})$						
1176	$\nu_{38}(B_{2g})$						
1123	$\nu_{21}(B_{1g})$						
		1051		1056			
1014	$\nu_{58}(B_{3g})$						
1000	$\nu_{59}(B_{3g})$						
990	$\nu_6(A_g)$	1000	999		0	–1	
919	$\nu_7(A_g)$						
889[a]	$\nu_{60}(B_{3g})$	891	891	892	+2	+2	+3
861	$\nu_{22}(B_{1g})$						
765	O.o.p.[b]	782		783	+17		+18
688	$\nu_{61}(B_{3g})$	685	673		–3	–15	
654	$\nu_8(A_g)$	650	647		–4	–7	
626	$\nu_{62}(B_{3g})$						
487	$\nu_9(A_g)$	502	500	499	+15	+13	+12
441	$\nu_{10}(A_g)$			445			+4
349	$\nu_{63}(B_{3g})$						
334	$\nu_{64}(B_{3g})$						
310	$\nu_{11}(A_g)$	317	314		+7	+4	

[a] Data taken from [5].
[b] Out-of-plane vibrations.

Table 2. Cation charges ρ and Raman frequencies $\nu_3(A_g)$ in different radical ion salts of the ET molecule

ρ	Compound[a]	$\nu_3(A_g)$, cm^{-1}	Compound[b]	$\nu_3(A_g)$, cm^{-1}
0	ET^0	1494	ET^0	1494
1			ETI_3	1431
0.5	$(ET)_8[Hg_4Br_{12}(C_6H_5Cl)_2]$	1456	κ-$(ET)_2Cu[N(CN)_2]Br$	1464
0.5	$(ET)_8[Hg_4Cl_{12}(C_6H_5Cl)_2]$	1472	κ-$(ET)_2Cu[N(CN)_2]Br$	1459
0.5	$(ET)_8[Hg_4Br_{12}(C_6H_5Br)_2]$	1474	κ-$(ET)_2Cu(NCS)_2$	1461
0.5	$(ET)_2Hg(SCN)Cl_2$	1455	κ-$(ET)_2Cu(CN)_3$	1471
0.5	$(ET)_4Hg_{2.89}Br_8$	1462	κ-$(ET)_4Hg_3Cl_8$	1464

[a] Data obtained in this work.
[b] Data taken from [10, 14].

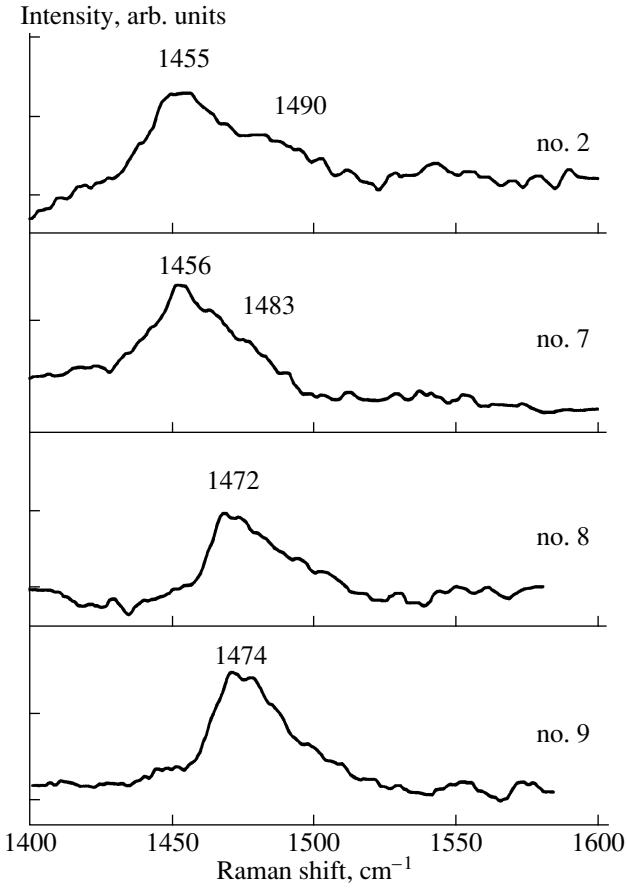

Fig. 4. Raman spectra of the κ-$(ET)_2[Hg(SCN)Cl_2]$ (no. 2), $(ET)_8[Hg_4Br_{12}(C_6H_5Cl)_2]$ (no. 7) $(ET)_8[Hg_4Cl_{12}(C_6H_5Cl)_2]$ (no. 8), and $(ET)_8[Hg_4Br_{12}(C_6H_5Br)_2]$ (no. 9) crystals in the frequency range 1400–1600 cm^{-1}. E_{exc} = 2.54 eV, T = 293 K.

$[Hg_4Br_{12}(C_6H_5Cl)_2]^{-4}$ and $[Hg(SCN)Cl_2]^{-1}$ anions, respectively. The spectra of the $(ET)_4Hg_{2.89}Br_8$ (no. 1) and $(ET)_8[Hg_4Cl_{12}(C_6H_5Cl)_2]$ (no. 8) metals were measured in the range 1400–1600 cm^{-1}, which involves the most intense lines attributed to the stretching vibrations of the central and ring C=C bonds, i.e., $\nu_2(A_g)$ and $\nu_3(A_g)$. The $\nu_3(A_g)$ frequencies for all the samples studied in this work and the available data [10, 14] for a number of other conducting ET salts are summarized in Table 2. The Raman spectra of samples nos. 2, 7, 8, and 9 in the range 1400–1600 cm^{-1} are compared in Fig. 4. The dependence of the $\nu_3(A_g)$ frequency on the cation charge ρ is shown in Fig. 5. The data taken from [10, 14] for other compounds are also displayed in this figure. In the studied compounds with a ribbon packing, the cation charge is formally equal to +0.5. As mentioned above, the data presented in Fig. 5 refer to the samples with considerably different packings of the ET molecules in the layer: these are the compounds with the κ phase, in which the ET molecules are arranged face-to-face to form mutually perpendicular dimers, and the crystals with a ribbon molecular packing. It can be seen that, at a cation charge of +0.5, the frequencies for all the samples differ by no more than 20 cm^{-1} and do not depend on the packing type. It is worth noting that the largest differences in the $\nu_3(A_g)$ frequencies are observed for the $(ET)_8[Hg_4Br_{12}(C_6H_5Cl)_2]$ (1456 cm^{-1}), $(ET)_8[Hg_4Cl_{12}(C_6H_5Cl)_2]$ (1472 cm^{-1}), and $(ET)_8[Hg_4Br_{12}(C_6H_5Br)_2]$ (1474 cm^{-1}) crystals, which have the same type of ET molecular packing but somewhat differ in the chemical formula of the anion. This suggests that the anion can appreciably affect the $\nu_3(A_g)$ frequency.

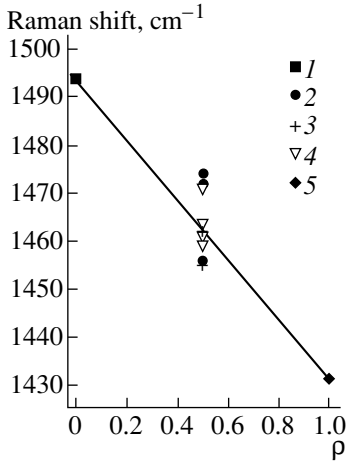

Fig. 5. Dependence of the $\nu_3(A_g)$ frequency on the cation charge ρ: (*1*) ET^0; (*2*) samples nos. 7, 8, and 9; (*3*) samples nos. 1 and 2; (*4*) samples studied in [10]; and (*5*) samples studied in [14].

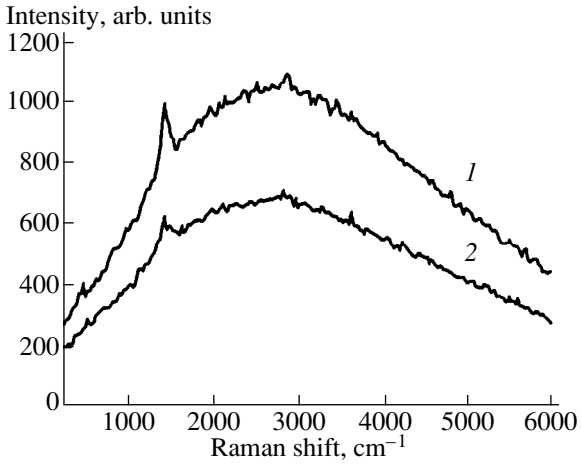

Fig. 6. Raman spectrum of sample no. 7 in the range 1000–5500 cm^{-1} for (*1*) *HH* and (*2*) *HV* polarizations. E_{exc} = 2.54 eV, T = 293 K.

As noted above, the $(ET)_8[Hg_4Br_{12}(C_6H_5Br)_2]$ crystal (no. 9) undergoes a transition to the dielectric state at 130 K [9]. The Raman spectrum of this crystal in the range 1400–1600 cm^{-1} was also taken at $T \approx 100$ K. However, no substantial changes in the $\nu_3(A_g)$ vibrations were observed in the spectra above and below the phase transition point.

It can be seen from Fig. 3 that the Raman spectrum is characterized by a structureless background comparable in intensity to the strongest phonon line. This background is observed for all the samples studied. It is established that this background is not caused by the Rayleigh scattering. The recording of the spectra in a wider frequency range revealed an increase in the background intensity with an increase in the Raman shift and also a very broad partly depolarized maximum at about 2500 cm^{-1} (upon excitation with the 488-nm line). The intensity of the maximum found in the *HH* polarization is higher than that for the *HV* polarization (Fig. 6). After the correction for spectral efficiency of the spectrometer, the maximum is retained and shifts to 3000 cm^{-1}. The maximum and the background for sample no. 9 are also observed at $T \sim 100$ K.

The shape of the maximum somewhat differs upon excitation with 488- and 541.5-nm lines. No maximum is observed upon excitation with the 632.3-nm line. In this case, an increase in the Raman shift up to 3000 cm^{-1} leads to a slight decrease in the intensity of the spectrum. With a further increase in the Raman shift (i.e., at larger wavelengths), the intensity increases drastically, which is likely explained by the luminescence. (Note that the maximum of luminescence for the ET^0 neutral molecule is located at 15492 cm^{-1}. A considerably weaker luminescence band in the same range is observed for sample no. 9 at a temperature of ~100 K upon excitation with the 488-nm line.)

The nature of the background and the broad maximum in the range of 3000 cm^{-1} remains unclear. Presumably, they can be associated with the resonance Raman scattering by one-particle and collective electronic excitations. In this respect, we note that Kostur and Éliashberg [15] theoretically treated the quasi-particle Raman spectrum in the high-temperature superconductors at $T > T_c$. It was demonstrated that this spectrum contains a broad maximum at about 2000 cm^{-1}, and its intensity and location depend on the phonon spectrum and the electron–phonon interaction. It should be also mentioned that the maximum in the range of 2000 cm^{-1} was observed in the conductivity spectrum (obtained from the reflectivity spectra by the Kramers–Kronig method) of the compounds studied.

Alternatively, the background and the broad maximum can be explained by the scattering in the surface layer degraded in air.

ACKNOWLEDGMENTS

This work was supported by the Russian Foundation for Basic Research, project nos. 98-02-18303 and 97-03-33686a.

REFERENCES

1. É. B. Yagubskiĭ, I. F. Shcheglov, V. N. Laukhin, *et al.*, Pis'ma Zh. Éksp. Teor. Fiz. **39**, 12 (1984) [JETP Lett. **39**, 12 (1984)].
2. J. M. Williams, J. R. Ferraro, R. J. Thorn, K. D. Carlson, U. Geiser, H. H. Wang, A. M. Kini, and M.-H. Whangbo, *Organic Superconductors (Including Fullerenes): Synthesis, Structure, Properties, and Theory* (Prentice Hall, Englewood Cliffs, NJ, 1992).
3. A. M. Kini, U. Geiser, H. H. Wang, *et al.*, Inorg. Chem. **29**, 2555 (1990).
4. M. Z. Aldoshina, R. N. Lyubovskaya, S. V. Konovalikhin, *et al.*, Synth. Met. **55–57**, 1905 (1993).
5. J. E. Eldridge, Y. Xie, H. H. Wang, *et al.*, Spectrochim. Acta, Part A **52**, 45 (1996).
6. O. O. Drozdova, V. N. Semkin, R. M. Vlasova, *et al.*, Synth. Met. **64**, 17 (1994).
7. R. N. Lyubovskaya, T. V. Afanas'eva, O. A. D'yachenko, *et al.*, Izv. Akad. Nauk SSSR, Ser. Khim. **12**, 2872 (1990).
8. M. G. Kaplunov and R. N. Lyubovskaya, J. Phys. I **2**, 1811 (1992).
9. V. V. Gritsenko, O. A. D'yachenko, G. V. Shilov, *et al.*, Izv. Akad. Nauk, Ser. Khim. **4**, 894 (1992).
10. H. H. Wang, J. R. Ferraro, J. M. Williams, *et al.*, J. Chem. Soc., Chem. Commun. 1893 (1994).
11. R. B. Lyubovskii, R. N. Lyubovskaya, and O. A. Dyachenko, J. Phys. I **6**, 1609 (1996).
12. R. M. Vlasova, S. Ya. Priev, V. N. Semkin, *et al.*, Synth. Met. **48**, 129 (1992).
13. R. M. Vlasova, O. O. Drozdova, R. N. Lyubovskaya, and V. N. Semkin, Fiz. Tverd. Tela (S.-Peterburg) **37**, 703 (1995) [Phys. Solid State **37**, 382 (1995)].
14. K. D. Truong, D. Achkir, S. Jandl, and M. Poirier, Phys. Rev. B **51**, 16168 (1995).
15. V. N. Kostur and G. M. Éliashberg, Pis'ma Zh. Éksp. Teor. Fiz. **53**, 373 (1991) [JETP Lett. **53**, 391 (1991)].

Translated by O. Borovik-Romanova

Physics of the Solid State, Vol. 42, No. 8, 2000, pp. 1394–1397. Translated from Fizika Tverdogo Tela, Vol. 42, No. 8, 2000, pp. 1357–1360.

METALS AND SUPERCONDUCTORS

Heat Conductivity of $LuInCu_4$

A. V. Golubkov*, L. S. Parfen'eva*, I. A. Smirnov*, H. Misiorek, J. Mucha**, and A. Jezowski****

**Ioffe Physicotechnical Institute, Russian Academy of Sciences, Politekhnicheskaya ul. 26, St. Petersburg, 194021 Russia*
e-mail: Igor.Smirnov@shuv.pop.ioffe.rssi.ru
***Institute of Low-Temperature and Structural Studies, Polish Academy of Sciences, Wroclaw, 53-529 Poland*
Received February 1, 2000

Abstract—Electrical resistivity and heat conductivity of the $LuInCu_4$ semimetal have been studied in the 4.2–300-K range. For $T \gtrsim 100$ K, the bipolar heat-conductivity component (κ_{bip}) was found to contribute. Data on κ_{bip} have been used to estimate the electron and hole subband-overlap energy (ε_0) as ~0.1 eV. © *2000 MAIK "Nauka/Interperiodica".*

Interest in $LnTCu_4$-type intermetallic compounds (with Ln standing for rare earth, and T, for transition metals), which crystallize in a $AuBe_5$-type fcc cubic lattice [$C15B$ structure, space group $F\bar{4}3m(T_d^2)$] has recently been demonstrated by experimenters and theoreticians in leading laboratories all over the world.

These materials exhibit unusual and interesting magnetic properties, but one representative of this family, $YbInCu_4$, has attracted particular attention because, at $T_v \sim 40$–80 K and atmospheric pressure, it undergoes a first-order isostructural phase transition in which, being a Curie–Weiss paramagnet (a state with localized magnetic moments) at $T > T_v$, it transforms into a Pauli paramagnet (nonmagnetic Fermi-liquid state), a compound with mixed valence of the rare earth ion (the so-called light heavy-fermion system) at $T < T_v$ [1, 2].[1]

When analyzing experimental data on $YbInCu_4$ (heat capacity, magnetic susceptibility, NMR, linear expansion coefficient, electrical conductivity), most studies used $LuInCu_4$ as a reference material, since it does not undergo the above phase transition and is nonmagnetic, while having the same lattice structure and lattice parameters close to those of $YbInCu_4$ [3–10]. Yb and Lu are neighbors in the Periodic Table.

Information literature in the on the heat conductivity of $LuInCu_4$ is lacking. However, it is necessary, and for many purposes. It could be used as a reference when analyzing heat conductivity data for $YbInCu_4$ [2]. It is also needed both for thermodynamic calculations and in estimating the thermal regimes of single-crystal growth. $LuInCu_4$ is a semimetal [11–13]. Data on the bipolar component of heat conductivity κ_{bip} could be used to estimate the electron and hole subband-overlap energy for this material.

[1] Papers [1, 2] summarize references to most of the experimental and theoretical studies on $YbInCuO_4$.

Measurements have been carried out of the heat conductivity κ_{tot} and electrical resistivity ρ of a cast polycrystalline sample of $LuInCu_4$ within the temperature range of 4.2 to 300 K.

The sample was prepared by the technique described elsewhere [14, 15]. The components used in the synthesis of $LuInCu_4$ were O-grade Lu, SVCh-grade In of 99.99% purity, and 99.998%-pure Cu. The components taken in the stoichiometric ratio were melted in a thin-walled tantalum container pumped to 10^{-4} mm Hg. The container diameter was 11 mm, and its wall was 0.1 mm thick. The samples were melted in an rf furnace. The substances loaded in the container were heated to 1150°C. After maintaining the container at 1150°C for 30 min, the temperature was reduced to 800°C by dipping the crucible into a cold zone. The ingot thus obtained was annealed for 75 h at 800°C.

The $LuInCu_4$ sample under study underwent x-ray characterization on a DRON-2 setup (CuK_α radiation). The lattice constant a was found to be 7.149(4) Å. Literature quotes $a = 7.193$ Å for $LuInCu_4$ [11].

The total heat conductivity κ_{tot} and ρ were measured on a setup similar to that described in [16].

Figure 1 presents our and literature [5, 9, 11, 17] data on $\rho(T)$ of $LuInCu_4$ samples. ρ depends linearly on temperature, which is characteristic of metals and semimetals. The $LuInCu_4$ sample studied here has a fairly high residual resistivity.

Figure 2 compares the data on $\rho(T)$ of $YbInCu_4$ taken from [2] with those for the $LuInCu_4$ sample under study here. As seen from the figure, $\rho(T)$ curves obtained on $YbInCu_4$ (for temperatures $T > T_v$) and $LuInCu_4$ (for $T > 100$ K) are similar in magnitude and follow the same temperature behavior.

Figure 3 displays data for κ_{tot} of $LuInCu_4$. No hysteresis was found in the $\kappa_{tot}(T)$ relation.

1063-7834/00/4208-1394$20.00 © 2000 MAIK "Nauka/Interperiodica"

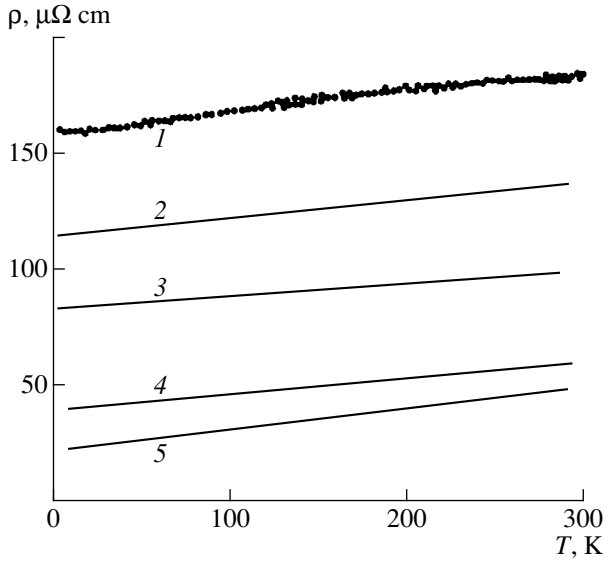

Fig. 1. Dependence of ρ on T: (*1*) this experiment, (*2*) data from [5], (*3*) [9], (*4*) [11], and (*5*) [17].

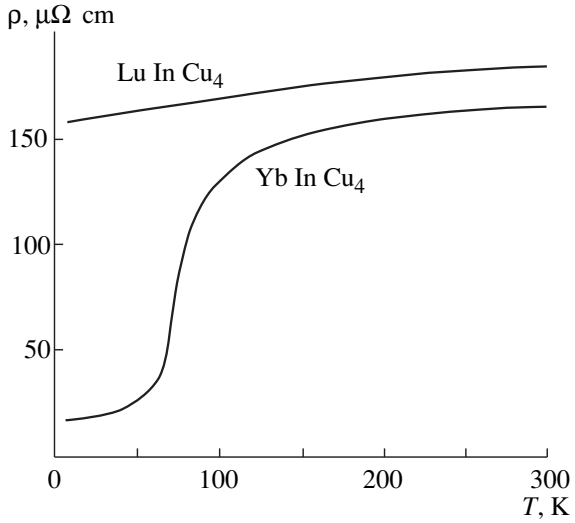

Fig. 2. A comparison of ρ(T) between the $LuInCu_4$ sample under study here and $YbInCu_4$ from [2].

By [11], the concentration of carriers (of both signs) in semimetallic $LuInCu_4$ is ~10^{20} cm^{-3} (which is supported by data of [4]), the Hall constant is positive, and the effective mass ratio of electrons (m_e) and holes (m_h) is ~2.

κ_{tot} of a semimetal obeys the relation

$$\kappa_{tot} = \kappa_{ph} + \kappa_e + \kappa_{bip}, \quad (1)$$

where κ_{ph}, κ_e, and κ_{bip} are the lattice, electronic, and bipolar heat conductivity components, respectively.

By the classical theory of heat conductivity of metals, semimetals, and strongly degenerate semiconductors [18–20], κ_e obeys the Wiedemann–Franz law

$$\kappa_e = L_0 T/\rho, \quad (2)$$

where L_0 is the Sommerfeld value of the Lorentz number ($L_0 = 2.45 \times 10^{-8}$ WΩ/K^2).

Figure 4a presents data for κ_{ph} derived from

$$\kappa_{ph} = \kappa_{tot} - \kappa_e \quad (3)$$

with due account of (2) and of the results on ρ(T) and $\kappa_{tot}(T)$ from Figs. 2 and 3, respectively. These calculations did not include the contribution of κ_{bip} to κ_{tot}.

As seen from Fig. 4a, at low temperatures $\kappa_{ph} \sim T^{1.6}$, while in the 50–100-K interval, $\kappa_{ph} \sim T^{-0.6}$. The latter temperature dependence of κ_{ph} is characteristic of moderately defective materials. For defect-free (or weakly defective) materials, theory [18–20] predicts a linear decrease in κ_{ph} with increasing temperature ($\kappa_{ph} \sim T^{-1}$). We believe that the "defectiveness" of our sample is not connected with impurities in the starting materials used in the preparation of $LuInCu_4$, but could rather be due to the substitution of indium for Lu or Cu for In, as this was observed in $YbInCu_4$ [2], where the experimentally observed "amorphous" behavior of $\kappa_{ph}(T)$ for $T > T_v$ was assigned to the substitution of either In for Yb [21], or Cu for In [22].

At $T > 100$ K, the $\kappa_{ph} \sim T^{-0.6}$ relation gives way to a fairly strong increase in κ_{ph} with temperature in $LuInCu_4$. It can be due to the onset of the bipolar heat-conductivity component, which can be expected in semimetals [see relation (1)].

The κ_{bip} component for a semimetal can be estimated from the expressions given in [20].

Assuming that the electrons and holes are scattered independently of one another and their behavior can be

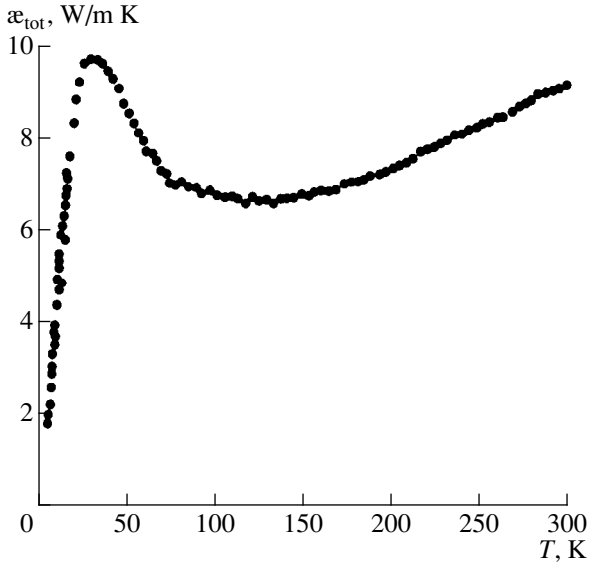

Fig. 3. Temperature dependence of κ_{tot} of the $LuInCu_4$ sample under study.

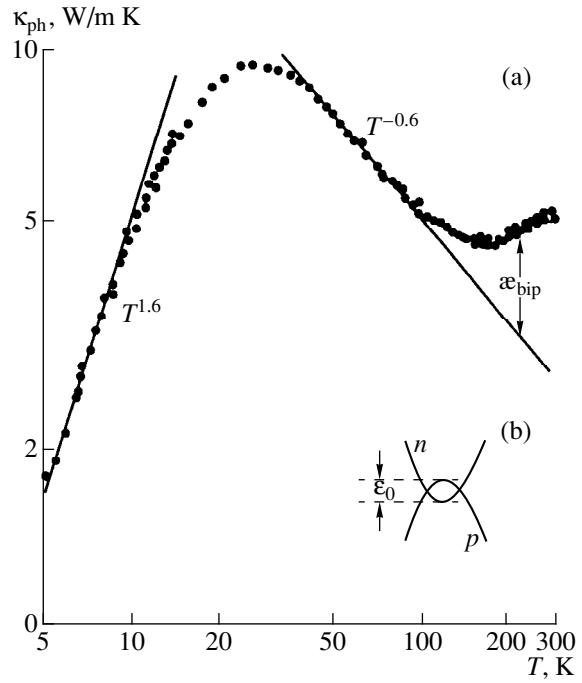

Fig. 4. (a) κ_{ph} of the $LuInCu_4$ sample and (b) band diagram of a semimetal (schematic).

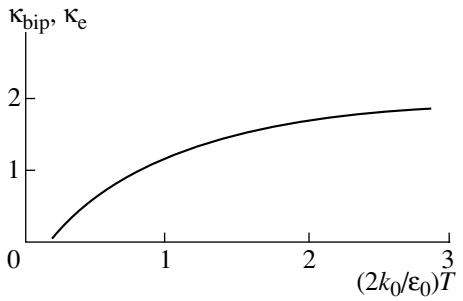

Fig. 5. Temperature dependence of κ_{bip}/κ_e for $r = -0.5$.

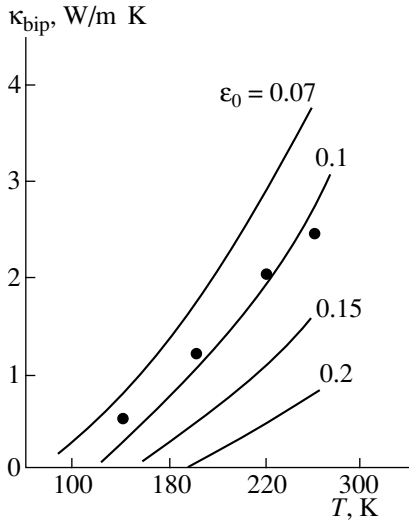

Fig. 6. Dependence of κ_{bip} on T for different values of ε_0: solid curves are the calculation and points are the present experiment.

described by a relaxation time $\tau \sim \varepsilon^r$, as well as the fact that the bands under consideration are parabolic, κ_{bip} can be cast in the form

$$\kappa_{bip} = T\left(\frac{k_0}{e}\right)^2\left\{\frac{A_n}{\rho_n} + \frac{A_p}{\rho_p} + \frac{1}{\rho_n + \rho_p}\left[\delta_n + \delta_p - \frac{\varepsilon_0}{k_0 T}\right]^2\right\}, \quad (4)$$

where k_0 is the Boltzmann constant; ρ_n and ρ_p are the electrical resistivities due to the electrons and holes, respectively; ε_0 is the band overlap energy (Fig. 4b)

$$\delta_{n,p} = \frac{[(r+5/2)F_{r+3/2}(\mu^*_{n,p})]}{[(r+3/2)F_{r+1/2}(\mu^*_{n,p})]}, \quad (5)$$

$$A_{n,p} = \left[\frac{(r+7/2)F_{r+5/2}(\mu^*_{n,p})}{(r+3/2)F_{r+1/2}(\mu^*_{n,p})} - \frac{(r+5/2)^2F^2_{r+3/2}(\mu^*_{n,p})}{(r+3/2)^2F^2_{r+1/2}(\mu^*_{n,p})}\right], \quad (6)$$

$F_r(\mu^*)$ are the Fermi integrals; $\mu^*_n = E_F/k_0T$, $\mu^*_p = (\varepsilon_0 - E_F)/k_0T$; and E_F is the Fermi energy.

Because accurate determination of all parameters entering (4)–(6) is impossible, a precise calculation of κ_{bip} for $LuInCu_4$ appears to be a complicated problem. Let us try to estimate κ_{bip} by assuming that $\rho_p = \rho_n$; the effective electron and hole masses are equal (which, as pointed out above, is wrong, because, by [11], $\mu^*_n/\mu^*_p \sim 2$ for $LuInCu_4$), so that the Fermi level $E_F = \varepsilon_0/2$, $\mu^*_p = \mu^*_n$, $\delta_p = \delta_n = \delta$, and $A_p = A_n = A$. Then, by [20],

$$\kappa_{bip}/\kappa_e = \frac{(\delta - \varepsilon_0/2k_0T)^2}{A}. \quad (7)$$

For $r = -0.5$ (in the case where carriers scatter from acoustic lattice vibrations, which is more probable in our case), equation (7) can be plotted as shown in Fig. 5 [20]. Using Fig. 5 and the experimental data on $\kappa_e(T)$, one can construct the dependence of κ_{bip} on T for different values of ε_0 (Fig. 6). The points in Fig. 6 are the experimental data for κ_{bip} of $LuInCu_4$ derived from Fig. 4a by subtracting from $\kappa_{ph}(T)$ calculated with (3) the values of the lattice heat conductivity obtained from the $\kappa_{ph} \sim T^{-0.6}$ relation extrapolated to high temperatures (see Fig. 4a). As seen from Fig. 6, the experimental points fall on the curve corresponding to $\varepsilon_0 \sim 0.1$ eV. This value is substantially less than that obtained by a theoretical calculation of ε_0 for $LuInCu_4$ in [11, 12].

ACKNOWLEDGMENTS

The authors are indebted to N.F. Kartenko and N.V. Sharenkova for the x-ray diffraction measurements.

The work was carried out under a bilateral agreement between the Russian and Polish Academies of Sciences.

Support of the Russian Foundation for Basic Research (grant no. 99-02-18078) is gratefully acknowledged.

REFERENCES

1. A. V. Goltsev and G. Bruls, submitted to Phys. Rev. B.
2. I. A. Smirnov, L. S. Parfen'eva, A. Jezowski, *et al.*, Fiz. Tverd. Tela (St. Petersburg) **41**, 1548 (1999) [Phys. Solid State **41**, 1418 (1999)].
3. A. Severing, E. Gratz, B. D. Rainford, and K. Yoshimura, Physica B (Amsterdam) **163**, 409 (1990).
4. K. Nakajima, H. Nakamura, Y. Kitaoka, *et al.*, J. Magn. Magn. Mater. **90–91**, 581 (1990).
5. I. Felner, I. Nowik, D. Vaknin, *et al.*, Phys. Rev. B **35**, 6956 (1987).
6. I. Nowik, I. Felner, J. Voiron, *et al.*, Phys. Rev. B **37**, 5633 (1988).
7. J. M. de Teresa, Z. Arnold, A. del Moral, *et al.*, Solid State Commun. **99**, 911 (1996).
8. T. Matsumoto, T. Shimizu, Y. Yamada, and K. Yoshimura, J. Magn. Magn. Mater. **104–107**, 647 (1992).
9. H. Müller, E. Bauer, E. Gratz, *et al.*, J. Magn. Magn. Mater. **76–77**, 159 (1988).
10. J. L. Sarrao, A. P. Ramizer, T. W. Darling, *et al.*, Phys. Rev. B **58**, 409 (1998).
11. H. Nakamura, K. Ito, and M. Shiga, J. Phys.: Condens. Matter **6**, 9201 (1994).
12. K. Takegahara and T. Kasuya, J. Phys. Soc. Jpn. **59**, 3299 (1990).
13. E. Figueroa, J. M. Lawrence, J. L. Sarrao, *et al.*, Solid State Commun. **106**, 347 (1998).
14. A. V. Golubkov, T. B. Zhukova, and V. M. Sergeeva, Izv. Akad. Nauk SSSR, Neorg. Mater. **2** (11), 77 (1966).
15. A. V. Golubkov and V. M. Sergeeva, Preprint Inst. Fiz. Met. UNTs AN SSSR (Institute of Metal Physics, Academy of Sciences of USSR, Sverdlovsk, 1977).
16. A. Jezowski, J. Mucha, and G. Pompe, J. Phys. D **20**, 1500 (1987).
17. N. Pillmayr, E. Bauer, and K. Yoshimura, J. Magn. Magn. Mater. **104–107**, 639 (1992).
18. V. S. Oskotskiĭ and I. A. Smirnov, *Crystal Defects and Thermal Conduction* (Nauka, Leningrad, 1972).
19. R. Berman, *Thermal Conduction in Solids* (Clarendon, Oxford, 1976; Mir, Moscow, 1979).
20. I. A. Smirnov and V. I. Tamarchenko, *Electronic Thermal Conduction in Metals and Semiconductors* (Nauka, Leningrad, 1977).
21. J. M. Lawrence, G. H. Kwei, J. L. Sarrao, *et al.*, Phys. Rev. B **54**, 6011 (1996).
22. A. Löffert, M. L. Aigner, F. Ritter, and W. Assmus, Cryst. Res. Technol. **34**, 267 (1999).

Translated by G. Skrebtsov

Physics of the Solid State, Vol. 42, No. 8, 2000, pp. 1398–1402. Translated from Fizika Tverdogo Tela, Vol. 42, No. 8, 2000, pp. 1361–1364.

METALS AND SUPERCONDUCTORS

Process of Magnetic Field Penetration into the High-Temperature Superconductor $YBa_2Cu_3O_{7-\delta}$

V. M. Arzhavitin*, N. N. Efimova, M. B. Ustimenkova**, and V. A. Finkel'***

** Kharkov Institute of Physics and Technology, ul. Akademicheskaya 1, Kharkov, 310108 Ukraine*

e-mail: vasil@kipt.kharkov.ua (TO: FINKEL)

*** Kharkov State University, pl. Svobody 4, Kharkov, 310077 Ukraine*

Received January 20, 2000

Abstract—The processes of magnetic field penetration into the ceramic samples of the HTSC $YBa_2Cu_3O_{\sim 6.95}$ at $T < T_c$ are studied by the methods of internal friction and magnetization measurements. A clearly manifested correlation is observed between the field dependences of the internal friction spectrum parameters (the logarithmic damping decrement Q^{-1} and the resonance frequency f) and the trapped magnetic flux ΔM. The magnetomechanical approach we used reveals a significant difference in the field dependences of the densities of pinned (N_p) and free (N_f) Abrikosov vortices for $H > H_{c1}$. © *2000 MAIK "Nauka/Interperiodica".*

A large number of publications (see, for example, [1–8]) have been devoted to studies of internal friction (IF) in bulk ceramics, thin films, and single crystals of HTSC at low temperatures over a wide range of frequencies (from a few hertz to tens of megahertz). Apparently, special interest is aroused by the effects associated with the magnetic flux penetration into a superconductor in a magnetic field (the penetration begins at $H = H_{c1}$, where H_{c1} is the lower critical field), terminating in the formation of the mixed state in a field $H = H_S$,[1] with the vortex lattice melting, magnetic flux pinning, and so on. The H–T phase diagrams of high-temperature superconductors are quite complicated, given the characteristic combination of a short coherence length ξ and a long magnetic field penetration length λ in HTSC, as well as the strong anisotropy of their electromagnetic properties. The available data point towards the existence of a large number of different magnetic states ("vortex phases") [11–16]. A spatial inhomogeneity[2] is observed in the process of magnetic field penetration in a sample of a macroscopic size in relatively weak magnetic fields $H_{c1} < H \ll H_{c2}$, where H_{c2} is the upper critical field [11–13].

Mechanical methods (including the low-frequency IF method) appear to be quite promising for investigations of HTSC in a magnetic field. Such a method makes it possible to appraise the dynamics of magnetic vortices from the attenuation of vibrations of the superconductor. Obviously, the processes of dissipation of energy of mechanical vibrations and HTSC magnetization must be interrelated, since they are governed by the same physical mechanisms associated with the magnetic field penetration in a superconductor.

In this connection, we set out in the present work to study the resonance and magnetic properties of the superconducting state of the metaloxide compound $YBa_2Cu_3O_{7-\delta}$ in weak magnetic fields ($T = 77.3$ K, $0 \le H \le 600$ Oe). Obviously, a correlation between these properties will provide new data on the dynamics of magnetic field penetration in HTSC.

1. SAMPLES AND MEASURING TECHNIQUE

Polycrystalline (ceramic) HTSC samples of $YBa_2Cu_3O_{\sim 6.95}$ with a characteristic granule size ~1–5 μm, obtained from a mixture of oxides and carbonates Y_2O_3, Ba_2CO_3, and CuO by using the standard ceramic technology (see, for example, [17]) were used as objects for measuring the IF parameters, viz., the IF logarithmic damping decrement $Q^{-1}(H)$ and the resonance vibrational frequency $f(H)$ (the vibrational frequency is connected with the "effective" elastic modulus E through the relation $f^2 \sim E$), as well as for magnetic measurements. According to the results of the x-ray phase analysis, the concentration of the main impurity phase $BaCuO_2$ did not exceed ~1%. Samples for measuring IF and the magnetization σ were pressed from an HTSC powder (rectangular parallelepipeds of characteristic size $2 \times 2 \times 20$ mm for resonance measurements and $2 \times 2 \times 8$ mm for magnetic measurements[3]) and then sintered in air at a temperature

[1] The field H_S is connected with Bean's field H^* [9] for a complete penetration of the magnetic field into superconducting grains or granules through the familiar relation $H_S = H_{c1} + 2H^*$ [10].

[2] The inhomogeneity concerns the distribution of various magnetic states in granules of an HTSC sample, viz., a mixed state (Shubnikov phase) on the outer side of the granule, and a perfect diamagnet (Meissner phase) inside it.

[3] These parallelepipeds were machined to nearly perfect cylinders of diameter ~2 mm; the demagnetization factor D for such a sample geometry was ~0.3.

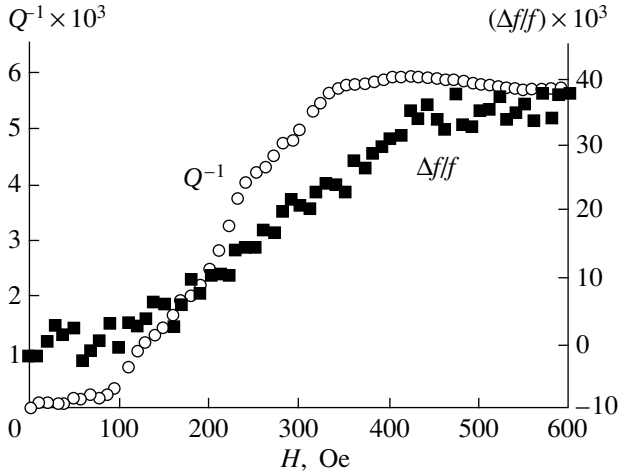

Fig. 1. Field dependence of the relative variation of the logarithmic damping decrement (ΔQ^{-1}) of IF and normalized shift in the resonance frequency ($\Delta f(H)/f(0)$) of the HTSC $YBa_2Cu_3O_{7-\delta}$.

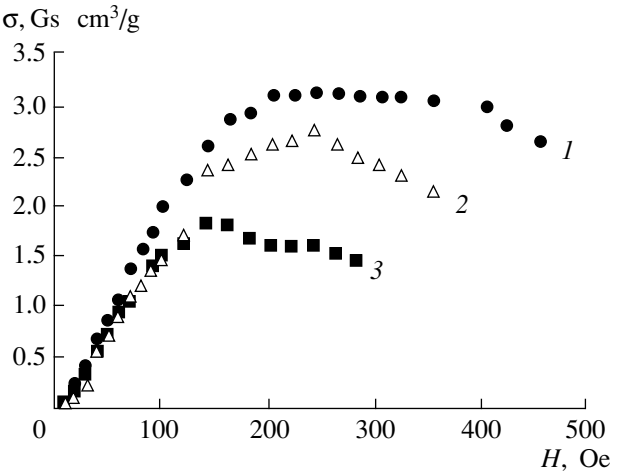

Fig. 2. Field dependence of the magnetization σ of the HTSC $YBa_2Cu_3O_{7-\delta}$ at T = 65 (*1*), (*2*) and 75 K (*3*).

~950°C, followed by slow cooling. The superconducting transition temperature T_c of the samples was ~92 K.

Measurements of the field dependences of Q^{-1} and f for the HTSC $YBa_2Cu_3O_{\sim 6.95}$ at nitrogen temperature were made according to the inverse pendulum technique using flexural vibrations in the range of acoustic frequencies up to 100 Hz for a relative deformation $\varepsilon \sim 10^{-6}$ on a specially constructed instrument [18]. The longitudinal magnetic fields of strength up to ~600 Oe were produced with the help of a solenoid with copper wire winding. The large length of the solenoid (~400 mm) ensured a high uniformity of the field along the sample.

The magnetization of the HTSC $YBa_2Cu_3O_{\sim 6.95}$ at low temperatures was measured using a ballistic magnetometer [19]. The relative measurement error ($\Delta\sigma$) was ~2%, and the sensitivity of the instrument was $\sim 10^{-3}$ G · cm³ g^{-1}.

2. RESULTS OF MEASUREMENTS

The results of measurements of the dependence of relative variation of the logarithmic damping decrement $\Delta Q^{-1}(H) = Q^{-1}(H) - Q^{-1}(H = 0) = Q^{-1}(H) - Q^{-1}(0)$ of IF and $\Delta f(H)/f(H = 0) = \Delta f(H)/f(0) = [f(H) - f(0)]/f(0)$ of the normalized shear of the resonance frequency of the HTSC $YBa_2Cu_3O_{7-\delta}$ on the magnetic field strength at T = 77 K are shown in Fig. 1. Three segments stand out clearly on the dependence $\Delta Q^{-1}(H)$ (curve *1* in Fig. 1):[4]

(1) for $H \leq$ ~90 Oe, the variation of Q^{-1} does not exceed the measurement error;

(2) the value of ΔQ^{-1} increases sharply in the interval ~90 $\leq H \leq$ ~350 Oe;

(3) for $H \geq$ ~350 Oe, the increase in the external field strength hardly affects the value of ΔQ^{-1}.

The variation of the resonance frequency shift $\Delta f(H)/f(0)$ for the HTSC $YBa_2Cu_3O_{7-\delta}$ in a magnetic field also begins at $H \sim$ 90 Oe (curve *2* in Fig. 1). An increase in $\Delta f(H)/f(0)$ is observed in stronger fields. However, the tendency towards saturation on this curve is much weaker than in the curve $\Delta Q^{-1}(H)$.

Qualitatively, the magnetization curves $\sigma(H)$ obtained under diamagnetic screening conditions (ZFC) at various temperatures close to T_c (Fig. 2) are similar: the initial linear segment of the $\sigma(H)$ dependence[5] is followed by a nonlinear segment on which the slope of the dependence of magnetization on the magnetic field strength decreases and then reverses its sign.

3. DISCUSSION OF RESULTS

Let us consider the observed variations in the parameters of the internal friction spectra (logarithmic damping decrement Q^{-1} and the resonance frequency f), and in the magnetization σ of the HTSC $YBa_2Cu_3O_{7-\delta}$, caused by applying an external longitudinal magnetic field at $T < T_c$.

In the first place, we observe that the behavior of the curves $\Delta Q^{-1}(H)$ and $\Delta f(H)/f(0)$ (Fig. 1) over the entire range of magnetic fields is reminiscent of the dependence of the trapped magnetic flux density ΔM on the magnetic field[6] (Fig. 3) obtained in the experiments on the measurement of magnetization under ZFC. The

[4] It should be remarked at the very outset that we shall not consider in this work the effects in very weak magnetic fields ($0 \leq H \leq 10$ Oe), when the magnetic field penetrates the "weak links" between the granules [19].

[5] In this case, the quantity $\chi \neq -1/(4\pi)$, since granular HTSC are ideal diamagnets only for $H \leq H_{c1J}$, where H_{c1J} is the lower critical field of Josephson's weak links.

[6] $\Delta M = \sigma_{trap}\rho/(4\pi)$, where ρ is the density of the HTSC sample; the "trapped magnetization" σ_{trap} is determined by subtracting from the experimentally determined value $\sigma(H)$ of the magnetization the quantity σ_{ext} obtained by extrapolating the linear segment of the dependence $\sigma(H)$.

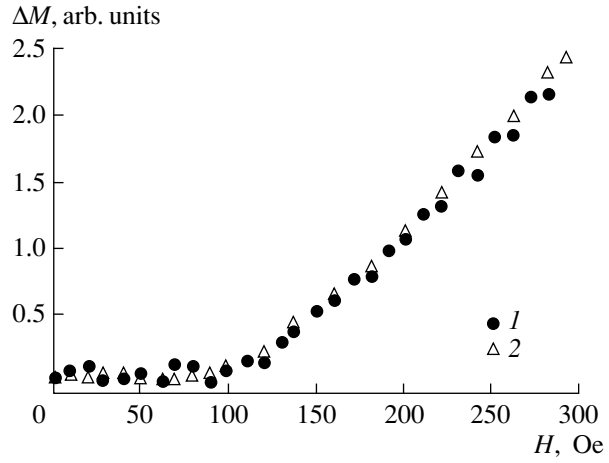

Fig. 3. Field dependence of the magnitude of the trapped magnetic flux density at $T \sim 77$ K according to magnetic measurements data (*1*) and results of IF measurements (*2*).

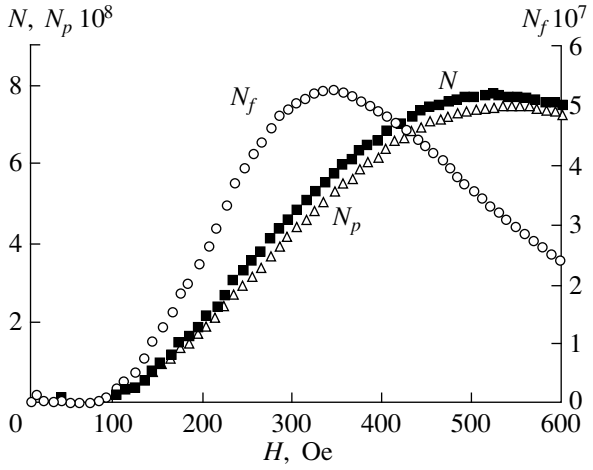

Fig. 4. Field dependence of the density of trapped magnetic vortices in the HTSC $YBa_2Cu_3O_{7-\delta}$.

qualitative agreement between the dependences $\Delta Q^{-1}(H)$ and $\Delta f(H)/f(0)$ on the one hand, and $\Delta M(H)$ on the other hand is symptomatic: the emergence of singularities on these curves is apparently associated with the same processes.

Significantly, no changes in the values of $\Delta Q^{-1}(H)$ and $\Delta f(H)/f(0)$ were observed at $T = 77$ K in fields up to ~90 Oe (the $\sigma(H)$ dependences are linear in this case). It is also worth noting that according to the results of electrophysical investigations carried out on the same HTSC samples at $T = 77$ K [20], the value of the field at which the magnetic field starts penetrating the granules of the HTSC $YBa_2Cu_3O_{7-\delta}$, i.e., the minimum value of the lower critical field $H_{c1}(H_{c1}^{\min})$, is about the same. Thus, the IF parameters are stable in the region of existence of Meissner's phase, i.e., until the penetration of the external magnetic field in the HTSC granules.

It was mentioned above that the logarithmic damping decrement (Q^{-1}) and the resonance vibrational frequency (f) of the HTSC sample $YBa_2Cu_3O_{7-\delta}$ begin to increase at $H > H_{c1}$. For $H \geq 250$ Oe, the dependence $\Delta Q^{-1}(H)$ shows a clearly manifested tendency towards saturation, while the saturation effect is much weaker for the dependence $\Delta f(H)/f(0)$ (Fig. 1). The increase in the values of $\Delta Q^{-1}(H)$ and $\Delta f(H)/f(0)$ for $H > 90$ Oe, which correlates qualitatively with the onset of the magnetic flux trapping, points towards the beginning of the penetration of Abrikosov vortices into superconducting granules, i.e., towards the formation of the mixed state in the HTSC $YBa_2Cu_3O_{7-\delta}$.

Apparently, the interval of fields $\sim 90 \leq H \leq \sim 350$ Oe corresponds to the process of vortex penetration in a superconductor, which is known to be accompanied by the emergence of spatial inhomogeneity in HTSC granules [10] and ends with the transition of the entire sample into the critical state for $H = H_S$ [9].[7]

The attainment of the field H_S (it should be emphasized that, like the Bean field H^*, the value of this field is not a physical constant of the material, but depends on the shape and size of the superconducting granules in the case of granular HTSC) at $H \geq 350$ Oe points towards the termination of a noticeable increase in the total number of vortices, as well as towards the onset of formation of an ordered vortex lattice.

The field dependences $Q^{-1}(H)$ and $\Delta f(H)/f(0)$ in fields $H > H_{c1}$ can be analyzed by using the familiar magnetomechanical approach [2, 21, 22]. According to this method, the displacement of a superconductor relative to the applied magnetic field **H** leads to the emergence of a restoring mechanical force acting on each magnetic vortex pinned by structural defects. Accordingly, the vibrational frequency of the entire sample also changes by the amount $\Delta f(H)$ [21]:

$$\Delta f(H) = \frac{N_p \Phi_0 H V}{16\pi^3 I f(0)}, \qquad (1)$$

where N_p is the density of pinned vortices (the number of vortices per unit longitudinal section of the superconductor), Φ_0 is a magnetic flux quantum ($\Phi_0 = 2.07 \times 10^{-7}$ G · cm^2), I is the moment of inertia of the superconducting sample, and V is the sample volume.

The change in the logarithmic damping decrement of a superconductor in a magnetic field is defined as [22]

$$\Delta Q^{-1}(H) = H^2 V \frac{N_p N_f}{(N_p + N_f)^2} : [\pi^4 I f^2(0)], \qquad (2)$$

[7] It should be recalled that for $H = H_S$, the dependence $\Delta M(H)$ for various HTSC samples displays a tendency towards the attainment of a peak [19].

where N_f is the density of free (unpinned) vortices.

Thus, in the framework of the magnetomechanical approach, the resonance frequency is found to be sensitive only to pinned magnetic vortices, while the logarithmic damping decrement depends on both pinned and free vortices. The results of IF measurements in HTSC make it possible to estimate the density of both types of magnetic vortices.[8] Without going into the computational details, we present in Fig. 4 the results of such computations. It can be seen that the fraction of free vortices is quite small in the entire range of fields (the ratio N_f/N does not exceed a few percent). The total vortex density N, as well as the density of pinned vortices N_p, increases in the entire range of fields, while the field dependence of the density of free vortices (N_f) has a well-defined peak in the vicinity of the field $H_S \sim 350$ Oe. Such behavior of the dependences $N_p(H)$ and $N_f(H)$ is quite understandable: the formation of an ordered lattice of pinned vortices occurs through the movement of free vortices. As this process is being completed, free magnetic vortices are pinned at the defects and their fraction in the total number of vortices ($N = N_p + N_f$) begins to decrease with the increasing magnetic field strength.

Estimating the density of magnetic vortices from the results of IF measurements allows us to compute certain magnetic properties of HTSC. Thus, knowing the vortex density N, we can estimate the density of the trapped magnetic flux in an HTSC:

$$\Delta M = N\Phi_0/(4\pi). \quad (3)$$

The dependences $[\Delta M(H)]_{\text{calc}}$ and experimentally determined curves $\Delta M(H)$ are found to coincide quite well (see Fig. 3).

Thus, the penetration of magnetic field in the high-temperature superconductor $YBa_2Cu_3O_{7-\delta}$ at $T < T_c$ is studied with the help of two independent methods. The magnetodynamic effects observed in HTSC indicate that the logarithmic damping decrement of internal friction (ΔQ^{-1}) and the resonant vibrational frequency ($\Delta f/f$) increase as the magnetic field increases from zero to 600 Oe. In the dynamic experiments we carried out, the value of the lower critical field $H_{c1}^{\min} = 90$ Oe, at which the first vortex filaments appear in the sample, was established reliably. The value of $H_{c1}^{\min}$ correlates well with the results of direct magnetic measurements.

The results of measurements of the IF parameters of an HTSC in a magnetic field were used to estimate the fraction of free and pinned vortices for $H > H_{c1}$. It was found that the density of pinned vortices increases monotonically with increasing magnetic field strength, while the field dependence of the density of free vortices has a peak at $H_{c1} < H < H_S$.

The magnetic flux ΔM trapped in the HTSC $YBa_2Cu_3O_{7-\delta}$ was estimated from the data on mechanical resonance in a superconducting sample placed in a magnetic field. These estimations agree well with the dependence $\Delta M(H)$ obtained in this work from the data on magnetic-field dependence of the magnetization in $YBa_2Cu_3O_{7-\delta}$.

On the whole, the results we obtained indicate that a considerable amount of information can be gathered by using the IF technique to study the process of magnetic flux penetration in HTSC, for constructing the H–T phase diagrams, etc.

[8] It should be emphasized that the value of the magnetization σ measured in constant magnetic fields is sensitive only to the total density of vortices ($N = N_p + N_f$).

ACKNOWLEDGMENT

This research was supported by the International Science Foundation (ISSP grant no. QSU082209).

REFERENCES

1. P. Esquinazi, J. Low Temp. Phys. **85**, 139 (1991).
2. C. Hunnekes and H.G. Bohn, J. Alloys Compd. **234**, 218 (1996).
3. J. X. Zhang, P. C. W. Fung, G. M. Lin, *et al.*, J. Phys. Chem. Solids **51**, 287 (1992).
4. V. G. Bar'yakhtar, V. N. Varyukhin, and F. B. Nazarenko, Sverkhprovodimost: Fiz., Khim., Tekh. **3**, 1145 (1990).
5. Y. T. Wen, T. S. Ke, G. H. Bohn, *et al.*, Physica C (Amsterdam) **193**, 99 (1992).
6. Y. T. Wen, L. X. Yuan, C. Y. Xie, *et al.*, J. Phys.: Condens. Matter **2**, 661 (1990).
7. I. M. Golev, O. N. Ivanov, I. M. Shushlebin, *et al.*, Fiz. Tverd. Tela (Leningrad) **31** (1), 220 (1989) [Sov. Phys. Solid State **31**, 120 (1989)].
8. V. S. Okovit, Ya. D. Starodubov, L. A. Chirkina, and S. D. Lavrinenko, Fiz. Nizk. Temp. **20**, 63 (1994) [Low Temp. Phys. **20**, 53 (1994)].
9. C. P. Bean, Phys. Rev. Lett. **8**, 250 (1962); Rev. Mod. Phys. **36**, 31 (1964).
10. E. Altshuler, S. García, and J. Barroso, Physica C (Amsterdam) **177**, 61 (1991); E. Altshuler and S. García, Physica C (Amsterdam) **200**, 195 (1992).
11. G. W. Crabtree and D. R. Nelson, Phys. Today **50**, 38 (1997).
12. E. H. Brandt, Physica C (Amsterdam) **169**, 91 (1991); **195**, 1 (1992).
13. G. Blatter, M. V. Feigel'man, V. B. Geshkenbein, *et al.*, Rev. Mod. Phys. **66**, 1125 (1994).
14. R. J. Soulen and S. A. Wolf, Physica C (Amsterdam) **166**, 95 (1990).
15. L. Xing, Phys. Rev. B **46**, 11084 (1992).
16. V. V. Moshalkov, Solid State Commun. **77** (5), 389 (1991).

17. V. A. Finkel', V. M. Arzhavitin, A. A. Blinkin, *et al.*, Physica C (Amsterdam) **235–240**, 303 (1994).
18. V. M. Arzhavitin, V. P. Golovin, G. F. Tikhinskiĭ, *et al.*, Sverkhprovodimost': Fiz., Khim., Tekh. **2**, 153 (1989).
19. N. N. Efimova, Yu. A. Popkov, M. B. Ustimenkova, and V. A. Finkel', Fiz. Nizk. Temp. **20**, 342 (1994) [Low Temp. Phys. **20**, 273 (1994)].
20. V. A. Finkel' and V.V. Toryanik, Fiz. Nizk. Temp. **23**, 824 (1997) [Low Temp. Phys. **23**, 618 (1997)].
21. V. E. Miloshenko, I. M. Shushlebin, and M. N. Zolotukhin, Fiz. Tverd. Tela (Leningrad) **31** (9), 281 (1989) [Sov. Phys. Solid State **31**, 1638 (1989)].
22. V. E. Miloshenko and I. M. Shushlebin, Sverkhprovodimost': Fiz., Khim., Tekh. **3**, 1836 (1990).

Translated by N. Wadhwa

Physics of the Solid State, Vol. 42, No. 8, 2000, pp. 1403–1409. Translated from Fizika Tverdogo Tela, Vol. 42, No. 8, 2000, pp. 1365–1371.

SEMICONDUCTORS AND DIELECTRICS

Effects of Aggregation of Squaryl Dye on Photogeneration of Charges in Amorphous Molecular Semiconductors Based on Poly-*N*-epoxypropyl Carbazole

N. A. Davidenko* and A. A. Ishchenko**

** Shevchenko National University, Vladimirskaya ul. 64, Kiev, 252033 Ukraine*

e-mail: daviden@ukrpack.net

*** Institute of Organic Chemistry, National Academy of Sciences of Ukraine, ul. Murmanskaya 5, Kiev, 253094 Ukraine*

Received November 30, 1999

Abstract—Peculiarities of photoconductivity, photoabsorption, and photoluminescence of poly-*N*-epoxypropyl carbazole films doped with an intraionic dye are investigated. The anomalous temperature dependences of the photoconductivity of the films in the dye absorption region are explained by studying the effect of the dye concentration, temperature, and external electric field on the liberation of captured charges from the traps formed in the films as a result of doping. It is concluded that an increase in the dye concentration enhances its aggregation, intensifies the photogeneration of triplet electron–hole pairs, and narrows the spatial distribution of traps for holes in the vicinity of the dye. The hole charges captured in such traps are connected through the Coulomb interaction with negatively charged fragments of dye molecules. The traps are destroyed through thermal activation. *© 2000 MAIK "Nauka/Interperiodica".*

Poly-*N*-epoxypropyl carbazole (PEPC) films doped with cationic polymethine dyes possess photosemiconducting properties and can be used for optical information recording and processing. Such films have a high photoconductivity and exhibit electroluminescence properties [1]. However, intraionic dyes [2] are preferable for applications in electrophotographic and holographic media, as these dyes can generate both positive (holes) and negative (electron) charges when exposed to light. Among intraionic compounds, organic dyes, which are derivatives of the squaric acid and called squaryl dyes, are very promising in this respect. These dyes are characterized by a high thermo- and photostability and have intense absorption bands [3]. At the present time, squarynes are widely used in polymeric materials of laser disks intended for information recording and storage [3]. The capture of nonequilibrium charges in traps whose presence in PEPC with ionic dyes at room temperature was established in [4], is one of the factors lowering the photoconductivity and luminescence intensity. The effect of traps on the photoconductivity and luminescence of PEPC films with intraionic dyes remained unclear. In addition, squaryl dyes exhibit a pronounced tendency to aggregation [5], which is also manifested in the electrical and physical properties of PEPC films [2]. The present work aims to establish peculiarities in the optical and photoelectric properties of PEPC films upon a change in the concentration of a squaryl dye.

1. SAMPLES AND EXPERIMENTAL TECHNIQUE

We used a squaryl dye based on a derivative of 1,3,3-trimethyl-3*H*-indoline (HISD):

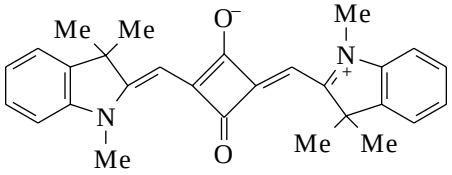

The molecule of this dye has a negatively charged (A^-) and a positively charged (D^+) centers. The optical absorption and photoluminescence spectra of PEPC films for various concentrations N of the dye are shown in Fig. 1.

We determined the effect of the dye concentration in PEPC on the photoabsorption and photoluminescence spectra of the films; the variation of photoluminescence intensity in the films as a function of the external electric field strength; the photocurrent in sandwich-type samples exposed to light in the dye absorption region at various temperatures; the ratio of concentrations of the singlet (n_1) and triplet (n_3) electron–hole pairs (EHP) in films illuminated by light in the dye absorption region, and the effect of trapped charge carriers on the photoconductivity of the investigated films.

The samples were prepared in the form of structures with a free surface (quartz substrate–polymer film) or in the form of sandwich-type structures (Al–polymer film–SnO_2). We used the PEPC + N wt % HISD films. The dye concentration N varied from 1×10^{-2} to 5 wt %. The polymer films were prepared by drying the solu-

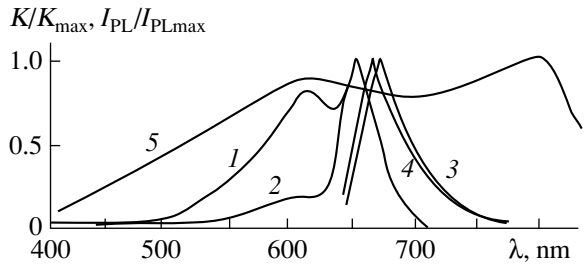

Fig. 1. Normalized absorption (curves *1* and *2*) and luminescence (*3*, *4*) spectra of PEPC + 0.01 wt % HISD (*1*, *3*) and PEPC + 1 wt % HISD (*2*, *4*) films as well as the absorption spectrum of polystyrene + 10 wt % PEPC films (curve *5*) obtained in [18] under γ-radiolysis.

tions of PEPC + *N* wt % HISD in dichloroethane poured on quartz substrates with or without a SnO_2 layer. The thickness of the dried films was $L = 0.5$–2 μm. The Al films were deposited by thermal sputtering in a vacuum chamber, and the thickness of the Al layer was 300–350 Å.

In the sandwich-type samples, we measured the photocurrent density j_{PH} in the photoresistance mode and the photoluminescence intensity I_{PL} in the optical wavelength range $\lambda = 350$–1200 nm during the exposure of the sample from the side of the SnO_2 electrode to light with a wavelength $\lambda_1 = 546$, 633, 680, or 711 nm (intensity I_1) or $\lambda_2 = 380$ nm (intensity I_2). The samples were exposed to light emitted by an incandescent lamp using light filters, by a He–Ne laser, and by a hydrogen lamp. The light intensity was $I_1 = 0.2$–20 and $I_2 = 0.1$–0.5 W/m^2.The electric field strength was varied in the range $E = 2 \times 10^7$–3×10^8 V/m. The measurements were made at a temperature T in the interval 290–355 K, at which PEPC films are used as recording media. The results of measurements of j_{PH} were used for calculating the relative quantum yield of charge carrier photogeneration $\eta = j_{PH}h\nu/qI_1\kappa L$, where q is the electron charge and $h\nu$ is the energy of a light quantum. Along with j_{PH}, we measured I_{PL} and determined the relative variation δI_{PL} of I_{PL} in the electric field E from the relation $\delta I_{PL} = [I_{PL}(E) - I_{PL}(0)]/I_{PL}(0)$, where $I_{PL}(E)$ is the quasistationary value of I_{PL} after the application of the electric field, and $I_{PL}(0)$ is the quasi-stationary value of I_{PL} before the application of the field.

In order to determine the ratio of n_1 to n_3, we used the technique proposed in [6, 7] for determining the change in the photoconductivity of amorphous molecular semiconductors (AMS) in the absorption range of dopants with the simultaneous photogeneration of triplet excitons. The latter are catalyzers of the *S*–*T* conversion of EHP [8, 9]. Consequently, the photogeneration of triplet excitons enhances the photoconduction of AMS connected with the dissociation of singlet EHP and suppresses the photoconduction of AMS connected with the dissociation of triplet EHP. As in [6, 7], the photogeneration of EHP was induced by the exposure of the sandwich-type structures to light of wavelength λ_1, while light of wavelength λ_2 was used for the photogeneration of excitons (the wavelength λ_2 does not belong to the absorption range of HISD and lies near the red boundary of the PEPC absorption, where an effective photogeneration of triplet excitons takes place [10]). In the samples exposed to the light of wavelength λ_1 or λ_2, we measured the quasi-stationary photocurrent j_1 or j_2, respectively. When the sample was illuminated simultaneously by the light of wavelength λ_1 and λ_2, the quasi-stationary photocurrent j_3 was recorded. For an analysis of the results, we calculated the ratio $\delta j = j_3/(j_1 + j_2)$ of photocurrents, and determined the dependences of j_1 and δj on N, E, and λ_1. The ratios of n_1 to n_3 in photogenerated EHP was estimated, following [6, 7], from the deviation of δj from unity: if $\delta j > 1$ or $\delta j < 1$, a larger number of singlet or triplet EHP, respectively, are formed during photogeneration.

For samples with a free surface of polymer films, the spectrocomputational complex KSVIP-23 was used for measuring the optical spectra of the absorption coefficient κ and the photoluminescence intensity I_{PL} in the optical wavelength range $\lambda = 350$–1200 nm. We also measured the optical density K_1 and K_2 of the films at the wavelengths λ_1 and λ_2, respectively, with the help of photodiodes whose amplified signals were recorded by a storage oscilloscope. We calculated the values of ΔK_1 and ΔK_2, viz., the deviation of the optical density of the films from the steady-state value during and after the exposure of films to light. Besides, we measured the variation of I_{PL}, K_1, and K_2 as a result of pulse heating of polymer films to a temperature of +(85–90)°C at a rate of 10^6 K/s. The pulse heating of the films was accomplished at the expense of Joule heat liberated in the conducting SnO_2 layer, deposited on the quartz substrates under the polymer films, due to the passage of a current pulse of duration 0.1 s.

In order to create a nonequilibrium concentration M of charges captured in traps, we exposed the samples to light of wavelength λ_2 during the time t_1. This led to the photogeneration and capture of mobile holes in the traps created by carbazole (Cz) cores of PEPC. A trapped hole corresponds to a cation radical ($Cz^{\bullet +}$) whose optical absorption spectrum lies in the visible optical range (curve *5* in Fig. 1). The buildup of M was detected from a decrease in K_2 and an increase in K_1, while the relaxation of M was judged from the recovery of K_1 and K_2 during the time t_2 after the discontinuation of illumination by light with wavelength λ_2.

2. EXPERIMENTAL RESULTS

Figure 1 shows the absorption and photoluminescence spectra of PEPC films with HISD. The increase in the dye concentration in the film is accompanied with a bathochromic shift of the peak and by a narrow-

ing of the bands. These results combined with the results of our previous spectroscopic studies in the temperature range T = 4.2–320 K [5] indicate that an increase in N enhances the aggregation of HISD molecules. We also proved earlier that the structure of aggregates is close to a "head–tail" structure.

In Al–PEPC + N wt % HISD–SnO_2 samples, the photocurrent increases with E and N. For $L = 1$ μm, $E = 1 \times 10^8$ V/m, and $N = 5$, η attains the value 0.02. The $\eta(E)$ dependence plotted in the ln η vs. $E^{1/2}$ coordinates is linear. The slopes of the straight lines describing these dependences are identical for all the samples under investigation. This suggests that the mechanism of photogeneration of free charge carriers in the films under investigation is similar to that proposed for AMS based on PEPC [11]. According to this mechanism, an EHP is formed from an excited photogeneration center as a result of absorption of light of wavelength λ_1. In an external electric field, the EHP dissociates so that the hole, formed as a result of the dissociation, jumps from one carbazole core of PEPC to another, away from the photogeneration center, leaving behind a quasi-stationary electron. The dissociation probability is determined by the probability of activation surmounting by a hole of the Coulomb barrier (W_{0ph}) equal to the energy of Coulomb attraction between a hole and an electron. In this case, the dependence of j and η on E and T can be presented in analytic form as follows:

$$j \sim \eta \sim \exp(-(W_{0ph} - \beta E^{1/2}))/(T^{-1} - T_0^{-1}), \qquad (1)$$

where k is the Boltzmann constant and T_0 is the characteristic temperature amounting to 490 ∓ 20 K for PEPC-based AMS. The value of the coefficient β calculated from the η(E) dependences plotted in the log η vs. $E^{1/2}$ coordinates is $(4.3 \mp 0.3) \times 10^{-5}$ eV $(\text{V/m})^{-1/2}$, which is close to the theoretical value of the Poole–Frenkel constant [11].

However, the photoconductivity mechanism for PEPC films with HISD differs considerably from that for other doped PEPC films. Figure 2 shows the results of measurements of the temperature dependence of j_1 for different values of N and E. These dependences are characterized by the nonlinearity of the experimental curves in the ln j_1 vs. $1/T$ coordinates. For small values of N and E, these curves have a flattened minimum that disappears with increasing N and E. These results are similar to those obtained for PEPC films with cationic dyes [5] and can be interpreted by the capture of photogenerated holes in the traps formed in the polymer in the vicinity of electrically charged dye molecules. However, a flattened minimum was not observed on the j_1 vs. T dependences for PEPC films with cationic dyes. This means that, although the dependences under investigation can be associated with the thermal degradation of the traps for photogenerated charges upon heating, the nature of these traps is more complicated than for PEPC with cationic dyes.

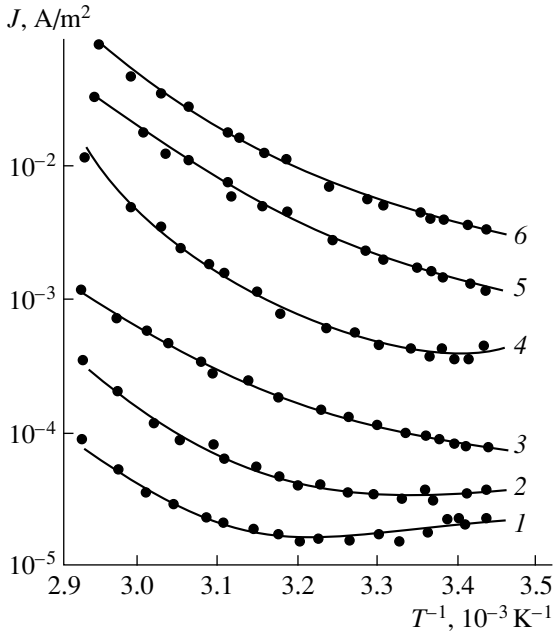

Fig. 2. Dependence of lnj_1 on $1/T$ for Al–PEPC + 0.01 wt % HISD–SnO_2 (curves *1–3*) and Al–PEPC + 1 wt % HISD–SnO_2 (curves *4–6*) samples for $E = 3 \times 10^7$ V/m (*1–4*), 5.2×10^7 V/m (*2, 5*), and 7×10^7 V/m (*3, 6*).

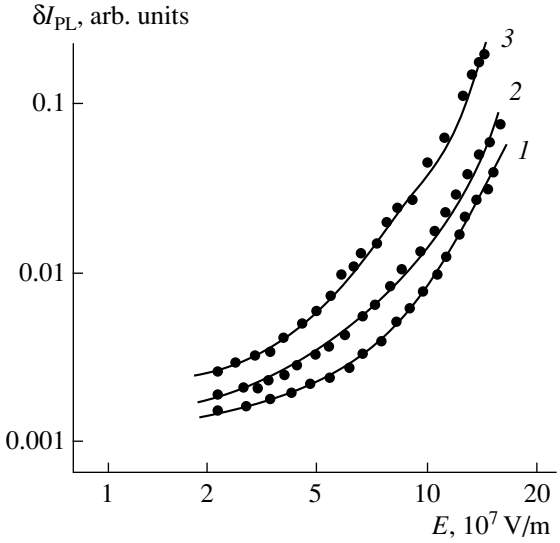

Fig. 3. Dependence of δI_{PL} on E in Al–PEPC + N wt % HISD–SnO_2 samples for $L = 1$ μm and $N = 0.1$ (*1*), 0.5 (*2*), and 5 (*3*) measured during their exposure to light of wavelength λ = 633 nm.

Figure 3 shows the curves describing the dependence of δI_{PL} on N for various values of E. The results of the measurements of these dependences indicate an increase in the quenching effect of the electric field on photoluminescence upon an increase in the aggregation of HISD. According to the results obtained in [12], such an increase in δI_{PL} can be associated with an increase in

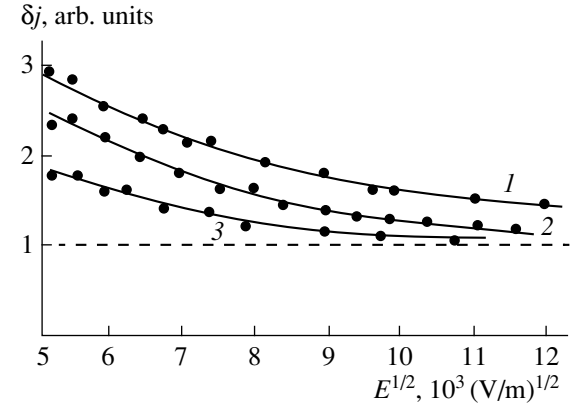

Fig. 4. Dependence of δj on E in Al–PEPC + N wt % HISD–SnO_2 samples for L = 1 μm and N = 0.01 (*1*), 0.1 (*2*), and 5 (*3*) measured during their exposure to light of wavelength λ = 633 nm.

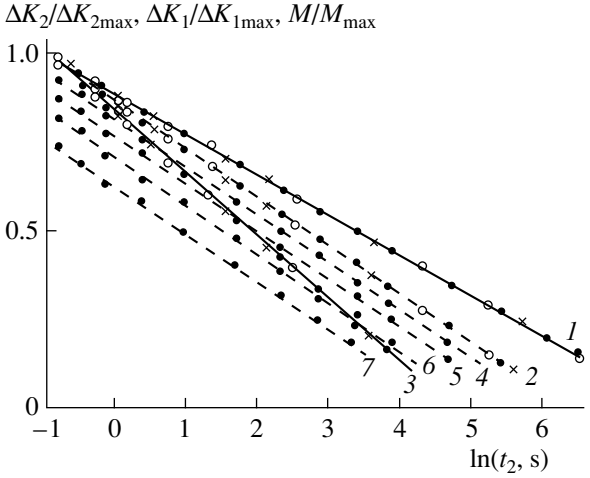

Fig. 5. Dependences of ΔK_1 (crosses), ΔK_2 (light circles), and M (dark circles) on ln t_2 for t_1 = 1 s, T = 293 K, λ_2 = 380 nm, λ_1 = 633 nm in samples with PEPC + 0.01 wt % HISD (*1*), PEPC + 0.1 wt % HISD (*2*, *4*–*7*), and PEPC + 1 wt % HISD (*3*) at a temperature T = 293 (*1*–*3*), 307 (*4*), 324 (*5*), 331 (*6*), and 340 K (*7*).

the dissociation probability of EHP (leading to an increase in η) due to an increase in the mobility of the other charge carrier (electron) in a EHP and/or due to an increase in the probability of photogeneration of long-lived (triplet) EHPs. Additional investigations were carried out in order to verify the second assumption.

Figure 4 shows the δj vs. E dependences plotted for various values of N. Since $\delta j > 1$, we can assume, according to [6, 7], that predominantly singlet EHPs are generated in PEPC + N wt % HISD films as a result of exposure of the investigated samples to the light of wavelength λ_1. However, since the value of δj decreases with increasing N, we can also assume that an enhancement of the dye aggregation diminishes the difference between photogenerated singlet and triplet EHPs, i.e., the ratio n_3/n_1 increases. This means that an increase in the EHP dissociation probability with the dye concentration in PEPC is also connected with an increase in their lifetime, in view of the triplet spin state of EHPs.

In Al–PEPC + N wt % HISD–SnO_2 samples exposed to light, the photocurrent first increases to a quasistationary value and then falls to zero when the illumination ceases. If, however, the sample exposed to the light of wavelength λ_2 for a time t_1 is illuminated by the light of wavelength λ_1 after a time t_2, the leading front of the current pulse exhibits a peak followed by a decrease to the quasi-stationary value. The height of this peak can be used for estimating the concentration M of charges formed as a result of illumination by the light of wavelength λ_2 and participating in photoconduction stimulated by light of wavelength λ_1. It is important to note that the strongest effect of illumination by light of wavelength λ_1 is observed for λ_1 = 633 nm and decreases to zero upon a transition to λ_1 = 711 nm. An analysis of the $M(t_1)$ curve shows that it can be approximated by a simple exponential function with a single time constant (3.1 ∓ 0.2 s for I_1 = 20 W/m^2).

The value of M decreases with increasing t_2 and does not depend on E in the time interval $t_1 + t_2$, but decreases to zero if the sample was exposed to the light of wavelength λ_1 during the time t_2, even for E = 0. The $M(t_2)$ dependences cannot be presented by a simple exponentially decreasing function, but the curves describing these dependences can be approximated in the M vs. ln t_2 coordinates by straight lines. Figure 5 shows that the slopes of these plots increase with the HISD concentration. As the value of N increases from 0.01 to 1, the slope of the $M(\ln t_2)$ dependences increases by a factor of 1.6. The slopes of the graphs are independent of E. The measurements of these dependences at different temperatures of the samples in the range T = 293–350 K (curves *1*, *5*, and *6* in Fig. 5) revealed that with increasing T the value of M decreases, and this decrease is of the activation nature with an activation energy 0.17 ∓ 0.03 eV. Figure 5 also presents the dependences of ΔK_1 and ΔK_2 on ln t_2. It can be seen that these correlate with each other and with the $M(t_2)$ dependences.

The value of I_{PL} decreases during the illumination of the samples; however, if the polymer film is rapidly heated during or after the exposure, the photoluminescence intensity is restored. In the case of pulse heating, the restoration of K_1 and K_2 is also observed, along with the restoration of I_{PL}.

3. DISCUSSION OF RESULTS

Let us return to Fig. 2. We proposed earlier that the nonexponential temperature dependence of j_1 can be due to the fact that, after their photogeneration from HISD, holes are captured in traps in PEPC. The con-

centration of such traps decreases upon heating, and they produce a weaker effect on the dissociation of EHPs. It is remarkable, however, that the value of j_1 for small N and E decreases with increasing T. In PEPC-based AMS, holes are mobile, and the dependence of the mobility (μ_p) on E and T can be presented in an analytical form [11, 13] similar to (1):

$$\mu_p \sim \mu_0 \exp(-(W_{0p} - \beta E^{1/2}))/(T^{-1} - T_0^{-1}), \qquad (2)$$

where μ_0 is the hole mobility in zero electric field and W_{0p} is the activation energy of the hole mobility, which amounts to 0.62 eV for PEPC [11]. Hence, we can assume that the drift mobility of holes in weak electric fields is low and insufficient for the holes, liberated from the traps in the vicinity of recombination centers as a result of heating, to move away from a center and to avoid recombination. The activation energy for the liberation of holes from the traps in the vicinity of dye molecules is smaller than $W_{0p} - \beta E^{1/2}$; as the temperature increases, the recombination probability for holes from the traps becomes higher than the EHP dissociation probability. With increasing E, the value of μ_p increases, and the holes liberated as a result of heating move away from the recombination centers with a higher probability. Such a mechanism allows us to explain the observed flattened minimum on the temperature dependences of j_1 (see Fig. 2). We also assume that, as the HISD concentration increases, additional conditions for the elevation of the EHP dissociation probability are created. One such condition is an increase in the EHP lifetime due to the triplet spin state. Indeed, according to the conclusion drawn in [12], an increase in the quenching effect of an electric field on photoluminescence (see Fig. 3) can be due to an increase in the fraction of triplet states in HISD aggregates, as well as an increase in the n_3/n_1 ratio. The results of measuring the δj vs. E dependences for various N also support this mechanism (see Fig. 4). Thus, as the aggregation of the dye becomes stronger, the energy levels of the excited states S and T of the dye become closer [14], and the probability of photogeneration of triplet EHP from such states becomes higher.

In order to analyze this assumption, let us consider the features of the formation and relaxation of traps near HISD in PEPC in greater detail. The results obtained indicate that nonequilibrium particles absorbing radiation in the visible and near IR ranges are accumulated in the AMS under investigation exposed to light of wavelength λ_2. After the cessation of the illumination, these particles disappear quite slowly. The photoluminescence intensity of dyes varies synchronously with the concentration of such particles. After illumination by light of wavelength λ_2 followed by pulse heating of the samples, the value of I_{PL} is restored. Besides, the excitation of HISD molecules by the light of wavelength λ_1 accelerates the relaxation of the concentration of such particles.

The results of measurements of the $M(t_2)$ dependences (Fig. 5) indicate that the exposure to light of wavelength λ_2 leads to the formation of some bound states consisting of positively and negatively charged particles that appear as a result of the photogeneration of molecular excitons [13]. A decrease in the concentration of such states can be considered by using the model of recombination of charge pairs with a finite spatial distribution over the distance between such charges [15, 16]. For a pair distribution of charges participating in recombination, the change in their concentration is defined as

$$M(t_2)/M_0 = \int_{r_1}^{\infty} f(r) \exp(-\omega(r)t)\, dr, \qquad (3)$$

where $\omega(r)$ is the transition probability rate of a hole to a recombination center, r_1 is the smallest separation between the charges in the pair distribution, and $f(r)$ is the distribution function of charge pairs over distances. For a rectangular distribution of charge pairs (a hole at a carbazole core of PEPC and an electron remaining after the dissociation of an exciton) with distances r_1 and r_2 between the electron and the hole, expression (3) can be written in the form

$$M(t_2)/M_0 = (r_2 - \alpha_p \ln(\nu_1 t_2)/2)/(r_2 - r_1), \qquad (4)$$

where α_p is the localization radius of the hole and ν_1 is the frequency factor of the hole transition during recombination. According to this model, an increase in the slope of the dependences with N in Fig. 5 is due to a decrease in the width of this spatial distribution. The latter is caused by the strengthening of bonds between the charges in pairs and a decrease in the probability of diffusion-induced dissociation during their lifetime. The fact that the charges in these pairs cannot be separated through diffusion is also confirmed by the results of measurements of the $M(t_2)$ dependences for various values of T (see Fig. 5), since the slope of the $M(t_2)/M_0$ vs. $\ln t_2$ graphs does not change with increasing temperature. Since holes are mobile charge carriers in PEPC and may diffuse over Cz, we can assume that an increase in N in these charge pairs does not deteriorate the transport of charge carriers due to the intensification of the dye aggregation, but suppresses the spatial distribution of traps and holes in the vicinity of dye aggregates.

The observed effects of hole trapping and liberation apparently cannot be explained by the formation of labile complexes or triplet exiplexes similar to those formed in PEPC with the cationic dye Rodamin 6Zh [17], as the relaxation of the formed states in our case cannot be described by a simple exponential function (see Fig. 5). The observed effects cannot be described by the photoliberation of trapped charges, either. The illumination by light of wavelength λ_2 leads to the formation of trapped holes, which absorb the light of

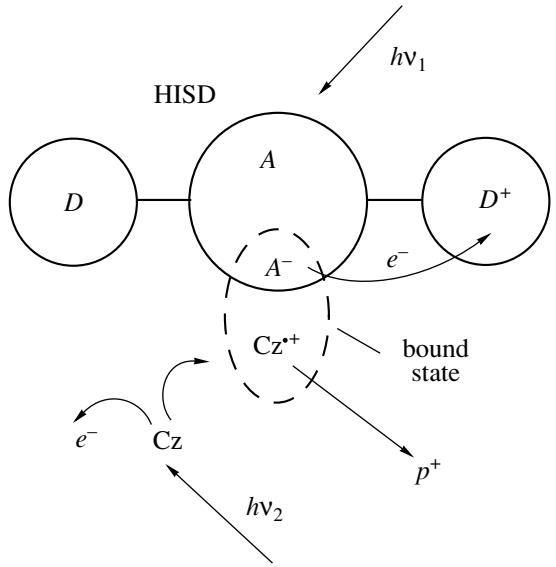

Fig. 6. Schematic diagram of the processes of formation and relaxation of bound states in a PEPC + HISD film.

wavelength λ_1 and which should participate in the induced photoconductivity. The peak in the electronic $Cz^{\bullet+}$ absorption spectrum lies near $\lambda = 800$ nm [18], but a photocurrent peak associated with preliminary illumination by light of wavelength λ_1 is not observed in Al–PEPC + N wt % HISD–SnO_2 samples.

The best model of the formation, relaxation, and effect of traps on photoconductivity can be the model based on the assumption concerning the trapping of $Cz^{\bullet+}$ holes in the vicinity of charged fragments of dye molecules. This model is illustrated in Fig. 6 and schematically shows the processes of formation and relaxation of bound states after the dissociation of molecular excitons in PEPC with HISD. This diagram can be presented by the following reactions.

(1) After the absorption of a light quantum with energy $h\nu_2$ in PEPC and the dissociation of a molecular exciton, a hole can be trapped in the vicinity of a negatively charged dye fragment, leading to the formation of the bound state $(Cz^{\bullet+}A^-)$.

(2) The relaxation of the state $(Cz^{\bullet+}A^-)$ is of the activation type and is accompanied by the recombination of $Cz^{\bullet+}$ with the electron remaining after the dissociation of an exciton. The energy of this activation process amounts to 0.17 ∓ 0.03 eV.

(3) An increase in the $Cz^{\bullet+}$ concentration leads to an increase in the optical density of the films in the absorption range of these cation radicals and to dye luminescence quenching.

(4) The absorption of a light quantum $h\nu_1$ by a dye molecule leads to a redistribution of the electron density in it (in Fig. 6, this is depicted by the transfer of an electron e^- from A^- to D^+), which in turn causes the rupture of the bond between the charges in the state $(Cz^{\bullet+}A^-)$.

(5) The liberation of a charge from $Cz^{\bullet+}$ is followed either by its recombination, or by the generation of a free hole p^+ participating in induced photoconductivity.

The same traps also capture the positive charges of holes in the case of photogeneration of EHP as a result of exposure of films to light of wavelength lying in the dye absorption region. As the dye aggregation becomes stronger, the spatial distribution of traps near negatively charged dye fragments decreases, and the probability of hole capture by these traps in an electric field becomes lower. The latter is an additional reason behind the vanishing of the shallow minimum on the curves describing the dependence of $\ln j_1$ on $1/T$ with increasing N (see Fig. 2). Consequently, we can assume that the conformation of carbazole fragments of PEPC in PEPC films with HISD changes near the negative fragments of dye molecules, and traps for holes are formed. As the HISD concentration increases, the spatial distribution of the conformation-type traps becomes narrower. With increasing temperature, the molecular movement of PEPC fragments is enhanced, and these traps are destroyed. When PEPC films with HISD are exposed to light from the absorption range of the dye, photogeneration of singlet electron–hole pairs predominantly takes place. In these pairs, holes are localized at carbazole fragments of PEPC and can be captured in conformation-type traps in the vicinity of negatively charged fragments of dye molecules. As these traps are destroyed by heating, the lifetime of photogenerated holes decreases and the probability of their recombination in weak electric fields increases. The aggregation of the dye is intensified with increasing HISD concentration. In this case, the *S* and *T* states of aggregated dye molecules become closer. The latter leads to an increase in the probability of photogeneration of triplet electron–hole pairs from excited states of the dye. The lifetime of triplet pairs is longer than that of singlet pairs, and hence the probability of their dissociation increases, even in weak electric fields.

REFERENCES

1. N. A. Davidenko and A. A. Ishchenko, Fiz. Tverd. Tela (St. Petersburg) **40**, 629 (1998) [Phys. Solid State **40**, 576 (1998)].
2. N. A. Davidenko, A. A. Ishchenko, and V. A. Pavlov, Zh. Nauchn. Prikl. Fotogr. **44** (2), 45 (1999).
3. *Chemistry of Functional Dyes*, Ed. by Z. Zochioda and J. Shirota (Mita Press, Tokyo, 1993).
4. N. A. Davidenko, A. A. Ishchenko, A. K. Kadashchuk, *et al.*, Fiz. Tverd. Tela (St. Petersburg) **41**, 203 (1999) [Phys. Solid State **41**, 179 (1999)].
5. Yu. A. Skryshevskiĭ, A. A. Ishchenko, A. K. Kadashchuk, *et al.*, Opt. Spektrosk. **88**, 399 (2000) [Opt. Spectrosc. **88**, 352 (2000)].

6. N. A. Davidenko and N. G. Kuvshinskiĭ, Fiz. Tverd. Tela (St. Petersburg) **39**, 1020 (1997) [Phys. Solid State **39**, 916 (1997)].
7. N. A. Davidenko and N. G. Kuvshinsky, Adv. Mater. Opt. Electron. **7**, 255 (1997).
8. V. L. Berdinskiĭ and A. L. Buchachenko, Kinet. Katal. **37**, 659 (1996).
9. A. L. Buchachenko and V. L. Berdinsky, J. Phys. Chem. **100**, 18292 (1996).
10. A. Undzenas, Yu. Grazhulyavichus, and Ya. Urbanavichene, Litov. Fiz. Sb. **21** (6), 106 (1981).
11. N. G. Kuvshinskiĭ, N. A. Davidenko, and V. M. Komko, *Physics of Amorphous Molecular Semiconductors* (Lybid', Kiev, 1994).
12. N. A. Davidenko and A. A. Ishchenko, Chem. Phys. **247**, 237 (1999).
13. M. Pope and C. E. Swenberg, *Electronic Processes in Organic Crystals* (Clarendon Press, Oxford, 1982).
14. A. A. Ishchenko, *Structure and Spectral Luminescence Properties of Polymethine Dyes* (Naukova Dumka, Kiev, 1994).
15. K. I. Zamaraev, R. F. Khaĭrutdinov, and V. P. Zhdanov, *Electron Tunneling in Chemistry* (Nauka, Novosibirsk, 1985).
16. V. P. Gol'danskiĭ, L. I. Trakhtenberg, and V. N. Flerov, *Tunnel Effects in Chemical Physics* (Nauka, Moscow, 1986).
17. N. A. Davidenko, N. G. Kuvshinsky, V. G. Syromyatnikov, and L. N. Fedorova, Adv. Mater. Opt. Electron. **7**, 207 (1997).
18. A. S. Kholmanskiĭ, B. M. Rumyantsev, and E. L. Kuz'mina, Khim. Vys. Énerg. **21**, 379 (1987).

Translated by N. Wadhwa

Physics of the Solid State, Vol. 42, No. 8, 2000, pp. 1410–1413. Translated from Fizika Tverdogo Tela, Vol. 42, No. 8, 2000, pp. 1372–1375.

SEMICONDUCTORS AND DIELECTRICS

Superluminescence of Er^{3+} in an Amorphous Silicon Matrix

V. I. Emel'yanov*, B. V. Kamenev*, P. K. Kashkarov*, E. I. Konstantinova*, V. Yu. Timoshenko*, E. I. Terukov, M. S. Bresler**, and O. B. Gusev****

** Moscow State University, Vorob'evy gory, Moscow, 119899 Russia*
e-mail: boris@ofme.phys.msu.su

*** Ioffe Physicotechnical Institute, Russian Academy of Sciences, Politekhnicheskaya ul. 26, St. Petersburg, 194021 Russia*
e-mail: Eug.terukov@pop.ioffe.rssi.ru

Received December 15, 1999

Abstract—The photoluminescence of Er^{3+} ions in thin films of amorphous silicon has been studied under conditions of intense pumping. A superlinear increase in the amplitude and a shortening of the photoluminescence relaxation times are revealed at a pumping intensity above 200 kW/cm^2. The data obtained are explained by the threshold "switching-on" of the superluminescence mechanism. © *2000 MAIK "Nauka/Interperiodica".*

1. INTRODUCTION

Searching for the methods of producing light-emitting silicon-based devices is an urgent problem of modern physics. As is known [1], the indirect-band-gap structure of silicon is responsible for the low probability of electron transitions with photon emission. In principle, there are two approaches. In the first of them, the spectrum of electronic states of Si is modified at the expense of the nanostructure formation. These conditions are realized, in particular, in the layers of porous silicon [2]. In the second approach, the silicon matrix is doped with luminescence activators, e.g., the ions of rare-earth elements [3]. Rather attractive optical properties are inherent in the trivalent ion Er^{3+}, whose radiation occurs through transitions in the inner 4*f* shell and is characterized by the wavelength $\lambda = 1.54$ μm. The latter corresponds to the transmission maximum of silica optical fibers [4].

Numerous attempts to introduce the Er^{3+} ions into crystalline silicon were made by researchers (see, e.g., [5]). However, the photoluminescence (PL) observed for Er^{3+} ions was sufficiently effective only at the liquid nitrogen temperature, and the heating of samples up to $T = 300$ K induced practically complete PL quenching [6, 7].

Much better results were obtained in the case when Er^{3+} ions were introduced into the matrix of amorphous hydrogenated silicon *a*-Si : H [8]: the effective luminescence at the wavelength $\lambda = 1.54$ μm was observed in these samples at room temperature upon optical and injection excitation [9]. A mechanism of the energy transport from the nonequilibrium electron–hole pairs in *a*-Si : H to the Er^{3+} ions with the subsequent radiative transition was proposed in [8].

In this work, the intracenter luminescence of Er^{3+} ions incorporated into amorphous hydrogenated silicon (*a*-Si : H⟨Er⟩) was studied under conditions of intense photoexcitation in order to elucidate the possibility of producing coherent radiation sources. The effect of a threshold superlinear increase in the intensity and a decrease in the PL relaxation time was found, the latter being treated as a result of "switching-on" stimulated radiation processes (superluminescence).

2. EXPERIMENTAL TECHNIQUE

The technology of forming the *a*-Si : H⟨Er⟩ samples and the subsequent determination of the hydrogen, oxygen, and erbium content were described in detail in [10]. We note only the use of a combined sputtering of the silicon and erbium targets and the magnetron silane decomposition. Concentrations of Er and O were 2.5×10^{20} and 9.8×10^{19} cm^{-3}, respectively. The samples were prepared in the form of an *a*-Si : H⟨Er⟩ film (thickness $h \sim 1$ μm) evaporated onto a silica substrate.

The samples were placed in a vacuum of 10^{-2} Pa and, prior to the measurements, were heated at $T = 520$ K for 20 min. The PL was studied either as a function of the excitation intensity I_{exc} at $T = 300$ K, or as a function of temperature at a constant value of I_{exc}.

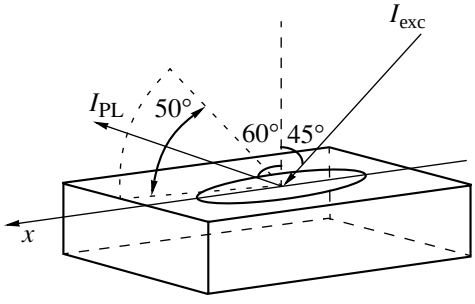

Fig. 1. Scheme of the PL excitation.

1063-7834/00/4208-1410$20.00 © 2000 MAIK "Nauka/Interperiodica"

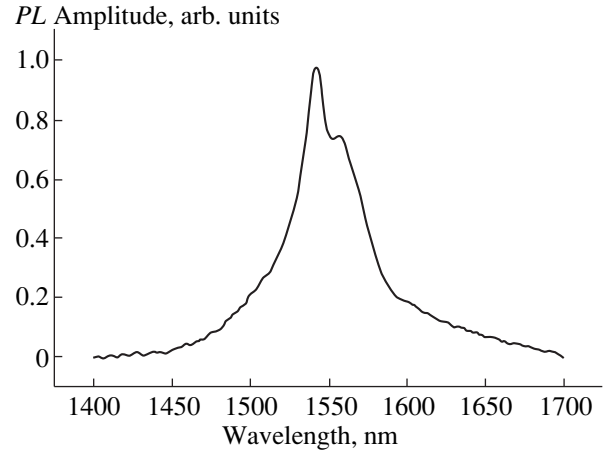

Fig. 2. PL amplitude spectrum at T = 300 K and I_{exc} = 50 kW/cm^2.

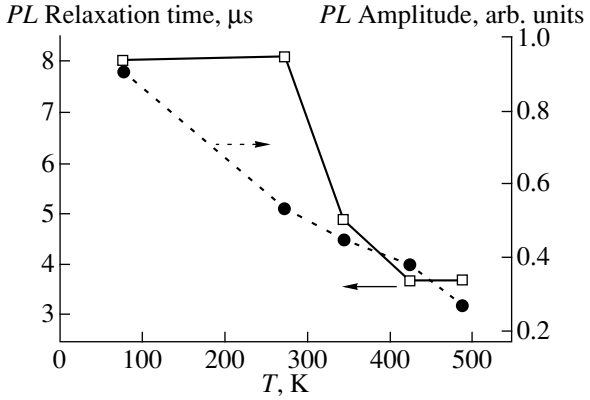

Fig. 3. Dependences of the PL amplitude I_{PL} and relaxation time τ_{PL} on the temperature for I_{exc} = 50 kW/cm^2.

For the PL excitation, two pulsed-periodic lasers were used: a copper vapor laser (λ_1 = 511 nm, τ_1 = 20 ns, single-pulse energy $E_1 \le 25$ μJ, pulse frequency ν_1 = 12 kHz) and a nitrogen laser (λ_2 = 337 nm, τ_2 = 10 ns, $E_2 \le 10$ μJ, ν_2 = 20–100 Hz). The radiation of each laser could be focused onto the sample in a spot ~0.5 mm in diameter (Fig. 1); in this case, the peak intensity I_{exc} reached 400–500 kW/cm^2. It should be noted that since $\nu_2 \ll \nu_1$, the mean radiation intensity of the copper vapor laser exceeded that of the nitrogen laser by more than two orders of magnitude.

The PL was recorded on an SDL-2 automated setup equipped with a Ge photodetector (time constant, ~1 μs) and an S-7-12 sampling oscilloscope.

3. RESULTS

For the *a*-Si : H⟨Er⟩ samples, the stable PL with a spectrum typical of Er in a silicon matrix was observed at T = 300 K. Indeed, the dependence of the PL amplitude (I_{PL}) on λ (Fig. 2) exhibits two maxima, which is usually related in the literature to the splitting of the Er^{3+} ground state in the crystal field of the matrix [11]. The shape of the spectrum virtually did not change when passing from the excitation with the wavelengths λ_1 and λ_2. The PL relaxation was satisfactorily approximated by the exponential law with the effective time $\tau_{PL} \sim 8$ μs for $I_{exc} < 50$ kW/cm^2.

Under sufficiently intense laser pumping of the PL, the thermal factor begins to play a significant role. Hence, first of all, we measured the dependences of I_{PL} and τ_{PL} on the sample temperature (Fig. 3). According to [6, 7], the PL quenching is revealed even at $T > 100$ K; however, a decrease in τ_{PL} is observed at higher T.

The dependences of I_{PL} and τ_{PL} on I_{exc} upon excitation by a copper vapor laser excitation are given in Fig. 4. As is seen from the figure, I_{PL} is proportional to I_{exc} at low levels of pumping and reaches saturation at $I_{exc} \sim 50$ kW/cm^2. Similar results were obtained upon excitation of PL by the radiation of continuous lasers [12]. However, unlike the data reported in [12], a superlinear increase in I_{PL} is observed beyond the saturation region as I_{exc} increases above 100 kW/cm^2.

Changes in the relaxation times of PL with an increase in I_{exc} are of obvious interest. As is seen from Fig. 4, τ_{PL} is virtually constant in the region of a linear increase and saturation of I_{PL}. However, at $I_{exc} >$ 100 kW/cm^2, the time τ_{PL} abruptly decreases (Fig. 4).

Similar dependences $I_{PL}(I_{exc})$ and $\tau_{PL}(I_{exc})$, except for the absence of saturation regions, were obtained upon excitation by a nitrogen laser (Fig. 5). Recall that the mean pumping intensity (responsible for the thermal effects) for the nitrogen laser is two orders of magnitude less than that of the copper vapor laser. Comparing Figs. 3 and 4, we can assume that, in the case of

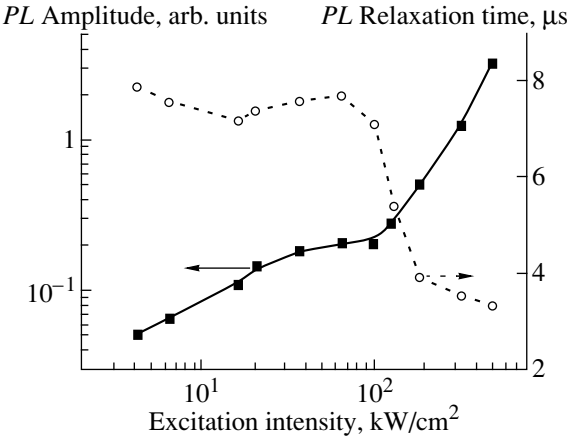

Fig. 4. Dependence of the PL amplitude I_{PL} and relaxation time τ_{PL} on the pumping intensity upon excitation by a copper vapor laser. T = 300 K.

using the latter laser, a horizontal portion of the dependence $I_{PL}(I_{exc})$ is caused by the sample heating. Apparently, the saturation observed in this dependence in the case of a continuous laser has a similar nature [12].

4. DISCUSSION

A superlinear increase in the PL amplitude followed by a simultaneous decrease in τ_{PL} is connected, in our opinion, with a threshold "switching-on" of the PL amplification through stimulated processes [13]. At a certain level of excitation, the inverse population of the levels $^4I_{13/2}$ and $^4I_{15/2}$ of erbium ions is realized and the medium possesses an optical gain.

The volume of a medium, which is occupied by the active Er^{3+} ions, will be modeled as a layer with thickness h and length L. This layer is extended along the x axis (Fig. 1) and filled by two-level atoms with the concentration n. Let a and b be the upper and lower energy levels of the signal transition of an atom, respectively, and ω_{ab} is the frequency of transition between these levels. The permittivity of the layer ($\varepsilon' \approx 12$) is larger than that of the substrate ($\varepsilon_s' \approx 2.2$). Since, from above, the layer borders the vacuum and h is of an order of the radiation wavelength, the layer forms a dielectric planar waveguide [14]. For the lowest waveguide modes, the longitudinal wave number $k \approx \omega\sqrt{\varepsilon'}/c$.

The radiation field inside the layer will be specified in the form of traveling wave

$$E(x) = E_0(x, t) \times \exp(-i\omega t - kx) + \text{complex conjugate}, \quad (1)$$

where $E_0(x, t)$ is the slowly varying field amplitude that is averaged over the cross-section of the waveguide. The equation for the radiation intensity inside the waveguide ($I_{PL} = c^*\varepsilon' E_0^2/2\pi$) has the form

$$\frac{\partial I_{PL}}{\partial t} + c^*\frac{\partial I_{PL}}{\partial x} = -4\pi\alpha''\omega I_{PL} + \left(\frac{\partial I_{PL}}{\partial t}\right)_{sp}, \quad (2)$$

where $c^* = c/(\varepsilon')^{1/2}$ is the velocity of light in a medium. The imaginary part of the resonance ($\omega = \omega_{ab}$) polarizability of the active ions is given by

$$\alpha'' = -\frac{nd_{ab}^2}{\hbar T_2^{-1}}D \equiv -\alpha_0'' D, \quad (3)$$

where d_{ab} is the matrix element of the transition between the operating levels, T_2 is the relaxation time of the active medium, $D = \rho_{aa} - \rho_{bb}$ is the difference between the populations of the upper and the lower levels ($\rho_{aa} + \rho_{bb} = 1$), $\hbar$ is the Planck constant, and n is the concentration of the active ions. The term $\sim\alpha''$ in relationship (2) describes the stimulated radiation, and the source of spontaneous radiation is expressed by the formula

$$\left(\frac{\partial I_{PL}}{\partial t}\right)_{sp} = \frac{1}{2}c^*\hbar\omega n T_1^{-1}(D + 1), \quad (4)$$

where T_1 is the radiative lifetime of the upper operating level.

The equation for the population difference under the condition $T_2 \ll T_1$ has the form

$$\frac{\partial D}{\partial t} + T_1^{-1}(D + 1) = -\frac{8\pi d_{ab}^2}{\hbar^2 T_2^{-1} c^*} I_{PL} D. \quad (5)$$

At the initial instant of time $t = 0$, the signal transition is assumed to be inverted; i.e., $D(t = 0) \equiv D(0)$, and $0 \le D(0) \le 1$.

A set of equations (2) and (5) describes the formation of the superluminescence pulse in the distributed medium of the initially inverted two-level atoms.

With the condition $L \ll c^* T_1$, relationship (2) can be replaced by the simplified equation

$$\frac{\partial I_{PL}}{\partial t} + \gamma_E I_{PL} = -4\pi\alpha''\omega I_{PL} + \left(\frac{\partial I_{PL}}{\partial t}\right)_{sp}, \quad (6)$$

where the term with the constant $\gamma_E = (1 - R)\dfrac{c^*}{L}$ takes into account the exit of the radiation beyond the limits of the operating volume. ($1 - R$ is the effective transmission coefficient of the "resonator" walls).

Under the condition $\gamma_E \gg T_1^{-1}$ from expression (6), with allowance made for (2) and (4), we have in the adiabatic approximation that

$$I_{PL} = \frac{c^*\hbar\omega n T_1^{-1}(D + 1)}{2\gamma_E(1 - \beta D)} \equiv \frac{I_{sp}}{(1 - \beta D)}, \quad (7)$$

where coefficient $\beta = 4\pi|\alpha_0''|\,\omega\gamma_E^{-1} > 0$, and I_{sp} specifies the intensity of the spontaneous PL in the operating volume. Formula (7) defines the excess of the PL intensity above the level of the spontaneous PL due to a stimulated radiation (superluminescence).

Substituting (7) in (5) gives the equation of the kinetics of the population difference for superluminescence

$$\partial D/\partial t = -\frac{(D + 1)}{T_1(1 - \beta D)}. \quad (8)$$

Equation (8), together with (7), describes the kinetics of superluminescence intensity.

Integration of equation (8) for the PL decay time τ_{PL} (defined as a time for which the initial value of the upper level population decreases e times) yields the following expression:

$$\tau_{PL} = T_1(1 - \beta D(0)). \quad (9)$$

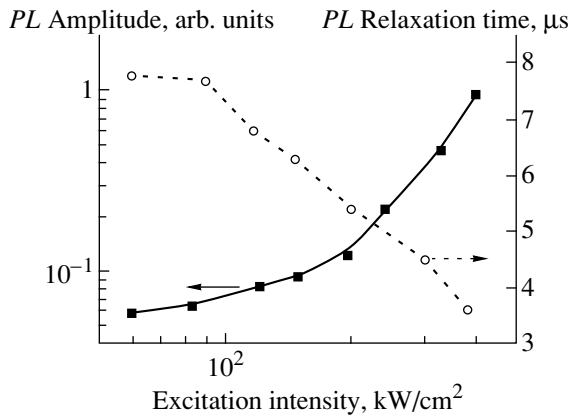

Fig. 5. Dependence of the PL amplitude I_{PL} and relaxation time τ_{PL} on the pumping intensity upon excitation by a nitrogen laser. T = 300 K.

A characteristic value of the initial inversion, at which the stimulated radiation becomes significant, can be evaluated from the condition $\beta D_{cr}(0) = 0.1$. Neglecting the dependence of n on the pumping intensity (i.e., on $D(0)$), we get the estimate

$$D_{cr}(0) = \frac{0.1\hbar T_2^{-1}\gamma_E}{4\pi d_{ab}^2 \omega}. \quad (10)$$

Substitute the known numerical values in formula (10): $L = 5 \times 10^{-2}$ cm^{-2} and $(\varepsilon')^{1/2} \sim 3.5$, then $c^* \sim 8.6 \times 10^9$ cm/s and $\gamma_E \sim 10^{10}$ s^{-1}; moreover, we use $n = 10^{20}$ cm^{-3}, $T_2 \sim 10^{-11}$ s, and $\omega = 1.2 \times 10^{15}$ s^{-1}. According to [15], the dipole moment of transition $d_{ab} = 5 \times 10^{-21}$ CGSE (forbidden transition). Then, from formula (10) for the characteristic initial inversion, at which the superluminescence starts, we have $D_{cr} \sim 10^{-2}$, which is easily achieved experimentally.

Let us correlate the results of the theoretical analysis with those obtained experimentally. It follows from comparing of relationships (7) and (9) that, at n = const, the duration of the superluminescence pulse decreases with an increase in the inversion $D(0)$ (i.e., with an increase in I_{exc}) as many times as the radiation intensity amplitude of Er ions increases. The dependences $I_{PL}(I_{exc})$ and $\tau_{PL}(I_{exc})$ (Figs. 4, 5) qualitatively agree with the calculations. However, the relative increase in the PL intensity is noticeably larger than follows from the comparison of formulas (7) and (9) for n = const. This difference is likely caused by the simplifications used in the calculations, which should affect the form of the analytical expressions (7) and (9).

In conclusion, it should be noted that the processes of radiation of the Er^{3+} ions incorporated into the matrix of amorphous silicon were studied under conditions of intense pumping. The threshold superlinear increase in the intensity I_{PL} and decrease in the PL relaxation time τ_{PL} were found at the power density $\geq$200 kW/cm^2. The data obtained qualitatively agree with the results of the calculations, which take into account the amplification of spontaneous radiation in the system under study. The latter fact indicates the possibility of producing sources of the coherent stimulated radiation in *a*-Si : H⟨Er⟩ thin films.

ACKNOWLEDGMENTS

We are grateful to B. P. Zakharchenya for the support of this work and fruitful discussions of the results.

This work was supported by the INCO-COPERNICUS (no. 977048-SIER), the Russian Foundation for Basic Research (no. 99-02-16664), and the State Program of the Ministry of Science and Technology of the Russian Federation "Surface Atomic Structures" (project nos. 4.1.99 and 1S91.1LF020).

REFERENCES

1. V. L. Bonch-Bruevich and S. G. Kalashnikov, *The Physics of Semiconductors* (Nauka, Moscow, 1977).
2. L. T. Canham, Appl. Phys. Lett. **57**, 1046 (1990).
3. *Rare Earth Doped Semiconductors*, Ed. by G. S. Pomrenke, P. B. Klein, and D. W. Langer (Materials Research Society, Pittsburgh, 1993), Vol. 301.
4. K. Iga and S. Kinoshita, *Progress Technology for Semiconductors Lasers*, Springer Ser. in Mater. Sci. (Springer-Verlag, Berlin, 1996), Vol. 30.
5. W. Jantsch, S. Lanzerstorfer, L. Palmetshofer, *et al.*, J. Lumin. **80**, 9 (1999).
6. F. Priolo, G. Franzo, S. Coffa, *et al.*, J. Appl. Phys. **78**, 3874 (1995).
7. J. H. Shin, R. Serna, G. N. van den Hoven, *et al.*, Appl. Phys. Lett. **68**, 997 (1996).
8. W. Fuhs, I. Ulber, G. Weiser, *et al.*, Phys. Rev. B **56**, 9545 (1997).
9. O. Gusev, M. Bresler, A. Kuznetsov, *et al.*, J. Non-Cryst. Solids **227–230**, 1164 (1998).
10. V. Marakhonov, N. Rogachev, J. Iskalov, *et al.*, J. Non-Cryst. Solids **137–138**, 1164 (1991).
11. H. Przybylinska, W. Jantsch, Yu. Suprun-Belevitch, *et al.*, Phys. Rev. B **54**, 2532 (1996).
12. M. S. Bresler, O. B. Gusev, V. Kh. Kudoyarova, *et al.*, Appl. Phys. Lett. **67**, 3599 (1995).
13. A. V. Andreev, V. I. Emel'yanov, and Yu. A. Il'inskii, *Cooperative Effects in Optics* (Inst. of Physics Publ., Bristol, 1993).
14. M. B. Vinogradova, O. V. Rudenko, and A. P. Sukhorokov, *The Theory of Waves* (Nauka, Moscow, 1990).
15. I. Yassievich, M. Bresler, and O. Gusev, J. Non-Cryst. Solids **226**, 192 (1998).

Translated by T. Galkina

Physics of the Solid State, Vol. 42, No. 8, 2000, pp. 1414–1421. Translated from Fizika Tverdogo Tela, Vol. 42, No. 8, 2000, pp. 1376–1383.

SEMICONDUCTORS AND DIELECTRICS

Peak in the Magnetic-Field Dependence of Diffusion-Induced Thermopower for *n*-Bi–Sb Semiconducting Alloys

V. D. Kagan, N. A. Red'ko, N. A. Rodionov, and V. I. Pol'shin

Ioffe Physicotechnical Institute, Russian Academy of Sciences, Politechnicheskaya ul. 26, St. Petersburg, 194021 Russia

e-mail: Nikolaj.A.Redko@shuvpop.ioffe.rssi.ru

Received January 20, 2000

Abstract—A peak is detected on the dependence of the diffusion-induced thermopower on transverse magnetic field in degenerate semiconducting alloys n-$Bi_{1-x}Sb_x$ ($0.07 \le x \le 0.15$) doped with tellurium donor impurity. The temperature gradient is directed along the bisector axis C_1 of the monocrystalline sample and the magnetic field is along the triad axis C_3. The electron spectrum of the Bi–Sb alloys under investigation consists of three equivalent ellipsoids with distinctly different effective masses along the axes of the ellipsoid ($m_\parallel/m_\perp \ge 250$). A simple kinetic theory shows that the presence of the peak on the diffusion thermopower is a manifestation of this strong anisotropy in the electron spectrum and of the additive contribution of all three ellipsoids to electron transport. The nonmonotonic dependence of thermopower on the transverse magnetic field makes it possible to determine the electron relaxation time, while the temperature dependence of this relaxation time can be used to separate the relaxation time for electrons scattered from ionized impurities and from acoustic phonons. © *2000 MAIK "Nauka/Interperiodica".*

An analysis of the diffusion thermopower of semiconductors provides vital information on the type of charge carriers, their effective mass, scattering mechanisms, and the value of the chemical potential. Thermopower emerges in semiconductors in the presence of a temperature gradient leading to diffusion of electrons with an energy higher than the chemical potential energy by ~kT from its hot end to the cold one. The electron concentration in the sample is redistributed, increasing at the cold end and decreasing at the hot end. The emerging electric field induces a countercurrent of "cold" electrons having an energy smaller than the chemical potential energy by ~kT. As the thermodynamic equilibrium sets in for the ongoing processes, an internal electric field determining the diffusion thermopower is induced. The countercurrents of "hot" and "cold" electrons persist, but the resultant current at each point of the semiconductor is equal to zero [1].

The diffusion thermopower for a semiconductor with an isotropic electron spectrum is a function of temperature, chemical potential ζ, the parameter r of electron scattering mechanism, contained in the energy dependence of the electron relaxation time $\tau \sim \mathscr{E}^{r-1/2}$ ($r = 0$ for electron scattering from acoustic phonons or from pointlike impurities, and $r = 2$ for scattering from impurity ions), and the parameter $\gamma = \{4\zeta(1 + \zeta/\mathscr{E}_g)\}/\{\mathscr{E}_g(1 + 2\zeta/\mathscr{E}_g)^2\}$ characterizing the extent of deviation from the parabolicity of the band and depending on the energy gap $\mathscr{E}_g$ and on the chemical potential [1]

$$\alpha(T) = -\frac{k}{e}\frac{\pi^2}{3}\left(\frac{kT}{\zeta}\right)(r + 1 - \gamma)\frac{(1 + 2\zeta/\mathscr{E}_g)}{(1 + \zeta/\mathscr{E}_g)}, \qquad (1)$$

where e is the absolute value of the electron charge. Formula (1) is written for a degenerate semiconductor of the n type.

Figure 1a shows the temperature dependence of the diffusion thermopower (1) for a degenerate semiconductor of the n-type taking into account the mechanism of electron scattering from impurity ions at $T \le T_1$ and from acoustic phonons or at pointlike impurities at $T \ge T_2$.

Diffusion thermopower of a semiconductor placed into a transverse magnetic field ($\mathbf{H} \perp \nabla\mathbf{T}$) depends monotonically on the magnetic field. The absolute value of the thermopower $\alpha(H)$ in a weak magnetic field is higher than the thermopower $\alpha(0)$ in zero magnetic field in the case of electron scattering from acoustic phonons or from pointlike impurities, but is smaller in the case of scattering from ionized impurities [1]. The diffusion thermopower variation for an n-type degenerate semiconductor in a magnetic field is given by

$$\Delta\alpha(H) = \alpha(H) - \alpha(0) = \frac{k}{e}\frac{\pi^2}{3}\frac{(uH/c)^2}{1 + (uH/c)^2} \times \left(\frac{kT}{\zeta}\right)\left(r - \frac{1}{2} - \gamma\right)\frac{(1 + 2\zeta/\mathscr{E}_g)}{(1 + \zeta/\mathscr{E}_g)}, \qquad (2)$$

where u is the electron mobility. Formula (2) shows that $\Delta\alpha(H) < 0$ and $|\alpha(H)| > |\alpha(0)|$ for an n-type semiconductor for $r = 0$, while $\Delta\alpha(H) > 0$ and $|\alpha(H)| < |\alpha(0)|$ for $r = 2$ (Fig. 1a).

Diffusion thermopower in a classically strong transverse magnetic field does not depend on the mechanism of electron scattering and attains the limiting value α_∞.

1063-7834/00/4208-1414$20.00

For a degenerate *n*-type semiconductor, α_∞ can be expressed as follows [1]:

$$\alpha_\infty = -\frac{k}{e}\frac{\pi^2}{2}\left(\frac{kT}{\zeta}\right)\frac{(1+2\zeta/\mathscr{E}_g)}{(1+\zeta/\mathscr{E}_g)}. \quad (3)$$

In actual practice, α_∞ is used for determining the chemical potential and the effective mass of a semiconductor from the known electron concentration.

Figure 1a shows the temperature dependence of α_∞ (3) for a degenerate *n*-type semiconductor, while Fig. 1b shows the magnetic-field dependence $\Delta\alpha(H)$ (2) and the limiting values of $\Delta\alpha_\infty$ for $uH/c \gg 1$: $\Delta\alpha_1(H)$ for electron scattering from impurity ions ($r = 2$) and $\Delta\alpha_2(H)$for scattering from acoustic phonons or from pointlike impurities ($r = 0$).

The measurement of the transverse Nernst–Ettingshausen effect along with the thermopower on the same semiconducting sample in a transverse magnetic field makes it possible to judge independently on the electron scattering mechanism. This effect is an analog of the Hall effect and can be described as follows: if there exists a temperature gradient $\nabla_x T$ along a semiconductor placed in a transverse magnetic field $H_z \perp \nabla_x T$, an electric field $E_y \perp H_z$, $\nabla_x T$ is induced [1]: $E_y = -QH_z\nabla_x T$, where Q is the Nernst–Ettingshausen coefficient.

The Nernst–Ettingshausen coefficient for a degenerate semiconductor in a weak magnetic field is independent of the field, its sign being determined by the electron scattering mechanism [1]:

$$Q_0 = \frac{k}{e}\frac{\pi^2}{3}\frac{u}{c}\left(\frac{kT}{\zeta}\right)\left(r-\frac{1}{2}-\gamma\right)\frac{(1+2\zeta/\mathscr{E}_g)}{(1+\zeta/\mathscr{E}_g)}, \quad (4)$$

where e is the absolute value of the electron charge.

In a classically strong magnetic field, the Nernst–Ettingshausen coefficient for a degenerate semiconductor is a function of the magnetic field and is smaller than Q_0 by a factor of $(uH/c)^2$:

$$Q_\infty = (uH/c)^{-2}Q_0. \quad (5)$$

Figure 1c shows the temperature dependence of the Nernst–Ettingshausen coefficient (4) for a degenerate semiconductor in a weak magnetic field. The coefficient Q is positive for electron scattering from ionized impurities ($r = 2$) and negative for scattering from acoustic phonons or pointlike impurities ($r = 0$).

For InSb, AsSb, GaAs, HgTe, InP, AlSb and other semiconductors with an isotropic electron spectrum, the theoretical dependences [1] (including the above dependences for α and Q, which together make it possible to determine the electron parameters in these materials) were confirmed experimentally.

In the present work, we present the results of investigation of *n*-Bi–Sb semiconducting alloys with a strongly anisotropic energy spectrum of *L*-electrons for which the diffusion thermopower exhibits a nonmonotonic dependence on the transverse magnetic field for $\mathbf{H} \parallel C_3$ and propose a theoretical interpretation of this dependence.

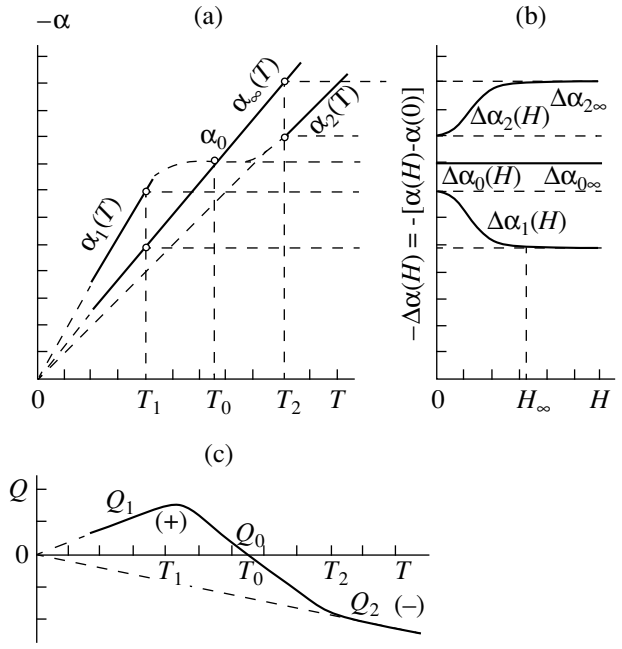

Fig. 1. Characteristic temperature dependences of the diffusion thermopower for *n*-type degenerate semiconductors in a transverse classically strong magnetic field (α_∞) and in zero magnetic field (calculated by using formulas (3) and (1), respectively) for different mechanisms of electron scattering: $\alpha_1(T)$ for scattering from impurity ions ($r = 2$) and $\alpha_2(T)$ for scattering from acoustic phonons or pointlike impurities ($r = 0$) (a); field dependence of the thermopower variation $\Delta\alpha(H) = \alpha(H) - \alpha(0)$ in a transverse magnetic field for degenerate *n*-type semiconductors, calculated by using formula (2) for different mechanisms of electron scattering: $\Delta\alpha_1(H)$ for scattering from impurity ions ($r = 2$) and $\Delta\alpha_2(H)$ for scattering from acoustic phonons or pointlike impurities ($r = 0$), as well as the limiting values of $\Delta\alpha_\infty$ for $uH/c \gg 1$ (b); the temperature dependence of the Nernst–Ettingshausen coefficient for degenerate semiconductors in a weak magnetic field, calculated by using formula (4), for different mechanisms of electron scattering: Q_1 for scattering from impurity ions ($r = 2$) and Q_2 for scattering from acoustic phonons or pointlike impurities ($r = 0$).

1. DISCUSSION OF EXPERIMENTAL RESULTS

The kinetic parameters, i.e., the thermopower α, the resistivity ρ, the Hall coefficient R and the Nernst–Ettingshausen coefficient Q as functions of temperature ($1.4\ \mathrm{K} \le T < 40\ \mathrm{K}$) and magnetic field ($0 \le H < 20$ kOe) were measured on monocrystalline samples of semiconducting alloys *n*-$Bi_{1-x}Sb_x$ ($0.07 \le x \le 0.15$). The samples were cut from monocrystalline ingots on an electrical-erosion setup in the form of $3 \times 3 \times 30$-mm right parallelepipeds with the faces perpendicular to the crystallographic axes C_1, C_2, C_3. After cutting, the samples were subjected to chemical etching in a mixture of C_2H_5OH and HNO_3 taken in the 1 : 1 ratio. The sample

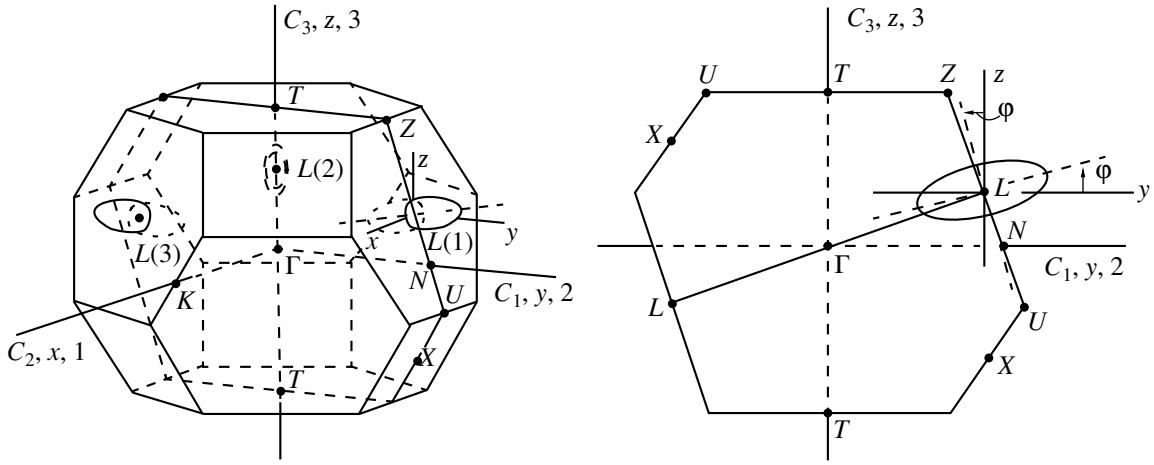

Fig. 2. Brillouin zone for degenerate semiconducting alloys *n*-Bi–Sb with three electron ellipsoids with the centers at the *L* points, through which the reflection planes pass. One of the three sections of the Brillouin zone by a reflection plane is shown separately. The ellipsoids in the zone are equivalent and are tilted to the crystal axes. One of the minor axes of an ellipsoid coincides with the binary axis C_2 of the crystal, while the other two ellipsoid axes form an angle φ with the trigonal axis C_3 and the bisector axis C_1.

length coincided with the bisector axis C_1 of the crystal, which made it possible to measure the tensor components $\rho_{22}(\mathbf{j} \parallel C_1)$ of resistivity and $\alpha_{22}(\nabla\mathbf{T} \parallel C_1)$ of thermopower.

The Fermi surface of Bi–Sb semiconducting alloys doped with a donor impurity consists of three electron ellipsoids [2] with the centers at *L* points of the Brillouin zone, which are located in reflection planes (Fig. 2). One of the smaller ellipsoid axes coincides with the binary axis C_2 of the crystal, about which the ellipsoids are turned through a small angle $\varphi = (5–6)°$ [2]. As a result of such a rotation, the other two axes form an angle φ with the crystallographic axes C_1 and C_3. The ellipsoids for Bi–Sb alloys are equivalent in view of the crystal symmetry and are characterized by strongly anisotropic effective masses ($m_\parallel/m_\perp \geq 250$) [3]. It is also important to note that if the direction of the magnetic field coincides with the trigonal axis of the crystal ($\mathbf{H} \parallel C_3$), the cyclotron frequency is the same for all electrons, and hence the conditions of a classically strong magnetic field simultaneously holds for all of them. The fulfillment of this condition is an important requirement for analyzing the diffusion thermopower as a function of the transverse magnetic field in Bi–Sb alloys and for determining its limiting value (α_∞) in a classically strong magnetic field. The value of α_∞ was used in [3] for determining the density of states and the electron density-of-states mass at the Fermi level for *n*-Bi–Sb alloys.

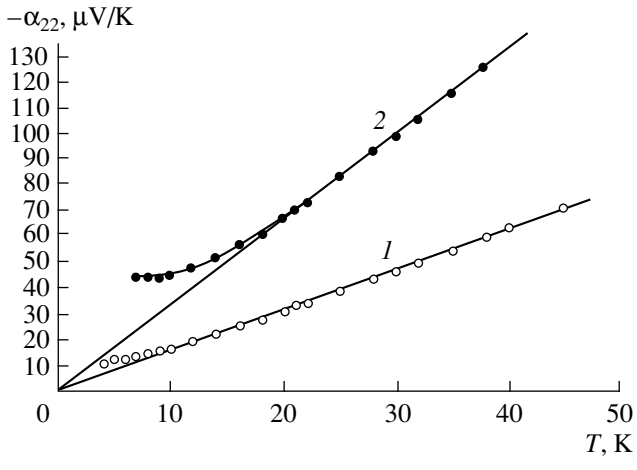

Fig. 3. Temperature dependence of the thermopower $\alpha_{22}(0)$ of a semiconducting alloy *n*-$Bi_{0.93}Sb_{0.07}$ in zero magnetic field ($\nabla\mathbf{T} \parallel C_1$) (*1*) and α_∞ in a transverse classically strong magnetic field for $\mathbf{H} \parallel C_3$ (*2*). The solid curves plotted from the experimental results on $\alpha_{22}(0)$ and α_∞ for $T > 18$ K extrapolate the linear dependence of diffusion thermopower.

The Bi–Sb alloys used for measurements were doped with a donor impurity ~0.001 at. % Te; as a result, the electron concentration in the samples amounted to ~$(1–2) \times 10^{17}$ cm^{-3} (the electron concentration in each sample was determined from Hall measurements).

Figure 3 shows the temperature dependences of the thermopower of an *n*-$Bi_{0.93}Sb_{0.07}$ semiconducting alloy both in zero magnetic field [$\alpha(0)$] and in a transverse classically strong magnetic field (α_∞). Such dependences are typical of all the studied *n*-$Bi_{1-x}Sb_x$ alloys ($0.07 \leq x \leq 0.15$). The data presented in the figure show that the linear dependence of the thermopower $\alpha_{22}(0)$ and α_∞ at high temperatures can be extrapolated exactly to zero as predicted by formulas (1) and (3) for the diffusion thermopower ($\alpha \sim kT/\zeta$), The electron concentration for the *n*-$Bi_{0.93}Sb_{0.07}$ alloy was 1.37×10^{17} cm^{-3}, the Fermi energy $\mathscr{E}_F = 18.6$ meV, the energy gap $\mathscr{E}_{gL} = 7.5$ meV, and $m_\parallel/m_\perp \cong 320$. The deviations from the linear temperature dependence observed for $\alpha_{22}(0)$ and α_∞ in Fig. 3 at $T < 18$ K are associated with the presence of

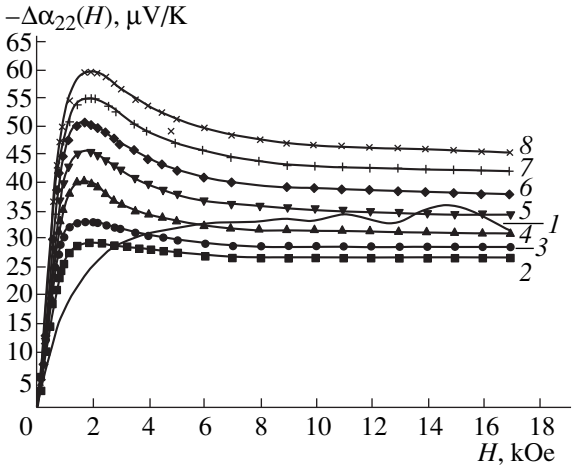

Fig. 4. Variation of the thermopower $\Delta\alpha_{22}(0) = \alpha_{22}(H) - \alpha_{22}(0)$ ($\nabla\mathbf{T} \parallel C_1$) in a transverse magnetic field for $\mathbf{H} \parallel C_3$ for a semiconducting alloy n-$Bi_{0.93}Sb_{0.07}$at various temperatures (K): 4.8 (*1*), 10.6 (*2*), 12.3 (*3*), 15.4 (*4*), 18.6 (*5*), 21 (*6*), 23.2 (*7*), and 25.1 (*8*).

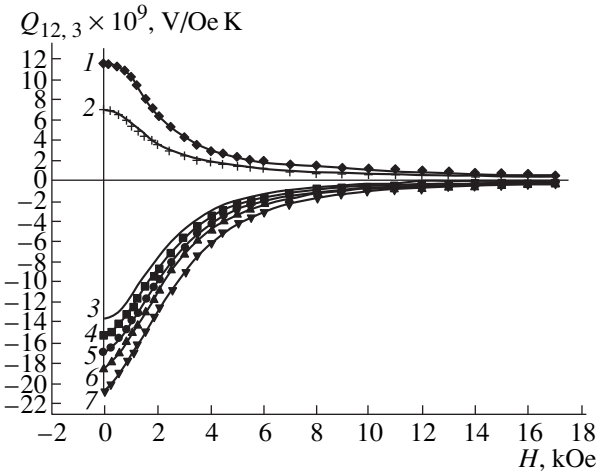

Fig. 5. Magnetic-field dependence of the Nernst–Ettingshausen coefficient $Q_{12,3}$ ($\nabla\mathbf{T} \parallel C_1$, $\mathbf{H} \parallel C_3$) for the semiconducting alloy n-$Bi_{0.93}Sb_{0.07}$ at various temperatures (K): 4.8 (*1*), 6.2 (*2*), 18.6 (*3*), 21 (*4*), 23.2 (*5*), 25.1 (*6*), and 29.3 (*7*).

the phonon component of thermopower associated with the electron drag effect.

In the Bi–Sb alloys under investigation, the variation of the diffusion thermopower $\Delta\alpha_{22}(H) = \alpha_{22}(H) - \alpha_{22}(0)$ ($\nabla\mathbf{T} \parallel C_1$) in a magnetic field $\mathbf{H} \parallel C_3$ is a nonmonotonic function of the magnetic field. The typical curves for the n-$Bi_{0.93}Sb_{0.07}$ alloy at temperatures above 18 K are presented in Fig. 4. We are not aware of any data concerning the diffusion thermopower for other anisotropic semiconductors exhibiting a nonmonotonic dependence on a transverse magnetic field. In contrast to diffusion thermopower, the phonon component of the thermopower in the $Bi_{0.93}Sb_{0.07}$ alloy exhibits a monotonic magnetic-field dependence at $T < 10$ K, which is shown in Fig. 4 (curve *1*).

The absolute value of the diffusion thermopower in Bi–Sb alloys increases in a transverse magnetic field (see Fig. 3), which can be due to electron scattering from acoustic phonons or from pointlike defects in accordance with the theoretical formula (2) in [1]. The temperature dependence of the resistivity of degenerate semiconducting Bi–Sb alloys is typically metallic. For $T < 10$ K, a temperature-independent residual resistivity is observed, while for $T > 10$ K the resistivity increases with temperature, indicating that the scattering of electrons from acoustic phonons comes into play, along with their scattering from impurities.

Figure 5 shows the magnetic-field dependence of the Nernst–Ettingshausen coefficient $Q_{12,3}$($\nabla\mathbf{T} \parallel C_1$, $\mathbf{H} \parallel C_3$) for the degenerate semiconducting alloy n-$Bi_{0.93}Sb_{0.07}$ at various temperatures. At $T > 10$ K, the Nernst–Ettingshausen coefficient is negative which, according to theory [1], corresponds to the electron scattering from acoustic phonons or pointlike impurities.

A theoretical analysis of the observed peak on the magnetic field dependence of the diffusion thermopower for semiconducting Bi–Sb alloys with a highly anisotropic energy spectrum of L-electrons is presented below.

The magnetic-field dependence of the diffusion thermopower tensor was determined by solving the kinetic equation for a strongly anisotropic nonparabolic energy–momentum relation for L-electrons for semiconducting Bi–Sb alloys in the Lax model,

$$\mathscr{E}_\mathbf{p} = \left[\left(\frac{\mathscr{E}_g}{2}\right)^2 + \frac{\mathscr{E}_g}{2}\left(\frac{p_1^2}{m_1} + \frac{p_2^2}{m_2} + \frac{p_3^2}{m_3}\right)\right]^{1/2} - \frac{\mathscr{E}_g}{2}, \qquad (6)$$

where $\mathscr{E}_g$ is the band gap, $\mathbf{p}$ is the electron quasimomentum, and m_i are the effective masses of electrons in an ellipsoid.

We can write the following kinetic equation for the nonequilibrium correction to the electron distribution function $\Delta f_\mathbf{p} = f_\mathbf{p} - f_0(\mathscr{E}_\mathbf{p})$ for an ellipsoid (in the coordinate frame based on its principal axes):

$$\frac{e}{c}[\mathbf{vH}]\frac{\partial \Delta f_\mathbf{p}}{\partial \mathbf{p}} + \frac{1}{\tau(\mathscr{E}_\mathbf{p})}\Delta f_\mathbf{p} = \left(-\frac{\partial f_0}{\partial \mathscr{E}_\mathbf{p}}\right)\left[e\mathbf{Ev} - \frac{\mathscr{E}_\mathbf{p} - \zeta}{T}\mathbf{v}\nabla\mathbf{T}\right], \qquad (7)$$

where $\mathbf{E}$ and $\mathbf{H}$ are the electric and magnetic field strengths, $v_i = \partial\mathscr{E}_\mathbf{p}/\partial p_i = \dfrac{p_i}{m_i(1 + 2\mathscr{E}_\mathbf{p}/\mathscr{E}_g)}$ are the electron velocity components, $f_0 = [\exp((\mathscr{E}_\mathbf{p} - \zeta)/kT) + 1]^{-1}$ is the Fermi distribution function and ζ is the chemical potential of the electrons.

We shall confine our analysis of electron scattering from phonons and impurities to the isotropic relaxation time approximation. In the case of an anisotropic energy spectrum of electrons, the action of the scattering operator on the distribution function can be replaced with simple multiplication by its relaxation time only in the simple case when the total relaxation time coincides with the "departure" time. The electron scattering frequency in this case is proportional to the electron density of states $\rho(\mathscr{E})$:

$$\rho(\mathscr{E}) = \frac{(2m_1m_2m_3)^{1/2}}{\pi^2\hbar^2}\left[\mathscr{E}\left(1+\frac{\mathscr{E}}{\mathscr{E}_g}\right)\right]^2\left(1+\frac{2\mathscr{E}}{\mathscr{E}_g}\right). \quad (8)$$

For solving equation (7), we first find the electrical conductivity tensor $\hat{\sigma}$ and thermoelectricity tensor $\hat{\beta}$ in the symmetry axes of an ellipsoid and then carry out a simple transformation, taking into account the inclination of the ellipsoid to the crystallographic axes of a Bi–Sb alloy. The thermopower tensor is obtained by multiplying the thermoelectricity tensor and the resistivity tensor, which is the inverse of the electrical conductivity tensor. The diagonal component of the resultant tensor equals the component of diffusion thermopower $\alpha(H)$, while the off-diagonal component defines the components of the Nernst–Ettingshausen coefficient Q.

The formula obtained for the diffusion thermopower $\alpha(H)$for $\mathbf{H} \perp \nabla\mathbf{T}$ takes into account the contribution of electrons from the three ellipsoids, as well as the anisotropy of the electron energy spectrum, the deviation from the parabolicity of the band, and the inclination of the ellipsoid axes to the crystallographic axes of the *n*-type semiconducting crystal:

$$\alpha(H) = -\frac{k}{e}\frac{\pi^2}{3}\frac{kT}{\zeta} \times\left\{\frac{3(1+2\zeta/\mathscr{E}_g)}{2(1+\zeta/\mathscr{E}_g)}+a\frac{\Omega^2\tau^2(\delta-2)-\delta}{(1+\Omega^2\tau^2)(\delta+\Omega^2\tau^2)}\right\}, \quad (9)$$

where

$$a = \frac{1}{2}+\frac{\zeta}{2\mathscr{E}_g(1+\zeta/\mathscr{E}_g)}+\frac{4\zeta}{\mathscr{E}_g(1+2\zeta/\mathscr{E}_g)}, \quad (10)$$

$\Omega = \dfrac{eH}{c\sqrt{M_1M_4}}$ is the cyclotron frequency for electrons, which has the same value for all ellipsoids for $\mathbf{H} \parallel C_3$; $M_i = m_i(1+2\zeta/\mathscr{E}_g)$ are the effective masses of electrons in an ellipsoid at the Fermi level; $\delta = (M_1 + M_4)^2/(4M_1M_4)$ is a parameter taking into account the anisotropy of the electron energy spectrum; and e is the absolute value of the electron charge. In view of the inclination of an ellipsoid in Bi–Sb alloys to the crystallographic axes C_1 and C_3 by the angle φ, the effective mass of an electron along the C_1 axis is defined by the formula

$$\frac{1}{M_4} = \frac{\cos^2\varphi}{M_2}+\frac{\sin\varphi}{M_3}. \quad (11)$$

If we disregard the inclination of the ellipsoid to the crystallographic axes, the value of M_4 will be equal to M_2, viz., the largest of the effective masses of the ellipsoid. If we take into account the inclination of the ellipsoid, the effective mass M_4 is determined, in accordance with (11), not only by the mass M_2, but also by the smaller mass M_3. It was found that the contribution of the second tern in (11) for Bi–Sb alloys is approximately twice as large as that of the first term, in view of the small angle of inclination $\varphi \cong (5\text{–}6)°$ and the small value of the effective mass M_3 ($M_2/M_3 \cong 300$).

The parameter a emerges in (9) and (10), owing to the differential nature of the diffusion thermopower, and is associated with the dependence of the electron relaxation time τ and effective mass M on the Fermi energy:

$$a = \frac{d\ln(1/\tau(\zeta))}{d\ln\zeta}+\frac{d\ln M}{d\ln\zeta}. \quad (12)$$

Formula (9) can be used to derive the expressions for the diffusion thermopower in a classically strong transverse magnetic field α_∞ ($\Omega\tau \gg 1$) and the variation of thermopower $\Delta\alpha(H) = \alpha(H) - \alpha(0)$ due to the transverse magnetic field for an *n*-type semiconductor:

$$\alpha_\infty = -\frac{k}{e}\frac{\pi^2}{2}\frac{kT}{\zeta}\frac{(1+2\zeta/\mathscr{E}_g)}{(1+\zeta/\mathscr{E}_g)}, \quad (13)$$

$$\Delta\alpha(H) = -\frac{k}{e}\frac{\pi^2}{3}\frac{kT}{\zeta}a\left\{1+\frac{\Omega^2\tau^2(\delta-2)-\delta}{(1+\Omega^2\tau^2)(\delta+\Omega^2\tau^2)}\right\}. \quad (14)$$

Expressions (3) and (13) for α_∞ coincide. After transformations taking into account equation (8), formula (13) for α_∞ depends only on the electron density of states and coincides with the general expression derived by Ravich [4]:

$$\alpha_\infty = -\frac{k}{e}\frac{\pi^2}{2}\frac{kT}{n}(3\rho(\zeta)), \quad (15)$$

where $n = \dfrac{(m_1m_2m_3)^{1/2}}{\pi^2\hbar^3}(2\zeta)^{3/2}(1+\zeta/\mathscr{E}_g)^{3/2}$ is the concentration and 3ρ is the electron density of states for the three ellipsoids.

The function $\Delta\alpha(H)$ is negative, since the parameter a is positive in view of the assumption on isotropic scattering of electrons.

The nonmonotonic behavior of $\Delta\alpha(H)$ as a function of the transverse magnetic field is determined by the existence of three electron ellipsoids and by the value of the anisotropy parameter δ. Equation (14) shows that

the function $\Delta\alpha(H)$ increases monotonically from zero to the limiting value $\Delta\alpha_\infty$ for $1 < \delta < 2$, while for $\delta > 2$ the function $\Delta\alpha(H)$ has a peak at

$$(\Omega\tau)^2_{\max} = \frac{\delta + (\delta - 1)\sqrt{2\delta}}{(\delta - 2)}. \quad (16)$$

For a single ellipsoid with an anisotropic energy spectrum for electrons, the electrical conductivity and thermoelectricity tensors acquire only the conventional factor $(1 + \Omega^2\tau^2)^{-1}$. However, the magnetic-field dependence in the resistivity tensor disappears, and the monotonic magnetic-field dependence $\alpha(H)$ is determined by the dependence of the thermoelectricity tensor. In the case of three ellipsoids in Bi–Sb alloys for $\mathbf{H} \parallel C_3$, the cyclotron frequency is the same, while the total electrical conductivity tensor is the sum of the electrical conductivity tensors for the three ellipsoids. As a result, the total resistivity tensor is proportional to $(1 + \Omega^2\tau^2)/(\delta + \Omega^2\tau^2)$. After the multiplication of the resistivity tensor by the thermoelectricity tensor, the denominator of formula (14) for $\Delta\alpha(H)$ acquires both factors $(\delta + \Omega^2\tau^2)$ and $(1 + \Omega^2\tau^2)$, which leads to a nonmonotonic dependence.

In order to determine the reciprocal relaxation time $1/\tau$ for electrons in Bi–Sb alloys, we constructed the temperature dependences for two characteristic magnetic fields H_1 and H_2. For the magnetic field H_1, the thermopower $\Delta\alpha(H_1)$ has a peak, while for the magnetic field H_2 (smaller than H_1), the equality $\Delta\alpha(H_2) = \Delta\alpha_\infty$ holds. The magnetic field H_1 is defined by formula (16), while the magnetic field H_2 can be found from the condition

$$\omega^2\tau^2 = \frac{\delta}{\delta - 2}. \quad (17)$$

The temperature dependences of H_1 and H_2 make it possible to determine an important kinetic parameter, viz., the reciprocal electron relaxation time, as a function of temperature. The quantity $1/\tau$ determined from the data on $H_1(T)$ and $H_2(T)$ has a linear dependence on temperature:

$$1/\tau = C_1 T + C_2. \quad (18)$$

The mechanisms of scattering for electrons are determined by impurities and acoustic phonons. The electron scattering from impurities in degenerate semiconductors is independent of temperature [1]. On the other hand, the electron scattering from acoustic phonons at $T > \Theta_e$ depends on temperature since $1/\tau_{e-ph}$ is proportional to the equilibrium number of phonons N_{ph}, which is determined by the Rayleigh distribution, $N_{ph} = kT/(\hbar\omega_{\mathbf{q}})$, where $\omega_{\mathbf{q}}$ is the phonon frequency. The Debye electron temperature $\Theta_e = 2p_F s$ is determined by the limiting phonons interacting with electrons on the Fermi surface ($q = 2p_F$). Here p_F is the Fermi momentum for electrons and s is the velocity of sound. According to our estimates, $\Theta_e \cong 4$ K in the investigated Bi–Sb alloys.

We assume that the first term in formula (18) is determined by the electron–phonon scattering, while the second term is determined by the scattering of electrons from the impurities. The existence of the temperature dependence of $1/\tau$ allowed us to separate $1/\tau_{e-ph}$ and $1/\tau_{e-im}$ in Bi–Sb alloys by plotting $1/\tau$ as a function of T. The value of $1/\tau_{e-im}$ was determined by extrapolating the temperature dependence of $1/\tau$ to low temperatures, and $1/\tau_{e-ph}$ was found from the slope of this curve. The reciprocal relaxation time for $Bi_{0.93}Sb_{0.07}$ alloy was found to be as follows: $1/\tau_{e-im} = 1.3 \times 10^{11}$ s^{-1} and $1/\tau_{e-ph} = 2 \times 10^9 T$ s^{-1}.

Although the temperature for which the diffusion thermopower of Bi–Sb alloys was investigated is relatively high ($T > 18$ K), the obtained value of $1/\tau_{e-im}$ proved to be several times larger than $1/\tau_{e-ph}$. This means that the electron scattering from impurities is much stronger than the electron scattering from acoustic phonons.

In the absence of phonon drag, the expression for the Nernst–Ettingshausen coefficient Q_{12} has the form

$$Q_{12} = -\frac{\pi^2}{6}\frac{k^2 T}{\zeta}\frac{(M_1 + M_4)a\tau}{M_1 M_4 c(\delta + \Omega^2\tau^2)}. \quad (19)$$

For semiconductors with an isotropic electron spectrum, the theory [1] explains the sign of the Nernst–Ettingshausen coefficient by the type of the scattering mechanism: the negative sign corresponds to electron scattering from acoustic phonons or from pointlike impurities, and the positive sign to scattering from charged impurities. The sign of Q_{12} (19) is determined by the coefficient a and depends on the first term in formula (10).

It should be noted that formulas (14) and (19) contain the same coefficient a defined by formula (10). In accordance with (14) and (19), our experimental data, i.e., the negative values of $\Delta\alpha_\infty$ and Q_{12}, are ensured by the positive value of a. Such a sign of a appears when the electron scattering from acoustic phonons (10) prevails. However, an analysis of experimental results based on formulas (16) and (17), and of the temperature dependence of $1/\tau$, leads to the conclusion about the prevailing contribution from electron scattering from ionized impurities. If the effective mass in alloys were isotropic, we would be able to calculate the value of a, and this scattering would correspond to its negative sign. Thus, we encounter a contradiction in our analysis. The reason behind this contradiction lies mainly in the theoretical assumption formulated above, where we replaced, in the kinetic equation, the result of the action of the integral collision operator on the nonequilibrium correction to the distribution function by the product of reciprocal electron relaxation time and this correction. Such a replacement can be substantiated in the case of

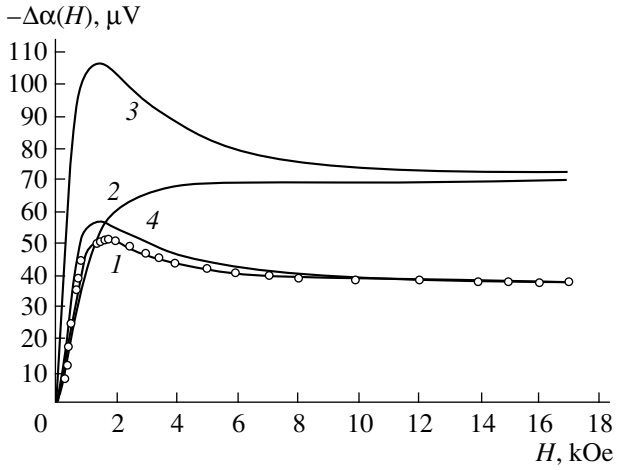

Fig. 6. Experimental and theoretical variation of the diffusion thermopower $\Delta\alpha(H) = \alpha(H) - \alpha(0)$ as a function of the transverse magnetic field with electron parameters for the alloy n-$Bi_{0.93}Sb_{0.07}$: experimental curve for $\Delta\alpha_{22}(H)$ ($\nabla\mathbf{T} \parallel C_1$, $\mathbf{H} \parallel C_3$) at $T = 21$ K (*1*), $\Delta\alpha(H)$ calculated by formula (2) for an isotropic electron spectrum taking into account the electron scattering for $r = 0$ (*2*), $\Delta\alpha(H)$ calculated by formula (14) for an anisotropic electron spectrum with $a = 2.52$ and with the same mechanism of electron scattering as for curve *2* (*3*), and $\Delta\alpha(H)$ calculated by formula (14) for an anisotropic electron spectrum with the value of $a = 1.33$, which was determined from the experimental value of $\Delta\alpha_\infty$ and corresponds to a mixed mechanism of electron scattering (*4*).

an isotropic electron spectrum. In the case of an anisotropic electron spectrum, such a replacement can be substantiated in the case when the collision operator is determined by electron scattering from phonons in the elastic approximation or by the electron scattering from pointlike impurities. However, for electron scattering from ionized impurities, such a replacement cannot be substantiated. It should be noted that Bi–Sb alloys were doped with ionized donor impurities. An analytic solution of the kinetic equation using a truly integral collision operator involves mathematical difficulties, and the field dependence of the thermopower can hardly be determined in such a solution. For this reason, we want to preserve the assumption on the relaxation time as a phenomenological description, in which the value of the reciprocal relaxation time obtained above is what is referred to as the norm of the collision operator.

It should be noted, however, that formulas (1)–(5) correspond to an isotropic electron spectrum; namely, they lead to the conclusion on the sign of the coefficient a (10) for a given scattering mechanism. In the case of an anisotropic electron spectrum, such a conclusion cannot be drawn, and we can assume that the sign of the coefficient a in the case of dominance of scattering of electrons from ionized impurities is nevertheless positive.

Figure 6 shows the experimental and theoretical dependences of diffusion thermopower on the transverse magnetic field corresponding to various theoretical assumptions. Curve *1* represents the experimental data on $\Delta\alpha_{22}(\nabla\mathbf{T} \parallel C_1, \mathbf{H} \parallel C_3)$ for the n-$Bi_{0.93}Sb_{0.07}$ alloy at $T = 21$ K. Curve *2* corresponds to $\Delta\alpha(H)$ calculated by formula (2) for an isotropic electron spectrum for the mechanism of electron scattering from acoustic phonons or pointlike impurities ($r = 0$). However, the chemical potential substituted into (2) was calculated for a real anisotropic Lax spectrum. Curve *2* corresponds to a monotonic dependence on the magnetic field, and the limiting value of $\Delta\alpha_\infty$ is approximately twice as large as the experimental value. Curve *3* was calculated by formula (14) for an anisotropic electron spectrum for the same scattering mechanism as for curve *2*. The presence of a peak on the field dependence $\Delta\alpha(H)$ is in qualitative agreement with the experimental data, but the value at the peak differs quantitatively. According to formulas (2) and (14), the limiting values of $\Delta\alpha_\infty$ for curves *2* and *3* are identical and are determined by the value of a given by (10) and $a = 2.52$. Since this calculated value of $\Delta\alpha_\infty$ differs from the experimental value, we plotted curve *4* corresponding to formula (14), in which we used the coefficient a that was determined from the experimental value of $\Delta\alpha_\infty$ and is equal to 1.33. It can be seen that this curve is close to the experimental curve *1*. The closeness of these two curves allows us to use formula (14) for determining the relaxation time from characteristic values of the magnetic fields for experimental curves at various temperatures (Figs. 4 and 6). The positive value of the coefficient a in the case of dominant scattering from ionized impurities for an anisotropic electron spectrum was discussed above.

It should be noted, in conclusion, that the semiconducting Bi–Sb alloys exhibit a very large ratio, $\eta = m_\parallel/m_\perp \geq 250$, of effective masses along and across the ellipsoids [3]. For the sake of comparison, we present the values of η for other anisotropic semiconductors: 19.3 for Ge [5], 4.8 for Si [5], 10 for n-PbTe [6], 14 for p-PbTe [6], $\cong$4.5 for Bi_2Te_3 of the n and p type [7], and 2 for Te [8]. We are not aware of any data concerning the nonmonotonic dependence of thermopower for these semiconductors in a transverse magnetic field, but such a dependence cannot be ruled out in general. This circumstance should be taken into account when determining the limiting value of the thermopower in a strong magnetic field, which can be used for determining the density of states of charge carriers. On the other hand, if such a peak were observed, it could be used for determining the relaxation parameters for electrons, as it was done by us here. Note that the electron spectrum of the Bi–Sb alloys under investigation was convenient, since the cyclotron frequency was identical for all the ellipsoids for $\mathbf{H} \parallel C_3$.

REFERENCES

1. B. M. Askerov, *Kinetic Effects in Semiconductors* (Nauka, Leningrad, 1970).

2. N. B. Brandt, R. Germann, G. I. Golysheva, *et al.*, Zh. Éksp. Teor. Fiz. **83**, 2152 (1982) [Sov. Phys. JETP **56**, 1247 (1982)].
3. N. A. Red'ko, V. I. Pol'shin, V. V. Kosarev, and G. A. Ivanov, Fiz. Tverd. Tela (Leningrad) **25**, 3138 (1983) [Sov. Phys. Solid State **25**, 1807 (1983)].
4. I. N. Dubrovskaya and Yu. I. Ravich, Fiz. Tverd. Tela (Leningrad) **8**, 1455 (1966) [Sov. Phys. Solid State **8**, 1160 (1966)].
5. G. Dresselhaus, A. F. Kip, and C. Kittel, Phys. Rev. **98**, 368 (1955).
6. K. F. Cuff, M. R. Ellett, C. D. Kuglin, and L. R. Williams, in *Proceedings of the International Conference on Physics of Semiconductors, Paris, 1964*, p. 667.
7. R. B. Mallinson, J. A. Rayne, and R. W. Ure, Phys. Lett. A **24** (13), 713 (1967); L. R. Testradi, P. J. Stiles, and E. Burstein, Solid State Commun. **1** (2), 28 (1963).
8. Y. Couder, M. Hulin, and H. Thome, Phys. Rev. B **7**, 4373 (1973).

Translated by N. Wadhwa

Physics of the Solid State, Vol. 42, No. 8, 2000, pp. 1422–1426. Translated from Fizika Tverdogo Tela, Vol. 42, No. 8, 2000, pp. 1384–1389.

SEMICONDUCTORS AND DIELECTRICS

Structural Defects in 6*H*-SiC Substrates and Their Effect on the Sublimation Growth of Epitaxial Layers in Vacuum

L. M. Sorokin, A. S. Tregubova, M. P. Shcheglov, A. A. Lebedev, and N. S. Savkina

Ioffe Physicotechnical Institute, Russian Academy of Sciences, Politekhnicheskaya ul. 26, St. Petersburg, 194021 Russia

e-mail: Lev.Sorokin@shuvpop.ioffe.rssi.ru

Received February 3, 2000

Abstract—The structural perfection of silicon carbide substrates and homoepitaxial layers grown on the substrates by sublimation has been studied by x-ray diffraction (topography and diffractometry) and optical microscopy. The optimum diffraction conditions (*hkil* reflections, radiation wavelength λ, and recording geometry) for revealing "micropipes" of the dislocation nature are determined. It is shown that the growth conditions used make it possible to obtain highly perfect epitaxial layers. © *2000 MAIK "Nauka/Interperiodica".*

1. INTRODUCTION

Recent progress in the growth of silicon carbide single crystals with sufficiently large sizes and modern technologies of growing epitaxial layers allow the use of SiC as a promising material in power devices, light emitting diodes, and other instruments operating under extreme conditions (high temperatures, radiation, corrosive media, etc.). The presence of structural defects in these crystals considerably restricts their use for the above purposes. The character of forming the dislocation structure and the distribution of dislocations and other defects over the surface and in the bulk depend on the substrate growth method responsible for the specific features in the defect structure of substrates. Since the structural defects in the layers affect many characteristics of semiconductor devices, they cannot be improved without systematic investigations into the structural perfection of both the initial materials (substrates) and epitaxial layers.

The purpose of this work was to investigate the features in the defect structures of silicon carbide substrates grown by the modified Lely method and epitaxial layers grown on the Si face by the sublimation technique.

2. EXPERIMENTAL TECHNIQUE

The SiC crystals (substrates) grown by the modified Lely method exhibit a high structural perfection but cannot be used in some cases due to their small sizes. The sizes of the SiC crystals grown by the modified Lely method can be sufficiently large (25–75 mm in diameter); however, their structural perfection is substantially lower than that of the former crystals [1].

Among all the known SiC polytypes, the 6*H*-SiC polytype studied in the present work is most frequently used for the growth of epitaxial layers. A SiC substrate (CREE, USA) with a diameter of ~25 mm was cut into several parts of area ~1 cm^2 for different experiments. The epitaxial layers were grown on the substrates by sublimation. Immediately prior to the epitaxial layer growth, the substrates were subjected to sublimation etching with the aim of removing the defect layer formed upon mechanical treatment of substrate surfaces. The *n*-type layers were grown on a Si face of the substrate under a vacuum of 10^{-6} torr at a growth source temperature of ~2000°C [2]. The temperature gradient of a growth chamber was changed by its displacement inside an inductor. The growth rate was equal to about 15 μm/h at a temperature of ~2000°C. The weakly compensated epitaxial silicon carbide layers with the hole concentration $N_d - N_a \sim 1 \times 10^{15}$ cm^{-3} and a hole diffusion length of ~2.5 μm were grown by this means.

In this work, structural defects were studied using a combination of nondestructive techniques—x-ray diffraction (topography and diffractrometry) and optical microscopy.

The transmission topography (the Lang method), the back-reflection technique in an asymmetric geometry (the Berg–Barrett method), and double-crystal topography were used in the x-ray topographic study. The Lang method permits detection and examination of defects throughout the bulk of a crystal under consideration. In order to avoid the contribution from surface defects at the untreated C surface to the diffraction image, the substrate was further polished and etched in a KOH melt. The second method makes possible the diffraction image of defects in near-the-surface layer. The depth of formation of the x-ray diffraction reflection is determined by the extinction length t_Λ. For the $(10\bar{1}.10)$ and $(11\bar{2}.12)$ reflections (CuK_α radiation), the calculated depths were equal to 13 and 27 μm, respectively. A germanium monochromator set in the symmetric reflection (111) was used in the double-crystal topography in the Bragg geometry. In this

1063-7834/00/4208-1422$20.00

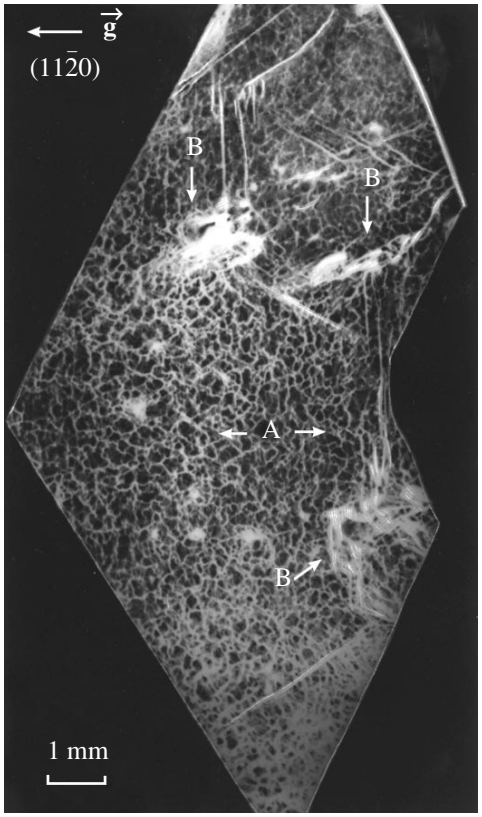

Fig. 1. Lang x-ray topogram [MoK_α radiation, (11$\bar{2}$0) reflection]. (A) Regions with a uniform distribution of the basal dislocations and (B) regions with strong local imperfections.

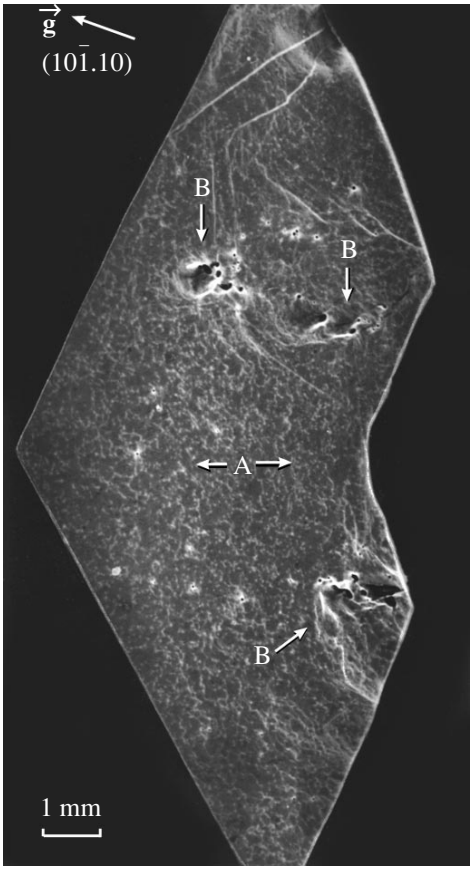

Fig. 2. Reflection Berg–Barrett x-ray topogram [CuK_α radiation, (10$\bar{1}$.10) reflection] of the same crystal as in Fig. 1.

method, an increase in the sensitivity of images to small misorientations of the crystallographic planes near defects is achieved at the expense of a decrease in the divergence of the beam incident on the studied crystal. This enables one to determine the geometry of defects.

3. RESULTS

A cellular structure brought about by an ordered dislocation arrangement in substrates is observed in the Lang topograms [MoK_α radiation, (11$\bar{2}$0) reflection]. Large regions with a sufficiently uniform distribution of the basal dislocations ($\leq 10^5$ cm^{-2}) and regions with rather strong imperfections in the form of continuous bright spots without indications of fine structure can be distinguished in the images of the substrates under consideration. From these images it is difficult to judge whether a pileup of dislocations or other defects are responsible for these imperfections (Fig. 1).

The resolution substantially increases when the image is obtained from the crystal region with a limited thickness. In order to reveal how structural defects in near-the-surface layer affect the epitaxial growth, we recorded the topograms in the reflection Bragg geometry [Berg–Barrett method, CuK_α radiation, (10$\bar{1}$.10) and (11$\bar{2}$.12) reflections]. Out of all the reflections used, the best contrast in the image of the dislocation structure is achieved with the above reflections. Figure 2 displays the Berg–Barrett topogram of the same crystal region as in Fig. 1. Only single dislocations or, more precisely, their portions that correspond to the emergence of dislocations on the surface under examination are seen as opposed to the cellular structure. Single defects in the form of a dark core with an asymmetric bright halo (rosette) are also seen in Fig. 2 in the regions that correspond to the homogeneous cellular structure shown in Fig. 1. The sizes of these defects vary in the range 1–10 μm. Moreover, aggregates of these defects with different sizes are observed in the regions with strong imperfections (continuous bright spots in Fig. 1). In the same regions, one can see long bright lines whose image width exceeds single dislocations. These defects can be considered regions with low-angle boundaries penetrating the whole of the crystal.

Figure 3 depicts the Berg–Barrett topogram of the same sample after the growth of the epitaxial layer ~5 μm thick. It should be noted that the dislocation

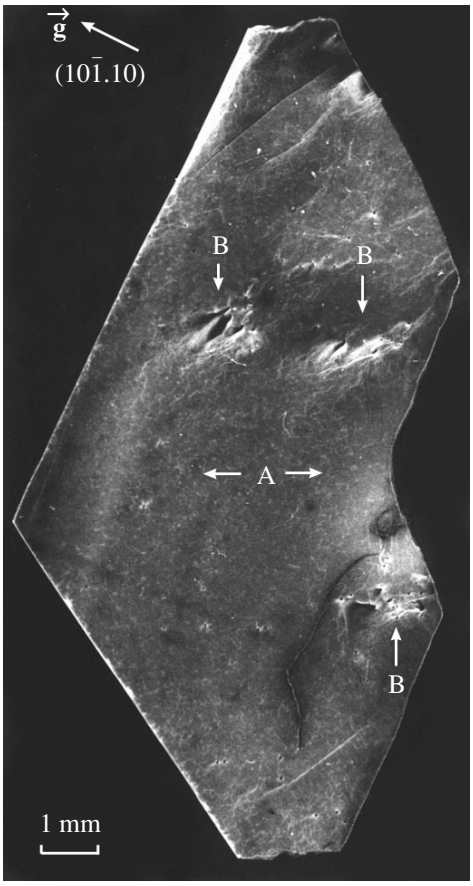

Fig. 3. Berg–Barrett topogram of the 6*H*-SiC substrate with a 5-μm-thick epitaxial layer. Diffraction conditions are the same as in Fig. 2.

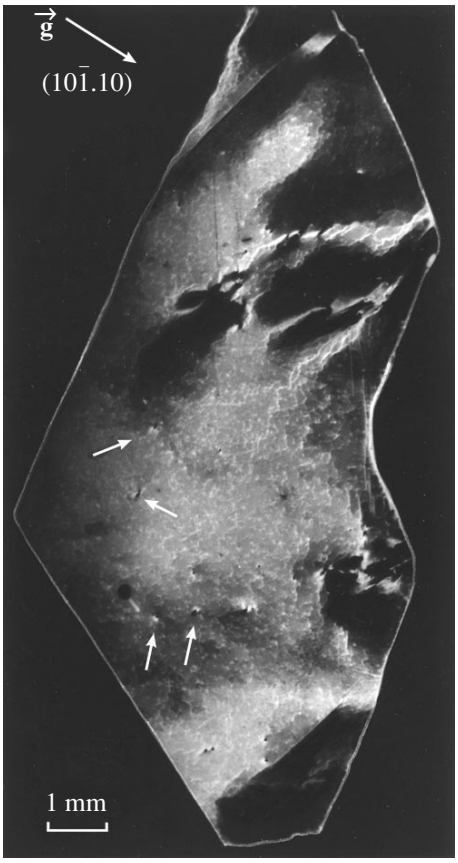

Fig. 4. Double-crystal x-ray topogram of the substrate with an epitaxial layer [CuK_α radiation, (10$\bar{1}$.10) reflection]. Defects with a dark core and bright halo are micropipes.

density on the image decreases substantially. Since the basal dislocations do not intergrow, the tilt dislocations become clearly seen in the Berg–Barrett topogram. As regards the more distorted and inhomogeneous regions of the substrate, for the most part, they are inherited by the epitaxial layer. The low-angle boundaries composed of tilt dislocations intergrow into the epitaxial layer. The substrate defects in the form of dark core with a bright halo intergrow into the layer and, like the low-angle boundaries, bring about a strong misorientation of regions with respect to each other. This misorientation is more pronounced in the double-crystal x-ray topogram (Fig. 4). The defects with a dark core and bright halo are also more clearly seen in this picture. The halo size decreases, and the defect geometry becomes all the more evident from the contours of the central part. Analysis of these defects in the topograms indicates their dislocation nature. Furthermore, additional smaller defects with a halo contrast manifest themselves in this picture, which indicates the efficiency of using double-crystal topography in this case.

The nature of the defects with a halo contrast, which were observed in the topograms, was further investigated by optical microscopy. Hollow pipes were revealed in the optical images after the preliminary etching of the substrate in a KOH melt. These pipes correspond to hexagonal etch pits on the substrate surface. The presence of a "tail" (shadow cast by the pit image) is strong evidence that an extended defect terminates in the etch pit. This effect can be observed when the micrograph of the surface has been obtained for the sample inclined with respect to the horizontal plane (Fig. 5). Similar defects found in single-crystal silicon carbide by using synchrotron x-ray topography [3] were interpreted by as pores—the outcrops of hollow channels ("micropipes") arising from screw superdislocations. According to Frank [4], in crystals with a large shear modulus, the screw dislocations with the Burgers vector exceeding a critical magnitude have an empty core. The relationship between the equilibrium diameter of the pipe associated with an empty core and the magnitude of the Burgers vector **b** of the screw dislocation is given by the following formula [4]:

$$D = \mu b^2/4\pi^2\gamma,$$

where μ is the shear modulus, and γ is the specific surface energy. In many works [5, 6], the pits observed at

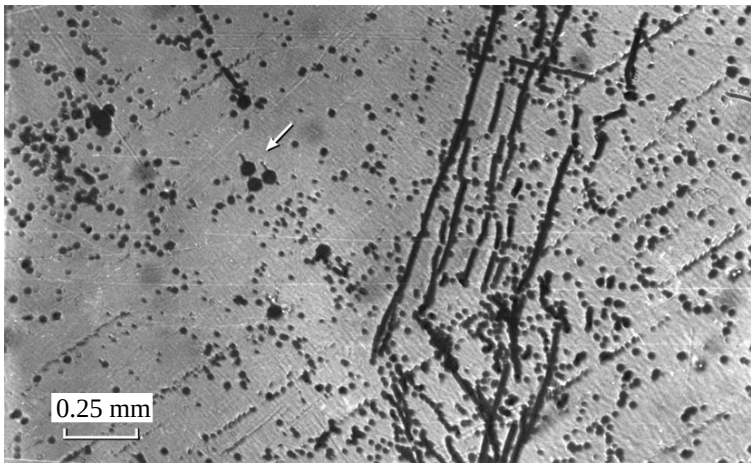

Fig. 5. Optical micrograph of the 6*H*-SiC substrate surface etched in a KOH melt. Hexagonal defect etch pits corresponding to the outcrops of micropipes are seen. Tails (projections of hollow channels—micropipes) off the pipes are observed for the inclined sample.

the center of growth spirals in silicon carbide are related to the screw dislocations. In our case, defects of this type occur in the substrates and can intergrow into the epitaxial layers.

In addition to the x-ray topographic studies, we measured the half-widths ω_θ of the diffraction reflection curves for the initial substrates and epitaxial layers. A 6*H*-SiC single crystal served as a monochromator. The diffraction reflection curves for the studied crystal were measured using the symmetric reflections (0006) and (000.12) and the nonsymmetric reflection $(10\bar{1}.10)$ (CuK_α radiation). For the symmetric (0006) and nonsymmetric $(10\bar{1}.10)$ reflections, the calculated depths of the formation of the diffraction reflection (extinction length t_Λ are equal to 3 and 5 μm, respectively. These values lie within the thickness of the epitaxial layer. For the (000.12) reflection, t_Λ is equal to ~17 μm. As follows from the measurements, the regions with a uniform distribution of dislocations correlate with smaller values of half-widths as compared to the regions with more defective structure observed in the topograms. The measurements of the diffraction reflection curves for epitaxial layers demonstrated that the half-widths have a tendency to decrease (as compared to the substrate) in the regions corresponding to the uniform distribution of dislocations. The half-widths of the diffraction reflection curves for regions with strong local distortions in the substrate are considerably larger and remain virtually constant after the layer growth. Therefore, it can be stated that virtually all defects responsible for nonuniform distortions intergrow from the substrate into the layer without loss of their "power".

The quantitative distribution of the half-widths of diffraction reflection curves over the surface is shown in Fig. 6. It can be seen that the spread in half-width is in the range from 14″ to 40″. For the sample regions with a uniform dislocation distribution, the half-width of diffraction curves for the (000.12) reflection is equal to 14″–16″ prior to the layer growth and 10″–14″ after the growth of the 15-μm-thick layer. For the $(10\bar{1}.10)$

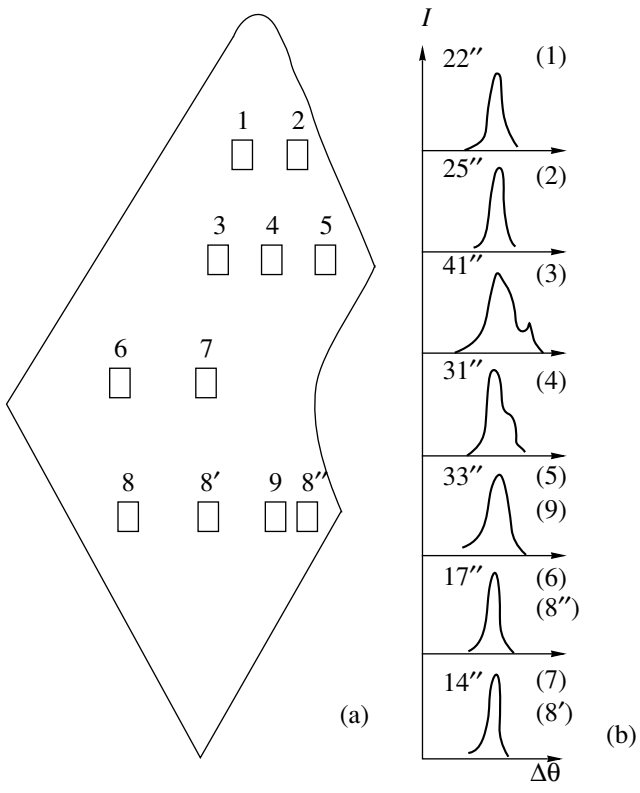

Fig. 6. (a) Contour of the initial sample with points of measuring the half-widths ω_θ of diffraction curves prior to and after growth of the epitaxial layer. (b) Diffraction curves. Numerals near curves correspond to ω_θ (in seconds).

nonsymmetric reflection, the half-width is equal to 18″–20″ for the substrate free of layer and 14″–16″ for the sample with the grown layer. These data indicate a substantial improvement in the structural perfection of the epitaxial layer as compared to the substrate, which is in good agreement with the results of the x-ray topographic investigations.

Thus, the results of the complex structural investigations can be summarized as follows:

(i) The optimum diffraction reflections that provide the best contrast of the microchannel (micropipe) image in the x-ray topograms were determined.

(ii) It was established that the pores revealed are the outcrops of the micropipes of dislocation origin.

(iii) The structural perfection of the epitaxial layers depends on the density of distribution of dislocations, micropipes, and other defects over the substrate surface.

(iv) The examination of the substrates and epitaxial layers with the use of double-crystal x-ray topography showed that the regions with strong imperfections contain defects of different types.

(v) It was demonstrated that the epitaxial layers grown by sublimation exhibit a better structural perfection compared to the substrates.

ACKNOWLEDGMENTS

This work was supported by the International Association of Assistance for the promotion of co-operation with scientists from the New Independent States of the former Soviet Union, project no. INTAS 97-30834.

REFERENCES

1. A. N. Andreev, A. S. Tregubova, M. P. Shcheglov, *et al.*, Fiz. Tekh. Poluprovodn. (S.-Peterburg) **29**, 1828 (1995) [Semiconductors **29**, 955 (1995)].
2. M. M. Anikin, A. A. Lebedev, S. N. Pyatko, and A. M. Strel'chuk, Mater. Sci. Eng. B **11**, 113 (1992).
3. M. Dudley, W. Si, S. Wang, *et al.*, Nuovo Cimento Soc. Ital. Fis., D **19** (2–4), 153 (1996); in *Proceedings of the Third European Symposium on X-ray Topography and High-Resolution Diffraction, Palermo, Italy, 1996*, Ed. by C. Bocchi *et al.* (Società Italiana di Fisica, Bologna, 1996).
4. F. S. Frank, Acta Crystallogr. **4**, 497 (1951).
5. I. Sunagawa and P. Bennema, J. Cryst. Growth **53**, 490 (1981).
6. H. Tanaka, Y. Uemura, and Y. Inomata, J. Cryst. Growth **53**, 630 (1981).

Translated by O. Borovik-Romanova

Physics of the Solid State, Vol. 42, No. 8, 2000, pp. 1427–1430. Translated from Fizika Tverdogo Tela, Vol. 42, No. 8, 2000, pp. 1389–1392.

SEMICONDUCTORS AND DIELECTRICS

XANES Calculation of Chalcogenide Spinel $CdIn_2S_4$

N. Yu. Safontseva and I. Ya. Nikiforov

Don State Technical University, Rostov-on-Don, 344010 Russia

e-mail: root@sintez.md.su

Received October 5, 1999; in final form, February 4, 2000

Abstract—The shape of the x-ray *K* absorption spectrum of sulfur in the normal spinel $CdIn_2S_4$ is calculated using the FEFF7 program. Local densities of free electron states of S, Cd, and In are calculated in the theory of multiple scattering in the local coherent potential approximation. A comparison of the obtained results with the experimental x-ray *SK* spectrum demonstrates good agreement between them. © *2000 MAIK "Nauka/Interperiodica".*

Ferrites, whose crystal lattice is a normal or an inverted [1] spinel, play a special role in engineering. Being semiconductors as a rule, many ferrites are used in communication technology. The overwhelming majority of ferrites also possess ferromagnetic properties; thus, nonferromagnetic cubic spinels Zn and Cd with a normal spinel structure would not be important for technical applications if they were not used as dopants to the ferromagnetic ferrites Cu, Mg, Ni, and Mn, which is responsible for their remarkable properties such as the lowering of the Curie temperature and an increase in the permeability and magnetic saturation in combination with a resistivity exceeding that of iron.

1. COMPUTATIONAL TECHNIQUE

The present work is devoted to an analysis of the free state of cadmium spinel $CdIn_2S_4$ by using various theoretical methods.

(1) The FEFF7 program developed by Rehr, Zabinsky, Albers, and Ankudinov [2–4] was used to calculate the *K* edge of the sulfur absorption spectrum. Since the main features of the x-ray absorption spectra are determined by the elastic scattering of a photoelectron wave in a complex potential relief of the nearest neighbors of an absorbing atom in a solid, the FEFF7 program uses the "Fermi golden rule" to calculate the x-ray photoabsorption cross section:

$$\mu(E) \sim \sum_f |\langle \psi_i | \hat{e}\mathbf{r} | \psi_f \rangle|^2 \delta(E - E_f), \qquad (1)$$

where $E \equiv \omega - E_i$, ω being the x-ray energy (in the Hartree atomic units, $h = 1$); $|\psi_i\rangle$, E_i, $|\psi_f\rangle$, and E_f are the wave functions and energies of the initial (core) and the final (empty) states of the electron being ionized; and $\hat{e}$ is the x-ray polarization vector.

(2) The crystal potentials calculated using the FEFF7 program according to the Mattheiss' standard algorithm were used to calculate scattering phases, the total *T* scattering matrix, and, finally, local partial densities of electron states in the cluster version of the local coherent potential (LCP)

$$n_l^A(E) = -\sqrt{E}\pi^{-1} \int_0^{r_{WS}} \{R_l^A(E, r)\}^2 dr \frac{\mathrm{Im} T r T_{lm}^{00, A}}{\mathrm{Im} t_l^A(E)}, \qquad (2)$$

where l is the orbital quantum number, $R_l^A(E, r)$ is the radial component of the wave function of an electron in the atom A, $T_{lm}^{00, A}$ is the matrix element of the scattering operator, $t_l^A(E)$ are single-site scattering matrices, and r_{WS} is the radius of the Wigner–Seitz cell.

The LCP method proposed by Gyorffy [5, 6] and executed in the packet of programs, which were developed under the guidance of Nikiforov and used successfully for studying both occupied and empty electron states with different crystal structures and types of chemical bonds of the compounds [7–10], was first used to calculate the free electron states of the compound with the $CdIn_2S_4$ spinel structure. This analysis has only now become possible, since the structure complexity (56 atoms per unit cell and their nonequivalent positions) necessitates an analysis of larger clusters and, thus, requires state-of-the-art computer technology.

In order to construct crystal potentials on the basis of the FEFF7 program, we used clusters containing up to 1000 atoms. The positions of atoms in a spinel cluster were determined with the help of formulas for the

Table 1. Radii of MT spheres (RMT) and lengths of bonds in $CdIn_2S_4$

RMT_{Cd}, Å	RMT_{In}, Å	RMT_S, Å	$l_{T,\,Cd–S}$, Å	$l_{O,\,In–S}$, Å
1.381	1.314	1.238	2.618	2.537

1063-7834/00/4208-1427$20.00

Table 2. Separations between principal peaks of the theoretical and experimental spectra and local partial densities of electrons states of S, Cd, and In

Separation, eV	$a' - a$	$a - b$	$a - b'$	$a - c$	$a - d$
Theoretical S*K* edge (single scattering)	–	2.85	–	–	13.13
Theoretical S*K* edge (multiple scattering)	–	3.24	–	9.01	–
S*K* edge (experiment [13])	~1	~3	~4.5	~10	~13
p states of S	0.82	3.26	6.44	9.25	12.24
p states of S^-	0.82	2.00	4.35	9.24	12.51
p, *d* states of Cd	–	2.72	4.08	9.52	12.24
p, *d* states of In	–	2.45	4.35	7.34	–

lengths of the tetrahedral l_T(Cd–S) and octahedral l_O(In–S) cation–anion bonds [1, 11]:

$$l_T = \sqrt{3}(1/8 + \delta)a; \quad (3)$$

$$l_O = (1/4 - \delta)a, \quad (4)$$

where a is the parameter of a cubic unit cell of the spinel, which is taken equal to 10.797 Å for $CdIn_2S_4$ according to [12], with $\delta \equiv u - 3/8$, u being the anion parameter determining the position of sulfur atoms and taking into account their displacement from ideal positions in the [111] direction. In this work, $u = 0.390$ [12].

The radii of the muffin-tin (MT) spheres, as well as the lengths of the Cd–S and In–S bonds used in our calculations, are presented in Table 1.

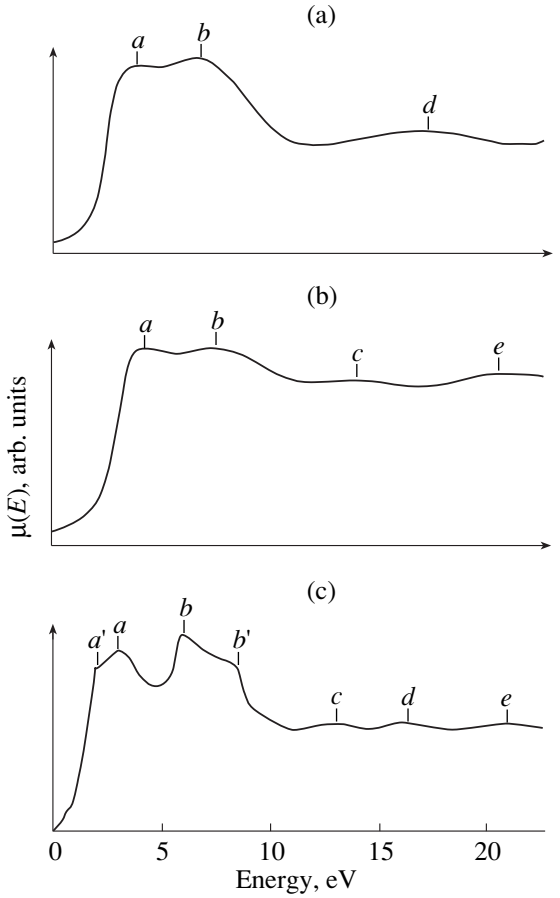

Fig. 1. S*K* absorption edge: (a) theoretical, obtained by using only single scattering routes (FEFF7); (b) theoretical, obtained by taking into account multiple scattering (FEFF7); and (c) experimental [13].

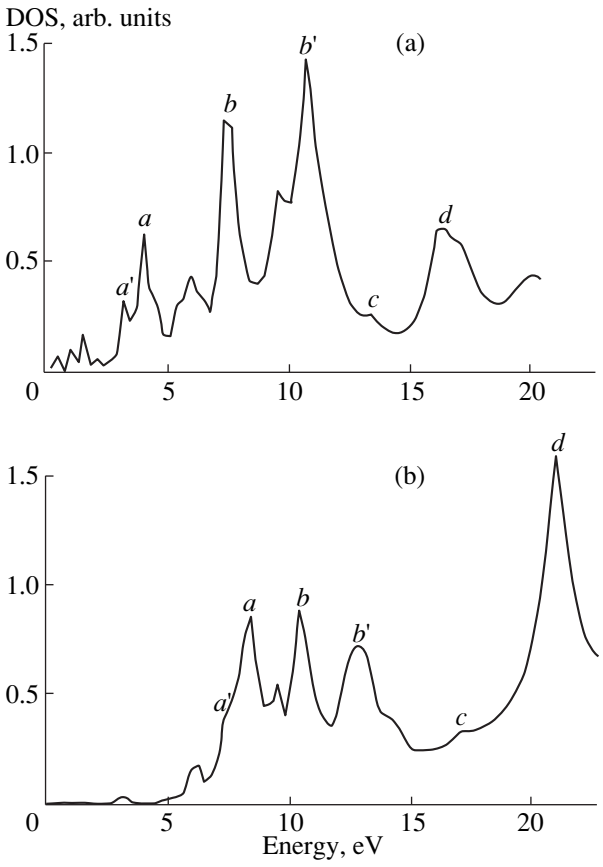

Fig. 2. Densities of free *p* states of sulfur (a) taking a core vacancy into account and (b) disregarding a core vacancy (ionized S atom).

2. DISCUSSION OF RESULTS

Figure 1 shows the theoretical and experimental [13] XANES spectra of sulfur in $CdIn_2S_4$ (the origin coincides with the absorption edge). The first theoretical S*K* absorption edge is calculated with the help of the FEFF7 program using only single scattering routes (i.e., bilateral routes) in a cluster consisting of 154 atoms. In the present analysis, we took into account 33 scattering routes. It can be seen from Fig. 1 and Table 2 that the separations between the principal peaks of the theoretical and experimental spectra coincide to within a high degree of accuracy. The second theoretical XANES spectrum was calculated for multiple scattering in a cluster composed of 106 atoms. Of all the scattering routes, we chose those whose amplitude constitutes at least 35% of the amplitude of the longest route. The maximum length of single, as well as multiple, scattering routes was chosen by the order of the lattice constant, and its increase did not lead to a change in the shape of theoretical XANES spectra. In the case of multiple scattering, we used a partially nonlocal exchange–correlation potential in contrast to the Hedin–Lundqvist potential applied for bilateral routes. It can be seen from Fig. 1 that the splitting of the theoretical XANES spectrum for sulfur could be observed even for single scattering. The spikes *a*' and *b*' appearing at the experimental S*K* edge on the low-, as well as high-energy side could not be obtained in calculations. It should also be noted that using multiple scattering routes leads to suppression of the main features in the vicinity of the S*K* absorption edge. Consequently, single scattering routes play a major role in the formation of the absorption edge profile. This fact can be interpreted as the absence of "shadow" effects [14] leading to the screening of an absorbing sulfur atom by the atoms of the nearest neighborhood. This can be associated with peculiarities of lattice symmetry and loose packing of cations (especially in tetrahedral positions).

Figure 2 shows local partial densities of free *p* states of sulfur, which were obtained in the LCP approximation, taking into account vacancies at the 1*s* core energy level. In order to include the vacancy screening on the 1*s* level, the number of electrons in an absorbing S atom was increased by unity, i.e., the S atom was ionized to minus one, and an extra *p* electron was taken into consideration. The density of *p* states of ionized sulfur is also presented in Fig. 2. A comparison of the separations between the principal peaks of the density of electron states of ionized sulfur shows that they agree well with the main features of the experimental S*K* edge. In Fig 2 (as well as in Fig. 3 below), zero coincides with the MT zero. An analysis of the densities of *p* states for sulfur shows that the presence of a core vacancy on the 1*s* level leads to an intensity redistribution among principal peaks and to a displacement of free electron states of sulfur by ~2 eV towards lower energies.

The calculation of the densities of state of Cd and In (Fig. 3) also proved that the bottom of the conduction band is formed not only by the *p* states of sulfur, which are considerably delocalized and strongly hybridized with the *d* states of sulfur, but also by the *p* and *d* states of cadmium and indium; the interaction with these states is responsible for the main features of the S*K* edge. The positions of the principal peaks of the *p* and *d* states of indium and cadmium are close to the positions of the main peaks of the *p* and *d* states of sulfur on the energy scale. The intensities of the principal peaks of the density of states for indium are much higher than for cadmium. This can be explained by the nearest neighbors of a sulfur atom being three indium atoms and only one cadmium atom. The separations between the principal peaks of the theoretical and experimental spectra, as well as between the peaks of the electron density of states for sulfur, cadmium, and indium, are presented in Table 2.

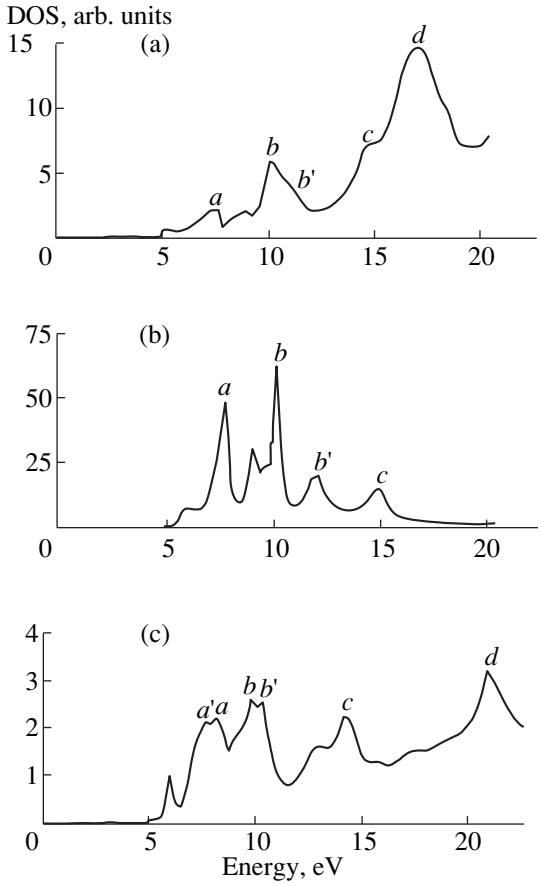

Fig. 3. Densities of free *p* and *d* states of atoms of $CdIn_2S_4$: (a) cadmium, (b) indium, and (c) sulfur without a core vacancy.

REFERENCES

1. E. V. Gorter, Usp. Fiz. Nauk **57** (8), 279 (1955).
2. S. I. Zabinsky, J. J. Rehr, A. Ankudinov, *et al.*, Phys. Rev. B **52**, 2995 (1995).

3. J. J. Rehr and R. C. Albers, Phys. Rev. B **41**, 8139 (1990).
4. J. Mustre de Leon, J. J. Rehr, S. I. Zabinsky, and R. S. Albers, Phys. Rev. B **44**, 4146 (1991).
5. B. L. Gyorffy, Phys. Rev. B **5**, 2382 (1972).
6. D. House, B. L. Gyorffy, and G. M. Stocks, J. Phys. (Paris) **35** (5), C4-75 (1974).
7. V. V. Ilyasov, I. Ya. Nikiforov, and N. Yu. Safontseva, Phys. Status Solidi B **185**, 171 (1994).
8. V. V. Ilyasov, N. Yu. Safontseva, and I. Ya. Nikiforov, Fiz. Tverd. Tela (St. Petersburg) **36**, 451 (1994) [Phys. Solid State **36**, 247 (1994)].
9. I. Ya. Nikiforov, V. V. Ilyasov, and N. Yu. Safontseva, J. Phys.: Condens. Matter **7**, 6035 (1995).
10. B. V. Gabril'yan, A. A. Lavrent'ev, and I. Ya. Nikiforov, Fiz. Tverd. Tela (St. Petersburg) **41**, 41 (1999) [Phys. Solid State **41**, 35 (1999)].
11. V. Talanov, Phys. Status Solidi B **106**, 99 (1981).
12. G. Blasse, *Crystal Chemistry of Spinels* (Metallurgiya, Moscow, 1968), Philips Res. Rep. Suppl., No. 3, 1 (1964).
13. A. A. Lavrentyev, I. Ya. Nikiforov, and B. V. Gabrelian, J. Phys. IV **7**, C2–285 (1997).
14. R. V. Vedrinskiĭ and L. A. Bugaev, Fiz. Tverd. Tela (Leningrad) **28**, 2516 (1986) [Sov. Phys. Solid State *28*, 1408 (1986)].

Translated by N. Wadhwa

Physics of the Solid State, Vol. 42, No. 8, 2000, pp. 1431–1434. Translated from Fizika Tverdogo Tela, Vol. 42, No. 8, 2000, pp. 1393–1396.

SEMICONDUCTORS AND DIELECTRICS

Effect of Contact with Air on the Photoluminescence Spectrum of Porous Silicon

V. F. Agekyan*, A. M. Aprelev*, R. Laiho, and Yu. A. Stepanov***

**Institute of Physics (Petrodvorets Branch), St. Petersburg State University, ul. Pervogo Maya 100, Petrodvorets, 198904 Russia*

***Wihuri Physical Laboratory, Turku University, Turku, 20014 Finland*

Received February 16, 2000

Abstract—A study has been made of the transformation of photoluminescence (PL) spectra of porous silicon (PS) induced by its ageing, including the early stages of contact with air. The sample was prepared under conditions that minimized this contact, and spectral measurements were carried out in a high vacuum or in liquid nitrogen. The PS PL spectra obtained under continuous measurement in high vacuum are always dominated by one emission band of PS nanoelements, which shifts toward shorter wavelengths with ageing by 150 nm. At 80 K, the band intensity is considerably higher than at 300 K, and this difference grows with ageing. Exposure of a sample to air for a few tens of seconds is long enough to strongly transform its time-resolved PL spectra, which is evidence of a change in the sample surface. The effect of immersion of PS samples in liquid nitrogen on PL spectra is associated not only with their cooling, but also with the field of adsorbed nitrogen molecules, whose influence becomes weaker with increasing thickness of the oxidized near-surface layer. The variation of the spectral properties and kinetics of the long-wavelength PS PL band with temperature, medium (liquid nitrogen or vacuum), and exposure time suggest that these factors affect carrier migration between silicon nanoelements. © *2000 MAIK "Nauka/Interperiodica".*

Despite intense studies of the optical properties of PS, no adequate model of its PL has yet been constructed. While it is currently believed that the exciting light is absorbed primarily in the bulk of the microstructures making up PS, the oxidized near-surface layer also contributes to the radiative recombination spectrum [1–3]. The dominant factor from the standpoint of technology is the ageing a PS sample undergoes when stored in air (see [4] and references therein). An essential aspect limiting the application potential of PS is its high surface reactivity, one of its manifestations being the strong ageing-induced variation of PL spectra of a sample. Determination of the contribution of surface states to the energy relaxation of photoexcited carriers offers the possibility of shedding light on the mechanism of photocarrier relaxation in PS. This is done by investigating the PL evolution with a variation of the composition of the near-surface layer. According to [5], ageing is governed by the increase of oxygen content in the near-surface layer of PS. The PS surface obtained immediately after anodization is extremely reactive; we have established that exposure to air for a few tens of seconds is long enough to change it dramatically. It is difficult to monitor the state of a sample in initial stages, and therefore, when studying degradation of steady-state PS PL, one usually accepts a partially oxidized sample as a starting material. Even in the cases where the sample is placed in vacuum after preparation, it usually remains in contact with air for a few minutes. Our work differs in the special measures taken to bring to a minimum the contact of a PS sample with air before the first PL spectral measurements made at 77 and 300 K.

1. EXPERIMENTAL TECHNIQUES

The samples were prepared by anodization of *n*-type silicon (ρ = 100 Ω/cm), usually in an ethanol/water solution of hydrofluoric acid. The process was run in the following conditions: the $H_2O : C_2H_5OH : HF(48\%)$ electrolyte component ratios of 1 : 2 : 1, the etching was performed for 30 min at a current density of 30 mA/cm^2, and the sample surface was illuminated by a krypton incandescent lamp. As already mentioned, measures were taken to preclude sample contact with air before the first emission spectrum measurement. After the anodization and rinsing, the sample still covered by a water layer was placed in a vacuum chamber, which was rapidly evacuated down to 2×10^{-7} Torr. This vacuum desiccation prevents oxidation of the PS surface up to the instant when air is admitted to the chamber. Alternately, the sample was dried after rinsing it in a flow of warm nitrogen and subsequently immersed in liquid nitrogen. This procedure also protects PS against oxidation, with the PL spectrum remaining unchanged for several hours at a time.

The PL was investigated on two setups. In the first one, the excitation was provided by an LGI-21 molecular-nitrogen laser operating at a wavelength of 337 nm with pulses about 5 ns long, thus permitting time-

1063-7834/00/4208-1431$20.00

resolved measurement of PL spectra and investigation of the PL decay kinetics. The maximum excitation level at the pulse peak was 5 kW/cm^2 at an average laser power of not over 1 mW. The second setup with CW photoexcitation was used to measure PL and PL excitation spectra in a high vacuum at 80 and 300 K and in air. The PL spectra taken under pulsed excitation were of two types, namely, a nanosecond-range (the interval from 2 ns to the laser-pulse maximum) and a microsecond one (the interval up to 1 μs), and in CW operation the PL was excited at 340 nm.

2. EXPERIMENTAL RESULTS AND DISCUSSION

The PL spectrum obtained under CW excitation and measurement of an as-prepared PS sample that had no contact with air and was placed in vacuum at 300 K exhibits the main band peaking at 700 nm and a weak band at 570 nm, both of a Gaussian shape (Fig. 1). The PL of PS observed in the 500–800-nm range is usually assigned to inhomogeneously broadened emission of nanocrystallites and nanofilaments, which is governed by size quantization [6–9]. As seen from Fig. 1, the maximum of the main band shifts to shorter wavelengths as PS undergoes ageing in air. The PL brightness increases with PS ageing, and cooling from 300 to 80 K also brings about an enhancement of the PL and a shortward shift of its maximum. Additional studies showed that the weak 570-nm band is observed only in the samples prepared by anodization in an ethanol-containing electrolyte, while when anodizing silicon in an aqueous solution of HF (1 : 1) this band does not appear. Thus, the 570-nm band can be assigned to organic complexes present on the PS surface.

It appears natural to associate the short-wavelength shift of the main PL band induced by ageing with a decrease of the average size of nanocrystallites and nanofilaments in the course of their oxidation [10], but in this case one would expect a corresponding change of the PL excitation spectrum in shape (the absorption edge shape). Such a change was observed to occur in our experiment, but only of samples stored in air for more than a month (illustrated by curves *5* and *6* in Fig. 1). We believe that the short-wavelength shift seen in the early stages of ageing is caused by changes in the carrier relaxation conditions, in particular, by suppression of carrier tunneling from smaller to larger nanocrystallites and nanofilaments. The first to become oxidized in the course of ageing are surface amorphous layers of silicon, which does not affect the size of crystalline nanoelements while being capable of efficiently reducing the transmission of the barriers separating them.

Photocarrier transfer from one nanoelement to another is also hindered by a lowering of temperature, which likewise shifts the spectrum toward shorter wavelengths. Increasing the extent of photocarrier localization increases the nonradiative relaxation time, as a result of which both the ageing and temperature decrease enhance the PL of PS. The change in the dynamics of photocarriers in the course of sample ageing is well illustrated by PS PL kinetics measurements performed at a fixed wavelength. As seen from Fig. 2, after exposure to air for five days, the PL decay time τ at a wavelength of 650 nm increases by an order of magnitude, because the PL shifts with sample oxidation toward shorter wavelengths, and the 650-nm region in the PL of a highly oxidized sample corresponds to the long-wavelength wing of the nanoele-

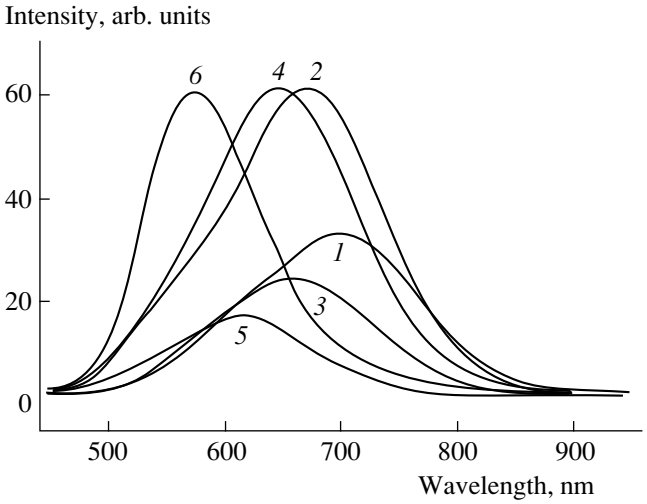

Fig. 1. PL spectra of PS placed in vacuum, which were measured in a continuous regime. As-prepared sample, no contact with air, T (K): (*1*) 300, (*2*) 80; sample exposed to air for 20 h, T (K): (*3*) 300, (*4*) 80; sample exposed to air for three months, T (K): (*5*) 300, (*6*) 80. The *1–2*, *3–4*, *5–6* pairs of spectra are normalized.

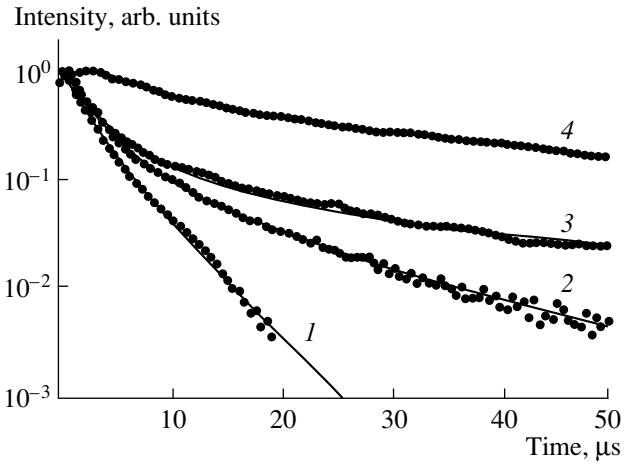

Fig. 2. PL decay kinetics of PS at a wavelength of 650 nm. As-prepared sample before contact with air (*1*) and after exposure to air for five min (*2*), 40 min (*3*), and five days (*4*). The solid lines are plots for decay times τ of 2.7, 3.2, 11, and 35 μs, respectively.

ment emission band. The kinetics of the long-wavelength PS emission is described in all ageing stages by a complex exponential $((t/\tau)^{\beta-1}\exp[-(t/\tau)^{\beta}]$ [11], with τ varying from a few to a few tens of μs, and with values of β from 0.6 to 0.8, which are characteristic of the emission of a system of coupled nanoelements having a size dispersion.

The "slow" long-wavelength PS emission was assigned [11] to surface states of nanocrystallites, which are suggested to also be responsible for the Urbach absorption tail in the gap. There are, however, grounds to believe that the exponential tail in the density of electronic states is related not to the surface, but rather to the crystallites being distributed in size [12]. In this case, it appears natural to associate the "slow" band with bulk carrier recombination in nanocrystallites differing in size.

The 470-nm band with a decay time $\tau < 0.5$ μs is weak in the time-resolved PL spectrum of an as-prepared sample, which was not brought in contact with air, but grows rapidly in intensity as PS undergoes oxidation (Fig. 3). This band should be assigned to defects in the SiO_x oxide layer, which forms even after a short exposure of a sample to air. The relation of the short-wavelength PL with the SiO_x layer (x = 1.4–1.6) was suggested in a number of publications [13]. Because of the decay time of this band being short compared to that of the long-wavelength radiation, the 470-nm band is strong only in time-resolved PL (Fig. 3), while being virtually unseen in continuously measured spectra. At 300 K, this band decays so quickly that it is weak even in a time-resolved μs-scale PL spectrum.

The maximum of the ns-scale PL spectrum of PS lies in the 550–600-nm region (Fig. 3). Immersion of a sample in liquid nitrogen precludes development of the long-wavelength tail of the "slow" emission, which becomes strongly manifest in the μs-range spectrum at T = 300 K (Fig. 3). While immersion in liquid nitrogen suppresses photocarrier-hopping migration, this is not a simple consequence of a temperature decrease, because cooling of PS in vacuum down to 80 K does not significantly change the spectral composition of its PL. An important part is apparently played here by the adsorption of nitrogen molecules, which affects the migration through a change in the rate of photocarrier nonradiative surface recombination. We have established that adsorption processes do not noticeably affect the PL of nanoelements in strongly oxidized PS samples, which were kept exposed to air for months. The reason for this difference is apparently as follows. Adsorption changes the near-surface electric field, which influences on the emission of nanoelements less, the thicker the oxide layer separating silicon nanoelements from adsorbed nitrogen is. Quenching of the "slow" PL was observed earlier in hydrogen-passivated free silicon nanoelements and PS immersed in methanol [14]. A second reason for the formation of electric fields could be the spatial separation of photocarriers in optically excited PS, which gives rise to a photoemf.

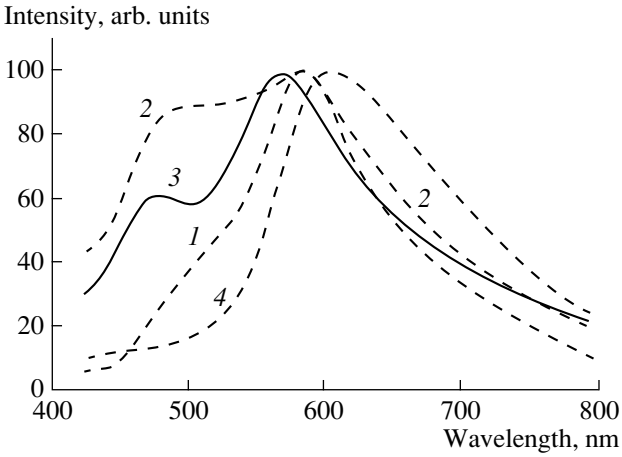

Fig. 3. Time-resolved normalized PL spectra of PS: (*1*) ns- and μs-range 77-K spectra of a sample which had no contact with air; (*2*) same sample exposed to air for five days, ns- and μs-range spectra measured at T = 77 K; (*3*) and (*4*) ns- and μs-range spectra, respectively, measured at T = 300 K.

Our interpretation of the PL spectrum of PS agrees also with the conclusion drawn in [15] that oxidation of PS in water and in air results in the nanoelements becoming isolated from nonradiative relaxation centers.

Thus, we have shown that, when the contact of a PS sample with air is brought to a minimum, its PL exhibits, even in the ns-scale range, only an emission band from the bulk of the PS nanoelements. Exposure of a sample to air for a few tens of seconds greatly affects its PL because of changes in the near-surface layer and hindered carrier migration among PS nanoelements.

ACKNOWLEDGMENTS

Support of the Program of Cooperation between St. Petersburg State University and the University of Turku, and of the MGVE (grant no. 97-0-7.2.65) is gratefully acknowledged.

REFERENCES

1. G. G. Qin and I. Q. Jia, Solid State Commun. **86**, 559 (1993).
2. R. Laiho, A. Pavlov, O. Hovi, and T. Tsuboi, Appl. Phys. Lett. **63**, 275 (1993).
3. H. D. Fuchs, M. Stutzman, M. S. Brandt, *et al.*, Phys. Rev. B **48**, 8172 (1993).
4. N. E. Korsunskaya, T. V. Torchinskaya, B. R. Dzhumaev, *et al.*, Fiz. Tekh. Poluprovodn. (St. Petersburg) **31**, 908 (1997) [Semiconductors **31**, 773 (1997)].
5. A. Bsiesy, J. C. Vial, F. Gaspard, *et al.*, Surf. Sci. **254**, 195 (1991).

6. S. Guha, G. Hendershot, D. Peeples, *et al.*, Appl. Phys. Lett. **64**, 613 (1994).
7. K. Ito, S. Ohyama, Y. Uehara, and S. Ushiroda, Surf. Sci. **363**, 423 (1996).
8. A. G. Cullis and L. T. Canham, Nature **333** (6342), 335 (1991).
9. G. D. Sanders and Yia–Chung Chang, Phys. Rev. B **45**, 9202 (1992).
10. B. Bessais, H. Ezzaouia, H. Elhouichet, *et al.*, Semicond. Sci. Technol. **11**, 1815 (1996).
11. Y. Kanemitsu and T. Ogawa, Surf. Rev. Lett. **3**, 1163 (1996).
12. N. P. Kovalenko, I. K. Doycho, S. A. Gevelyuk, *et al.*, J. Phys.: Condens. Matter **11**, 4783 (1999).
13. R. Laiho, A. Pavlov, and T. Tsuboi, J. Lumin. **57**, 89 (1995); S. M. Prokes, Appl. Phys. Lett. **62**, 3244 (1993); L. Tsybeskov, Ju. V. Vandyshev, and P. M. Fauchet, Phys. Rev. B **49**, 7821 (1994); A. Kux, D. Kovalev, and F. Koch, Appl. Phys. Lett. **66**, 49 (1995).
14. A. A. Seraphin, S.-T. Ngiam, and K. D. Kolenbrander, J. Appl. Phys. **80**, 6429 (1996); J. M. Rehm, G. L. McClendon, L. Tsybeskov, and P. M. Fauchet, Phys. Lett. **66**, 3669 (1995).
15. D. R. Tallant, M. J. Kelly, T. R. Guilinger, and L. Simpson, J. Appl. Phys. **80**, 7009 (1996).

Translated by G. Skrebtsov

Physics of the Solid State, Vol. 42, No. 8, 2000, pp. 1435–1442. Translated from Fizika Tverdogo Tela, Vol. 42, No. 8, 2000, pp. 1397–1403.

SEMICONDUCTORS AND DIELECTRICS

Two-Wave Interaction on a Photorefractive Grating in Cubic Gyrotropic Crystals in the Case of Strong Coupling

R. V. Litvinov, S. M. Shandarov, and S. G. Chistyakov

Tomsk State University of Control Systems and Radioelectronics, Tomsk, 634050 Russia

e-mail: shand@stack.ru

Received November 24, 1999

Abstract—The effect of nonunidirectional energy exchange on the intensity and polarization state of the signal wave is analyzed in the case of symmetric two-wave coupling on a transmission photorefractive grating produced by a diffusion mechanism in a gyrotropic cubic crystal belonging to the point group 23. © *2000 MAIK "Nauka/Interperiodica".*

INTRODUCTION

Coupling of light waves due to photorefractive nonlinearity in cubic gyrotropic crystals has been studied intensively in recent years [1–15]. Analytical expressions were obtained [7, 11] for the two-beam gain coefficient in the case of a grating recorded by a diffusion mechanism with a vector **K** lying in the (110) plane of a sillenite crystal. In deriving these expressions, the inexhaustible-pump wave approximation was used and the two-beam coupling constant γ was assumed to be small in comparison to the specific rotation ρ of the polarization plane.

In [10, 13], it was shown that, in the case of strong wave coupling, when a crystal is placed in an external alternating field and the condition $\gamma \ll \rho$ is not fulfilled, the contribution from nonunidirectional energy exchange to the total gain becomes detectable in the two-beam interaction. This contribution is always transferred from the strong to the weak beam and its polarization is orthogonal to the polarization of the weak wave in the absence of the strong one if the waves incident on the crystal have identical polarization.

The wave coupling on a photorefractive grating produced by diffusion also does not meet the condition $\gamma \ll \rho$ in some cases. For instance, in a $Bi_{12}TiO_{20}$ crystal, the specific rotation is $\rho = 1.13$ cm^{-1} for a wavelength of $\lambda =$ 633 nm [16], which is comparable to the two-beam coupling constant for photorefractive gratings with a spatial period of $\Lambda < 2$ μm.

In this paper, expressions for the two-beam gain on a photorefractive grating of the diffusion type are derived in the inexhaustible-pump wave approximation for any values of the wave coupling constant and the interaction length. The polarization dependence of two-wave interaction is analyzed for two opposite directions of the light wave propagation in the crystal, [110] and $[\bar{1}\bar{1}0]$. The variation of the polarization state of the signal wave in the presence of a pump wave is considered.

1. BASIC EQUATIONS

Following [4, 5], we consider the case of two coherent polarized plane waves, signal (S) and reference (R) ones, symmetrically incident on a photorefractive crystal (Fig. 1). The field of a light wave can be resolved into two components, one of which is parallel to the plane of incidence (TM component), while the other is perpendicular to the plane (TE component). Using the paraxial approximation and neglecting wave absorption, we can write equations for the coupled waves in the form [8]

$$\frac{dR_M}{dx} = \rho R_E - \frac{\gamma}{2I_0}(S_M^* R_M + S_E^* R_E)(H_{MM} S_M + H_{ME} S_E), \quad (1)$$

$$\frac{dR_E}{dx} = -\rho R_M - \frac{\gamma}{2I_0}(S_M^* R_M + S_E^* R_E)(H_{EM} S_M + H_{EE} S_E), \quad (2)$$

$$\frac{dS_M}{dx} = \rho S_E + \frac{\gamma}{2I_0}(S_M R_M^* + S_E R_E^*)(H_{MM} R_M + H_{ME} R_E), \quad (3)$$

$$\frac{dS_E}{dx} = -\rho S_M + \frac{\gamma}{2I_0}(S_M R_M^* + S_E R_E^*)(H_{EM} R_M + H_{EE} R_E), \quad (4)$$

1063-7834/00/4208-1435$20.00

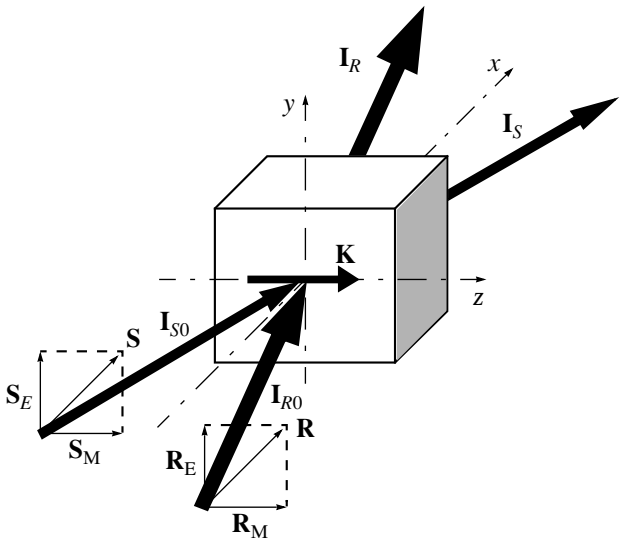

Fig. 1. Geometry of symmetric two-wave interaction on a transmission photorefractive grating produced by diffusion in a crystal plate having an arbitrary orientation relative to the crystallographic axes.

where R_M and R_E are the TM and TE components, respectively, of the electric field strength of the reference (pump) wave; S_M and S_E are the respective components of the signal wave; $I_0 = |R_M|^2 + |R_E|^2 + |S_M|^2 + |S_E|^2$ is the total intensity of the light wave in the crystal; $\gamma = 2\pi n_0^3 r_{41}^s E_{sc}/\lambda_0$ is the coupling constant; n_0 is the index of refraction of the unperturbed crystal; and r_{41}^s is the electrooptical constant of the mechanically clamped crystal. The quantity E_{sc} characterizes the electric field set up by the space charge of the grating produced by a diffusion mechanism and is given by the following expression [16] in the single-level band model of a photorefractive crystal:

$$E_{sc} = \frac{E_D}{1 + (E_D/E_q)}, \tag{5}$$

where $E_D = (k_B T/e)K$ is the diffusion field; $E_q = eN_A/(\varepsilon K)$ is the saturation field of traps; $K = 2\pi/\Lambda$, with Λ being the spatial period of the grating; and ε is the static permittivity of the crystal. The elements of the coupling matrix H_{MM}, H_{EE}, and $H_{EM} = H_{ME}$ include the electrooptical effect, as well as the piezoelectric and photoelastic effects, and are given by the following expressions in the paraxial approximation [8]:

$$H_{MM} = \mathbf{e}_M(\mathbf{H}_{G1} + \mathbf{H}_{G2})\mathbf{e}_M = \mathbf{z}^0(\mathbf{H}_{G1} + \mathbf{H}_{G2})\mathbf{z}^0, \tag{6}$$

$$H_{EE} = \mathbf{e}_E(\mathbf{H}_{G1} + \mathbf{H}_{G2})\mathbf{e}_E = \mathbf{y}^0(\mathbf{H}_{G1} + \mathbf{H}_{G2})\mathbf{y}^0, \tag{7}$$

$$H_{EM} = \mathbf{e}_M(\mathbf{H}_{G1} + \mathbf{H}_{G2})\mathbf{e}_E = \mathbf{z}^0(\mathbf{H}_{G1} + \mathbf{H}_{G2})\mathbf{y}^0, \tag{8}$$

where the unit vectors $\mathbf{e}_M$ and $\mathbf{e}_E$ of the TM and TE components coincide with the z and y axes, respectively (Fig. 1). The matrices $\mathbf{H}_{G1}$ and $\mathbf{H}_{G2}$ have the form

$$\mathbf{H}_{G1} = \begin{bmatrix} 0 & q_3 & q_2 \\ q_3 & 0 & q_1 \\ q_2 & q_1 & 0 \end{bmatrix}, \tag{9}$$

$$(\mathbf{H}_{G2})_{mn} = \frac{p^E_{mnkl}\gamma_{ki}e'_i q_l}{r^s_{41}}, \tag{10}$$

where q_i are the direction cosines between the grating vector $\mathbf{K}$ and the crystal axes; γ_{ki} are the components of the tensor $\gamma = \Gamma^{-1}$, the inverse of the Christoffel tensor with components $\Gamma_{ik} = c^E_{ijkl} q_j q_l$; c^E_{mnkl} and p^E_{mnkl} are the elastic constants and photoelastic constants, respectively, measured at a constant electric field; and $e'_k = e_{nkl} q_n q_l$, with e_{nkl} being the piezoelectric coefficients.

2. WAVE INTERACTION IN THE INEXHAUSTIBLE PUMP WAVE APPROXIMATION

In this approximation, the photorefractive grating does not affect the pump wave, because the terms involving the coupling constant γ are dropped in the right-hand side of equations (1) and (2). In this case, when propagating through the crystal, the plane of polarization of the pump wave is rotated due to gyrotropy of the crystal, and the corresponding solution can be written in the form

$$R_M(x) = R_{M0}\cos(\rho x) + R_{E0}\sin(\rho x), \tag{11}$$

$$R_E(x) = R_{E0}\cos(\rho x) + R_{M0}\sin(\rho x), \tag{12}$$

where R_{M0} and R_{E0} are the boundary values of the TM and TE components, respectively, of the amplitude of the pump wave.

The general solution of equations (3) and (4) is

$$S_M(x) = S^0_M(x)\exp(G(x)x) + \frac{\gamma}{2I_0}R^*_E(x)\Phi(x), \tag{13}$$

$$S_E(x) = S^0_E(x)\exp(G(x)x) - \frac{\gamma}{2I_0}R^*_M(x)\Phi(x), \tag{14}$$

where the functions

$$S^0_M(x) = S_{M0}\cos(\rho x) + S_{E0}\sin(\rho x), \tag{15}$$

$$S^0_E(x) = S_{E0}\cos(\rho x) - S_{M0}\sin(\rho x) \tag{16}$$

are a solution of the set of equations for $\gamma = 0$. These functions describe the rotation of the plane of polarization of the signal wave due to gyrotropy of the crystal in the absence of photorefractive interaction; S_{M0} and

S_{E0} are the boundary values of the TM and TE components, respectively, of the amplitude of the signal wave.

The functions $G(x)$ and $\Phi(x)$ are two independent integrals of the set of equations (3) and (4) and have the form

$$G(x) = \frac{\gamma}{2}\left\{H_\Sigma - 2\mathrm{Im}\left[\frac{1-\exp(i2\rho x)}{2\rho x}(H_{EM} - iH_\Delta)\right.\right.$$
$$\left.\left.\times\left(\mathrm{Re}\left(\frac{R^*_{M0}R_{E0}}{I_0}\right) + i\frac{|R_{M0}|^2 - |R_{E0}|^2}{2I_0}\right)\right]\right\}, \quad (17)$$

$$\Phi(x) = \int_0^x [J_0 + J_c\cos(2\rho\xi) - J_s\sin(2\rho\xi)]$$
$$\times \exp(G(\xi)\xi)d\xi, \quad (18)$$

where we have introduced the notation

$$J_0 = H_\Sigma(R_{M0}S_{E0} - R_{E0}S_{M0}), \quad (19)$$

$$J_c = H_{EM}(R_{E0}S_{E0} - R_{M0}S_{M0}) + H_\Delta(R_{E0}S_{M0} + R_{M0}S_{E0}), \quad (20)$$

$$J_s = H_\Delta(R_{M0}S_{M0} - R_{E0}S_{E0}) + H_{EM}(R_{E0}S_{M0} + R_{M0}S_{E0}), \quad (21)$$

$$H_\Sigma = \frac{H_{MM} + H_{EE}}{2}, \quad (22)$$

$$H_\Delta = \frac{H_{MM} - H_{EE}}{2}. \quad (23)$$

We note that expressions (13), (14), (17), and (18) are similar in structure to the expressions for the field of the signal light wave derived in [10] using a mode approach. The equations we obtained are valid for an arbitrary cut of a gyrotropic cubic crystal and for any orientation of the vector **K** of the transmission photorefractive grating.

In the case where the light waves falling on the crystal have the same polarization, the amplitude of the signal wave can be written as the sum of two components

$$\mathbf{S}(x) = \mathbf{S}_\parallel(x)\exp[G(x)x] + \mathbf{S}_\perp(x)\frac{\gamma\Phi(x)}{2\sqrt{I_{S0}I_{R0}}}, \quad (24)$$

where the first term $\mathbf{S}_\parallel(x) = (S_{M0}\mathbf{z}^0 + S_{E0}\mathbf{y}^0)\cos(\rho x) + (S_{E0}\mathbf{z}^0 - S_{M0}\mathbf{y}^0)\sin(\rho x)$ is the vector amplitude of the signal wave in the absence of the pump wave (with no coupling), while the second term $\mathbf{S}_\perp(x) = (S^*_{E0}\mathbf{z}^0 - S^*_{M0}\mathbf{y}^0)\cos(\rho x) - (S^*_{M0}\mathbf{y}^0 + S^*_{E0}\mathbf{z}^0)\sin(\rho x)$ is orthogonal to the vector $\mathbf{S}_\parallel(x)$ ($\mathbf{S}_\perp(x)\mathbf{S}^*_\parallel(x) = 0$); I_{S0} and $I_{R0} = I_R$ in (24) are the intensity of the signal wave at the boundary $x = 0$ and the intensity of the pump wave, respectively. Therefore, the interaction of the signal and reference waves on the photorefractive grating produced by diffusion not only leads to an increase in the amplitude of the signal wave, but also changes its polarization state.

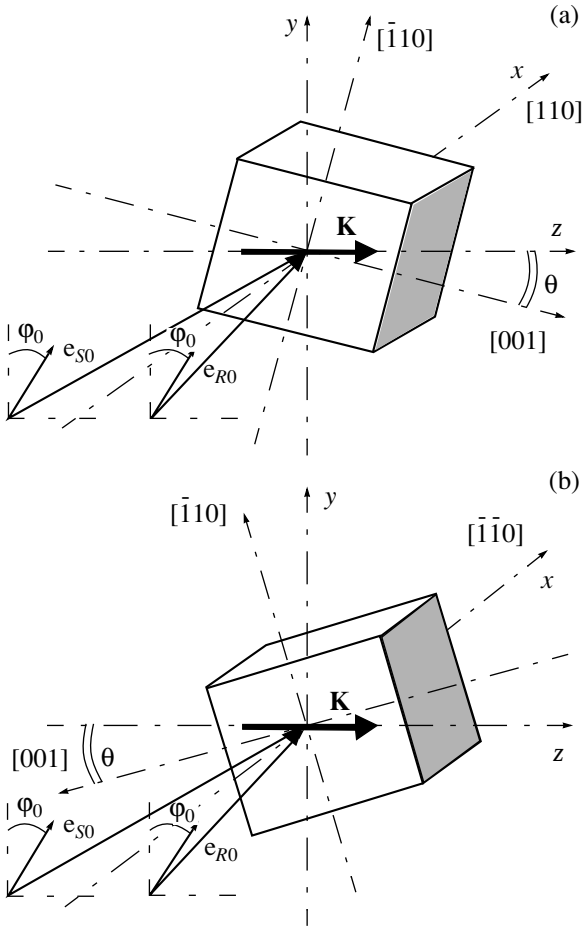

Fig. 2. Schemes of two-wave interaction in passing in the (110) cut of a cubic photorefractive crystal for two opposite orientations of the crystal with respect to the signal and reference waves: (a) $\mathbf{x}^0 \parallel [110]$ and (b) $\mathbf{x}^0 \parallel [\bar{1}\bar{1}0]$.

For the waves having the same polarization at the boundary of the crystal, the two-wave gain $\Gamma = \ln[I_S(x)/I_{S0}]/x$ is

$$\Gamma = 2G(x) + \frac{1}{x}\ln\left[1 + \frac{\gamma^2\exp(-2G(x)x)}{4I_{S0}I_{R0}}|\Phi(x)|^2\right], \quad (25)$$

where the first term describes the conventional unidirectional energy transfer, while the second corresponds to a nonunidirectional energy transfer that always enhances the weak signal wave [10, 13].

For coupled waves having the same linear polarization, the functions $G(x)$ and $\Phi(x)$ are conveniently expressed in terms of the angle φ_0 between the polarization vector at the entrance face of the crystal and the

normal $\mathbf{y}^0$ to the plane of incidence (Fig. 2)

$$G_{\mathrm{LP}}(x) = \frac{\pi n_0^3 r_{41}^s E_{\mathrm{sc}}}{\lambda}\left\{H_\Sigma + \frac{\sin\rho x}{\rho x} \times [H_{\mathrm{EM}}\sin(\rho x + 2\varphi_0) - H_\Delta\cos(\rho x + 2\varphi_0)]\right\}, \quad (26)$$

$$\Phi_{\mathrm{LP}}(x) = \int_0^x \{H_\Delta\sin[2(\rho\xi + \varphi_0)] + H_{\mathrm{EM}}\cos[2(\rho\xi + \varphi_0)]\}\exp(G_{\mathrm{LP}}(\xi)\xi)d\xi, \quad (27)$$

where the integral $\Phi_{\mathrm{LP}}(x)$ is normalized to the quantity $\sqrt{I_{S0}I_{R0}}$. In this case, the polarization of the signal wave remains linear in the crystal, and the corresponding vector components in (24) are

$$\mathbf{S}_\parallel^{\mathrm{LP}}(x) = \sqrt{I_{S0}}[\mathbf{y}^0\cos(\rho x + \varphi_0) + \mathbf{z}^0\sin(\rho x + \varphi_0)],$$
$$\mathbf{S}_\perp^{\mathrm{LP}}(x) = \sqrt{I_{S0}}[-\mathbf{y}^0\sin(\rho x + \varphi_0) + \mathbf{z}^0\cos(\rho x + \varphi_0)]. \quad (28)$$

The angle of rotation of the polarization vector of the signal wave $\Delta\varphi$ in the presence of the pump wave from its direction in the absence of wave coupling is given by

$$\Delta\varphi = -\arctan\left(\frac{\pi n_0^3 r_{41}^s E_{\mathrm{sc}}}{\lambda}\Phi_{\mathrm{LP}}(x)\exp(-G_{\mathrm{LP}}(x)x)\right). \quad (29)$$

If the polarization vector of the signal wave is rotated clockwise in the absence of the pump wave, a positive (negative) value of the angle $\Delta\varphi$ can be interpreted as an increase (decrease) in the value of the specific rotation due to wave coupling.

In the case where the coupled waves have right- or left-circular polarization (which will be indicated by subscripts *r* and *l*, respectively), the field of the signal light wave is the sum of two components, circularly polarized on the left and right, and its vector amplitude has the form

$$\mathbf{S}_r(x) = \sqrt{I_{S0}}\exp\left[\left(\frac{\gamma}{2}H_\Sigma + i\rho\right)x\right]\left\{\frac{\mathbf{z}^0 + i\mathbf{y}^0}{\sqrt{2}} + \frac{\mathbf{z}^0 - i\mathbf{y}^0}{\sqrt{2}}\frac{H_\Delta + iH_{\mathrm{EM}}}{H_\Sigma + i(4\rho/\gamma)} \times\left(1 - \exp\left[-\left(\frac{\gamma}{2}H_\Sigma + i2\rho\right)x\right]\right)\right\}, \quad (30)$$

$$\mathbf{S}_l(x) = i\sqrt{I_{S0}}\exp\left[\left(\frac{\gamma}{2}H_\Sigma - i\rho\right)x\right]\left\{\frac{\mathbf{z}^0 - i\mathbf{y}^0}{\sqrt{2}} + \frac{\mathbf{z}^0 + i\mathbf{y}^0}{\sqrt{2}}\frac{H_\Delta - iH_{\mathrm{EM}}}{H_\Sigma - i(4\rho/\gamma)} \times\left(1 - \exp\left[-\left(\frac{\gamma}{2}H_\Sigma + i2\rho\right)x\right]\right)\right\}. \quad (31)$$

Thus, because of the interaction with the pump wave, the polarization of the signal wave becomes elliptical. The ratio of the minor axis of the polarization ellipse to the major axis, $\delta = b/a$, can be written as

$$\delta = \frac{A - B(x)}{A + B(x)}, \quad (32)$$

where

$$A = \sqrt{H_\Sigma^2 + (4\rho/\gamma)^2},$$

$$B(x) = \sqrt{(H_\Delta^2 + H_{\mathrm{EM}}^2)[1 - 2\exp(-\gamma H_\Sigma x/2)\cos(2\rho x) + \exp(-\gamma H_\Sigma x)]}.$$

The tilt of the polarization ellipse, depending on the interaction length, is characterized by the angle χ between the semiaxis *b* and the *y* axis

$$\chi = \frac{1}{2}\left\{\arctan\left[\frac{\sin(2\rho x)}{\exp(\gamma H_\Sigma x/2) - \cos(2\rho x)}\right] + \arctan\left[\frac{H_\Sigma H_\Delta H_{\mathrm{EM}} - H_\Delta(4\rho/\gamma)}{H_\Sigma H_\Delta + H_{\mathrm{EM}}(4\rho/\gamma)}\right]\right\}. \quad (33)$$

If the coupled waves have a circular polarization, expression (25) for the two-wave gain becomes

$$\Gamma = \gamma H_\Sigma + \frac{1}{x}\ln\left\{1 + \frac{H_\Delta^2 + H_{\mathrm{EM}}^2}{H_\Sigma^2 + (4\rho/\gamma)^2} \times\left[1 - 2\exp\left(-\frac{\gamma}{2}H_\Sigma x\right)\cos(2\rho x) + \exp(-\gamma H_\Sigma x)\right]\right\}. \quad (34)$$

3. COUPLED WAVES OF THE SAME LINEAR POLARIZATION IN THE (110) CUT

We consider the (110) cut of a crystal and assume that the grating vector **K** lies in the (110) plain and

makes an angle θ with the [001] direction (Fig. 2). In this case, there are two "opposite" orientations of the crystal with respect to the signal and reference waves, producing a transmission photorefractive grating. The coefficients H_Σ, H_Δ, and H_{EM} [see (22), (23), (6)–(8)] corresponding to these orientations can be expressed in terms of the components H_{mn} of the matrix $\mathbf{H}_G = \mathbf{H}_{G1} + \mathbf{H}_{G2}$ as follows:

$$H_\Sigma^\pm = \frac{\pm 1}{4}(H_{11} + H_{22} + 2H_{33} - 2H_{12}), \quad (35)$$

$$H_\Delta^\pm = \frac{\mp 1}{4} \times [(H_{11} + H_{22} - 2H_{33} - 2H_{12})\cos\theta + 4\sqrt{2}H_{13}\sin 2\theta], \quad (36)$$

$$H_{EM}^\pm = \frac{1}{4}(H_{11} + H_{22} - 2H_{33} - 2H_{12})\sin 2\theta - \sqrt{2}H_{13}\cos 2\theta, \quad (37)$$

where the indices "+" and "–" refer to the orientations of the x axis along the [110] (Fig. 2a) and $[\bar{1}\bar{1}0]$ (Fig. 2b) directions, respectively. Analytical expressions for the components H_{mn} for the (110) cut of crystals belonging to the point group 23 are well known [7, 17] and presented in the Appendix.

It should be noted that one of the two "opposite" orientations of the crystal can be obtained from the other by rotating the crystal through 180° about the y axis, perpendicular to the grating vector. From (32)–(34), it follows that, under this rotation, the coefficients $H_\Sigma^\pm$ and $H_\Delta^\pm$ become negative, while the coefficient $H_{EM}^\pm$ remains unchanged. For this reason, upon interaction with the reference wave, the intensity and polarization of the signal wave will generally be different for these two opposite orientations of the crystal.

In the transverse geometry [11], where the grating vector **K** is parallel to the $[\bar{1}10]$ axis (**K** ⊥ [001]), the coefficients $H_\Sigma^\pm$ and $H_\Delta^\pm$ vanish. The coefficient $H_{EM}^\pm = r_{41}^T / r_{41}^s$ is independent of the orientation of the crystal, and the polarization dependences of the two-wave gain $\Gamma(\varphi_0)$ (curves *1* in Fig. 3) and of the rotation angle of the polarization vector of the signal wave $\Delta\varphi(\varphi_0)$ (curves *2* in Fig. 3) remain unchanged under the rotation of the crystal through 180° about the y axis. The dependences presented in Fig. 3 correspond to the interaction of light waves (λ = 633 nm) on photorefractive gratings with spatial periods Λ = 1 (Figs. 3a, 3b) and 6 μm (Fig. 3c), produced by a diffusion mechanism in a $Bi_{12}TiO_{20}$ crystal with a specific rotation of the plane of polarization ρ = 6.3 deg/mm. Because bismuth titanate has a high acceptor concentration, $N_A = 3 \times 10^{22}$ m^{-3} [18], we can assume that traps are not saturated and put $E_{sc} \cong E_D$ [see (5)] for gratings with a period of Λ > 1 μm. Here and henceforth, the calculations are performed using the parameters of the $Bi_{12}TiO_{20}$ crystal dealt with in [19]

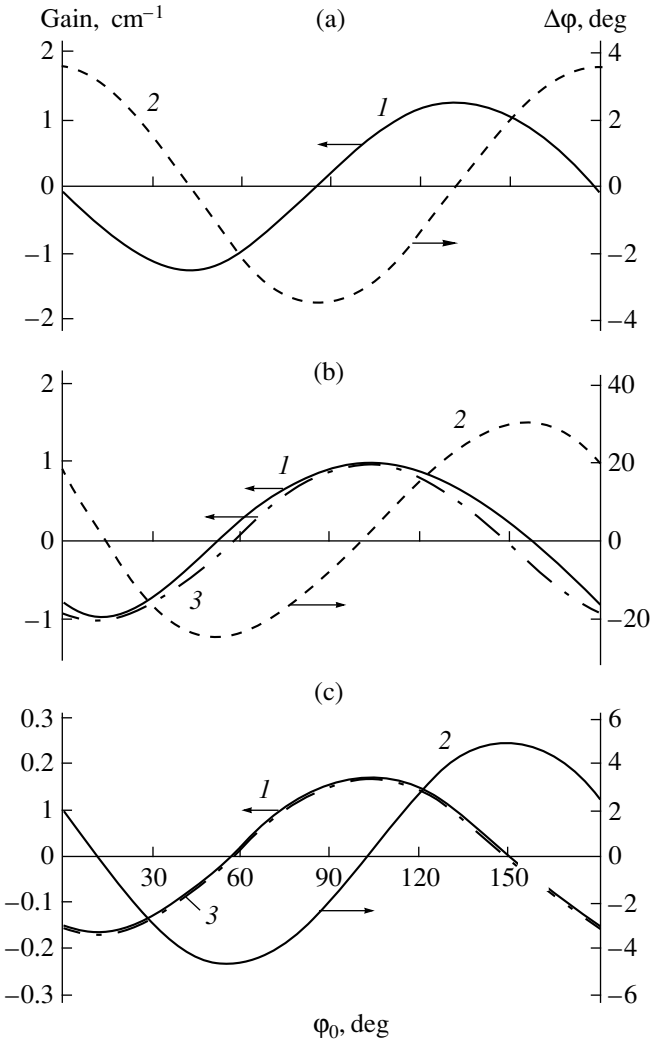

Fig. 3. Dependence of the two-wave gains Γ (*1*) and $2G_0$ (*3*) and of the rotation angle of the polarization vector of the signal wave Δφ at the exit from a $Bi_{12}TiO_{20}$ crystal (*2*) on the angle of the polarization vector at the entrance φ_0 (the same for both waves) for the vector of the photorefractive grating **K** directed along the $[\bar{1}10]$ axis and the following values of the parameters: (a) d = 1 mm, Λ = 1 μm; (b) d = 1 cm, Λ = 1 μm; and (c) d = 1 cm, Λ = 6 μm. The curves for $\mathbf{x}^0 \parallel [110]$ and $\mathbf{x}^0 \parallel [\bar{1}\bar{1}0]$ coincide.

In Fig. 3b, curve *3* is the polarization dependence of the conventional gain $2G(\varphi_0)$ [see (25)], not including the contribution from nonunidirectional energy transfer. This energy exchange can be seen to materially affect the polarization dependences $\Gamma(\varphi_0)$ for thick crystals with small grating periods, especially in the region where $2G \approx 0$. At the same time, the contribution from this energy exchange to the two-wave gain can be

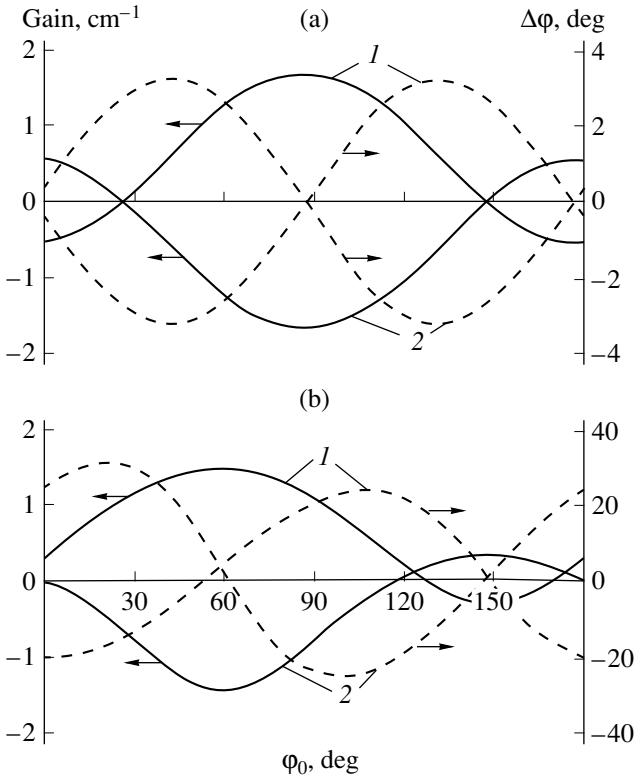

Fig. 4. Dependence of the two-wave gain (solid lines) and of the rotation angle of the polarization vector of the signal wave $\Delta\varphi$ at the exit from a $Bi_{12}TiO_{20}$ crystal (dashed lines) on the angle of the polarization vector φ_0 of the waves at the entrance for the grating vector **K** directed along the $[\bar{1}11]$ axis and different thicknesses of the crystal: (a) d = 1 mm and (b) d = 1 cm; the unit vector $\mathbf{x}^0 \parallel [110]$ (curves *1*) or $[\bar{1}\bar{1}0]$ (curves *2*). The spatial period of the grating is Λ = 1 μm.

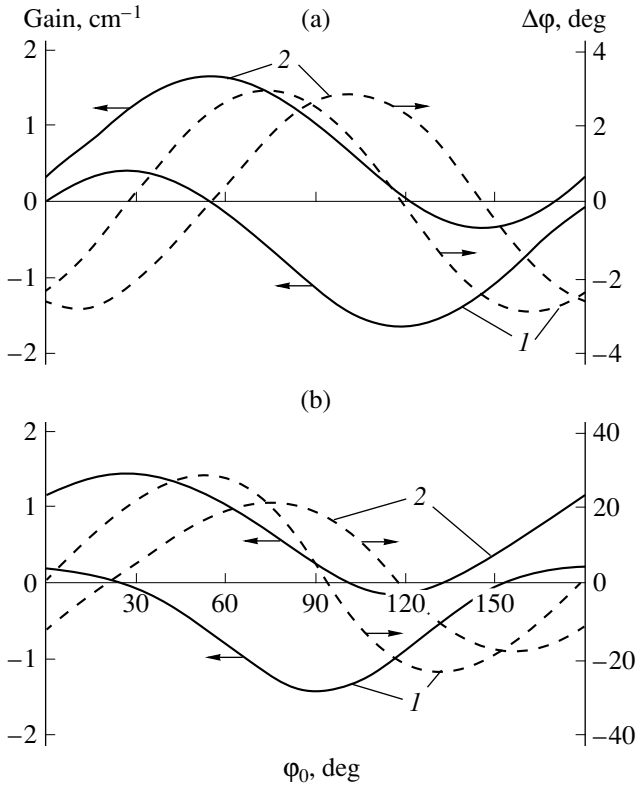

Fig. 5. Dependences $\Gamma(\varphi_0)$ (solid lines) and $\Delta\varphi(\varphi_0)$ (dashed lines) at the exit from a $Bi_{12}TiO_{20}$ crystal for $\mathbf{K} \parallel [\bar{1}1\bar{2}]$, Λ = 1 μm, and different thicknesses of the crystal: (a) d = 1 mm and (b) d = 1 cm; the unit vector $\mathbf{x}^0 \parallel [110]$ (curves *1*) or $\mathbf{x}^0 \parallel [\bar{1}\bar{1}0]$ (curves *2*).

neglected and, hence, $\Gamma(\varphi_0) \cong 2G(\varphi_0)$ for thin crystals or small grating periods. A large amount of nonunidirectional energy transfer produces a substantial change in the polarization of the signal wave, being as large as $\Delta\varphi_m \approx 30°$ for Λ = 1 μm and d = 10 mm. For the orientation of the grating vector in question, $\mathbf{K} \parallel [\bar{1}10]$, the rotation angle of the polarization vector reaches its maximum value $\Delta\varphi_m$ when Γ = 0. In this case, the conventional energy transfer proceeds from the weak to the strong beam and is exactly balanced out by the nonunidirectional transfer of energy to the orthogonally polarized component. The rotation angle of the polarization plane of the signal beam produced by the nonunidirectional energy transfer from the reference wave is decreased with the increasing grating period and decreasing interaction length. However, in the cases of Λ = 1 μm, d = 1 mm (Fig. 3b) and Λ = 6 μm, d = 10 mm (Fig. 3c), where the contribution from the nonunidirectional energy transfer to the two-wave gain can be neglected, this rotation angle has noticeable values, as large as $\Delta\varphi_m \approx 3.5°$ and ≈4.9°, respectively.

The coefficient $H_{EM}^{\pm}$ vanishes for two specific orientations of the grating vector: $\mathbf{K} \parallel [001]$ (longitudinal geometry [11]) and $\mathbf{K} \parallel [\bar{1}11]$. In these cases, the two-wave gain without the nonunidirectional energy transfer $2G_{LP}(\varphi_0)$ changes its sign under the rotation of the crystal through 180° about the y axis. These features of the two-wave interaction are illustrated by Fig. 4a, where the polarization dependences $\Gamma(\varphi_0)$ and $\Delta\varphi(\varphi_0)$ are presented for a grating with $\mathbf{K} \parallel [\bar{1}11]$ in a thin crystal plate (d = 1 mm). For small interaction lengths, the contribution from the nonunidirectional energy exchange is insignificant, and the $\Gamma(\varphi_0)$ and $\Delta\varphi(\varphi_0)$ curves for two opposite orientations of the crystal ($\mathbf{x}^0 \parallel [110]$ and $\mathbf{x}^0 \parallel [\bar{1}\bar{1}0]$) are virtually symmetric to each other with respect to the zero level. As the interaction length increases (Fig. 4b), the mutual symmetry of the

curves disappears, because the nonunidirectional energy transfer (always leading to an increase in the amplitude of the weak wave [10, 13]) makes a noticeable, positive contribution to the two-wave gain.

Figure 5 illustrates the features of the polarization dependences in a more general case, where the coefficients $H_{\Sigma}^{\pm}$, $H_{\Delta}^{\pm}$, and $H_{EM}^{\pm}$ are all nonzero. The curves presented in this figure correspond to the grating vector pointing along the $[1\bar{1}2]$ direction and possess no symmetry under the rotation of the crystal through 180° about the y axis for both large and small interaction lengths.

An analysis of the $\Delta\varphi(\varphi_0)$ and $\Gamma(\varphi_0)$ dependences presented in Figs. 3–5 and of expressions (25)–(27) and (29), describing them, reveals that the extremal values $\Delta\varphi_m$ of the rotation angle of the polarization vector of the signal wave are observed at an extremal rate of change of the two-wave gain $\Gamma(\varphi_0)$, with maximum (minimum) values $\Delta\varphi_m$ corresponding to minimum (maximum) values of the derivative $d\Gamma/d\varphi_0$.

Thus, we have shown that nonunidirectional energy transfer can significantly affect the intensity and polarization state of the signal wave in the case of two-wave interaction on a photorefractive grating produced by diffusion in a cubic gyrotropic crystal.

ACKNOWLEDGMENTS

This work was supported in part by the Intant company (Tomsk).

APPENDIX

For a crystal belonging to the point group 23, the dependence of the components of the symmetric matrix $\mathbf{H}_G = \mathbf{H}_{G1} + \mathbf{H}_{G2}$ on the angle θ defining the direction of the grating vector $\mathbf{K}$ in the (110) plane (Fig. 2) has the form [17]

$$H_{11} = \frac{e_{14}\sin^2\theta\cos\theta}{r_{41}^u C(\theta)} \times \{(p_{11}+p_{12})[2C_{11}\cos^2\theta + (C_{44}^{\mathrm{E}} - C_{12})\sin^2\theta] + p_{21}[C_{11}\sin^2\theta + C_{12}(1-5\cos^2\theta) - 2C_{44}^{\mathrm{E}}\cos 2\theta]\}, \quad \text{(A1)}$$

$$H_{22} = \frac{e_{14}\sin^2\theta\cos\theta}{r_{41}^u C(\theta)} \times \{(p_{11}+p_{21})[2C_{11}\cos^2\theta + (C_{44}^{\mathrm{E}} - C_{12})\sin^2\theta] + p_{12}[C_{11}\sin^2\theta + C_{12}(1-5\cos^2\theta) - 2C_{44}^{\mathrm{E}}\cos 2\theta]\}, \quad \text{(A2)}$$

$$H_{33} = \frac{e_{14}\sin^2\theta\cos\theta}{r_{41}^u C(\theta)} \times \{(p_{12}+p_{21})[2C_{11}\cos^2\theta + (C_{44}^{\mathrm{E}} - C_{12})\sin^2\theta] + p_{11}[C_{11}\sin^2\theta + C_{12}(1-5\cos^2\theta) - 2C_{44}^{\mathrm{E}}\cos 2\theta]\}, \quad \text{(A3)}$$

$$H_{12} = \cos\theta + \frac{2e_{14}p_{44}^{\mathrm{E}}\sin^2\theta\cos\theta}{r_{41}^u C(\theta)} \times [(C_{12} - C_{44}^{\mathrm{E}})\sin^2\theta - 2C_{11}\cos^2\theta], \quad \text{(A4)}$$

$$H_{13} = \frac{\sin\theta}{\sqrt{2}} + \frac{e_{14}p_{44}^{\mathrm{E}}\sin\theta}{\sqrt{2}r_{41}^u C(\theta)} \times [C_{12}\sin^2\theta(6\cos^2\theta - \sin^2\theta) - C_{11}(4\cos^4\theta + \sin^4\theta) - 2C_{44}^{\mathrm{E}}\sin^4\theta], \quad \text{(A5)}$$

$$H_{23} = -H_{13}, \quad \text{(A6)}$$

where we have introduced the notation

$$C(\theta) = \sin^2\theta[(2C_{12}^2 - C_{11}^2)\cos^2\theta - 2C_{44}^{\mathrm{E}}\sin^2\theta] - C_{11}C_{12}\sin^2\theta\cos^2\theta + C_{12}C_{44}^{\mathrm{E}}\sin^2\theta(5\cos^2\theta - 1) - C_{11}C_{44}^{\mathrm{E}}(1+\cos^4\theta). \quad \text{(P7)}$$

REFERENCES

1. D. J. Webb, A. Kieβling, B. I. Sturman, *et al.*, Opt. Commun. **108**, 31 (1994).
2. V. V. Shepelevich, N. N. Egorov, and V. V. Shepelevich, Jr., J. Opt. Soc. Am. B **11**, 1394 (1994).
3. J. R. Goff, J. Opt. Soc. Am. B **12**, 99 (1995).
4. H. C. Pedersen and P. M. Johansen, J. Opt. Soc. Am. B **12**, 592 (1995).
5. H. Tuovinen, A. A. Kamshilin, R. Ravattinen, *et al.*, Opt. Eng. **34**, 2641 (1995).
6. H. C. Ellin and L. Solimar, Opt. Commun. **130**, 85 (1996).
7. S. M. Shandarov, A. V. Reshet'ko, A. A. Emelyanov, *et al.*, Proc. SPIE **2969**, 202 (1996).
8. H. Touvinen, A. A. Kamshilin, and T. Jaaskelainen, J. Opt. Soc. Am. B **14**, 3383 (1997).
9. V. V. Shepelevich, Opt. Spektrosk. **83**, 172 (1997) [Opt. Spectrosc. **83**, 161 (1997)].
10. R. V. Litvinov and S. M. Shandarov, Opt. Spektrosk. **83**, 334 (1997) [Opt. Spectrosc. **83**, 313 (1997)].
11. E. Shamonina, V. P. Kamenov, K. H. Ringhofer, *et al.*, Opt. Commun. **146**, 62 (1998).
12. E. Shamonina, V. P. Kamenov, K. H. Ringhofer, *et al.*, J. Opt. Soc. Am. B **15**, 2552 (1998).

13. V. Yu. Krasnoperov, R. V. Litvinov, and S. M. Shandarov, Fiz. Tverd. Tela (St. Petersburg) **41**, 632 (1999) [Phys. Solid State **41**, 568 (1999)].

14. V. V. Shepelevich, Y. Hu, A. Firsov, *et al.*, Appl. Phys. B **68**, 923 (1999).

15. B. I. Sturman, E. V. Podivilov, K. H. Ringhofer, *et al.*, Phys. Rev. E **60**, 3332 (1999).

16. M. P. Petrov, S. I. Stepanov, and A. V. Khomenko, *Photorefractive Crystals in Coherent Optics* (Nauka, St. Petersburg, 1992).

17. S. M. Shandarov, V. V. Shepelevich, and N. D. Khat'kov, Opt. Spektrosk. **70**, 1068 (1991) [Opt. Spectrosc. **70**, 627 (1991)].

18. J. E. Millerd, E. M. Garmire, M. B. Klein, *et al.*, J. Opt. Soc. Am. B **9**, 1449 (1992).

19. S. I. Stepanov, S. M. Shandarov, and N. D. Khat'kov, Fiz. Tverd. Tela (Leningrad) **29**, 3054 (1987) [Sov. Phys. Solid State **29**, 1754 (1987)].

Translated by Yu. Epifanov

Physics of the Solid State, Vol. 42, No. 8, 2000, pp. 1443–1446. Translated from Fizika Tverdogo Tela, Vol. 42, No. 8, 2000, pp. 1404–1407.

SEMICONDUCTORS AND DIELECTRICS

Raman Scattering in the Bi_2TeO_5 Single Crystal

K. V. Domoratskiĭ*, V. I. Pastukhov*, A. Yu. Kudzin*, L. Ya. Sadovskaya*, V. M. Rizak, and V. A. Stefanovich****

** Dnepropetrovsk State University, pr. Gagarina 72, Dnepropetrovsk 10, 320625 Ukraine*

*** Uzhgorod State University, Podgornaya ul. 46, Uzhgorod, 294000 Ukraine*

e-mail: elf@ff. dsu. dp. ua

Received November 24, 1999

Abstract—Polarized Raman spectra of the Bi_2TeO_5 single crystal have been investigated for the first time. The group-theoretic analysis of the first–order vibrational spectra is performed. The number of the experimentally observed bands is less than the predicted number of normal modes. The spectral ranges with similar bands are revealed. Some ranges in the spectra of Bi_2TeO_5 are identified from the spectral data for the materials containing bismuth–oxygen and tellurium–oxygen complexes. © *2000 MAIK "Nauka/Interperiodica".*

1. INTRODUCTION

Bismuth tellurite (Bi_2TeO_5) has been investigated [1–4] as a promising material with photorefractive and acousto-optic properties. It is of interest to study the lattice dynamics of its single crystal. The vibrational spectra of Bi_2TeO_5 in the frequency range 4000–400 cm^{-1} were studied by IR spectroscopy in [3, 4]. However, data on Raman spectra for single crystals of this material are unavailable.

The purpose of this work was to perform the symmetry analysis of fundamental vibrations in the Bi_2TeO_5 single crystal and to study these vibrations experimentally by Raman spectroscopy.

2. GROUP-THEORETIC ANALYSIS

Bismuth tellurite crystallizes in an orthorhombic crystal system and belongs to the noncentrosymmetric space group *Abm*2. The unit cell of Bi_2TeO_5 with the parameters a = 11.602 Å, b = 16.461 Å, and c = 5.523 Å contains formula units Z = 8 ($N = 8Z$ = 64 atoms) [5].

The group-theoretic analysis of the first-order vibrational spectrum of Bi_2TeO_5 was based on the atomic site symmetry [6]. The number of bands assigned to the single-particle interactions should correspond to the number of atoms in the primitive cell. Since bismuth tellurite has the base-centered unit cell, we have accounted for vibrations of only half its atoms in our analysis (n = 32). It is found that $3n$ = 96 normal atomic vibrations of Bi_2TeO_5 are distributed over the symmetry types as follows:

$$24A_1 + 22A_2 + 25B_1 + 22B_2 \text{ (optical)},$$

$$A_1 + B_1 + B_2 \text{ (acoustic)}.$$

Vibrations of the $A_1(z)$, $B_1(x)$, and $B_2(y)$ types are the polar ones (IR active).

3. EXPERIMENTAL TECHNIQUE

Single crystals of bismuth tellurite were grown by the Czochralski technique. The batch was prepared from a mixture of 47 mol % Bi_2O_3 and 53 mol % TeO_2 (high-purity grade). The procedure of preparing the Bi_2TeO_5 single crystals was described in [7]. Two samples were obtained in the from of parallelepipeds $4.5 \times 7.5 \times 9$ mm and $5 \times 12 \times 6$ mm in size with the edges along the orthorhombic crystallographic axes $X \parallel a$, $Y \parallel b$, $Z \parallel c$.

The polarized Raman spectra were measured on a DFS-24 spectrometer (excitation by a He–Ne laser; wavelength, 632.8 nm; power, 50 mW) and a DFS-12 spectrometer (excitation by the second harmonic of a YAG : Nd^{3+} laser; wavelength, 532.05 nm; power, 300 mW). The spectral resolution was 1 cm^{-1}. The measurements were performed in a 90° geometry. The exciting radiation was focused on the sample by a collecting lens. The spectra were recorded using the photon-counting method with a FEU-79 cooled photomultiplier. In the present paper, we report and discuss the results obtained with the DFS-12 spectrometer, because a better signal-to-noise ratio has been achieved in this case.

4. DISCUSSION OF RAMAN SPECTRA

Figures 1 and 2 demonstrate the Raman spectra of the Bi_2TeO_5 single-crystal sample, which were obtained on a DFS-12 spectrometer at room temperature. The experimentally found number of vibrational bands (parenthesized in the figures behind the geometry of scattering) is less than the number of normal modes predicted by the group-theoretic analysis. The

1063-7834/00/4208-1443$20.00

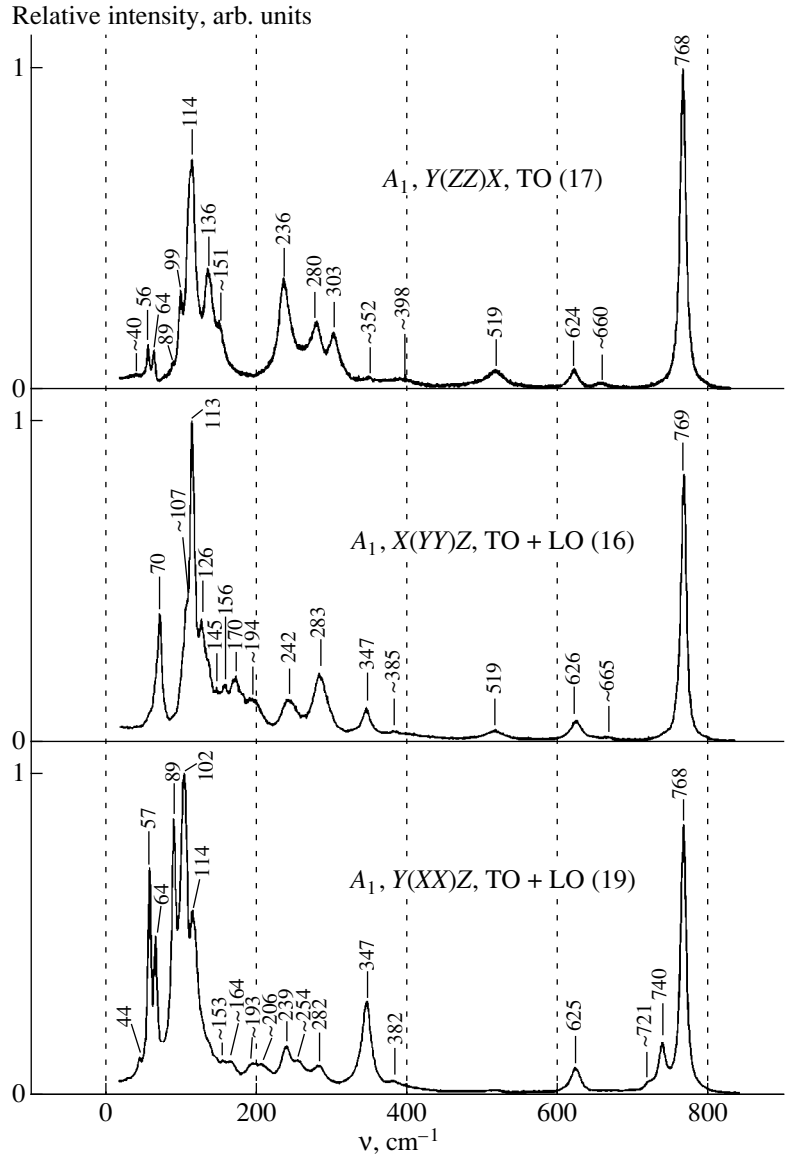

Fig. 1. Raman spectra of Bi_2TeO_5 for diagonal components of the Raman tensor.

spectra of mixed vibrations shown in Fig. 2, together with fragments of the spectra for the totally transverse phonons, indicate the longitudinal-transverse splitting of polar vibrations in Bi_2TeO_5 for the B_1 and B_2 representations. Since the splitting is small, we can assume that the ion contribution to the polarization is insignificant. However, it is quite detectable by Raman spectroscopy.

The spectral range below 150 cm^{-1} is characterized by the presence of narrow, partially overlapping bands, among which are rather intense bands and bands with a low intensity. Above this range (150–400 cm^{-1}), the spectra contain broader bands of lower intensity. The bands are actually absent in the range 400–600 cm^{-1}. A high-frequency range (above 600 cm^{-1}) is characterized by the presence of individual bands with different degrees of damping. In molecular crystals, the interaction between molecules, their translations, and librations manifest themselves in the low-frequency range (external vibrations). The intramolecular vibrations are observed at higher frequencies (internal vibrations). In some cases, such a separation is carried out for ionic complexes in ionic-covalent crystals. Bismuth telluride exhibits several structural units [5]. Apparently, the frequency range below 150 cm^{-1} is promarily attributed to the bending vibrations of the Bi–O–Bi, Bi–O–Te, and Te–O–Te bonds, which can be conditionally treated as the interactions between coordination polyhedra of different types. The bands above 150 cm^{-1} are most probably associated with the vibrations inside the complexes involved in Bi_2TeO_5.

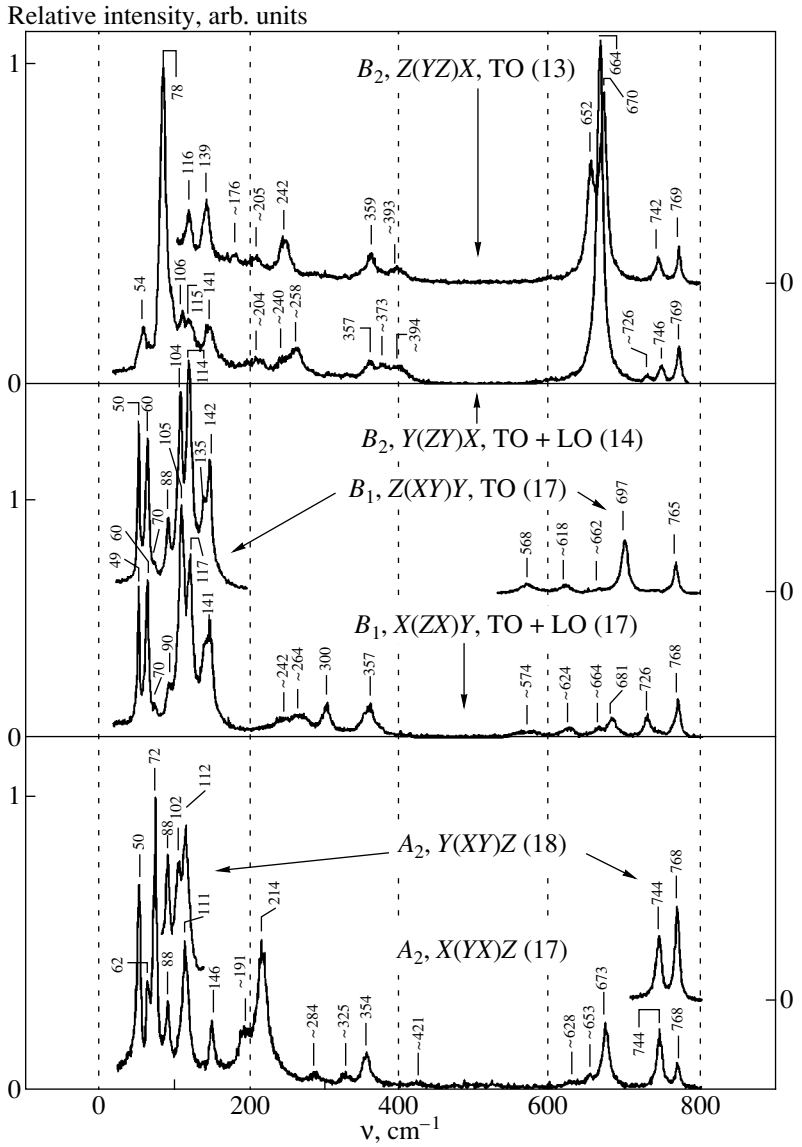

Fig. 2. Raman spectra of Bi_2TeO_5 for off-diagonal components of the Raman tensor.

Three types of bismuth–oxygen polyhedra with sevenfold- and eightfold-coordinated oxygens are found in the structure of Bi_2TeO_5 [5]. Similar sevenfold-coordinated bismuth–oxygen polyhedra are observed in sillenites, for example, in $Bi_{12}GeO_{20}$ [8]. The Raman spectra for α-Bi_2O_3 and sillenites are similar to each other [9]. The spectral range that corresponds to the vibrational modes of α-Bi_2O_3 is limited by the band at 445 cm^{-1}. For sillenites, this band correlates with the band at about 530 cm^{-1}. However, according to [9], the vibrational range of the Bi–O bonds is limited by the frequency of 650 cm^{-1}. It is quite probable that the majority of bands in the range 150–650 cm^{-1} in the spectra of Bi_2TeO_5 can be attributed to vibrations in the bismuth–oxygen polyhedra.

The tellurium atom in the Bi_2TeO_5 lattice has the nearest anionic environment, which consists of five oxygen atoms. As follows from comparison of the Te–O bond lengths, the main structural unit is the TeO_3 pyramidal complex [5], whose molecular symmetry in the given crystal is described by the symmetry group C_1. According to [10], the frequencies of internal vibrations obtained for a free TeO_3^{2-} ion with the C_{3v} symmetry in an aqueous solution of α-TeO_3 are as follows: $\nu_1^v(A_1) = 758$, $\nu_3^v(E) = 703$, $\nu_2^d(A_1) = 364$, and $\nu_4^d(E) = 326$ cm^{-1} (superscripts v and d designate the stretching and bending vibrations, respectively). A certain correlation between the band frequencies in the range 650–800 cm^{-1} and the ν^d values for TeO_3^{2-} is observed in the

spectra of Bi_2TeO_5. This correlation, together with the actual absence of phonon activity in the adjacent lower-frequency range (Figs. 1, 2), permits us to attribute the bands in the range 650–800 cm^{-1} in the spectra of Bi_2TeO_5 to the stretching vibrations of the TeO_3 complex.

A similar assignment of the bands in the range 400–800 cm^{-1} to the vibrations of bismuth–oxygen and tellurium–oxygen bonds was made in the IR spectroscopic study of bismuth tellurite [3].

The majority of the Bi–O bonds in the bismuth–oxygen polyhedra of Bi_2TeO_5 and sillenites are close in length. As is seen from Fig. 1, the bands at 519 and ~625 cm^{-1} of the totally symmetric representation A_1 are located separately from the neighboring bands. These bands correlate with the bands at ~537 and 621 cm^{-1} in the spectra of sillenites [9]. It is evident that the former bands can be interpreted in a similar way; i.e., they can be assigned to the stretching vibrations of the Bi–O bonds, which are identical for the materials under consideration [11]. In Bi_2TeO_5, the bond that corresponds to the former band is weaker and its vibrations occur at a lower frequency. The location of the latter band can indicate that the strength of the given Bi–O bond in bismuth telluride is somewhat higher than that in sillenites.

The difference in widths of the spectral bands in the ranges above and below 150 cm^{-1}, which is characteristic of bismuth tellurite, is also observed for other bismuth-containing oxides considered previously [9]. Broad bands widths of the spectral bands in the range of "intracomplex" vibrations are due to the site disordering in polyhedral complexes. Within the crystal-chemical approach, this disordering is explained by the hybridization of the bonds between elements that have uncompleted core orbitals (when the outer orbitals are completely occupied) and occur in oxygen polyhedral environment [9, 12]. This character of the bonds is responsible for both the considerable width of the bands in the higher-frequency range and its temperature sensitivity [9]. The decisive role of the site disordering mechanism for Bi_2TeO_5 is shown by a considerable increase in the width of the bands in the range 150–650 cm^{-1}, which is observed upon heating the samples from 100 to 633 K in the geometry $y(zz)x$ (for example, from 10 to 30 cm^{-1} for the band at 236 cm^{-1}). The broadening of the bands attributed to the Te–O stretching vibrations was also observed with an increase in the temperature. It is probable that the tellurium–oxygen complexes are disordered in a similar manner. This can be the major reason for the discrepancy between the experimental spectra obtained at room temperature and the results of the group-theoretic analysis.

ACKNOWLEDGMENTS

We thank V. M. Gorbenko for help in sample preparation.

REFERENCES

1. I. Foldvari, Huimin Liu, Richard C. Powell, and A. Peter, J. Appl. Phys. **71**, 5465 (1992).
2. A. M. Antonenko, V. M. Gorbenko, L. Ya. Sadovskaya, and S. Yu. Ermakov, Fiz. Tverd. Tela (S.-Peterburg) **38**, 938 (1996) [Phys. Solid State **38**, 518 (1996)].
3. V. V. Kucha, A. V. Khomich, V. B. Kravchenko, and P. I. Perov, Neorg. Mater. **20**, 314 (1984).
4. I. Folvari, A. Peter, L. A. Kappers, *et al.*, J. Mater. Sci. **27**, 750 (1992).
5. D. Mercurio, M. El Farissi, B. Frit, and P. Goursat, Mater. Chem. Phys. **12** (9), 467 (1983).
6. G. N. Zhizhin, B. N. Mavrin, and V. F. Shabanov, *Optical Vibrational Spectra of Crystals* (Nauka, Moscow, 1984).
7. K. V. Domoratsky, A. Yu. Kudzin, L. Ya. Sadovskaya, and G. Ch. Sokolyanskii, Ferroelectrics **214**, 191 (1998).
8. S. C. Abrahams, P. B. Jamieson, and J. L. Berdstein, J. Chem. Phys. **47**, 4034 (1967).
9. R. J. Betsch and W. B. White, Spectrochim. Acta A **34**, 505 (1978).
10. K. Nakamoto, *Infrared and Raman Spectra of Inorganic and Coordination Compounds* (Wiley, New York, 1986; Mir, Moscow, 1991).
11. W. Wojdovski, Phys. Status Solidi B **130**, 121 (1985).
12. A. K. Yakhkind, in *Structure and Physicochemical Properties Inorganic Glasses*, Ed. by A. G. Vlasov and V. A. Florinskaya (Khimiya, Leningrad, 1974).

Translated by N. Korovin

Physics of the Solid State, Vol. 42, No. 8, 2000, pp. 1447–1450. Translated from Fizika Tverdogo Tela, Vol. 42, No. 8, 2000, pp. 1408–1411.

SEMICONDUCTORS AND DIELECTRICS

Nonempirical Quantum-Chemical Calculations of the Magnetic Shielding Tensor of Nuclei $^{47, 49}$Ti in Crystalline Titanium Oxides

L. S. Vorotilova, L. V. Dmitrieva, and B. F. Shchegolev

Grebenshchikov Institute of Silicate Chemistry, Russian Academy of Sciences, ul. Odoevskogo 24/2, St. Petersburg, 199155 Russia

e-mail: lvs@isc.nw.ru

Received January 18, 2000

Abstract—Nonempirical computations are carried out for the chemical shift tensor for the $^{47, 49}$Ti nuclei in crystalline modifications of titanium dioxide and barium titanate. Computations are made using the cluster approach and the GAUSSIAN-94 program. A comparison with the experiment shows that such an approach can be used for titanium oxides containing TiO_6 complexes. It is noted that the choice of the basic wave functions for the titanium atoms plays a significant role. © *2000 MAIK "Nauka/Interperiodica".*

The modern techniques of magnetic radiospectroscopy of solids provide abundant information about the electronic structure of the crystal lattice, the local symmetry of the structural positions, and the nature of the chemical bond in the crystal. In the NMR technique, the electric field gradient (EFG) and the chemical shift tensor provide rich information concerning crystal chemistry [1]. The chemical shift tensor reflects the effects associated with the magnetic shielding of nuclei in an external magnetic field. Its theoretical analysis is based on the Ramsay theory. Quantitative computation of magnetic shielding not only allows a detailed interpretation of the experimental results, but also establishes possible correlations of the parameters of the chemical shift with the structure and a number of properties of the crystal.

Recently published experimental NMR data on the chemical shift of the ^{49}Ti nuclei in two modifications (anatase and rutile) of titanium dioxide [2] have triggered investigations concerning the computation of the magnetic shielding effect in these crystals. Additional verification of the proposed computational technique was made possible by the experimental results for the $^{47, 49}$Ti nuclei in $BaTiO_3$ [3, 4].

Of special interest are the nonempirical quantum chemical computations of the magnetic shielding (MS) for atomic nuclei. For light nuclei (^{1}H, ^{13}C, ^{17}O, ^{29}Si), such computations have been carried out quite successfully for a long time. An entirely different situation arises in the case of heavier nuclei, including $^{47, 49}$Ti. So far, the results of theoretical estimation of MS for titanium have only been reported in a few publications [5–7], and Tossell [5, 6] was the only one to consider not only molecular, but also some crystalline titanium compounds.

In this work, it is proposed to carry out MS computations using the cluster approach, which was successfully applied for computing the EFG tensor at the sites of quadrupole nuclei in crystals [8].

1. COMPUTATION OF THE MS TENSORS FOR $^{47, 49}$Ti NUCLEI IN RUTILE AND ANATASE

The crystal structure of rutile and anatase, the two modifications of TiO_2, has been investigated thoroughly [9]. Both types of crystals are comprised of TiO_6 octahedra. This structural unit, viz., the titanium–oxygen octahedron, was treated as a cluster in which the lengths of bonds between atoms and the angles in the cluster were taken directly from the structural data for each crystal. All computations were carried out for the cluster $(TiO_6)^{8-}$ using the MO LCAO SCP (Hartree–Fock–Roothaan) technique and the GAUSSIAN-94 program. The atomic bases (13*s*7*p*5*d*) for Ti [10] and (10*s*, 6*p*)/[5*s*, 3*p*] for O [11], supplemented by the *d* function with an exponent 0.85, were used. These bases were found to be quite effective in quantum-chemical cluster computations of a number of properties of crystalline titanium oxides [12]. Computations of the MS tensor were based on the GIAO method [13, 14].

The principal values of the MS tensor computed for $^{47, 49}$Ti in rutile (σ_{xx}, σ_{yy}, σ_{zz}), and anatase [$\sigma_{xx} = \sigma_{yy} = \sigma_\perp$, $\sigma_{zz} = \sigma_\parallel$ (axial symmetry)] are presented in Table 1. These quantities are usually expressed in parts per million, or ppm. The direction of the axes in the titanium–oxygen octahedra are shown in the figure.

It should be remarked that, instead of the magnetic shielding tensor, the relative quantity normally determined in experiments is the chemical shift tensor δ.

1063-7834/00/4208-1447$20.00

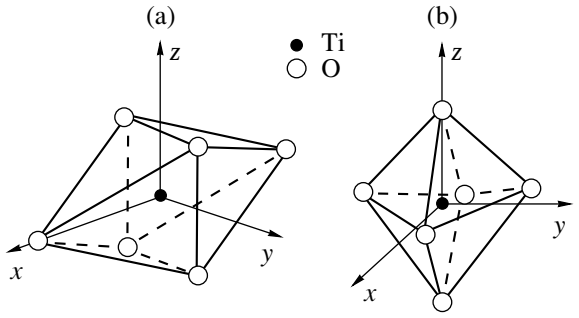

Choice of the direction of coordinate axes in the titanium–oxygen octahedra of rutile (a) and anatase (b).

(The absolute scale for the shifts is only introduced for a few nuclei.) The following relation holds for $|\sigma| \ll 1$: $\delta = \sigma_{ref} - \sigma_s$, where σ_s is the MS tensor for the given nucleus in the sample, and σ_{ref} is the MS tensor for the given nucleus in the reference material.

In this connection, it would be expedient to compute the MS tensor σ_{ref}^{Ti} for Ti nuclei in the reference material for comparing the theoretical values of the MS tensor σ_s^{Ti} with the experimental values of δ^{Ti}. Liquid $TiCl_4$ was used as the reference material as in [3].

For computing σ_{ref}^{Ti} in the $TiCl_4$ molecule, we first chose the same basis for the Ti atom as in TiO_2. However, the value of the MS tensor was found to differ significantly (by a factor of 1.5–3 depending on the basis on Cl) from the available experimental data [5, 7] for the optimized, and the experimental geometry of the molecule. This discrepancy is probably associated with the peculiarities of the basis for Ti in [10], which was optimized not for the ground state, but for an excited state (^5F) of the Ti atom. It was mentioned above that the efficiency of such a basis was proved in the computations of a number of properties of crystalline oxides of titanium, whose basic structural fragment is the titanium–oxygen octahedron. Apparently, such a basis may not be effective for other titanium compounds. Hence, we computed the MS tensor for $^{47, 49}$Ti nuclei for several standard balanced bases on Ti and Cl atoms, e.g., 3–21*G**, 6– 31*G**, and 6–311*G**. It follows from Table 2 that the value of σ_{ref}^{Ti} (in view of the symmetry of the molecule, the MS tensor is isotropic and has only one independent component) changes monotonically with the broadening of bases in the series under consideration, and agrees well with the data available in the literature [5, 7]. For a theoretical estimation of the chemical shift tensor in both modifications of TiO_2, two values of σ_{ref}^{Ti} obtained in the most comprehensive bases 6–31*G** and 6–311*G** were tried:

$$\sigma_{ref}^{Ti}(1) = -472 \text{ ppm}, \quad \sigma_{ref}^{Ti}(2) = -502 \text{ ppm}.$$

Table 3 shows the theoretical values of the chemical shift for rutile and anatase.[1] A comparison with the experiment shows a good agreement between these quantities for anatase (3–5%) and a slightly worse agreement for rutile (8–15%). Apparently, this discrepancy is due to the different accuracies of measurement of δ^{Ti} in the two modifications of TiO_2. Indeed, while measuring the chemical shift in rutile [2], we used the data on quadrupole interaction obtained by Kanert and Kolem [15] without taking into account the magnetic shielding of Ti nuclei. On the other hand, the parameters of chemical shift tensor and quadrupole interaction tensor for anatase were determined from the same experimental spectra [2]. However, it is quite likely that the discrepancy between the theory and experiment is due to the error in computations that were carried out without taking into account the effect of the crystal surrounding of the cluster, among other things. It is quite difficult to take this effect into consideration for materials like TiO_2, which have a rather low symmetry.

During an analysis of the experimental values of shifts in TiO_2, it was observed that the direction of the minimum component of the shielding tensor coincides with the longest Ti–O bond [2]. This observation was confirmed by the computations: it gives the minimum value of σ along the maximum length of the bond in both rutile and anatase. On the other hand, another correlation mentioned in [2], viz., the relation between the isotropic part of the MS tensor and the average Ti–O

Table 1. Cluster computations of the tensor of magnetic shielding for $^{47, 49}$Ti in rutile and anatase

$(TiO)_6^{8-}$	σ^{Ti}, ppm		
	σ_{xx}	σ_{yy}	σ_{zz}
Rutile	416	437	514
Anatase	440	440	378

Table 2. Computations of the tensor of magnetic shielding for $^{47, 49}$Ti in the $TiCl_4$ molecule

Basis	σ^{Ti}, ppm	References
3–21*G**	−298	Our work
6–31*G**	−472	Our work
6–311*G**	−502	Our work
Double-zeta with auxiliary functions	−404	[7]
Polarized double-zeta	−482	[5]

[1] The advantage of the 6–31*G** basis for Ti in the molecule of $TiCl_4$ over the basis (13*s*7*p*5*d*) was further confirmed by the following computations: within the first basis, the optimized geometry of the molecule and its IR frequencies coincide to within 2–7% with the experimental results, while the introduction of the second basis deteriorates the result and causes a 5–15% deviation of these quantities from the experimental values.

Table 3. Comparison of the theoretical values of the chemical shift tensor for ^{47,49}Ti in rutile and anatase with the experimental results

	σ_{ref}, ppm	δ, ppm				
		rutile			anatase	
		δ_{xx}	δ_{yy}	δ_{zz}	$\delta_\perp$	$\delta_\parallel$
Theory	−472	−888	−909	−986	−912	−850
	−502	−918	−939	−1016	−942	−880
Experiment		−815	−885	−885	−960	−840

bond length in the octahedron, was not confirmed by computations.

2. COMPUTATION OF THE MS TENSOR FOR ^{47,49}Ti NUCLEI IN BARIUM TITANATE

Technologically, barium titanate $BaTiO_3$ is the most important and intensively studied ferroelectric crystal. It has a perovskite cubic structure at temperatures higher than the Curie temperature (T = 130°C), and undergoes a series of structural phase transformations upon cooling: from cubic to tetragonal symmetry and further to orthorhombic and rhombohedral symmetry.

The NMR spectra of the ^{47,49}Ti nuclei in $BaTiO_3$ were studied in [3, 4]. The chemical shift δ^{Ti} relative to $TiCl_4$ was determined for the cubic phase. In the tetragonal phase, we measured the anisotropic component of the chemical shift tensor δ_a, which was defined in [4] for the case of axial symmetry as follows:

$$\delta_a = \delta_{iso} - \delta_\parallel = (\delta_\parallel + 2\delta_\perp)/3 - \delta_\parallel = 2/3(2\delta_\perp - \delta_\parallel).$$

The technique for calculating the magnetic shielding proposed above is also applicable to these two phases of $BaTiO_3$. For the $(TiO_6)^{8-}$ clusters having the geometry of the corresponding phases, the results of computations are presented in Table 4.

A comparison with the experimental results shows that computations for the cubic phase do not yield a good agreement between the theoretical and experimental values of the shift δ^{Ti}. To improve the results, one can try to take into account the crystalline surroundings of the cluster, simulating it by a set of point charges while preserving the electric neutrality of the system. In the case under consideration, we surrounded the cluster $(TiO_6)^{8-}$ by eight charges $q = +1.0e$ (e is the elementary charge) occupying the Ba ion positions. The correctness of such a choice is confirmed by calculations of the potential at the site of the Ti nucleus under consideration. We compared the values of the potential created by the above-mentioned eight charges, on the one hand, and the infinite lattice of point charges on the other. For the lattice formed by the point charges $q_{Ba} = +2.0e$, $q_O = -1.5e$, $q_{Ti} = +2.5e$ (q_{Ti} has a value close to the Millikan's charge in the cluster computations), it is shown by the results of computations that these two potentials coincide to within 5%. The value of the tensor δ^{Ti} in the cubic phase of $BaTiO_3$ for the system $[(TiO_6)^{8-} + 8e]$ agrees well with the experimental data (Table 4). Table 4 also shows the results of computations of the MS tensor for the tetragonal phase of barium titanate. Since only the anisotropic part of the chemical shift tensor was determined in the experiments, a comparison with the computational results was confined only to this quantity. In view of the smallness of the quantity δ_a and the fact that it is the difference between two large quantities, we can assume that the agreement between the theory and the experiment is quite satisfactory.

Thus, the following conclusions can be drawn from the results of our investigations:

(1) The proposed cluster approach is completely applicable for nonempirical computations of the MS tensor of nuclei ^{47,49}Ti in the crystals containing TiO_6 octahedra. It provides a qualitative, as well as quantitative, description of the magnetic shielding effects.

(2) The choice of a basis for Ti atoms in the MS computations is the most important problem. Different

Table 4. Computation of tensors σ^{Ti} and δ^{Ti} for two phases of $BaTiO_3$

$BaTiO_3$	Theory				Experiment	
	σ, ppm	σ_{ref}, ppm	δ, ppm	δ_a, ppm	δ, ppm	δ_a, ppm
$(TiO_6)^{8-}_{cub}$	433	−472 −502	−905 −935	0	−741 [5]	0
$[(TiO_6)^{8-} + 8e]_{cub}$	267	−472 −502	−739 −769			
$(TiO_6)^{8-}_{tetr}$	$\sigma_\perp$: 418 $\sigma_\parallel$: 436			12	–	40 [6]

sets of bases are found to be optimal for oxides and halogenides of titanium.

(3) A proper consideration of the effect of the cluster surroundings may turn out to be important for refining the isotropic part of the MS tensor.

ACKNOWLEDGMENTS

The authors are indebted to O. E. Kvyatkovskiĭ for a fruitful discussion of the results.

This research was supported by the Federal Program "Integration" (project no. 326.44).

REFERENCES

1. *Multinuclear NMR*, Ed. by J. Mason (Plenum, New York, 1987).
2. L. V. Dmitrieva, L. S. Vorotilova, and M. V. Razumeenko, Fiz. Tverd. Tela (St. Petersburg) **39**, 1194 (1997) [Phys. Solid State **39**, 1057 (1997)]; L. V. Dmitrieva, L. S. Vorotilova, I. S. Podkorytov, and M. G. Shelyapina, Fiz. Tverd. Tela (St. Petersburg) **41**, 1204 (1999) [Phys. Solid State **41**, 1097 (1999)].
3. O. Kanert and H. Schulz, Solid State Commun. **91**, 465 (1994).
4. T. J. Bastow, J. Phys.: Condens. Matter **1**, 4985 (1989).
5. J. A. Tossell, J. Magn. Reson. **94**, 301 (1991).
6. J. A. Tossell, J. Phys. Chem. A **102**, 3368 (1998).
7. H. Nakatsuji and T. Nakao, Chem. Phys. Lett. **167**, 571 (1990).
8. L. S. Vorotilova, L. V. Dmitrieva, and B. F. Shchegolev, Fiz. Tverd. Tela (Leningrad) **33**, 1527 (1991) [Sov. Phys. Solid State **33**, 861 (1991)]; L. S. Vorotilova, L. V. Dmitrieva, O.E. Kvyatkovskiĭ, and B. F. Shchegolev, Fiz. Tverd. Tela (St. Petersburg) **39**, 618 (1997) [Phys. Solid State **39**, 540 (1997)].
9. K. V. Krishna Rao, S. V. Nagender Naidu, and L. Iyengar, J. Am. Ceram. Soc. **53** (3), 124 (1970).
10. Hyla-Kryspin, J. Demuynck, A. Strich, and M. Benard, J. Chem. Phys. **75**, 3954 (1981).
11. T. H. Dunning, J. Chem. Phys. **55**, 716 (1971).
12. L. S. Vorotilova, L. V. Dmitrieva, O. E. Kvyatkovskiĭ, and B. F. Shchegolev, in *Proceedings of the VII International Conference on High-temperature Chemistry of Silicates and Oxides, St. Petersburg, 1998*, p. 59; O. E. Kvyatkovskiĭ and B. F. Shchegolev, in *Proceedings of the XV All-Russia Conference on Physics of Ferroelectrics, Rostov-on-Don, 1999*, p. 247.
13. R. Ditchfield, Mol. Phys. **27**, 789 (1974).
14. K. Wolinski, J. F. Hinton, and P. Pulay, J. Am. Chem. Soc. **112**, 8251 (1990).
15. O. Kanert and H. Kolem, J. Phys. C **21**, 3909 (1988).

Translated by N. Wadhwa

Physics of the Solid State, Vol. 42, No. 8, 2000, pp. 1451–1455. Translated from Fizika Tverdogo Tela, Vol. 42, No. 8, 2000, pp. 1412–1416.

SEMICONDUCTORS AND DIELECTRICS

Energy Features of Bound Polaron States in Colored NaCl and KBr Crystals

E. V. Korovkin and T. A. Lebedkina

Institute of Solid-State Physics, Russian Academy of Sciences, Chernogolovka, Moscow oblast, Chernogolovka, 142432 Russia

e-mail: korovkin@issp.ac.ru; tlebyod@issp.ac.ru

Received January 31, 2000

Abstract—Thermoionization of bound polaron states in γ-irradiated KBr and NaCl crystals is studied in the temperature range 71–104 K. It is shown that the complex shape of the thermoionization curves in this temperature range is determined by the presence of three types of electron traps that are unstable (each trap decays according to an exponential law) and one type of stable trap. This explains a sharp break on the dependence of the logarithm of the lifetime on the reciprocal temperature, which is observed for a KBr crystal, as well as a number of discrepancies in the results obtained by other authors. The physical parameters (activation energy H for thermoionization, the optical absorption peak E_{op}, the spectral photoionization threshold E_i, and the energies of phonons participating in the optical absorption, L_{op}, and in photoionization, L_{phc}) obtained in the present paper and in our earlier studies on KCl, NaCl, and KBr crystals are analyzed, and the relations between these quantities predicted by available theories are considered. © *2000 MAIK "Nauka/Interperiodica".*

1. In 1987, a two-step photoconductivity was discovered in γ-irradiated NaCl crystals at low temperatures (4.2–70 K) [1]. The essence of this phenomenon can be described as follows. It is well known that the illumination of colored alkali halide crystals (AHCs), i.e., crystals containing F centers, by F-light (2–3 eV) may lead to photoconduction in them [2]. Infrared light does not cause noticeable photoconduction. However, the combined effect of IR and F-light can induce photoconductivity that is several times stronger than that induced by F-light alone. Moreover, if a sample preliminarily exposed to F-light is illuminated by IR radiation even after some time following the first exposure, photoconduction, which will be henceforth referred to as IR photoconduction stimulated by F-light, is also induced. It disappears when the sample is exposed to an intense IR pulse or a low-intensity IR pulse of long duration. This effect leads to the conclusion that γ-colored AHCs contain traps that can capture electrons from the excited F centers and lose them under the action of IR light. It was established that these traps are virtually stable at low temperatures, but they lose the electrons trapped in them upon heating (thermoionization process). The spectrum of IR photoconductivity stimulated by F-light and the kinetics of the two-step photoconduction in NaCl were investigated in detail in [3, 4]. Later, similar effects were observed in colored crystals KBr and KCl [5].

At low temperatures, the concentration of filled traps could attain large values owing to the stability of the created electron states, which allowed us to observe their optical absorption spectrum [6, 7]. An analysis of the spectra of photoconduction and photoabsorption stimulated by F-light revealed that this new type of traps exhibits the properties of polarons [5–7], i.e., the presence of a periodic structure corresponding to a longitudinal optical phonon participating in absorption, the specific temperature dependence of the photoabsorption spectrum, and a considerable difference in the positions of spectral peaks of optical absorption and stimulated IR photoconduction. Since the lifetime of electrons in the traps under investigation is long at low temperatures (the value of a photocurrent in a sample with filled traps remains unchanged after holding it for 50 min in the dark at T = 4.2–65 K), it was concluded that these states are probably bound polarons. It turned out that the optical absorption spectra of the traps responsible for IR photoconductivity stimulated by F-light in various AHCs perfectly coincide with the data reported in [8–11]. Jacobs [11] called the new type of centers the I_e centers. However, the results of experiments on the thermoionization of I_e centers reported in those papers are controversial. In order to explain the dependence of the lifetime t of the I_e centers on the reciprocal temperature $1/T$, the authors of those publications proposed various models presuming hyperbolic and logarithmic time dependences $C(t)$ of the concentration of I_e centers at a given temperature T during thermoionization. Although the experimental points fit the theoretical $C(t)$ curve well, neither model can explain the emergence of a kink on the temperature dependence $t(1/T)$ of the lifetime for KBr crystals [11]. A clear physical pattern of the processes occurring in a crystal during the thermoionization of I_e centers at a given temperature was not given, even in the last publication [11], by these authors. We have already pub-

1063-7834/00/4208-1451$20.00

lished the results of an investigation of the thermoionization of IR traps in colored KCl crystals [12]. In the present work, we describe the results of similar experiments on colored KBr and NaCl crystals.

2. Experiments were made on samples prepared from γ-irradiated NaCl and KBr single crystals. The concentration of *F* centers was as high as 10^{17}–10^{18} cm^{-3}. The temperature range in our experiments was 71–104 K for KBr and 73–89 K for NaCl, which ensured the characteristic decay time from 5 to 4000 s accessible for measurements. The details of the experimental technique are described in detail in [12]. Before each measurement, a sample was exposed to *F*-light in order to create the required states, and after each measurement the sample was cleared of the filled traps by a high-intensity IR pulse in order to avoid their uncontrollable accumulation. Naturally, the intensity of *F*-light and the exposure time in the entire measuring cycle were maintained constant to the maximum possible extent. As an *F*-light source, we used a tungsten lamp SI-8 with light filters SS-8 + SZS-25 for NaCl and ZhS-18 + SZS-25 for KBr. The same lamp was used as a source of a high-intensity IR source with light filters IKS-1 for NaCl and IKS-1 + germanium light filter for KBr. The two procedures were accomplished with a disconnected power supply to avoid the polarization of the sample. At time *t* after switching off the *F*-light, the power source was switched on, the electrometer was connected, and a testing monochromatic IR pulse was supplied. For this purpose, an IKS-21 spectrophotometer with a lithium fluoride prism was used with a globar as a light source. The photon energy of this light (0.51 eV for both NaCl and KBr) was chosen such that the signal was maximal. The light pulse induced a photocurrent detected by the electrometer. For each measuring point (for a given holding time *t* in this research, or for each wavelength λ of IR light in spectroscopic experiments), the entire cycle was repeated twice, but for opposite polarities of the voltage applied to the sample. This complex procedure significantly increased the time of measurements, but completely eliminated the effect of sample polarization, emerging in each measurement, on subsequent measurements and precluded its gradual accumulation. The dependence of the results of measurements on the mode of movement on the time scale in this work and on the wavelength scale in spectral studies was also ruled out. The photocurrent $I(t)$ being detected was taken to be a measure of the concentration of traps filled with electrons (bound polaron states) since the concentration of electron states filled with electrons was a few orders of magnitude lower than the concentration of other traps (e.g., *F* centers) for a short duration of the *F*-light pulse (normally, 10 s), and we could thus neglect the change in the electron mean free path in the course of the experiment.

3. Figures 1 and 2 show the experimental dependences of photocurrent *I* on the time *t* at a given temperature for KBr and NaCl crystals, respectively. As in the experiments with KCl crystals, the shape of the curves for all the crystals depends on the wavelength of the testing light, which indicates the presence of several types of traps. The thermoionization curves for KBr crystals (Fig. 1) intersect one another like the curves for KCl crystals in [12]. This is not observed for NaCl (Fig. 2). The results were processed under the assumption that the crystal contains several different electron states whose thermoactivated decay involves the loss of an electron captured earlier (i.e., thermoionization), and that the process occurs according to an exponential

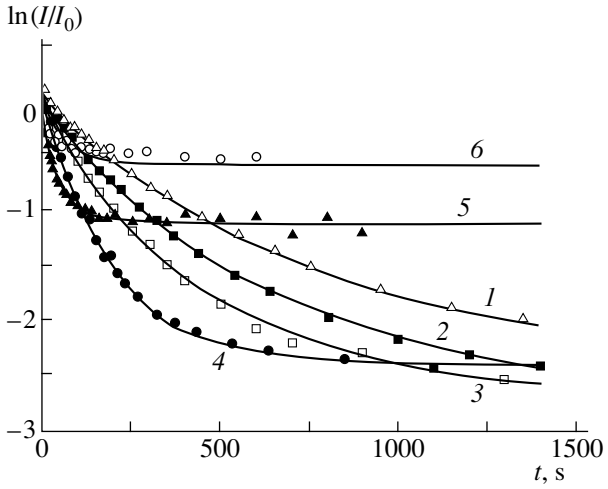

Fig. 1. Thermoionization curves for electron traps in γ-colored KBr crystals for various temperatures *T* (K): 72 (*1*), 77 (*2*), 82 (*3*), 90 (*4*), 101 (*5*), and 104 (*6*).

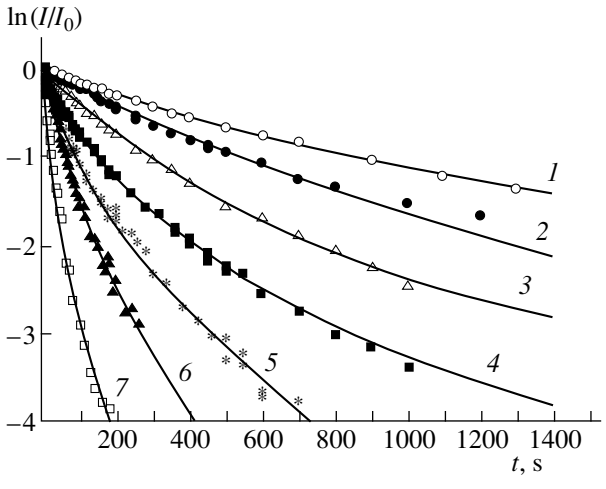

Fig. 2. Thermoionization curves for electron traps in γ-colored NaCl crystals at various temperatures *T* (K): 73 (*1*), 75 (*2*), 81 (*3*), 82 (*4*), 84 (*5*), 85 (*6*), and 89 (*7*).

law. The thermoionization curves for the KBr crystal (see Fig. 1) are correctly described by the formula

$$I/I_0 = a\exp(-t/\tau_a) + b\exp(-t/\tau_b) + c\exp(-t/\tau_a) + d$$

under the condition that $a + b + c + d = 1$, where I_0 is the photocurrent at the instant of time $t = 0$; a, b, c, and d are the coefficients reflecting the contributions of the a-, b-, c-, and d-type traps, respectively; and τ_a, τ_b, and τ_c are the lifetimes of electron traps of the corresponding types. The electron states of the d type are deeper traps, stable in the given temperature range. The photoconductivity spectrum (Fig. 3) contains a long-wave edge of these states, whose maximum was not attained ($E_{max} > 0.85$ eV). Figure 4 shows the temperature dependence of the lifetimes. The graphs in the figure were used for obtaining the following values of the activation energy: $H_a = 0.125$, $H_b = 0.026$, and $H_c = 0.017$ eV. The graphs explain the presence of a sharp break on the ln t vs. $1/T$ curve for KBr crystals in [11]. When the characteristic lifetime t is determined from the slope of the initial segment of the thermoionization curve plotted in the ln t vs. $1/T$ coordinates, only the "faster" segments of the two intersecting straight lines are left for each temperature, forming a sharp break.

The experimental curves for NaCl crystals (see Fig. 2) can also be described by the above formula. The constant component is very small, but it plays a significant part. The activation energies for various traps in NaCl crystals, which are derived from the graphs in Fig. 4, are as follows: $H_a = 0.146$, $H_b = 0.126$, and $H_c = 0.111$ eV.

4. This model can interpret not only the experimental facts described above (such as the change in the thermoionization curves with the wavelength of the testing light and the presence of a break on the curve describing the lifetime of the I_e centers in [11]), but also the discrepancies in the results obtained by different authors. Schneider [13] proposed a model in which a trap is assumed to be an impurity of another alkali cation in the crystal (e.g., Na^+ impurity in KCl). In his experiments, the IR absorption stimulated by F-light increases with the concentration of Na^+ impurity in KCl. However, the absorption peak corresponds to 170 K, while the maximum absorption in our experiments and in [11] is observed at lower temperatures. Moreover, Jacobs [11] observed a decrease in the IR absorption stimulated by F-light upon an increase in the concentration of Na^+ impurities in KCl. A comparison of the results obtained in [13] and [11] leads to the conclusion that the electron traps observed in these experiments were different. According to our experiments, the electron traps under investigation are not identical. At low temperatures, the absorption due to a-, b- and c-type traps prevails; these traps are vacated almost completely at 170 K and, at high temperatures, the absorption by d-type traps dominates. Schneider [13], who studied the impurity concentration dependence of absorption, apparently dealt with d-type traps, while Jacobs [11] studied the traps of the a, b, and c types. It was mentioned above that the electron states under investigation exhibit polaron properties. At the same time (at any rate, at low temperatures), they are stationary; otherwise, their lifetime could not be long, even at low temperatures. Consequently, we are dealing either with a so-called bound polaron, viz., a polaron localized at a crystal defect due to a weak interaction with it (for this reason, it exhibits the properties of a

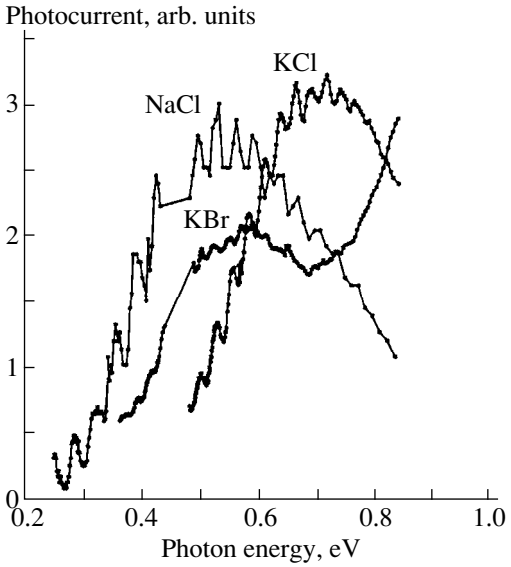

Fig. 3. IR photoconduction stimulated by F-light in γ-colored AHCs. The sample temperature $T = 9$ K for all crystals. The error of measurements was 4% for NaCl crystals and 2% for KBr and KCl crystals.

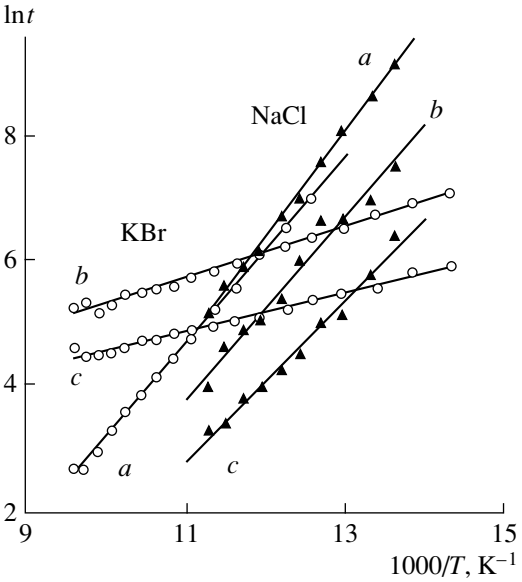

Fig. 4. Temperature dependence of the lifetime for traps in γ-colored KBr and NaCl crystals.

Parameters of investigated polaron states in NaCl, KCl, and KBr

Parameters	NaCl		KCl		KBr	
H_a, eV	0.146		0.303	[12]	0.125	
	0.22	[11]	0.33	[11]	0.17	[11]
H_b, eV	0.126		0.18	[12]	0.026	
H_c, eV	0.111				0.017	
E_{op}, eV	0.32	[6]	0.36	[7]	0.32	[7]
	0.33	[11]	0.36	[11]	0.32	[11]
E_{phc}, eV	0.53	[3]	0.71	[5]	0.57	[5]
E_i, eV	0.25	[3]	0.48	[5]	0.35	[5]
L_{op}, meV	31.6	[6]	24.8	[7]	20.0	[7]
	31.0	[11]	25.0	[11]	19.8	[11]
L_{phc}, meV	35.44	[3]	26.78	[5]	21.08	[5]
D, %	10.8	[5]	7.4	[5]	5.2	[5]

Note: Here, E_{op} is the position of the optical absorption peak for bound polaron states, E_{phc} and E_i are the position of the peak and the spectral photoionization threshold for the same states, L_{op} and L_{phc} are the energies of a longitudinal optical phonon obtained from the optical absorption and photoionization spectra, respectively, and $D = (L_{phc} - L_{op})/L_{phc}$ is the degree of softening of the phonon modes according to [5].

conventional polaron), or with a small-radius polaron localized at a conventional lattice site, which can only jump over similar sites due to tunneling or thermoactivation. For this reason, it would be interesting to compare the experimental parameters obtained for the object under investigation with the corresponding quantities predicted by the existing theories. The temperature dependence of the optical absorption spectrum completely coincides with the theoretical prediction by Loos and Straka [14] on the infrared absorption produced by small polarons.

Periodic oscillations observed in the optical absorption and photoionization spectra made it possible to determine the energy of a longitudinal optical phonon participating in the corresponding process [5]. The accuracy of its determination is large enough to reliably establish that the energy of a phonon participating in the photoionization process is greater than the corresponding value determined from the optical absorption spectra (see table).

If we assume that an electron is ejected to the conduction band during photoionization, it is reasonable to assume that the phonons required for this process are ordinary *LO*-phonons of the crystal, while the phonons participating in the formation of optical absorption spectra are connected with the excitation of intrinsic degrees of freedom of the polaron. The theoretical analysis carried out by Alexandrov and Capellman [15] predicts the "softening" of active phonon modes of a polaron as compared to analogous modes of the crystal. In this case, the experimentally determined value of D is the degree of "softening" of the phonon modes corresponding to the bound polaron. It is possible, however, that an electron leaves the bound polaron not in the form of a band electron, but together with a certain deformation of the lattice surrounding it, i.e., in the form of a free polaron. In this case, this quantity is the difference between the "softenings" of the phonon modes of a free and a bound polaron.

According to Pekar [16], the ratios of the polaron energy E_p, the optical absorption peak E_{op} of a polaron, and the spectral threshold E_i of its photoionization are $E_p : E_{op} : E_i = 1 : 2 : 3$. The ratio $E_p : E_{op} = 1 : 2$ satisfactory agrees with the experimental data for *a*-type traps in NaCl and KBr, as well as for *b*-type traps in KCl: $2H_a = 0.29$ eV ($\simeq$0.32 eV) in NaCl, $2H_b = 0.36$ eV ($\simeq$0.36 eV) in KCl, and $2H_a = 0.25$ eV ($\simeq$0.32 eV) in KBr (see table). Calculating the spectral photoconduction threshold for the shallowest electron states according to Pekar's theory, we obtain the following values: $3H_c = 0.33$ eV in NaCl and $3H_b = 0.54$ eV in KCl, which are in satisfactory agreement with the spectral photoconductivity threshold (see Fig. 3) ~0.25 and ~0.48 eV in NaCl and KCl, respectively. This probably indicates the presence of even shallower polaron states. The spectral photoionization threshold for the shallowest trap in KBr crystals was 0.05 eV. Our setup did not allow us to work with a phonon energy lower than 0.2 eV, and the actual possible range was even smaller (see Fig. 3) and was determined by the intensity of the signal required for reliable measurements.

5. Our experiments revealed that the polaron states responsible for the IR photoconduction stimulated by *F*-light in colored AHCs are electron traps of several types. The table contains the physical parameters of polaron states corresponding to various types of traps. The origin of the traps investigated by us remains unclear. New information concerning this problem can

be obtained, for example, from an analysis of electron states in additively colored AHCs.

REFERENCES

1. E. V. Korovkin and T. A. Lebedkina, Fiz. Tverd. Tela (Leningrad) **29**, 2807 (1987) [Sov. Phys. Solid State **29**, 1612 (1987)].
2. R. L. Wild and F. C. Brown, Phys. Rev. **121**, 1296 (1961).
3. E. V. Korovkin and T. A. Lebedkina, Fiz. Tverd. Tela (Leningrad) **33**, 120 (1991) [Sov. Phys. Solid State **33**, 67 (1991)].
4. E. V. Korovkin and T. A. Lebedkina, Fiz. Tverd. Tela (Leningrad) **33**, 2483 (1991) [Sov. Phys. Solid State **33**, 1400 (1991)].
5. E. V. Korovkin and T. A. Lebedkina, Fiz. Tverd. Tela (St. Petersburg) **37**, 3536 (1995) [Phys. Solid State **37**, 1945 (1995)].
6. E. V. Korovkin and T. A. Lebedkina, Fiz. Tverd. Tela (Leningrad) **33**, 2807 (1991) [Sov. Phys. Solid State **33**, 1586 (1991)].
7. E. V. Korovkin and T. A. Lebedkina, Fiz. Tverd. Tela (St. Petersburg) **35**, 642 (1993) [Phys. Solid State **35**, 329 (1993)].
8. F. Borms and G. Jacobs, Phys. Status Solidi B **43**, 283 (1971).
9. F. Carlier and G. Jacobs, Phys. Status Solidi B **89**, 193 (1978).
10. F. Carlier and G. Jacobs, Phys. Status Solidi B **89**, K95 (1978).
11. G. Jacobs, Phys. Status Solidi B **129**, 755 (1985).
12. E. V. Korovkin and T. A. Lebedkina, Fiz. Tverd. Tela (St. Petersburg) **38**, 3327 (1996) [Phys. Solid State **38**, 1815 (1996)].
13. I. Schneider, Solid State Commun. **25**, 1027 (1978).
14. J. Loos and J. Straka, Czech. J. Phys., Sect. B **39**, 316 (1989).
15. A. S. Alexandrov and H. Capellman, Phys. Rev. B **43**, 2042 (1991).
16. S. I. Pekar, Zh. Éksp. Teor. Fiz. **16**, 341 (1946).

Translated by N. Wadhwa

Physics of the Solid State, Vol. 42, No. 8, 2000, pp. 1456–1459. From Fizika Tverdogo Tela, Vol. 42, No. 8, 2000, pp. 1417–1419.

DEFECTS, DISLOCATIONS, AND PHYSICS OF STRENGTH

Grain Size, Stress, and Creep in Polycrystalline Solids

F. R. M. Nabarro

Condensed Matter Physics Research Unit, University of the Witwatersrand, Private Bag 3, WITS 2050, Johannesburg, South Africa

Division of Manufacturing and Materials Technology, CSIR, P.O. Box 395, Pretoria 0001, South Africa

Received November 29, 1999; in final form, January 11, 2000

Abstract—If a stress σ is applied to a polycrystal of grain size L, the mode of creep deformation depends on the answers to the following questions: (I) Does σ exceed the Peierls stress σ_p; (II) Does L exceed the dislocation spacing in a Taylor lattice stabilized by σ_p; (III) Does $L\sigma$ exceed the value required for a Frank–Read or Bardeen–Herring source to operate within the grain? (IV) Does $L^{1/2}\sigma$ exceed the Hall–Petch value required for slip to propagate across a grain boundary? The (L, σ) plane is thus partitioned into regions in which different creep modes predominate. © *2000 MAIK "Nauka/Interperiodica".*

1. DIFFUSIONAL CREEP AND HARPER–DORN CREEP

In diffusional creep, transport of matter occurs by the migration of vacancies from grain boundaries roughly normal to a tensile stress to boundaries roughly parallel to this stress. The migration occurs either through the body of the grain [1, 2] or along the grain boundaries [3]. In Harper–Dorn creep, vacancies migrate from edge dislocations with their Burgers vectors roughly parallel to the tensile axis to edge dislocations with their Burgers vectors roughly perpendicular to the tensile axis. The spacing l between adjacent dislocations, which are modeled as forming a Taylor lattice, reaches an equilibrium value such that the stress each dislocation exerts on its neighbor is of the order of the Peierls stress σ_p [4, 5]. Thus,

$$b\mu/2\pi l \approx \sigma_p, \quad l \approx b\mu/2\pi\sigma_p, \tag{1}$$

and Harper–Dorn creep is possible only if $l < L$, i.e.,

$$L > b\mu/2\pi\sigma_p. \tag{2}$$

When this condition is satisfied, the diffusion paths for Harper–Dorn creep are shorter than those for diffusional creep, and Harper–Dorn creep will be faster than Nabarro-Herring creep provided that [6]

$$L/b > 7\mu/\sigma_p. \tag{3}$$

Different modes of creep will operate depending on whether the product $L\sigma$ is or is not large enough for Bardeen–Herring climb sources to operate within or on the surface of the grain. If the line tension of a dislocation is Γ, sources can operate freely if

$$b\sigma > 4\Gamma/L. \tag{4}$$

With $\Gamma \approx b^2\mu/2$, where μ is the shear modulus, this becomes

$$L\sigma > 2b\mu. \tag{5}$$

The authors of [7, 8] interpret this kind of formula in the following way. As diffusional creep occurs, edge dislocations climb along the grain boundaries. Inequality (5) represents the condition that, if these dislocations are removed, they can be replaced by new dislocations generated by Bardeen–Herring sources in the grain boundaries. This interpretation seems to be incorrect on two grounds. First, a typical large-angle boundary contains edge dislocations all of the same sign separated by distances of the order of $b/3$. If these dislocations all climbed out of the boundary and were not replaced, the total deformation would be of the order of 30%, larger than that normally observed in diffusional creep. In fact, the dislocations will not disappear, but will, statistically, continue to climb in adjacent grain boundaries. Second, it is not clear why Bardeen–Herring sources should operate preferentially in grain boundaries. When inequality (5) is satisfied, sources can operate within the grains, probably even more freely than in the grain boundaries.

Inequality (5) should rather be interpreted in the following way. The equilibrium spacing l of Eq. (1) is achieved by a balance of the multiplication of dislocations by the operation of Bardeen–Herring sources within the grain and the annihilation of dislocation pairs under their mutual attraction. This process occurs and Harper–Dorn creep is possible if inequality (4) is satisfied. If the inequality is not satisfied, dislocations climb into the grain boundaries and are absorbed, and, after a possible transient, diffusional creep, rather than Harper–Dorn creep, occurs.

2. STRESSES ABOVE THE PEIERLS STRESS

When the applied stress σ exceeds the Peierls stress σ_p,

$$\sigma > \sigma_p, \tag{6}$$

dislocations can move freely by glide.

If, in addition, inequality (5) is satisfied, dislocations will multiply by glide within the cell much more rapidly than they can annihilate by climb. Harper–Dorn creep gives way to power-law creep [9]. If the product $L^{1/2}\sigma$ is less than the Hall–Petch stress-intensity factor k_{HP}

$$L^{1/2}\sigma < k_{\mathrm{HP}}, \tag{7}$$

glide cannot percolate from one grain to its neighbor.

A possible mode of deformation is then that considered by Spingarn and Nix [10], which can be outlined as follows. The reduced stress is large enough to support glide on only one system in each grain. Coherence between the grains is maintained largely by sliding on the grain boundaries. This sliding is impeded by ledges formed on the boundaries by pile-ups of dislocations. The rate-controlling process is the smoothing of these ledges by the diffusion of vacancies between adjacent ledges. The distance λ between adjacent slip planes in a grain is likely to be of the order of the dislocation passing distance, given by

$$b\sigma = b^2\mu/2\pi\lambda$$

or

$$\lambda = b\mu/2\pi\sigma. \tag{8}$$

Allowing for the piling-up of dislocations, the work done by the external stress when a vacancy is transferred from the head of a pile-up is easily seen to be of the order of

$$W = Lb^2\sigma^2/2\mu. \tag{9}$$

On average, a vacancy travels a distance $\lambda/4$ to relieve the local strain, and so the thermodynamic driving force on a vacancy is

$$4W/\lambda = 4\pi Lb\sigma^3/\mu^2. \tag{10}$$

If the effective diffusion constant is D_e, the flux ϕ of vacancy is D_e/kT times the thermodynamic force, or

$$\phi = 4\pi Lb\sigma^3 D_e/\mu^2 kT. \tag{11}$$

At high temperatures, diffusion will occur through the bulk, D_e will be the bulk coefficient of diffusion D, and the flow of vacancies at each step will occur through an area of order $L\lambda/2 = Lb\mu/4\pi\sigma$. The volume V of matter transported at each step in unit time is then

$$V = Lb\mu\phi/4\pi\sigma = L^2b^2\sigma^2 D/\mu kT. \tag{12}$$

The time t taken to remove a step is

$$t = b\lambda L/8V = \mu^2 kT/16\pi L\sigma^3 D. \tag{13}$$

The shear strain is b/λ, and so the strain rate $\dot{\varepsilon}$ is given by

$$\dot{\varepsilon} = b/\lambda t = 32\pi^2 L\sigma^4 D/\mu^3 kT. \tag{14}$$

At low temperatures, D is replaced by the grain-boundary diffusion coefficient D_b, and the flux of vacancies occurs over an area of order Lb. The strain rate is then

$$\dot{\varepsilon} = 128\pi^3 L\sigma^5 D_b/\mu^4 kT. \tag{15}$$

Both processes occur within the normal range of power-law creep.

At higher stresses, several glide systems operate in each grain, and dislocation cells are formed having widths w given approximately by

$$w = 10.5b\mu/\sigma. \tag{16}$$

Under these conditions, power-law creep with an exponent 4–5 is observed. As the discussion in [11] shows, simple mechanisms of creep in this structure lead to the "natural" exponent of 3. An exponent of 5 can be obtained by assuming that diffusion occurs along the cores of dislocations, which are present with a density proportional to σ^2, but such a process would have an activation energy of only about half the observed value, which is close to that for the lattice self-diffusion. Other models of power-law creep [12, 13], which take into account the formation of dislocation cells within the grains, involve rather arbitrary assumptions.

3. POWER-LAW BREAKDOWN

When inequality (7) is not satisfied, a slip in one grain can transfer to a neighboring grain. While there is still some thermal activation of the slip process, as is shown by the slow decrease in flow stress with increasing temperature, the rate of deformation is no longer controlled by diffusion, but is a rapidly increasing function of stress. This is the domain of power-law breakdown.

4. NUMERICAL VALUES

The quantities entering this analysis are b and μ, which are well determined, and σ_p and k. Both theoretical and experimental values of the Peierls stress σ_p fall into two classes, with one class being several hundred times greater than the other. There are reasons to believe that, in problems of progressive plastic deformation, it is the values of the lower class that are relevant [14], and we use these. There are no satisfactory theoretical estimates of the Hall–Petch coefficient k, and we use values from the review by Hansen [15].

For aluminum, the relevant parameters are $b = 2.86 \times 10^{-10}$ m, $\mu = 26 \times 10^9$ Pa, $\sigma_p = 2.5 \times 10^{-5}\,\mu$, $k_{\mathrm{HP}} = 0.53 \times 10^5$ Nm$^{-3/2}$, and the relevant diagram is shown in Fig. 1.

The present analysis does not apply to very high stresses, where the lattice may break down, or at high stresses and very small grain size, where the Hall–Petch criterion may not apply because a pile-up of sev-

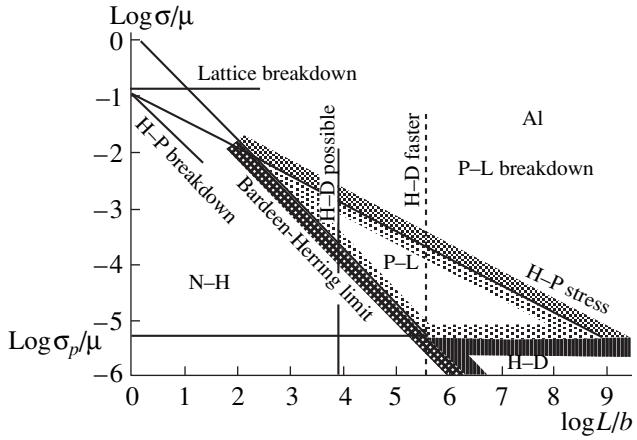

Fig. 1. The plane of grain size L and applied stress σ is divided into domains of different creep models in aluminum by four boundaries: the Peierls stress σ_p, the grain size at which Harper–Dorn creep becomes possible (or becomes faster than diffusional creep), the product $L\sigma$ above which Bardeen–Herring (or Frank–Read) sources can operate within the grain, and the Hall–Petch product $L^{1/2}\sigma$ above which glide can percolate between grains.

eral dislocations within the cell is not possible. The regions where the analysis does not apply are indicated in the figure.

When $L\sigma$ is below the Bardeen–Herring limit, dislocations cannot multiply within the grain even if $\sigma > \sigma_p$. Dislocations are swept into the grain boundaries, and only diffusional creep is possible in the steady state. Above the Bardeen–Herring limit, Harper–Dorn creep occurs when $\sigma < \sigma_p$, and the grain size is not too small, or, more precisely, for very large grain sizes where $L^{1/2}\sigma$ is large enough to allow dislocations to cross the grain boundary. For σ somewhat below σ_p, the Bardeen–Herring limit occurs at about $\log(L/b) = 6$, corresponding to $L = 290$ μm, in reasonable agreement with the value of 400 μm estimated by Mohamed [16] from the experimental data. Power-law creep occurs in the region bounded by the Bardeen–Herring limit, the Peierls stress, and the Hall–Petch stress line. The region above both the Bardeen–Herring and the Hall–Petch lines is that of a power-law breakdown.

For copper, $b = 2.56 \times 10^{-10}$ m, $\mu = 48 \times 10^9$ Pa, $\sigma_p = 10^{-5}\,\mu$, $k_{HP} = 1.6 \times 10^5$ Nm$^{-3/2}$, and the resulting diagram in the (L, σ) plane is shown in Fig. 2.

The topology of the diagram is different from that of Fig. 1. There is a region that lies below the Peierls stress, above the Bardeen–Herring limit, and at grain sizes so small that Harper–Dorn creep is either impossible or slower than diffusional creep. In this new region, diffusional creep will dominate.

5. INFLUENCE OF DISLOCATION CELLS

The discussion so far has assumed that the only obstacles to dislocation motion are the Peierls stress and the grain boundaries. However, dislocations can also assemble into cells of width $w(\sigma)$, where [11]

$$w(\sigma) \approx 10.5 b\mu/\sigma \qquad (17)$$

and usually do so provided that $w < L$. On the rather drastic assumption that the cell walls are as effective barriers to dislocation motion as grain boundaries, L must be replaced by $w(\sigma)$ in the preceding discussion. In Fig. 3, the diagram for aluminum is augmented by the line $w(\sigma)$. At large grain sizes, where the Hall–Petch line lies above the line $w(\sigma)$, the effective grain size is $w(\sigma)$, and power-law breakdown occurs at a constant stress given by the intersection of the $w(\sigma)$ and H–P stress lines. Then, as is observed, the regimes of

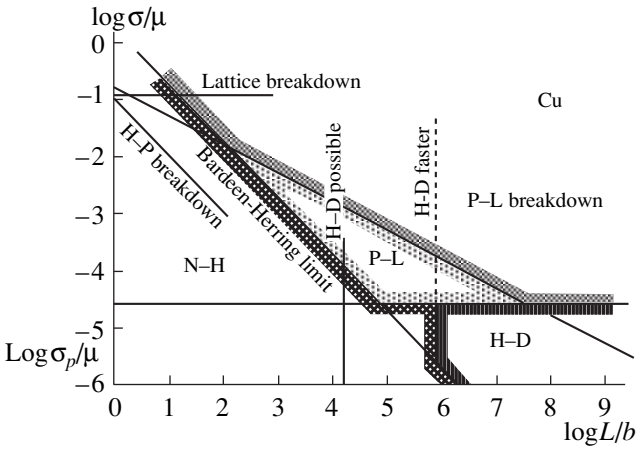

Fig. 2. A creep-mode diagram for copper similar to that of Fig. 1 for aluminum. There is a new domain, in which $\sigma < \sigma_p$. $L\sigma$ exceeds the Bardeen–Herring limit, but $L^{1/2}\sigma$ is below the value at which Harper–Dorn creep is faster than diffusional creep.

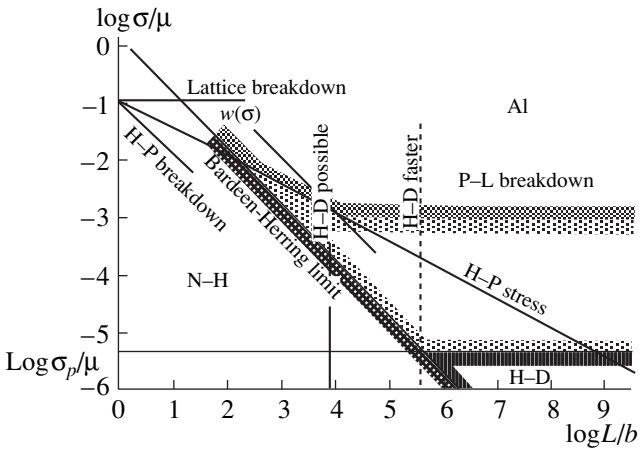

Fig. 3. Diagram for aluminum augmented by the line $w(\sigma)$ determining the dislocation cell size. Where $w < L$, power-law breakdown occurs at a stress independent of grain size.

Harper–Dorn creep and power-law breakdown are separated by a regime of power-law creep. It appears that this regime covers a factor of several hundreds in stress, in agreement with the observations reported by Wu and Sherby [17].

REFERENCES

1. F. R. N. Nabarro, *Report of a Conference on the Strength of Solids* (The Physical Society, London, 1948).
2. C. Herring, J. Appl. Phys. **21**, 437 (1950).
3. R. Coble, J. Appl. Phys. **34**, 1679 (1963).
4. F. R. N. Nabarro, Acta Metall. **37**, 2217 (1989).
5. J. N. Wang, Scr. Metall. Mater. **29**, 1505 (1993).
6. J. N. Wang, Philos. Mag. A **71**, 105 (1995).
7. E. Arzt, M. F. Ashby, and R. A. Verrall, Acta Metall. **31**, 1977 (1983).
8. E. Arzt, Acta Mater. **46**, 5611 (1998).
9. J. N. Wang, Scr. Metall. Mater. **29**, 733 (1993).
10. J. R. Spingarn and W. D. Nix, Acta Metall. **27**, 171 (1979).
11. J. Čadek, *Elsevier Materials Science Monographs* (Elsevier, Amsterdam, 1988), Vol. 48.
12. J. Weertman, Trans. Am. Soc. Met. **61**, 681 (1968).
13. R. C. Gifkins, J. Aust. Inst. Met. **18**, 137 (1973).
14. F. R. N. Nabarro, Philos. Mag. A **75**, 703 (1997).
15. N. Hansen, Metall. Trans. A **16**, 2167 (1985).
16. F. A. Mohamed, Mater. Sci. Eng. **32**, 37 (1978).
17. M. Y. Wu and O. D. Sherby, Acta Metall. **32**, 1561 (1984).

Physics of the Solid State, Vol. 42, No. 8, 2000, pp. 1460–1464. Translated from Fizika Tverdogo Tela, Vol. 42, No. 8, 2000, pp. 1420–1424.

DEFECTS, DISLOCATIONS, AND PHYSICS OF STRENGTH

Effect of Annealing on the Excess Free Volume and Strength of Amorphous Alloys

V. I. Betekhtin*, E. L. Gyulikhandanov, A. G. Kadomtsev*, A. Yu. Kipyatkova*, and O. V. Tolochko****

** Ioffe Physicotechnical Institute, Russian Academy of Sciences, Politekhnicheskaya ul. 26, St. Petersburg, 194021 Russia*

*** St. Petersburg State Technical University, Politekhnicheskaya ul. 29, St. Petersburg, 195251 Russia*

e-mail: vladimir.betekhtin@pop.ioffe.rssi.ru

Received February 1, 2000

Abstract—The regularities of annealing of an excess free volume in amorphous alloys have been investigated. It is shown that the mechanism for the healing of excess free volume is associated with the viscous flow. It is revealed that a decrease in this volume at high temperatures or pressures leads to an increase in the strength and provides an explanation for the features of its temperature dependence. The decrease in the excess free volume is enhanced under a tensile load. © *2000 MAIK "Nauka/Interperiodica".*

1. INTRODUCTION

Amorphous alloys possess unique physicomechanical properties. The thermal instability of amorphous alloys is a central problem limiting the field of their application. The structural relaxation resulting in the transition from an unstable to a metastable state proceeds already in as-prepared amorphous alloys produced by ultrafast quenching of the melt. The relaxation processes, which are drastically accelerated upon heating, stem from changes in the topological short-range order due to the atomic rearrangement, the "release" of free volume typical of the amorphous state, and a change in the internal stresses and the viscosity. Annealing at higher temperatures leads to a crystallization whose early stages are characterized by the formation of nanocrystals. After the completion of crystallization, the alloys transform to the stable state.

It is believed that the free volume in many respects plays the decisive role in the transition to metastable and stable states and, consequently, the change in the physicomechanical properties [1, 2]. The free volume in amorphous alloys can be separated into two components, namely, structure-sensitive and excess free volumes. The former component of the free volume is an integral characteristic of the amorphous state and completely disappears only after the completion of crystallization. The excess free volume is considered a structural defect whose elimination leaves the symmetry and topological characteristics of the amorphous state unchanged. However, it is this mobile component of the free volume that can be responsible for structural transformations and variations in the physicomechanical properties of amorphous alloys during the structural relaxation and, possibly, at early stages of crystallization. In our earlier work [3], it was demonstrated that a considerable part of the excess free volume in the amorphous alloys prepared by ultrafast quenching is localized in the form of porous microdiscontinuities about 20–100 nm in size.

From the aforesaid, it follows that the effect of annealing on the excess free volume and the strength properties of amorphous alloys is of crucial importance. The main objective of the present work was to obtain detailed data on this problem. In order to gain a better understanding of the role of the excess free volume in the formation of strength properties, we also analyzed recent data on the influence of high hydrostatic pressure on the excess free volume and the strength of amorphous alloys [3].

2. SAMPLE PREPARATION AND EXPERIMENTAL TECHNIQUE

The amorphous alloys to be studied had the following compositions: $Co_{59}Fe_5Si_{11}Ni_{10}B_{15}$ (alloy 1), $Fe_{61}Co_{20}Si_5B_{14}$ (alloy 2), and $Fe_{77}Ni_1Si_9B_{13}$ (alloy 3). The alloys in the form of ribbons 20–30 μm thick and 20 mm wide were prepared by ultrafast quenching. The amorphous state of the alloys was confirmed by the structural investigations.

The parameters of the excess free volume were examined by the modified small-angle x-ray scattering (SAXS) technique. The width of an x-ray beam was varied from 4 to 120 μm. The intensity of x-ray scattering by the amorphous alloys was measured in the angle range from 0.7′ to ~1°. This made possible a reliable evaluation of scattering inhomogeneities with sizes varying from several nanometers to several hundreds of nanometers.

The inhomogeneity parameters were determined from the SAXS data by using the tangent method (the Guinier method) and the second invariant.

1063-7834/00/4208-1460$20.00

It is known that the identification of the scattering inhomogeneities is a prime consideration in analysis of the SAXS data. For amorphous alloys, these are the regions with excess free volume (i.e., porous discontinuities), regions with an increased dopant concentration (such as the Guinier zones) or regions with increased internal stresses, and particles of the second phase.

Earlier [3], it was shown that the treatment of amorphous alloys under a high hydrostatic pressure (up to 1 GPa) affects only the scattering component governed by the excess free volume. Specifically, the excess free volume under pressure decreases more than twofold; moreover, the quantitative estimates of the decrease in the scattering intensity due to the healing under pressure confirm the hole nature of scattering inhomogeneities. Note that the pressure virtually does not affect the parameters of scattering inhomogeneities unrelated to the excess free volume.

Therefore, the treatment of amorphous alloys under hydrostatic pressure makes it possible to reveal the inhomogeneities arising from the excess free volume and, then, to trace the change in these inhomogeneities upon annealing with the SAXS technique. The samples were treated in a high-pressure bomb in an oil medium.

The strength of amorphous alloys and its temperature dependence were determined under tension at a loading rate of 25 MPa/s. The tentative dependence of the strength on the loading rate was also obtained in the loading rate range covering about three orders of magnitude.

The samples for mechanical testing were cut in the form close to "eight" on a special contrivance. The length of quasi-uniform part of the samples was equal to about 8 mm, and its width was ~3 mm. The shape of the samples and their careful alignment in a test machine led to a decrease in the scatter of strength from sample to sample down to 5%.

3. RESULTS

The second-invariant curves for all three alloys prior to and after the treatment under a hydrostatic pressure of 1 GPa were examined first. The results obtained completely confirmed the regularities revealed earlier in [3]: after the compression experiments, the area under the second-invariant curves decreases and certain maxima observed in the curves are shifted toward the right. As is known [4], the area under the second-invariant curve is proportional to the volume of scattering fractions, and the location of each maximum depends on the characteristic size of these fractions. Consequently, the treatment under pressure brings about a decrease in the volume of certain scattering fractions due to a decrease in their size. In this respect, the fractions with a decreased size were interpreted as pores, and the remaining fractions were considered structural inhomogeneities of the nonhole nature. The preliminary investigation of three alloys revealed that each alloy involves one or two fractions of inhomogeneities interpreted as pores. The sizes of these fractions were equal to 177 and 66 nm for alloy 3, 200 and 90 nm for alloy 2, and 133 nm for alloy 1.

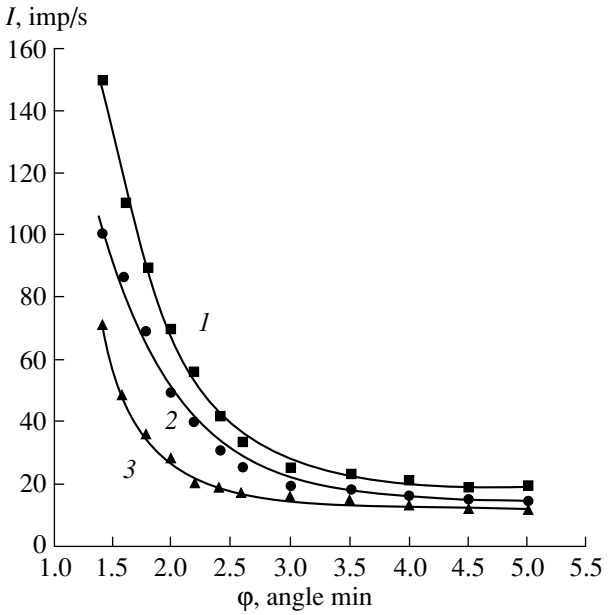

Fig. 1. SAXS indicatrices for samples of amorphous alloy 3 (*1*) prior to and after annealing at temperatures of (*2*) 200 and (*3*) 300°C (t = 1800 s).

Subsequently, the changes observed in these defects upon annealing were analyzed in the study of the structural relaxation.

The effect of annealing on the micropores in alloy 3 was examined in more detail. The temperature and the time of annealing were chosen so that the influence of phase separation and crystallization processes on the scattering could be ignored. The absence of these processes was checked by the x-ray diffraction analysis.

Figure 1 illustrates the change in the scattering by pores of one of the fractions in alloy 3 upon isochronal annealing (t = 1800 s). It can be seen that the intensity and the slope of the curve decrease, which indicates a decrease in the volume of scattering micropores.

The dependences of the volume of the same pore fraction on the temperature and the time of annealing are depicted in Figs. 2 and 3, respectively. As can be seen, the annealing at temperatures of 200–300°C for 10^3–10^4 s leads to a considerable decrease (by a factor of ~2) in the micropore volume. In order to determine the activation energy of pore healing, the data obtained were processed according to the isochronal–isothermal annealing procedure [5]. It turned out that the healing cannot be described by one activation energy. Its value was equal to ~0.5 eV at relatively low temperatures and ~1 eV at T > 250°C. The results obtained for alloy 3 with the initial fraction of pores ~88 nm in size are

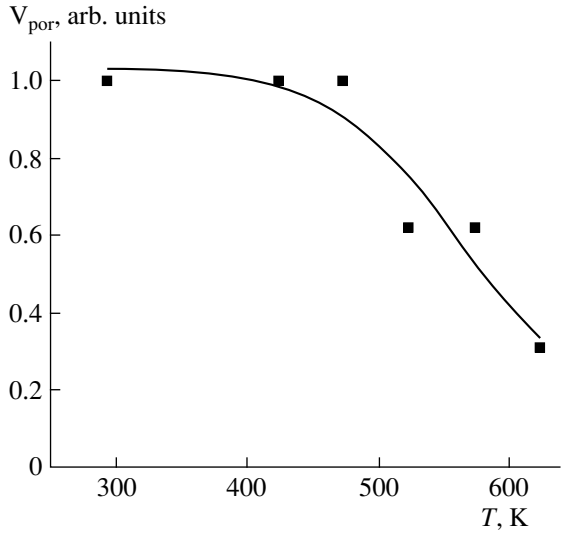

Fig. 2. Isochronal annealing curve for pores in amorphous alloy 3 (t = 1800 s).

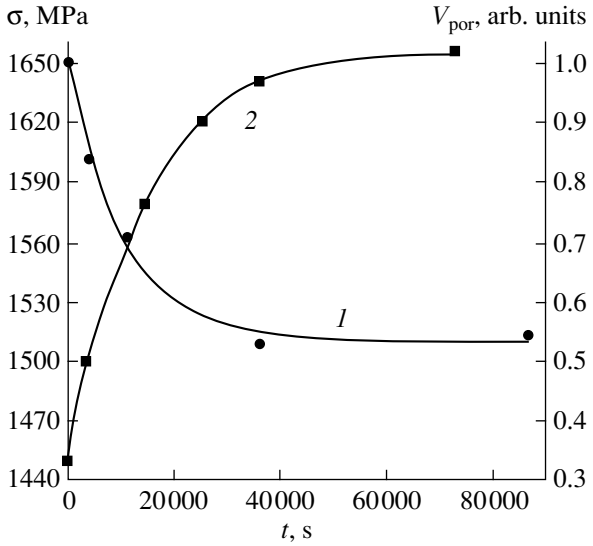

Fig. 3. (*1*) Isothermal (240°C) annealing curve for pores in alloy 3 and (*2*) dependence of the tensile strength of the samples after their annealing.

qualitatively similar to data for the other alloys and fractions.

Thus, the annealing at relatively low temperatures (below the glass transition point) results in a substantial decrease in the micropore volume and, correspondingly, in the SAXS intensity. Note that the fractions of inhomogeneities interpreted as "nonpores" remain virtually unchanged after their annealing. A certain change in the intensity of scattering by these fractions is observed at the maximum temperature of annealing ~350°C), which is likely explained by the phase separation and precrystallization processes. However, as already mentioned, these problems are beyond the scope of the present work.

The temperature–rate dependences of the strength of the amorphous alloys were also investigated in this work. The strength was examined with due regard for the above data on the influence of high temperatures and pressures on the excess free volume [3]. The temperature dependences of the strength for two alloys are displayed in Figs. 4 and 5. It can be seen that this dependence exhibits a complex behavior and can be conventionally divided into three portions. In two temperature ranges (18–100°C and 200–350°C), the strength linearly (or quasi-linearly) decreases with an increase in the temperature. In the range from 100–150 to 200°C, there appears an anomalous dependence of the strength. After the elimination of a certain excess free volume due to prolonged annealing at a high temperature or under a high pressure, the strength linearly decreases with an increase in the temperature and has no anomalous behavior. Moreover, the strength increases over the entire temperature range covered.

The data obtained allow us to draw two conclusions.

(1) A decrease in the excess free volume under high pressure (0.7 GPa) or upon annealing at 240°C for 5.5 h brings about an increase in the strength over the entire temperature range studied.

(2) An anomalous increase in the strength observed in the experiments at a constant loading rate can be explained by the fact that the elimination of a certain excess free volume under load occurs even at 150–200°C; the latter process leads to an anomalous increase in the strength at these temperatures.

The intimate connection between the excess free volume and the strength is corroborated by their direct correlation with an increase in the time of preliminary isothermal annealing (Fig. 3). The fact that loading enhances the elimination of the excess free volume at temperatures in the range of anomalous dependence was confirmed by the SAXS technique. It was found that the annealing of alloy 3 at 150°C for 40 min under the load equal to 0.8 of the breaking load leads to a decrease in the pore diameter from 90 to 60 nm. (A similar annealing without load caused the diameter of pores to decrease from 90 to 86 nm, i.e., left the pores virtually unhealed.)

Moreover, we elucidated how the strength of the amorphous alloys depends on the loading rate. At a temperature of 18°C, the tensile strengths at loading rates of 0.5, 25, and 300 MP s were equal to 1800, 1540, and 1200 MPa. Therefore, the dependence of the strength of amorphous alloys on the loading rate has an anomalous behavior: as the loading rate increases, the strength of amorphous alloys decreases.

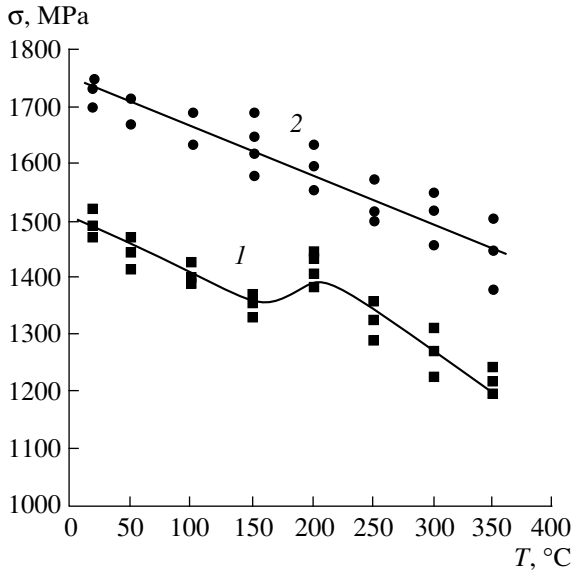

Fig. 4. Temperature dependences of the strength for alloy 1 (*1*) prior to and (*2*) after the annealing.

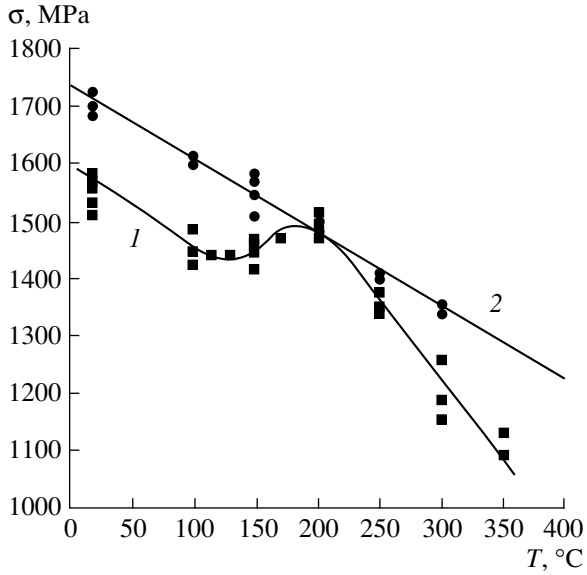

Fig. 5. Temperature dependences of the strength for alloy 3 (*1*) prior to and (*2*) after the treatment under a pressure of 0.7 GPa at 18°C.

4. DISCUSSION

First, let us consider the data on the annealing of amorphous alloys. According to the independent dilatometric measurements [6], the heating of amorphous alloys up to the glass transition temperature leads to an increase in their density by ≈0.5%; it is this value that is primarily associated with the excess free volume. As follows from the estimates obtained from the SAXS data, a decrease in the density of the initial amorphous alloys (prior to their annealing) due to the presence of pores is equal to $\approx 0.45 \pm 0.15\%$, which is in reasonable agreement with the dilatometric results and confirms the hole nature of the excess free volume.

Consequently, the obtained data on the annealing and the aforementioned estimate suggest that a considerable part of the excess free volume actually represents pores which are capable of healing at high temperatures. This inference does not rule out the possibility of forming the regions with a highly correlated atomic arrangement in the amorphous matrix upon annealing, which also should be accompanied by an increase in the density. The occurrence of the regions whose sizes can be equal to several nanometers and less is difficult to reveal reliably with the SAXS technique (owing to a low intensity of scattering by the regions).

In the course of annealing under conditions used in this work (Fig. 2), the excess free volume decreases about two times. Evidently, the remaining part of pores are healed upon annealing at higher temperatures. Note that this process can be retarded owing to both an increase in its activation energy and the competing coalescence of pores. (As noted above, the effect of higher annealing temperatures was not investigated in the present work, because the phase separation and early stages of crystallization make interpretating the SAXS data more difficult.) Under the chosen annealing conditions, a portion of pores are retained in the amorphous alloys. It is clear that the largest pores formed upon quenching or as a result of the coalescence of small-sized pores upon annealing are retained. This is supported by the data reported in [1]: it was found that prolonged annealing is attended by a certain increase in the size of one of the pore fractions (or, more exactly, the fraction attributed to pores according to the SAXS data).

With the aim of elucidating the mechanism for the healing of the excess free volume, let us compare the activation energies determined upon isochronal–isothermal annealing and the activation energies available in the literature for the amorphous alloys. According to [1, 2, 7], the activation energies (~0.5 eV at low temperatures and ~1 eV at relatively high temperatures) are close to the activation energies of viscous flow in the amorphous alloys. An increase in the activation energy of viscous flow with an increase in the temperature is explained by an enhancement of the cooperative process and a decrease in the free volume and internal stresses. Thus, the found activation energies for healing of the excess free volume at low and high temperatures give grounds to believe that the mechanism of healing is associated with the viscous flow.

As was noted in [1], the relaxation processes in the amorphous alloys have much in common with relaxation processes in amorphous polymers. In this respect, it is of interest to compare our data on the annealing of porosity in the amorphous alloys and the regularities of the pore healing in the amorphous–crystalline polymers for which the activation energy of healing increases (from ~0.5 to ~1.5 eV) at higher temperatures of annealing [8]. The found values agree well with the

activation energy of viscous flow, and an increase in the energy with an increase in the temperature correlates with an enhancement of the cooperative character of the mass transfer to the healing pores. As in polymers [9], the driving forces of the healing of excess free volume in the amorphous alloys are likely governed by internal stresses. Unfortunately, the calculated data on the internal stresses in the amorphous alloys are rather contradictory. Furthermore, allowance should be made for the fact that these stresses are very nonuniformly distributed among the contact and free surfaces of amorphous ribbons [8, 10]. When analyzing the driving forces of healing, the bubble pressure forces resulting from the curvature of pore surface should be taken into account. For excess free volume elements of size several nanometers, the bubble pressure is found to be of the order of tens of MPa [11].

The data obtained in this work conclusively indicate the connection between the excess free volume and the strength: a decrease in the excess free volume leads to a proportional increase in the strength of amorphous alloys. Note that an increase in the strength is observed independently of the particular factor (temperature or pressure) affecting the excess free volume. However, the annealing (which results in about the same decrease in the excess free volume as the pressure) leads to a somewhat larger increase in the strength (Figs. 4, 5). This can be due to the fact that the annealing accompanied by a decrease in the excess free volume (revealed by the SAXS technique) brings about further structural transformations (healing of the excess free volume elements of several nanometers in size, relaxation of internal stresses, etc.).

The found effect of the porosity on the strength of amorphous alloys seems to be natural: it is observed in metals, ceramics, films, alloys [12], polymers [13], and cement [14]. It is clear that the porosity not only promotes the nucleation of microcracks, but also facilitates their growth and, in a number of cases, can be responsible for the trajectories of the main crack propagation. As was shown in [15], the excess free volume substantially affects the development of the microfracture in amorphous alloys. The tendency toward nucleation and the further propagation of cracks can be considerably changed by affecting the excess free volume.

In closing, we dwell briefly on the possible explanation for the nature of the anomalous dependence of the strength in the temperature range from 100 (150) to 200°C. A similar anomaly was observed earlier for the temperature dependence of the strength of ionic single crystals in a temperature range in which the rate of fracture in the course of loading became comparable to the rate of relaxation processes [16]. Relaxation in crystalline materials is primarily associated with the evolution of the dislocation structure, whereas the relaxation in amorphous metallic glasses is likely determined by the evolution of the excess free volume. Then, an increase in the strength with a rise in temperature from ~150 to 200°C is caused by an increase in the release rate of the excess free volume in the amorphous alloys under the given loading conditions. Indeed, the annealing at 150°C under the load leads to a decrease in the size of one fraction of the excess free volume by a factor of ~1.5, and the elimination of a part of excess free volume upon prolonged annealing or treatment under pressure brings about an increase in the strength and the disappearance of the anomaly.

Thus, the data obtained allowed us to conclude that the excess free volume in the form of submicropores considerably affects the strength properties of amorphous alloys. Moreover, the effect of the porosity on the strength is sufficiently general in character for a wide variety of solids.

ACKNOWLEDGMENTS

This work was supported by the Russian Foundation for Basic Research, project no. 99-02-18287.

REFERENCES

1. A. M. Glezer and B. V. Molotilov, *Structure and Mechanical Properties of Amorphous Alloys* (Metallurgiya, Moscow, 1992).
2. *Metastable and Nonequilibrium Alloys*, Ed. by Yu. V. Efimov (Metallurgiya, Moscow, 1988).
3. V. I. Betekhtin, A. G. Kadomtsev, A. Yu. Kipyatkova, and A. M. Glezer, Fiz. Tverd. Tela (S.-Peterburg) **40**, 85 (1998) [Phys. Solid State **40**, 74 (1998)].
4. D. I. Svergun and L. A. Feĭgin, *X-ray and Neutron Small-Angle Scattering* (Nauka, Moscow, 1986).
5. A. C. Damask and G. J. Dienes, *Point Defects in Metals* (Gordon and Breach, New York, 1963; Mir, Moscow, 1966).
6. I. V. Zolotukhin and Yu. V. Barman, *Stability and Relaxation Processes in Metallic Glasses* (Metallurgiya, Moscow, 1991).
7. K. Suzuki, H. Fuzimori, and K. Hasimoto, *Amorphous Alloys* (Metallurgiya, Moscow, 1987).
8. H. S. Chen, Rep. Prog. Phys. **43**, 353 (1980).
9. A. I. Petrov, A. B. Sinani, M. V. Razuvaeva, *et al.*, Mekh. Kompoz. Mater. (Zinatne) **2**, 273 (1990).
10. A. R. Yavari and P. Desre, J. Mater. Sci. Lett. **2** (9), 516 (1982).
11. Ya. E. Geguzin, *Physics of Sintering* (Nauka, Moscow, 1974).
12. P. G. Cheremskoĭ, V. V. Slezov, and V. I. Betekhtin, *Pores in Solids* (Énergoatomizdat, Moscow, 1990).
13. S. B. Aĭnbinder, V. I. Betekhtin, A. A. Dzenis, *et al.*, Mekh. Polim., No. 4, 742 (1977).
14. V. I. Betekhtin, A. G. Kadomtsev, E. A. Egorov, *et al.*, Tsement **5–6**, 16 (1991).
15. A. M. Glezer and V. I. Betekhtin, Fiz. Tverd. Tela (S.-Peterburg) **38**, 1784 (1996) [Phys. Solid State **38**, 983 (1996)].
16. V. I. Betekhtin, V. I. Vladimirov, and N. A. Gorobeĭ, Probl. Prochn., No. 9, 3 (1979).

Translated by O. Borovik-Romanova

Physics of the Solid State, Vol. 42, No. 8, 2000, pp. 1465–1470. Translated from Fizika Tverdogo Tela, Vol. 42, No. 8, 2000, pp. 1425–1429.

MAGNETISM AND FERROELECTRICITY

Local Spin Configurations of Fe Atoms in the $Rh_{1-x}Fe_x$ (x = 0.1, 0.2, and 0.3) System with Competing Exchange Interactions

V. P. Parfenova, N. N. Delyagin, A. L. Erzinkyan, and S. I. Reĭman

Skobeltsyn Research Institute of Nuclear Physics, Moscow State University, Vorob'evy gory, Moscow, 119899 Russia

e-mail: parf@srdlan.npi.msu.su

Received November 24, 1999

Abstract—The local spin configurations of Fe atoms in the magnetically ordered alloys $Rh_{1-x}Fe_x$ (x = 0.1, 0.2, and 0.3) have been investigated by Mössbauer spectroscopy. The Mössbauer absorption spectra are measured in the range from 5 K to temperatures of the transition to the paramagnetic state. The measurements in magnetic fields with a strength up to 5 T are carried out at a temperature of 4.2 K. Analysis of the magnetic-hyperfine-field distribution functions demonstrates that Fe atoms form discrete sets of collinear spin configurations corresponding to different net moments of the nearest coordination sphere. The spin structure of the alloys is governed by a random distribution of Fe atoms over the lattice sites and the competition between the Fe–Rh ferromagnetic exchange interaction and the antiferromagnetic interaction of the neighboring Fe atoms. No spin frustration and spin "melting" effects characteristic of spin glasses are revealed in the Rh–Fe alloys. © *2000 MAIK "Nauka/Interperiodica".*

1. INTRODUCTION

The binary alloys $Rh_{1-x}Fe_x$ ($x < 0.4$) have a disordered face-centered cubic structure. At low temperatures, these alloys undergo a transition to the magnetically disordered state. Window *et al.* [1] found that the temperature of magnetic transition T_m for the alloys with $x \le 0.25$ increases linearly with an increase in the iron concentration according to the formula

$$T_m = 400(x - 0.01)\ \text{K}. \qquad (1)$$

The properties of the magnetically ordered phase in these alloys are as yet little understood. Murani and Coles [2] observed maxima of the magnetic susceptibility for the alloys with concentrations $0.03 < x < 0.15$ and interpreted them as indications of the transition to the spin glass phase. It was assumed that the magnetic structure of this phase is similar to the structure of the spin glass phase in the Au–Fe alloys. The results of Mössbauer investigations of the $Rh_{1-x}Fe_x$ ($0.01 < x < 0.25$) alloys [1, 3] were interpreted in the framework of the same concept. As far as we know, no detailed studies of the magnetic structure of these alloys have been performed.

The available data have cast some doubt on the similarity of the magnetic structures of the low-temperature phases in the Rh–Fe and Au–Fe alloys. Rhodium is the transition metal with the exchange-enhanced susceptibility. It is known that, in this case, the alternating exchange interaction necessary for forming the spin glass phase of the type observed in the Au–Fe alloys is considerably suppressed [4]. The linear dependence of T_m on the iron content [relationship (1)] is not characteristic of "classical" spin glasses and differs essentially from the behavior of T_m in the Au–Fe system [5]. At the same time, the linear dependence (1) is similar to the behavior of T_m in the Pd–Fe and Pd–Co alloys [6], in which the polarization of the Pd matrix with a high exchange-enhanced susceptibility gives rise to a ferromagnetic ordering even at a low Fe or Co content. The exchange enhancement of the susceptibility in Rh is not so high, but it can produce a substantial effect on the formation of the magnetic structure in the $Rh_{1-x}Fe_x$ alloys. The $Rh_{1-x}Fe_x$ system is a convenient model object for studying the behavior of the magnetic Fe atoms in a metallic matrix whose exchange polarization can be important, if not absolutely predominant, among the factors responsible for the spin structure.

New data on the magnetic structure of the $Rh_{1-x}Fe_x$ alloys can be obtained in the study of spin states of Fe atoms at the microscopic level. The Mössbauer spectroscopy provides a means of performing these investigations at different iron concentrations over a wide range of temperatures. This technique makes possible both a direct detection of different-type spin configurations and the classification of these states by analyzing the magnetic-hyperfine-field distribution functions $P(B_{\text{hf}})$. In the present work, the magnetic hyperfine interaction of the ^{57}Fe atoms in the $Rh_{1-x}Fe_x$ (x = 0.1, 0.2, and 0.3) alloys was studied by Mössbauer spectroscopy. The preliminary results obtained for the alloy with x = 0.1 were reported earlier in [7].

1063-7834/00/4208-1465$20.00

2. EXPERIMENTAL TECHNIQUE AND RESULTS

Samples of the $Rh_{1-x}Fe_x$ (x = 0.1, 0.2, and 0.3) alloys were produced by the arc melting of metals in an argon atmosphere. Iron enriched with a ^{57}Fe isotope was used. Ingots were homogenized at a temperature of 1200 K and then rapidly quenched. Resonance absorbers were prepared from the alloy powders. The powders were annealed at a temperature of 100 K and quenched. The Mössbauer absorption spectra were measured in the temperature range from 5 K to T_m. The measurements in external magnetic fields with a strength as high as 5 T were carried out at a temperature of 4.2 K. Resonance detectors were employed in order to increase the resonance absorption and the resolution of recording the 14.4-keV Mössbauer radiation.

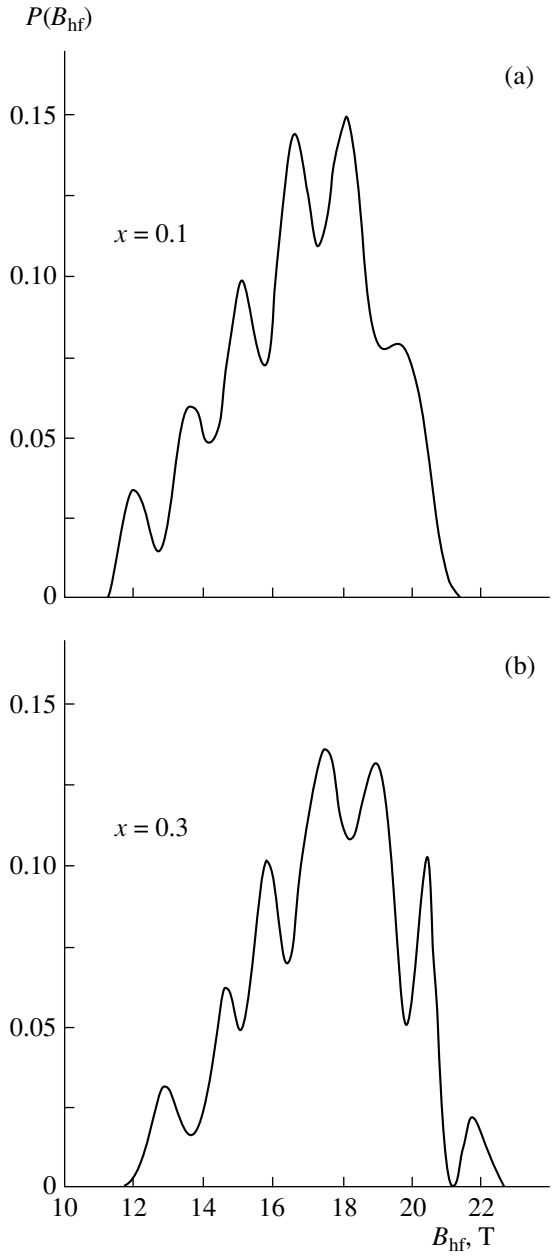

Fig. 1. Magnetic-hyperfine-field distributions for ^{57}Fe in the $Rh_{1-x}Fe_x$ alloys. x = (a) 0.1 and (b) 0.3.

At the first stage of the experimental data processing, the magnetic-hyperfine-field distribution functions $P(B_{hf})$ were calculated from the histograms [8]. As was shown earlier [1, 9], in the $Rh_{1-x}Fe_x$ alloys, the quadrupole shift of magnetic-hyperfine-structure components is absent, and the isomer shift is very weakly depends on the composition. These features are favorable to the reliable interpretation of the $P(B_{hf})$ distribution functions. It was found that the $P(B_{hf})$ distributions exhibit pronounced maxima with a width close to the instrumental resolution width of the resonance lines for all the alloys over a wide range of temperatures (up to $T/T_m \sim 0.85$). As an example, Fig. 1 demonstrates the $P(B_{hf})$ distributions for the alloys with x = 0.1 and 0.3 at 5 K. It is essential that the location of the main maxima in the distribution does not depend (or only slightly depends) on the iron concentration and smoothly varies with an increase in the temperature. This shape of the $P(B_{hf})$ distribution can be explained under the assumption that the hyperfine-field distribution is a superposition of discrete fields B_{hf} corresponding to particular spin configurations. This assumption was corroborated by the results of spectrum processing within the model of superposition of discrete magnetic sextets. The number of sextets was not fixed beforehand and was determined in the course of data processing. The values of B_{hf}, intensities of the partial spectra, linewidths, and isomer shifts served as variable parameters. For all the samples, the χ^2 criterion was no worse than that in calculations of the continuous hyperfine-field distribution. The found linewidths agree well with those expected for the superposition of a discrete set of hyperfine fields. It is important that the change in the iron concentration leads to a change in the intensity of partial spectra, but the values of B_{hf} for the main partial spectra (at T = 5 K) coincide within the limits of experimental error. These results demonstrate that the discrete set of spin configurations is formed in the studied alloys; moreover, the configurations with the same set of B_{hf} predominate in the alloys considerably differing in composition. In particular, this explains weak composition dependences of the $P(B_{hf})$ distribution shape and the mean hyperfine field $\langle B_{hf} \rangle$. The values of the latter for the alloys with x = 0.1, 0.2, and 0.3 at T = 5 K are equal to 16.7, 17.7, and 17.8 T, respectively.

The results of calculations (the fields B_{hf} and the relative intensities I of partial spectra) are listed in the table and displayed in Fig. 2. The magnetic transition temperatures T_m determined from the temperature dependences of $\langle B_{hf} \rangle$ for the alloys with x = 0.1, 0.2, and 0.3 are equal to 33, 75, and 94 K, respectively. For the alloys with x = 0.1 and 0.2, these temperatures agree with the data obtained in [1, 2].

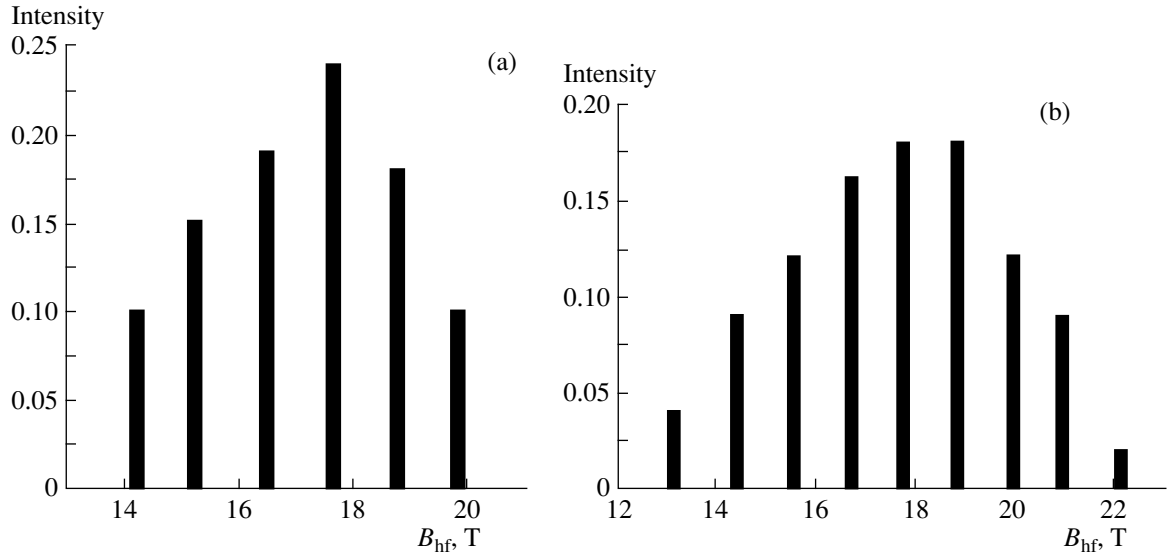

Fig. 2. Magnetic-hyperfine-field distributions obtained within the model of superposition of discrete magnetic partial spectra for the alloys with x = (a) 0.1 and (b) 0.3.

As follows from the Mössbauer absorption spectra measured in external magnetic fields, no considerable spin ordering of the Fe atoms is observed even in the field with a strength of 5 T. The degree of spin ordering does not exceed 3–5%, which is within the limits of experimental error. This differs drastically from the results of similar measurements for the Au–Fe alloys [10].

3. FERROMAGNETIC AND ANTIFERROMAGNETIC ORDERING OF SPINS IN THE $Rh_{1-x}Fe_x$ ALLOYS

The magnetic hyperfine field at Fe atoms in metallic magnets is determined by the intrinsic magnetic moment of a given atom and the magnetic moments of adjacent atoms. If the magnetic moment of the Fe atom is constant, the hyperfine-field distribution is completely governed by variations in the net magnetic moment of the environment. In the $Rh_{1-x}Fe_x$ alloys under consideration, the hyperfine-field distribution has the following characteristic features, which differ from those usually observed in disordered magnetic alloys. First, the shape of the $P(B_{hf})$ distribution only slightly depends on the composition. An increase in the iron concentration does not result in shift of the distribution as a whole, which manifests itself in a very small change in the mean field $\langle B_{hf}\rangle$. Second, the $P(B_{hf})$ distribution is well described within the model of a discrete set of hyperfine fields. Within the limits of exper-

Magnetic hyperfine fields B_{hf} and relative intensities I of partial spectra for the $Rh_{1-x}Fe_x$ (x = 0.1, 0.2, and 0.3) alloys at T = 5 K

	A	B	C	D	E	F	G	H	I
M, μ_{Fe}	–4	–3	–2	–1	0	+1	+2	+3	+4
					x = 0.1				
B_{hf}, T	–	14.23	15.23	16.49	17.66	18.78	19.83	–	–
I	–	0.10	0.15	0.19	0.24	0.18	0.10	–	–
					x = 0.2				
B_{hf}, T	13.02	14.31	15.61	16.78	17.94	18.99	20.04	21.29	–
I	0.02	0.07	0.15	0.17	0.20	0.19	0.15	0.05	–
					x = 0.3				
B_{hf}, T	13.11	14.35	15.44	16.68	17.61	18.78	19.83	20.90	22.02
I	0.04	0.09	0.12	0.16	0.18	0.18	0.12	0.09	0.02

Note: Root-mean-square errors for B_{hf} and I are equal to 0.05–0.10 T and 0.01–0.02, respectively. M is the net magnetic moment of the nearest coordination sphere of the Fe atom (see text).

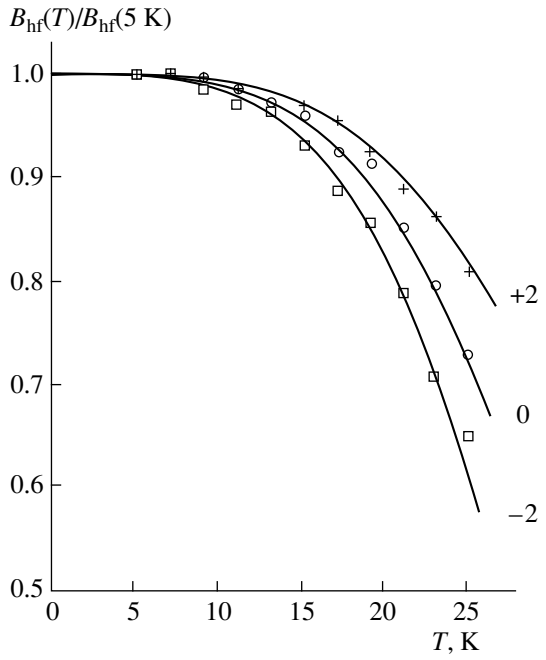

Fig. 3. Temperature dependences of the reduced hyperfine fields $B_{hf}(T)/B_{hf}$(5 K) for the magnetic partial spectra with $M = -2, 0, +2$ for the alloy with $x = 0.1$. The root-mean-square errors are equal to 0.01–0.02. Solid lines represent the Brillouin functions for spin $S = 1$.

imental error, the found values of B_{hf} are independent of the iron concentration; i.e., the same spin configurations predominate in the alloys of different compositions. Third, as is seen from the table, the sets of the fields B_{hf} are equidistant: the difference between the neighboring values of B_{hf} is equal to 1.13 ± 0.15 T. This means that the change in B_{hf} for any two neighboring partial spectra corresponds to the change in the net moment of adjacent atoms by the same magnitude.

In order to explain these features, it is sufficient to assume that the magnetic moments of the adjacent Fe atoms can be aligned both parallel and antiparallel to the moment of the central atom. The sign of the corresponding contribution to the hyperfine field is determined by the orientation of the net magnetic moment of the environment with respect to the moment of the central atom. In this approximation, the magnetic hyperfine field can be written as

$$B_{hf} = a\mu_{Fe} + bM\mu_{Fe}, \quad (2)$$

where μ_{Fe} is the magnetic moment of the Fe atom, M is the net magnetic moment of the nearest environment (in terms of μ_{Fe}), and a and b are the constant parameters. The number of Fe atoms n_{Fe} in the nearest coordination sphere is determined by the binomial distribution. For the alloy with $x = 0.1$, the most probable numbers $n_{Fe} = 0$ and 1 correspond to $M = 0$ and ± 1. It is clear that the most intense partial spectra D, E, and F (see table) should correspond to these configurations. According to [1], $B_{hf} = 17.6 \pm 0.3$ T for an isolated impurity Fe atom in the rhodium matrix. This value coincides with B_{hf} for the partial spectrum E (table), which gives grounds to assign this partial spectrum to the configuration with $M = 0$ (the Fe atoms with zero magnetic moment of the nearest environment). By assuming that the magnetic moment M for each pair of the adjacent partial spectra differs by the value $\Delta M = \pm 1$, the remaining partial spectra are uniquely identified. The M values found in this manner are given in the upper row of the table. Setting $\mu_{Fe} = 2.2\mu_B$ for the magnetic moment of the Fe atom in Rh [11], we obtain the following coefficients a and b in formula (2):

$$a = 8.1\text{T}/\mu_B, \quad b = 0.5\text{T}/\mu_B.$$

These values are typical of Fe in alloys with transition metals (see, for example, [8]).

For the alloy with $x = 0.1$, it is possible to compare the intensities of partial spectra with the probabilities $W(n_{Fe})$ of atomic configurations with different numbers n_{Fe}. At a random distribution of the Fe atoms over the lattice sites, we have the following probabilities: $W(0) = 0.28$, $W(1) = 0.38$, $W(2) = 0.23$, and $W(3) = 0.09$. The experimental values of $W(n_{Fe})$ are as follows: $W(0) = I(\text{E}) = 0.24 \pm 0.02$, $W(1) = I(\text{D}) + I(\text{F}) = 0.37 \pm 0.02$, $W(2) = I(\text{C}) + I(\text{G}) = 0.25 \pm 0.02$, and $W(3) = I(\text{B}) = 0.10 \pm 0.01$. A good agreement between the calculated and experimental probabilities $W(n_{Fe})$ can be considered a corroboration of the above identification of the partial spectra. In the alloys with $x = 0.2$ and 0.3, the probabilities of the atomic configurations with $n_{Fe} = 4$ and 5 become significant. However, the spin configurations with $M = \pm 5$ are not observed at all, and the intensity of the partial spectra with $M = \pm 4$ turns out to be very small (see table). This implies that the high-spin configurations ($M > 3$) with a large number of spins with identical orientation are unstable and easily transform into the states characterized by a smaller spin. In turn, this leads to an increase in the intensity of the partial spectra corresponding to the configurations with $M = 0, \pm 1$, and ± 2.

The temperature dependences of the hyperfine field B_{hf} for different spin configurations differ from each other and depend on the moment M in a regular fashion. Figure 3 displays the temperature dependences of the reduced hyperfine field $B_{hf}(T)/B_{hf}$(5 K) for three spin configurations in the alloy with $x = 0.1$. It can be seen that the larger the number of spins in the nearest environment that are aligned antiparallel to the spin of the central atom, the steeper the dependence $B_{hf}(T)$. For the alloy with $x = 0.1$, the dependences of the exchange field on M can be quantitatively evaluated in the mean field approximation. For this purpose, the $B_{hf}(T)$ dependences were approximated by the Brillouin functions (Fig. 3). The effective temperatures T_C, which characterize the local exchange field, were determined for each spin configuration. It was found that the T_C tem-

perature monotonically increases with an increase in M, and, for the configurations with $M = -3, -2, -1, 0, +1$, and $+2$, its values are equal to 29.5, 30.0, 31.2, 32.7, 34.7, and 37.0 K, respectively. These values can be compared with the nominal magnetic transition temperature $T_m = 33$ K. It is evident that the T_m temperature can be treated only as a parameter characterizing the exchange interaction averaged over the spin configurations. (Note that the T_m temperature coincides with the value of T_C for the spin configuration with $M = 0$.) A similar interrelation between the temperature dependence $B_{hf}(T)$ and M are observed for the spin configurations in the alloys with $x = 0.2$ and 0.3.

4. COMPETITION OF EXCHANGE INTERACTIONS IN THE $Rh_{1-x}Fe_x$ ALLOYS

The formation of local spin configurations of Fe atoms with parallel and antiparallel mutual spin orientations suggests that the competing exchange interactions with opposite signs occur in the $Rh_{1-x}Fe_x$ alloys. It is quite reasonable that the direct Fe–Rh interaction (the polarization of the matrix with the exchange-enhanced susceptibility) favors the ferromagnetic orientation of magnetic moments (as is the case, for example, in the Pd–Fe alloys). In order to explain the experimental data, it is necessary to assume that this interaction competes with the antiferromagnetic exchange interaction between the nearest neighbor Fe atoms. The fact that the configurations with positive and negative moments M are formed with approximately equal probabilities implies that the Fe–Rh and Fe–Fe competing interactions are comparable in magnitude. The random distribution of the Fe atoms over the lattice sites is responsible for a strong spatial nonuniformity of the composite exchange field and leads to the formation of regions with a predominant ferromagnetic or antiferromagnetic orientation of magnetic moments.

For the alloy with the given composition, the local exchange field at the Fe sites changes depending on the configuration of spins in the nearest environment. As follows from the temperature dependences $B_{hf}(T)$ (Fig. 3), the local exchange field regularly depends on M. An increase in the exchange field at the atoms in the configurations with positive M is due to an increase in the total polarization of the neighboring Rh atoms and the corresponding contribution from the Fe–Rh ferromagnetic interaction to the total energy of the system. By contrast, in the configurations with negative M, the contributions from the spin of the central atoms and the spins of the neighboring atoms to the polarization partly compensate each other, which brings about a decrease in the local exchange field at the central atom.

In the regions with a large local iron concentration, the probability of the formation of spin configurations in which the Fe–Fe antiferromagnetic interaction becomes predominant is rather high. This explains the aforementioned instability of the high-spin configurations with $M > 3$. It should be expected that a decrease in the mean iron concentration in the alloy will be accompanied by a decrease in the overlap of the polarization regions. This brings about, first, a decrease in the T_m temperature and, second, the formation of regions with a considerably weaker exchange field. The $P(B_{hf})$ distribution for the alloy with $x = 0.1$ (Fig. 1) exhibits a weak unidentified line ($B_{hf} = 12.3$, $I = 0.05$). It can be assumed that this line corresponds to the Fe atoms in the atomic configurations with $n_{Fe} = 0$, which are localized in the regions with the weaker exchange interaction. This interpretation becomes all the more probable with due regard for the fact that the intensity of the partial spectrum with $M = 0$ for this alloy is approximately 4% less than the calculated intensity (see the preceding section).

The discrete structure of the hyperfine-field distribution is retained up to temperatures $T/T_m \sim 0.85$, which reflects the high thermal stability of local spin configurations. An increase in the intensity of the $P(B_{hf})$ distribution in the range of zero fields is observed only in the immediate vicinity of T_m, i.e., in the range of the transition to the paramagnetic state. The appearance of zero (or very weak) hyperfine fields in the $P(B_{hf})$ distribution at relatively low temperatures is characteristic of the Au–Fe [10] and Fe–Ni–Mn [8] spin glasses. According to Saslow and Parker [12], this is due to the presence of frustrated spin states and the spin "melting" effect. No similar phenomena are observed in the Rh–Fe alloys under study.

Thus, the experimental data indicate that a specific spin structure is formed in the $Rh_{1-x}Fe_x$ ($x = 0.1$, 0.2, and 0.3) magnetically ordered alloys. The formation of this structure is caused by both the competition of exchange interactions comparable in magnitude and opposite in sign and the random distribution of the Fe atoms over the lattice site. The probability that the local spin configurations with preferred parallel or antiparallel mutual orientation of spins of the Fe atoms are formed in the system depends on the ratio between the parameters of the Fe–Rh and Fe–Fe competing interactions. An increase in the exchange enhancement of the matrix susceptibility can change the ratio between the competing interactions and induce a transition of the system to the ferromagnetic state similar to that observed in the Pd–Fe alloys. In order to verify this assumption and refine the proposed model of spin structure, similar investigations will be performed with the alloys in which the Rh atoms are partly replaced by the Pd atoms.

REFERENCES

1. B. Window, G. Longworth, and C. E. Johnson, J. Phys. C: Solid State Phys. **3**, 2156 (1970).
2. A. P. Murani and B. R. Coles, J. Phys. C: Solid State Phys., Suppl. **3**, S159 (1970).

3. C. Meyer, F. Hartman-Boutron, and Y. Gros, J. Phys. (Paris) **47**, 1395 (1986).
4. G. J. Nieuwenhuys, B. H. Verbeek, and J. A. Mydosh, J. Appl. Phys. **50**, 1685 (1979).
5. B. H. Verbeek and J. A. Mydosh, J. Phys. F: Met. Phys. **8**, L109 (1978).
6. G. J. Nieuwenhuys, Adv. Phys. **24**, 515 (1975).
7. V. P. Parfenova, N. N. Delyagin, A. L. Erzinkyan, and S. I. Reyman, Phys. Status Solidi B **214** (1), R1 (1999).
8. N. N. Delyagin, A. L. Erzinkyan, G. M. Gurevich, *et al.*, Fiz. Tverd. Tela (S.-Peterburg) **40**, 1650 (1998) [Phys. Solid State **40**, 1500 (1998)].
9. C. C. Chao, P. Duwez, and C. C. Tsuei, J. Appl. Phys. **42**, 4282 (1971).
10. N. N. Delyagin, G. M. Gurevich, A. L. Erzinkyan, *et al.*, Zh. Éksp. Teor. Fiz. **109**, 1451 (1996) [JETP **82**, 783 (1996)].
11. A. Clogston, B. Matthias, M. Peter, *et al.*, Phys. Rev. **125**, 541 (1962).
12. W. W. Saslow and G. Parker, Phys. Rev. Lett. **56**, 1074 (1986).

Translated by O. Borovik-Romanova

Physics of the Solid State, Vol. 42, No. 8, 2000, pp. 1471–1477. Translated from Fizika Tverdogo Tela, Vol. 42, No. 8, 2000, pp. 1430–1436.

MAGNETISM AND FERROELECTRICITY

Modification of Spin-Wave Resonance Spectra in Films due to Damping and Finite Surface-Spin Pinning

R. N. Nosov and D. I. Sementsov

Ul'yanovsk State University, ul. L. Tolstogo 42, Ul'yanovsk, 432700 Russia

e-mail: sements@quant.univ.simbirsk.su

Received December 20, 1999

Abstract—The influence of the extent of the surface spin pinning on the spin-wave resonance spectrum is investigated for the case of a perpendicularly magnetized thin ferromagnetic layer in the presence of damping in the spin system. For surface pinning of different types, the results of the numerical analysis of the imaginary part of susceptibility, which determines the amplitude, width, and position of resonance peaks in spin-wave spectra, are presented. © *2000 MAIK "Nauka/Interperiodica".*

INTRODUCTION

In the case of uniformly magnetized films, a necessary condition for spin-wave resonance (SWR) is the existence of the surface anisotropy, which differs from the bulk one and determines the extent of spin pinning on the film surface [1]. There is a considerable body of work devoted to the question of how the boundary conditions affect the spin-wave spectrum (SWS) [2–6]. The features of SWR spectra were investigated for symmetrical, antisymmetrical, and other special cases of surface-spin pinning. However, the analysis carried out in most of the works did not take damping, inherent in any spin system, into account. In the films that exhibit incomplete pinning of the surface spins and finite damping, the features of SWR spectra and its modification with variations of the above-mentioned characteristics have been little studied [7–9]. At the same time, the increased requirements for interpreting SWR spectra in mono- and multilayers necessitate a more detailed study on the influence of different parameters on the SWR spectra and, especially, of the symmetry of boundary conditions, the extent of spin pinning, and damping [10, 11]. In this work, the modification of the SWR spectrum with variations in the extent of surface-spin pinning and with change in the type of surface anisotropy is examined with allowance made for damping in the spin system.

1. EQUATIONS OF MOTION

In the presence of damping in the spin system, the motion of the magnetization vector **M** is described by the Landau–Lifshitz equation

$$\dot{\mathbf{M}} = \gamma[\mathbf{M}\mathbf{H}^{\text{eff}}] + \frac{\xi}{M}[\mathbf{M}\dot{\mathbf{M}}], \qquad (1)$$

where γ is the gyromagnetic ratio, ξ is the dimensionless damping parameter. The effective internal field is defined by the expression

$$\mathbf{H}^{\text{eff}} = \mathbf{H}_0 + \mathbf{h} + \alpha\nabla^2\mathbf{M} + \beta\mathbf{n}(\mathbf{n}\mathbf{M}) - 4\pi\hat{N}\mathbf{M}, \qquad (2)$$

where $\mathbf{H}_0$ and $\mathbf{h}$ are external static and high-frequency fields, respectively; α and β are the exchange and uniaxial anisotropy constants, respectively; $\mathbf{n}$ is the unit vector of the easy magnetization axis; and $\hat{N}$ is the demagnetizing coefficient tensor. Let the static field $\mathbf{H}_0$ and the unit vector $\mathbf{n}$ be orthogonal to the film surface, and the high-frequency field $\mathbf{h}$, orthogonal to $\mathbf{H}_0$. The bias magnetic field $\mathbf{H}_0$ is assumed to be of such a magnitude that the orientation of the steady-state magnetization $\mathbf{M}_0$ coincides with $\mathbf{n}$. Introducing small deviations $\mathbf{m}(\mathbf{r}, t)$ from the equilibrium magnetization in (1) and linearizing this equation, we obtain the following set of equations for the components m_x and m_y:

$$\begin{aligned}\dot{m}_x - \xi\dot{m}_y &= \gamma(\alpha M_0\nabla^2 - \beta M_0 - H_0 + 4\pi M_0)m_y - \gamma M_0 h_y,\\ \dot{m}_y - \xi\dot{m}_x &= (\gamma(\alpha M_0\nabla^2 - \beta M_0 - H_0 + 4\pi M_0)m_x + \gamma M_0 h_x.)\end{aligned} \qquad (3)$$

A film magnetized normally to its surface possesses axial symmetry; therefore, it is convenient to describe the deviation of the magnetic moment from the equilibrium in terms of rotational components $m^{\pm} = m_x \pm im_y$. If the high-frequency field is also circularly polarized ($h^{\pm} = h_x \pm ih_y$) and varies harmonically in time, the equation of motion for the component $m^+ \equiv m$, responsible for free oscillations of the spin system, has the form

$$\frac{d^2m}{dz^2} + \nu^2 m = -\frac{h}{\alpha}, \qquad (4)$$

1063-7834/00/4208-1471$20.00

where the wave number of a spin wave is determined by the dispersion law

$$\omega = (1 - i\xi)\omega_0 + \alpha\gamma M_0 \nu^2, \quad (5)$$

and $\omega_0 = \gamma(H_0 + \beta M_0 - 4\pi M_0)$ is the frequency of the uniform (ferromagnetic) resonance. The solution of (4) can be presented as

$$m(z) = A_1 \exp(i\nu z) + A_2 \exp(-i\nu z) - \frac{h}{\alpha\nu^2}. \quad (6)$$

The coefficients A_1 and A_2 are determined from the exchange boundary conditions [1] for each of the film surfaces

$$\frac{dm}{dz} - d_1 m\Big|_{z=-L} = 0, \quad \frac{dm}{dz} + d_2 m\Big|_{z=L} = 0, \quad (7)$$

where $d_i = a\Delta\beta_i/\alpha$ are parameters of the surface-spin pinning, a is a coefficient of the order of the lattice constant, and $\Delta\beta_i$ is the difference between the surface and bulk anisotropy constants.

A simultaneous solution of Eqs. (6) and (7) leads to the following expression for the magnetization averaged over the thickness of the film:

$$\langle m \rangle = \frac{1}{2L}\int_{-L}^{L} m(z)dz = \chi h, \quad (8)$$

where the high-frequency susceptibility of the film is

$$\chi = \frac{1}{2\alpha\nu^2} \times \left\{ \frac{2d_1 d_2 \tan\nu L + (d_1 + d_2)\nu}{\nu L[d_1 d_2 + (d_1 + d_2)\nu\cot 2\nu L - \nu^2]} - 2 \right\}. \quad (9)$$

This expression describes the excitation spectrum of the spin system of a magnetic film in the general form. In the absence of damping ($\xi = 0$), the position of spin wave peaks is determined by the poles of χ.

2. ANALYSIS OF THE MODEL WITHOUT DAMPING

In the general case of arbitrary spin pinning on the film surface, there can be three different kinds of boundary conditions, depending on the signs of the parameters d_i: when $d_i > 0$, uniaxial anisotropy of the "easy-axis" type is realized on both film surfaces; $d_i < 0$ corresponds to the surface anisotropy of the "easy-plane" type; and the case of $d_1 > 0$, $d_2 < 0$ corresponds to mixed boundary conditions. In what follows, we will consider several cases of surface pinning of spins that are of frequent occurrence.

(1) $d_1 = -d_2 = d$, the case of antisymmetrical pinning. In this case,

$$\chi = \frac{1}{\alpha\nu^2}\left[\frac{d^2 \tan\nu L}{\nu L(d^2 + \nu^2)} - 1\right], \quad (10)$$

and the spin-wave spectrum is determined by the wave numbers $\nu_p L = (2p - 1)\pi/2$, where p are integers. The position of spin-wave modes does not depend on the extent of pinning. In accordance with the number $2p - 1$, these modes may be specified as odd. The difference in the wave number between the "neighboring" modes depends on the film thickness: $\Delta\nu_{p,p+1} = \pi/L$ and, hence, it increases with decreasing thickness.

(2) $d_1 = d_2 = d$, the case of symmetrical pinning. In this case

$$\chi = \frac{1}{\alpha\nu^2}\left[\frac{d}{\nu L(d\cot\nu L - \nu)} - 1\right], \quad (11)$$

the spin-wave spectrum is determined by solutions of the equation

$$\cot\nu L - \nu/d = 0. \quad (12)$$

From (12), it follows that, in this case, the position of spin-wave modes depends on the extent of surface-spins pinning. In the case of complete pinning ($d \longrightarrow \pm\infty$), the spectrum of spin-wave modes is determined by the wave numbers $\nu_p L = (2p - 1)\pi/2$, and, similarly to the case of antisymmetrical pinning, they can be classified as odd.

(3) $d_1 \longrightarrow \infty$, $d_2 = 0$, i.e., there is complete pinning on one of the surfaces, and no pinning on the other. In this case,

$$\chi = \frac{1}{\alpha\nu^2}\left(\frac{1}{2\nu L\cot 2\nu L} - 1\right), \quad (13)$$

and the spin-wave spectrum is characterized by the wave numbers $\nu_p L = (2p - 1)\pi/4$; hence, the number of modes is doubled in comparison with the above cases of complete and symmetrical pinning.

In all considered cases, when pinning is entirely absent on both surfaces of the film ($d_1 = d_2 = d$), spin-wave modes disappear, and only the uniform mode of $\nu = 0$ remains in the spectrum (ferromagnetic resonance), the mode, for which $\chi = 1/\alpha\nu^2$. The considered spin-wave modes are of the bulk type, their wave numbers are real, and the solution of (6) can be presented in terms of trigonometric functions. According to (5), these modes are realized in the frequency range higher than the frequency of the uniform resonance ($\omega > \omega_0$). The derived solutions of (4) also admit the existence of surface spin-wave modes for which the wave numbers in (6) are purely imaginary. They exist at $\omega < \omega_0$ and are expressed in terms of hyperbolic functions. An expression for the susceptibility χ for the case of surface modes can be obtained by replacing ν with $i\nu$ in the

corresponding expressions for bulk modes. Thus, in the case of symmetrical pinning, instead of (11), we obtain

$$\chi = \frac{1}{\alpha\nu^2}\left[\frac{d}{\nu L(d\coth\nu L + \nu)} - 1\right], \qquad (14)$$

and, hence, the spectrum of these modes is given by a solution of the equation

$$\coth\nu L + \nu/d = 0. \qquad (15)$$

Figure 1 shows graphical solutions of the equations, corresponding to the wave-number spectrum of the bulk (a) and surface (b) modes in the case of symmetrical surface pinning of spins. It is evident that, at $d \longrightarrow \pm\infty$, the spectrum of bulk modes is determined by the wave numbers $\nu_p L = (2p-1)\pi/2$, while, at $d \longrightarrow 0$, the spectrum contains only one uniform mode with $\nu = 0$. In the considered case of symmetrical pinning, the surface mode exists only for surface anisotropy of the "easy-plane" type, i.e., at $d < 0$.

At nonsymmetrical boundary conditions, when $d_1 \neq \pm d_2$, analyzing (9) is generally rather difficult. However, for every specific type of the surface anisotropy and for given values of the parameters d_i, the wave-number spectrum of the bulk and surface modes can be found numerically.

3. THE MODEL WITH DAMPING

Expression (9) with pure real (or pure imaginary) wave numbers ν allows us to determine only the position of the spin-wave modes on the frequency scale (or on the scale of field amplitudes). The width of a peak and its amplitude can be found from (9), if we take into account that the value of ν is complex because of damping in the system. To examine the spin-wave spectrum of the system in the case of $\xi \neq 0$, we write the dispersion relation for the spin waves in terms of the real and imaginary parts of the wave number $\nu = \nu_1 - i\nu_2$,

$$\nu_1^2 - \nu_2^2 = \Omega - \Omega_0 \equiv \Delta\Omega, \quad 2\nu_1\nu_2 = \xi\Omega, \qquad (16)$$

where $\Omega = \omega/\alpha\gamma M_0$, and Ω_0 is defined by a similar relation. After solving (16), we obtain the frequency dependencies of the real and imaginary parts of the wave numbers of spin waves

$$\nu_j = \frac{1}{\sqrt{2}}\left[\sqrt{\Delta\Omega^2 + \xi^2\Omega^2} - (-1)^j\Delta\Omega\right]^{\frac{1}{2}}, \quad j = 1, 2. \qquad (17)$$

At $\Omega = \Omega_0$, i.e., when $\Delta\Omega = 0$, which corresponds to the uniform (ferromagnetic) resonance, we have $\nu_1 = \nu_2 = (\xi\Omega/2)^{\frac{1}{2}}$. In Fig. 2, the frequency dependencies of the parameters ν_j are plotted, which represent the dispersion curves for damping spin waves in the thin film.

The power of the high frequency field that is absorbed by the film is determined by the imaginary

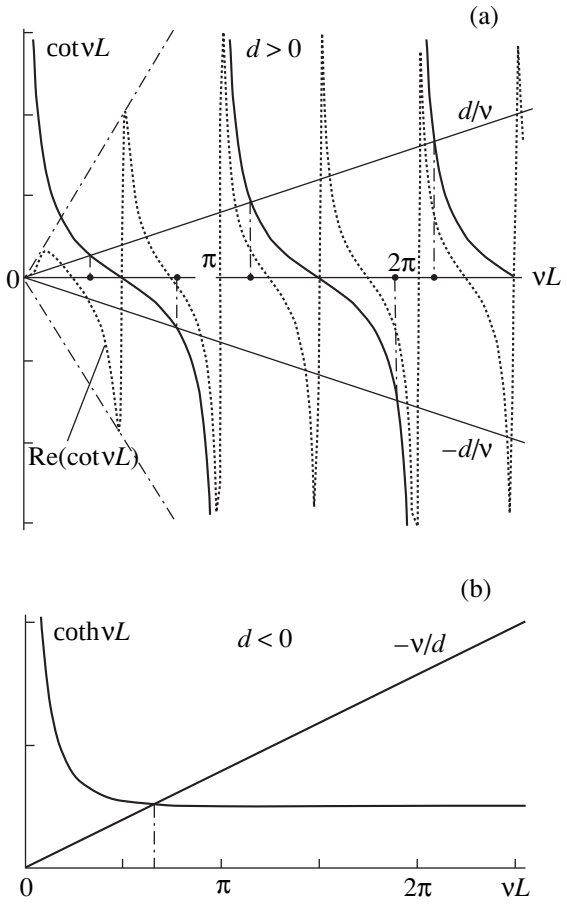

Fig. 1. Graphical solution of the dispersion equations for the bulk (a) and surface (b) modes at symmetrical pinning.

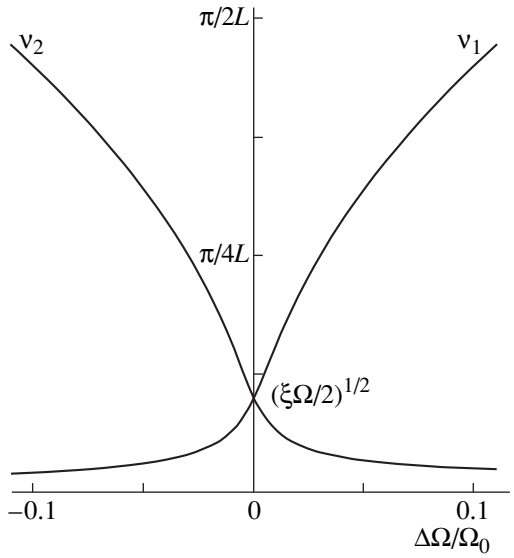

Fig. 2. Frequency dependencies of the real ν_1 and imaginary ν_2 parts of the wave numbers of spin waves.

part of the complex susceptibility $\chi = \chi' - i\chi''$ and is equal to $P = \omega\chi''h^2/2$. The maxima of χ'' are associated with spin wave modes of the corresponding type and order excited in the film. In what follows, we will consider in greater detail the spin wave spectrum for one of the most important cases, the symmetrical pinning. From (11), we obtain an expression for the imaginary part of the high-frequency susceptibility

$$\chi'' = \frac{1}{\alpha g L}\{\Delta\Omega(\nu_1 q_2 + \nu_2 q_1) + \xi\Omega[\nu_1 q_1 - \nu_2 q_2 - L(\nu_1^2 + \nu_2^2)(q_1^2 + q_2^2)]\}, \quad (18)$$

where the following notation has been introduced: $g = (q_1^2 + q_2^2)(\nu_1^2 + \nu_2^2)^3$ and

$$q_1 = \cot\nu_1 L \frac{\coth^2\nu_2 L - 1}{\cot^2\nu_1 L + \coth^2\nu_2 L} - \frac{\nu_1}{d},$$

$$q_2 = \coth\nu_2 L \frac{\cot^2\nu_1 L + 1}{\cot^2\nu_1 L + \coth^2\nu_2 L} + \frac{\nu_2}{d}.$$

Analysis of (18) reveals that the absorption maxima are located at the points that correspond either to a solution of the equation $q_1 = 0$ at $\Omega > \Omega_0$ (bulk modes) or, at $\Omega < \Omega_0$ and $d < 0$, to a solution of $q_2 = 0$ (surface modes). These equations are a generalization of Eqs. (12) and (15) to the case of nonzero damping. The spectrum of the bulk modes is determined by solutions of the equation $q_1 = 0$, which fall into two groups, namely:

$$L\nu_{1p}^{(1)} = \left(p - \frac{1}{2} - \Delta_p\right)\pi, \quad L\nu_{1p}^{(2)} \cong \pi p, \quad (19)$$

where Δ_p is a displacement that is dependent on the extent of pinning and on the mode's number.

As it follows from Fig. 1, at $\xi \neq 0$, the function $\mathrm{Re}(\cot\nu L)$ is bounded. The envelopes of its maxima are straight lines $\pm\nu_1\Omega L/\xi$, whence it follows that solutions of (19) exist only when the inequality $|d| \geq \xi\Omega L$ is fulfilled. The first type of solutions $\nu_{1p}^{(1)}$ corresponds to odd spin-wave modes and virtually coincides with the solutions of (12) in the case of no damping. The second type of solutions $\nu_{1p}^{(2)}$ corresponds to even modes. They appear as the result of distortions of standing spin waves due to damping in the spin system. When surface anisotropy grows, at $d > 0$, the wave numbers of odd modes increase, while the wave numbers of even modes do not vary for all practical purposes (they decrease very slightly). Hence, it follows that, with d growth, odd modes are shifted toward higher resonance frequencies (lower resonance fields). At $d < 0$, as the pinning becomes stronger, i.e., $|d|$ increases, the shift of spin-wave modes will take place in the reverse direction. The shift occurs until odd and even modes merge together, i.e., $|d|$ becomes equal to $\xi\Omega L$. In that case, the straight lines $\pm\nu_1/d$ merge with the envelopes of the maxima of the function $\mathrm{Re}(\cot\nu L)$, and it becomes impossible to identify the spin-wave modes as odd or even.

At the frequencies, corresponding to the wave numbers (19), in the approximation $\Delta\Omega \gg \xi\Omega$, the maxima of absorption are given by the expressions

$$\chi'' \cong \begin{cases} \dfrac{1}{\alpha\xi\Omega\Delta\Omega L^2}\left(\dfrac{2}{f} + \dfrac{\xi^2\Omega^2L^2}{\Delta\Omega}\right), & \nu_1 = \nu_1^{(1)} \\ \dfrac{\xi\Omega}{\alpha\Delta\Omega}\left(\dfrac{2d}{4d\Delta\Omega + \xi^2\Omega^2 L} + \dfrac{1}{\Delta\Omega}\right), & \nu_1 = \nu_1^{(2)}, \end{cases}$$

$$f = \frac{\nu_1^2 + d^2}{d^2 + \xi^2\Omega^2L^2/4} + \frac{1}{Ld}, \quad \nu_1^2 \cong \Delta\Omega. \quad (20)$$

From these expressions, it follows that the amplitudes of odd modes are proportional to ξ^{-1}, while the amplitudes of even modes are proportional to $\sim\xi$. At the damping parameter $\xi \leq 10^{-2}$, which usually takes place in the real magnetic films, the intensity of even modes is at least four orders of magnitude less than the intensity of odd modes.

In the limit case of complete pinning ($d \longrightarrow \infty$), expression (20) gives the following dependence of the amplitude of odd modes on the wave number ν_1:

$$\chi''_{\max} = \frac{1}{\alpha\xi\Omega\nu_1^2L^2}\left(2 + \frac{\xi^2\Omega^2L^2}{\nu_1^2}\right). \quad (21)$$

Neglecting the small second term in the parentheses in (21), we obtain the well-known "quadratic" distribution of the amplitudes of the spin-wave modes ($\chi''_{\max} \sim \nu^{-2}$). In the case of no pinning ($d = 0$), the spin-waves spectrum disappears, and expressions (20) describe the "tail" of the uniform resonance $\chi''_{\mathrm{unif}} \cong \xi\Omega/\alpha\Delta\Omega^2$. The finite values of the parameters d and ξ cause the departure of spin-wave amplitudes from the quadratic distribution, decreasing them in comparison with $\chi'' = 2/\alpha\xi\Omega\nu_1^2L^2$.

Let us examine the absorption χ'' in the vicinity of the uniform-resonance frequency $\Omega = \Omega_0$. Taking into account that $\nu_1 \cong \nu_2 \cong (\xi\Omega/2)^{\frac{1}{2}}$ and $\nu_i L \ll 1$ in this region, we obtain

$$\chi''_{\mathrm{unif}} = \frac{\xi\Omega}{\alpha(\Delta\Omega^2 + \xi^2\omega^2)} \times\left[1 - \frac{d(d - 3\Delta\Omega L/2)}{(d - \Delta\Omega L)^2 + (d + 1/2L)^2\xi^2\Omega^2L^4}\right]. \quad (22)$$

In the case of no pinning, the maximal value of the ferromagnetic-resonance amplitude takes place at $\Delta\Omega = 0$,

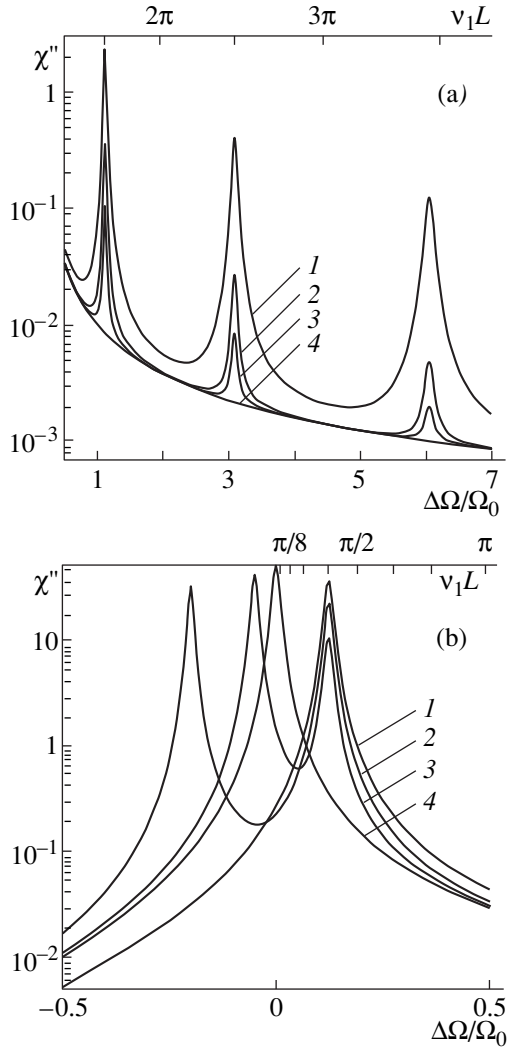

Fig. 3. Spin-wave resonance spectrum at antisymmetrical pinning and different values of the pinning parameter d; $L = 10^{-4}$ cm, $M_0 = 10^3$ G, and $\xi = 10^{-2}$.

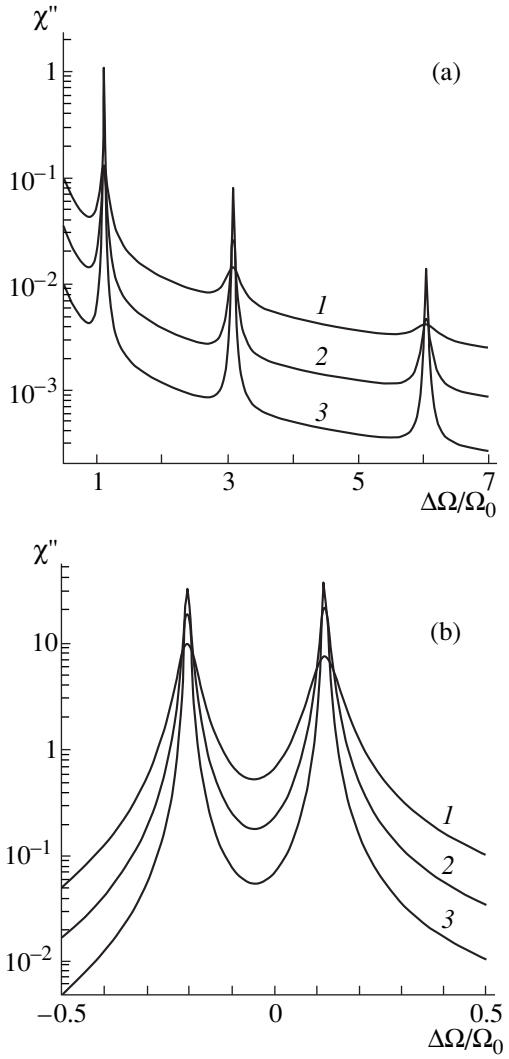

Fig. 4. Spin-wave resonance spectrum at antisymmetrical pinning and different values of the damping parameter ξ; $d = 1$.

and it is equal to $\chi''_{FMR} = 1/\alpha\xi\Omega$. At $d \neq 0$, the peak of absorption of the "uniform" mode is displaced: at $d > 0$, the shift is positive, and the uniform mode transforms into the bulk spin-wave mode specified by the index $p = 1$; at $d < 0$, the shift is negative, and the uniform mode transforms into the surface mode. Similarly, one can obtain the amplitudes of spin-wave modes in any particular case of the surface pinning of spins.

4. NUMERICAL RESULTS

In what follows, we present the results of numerical analysis, which describe how the main features of the modification of the spin-wave spectrum resulted from surface spin pinning and damping in the spin system. In Fig. 3, the dependence of χ'' on the normalized detuning from the frequency of the uniform resonance $\Delta\Omega/\Omega_0$ is shown for the case of antisymmetrical surface-spin pinning ($d_1 = -d_2 = d$) at different values of the pinning parameter ($d = \infty$, 2, 1, 0; curves *1–4*, respectively) and at the value of the damping parameter $\xi = 10^{-2}$. This dependence characterizes the frequency spectrum of spin-wave modes. The part of the spectrum that corresponds to the bulk modes of indices $p = 2$, 3, 4 is shown in Fig. 3a, while the part that corresponds to the bulk mode of index $p = 1$, as well as to the uniform and surface modes, is shown in Fig. 3b. From these dependencies, it follows that, with variations in the extent of surface-spin pinning, in the case under consideration, there is no frequency (and field) displacement of the bulk modes, but there is a displacement of the surface mode: at complete pinning, there is no surface mode; with a decrease of the extent of pinning, the surface mode displaces toward higher frequencies, and, in going to the case of no pinning ($d \longrightarrow 0$), it transforms to the uniform mode ($\Omega_S \longrightarrow \Omega_0$). At $d \neq 0$, there

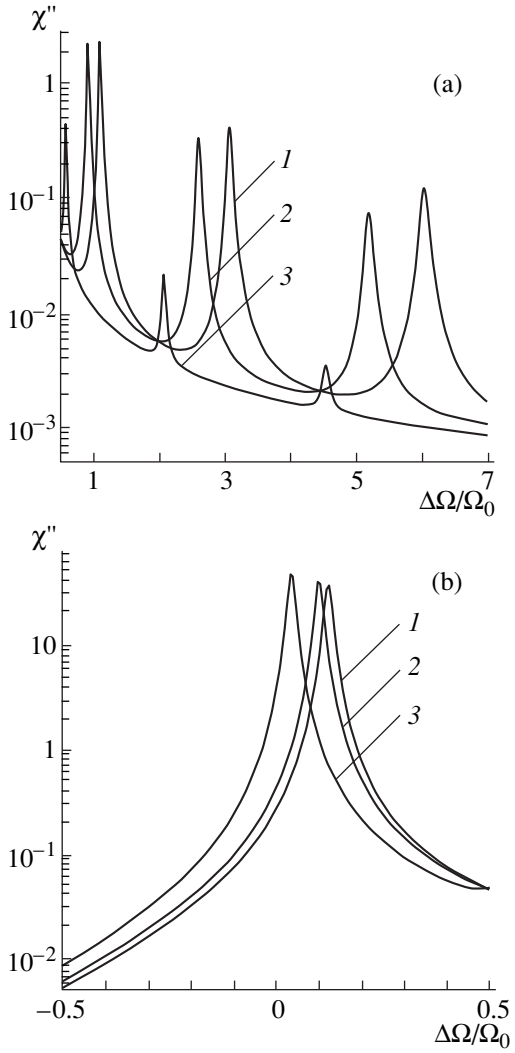

Fig. 5. Spin-wave resonance spectrum at symmetrical pinning and different values of the parameter $d > 0$; $\xi = 10^{-2}$.

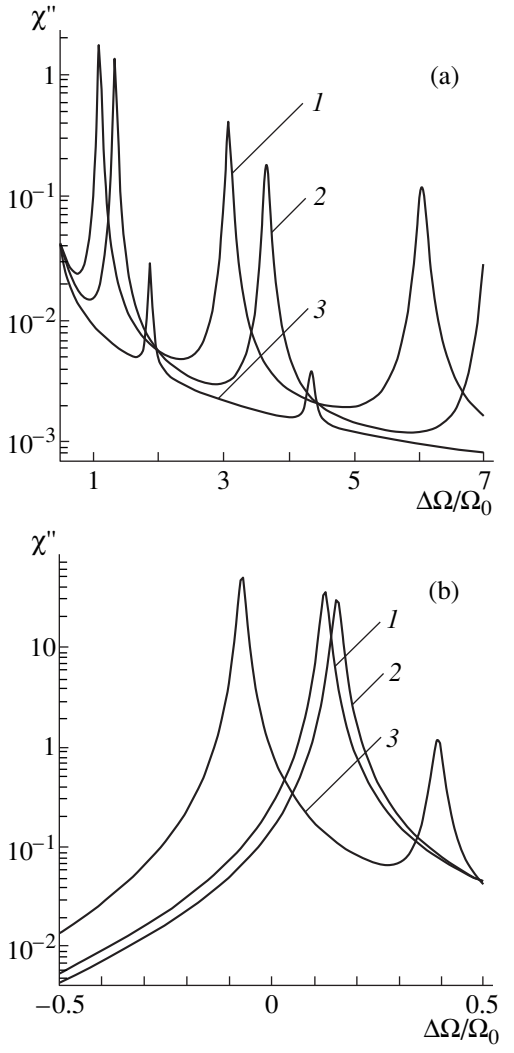

Fig. 6. Spin-wave resonance spectrum at symmetrical pinning and different values of the parameter $d < 0$; $\xi = 10^{-2}$.

is no uniform mode in the spectrum. It is also evident that an increase in the extent of pinning results in a significant increase in the amplitudes of bulk modes and in an insignificant decrease in the amplitude of the surface mode. The change in sign of the surface anisotropy on both sides of the film ($d_1 = -d_2 = d < 0$) has no effect on the wave number and amplitude of the spin-wave modes, which is a distinctive feature of the spin-wave spectrum in the case of surface-spin pinning of the antisymmetrical type.

In Figs. 4a and 4b, for antisymmetrical pinning characterized by the parameter $d = 1$, the spin-wave spectrum is shown at different values of the damping parameter $\xi = (0.3; 1; 3) \times 10^{-2}$ (curves *1–3*). As should be expected, the growth of the extent of damping in the spin system leads to a decrease in the amplitude of the resonance peaks and to an increase in their width. The extent of damping has no effect on the position of these peaks.

In Fig. 5, for the case of surface-spin pinning of the symmetrical type ($d_1 = d_2 = d$) and of the surface anisotropy of the "easy-axis" type ($d > 0$), the parts of the spectrum that correspond to the bulk spin-wave modes of indices $p = 2$, 3, and 4 (a) and to the mode of index $p = 1$ (b) are shown. A distinctive feature of this case is the absence of any surface mode in the spectrum and the dependence of the resonance-peak position on the strength of pinning. With an increase in the pinning strength, all resonance peaks displace toward higher frequencies. The amplitudes of peaks with $p > 1$ increase with the strength of pinning. However, for the mode of $p = 1$, the amplitude growth takes place with a decrease in pinning strength, and, at $d = 0$, this mode is transformed into the uniform resonance mode having a maximal amplitude. In Fig. 6, the spectrum at symmetrical pinning is shown, but for the case of surface anisotropy of the "easy-plane" type ($d < 0$). In this case, in the region $\Omega < \Omega_0$, a surface mode appears, with its

amplitude being much larger than the amplitude of the bulk mode with $p = 1$ (curve *3* in Fig. 6b); the growth of the strength of spin pinning results in an increase in the peak amplitudes of all bulk modes ($p \geq 1$) and in a displacement of resonance peaks of the bulk modes toward lower frequencies. A comparison of the spectra presented in Figs. 5 and 6 shows that, at the same values of $|d|$, but different types of surface anisotropy, the same interval of frequencies may be associated with spin-wave modes of different indices p. For example, in the frequency region $\Delta\Omega/\Omega_0 \cong 2$ and $|d| = 2$, we have the mode of $p = 3$ in Fig. 5a and the mode of $p = 2$ in Fig. 6a.

Thus, damping and incomplete surface-spin pinning lead to a significant rearrangement of the spectrum of spin-wave modes. The spectrum sensitivity to the type of surface anisotropy and to the extent of pinning demands the adequate theoretical approach in spin-wave mode identification. For the experimental determination of the spectral parameters to be more accurate, it is desirable to use films exhibiting low damping ($\xi \leq 10^{-2}$) and having a small thickness ($L \leq 10^{-4}$ cm), for which there is no overlapping of modes of different orders.

REFERENCES

1. A. G. Gurevich and G. A. Melkov, *Magnetic Oscillations and Waves* (Nauka, Moscow, 1994).
2. Yu. A. Korchagin, R. G. Khlebopros, and N. S. Chistyakov, Fiz. Tverd. Tela (Leningrad) **14**, 2121 (1972) [Sov. Phys. Solid State **14**, 1826 (1972)].
3. Yu. A. Korchagin, A. V. Nabatov, G. I. Fish, *et al.*, Fiz. Met. Metalloved. **35** (1), 196 (1973).
4. B. Hoekstra, R. P. Stapele, and J. M. Robertson, J. Appl. Phys. B **48**, 382 (1977).
5. L. V. Lutsev and Yu. M. Yakovlev, Fiz. Tverd. Tela (Leningrad) **30**, 1675 (1988) [Sov. Phys. Solid State **30**, 965 (1988)].
6. S. L. Vysotskiĭ, G. T. Kazakov, M. L. Kats, and Yu. A. Filimonov, Fiz. Tverd. Tela (St. Petersburg) **35**, 1190 (1993) [Phys. Solid State **35**, 606 (1993)].
7. D. I. Sementsov, Fiz. Tverd. Tela (Leningrad) **38**, 247 (1974).
8. P. E. Zil'berman, V. I. Kozlov, and A. V. Pomyalov, Fiz. Tverd. Tela (Leningrad) **28**, 352 (1986) [Sov. Phys. Solid State **28**, 195 (1986)].
9. R. S. Iskhakov, A. S. Chekanov, and L. A. Chekanova, Fiz. Tverd. Tela (Leningrad) **30**, 970 (1988) [Sov. Phys. Solid State **30**, 563 (1988)].
10. M. Jirsa, Phys. Status Solidi B **125**, 187 (1984).
11. A. M. Zyuzin and A. G. Bazhanov, Zh. Éksp. Teor. Fiz. **111**, 1667 (1997) [JETP **84**, 912 (1997)].

Translated by N. Ostrovskaya

Physics of the Solid State, Vol. 42, No. 8, 2000, pp. 1478–1482. Translated from Fizika Tverdogo Tela, Vol. 42, No. 8, 2000, pp. 1437–1440.

MAGNETISM AND FERROELECTRICITY

The Dependence of Pulse Properties of Ferrous Borate Single Crystals on Their Thickness

A. V. Bukvin, O. S. Kolotov, and V. A. Pogozhev

Moscow State University, Vorob'evy gory, Moscow, 119899 Russia

Received December 24, 1999

Abstract—It is established that the magnitude of the discontinuity in the slope of a pulse-switching curve defined as the ratio between the switching coefficients S_{w1} and S_{w2} corresponding to the first and second parts of the switching curve, respectively, decreases with an increase in the thickness of a ferrous borate single crystal. This change is generally caused by a decrease in the coefficient S_{w1}, whose magnitude is inversely proportional to the sample's thickness. In order to analyze the results obtained, we used the early proposed expression $\tau^{-1} = aH_s - bA^2$, connecting the switching rate τ^{-1} with the amplitude of the magnetic field H_s and the intensity A of the magnetoelastic vibrations accompanying the pulse switching. It is found that the coefficient a depends only slightly on the sample's thickness, while the coefficient b is inversely proportional to the thickness squared. Thus, the main part of the energy losses due to magnetoelastic vibrations is associated with elastic lattice vibrations. © *2000 MAIK "Nauka/Interperiodica".*

It is well known [1–3] that the pulse properties of magnets are most fully characterized by a switching curve, which is the dependence of the inverse switching time τ^{-1} (or the magnetization rate [4]) on the amplitude of a magnetic field pulse H_s. The shape of this curve reflects the qualitative and quantitative changes in the pulse-switching mechanisms. Searching and investigation of the changes associated with peculiarities of the interaction between the magnetic and elastic subsystems of the crystal are of great physical interest. These changes have until now only been found in single crystals of ferrous borate $FeBO_3$. It was established [5–7] that the shape of a switching curve of ferrous borate is determined not by the change in the magnetization nature, in contrast to other magnets investigated to date [2, 3, 8–10], but by the character of the dependence of energy losses associated with the excitation of shock magneto-elastic vibrations on the duration τ of the transient process. It was found that a delay in the elastic subsystem of the crystal from the magnetic one is observed when $\tau < \tau^* \approx 13$–17 ns, with τ^* depending only slightly on the sample's thickness and the period of vibrations determined by it. As a result, the energy losses due to the excitation of magnetoelastic vibrations decrease, the magnetization rate increases, and there appears a discontinuity in the slope of the $\tau^{-1}(H_s)$ curve.

Obviously, to understand the physics of the pulse switching of $FeBO_3$ single crystals (as well as other magnets characterized by a clearly pronounced magnetoelastic interaction), it is necessary to investigate the dependence of the shape of the switching curve on the properties and characteristics of the single crystals. The results of the investigation of the dependence of the discontinuity in the slope of a switching curve on the thickness of single crystals are reported in this paper. The case of 180° switching is considered. The analysis of the results obtained is carried out by means of an expression proposed in [11], which describes the dependence of the switching rate τ^{-1} on the amplitude of the switching field H_s and the intensity of magnetoelastic vibrations A,

$$\tau^{-1} = aH_s - bA^2, \tag{1}$$

where a is a proportionality coefficient depending on the Gilbert damping factor (i.e., on the losses in the magnetic subsystem) and the type of the transient process. For 180° switching, the coefficient b is equal to $ak/2M_s$, where M_s is the saturation magnetization and k is a coefficient in the expression $w_{me} = kA^2$ for the energy loss density associated with the excitation of magnetoelastic vibrations.

1. EXPERIMENTAL TECHNIQUE

The investigations were carried out on an induction setup with a time resolution of ~1 ns [12]. The initial single-domain state of a sample was created by a constant bias field H_b parallel to the sample's plane and exceeding the field of its technical saturation H_{sat} by 20–25%. The process under investigation was initiated by a magnetic field pulse H_p, whose direction was opposite to that of the field H_b. The resulting value of the switching field $H_s = H_p - H_b$ was used when constructing the $\tau^{-1}(H_s)$ dependences.

Eight samples with thicknesses ranging from 24 to 130 μm were investigated. The samples had an irregu-

1063-7834/00/4208-1478$20.00

lar-polygonal shape and diameters ranging from 4 to 8 mm. The plane of a sample was perpendicular to the crystallographic *C* axis. The parameters of four samples, which are used to illustrate the main results, are presented in the table. The table lists the thickness *d*, the saturation field H_{sat}, the period of magnetoelastic vibrations *T* (measured at the same field H_s = 3.5 Oe), and the values of the coefficients *a* and *b* in expression (1) found by the method described below. It should be noted that the value of the coefficient *k* and, therefore, the coefficient *b* depend on the method of determination of the intensity of magnetoelastic vibrations. As in our previous experiments [5–7], the amplitude *A* of stress oscillations of the longitudinal switching signal, which was observed immediately after the main stage of the magnetization reversal, was treated as a measure of the intensity of these vibrations. The switching time τ was supposed to be equal to the time interval between the instants at which the stress signal was 0.1 of its amplitude.

Parameters of the samples

Sample	*d*, μm	H_{sat}, Oe	*T*, ns	*a*, $Oe^{-1}\ \mu s^{-1}$	*b*, $\mu s^{-1}\ mV^{-2}$
1	24	1.3	13	36	9.9
2	45	1.4	22	33	3.1
3	80	1.8	40	33	1.1
4	110	2.1	56	30	0.65

2. RESULTS AND DISCUSSION

The investigations carried out indicate that the shape of a pulse-switching curve obviously depends on the sample's thickness. For curves obtained for the thinnest (No. 1) and the thickest (No. 4) samples (solid lines in Figs. 1, 2) illustrate this result. According to data published earlier [13], these curves consist of two parts, each of which is well approximated by a straight line. It is seen that, for the thickest sample, the discontinuity in slope of the pulse-switching curve (the difference in the slope of the approximating straight lines with respect to the abscissa axis) is obviously smaller than that for the thinnest one. In magnetodynamics [1–3], the rate of change in the switching rate (the so-called switching coefficient $S_w = dH_s/d\tau^{-1}$) is usually characterized by a quantity that is inversely proportional to the slope mentioned above. Accordingly, the discontinuity in slope can be characterized by the ratio between the switching coefficients S_{w1} and S_{w2} for the first and second parts, respectively, of the curves under discussion. We have S_{w1} = 0.29 and S_{w2} = 0.022 Oe μs for the 24 μm-thick sample (sample 1) and S_{w1} = 0.06 and S_{w2} = 0.025 Oe μs for sample 4. Thus, an increase in a sample's thickness gives rise to an essential decrease in the discontinuity in slope of the pulse-switching curve.

Figure 3 shows the dependences of the coefficients S_{w1} and S_{w2} on the thickness of all samples investigated. The coefficient S_{w1} becomes approximately 5.3 times smaller as the thickness grows from 24 to 130 μm. The experiment shows that the $S_{w1}(d)$ dependence is well

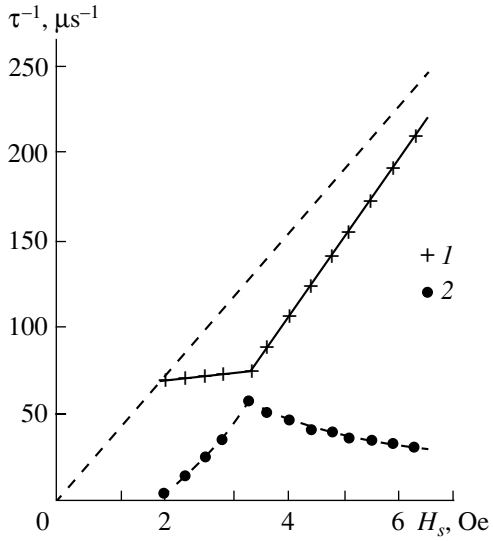

Fig. 1. Comparison between the experimental and calculated switching rates for sample 1. The solid line is an experimental pulse-switching curve; the dashed line is the τ^{-1} = aH_s straight line; (*1*) are the calculated switching rates; (*2*) are the values of bA^2.

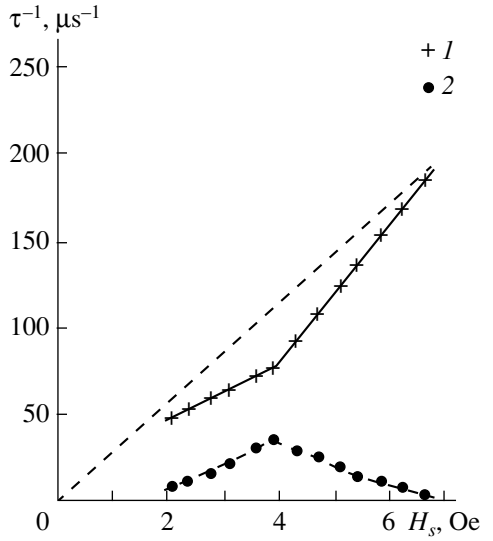

Fig. 2. Comparison between the experimental and calculated switching rates for sample 4. The solid line is an experimental pulse-switching curve; the dashed line is the τ^{-1} = aH_s straight line; (*1*) are the calculated switching rates; (*2*) are the values of bA^2.

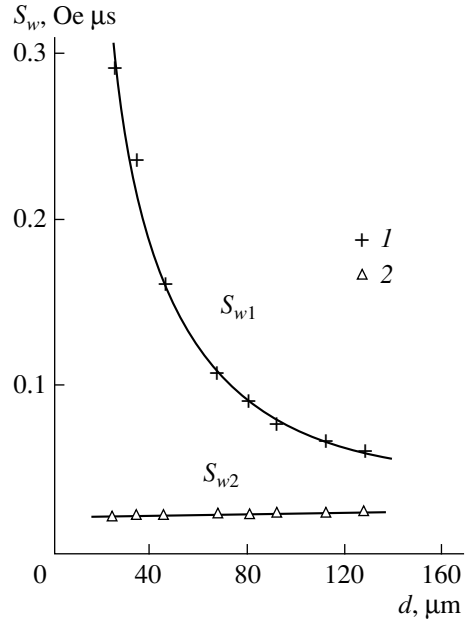

Fig. 3. Dependences of the switching coefficients on the sample thickness d: (*1*) correspond to the experimental values of S_{w1}, (*2*) are the experimental values of S_{w2}. The solid line is the hyperbola $S_{w1} = f/d$.

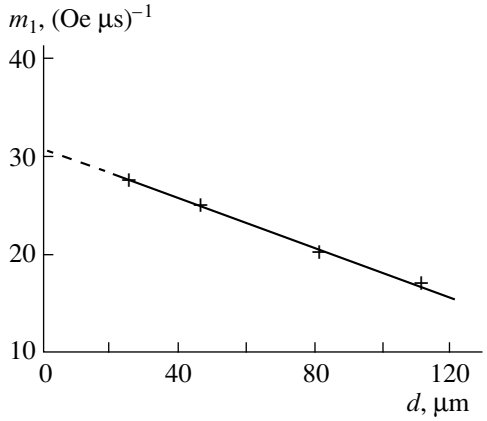

Fig. 4. Dependence of the coefficient m_1 on the sample's thickness d.

approximated by the hyperbola $S_{w1} = f/d$ (see Fig. 3), with f being approximately 7.3 Oe μm μs for the samples under investigation. At the same time, it is seen that the coefficient S_{w2} changes only slightly, growing from 0.02 to 0.25 Oe μs. Thus, the ratio S_{w1}/S_{w2} changes up to 6 times in the thickness range investigated.

To discuss the results obtained, let us consider expression (1). It should be reminded that the validity of this expression was proven [11], in general, for 90° switching. Therefore, it is necessary, first and foremost, to verify the validity of this expression in the case of the transient process considered in this paper. Figures 1 and 2 show the inverse switching time calculated from expression (1). The experimental values of the intensity of magnetoelastic vibrations and the values of the coefficients a and b fitted by the least-square procedure to the experimental data (see table) were used in the calculations. It is seen that the calculated values are consistent with the experimental pulse-switching curves and, therefore, expression (1) is also valid for the 180°-pulse magnetization reversal. Using this result, one can infer the influence of the energy losses due to magnetoelastic vibrations on the switching rate.

The influence of the energy losses is characterized by the quantity bA^2 in expression (1). This quantity is proportional to the energy density of magnetoelastic vibrations. Figures 1 and 2 show that the energy losses initially increase with a growth in the field H_s, then pass through a maximum at the field strength close to the field H_s^* corresponding to the discontinuity in slope of the $\tau^{-1}(H_s)$ curve, and begin to decrease. There is practically no influence of magnetoelastic vibrations on the switching rate at fields of ~10–15 Oe. Hence, the first term in expression (1) determines the switching rate that would be present if the magnetoelastic vibrations were absent. In other words, the equation of the asymptote of the pulse-switching curve at large fields has the form $\tau^{-1} = aH_s$. The asymptotes are represented by dashed straight lines in Figs. 1 and 2. A comparison of these asymptotes with the other lines presented in the figures reveals that the drag effect of magnetoelastic vibrations decreases as the sample's thickness grows. Obviously, the discontinuity in slope of a pulse-switching curve can also be characterized by the curve "sag" $aH_s^* - (\tau^*)^{-1} = bA^2(H_s^*)$.

A decrease in the energy losses that is observed with an increase in the thickness of the single crystal thus leads to a decrease in the magnitude of the discontinuity in slope (or "sag") of the pulse-switching curve. It also gives rise to a decrease in the switching coefficient S_{w1}. Let us consider this question in detail. Figures 1 and 2 show that, in the first approximation, the quantity bA^2 increases according to a linear law

$$bA^2 \approx (H_s - H_0)m_1, \tag{2}$$

as the strength of the switching field grows up to $H_s = H_s^*$. At that the field H_0 (~1.4–1.8 Oe) is close to the value of the field H_s at which the pulse-switching curve intersects its asymptote. The dependence of the proportionality coefficient m_1 on the sample's thickness is shown in Fig. 4. It is seen that this dependence is practically linear:

$$m_1 = m_{10} - pd, \tag{3}$$

where the proportionality coefficient is $p = 0.125$ (Oe μm μs)$^{-1}$, and $m_{10} = 31$ (Oe μs)$^{-1}$ determines the value of m_1 at $d \longrightarrow 0$.

Based on the results presented above, one can suppose that the switching coefficient S_{w1} increases with no limit with decreasing single-crystal thickness. In other words, the slope of the first part of the pulse-switching curve with respect to the abscissa axis is close to zero at $d \longrightarrow 0$. Since, in accordance with Eqs. (1) and (2), we have the relationship

$$S_{w1} = \frac{1}{a - m_1}, \quad (4)$$

it follows from formula (3) that the coefficients a and m_{10} have close values. The validity of this conclusion can be verified by comparing the average value of the coefficients a presented in the table (≈ 33 (Oe μs)$^{-1}$) to the above-mentioned value of m_{10}. It follows, in turn, that the relationship $S_{w1} \cong (pd)^{-1}$ takes place. This approximate expression agrees well with the experimental results presented earlier: the switching coefficient corresponding to the first part of the pulse-switching curve is inversely proportional to the sample's thickness, and the value $f = 7.3$ Oe μm μs is close to the predicted value of the proportionality coefficient $p^{-1} = 8$ Oe μm μs.

It is obvious that the analysis carried out is semiempirical. A rigorous explanation requires more detailed ideas of the energy losses in the elastic and magnetic subsystems of the crystal and their influence on the transient processes. Unfortunately, the experimental and theoretical investigations of these questions are presently in embryo. Nevertheless, we can reveal one factor that gives rise to a decrease in energy losses with a growth in the sample's thickness, everything else being equal. We found that the coefficient b in expression (1) is approximately inversely proportional to the single-crystal thickness squared. In Fig. 5, the values of the coefficient b taken from the table are indicated and the quadratic hyperbola q/d^2 with $q = 620$ (μm/mV)^2 μs^{-1} is plotted. Such a type of dependence under discussion indicates that the main part of the energy associated with magnetoelastic vibrations is the energy of elastic lattice vibrations. Indeed, the energy density of these vibrations (averaged over their period) is proportional to the vibration frequency squared [14]. The frequency of the magnetoelastic vibrations is inversely proportional to the thickness of the single crystal [15, 16].

Now let us briefly consider the switching coefficient S_{w2}. On the basis of the data presented in Figs. 1 and 2, one can think that, in the fields $H_s > H_s^*$, the quantity bA^2 decreases as the switching field grows, approximately following the linear law

$$bA^2 \approx bA^2(H_s^*) - (H_s - H_s^*)m_2,$$

where the proportionality coefficient $m_2 > 0$. Thus, the switching coefficient $S_{w2} \approx (a + m_2)^{-1}$ is smaller than the limiting switching coefficient $S_{w0} = a^{-1}$ characterizing the asymptote. For example, for sample 1, we have

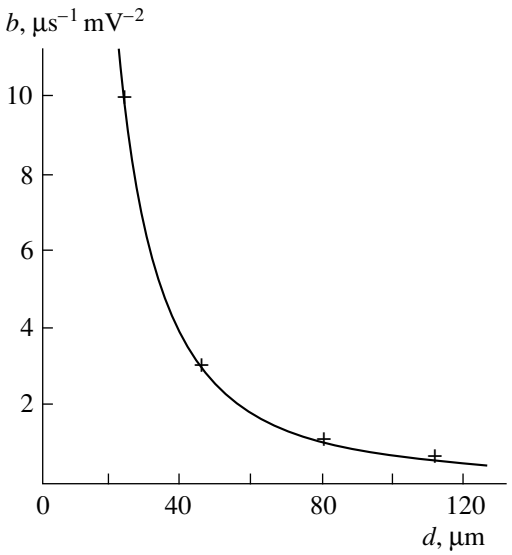

Fig. 5. Dependence of the coefficient b on the sample's thickness d. The solid line is the quadratic hyperbola $b = q/d^2$.

$S_{w0} = 0.028$ Oe μs, while the experimental value is $S_{w2} = 0.022$ Oe μs. The corresponding parameters for sample 4 are $S_{w0} = 0.033$ Oe μs and $S_{w2} = 0.025$ Oe μs. It is seen that the difference in value of S_{w0} and S_{w2} is noticeable. However, the values themselves are small, which is why an increase in the time resolution of the experimental setup is needed to investigate them in more detail and obtain the asymptote experimentally.

REFERENCES

1. F. B. Humphrey and E. M. Gyorgy, J. Appl. Phys. **30**, 935 (1959).
2. O. S. Kolotov, V. A. Pogozhaev, and R. V. Telesnin, Usp. Fiz. Nauk **113**, 569 (1973) [Sov. Phys. Usp. **17**, 528 (1973)].
3. S. Krupičˇka, *Physik der Ferrite und der Verwandten Magnetischen Oxide* (Academia, Prague, 1973; Mir, Moscow, 1976), Chap. II.
4. *Handbook on the Magnetism and Magnetic Materials Nomenclature*, Ed. by F. V. Lisovskiĭ and L. I. Antonov (Moscow, 1997).
5. O. S. Kolotov, J. H. Kim, A. P. Krasnozhon, and V. A. Pogozhev, Pis'ma Zh. Éksp. Teor. Fiz. **58**, 52 (1993) [JETP Lett. **58**, 53 (1993)].
6. O. S. Kolotov, J. H. Kim, A. P. Krasnozhon, and V. A. Pogozhev, Fiz. Tverd. Tela (St. Petersburg) **36**, 231 (1994) [Phys. Solid State **36**, 127 (1994)].
7. O. S. Kolotov, A. P. Krasnozhon, and V. A. Pogozhev, Fiz. Tverd. Tela (St. Petersburg) **40**, 305 (1998) [Phys. Solid State **40**, 277 (1998)].
8. A. S. Kashintsev, O. S. Kolotov, and V. A. Pogozhev, Fiz. Met. Metalloved. **64**, 891 (1987).
9. O. S. Kolotov and V. A. Pogozhev, Vestn. Mosk. Univ., Ser. 3: Fiz., Astron. **32** (5), 3 (1992).

10. A. A. Glazer, A. S. Kashintsev, O. S. Kolotov, *et al.*, Fiz. Met. Metalloved., No. 2, 154 (1992).
11. O. S. Kolotov, Fiz. Tverd. Tela (St. Petersburg) **41**, 654 (1999) [Phys. Solid State **41**, 589 (1999)].
12. O. S. Kolotov, V. A. Pogozhev, and R. V. Telesnin, *Methods and Instrumentation for Studying Pulse Properties of Thin Magnetic Films* (Mosk. Gos. Univ., Moscow, 1970).
13. O. S. Kolotov, V. A. Pogozhev, R. V. Telesnin, *et al.*, Phys. Status Solidi A **72** (2), K197 (1982).
14. V. A. Krasil'nikov and V. V. Krylov, *Introduction to the Physical Acoustics* (Moscow, 1984).
15. M. H. Seavey, Solid State Commun. **10**, 219 (1973).
16. O. S. Kolotov, V. A. Pogozhev, G. V. Smirnov, and Yu. V. Shvyd'ko, Fiz. Tverd. Tela (Leningrad) **29**, 2548 (1987) [Sov. Phys. Solid State **29**, 1471 (1987)].

Translated by A. Pushnov

Physics of the Solid State, Vol. 42, No. 8, 2000, pp. 1483–1487. Translated from Fizika Tverdogo Tela, Vol. 42, No. 8, 2000, pp. 1441–1445.

MAGNETISM AND FERROELECTRICITY

Microscopic Stability Mechanisms of a Charge-Ordered Phase of $La_{1.5}Sr_{0.5}NiO_4$

A. Yu. Zakharov, A. E. Nikiforov, and V. A. Smorkalov

Ural State University, pr. Lenina 51, Yekaterinburg, 620083 Russia

e-mail: Anton.Zaharov@usu.ru

Received January 24, 2000

Abstract—Using a pairwise potential approximation and a shell model, computer simulation is performed of a charge-ordered crystal phase of $La_{1.5}Sr_{0.5}NiO_4$, in which Ni^{2+} and Ni^{3+} ions are arranged in staggered rows in perovskite layers. This phase is found to be stable, and, in the process of its formation, the contribution to the lowering of the total crystal energy from the charge rearrangement is smaller than that from the relaxation of the crystal structure (the structure of NiO_2 layers, first of all) caused by this rearrangement. The decrease in the total energy is due to the long-range Coulomb interaction, predominantly the attraction between Ni^{3+} and oxygen ions in NiO_2 layers. *© 2000 MAIK "Nauka/Interperiodica".*

INTRODUCTION

$La_{2-x}Sr_xNiO_4$ crystals have attracted particular interest in the last few years. Originally, this was due to the conjecture that, when appropriately doped, this nickelate can be a superconductor, because its structure is identical to that of the cuprate $La_{2-x}Sr_xCuO_4$, which is superconducting in a wide composition range. However, these expectations have not been realized. Although pure La_2NiO_4 and La_2CuO_4 are both antiferromagnetic insulators, and their doping with strontium results in the injection of holes into the MeO_2 perovskite layers (*Me* = Ni, Cu), there are also some significant distinctions between them. For instance, the Ni^{2+} ion has a $3d^8$ configuration with a spin of $S = 1$, and the band gap in nickelates equals 4 eV [1]. In cuprates, by contrast, the Cu^{2+} ion has the 1/2 spin and the band gap is half as narrow [2]. For this reason, $La_{2-x}Sr_xCuO_4$ becomes a superconductor even for $x > 0.05$, whereas $La_{2-x}Sr_xNiO_4$ is an insulator up to $x \approx 1$ [3], because the holes in NiO_2 layers are in localized polaron states. The interpretation of transport properties of $La_{2-x}Sr_xNiO_4$ in terms of the polaron model is confirmed by the experiment. For example, the interaction of vibrational "breather" modes with holes leads to infrared [4, 5] and other anomalies [6].

Electron-diffraction experiments on $La_{2-x}Sr_xNiO_4$ ($x = 1/3$) [7] revealed satellite spots near each fundamental Bragg reflection. These satellites are associated with the formation of a superlattice and are only observed at temperatures below $T_{CO} \approx 220$ K. In terms of the space group D_{4h}^{17}, their positions are given by the wave vectors $\mathbf{q}_1 = (1, \pm\delta, 0)$ and $\mathbf{q}_2 = (\pm\delta, 1, 0)$, which correspond to two different superstructure domains. The value of δ was measured to be close to a rational number of 1/3. This allowed one to suppose that, in the crystal, there occurred a structural phase transition that resulted in unit-cell tripling along the two crystal axes in the plane of perovskite layers. Investigations of the electrical properties revealed that the phase transition is accompanied by an increase in the planar resistivity [3, 8]. On the basis of this, a proposal was made that the change in symmetry is due to hole localization, which is arranged in the NiO_2 layers in a periodic array, which is referred to as a charge- or polaron-ordered structure [7]. This name arose from the fact that a localized hole causes the formation of a polaron, which consists of a nickel ion and four in-plane oxygens around it. The array of polarons in the charge-ordered phase is also called the stripe structure, because they are arranged in stripes in real space.

Numerous experimental studies revealed that, unlike superconductivity, the charge ordering is a more universal property of layered perovskites; it is observed in differently doped $La_{2-x}Sr_xNiO_4$, e.g., for $x = 1/8$, 1/4, and 1/2 [7, 9], as well as in cuprates ($La_{2-x}Sr_xCuO_4$, $x = 1/8$) [10] and manganates. In the latter case, the transition to the charge-ordered phase occurs in the single-layer $La_{1.5}Sr_{0.5}MnO_4$ compound at a temperature $T_{CO} \approx 230$ K [11] and in the two-layer $LaSr_2Mn_2O_7$ at $T_{CO} = 210$ K [12]. Thus, the charge-ordering phenomenon is one of the key subjects of the study on oxides with the layered perovskite structure. In order to gain insight into this phenomenon, one should solve two fundamental problems.

First, it is not clear which ions the holes are localized on: metal (Ni, Cu, Mn) or oxygen ions. The major difficulty is that there are no available experimental data that allow one to unambiguously decide between these two cases. For this reason, one has to gain the information theoretically by using, for example, vari-

1063-7834/00/4208-1483$20.00 © 2000 MAIK "Nauka/Interperiodica"

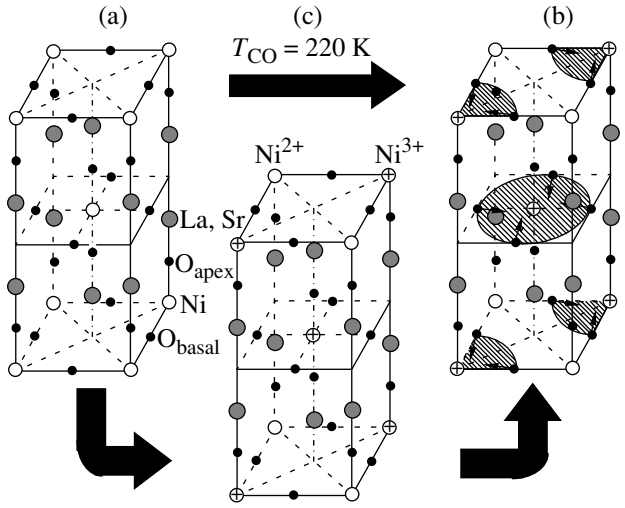

Fig. 1. Structures of (a) the high-temperature tetragonal (HTT), (b) charge-ordered (CO), and (c) pseudo-HTT phases of an $La_{2-x}Sr_xNiO_4$ crystal (schematic).

ous computer simulation methods. Relevant calculations were performed, for instance, for a two-dimensional system of the "perovskite layer" type by using a nonhomogeneous Hartree–Fock approximation [13]. Spectral characteristics of the system were predicted for the two cases of hole localization, and, on the basis of the calculations, the important conclusion was drawn that the electron–phonon interaction strongly affects the state of a localized hole: it is energetically favorable for a hole to be localized on oxygen ions when the electron–lattice coupling is weak and on metal ions in the opposite case. It should be noted in this connection that, from experimental data on the total phonon density in $La_{2-x}Sr_xNiO_4$ [9], it follows that the electron–lattice coupling is strong in this material.

The other fundamental problem that should be solved in studying the charge-ordering phenomenon is to elucidate microscopical mechanisms responsible for the formation of polarons and their spatial ordering. Theoretical investigations revealed that the formation of polaron states is determined by the balance of the long-range Coulomb repulsion between holes, on the one hand, and short-range interaction between ions of the crystal, on the other hand [14–18]. The latter can be due, for example, to the electron–lattice coupling or, as in manganates, to the orbital ordering in the 3*d*-ion sublattice, which results in Jahn–Teller distortions stabilizing-polaron states [19]

Thus, in studying the charge ordering in layered perovskites, a number of problems arise that have to be solved theoretically. Some of the problems are of fundamental importance, because they are a serious handicap to further experimental investigations of this phenomenon. Therefore, to theoretically elucidate the physical picture of the charge ordering is an urgent problem now.

The present paper is devoted to modeling the transition of an $La_{1.5}Sr_{0.5}MnO_4$ crystal from the high-temperature tetragonal (HTT) phase to a charge-ordered (CO) one. The objective of this work is, first, to theoretically demonstrate that the charge ordering can occur in layered perovskites and that this ordering is stable; second, to argue that this charge rearrangement directly or indirectly causes the total energy of the system to decrease; and, third, to elucidate the microscopical reasons for the charge ordering in nickelates.

1. THE STRUCTURE OF HIGH-TEMPERATURE TETRAGONAL AND CHARGE-ORDERED PHASES

The $La_{1.5}Sr_{0.5}NiO_4$ compound is a single-layer perovskite, which consists of alternate NiO_2 and (La, Sr)O layers, with the layer sequence being such that there are two layers of (La, Sr)O between nearest-neighbor NiO_2 layers (Fig. 1). The characteristic element of this structure is the octahedron NiO_6, which is deformed when any change in crystal symmetry occurs. The latter may be of a different origin. Specifically, the HTT and CO phases differ in structure because the distributions of holes in these phases are radically different.

For example, if the strontium doping of the crystal is $x = 1/2$, we have one hole per two formula units. From the results of the theoretical paper [13] and the experimental data [9], it follows that a hole is localized on nickel ions and distributed uniformly between them in the high-temperature tetragonal phase. Therefore, all nickel ions are equally charged (+2.5) and occupy symmetry-equivalent positions in the crystal (Fig. 1a). In the charge-ordered phase, the hole is localized entirely on one of the two nickel ions (a formula unit contains one Ni ion) and, hence, we have two species of Ni ion, +3 and +2. These ions are in equal amounts and distributed not randomly over the crystal, but arranged in staggered rows in perovskite layers. In this case, the unit cell is doubled along each of the two crystal axes in the NiO_2 layer plane. This structure was suggested in [7]; one quarter of its unit cell is depicted in Fig. 1b.

To treat the effect of Sr doping, we use the following method. Strontium is assumed to be distributed randomly over the crystal in both phases. Therefore, instead of the lanthanum sublattice in which Sr^{2+} ions substitute for a part of La^{3+} ions, we can introduce a homogeneous sublattice of an effective $(La_{1.5}, Sr_{0.5})$ ion (see below). Taking the crystal doping into account by this means, we preserve the long-range order and can perform symmetry phase analysis. The analysis revealed that the HTT and CO phases belong to the symmorphic symmetry groups D_{4h}^{17} and D_{2h}^{19}, respectively. These space groups essentially differ in that the in-plane oxygens O_{basal} are fixed in the $(\pm 1/2, \pm 1/2, 0)$ positions in the case of the D_{4h}^{17} group, whereas the D_{2h}^{19} group leaves room for displacements of these ions in

the NiO_2 plane. Furthermore, the positions of apical oxygens O_{apex}, which are equivalent in D_{4h}^{17}, are separated in D_{2h}^{19} into two different groups of equivalent positions, being in line with Ni^{2+} ions and in line with Ni^{3+} ions, respectively. This separation also takes place in the sublattice of effective ions, and we assume that the Sr population of the two groups of positions is the same.

The transition itself from the high-temperature tetragonal to a charge-ordered phase is treated as follows. From the above discussion, it follows that the CO phase has two nickel sublattices differing only in the charge of ions. Although all Ni-ion positions are equivalent in the HTT phase, they can also be separated into the corresponding sublattices. Then, the transition between the phases consists in the charge transfer from one sublattice to the other. This redistribution of charges is accompanied by the relaxation of the crystal structure. As the parameter characterizing the phase transition, we take the fraction of the hole charge Δ that is on the Ni ion with a higher charge. This parameter equals 0.5 in the HTT phase and lies in the range $0.5 < \Delta \leq 0.1$ in the CO phase.

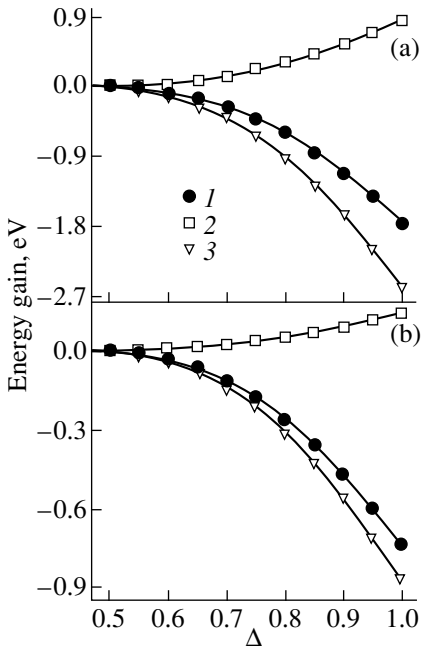

Fig. 2. Changes in the total energy (circles) and in its short-range (squares) and long-range (triangles) components as a function of parameter Δ in the process of (a) HTT ⟶ CO and (b) HTT ⟶ pseudo-HTT phase transitions.

2. MODEL EXPRESSION FOR THE CRYSTAL ENERGY

The total energy of the crystal is considered as a function of all unknown structure parameters (lattice parameters and displacements of the cores and shells of ions). Their optimum values are determined by the numerical minimization of the energy. The calculations are carried out in a pairwise potential approximation and the shell model, which are commonly used in modeling ion dielectrics [20]. In this case, the total energy of the crystal is the sum of only pairwise interactions between its ions. The interaction energy V_{ij} between the ith and jth ions is written as

$$V_{ij} = Z_i Z_j / r + U_{ij}, \quad (1)$$

where Z_i and Z_j are the ion charges. In (1), the first term corresponds to the interaction of the ions treated as point charges. The corresponding lattice sum is calculated by the Ewald method. The second term, U_{ij}, contains short-range quantum-mechanical contributions, and electrostatic corrections to the classical Coulomb interaction of ions that are due to the ions not being point charges.

In this paper, the quantum-mechanical contributions are approximated by the Born–Mayer potential g_{ij}, which is considered as the function of the distance between the shells, rather than between the cores of the ions. We also include a short-range term f_{ij}, which allows for the interpenetration (or screening) of the electron shells of interacting ions. Although Ni^{3+} is a Jahn–Teller-type ion, we do not take into account the many-particle contribution to the energy, assuming it to be small in comparison to the pairwise interactions. The weak exchange interaction of magnetic Ni ions is also ignored.

Thus, the final model expression for the crystal energy is

$$E_{tot} = \sum_{i \neq j} (Z_i Z_j / r + g_{ij}(|\mathbf{r}_{ij} - \mathbf{l}_i + \mathbf{l}_j|) + f_{ij}(r) + U_{ij}^{pol}), \quad (2)$$

where

$$g_{ij}(r) = C_{ij} \exp(-D_{ij} r) - \lambda_{ij}/r, \quad (3)$$

$$f_{ij}(r) = -A_{ij} \exp(-B_{ij} r)/r, \quad (4)$$

$$U_{ij}^{pol} = \frac{X_i X_j}{r} + \frac{Y_i X_j}{|\mathbf{r}_{ij} - \mathbf{l}_i|} + \frac{X_i Y_j}{|\mathbf{r}_{ij} + \mathbf{l}_j|} + \frac{Y_i Y_j}{|\mathbf{r}_{ij} + \mathbf{l}_i + \mathbf{l}_j|} - \frac{Z_i Z_j}{r} + \frac{1}{2} K_i \mathbf{l}_i^2 + \frac{1}{2} K_j \mathbf{l}_j^2. \quad (5)$$

Here, X_i and Y_i are the charges of the core and shell of the ith ion, respectively; $\mathbf{l}_i$ is the shift of the shell of the ith ion relative to its core; K_i is the elastic constant in the shell model; and $r = |\mathbf{r}_{ij}|$ is the distance between the cores of the ith and jth ions. The constants A_{ij}, B_{ij}, C_{ij}, D_{ij}, and λ_{ij} in the above formulas are parameters of the potentials; they are defined in [21, 22]. It should be noted that we ignore the difference in the short-range potentials of Ni^{2+} and Ni^{3+} ions.

Table 1. Change in the total energy (per formula unit) of $La_{1.5}Sr_{0.5}NiO_4$ as compared to the pseudo-HTT-phase energy caused by the introduction of additional degrees of freedom

Degrees of freedom (phases)	$E_{tot} - R_{tot}^{pseudo\ HTT}$, eV
HTT	0.74
Pseudo-HTT	0.0
Pseudo-HTT in the presence of structure relaxation along the normal to NiO_2 layers	−0.354
Pseudo-HTT in the presence of structure relaxation in NiO_2 layers	−0.98
CO	−1.00

Table 2. Change in the Coulomb interaction energy (per formula unit) between different sublattices caused by the HTT ⟶ CO phase transition

Sublattice *A*	Sublattice *B*	$E_{AB}^{Coulomb}$ (HTT) − $E_{AB}^{Coulomb}$ (CO), eV
Ni^{3+}	O_{basal}^{2-}	−8.3
Ni^{2+}	O_{basal}^{2-}	5.5
Ni^{3+}	Ni^{3+}	−4.7
Ni^{2+}	Ni^{2+}	3.86
Ni^{3+}	O_{apex}^{2-}	3.86
Ni^{2+}	O_{apex}^{2-}	−1.52

Note: The charges of Ni ions indicated correspond to the CO phase. In the HTT phase, all Ni ions have a charge of +2.5.

As was indicated above, we replace the disordered sublattice of La and Sr ions by the sublattice of an effective ion *A*. For this ion, the pairwise potentials are taken to be equal to a weighted sum of the corresponding potentials for lanthanum and strontium, with the weighting factors being proportional to the corresponding concentrations (*x* for strontium). For example, the screened interaction potential between the *A* and O^{2-} ions is

$$\begin{aligned} f_{A-O}(r) &= \frac{(2-x)f_{La-O}(r) + x f_{Sr-O}(r)}{2} \\ &= -\frac{1}{2}\{(2-x)A_{La-O}\exp(-B_{La-O}r)/r \\ &\quad + xA_{Sr-O}\exp(-B_{Sr-O}r)/r\}. \end{aligned} \tag{6}$$

In order to analyze the stability of the structure obtained by the minimization of the total energy, we carried out lattice dynamics calculations. In particular, we calculated the squared frequencies of phonon modes, and the absence (or presence) of negative quantities among them was taken as evidence that the crystal was stable (or unstable). Details of this analysis will be presented elsewhere.

3. RESULTS AND DISCUSSION

The calculated total energy for the HTT and CO phases is –166.7 and –168.5 eV per formula unit, respectively. Thus, the charge-ordered phase is energetically favored over the high-temperature tetragonal phase. In addition, dynamics calculations showed that the CO phase is stable.

In order to separate the mechanisms responsible for the charge redistribution between the Ni sublattices and for the relaxation of the crystal structure, we considered a model pseudo-HTT-phase whose structure parameters are equal to the equilibrium structure parameters of the HTT phase, but the charge distribution coincides with that in the CO phase. Clearly, the difference in the total energy of the HTT and pseudo-HTT phases is entirely due to the charge redistribution, whereas the difference in the total energy of the pseudo-HTT and CO phases is associated with the structure relaxation caused by the charge redistribution.

Figure 2 shows the changes in the total energy and in its long-range (Coulomb) and short-range components as a function of the parameter Δ (see Section 1) for the HTT ⟶ CO and HTT ⟶ pseudo-HTT phase transitions. The decrease in the total energy is roughly 1.74 eV in the first transition and 0.74 eV in the second. Therefore, the lowering of the crystal energy due to the structure relaxation is greater than that due to the charge redistribution taken alone. Indeed, the energy is reduced in the first case by 1.00 eV, whereas in the second case it is only reduced by 0.74 eV. The calculations also showed that the relaxation of the NiO_2 layer structure produces a decrease in energy, which is larger than that due to the relaxation of the crystal structure along the normal to these layers. The results are presented in Table 1.

Analysis of the variations of all components of the total energy in the process of transition to the charge-ordered phase revealed that the total energy is reduced predominantly due to the long-range Coulomb interaction (Fig. 2a). In this interaction, in turn, the dominant contribution is not from the interaction between Ni^{3+} ions in which the holes tend to repel each other to the optimum distances, but from the interaction between the Ni^{3+} and O_{basal}^{2-} sublattices, which leads to the formation of polarons (see Table 2).

4. CONCLUSIONS

Thus, using pairwise potentials, we performed computer simulation of the charge-ordered phase of $La_{1.5}Sr_{0.5}NiO_4$, in which there occurs a purely two-dimensional arrangement of Ni^{2+} and Ni^{3+} ions in stag-

gered rows in perovskite layers. This structure was found to be stable and energetically favored over the high-temperature tetragonal phase. On the HTT $\longrightarrow$ CO phase transition, the structure relaxation caused by the hole redistribution over the Ni sublattice produces a larger gain in energy than the redistribution itself does. The crystal energy is reduced more significantly due to the relaxation of the structure in the NiO_2 planes than in the direction perpendicular to these planes. Finally, the calculations showed that the interaction determining the decrease in the total energy of the crystal is the Ni^{3+}–O^{2-}_{basal} Coulomb interaction, which is responsible for the formation of polarons.

REFERENCES

1. T. Ido, K. Magoshi, H. Eisaki, and S. Uchida, Phys. Rev. B **44**, 12094 (1991).
2. S. Uchida, T. Ido, H. Takagi, *et al.*, Phys. Rev. B **43** (10-A), 7942 (1991).
3. R. J. Cava, B. Batlogg, T. T. Krajewski, *et al.*, Phys. Rev. B **43**, 1229 (1991).
4. N. Ogita, S. Takanashi, M. Udagawa, and K. Ohbayashi, J. Phys. Soc. Jpn. **61**, 3009 (1992).
5. X. X. Bi and P. C. Eklund, Phys. Rev. Lett. **70**, 2625 (1992).
6. J. Gopalakrishnan, G. Colsman, and B. Reuter, J. Solid State Chem. **22** (1), 145 (1977).
7. C. H. Chen, S.-W. Cheong, and A. S. Cooper, Phys. Rev. Lett. **71**, 2461 (1993).
8. Y. Takeda, R. Kanno, M. Sakano, *et al.*, Mater. Res. Bull. **25** (1), 293 (1990).
9. R. J. McQueeney, J. L. Sarrao, and R. Osborn, Phys. Rev. B **60**, 80 (1999).
10. J. M. Tranquada, B. Y. Hwang, C. H. Chen, *et al.*, Phys. Rev. B **49**, 7088 (1994).
11. Y. Moritomo, Y. Tomioka, A. Asamitsu, and Y. Tokura, Phys. Rev. B **51**, 3297 (1995).
12. J. Q. Li, Y. Matsumi, T. Kimura, and Y. Tokura, Phys. Rev. B **57**, 3205 (1998).
13. Y.-S. Yi, Z.-G. Yu, A. R. Bishop, and J. T. Gammel, Phys. Rev. B **58**, 503 (1997).
14. J. Zaanen and O. Gunnarsson, Phys. Rev. B **40**, 7391 (1989).
15. V. J. Emery, S. A. Kivelson, and H. Q. Lin, Phys. Rev. Lett. **64**, 475 (1990).
16. K. Yonemitsu, A. R. Bishop, and J. Lorenzana, Phys. Rev. B **47**, 12 059 (1993).
17. J. Zaanen and P. B. Littlewood, Phys. Rev. B **50**, 7222 (1994).
18. V. I. Anisimov, M. A. Korotin, J. Zaanen, and O. K. Andersen, Phys. Rev. Lett. **68**, 345 (1992).
19. Y. Moritomo, A. Nakamura, S. Mori, *et al.*, Phys. Rev. B **56**, 14879 (1997).
20. *Computer Simulation of Solids*, Ed. by C. R. A. Catlow and W. C. Mackrodt (Springer, Berlin, 1982).
21. A. E. Nikiforov and S. Yu. Shashkin, Fiz. Tverd. Tela (St. Petersburg) **39**, 1094 (1997) [Phys. Solid State **39**, 981 (1997)].
22. A. Yu. Zakharov, A. E. Nikiforov, and S. Yu. Shashkin, Fiz. Tverd. Tela (St. Petersburg) **41**, 1096 (1999) [Phys. Solid State **41**, 999 (1999)].

Translated by Yu. Epifanov

Physics of the Solid State, Vol. 42, No. 8, 2000, pp. 1488–1491. Translated from Fizika Tverdogo Tela, Vol. 42, No. 8, 2000, pp. 1446–1448.

MAGNETISM AND FERROELECTRICITY

Temperature Dependence of Spontaneous Magnetization of Spinel Ferrites with a Frustrated Magnetic Structure

L. G. Antoshina, A. N. Goryaga, and V. V. San'kov

Moscow State University, Vorob'evy gory, Moscow, 119899 Russia

Received in final form, January 25, 2000

Abstract—The spontaneous magnetization of the $Ni_{0.4}Fe_{0.6}[Ni_{0.6}Cr_{1.4}]O_4$, $Cu_{0.4}Fe_{0.6}[Ni_{0.6}Cr_{1.4}]O_4$, and $Zn_{0.4}Fe_{0.6}[Ni_{0.6}Cr_{1.4}]O_4$ samples has been investigated. Based on the results obtained, it is concluded that the anomalous temperature dependences of spontaneous magnetization stem from the presence of a frustrated magnetic structure in at least one of the sublattices. © *2000 MAIK "Nauka/Interperiodica".*

Investigations into the magnetic properties of the materials with a frustrated magnetic structure have been topical in recent years. The frustrated magnetic structure in ferrites with a spinel-type structure is usually formed because of the dilution of both sublattices by nonmagnetic ions [1]. For spinel ferrites with a frustrated magnetic structure, the long-range magnetic order does not extend over the bulk of samples. In this case, there are separate regions of spontaneous magnetization whose formation is caused by both long-range and short-range magnetic orders.

However, recent Mössbauer investigations revealed that the frustrated magnetic structure also occurs in undiluted spinel ferrites at a high Cr^{3+} content [2, 3].

The purpose of this work was to elucidate how the frustrated magnetic structure in the ferrite–chromite affected the temperature dependence of spontaneous magnetization $\sigma_s(T)$.

Néel was the first to demonstrate that the crystal lattice of magnetic compounds with a spinel-type structure consists of two sublattices (octahedral and tetrahedral), in which the magnetic moments $\mathbf{M}_{oct}$ and $\mathbf{M}_{tetr}$ are oppositely directed, so that the total magnetic moment is $\mathbf{M}_s = \mathbf{M}_{oct} - \mathbf{M}_{tetr}$ [4]. Based on his theory of ferrimagnetism, Néel calculated that, unlike normal ferromagnets, spinel ferrites can have the *N*-, *P*-, and *L*-type anomalous temperature dependences of the spontaneous magnetization $\sigma_s(T)$.

More recently, some researchers found ferrites with the *N*-type anomalous curves, i.e., with the compensation point. These are lithium chromites $Li_{0.5}Fe_{2.5-x}Cr_xO_4$ with x = 1.0–1.6 [5] and nickel chromites $NiFe_{2-x}Cr_xO_4$ with x = 0.75–1.5 [6]. According to these authors, the major factor responsible for the anomalous dependences $\sigma_s(T)$ is the direct negative exchange interaction between octahedral ions Cr^{3+}–Cr^{3+}, which leads to an abrupt decrease in the spontaneous magnetization of the octahedral sublattice $\sigma_{soct}(T)$ with an increase in the temperature.

In our opinion, the appearance of the *N*-type anomalous dependence $\sigma_s(T)$ for the ferrite–chromites $Li_{0.5}Fe_{2.5-x}Cr_xO_4$ and $NiFe_{2-x}Cr_xO_4$ can be due to one more factor. For example, the $\sigma_s(T)$ curves for the ferrite–chromites $CoFeCrO_4$ [7] and $CuFeCrO_4$ [8] are not the anomalous curves with the compensation points, whereas the *N*-type $\sigma_s(T)$ curve is characteristic of the nickel ferrite–chromite $NiFeCrO_4$ [6] with the same Cr^{3+} content.

The objects to be studied were the nickel ferrite–chromite $Ni_{0.4}Fe_{0.6}[Ni_{0.6}Cr_{1.4}]O_4$ with the compensation point [6] and two ferrites, in which the Cu^{2+} and Zn^{2+} ions are substituted for the Ni^{2+} tetrahedral ions, namely, $Cu_{0.4}Fe_{0.6}[Ni_{0.6}Cr_{1.4}]O_4$ and $Zn_{0.4}Fe_{0.6}[Ni_{0.6}Cr_{1.4}]O_4$.

The samples were prepared by the ceramic technique with annealing in air and subsequent slow cooling. The first annealing of the $Ni_{0.4}Fe_{0.6}[Ni_{0.6}Cr_{1.4}]O_4$ and $Zn_{0.4}Fe_{0.6}[Ni_{0.6}Cr_{1.4}]O_4$ samples was carried out at 1000°C for 4 h, and the second annealing was performed at 1350°C also for 4 h. Both annealings of the $Cu_{0.4}Fe_{0.6}[Ni_{0.6}Cr_{1.4}]O_4$ sample were carried out at 1000°C for 20 h. The X-ray diffraction analysis revealed that the samples were single-phase and had a cubic spinel structure at room temperature. The magnetization was measured by the ballistic technique in the fields up to 10 kOe in the temperature range 80–600 K. The remanent magnetization σ_r and the coercive force H_c were determined from the hysteresis loop measurements.

The temperature dependences of spontaneous magnetization $\sigma_s(T)$ and coercive force $H_c(T)$ for the nickel ferrite–chromite $Ni_{0.4}Fe_{0.6}[Ni_{0.6}Cr_{1.4}]O_4$ are shown in Fig. 1. It is seen that the compensation temperature T_K is equal to ≈340 K, and the Curie temperature T_C is ≈450 K. This is in good agreement with the data reported in [6]. The Cr^{3+} content is identical for all three

1063-7834/00/4208-1488$20.00

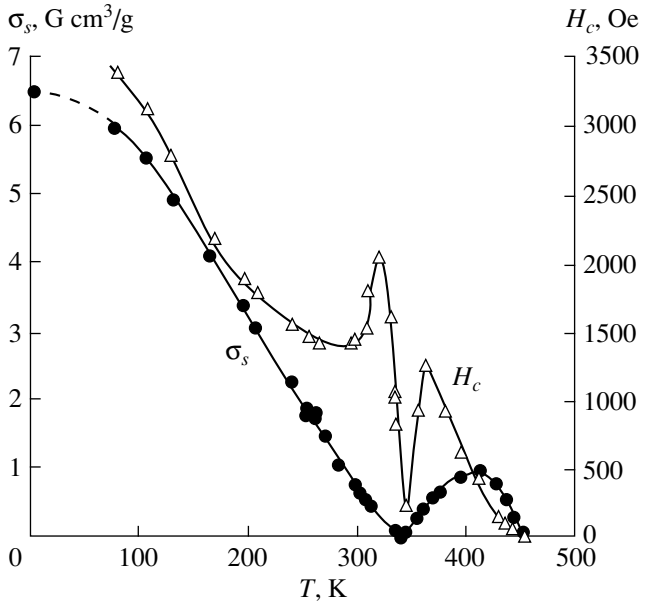

Fig. 1. Temperature dependences of spontaneous magnetization $\sigma_s(T)$ and coercive force $H_c(T)$ for the ferrite–chromite $Ni_{0.4}Fe_{0.6}[Ni_{0.6}Cr_{1.4}]O_4$.

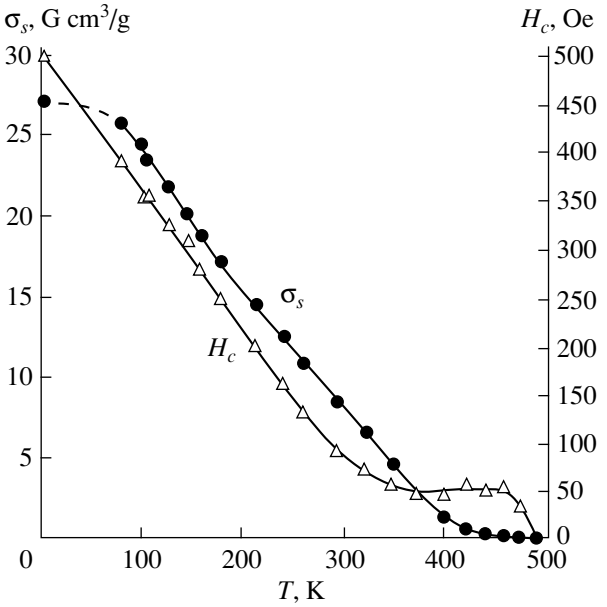

Fig. 2. Temperature dependences of spontaneous magnetization $\sigma_s(T)$ and coercive force $H_c(T)$ for the ferrite–chromite $Cu_{0.4}Fe_{0.6}[Ni_{0.6}Cr_{1.4}]O_4$.

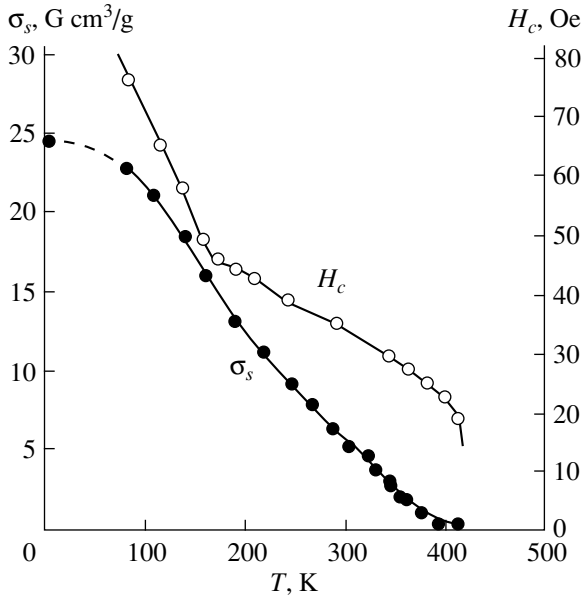

Fig. 3. Temperature dependences of spontaneous magnetization $\sigma_s(T)$ and coercive force $H_c(T)$ for the ferrite–chromite $Zn_{0.4}Fe_{0.6}[Ni_{0.6}Cr_{1.4}]O_4$.

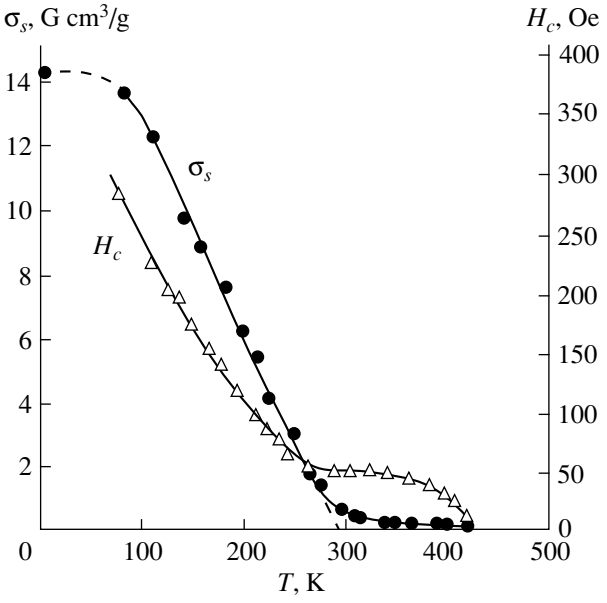

Fig. 4. Temperature dependences of spontaneous magnetization $\sigma_s(T)$ and coercive force $H_c(T)$ for the ferrite–chromite $CuFe_{0.6}Cr_{1.4}O_4$ taken from [9].

ferrites under study. For this reason, it could be expected that the $\sigma_s(T)$ curves for the samples containing the Cu^{2+} and Zn^{2+} ions should also have the compensation point.

However, the magnetization measurements demonstrated that the $Cu_{0.4}Fe_{0.6}[Ni_{0.6}Cr_{1.4}]O_4$ and $Zn_{0.4}Fe_{0.6}[Ni_{0.6}Cr_{1.4}]O_4$ samples have no compensation temperature. The dependences $\sigma_s(T)$ and $H_c(T)$ for the

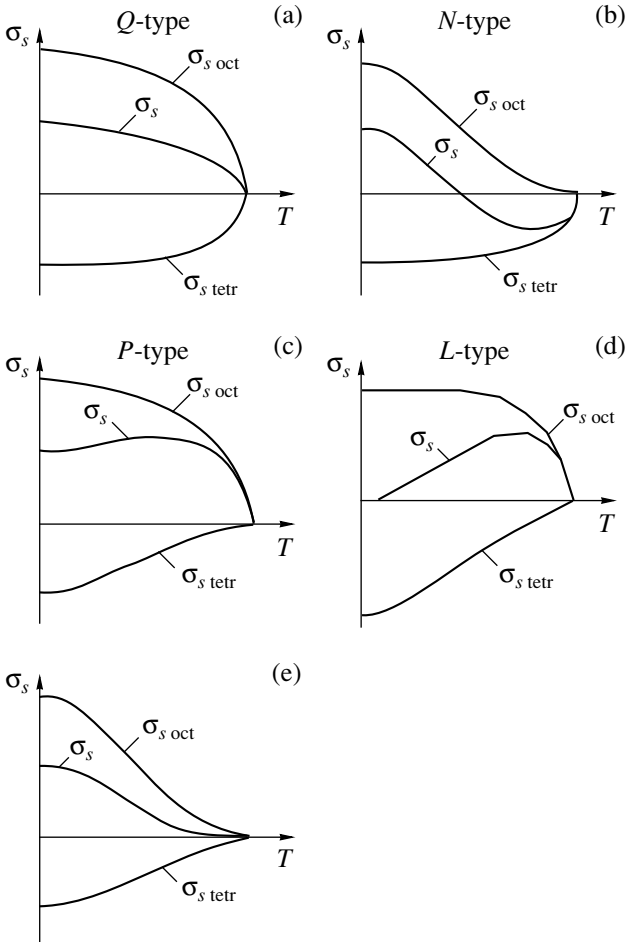

Fig. 5. Schematic curves of spontaneous magnetization $\sigma_s(T)$ for spinel ferrites.

$Cu_{0.4}Fe_{0.6}[Ni_{0.6}Cr_{1.4}]O_4$ and $Zn_{0.4}Fe_{0.6}[Ni_{0.6}Cr_{1.4}]O_4$ samples are presented in Figs. 2 and 3, respectively. It is seen that the shape of the $\sigma_s(T)$ curves for these ferrite–chromites differs sharply from the usual curves $\sigma_s(T)$ for the *Q*-type ferrimagnets. For both samples, the $\sigma_s(T)$ dependences can be described by a linear function in a rather wide temperature range (more than 200 K). It was found that an abrupt decrease in the σ_s magnitude for these ferrite–chromite materials occurs at a lower temperature as compared to H_c: when the spontaneous magnetization becomes small, the coercive force remains rather large and becomes zero only at $T = T_C$. When measuring the remanent magnetization σ_r, we found that its sign does not change for both samples; i.e., these samples have no compensation temperatures. Similar dependences $\sigma_s(T)$ and $H_c(T)$ were observed earlier for the copper ferrite–chromite $CuFe_{2-x}Cr_xO_4$ at a high Cr^{3+} content [8, 9]. For samples in this system, it was shown that the anomalous behavior of $\sigma_s(T)$ and $H_c(T)$ for copper ferrite–chromite materials is associated with the formation of the frustrated magnetic structure.

From comparison of the $\sigma_s(T)$ and $H_c(T)$ dependences for ferrites $Cu_{0.4}Fe_{0.6}[Ni_{0.6}Cr_{1.4}]O_4$ and $Zn_{0.4}Fe_{0.6}[Ni_{0.6}Cr_{1.4}]O_4$ (Figs. 2, 3) and the previously studied sample of $CuFe_{0.6}Cr_{1.4}O_4$ (Fig. 4) [9], we can assume that the ferrite–chromite samples under investigation also possess the frustrated magnetic structure over the entire temperature range. Apparently, the formation of the frustrated magnetic structure in the tetrahedral sublattice of these ferrites–chromites is explained by the fact that either the Zn^{2+} diamagnetic ion or the Cu^{2+} ion with a small magnetic moment was introduced into the sublattice, which supposedly violated the balance of exchange interactions.

As regards the ferrite–chromite $Ni_{0.4}Fe_{0.6}[Ni_{0.6}Cr_{1.4}]O_4$, we assume that the frustrated magnetic structure occurs solely in its octahedral sublattice, which is responsible for the magnetic moment of the ferrite below the compensation temperature T_K, and that no frustrated magnetic structure is observed in the tetrahedral sublattice, which is responsible for the magnetic moment above T_K.

Based on the results obtained, we believe that the formation of the frustrated magnetic structure in one of the sublattices of spinel ferrites should substantially affect the shape of the $\sigma_s(T)$ curve.

The schematic curves depicted in Fig. 5 demonstrate the formation of the resulting curve $\sigma_s(T)$ of the net spontaneous magnetization, depending on the types of spontaneous magnetization of the octahedral $\sigma_{soct}(T)$ and tetrahedral $\sigma_{stetr}(T)$ sublattices, respectively. For example, if the frustrated magnetic structure is absent in both sublattices and both curves $\sigma_{soct}(T)$ and $\sigma_{stetr}(T)$ are the *Q*-type curves, the resulting dependence $\sigma_s(T)$ should also be the *Q*-type curve (Fig. 5a). If the frustrated magnetic structure is present in the octahedral sublattice, and is responsible for the magnetic moment of the ferrite, and no frustrated magnetic structure occurs in the tetrahedral sublattice, then the resulting curve $\sigma_s(T)$ is the anomalous *N*-type curve (Fig. 5b). The *P*-type curve is observed when the frustrated magnetic structure is present in the tetrahedral sublattice and no frustrated magnetic structure occurs in the octahedral sublattice (Fig. 5c). In the specific case when the spontaneous magnetizations for both sublattices are identical at 0 K; i.e., $\sigma_{s0\,oct}(T) = \sigma_{s0\,tetr}(T)$, the anomalous *L*-type curve is observed (Fig. 5d). Thus, we can conclude that the condition for the appearance of the *N*-, *P*-, and *L*-type anomalous dependences $\sigma_s(T)$ is the presence of the frustrated magnetic structure in at least one of the sublattices.

The anomalous dependence of the novel type shown in Fig. 5e is observed when the frustrated magnetic structure is present in both sublattices.

REFERENCES

1. C. P. Poole and H. A. Farach, Z. Phys. B **47**, 55 (1982).
2. K. Muraleedharan, J. K. Srivastava, V. R. Marathe, and R. Vijayaragharan, J. Magn. Magn. Mater. **49**, 333 (1985).
3. H. Mohan, I. A. Shaikh, and R. G. Kulkarni, Physica B (Amsterdam) **217**, 292 (1996).
4. L. Néel, Ann. Phys. (Paris) **3**, 137 (1948).
5. E. W. Gorter, Philips Res. Rep. **9**, 403 (1954).
6. T. R. McGuire and S. W. Greenwald, Solid State Phys. Electron. Telecommun. **3** (1), 50 (1960).
7. K. P. Belov, A. N. Goryaga, R. R. Annaev, *et al.*, Fiz. Tverd. Tela (Leningrad) **31** (5), 117 (1989) [Sov. Phys. Solid State **31**, 785 (1989)].
8. L. G. Antoshina, A. N. Goryaga, E. N. Kukudzhanova, and I. A. Fil'gus, Zh. Éksp. Teor. Fiz. **111**, 1732 (1997) [JETP **84**, 948 (1997)].
9. L. G. Antoshina, A. N. Goryaga, and E. N. Evstafieva, J. Magn. Magn. Mater. **185** (1), 101 (1998).

Translated by N. Korovin

Physics of the Solid State, Vol. 42, No. 8, 2000, pp. 1492–1493. Translated from Fizika Tverdogo Tela, Vol. 42, No. 8, 2000, pp. 1449–1450.

MAGNETISM AND FERROELECTRICITY

Magnetic Properties of $TlCoS_2$ and $TlCoSe_2$ Layered Compounds

R. Z. Sadykhov, É. M. Kerimova, Yu. G. Asadov, and R. K. Veliev

Institute of Physics, Academy of Sciences of Azerbaijan, pr. Dzhavida 33, Baku, 370143 Azerbaijan

Received February 7, 2000

Abstract—The $TlCoS_2$ and $TlCoSe_2$ compounds are synthesized and their magnetic properties are studied in the temperature range 77–300 K. It is established on the basis of x-ray diffraction analysis that these compounds possess a hexagonal structure. Examination of the magnetization and paramagnetic susceptibility has shown that $TlCoS_2$ and $TlCoSe_2$ are ferrimagnets. The Curie temperature for $TlCoS_2$ is equal to 112 K, and T_C for $TlCoSe_2$ is less than 77 K. The effective magnetic moments are equal to 4.6 μ_B ($TlCoS_2$) and 4.85 μ_B ($TlCoSe_2$) and agree well with the theoretical values. © *2000 MAIK "Nauka/Interperiodica".*

Some physical properties of a series of low-dimensional compounds with the general formula $TlMeX_2$ (Me = Cr, Fe; X = S, Se, Te) were first observed and studied in [1–6]. It is of interest to study the magnetic properties of $TlCoS_2$ and $TlCoSe_2$, which belong to this group of compounds.

The $TlCoS_2$ and $TlCoSe_2$ compounds were synthesized in evacuated (up to 10^{-3} Pa) silica tubes upon interaction of the initial components of high purity. To prevent the explosion of the tube, the temperature of the furnace was increased up to the melting temperature of S (391 K) or Se (493 K), which was then held constant for 3 h. After that, the temperature was gradually increased up to 1200 K, at which the tubes were allowed to stand for 6 h with the subsequent cooling at a rate of 100 K/h down to 600 K. The annealing was carried out at this temperature for 480 h.

The x-ray powder diffraction analysis was performed on a DRON-3M diffractometer (CuK_α radiation). The angular resolution was ~0.1°. The x-ray powder diffraction patterns were recorded continuously, and the diffraction angles were determined from the measurements of the intensity peak. The error of the angle determination did not exceed ±0.02°.

The synthesized $TlCoS_2$ and $TlCoSe_2$ samples readily underwent lamination. Only the reflections with the (0.0.2*l*) indices were obtained from the natural surface of the $5 \times 5 \times 1$-mm layers in the angle range $10° \le 2\theta \le 80°$. The lattice parameter *c* was calculated using these reflections. Parameter *a* was calculated from the x-ray powder diffraction patterns, which contained the (*h* 0 0) and (*h k* 0) reflections. The results of the calculations are given in the table.

The $TlCoS_2$ and $TlCoSe_2$ compounds are isostructural to $TlCrS_2$ and $TlCrSe_2$ crystals [3]. There are groups in the structure of $TlCoS_2$ and $TlCoSe_2$ which consist of four equidistant layers formed by the Tl, Co, S(1) [or Se(1)], and S(2) [or Se(2)] atoms in the same packing position. The hexagonal cell contains three similar interpenetrating groups.

In the structure, the Co atoms center the S (Se) trigonal prisms, and the Tl atoms are tetrahedrally surrounded by the S (Se) atoms. Each S(1) or Se(1) atom is tetrahedrally surrounded by three Co atoms and one Tl atom, and the S(2) or Se(2) atoms center the trigonal prisms formed by three Co atoms and three Tl atoms.

All the above suggests that $TlCoS_2$ and $TlCoSe_2$ compounds are layered magnets. A sufficiently large ratio *c*/*a* (~6) for both compounds counts in favor of this statement.

The magnetization (σ) and paramagnetic susceptibility (χ) of the compounds under consideration were studied in the temperature range 77–300 K. The magnetization was measured on a Domenicalli pendulum magnetometer, and the paramagnetic susceptibility, on a magnetoelectrical balance by the Faraday method. The spontaneous magnetization (σ_s) at a constant temperature was determined by extrapolating the magnetization measured in different magnetic fields to the zero field. The dependence of the specific magnetization on the magnetic field for $TlCoS_2$ and $TlCoSe_2$ is given in Fig. 1. As is seen, the dependence $\sigma(H)$ for $TlCoS_2$ is characteristic of the materials, which possess a spontaneous magnetization. The enhancement of the paraprocess in the $\sigma(H)$ dependence at 90 and 100 K indicates the approach of the magnetic transformation temperature. This is clearly seen from Fig. 2, which shows the temperature dependence of the magnetization for $TlCoS_2$. The Curie temperature of this compound was determined by the method of thermodynamic coeffi-

Crystal lattice parameters

Compound	*a*, Å	*c*, Å	*z*	ρ, g/cm^3	*c*/*a*
$TlCoS_2$	3.726	22.510	3	6.026	6.04
$TlCoSe_2$	3.747	22.772	3	7.577	6.08

1063-7834/00/4208-1492$20.00

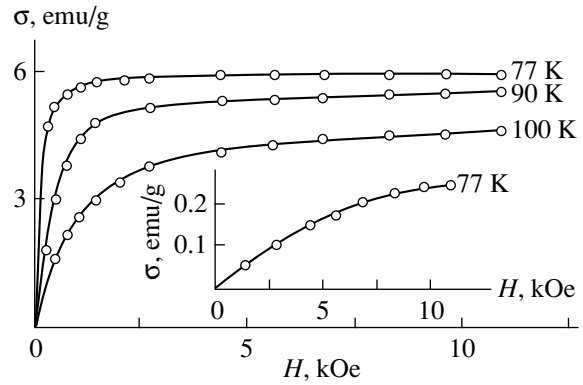

Fig. 1. Dependences of the specific magnetization of $TlCoS_2$ on the magnetic field. The inset shows the dependence of the specific magnetization of $TlCoSe_2$ on the magnetic field.

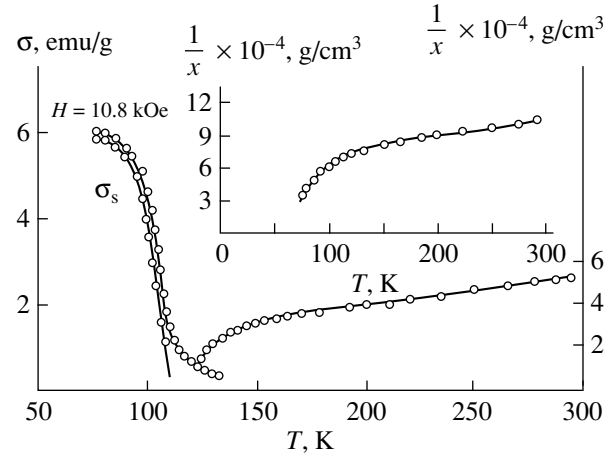

Fig. 2. Temperature dependences of the magnetization and the reverse paramagnetic susceptibility for $TlCoS_2$. The inset shows the temperature dependence of the reverse paramagnetic susceptibility for $TlCoSe_2$.

cients [7] and turned out to be equal to 112 K. The saturation magnetic moment of $TlCoS_2$ at 77 K is equal to 0.36 μ_B.

The temperature dependence of the reverse paramagnetic susceptibility of both compounds has a hyperbolic form (Fig. 2), which is an indication of ferrimagnetism. As is seen from the curve $1/\chi(T)$ (inset in Fig. 2), the magnetic transformation temperature of $TlCoSe_2$ is less than 77 K; therefore, the $\sigma(H)$ dependence for this compound at 77 K (inset in Fig. 1) has a form characteristic of the paramagnetic state.

The experimental effective magnetic moments for the compounds under study were calculated from the dependence $1/\chi(T)$; their values turned out to be equal to 4.6 ($TlCoS_2$) and 4.85 μ_B ($TlCoSe_2$). The theoretical value of the effective magnetic moment (4.9 μ_B) was calculated with due regard for the pure spin of the trivalent Co ion. As is seen, the experimental and theoretical results are in good agreement.

The experimental results obtained can be interpreted on the basis of the crystalline structure of the studied compounds. This structure can be represented in the form of alternating two-dimensional layers of the Co^{3+}, Tl^+, and S^{2-} (or Se^{2-}) ions, which are perpendicular to the hexagonal axis *c*. In this case, the layers of Tl^+ and S^{2-} (or Se^{2-}) are located between the nearest layers of the Co^{3+} ions. In the plane, which contains the Co^{3+} ions, ferromagnetic ordering takes place; therefore, the layers of Co^{3+} ions represent two-dimensional ferromagnets. These layers are linked by weaker exchange forces of the antiferromagnetic type. The ferrimagnetic ordering in $TlCoS_2$ and $TlCoSe_2$ is likely the result of the coexistence of two interactions—ferromagnetic (inside the layers) and antiferromagnetic (between the layers). This ordering can result, for example, from an incomplete compensation of spin magnetic moments of the ferromagnetic layers.

Thus, the studies of the magnetic properties showed that $TlCoS_2$ and $TlCoSe_2$ compounds are low-dimensional magnets with a ferrimagnetic ordering.

REFERENCES

1. Kosenberg, J. Phys. Chem. Solids **43** (2), 87 (1982).
2. G. I. Makovetskiĭ and E. I. Kasinskiĭ, Neorg. Mater. **20**, 1752 (1984).
3. M. A. Aljanov, E. M. Kerimova, and M. D. Nadjafzade, in *Abstract of the 14 IUPAC Conference on Chemical Thermodynamics, ICCT-96, Osaka, Japan, 1996*, p. 25.
4. M. Aljanov, M. Nadjafzade, Z. Seidov, and M. Gasumov, Turk. J. Phys. **20**, 1071 (1996).
5. A. I. Dzhabbarly, É. M. Kerimova, F. M. Seidov, and A. K. Zamanova, Neorg. Mater. **32** (1), 118 (1996).
6. É. M. Kerimova, F. M. Seidov, S. N. Mustafaeva, and S. S. Abdinbekov, Neorg. Mater. **35** (2), 157 (1999).
7. K. P. Belov and A. N. Goryaga, Fiz. Met. Metalloved. **2** (3), 441 (1956).

Translated by T. Galkina

Physics of the Solid State, Vol. 42, No. 8, 2000, pp. 1494–1498. Translated from Fizika Tverdogo Tela, Vol. 42, No. 8, 2000, pp. 1451–1455.

MAGNETISM AND FERROELECTRICITY

Relation between Giant Volume Magnetostriction and Colossal Magnetoresistance near the Curie Temperature of $Sm_{0.55}Sr_{0.45}MnO_3$

A. I. Abramovich, L. I. Koroleva, A. V. Michurin, O. Yu. Gorbenko, and A. R. Kaul'

Moscow State University, Vorob'evy gory, Moscow, 119899 Russia

e-mail: abram@ofef343.phys.msu.su

Received November 10, 1999; in final form, February 10, 2000

Abstract—The magnetic, transport, and elastic properties of $Sm_{0.55}Sr_{0.45}MnO_3$ have been established to be interrelated. At the Curie point, one observes a large volume compression $\Delta V/V \approx 0.1\%$, a sharp minimum in the temperature dependence of negative volume magnetostriction $\omega(T)$, and a maximum in the temperature dependence of the electrical resistivity. Giant negative volume magnetostriction $\omega = -5 \times 10^{-4}$ has been found in a magnetic field $H = 0.9$ T, which is accompanied by a colossal negative magnetoresistance of 44% in the same field. The results obtained are discussed in terms of a model of electronic phase separation. © *2000 MAIK "Nauka/Interperiodica".*

The discovery of high-temperature superconductors stimulated interest in the investigation of materials with a similar crystallographic structure, in particular, of the manganites with the perovskite structure. These materials exhibit anomalies in magnetic, electrical, optical, and other properties. The most impressive effect of all is certainly the colossal magnetoresistance (CMR) observed in them near the Curie temperature T_C (see reviews [1–3] and references therein). To have application potential, the T_C of these materials must be higher than room temperature and the CMR must be obtained in weak magnetic fields. However, CMR > 90% is usually achieved in manganites in fields of 6–12 T. A record-high CMR of 96% in a relatively weak magnetic field of 0.67 T was obtained in $La_{1/3}Nd_{1/3}Ca_{1/3}MnO_3$ at $T = 90$ K [4]. Room-temperature CMR was found to exist in $La_{0.77}Sr_{0.23}MnO_3$ thin films [5]. An intense discussion of a strong coupling of the electronic and magnetic subsystems of the manganites with the lattice is presently also under way. To reveal this relation, we prepared a $Sm_{0.55}Sr_{0.45}MnO_3$ polycrystal and studied its magnetization σ, the initial ac magnetic and paramagnetic susceptibility χ, resistivity ρ, magnetoresistance $\Delta\rho/\rho$, and thermal expansion $\Delta l/l$, as well as the longitudinal, $\lambda_{\parallel}$, and transverse, $\lambda_{\perp}$, magnetostriction. Note that $Sm_{1-x}Sr_xMnO_3$ is a poorly studied system. There are only a few publications devoted to its investigation [6–12].

Despite a wealth of experimental data on the manganites, no common viewpoint on the nature of their unusual properties has evolved thus far. Their interpretation is based on the following models: a transition from polaron to hopping conduction near T_C, magnetic-field-induced melting of the charge-ordered state, electronic phase separation initiated by strong *s–d* exchange, etc. We treat the results obtained in this work in terms of the latter model.

1. SAMPLE PREPARATION

The $Sm_{0.55}Sr_{0.45}MnO_3$ ceramics were prepared in the following way. Ash-free filters were impregnated with an aqueous solution of metal nitrates with a total concentration of about 1 mol/l. The residue left after the burning of these filters was calcined at 973 K, pressed into pellets, and sintered at 1473 K for 12 h. The phase composition of the ceramics and the lattice parameters were characterized by x-ray diffraction with a Siemens D5000 diffractometer. The ceramics obtained were found to be a single-phase perovskite with orthorhombic structure (*Pnma* group) and the following lattice parameters: $a = 5.424(1)$ Å, $b = 7.678(2)$ Å, and $c = 5.434(2)$ Å (Fig. 1). The orthorhombicity parameter derived from these figures is 0.2%, which suggests closeness to the cubic structure. The ratio $a < b/\sqrt{2} < c$ is characteristic of orthorhombic manganites with a tolerance factor of ~0.92. The single-phase state of the ceramics was also confirmed by Raman spectrum measurements made with a Jobin–Yvon T64000 triple-grating monochromator, which revealed only the presence of the phonon modes typical of orthorhombic manganites with *Pnma* symmetry.

2. EXPERIMENTAL RESULTS

Magnetization measurements performed at 4.2 K showed that saturation is not reached in magnetic fields of up to 4 T and that the spontaneous magnetic moment

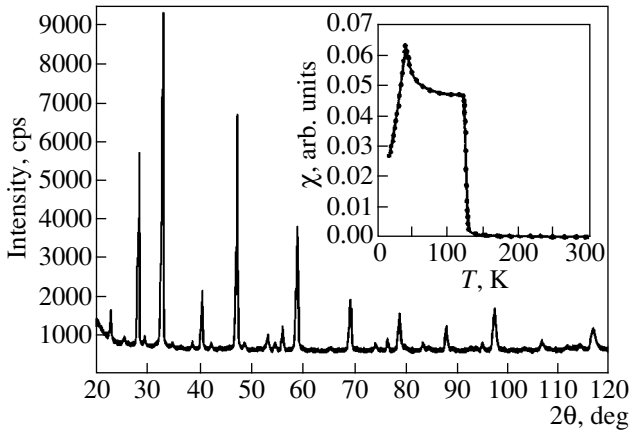

Fig. 1. X-ray diffraction pattern of $Sm_{0.55}Sr_{0.45}MnO_3$ powder (CuK_α radiation with silicon as internal standard). Inset: temperature dependence of initial ac (8-kHz) magnetic susceptibility in a field of 10^{-4} T.

is 3.18 μ_B/mol, which is 89% of the moment expected for the case of complete ferromagnetic (FM) ordering. It was found that the transition from the ferromagnetic to paramagnetic state is very diffuse and that the Curie temperature T_C derived by extrapolation of the steepest part of the $\sigma(T)$ curve to the temperature axis depends on the magnetic field. For instance, it varies from 135 to 150 K with the magnetic field varied from 0.1 to 0.8 T. Hence, the T_C in this compound should be determined only by the methods that do not require application of an external magnetic field, or in a very weak magnetic field. We succeeded in obtaining a more accurate value of T_C from measurements of the initial magnetic susceptibility in an ac magnetic field $H = 10^{-4}$ T. As seen from the inset to Fig. 1, the temperature dependence $\chi(T)$ has a sharp maximum at $T_N = 36$ K and an abrupt falloff at $T_C = 126$ K. Within the 300–500-K temperature region, the paramagnetic susceptibility obeys the Curie–Weiss law with a paramagnetic Curie point $\theta = 250$ K and an effective magnetic moment $\mu = 5.6\ \mu_B$/mol. For $T \le 300$ K, deviations from the Curie–Weiss relation are observed, which implies that, in this temperature region, the magnetic state is not uniform.

Near T_C, the temperature dependence of the electrical resistivity exhibits a maximum which is suppressed by the application of a magnetic field, its location shifting toward higher temperatures (Fig. 2). In other words, we have found a CMR of 44% in a relatively weak magnetic field of 0.9 T (Fig. 2), and of 20% in a field of 0.4 T at $T = 100$ K, which is important from the standpoint of applications.

Figure 3 presents temperature dependence of thermal expansion $\Delta l/l(T)$ measured in a heating and a cooling run and under heating a sample following its cooling in a magnetic field of 0.9 T. Near T_C, one sees a sharp decrease of $\Delta l/l$, which corresponds to a volume compression of 0.1% ($\Delta V/V = 3\Delta l/l$). Application of a magnetic field reduces the jump in the $\Delta l/l(T)$ relation and shifts it toward higher temperatures (the inset to Fig. 3). Cooling in a magnetic field also brings about a decrease in $\Delta l/l$ by an amount directly proportional to the applied field and independent of its direction within a broader temperature region (122–300 K). There is a considerable temperature hysteresis in $\Delta l/l$ below T_C. The temperature dependence of volume magnetostriction $\omega = \lambda_{\parallel} + 2\lambda_{\perp}$ and of the anisotropic part of magnetostriction $\lambda_t = \lambda_{\parallel} - \lambda_{\perp}$ in a magnetic field of 0.9 T is displayed in Fig. 4. One readily sees that the $\omega(T)$ dependence passes through a sharp minimum at T_C, where $|\omega|$ reaches a very large value of 5×10^{-4} in a field $H = 0.9$ T. Magnetostriction of about the same magnitude

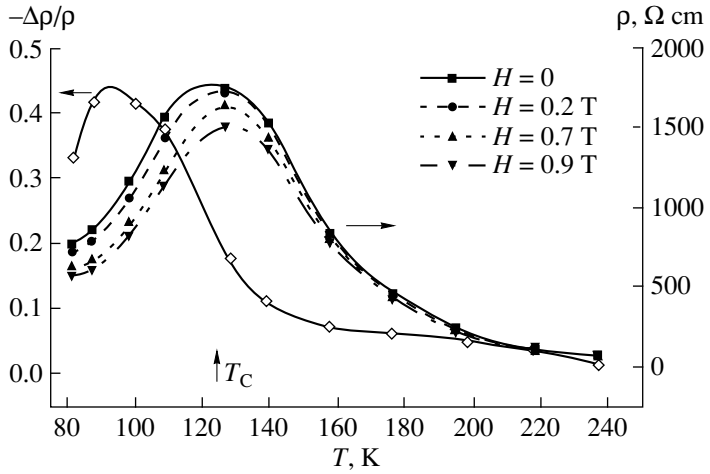

Fig. 2. Temperature dependences of the electrical resistivity in various magnetic fields and of magnetoresistance in a field of 0.9 T.

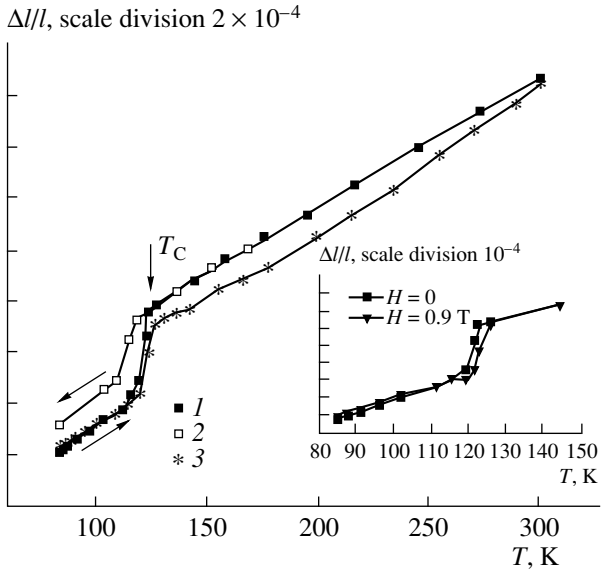

Fig. 3. Temperature dependences of thermal expansion obtained in various conditions: (*1*) heating, (*2*) cooling, and (*3*) heating after field cooling in $H = 0.9$ T. Inset: effect of a magnetic field on thermal expansion.

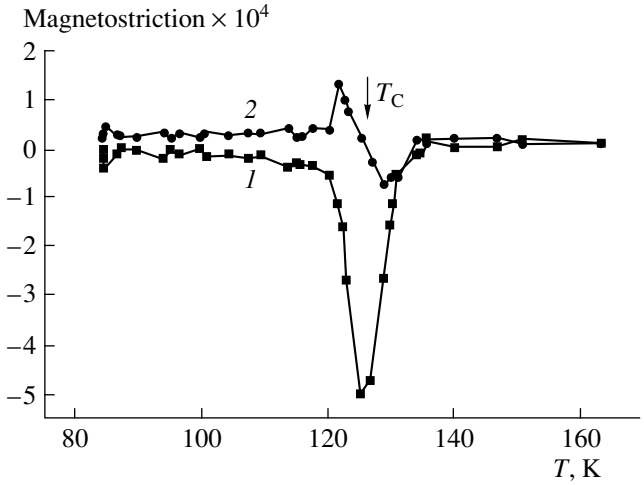

Fig. 4. Temperature dependences of (*1*) the volume magnetostriction and (*2*) the anisotropic part of magnetostriction in a magnetic field of 0.9 T.

was found earlier in $La_{0.60}Y_{0.07}Ca_{0.33}MnO_3$, but in a considerably stronger magnetic field of 14 T [13]. The anisotropic magnetostriction reverses its sign at T_C; below T_C it is positive, while above T_C is negative. As seen from Fig. 5, the $\omega(H)$ curves exhibit a sharp growth of $|\omega|$ at a certain critical magnetic field H. The $\omega(H)$ curves do not saturate in fields of up to 1 T and reveal hysteresis with an increasing or decreasing magnetic field (Fig. 5). In addition, the authors observed a temperature hysteresis of thermal expansion (Fig. 3) and of magnetostriction below T_C. These observations indicate a first-order thermodynamic phase transition at the Curie point accompanied by changes in the conduction type and the sample volume. Note the unusual behavior of the field dependences of the anisotropic magnetostriction $\lambda_t(H)$ in the vicinity of T_C. As the field is increased, λ_t first increases in magnitude, as is the case with conventional ferromagnets, after which, starting from a certain critical magnetic field, whose value depends on temperature, it falls off. This becomes manifest particularly clearly for the isotherms corresponding to 126 and 128 K (Fig. 6).

3. DISCUSSION OF RESULTS

We attribute the anomalies in the magnetic, elastic, and transport properties to the existence in $Sm_{0.55}Sr_{0.45}MnO_3$ of a magnetic diphase state originating from a strong *s–d* exchange coupling, similar to that observed in the classical EuSe- and $CdCr_2Se_4$-type magnetic semiconductors [1, 14]. The compound studied here is a heavily doped antiferromagnetic semiconductor $SmMnO_3$ which, as we believe, maintains at low temperatures a magnetic diphase state consisting of an insulating antiferromagnetic matrix with embedded conducting FM clusters, where carriers are localized because of the gain in energy involved in the *s–d* exchange [14]. This type of magnetic diphase state is also indicated by a fairly high resistivity, namely, $\rho = 260\ \Omega$ cm at 4.2 K. As shown by Nagaev [14], such FM clusters exist at temperatures $T \geq 0$ K, but are destroyed under heating near T_C. The carriers residing for $T < T_C$ in the FM clusters become free, and this brings about a strong decrease in the resistivity for $T > T_C$ (Fig. 2). Application of an external magnetic field results in an increase in the FM clusters in volume and their magnetic moments orienting along the magnetic field, as well as in an increase of the electron kinetic energy inside the clusters, which facilitates carrier tunneling among the clusters and favors cluster destruction. It is these factors that account for the CMR (Fig. 2). We believe that, if one accepts the above insulating magnetic diphase state, the low-temperature peak in the $\chi(T)$relation occurring at $T_N = 36$ K signals destruction of the long-range magnetic order in the AFM matrix, while the sharp decrease at $T_C = 126$ K corresponds to the destruction of the FM order in the clusters. As already mentioned, the spontaneous magnetization at 4.2 K is less than that expected for complete FM ordering and, hence, FM clusters occupy only a part of the sample volume, more specifically, 89%. It was shown [15] that the lattice parameters decrease inside the FM clusters of the diphase magnetic state, because this results in screening of the new charge distribution and in a decrease in their energy through increasing charge-cloud overlap of the central ion and its nearest neighbors. Lattice compression in a related compound $La_{1-x}Ca_xMnO_3$ near T_C is supported by neutron diffraction measurements [16]. In the absence of a magnetic

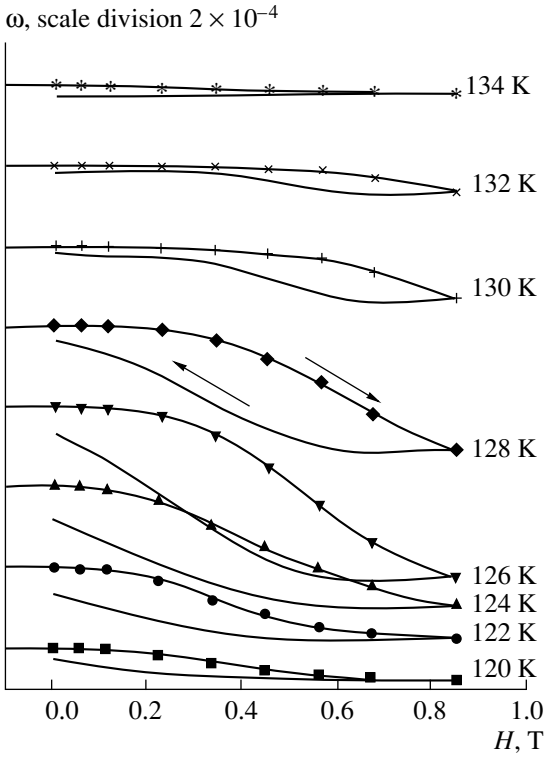

Fig. 5. Volume magnetostriction isotherms obtained near T_C.

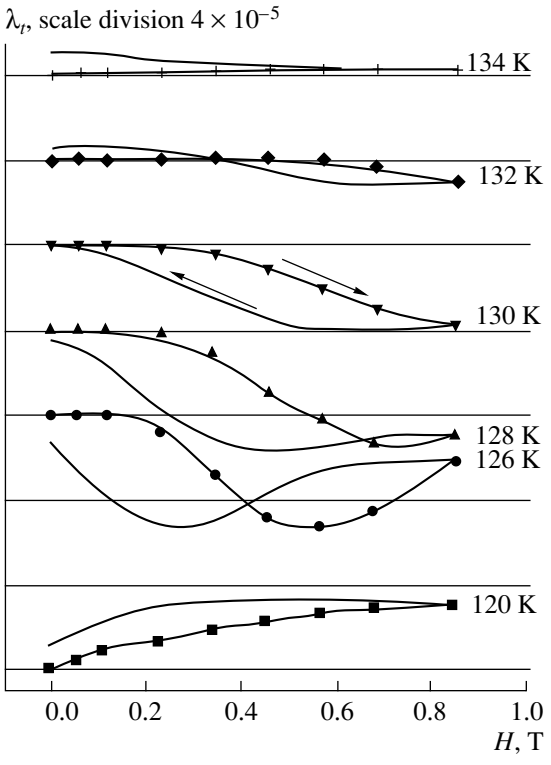

Fig. 6. Isotherms of anisotropic magnetostriction near T_C.

field, the FM clusters are destroyed in the vicinity of T_C to give rise to excess thermal expansion, and it is this jump that we observed (Fig. 3). It is known that, at $T \geq T_C$, an external magnetic field increases the extent of FM order near impurities more than it does on average over the crystal, because its influence is enhanced by *s–d* exchange; in other words, an external magnetic field restores the temperature-destroyed FM clusters and the lattice compression characteristic of the latter. This results in a reduced thermal expansion jump (see inset to Fig. 3) and a negative volume magnetostriction. Note that this magnetostriction is large enough to bring about apparently substantial changes in the crystal lattice type. This assumption is buttressed by the sign reversal of the anisotropic magnetostriction at T_C (Fig. 4). The restoration of FM clusters by a magnetic field occurs, however, in a limited temperature region slightly above T_C. As a result, the $\omega(T)$ curves pass through a minimum at T_C, and the volume magnetostriction decreases rapidly in absolute magnitude as the temperature increases still more (Fig. 4). Field-cooling a sample also initiates the creation of FM clusters and the lattice compression accompanying it, but over a broader temperature interval. Therefore, the $\Delta l/l(T)$ curve of a field-cooled sample passes lower than that of the zero-field-cooled one (Fig. 3). As already mentioned, it is the temperature of destruction of the FM clusters that is the T_C in this case. An external magnetic field increases the temperature of this destruction, exactly what was observed experimentally. It is this effect that accounts for the shift of the maximum in the $\rho(T)$ curves (Fig. 2), of the minimum in the $\omega(T)$ curves (Fig. 4), and of the jump in the $\Delta l/l(T)$ curves (Fig. 3) toward higher temperatures when subjected to a magnetic field. Thus, the anomalies in magnetic, elastic, and transport properties observed to occur in $Sm_{0.55}Sr_{0.45}MnO_3$ are interpreted satisfactorily in the model of electronic phase separation.

ACKNOWLEDGMENTS

Support of the Russian Foundation for Basic research (grant no. 96-15-96429), INTAS-97-open-30253, and NATO-HTECH LG 972942 is gratefully acknowledged.

REFERENCES

1. É. L. Nagaev, Usp. Fiz. Nauk **166**, 833 (1996) [Phys. Usp. **39**, 781 (1996)].
2. A. P. Ramírez, J. Phys.: Condens. Matter **9**, 8171 (1997).
3. C. N. R. Rao, A. K. Cheetham, and R. Mahesh, Chem. Mater. **8**, 2421 (1996).
4. G. H. Rao, L. R. Sun, J. K. Liang, *et al.*, Appl. Phys. Lett. **69**, 424 (1996).
5. O. Yu. Gorbenko, R. V. Demin, A. R. Kaul', *et al.*, Fiz. Tverd. Tela (St. Petersburg) **40**, 290 (1998) [Phys. Solid State **40**, 263 (1998)].

6. Y. Tomioka, H. Kuwahara, A. Asamitsu, *et al.*, Appl. Phys. Lett. **70**, 3609 (1997).
7. F. Damay, A. Maignan, N. Nguyev, and B. Raveau, J. Solid State Chem. **124**, 385 (1996).
8. F. Damay, N. Nguyev, A. Maignan, *et al.*, Solid State Commun. **98**, 997 (1996).
9. R. M. Thomas, L. Ranno, and J. M. D. Coey, J. Appl. Phys. **81**, 5763 (1997).
10. V. Caignaert, A. Maignan, and B. Raveau, Solid State Commun. **95**, 357 (1995).
11. S. M. Dunaevskiĭ, A. L. Malyshev, V. V. Popov, and V. A. Trunov, Fiz. Tverd. Tela (St. Petersburg) **39**, 1831 (1997) [Phys. Solid State **39**, 1636 (1997)].
12. S. M. Dunaevskiĭ, I. A. Kurbakov, V. A. Trunov, *et al.*, Fiz. Tverd. Tela (St. Petersburg) **40**, 1271 (1998) [Phys. Solid State **40**, 1158 (1998)].
13. M. R. Ibarra, P. A. Algarabel, and C. Marquina, Phys. Rev. Lett. **75**, 3541 (1995).
14. É. L. Nagaev, Pis'ma Zh. Éksp. Teor. Fiz. **6**, 484 (1967) [JETP Lett. **6**, 18 (1967)]; Zh. Éksp. Teor. Fiz. **54**, 228 (1968) [Sov. Phys. JETP **27**, 122 (1968)]; *Physics of Magnetic Semiconductors* (Nauka, Moscow, 1979).
15. A. Yanase and T. Kasuya, J. Phys. Soc. Jpn. **25**, 1025 (1968).
16. P. G. Radaelli, D. E. Cox, M. Marezio, *et al.*, Phys. Rev. Lett. **75**, 4488 (1995).

Translated by G. Skrebtsov

Physics of the Solid State, Vol. 42, No. 8, 2000, pp. 1499–1507. Translated from Fizika Tverdogo Tela, Vol. 42, No. 8, 2000, pp. 1456–1464.

MAGNETISM AND FERROELECTRICITY

Anomalous Increase in the Unipolarity of Doped Lithium Niobate Crystals in the Temperature Range 300–400 K

M. N. Palatnikov*, V. A. Sandler, N. V. Sidorov*, A. V. Gur'yanov**, and V. T. Kalinnikov***

** Institute of Chemistry and Technology of Rare Elements and Mineral Raw Materials, Kola Scientific Center, Russian Academy of Sciences, Apatity, Murmansk oblast, 184200 Russia*

*** Ivanovo State University, Ivanovo, Russia*

e-mail: palat_mn@chemy.kolasc.net.ru

Received in final form, October 15, 1999

Abstract—The lithium niobate single crystals doped with B, Zn, and Gd at a content of 0.002–0.44 wt % have been grown. Their domain structure, static and dynamic piezoelectric properties, dielectric properties, and conductivity are investigated over a wide range of frequencies. The dielectric dispersion associated with the Debye-type relaxation process and considerable anomalies in $\varepsilon'_{22}(T)$ and conductivity are revealed in the temperature range ~300–400 K. At these temperatures, the piezoelectric modulus d_{33} of the initial polydomain crystals $LiNbO_3$: Gd jumpwise increases up to the values close to those for the undoped single-domain crystal. This increase is accompanied by a substantial change in the etch patterns due to the domain structure of the crystal. The nature of the anomalies observed in $LiNbO_3$ in the above temperature range is discussed. © *2000 MAIK "Nauka/Interperiodica".*

1. INTRODUCTION

The anomalous temperature dependences of the conductivity and optical, dielectric, and pyroelectric properties and also the characteristic temperature evolution of the polarized light images for undoped and doped $LiNbO_3$ crystals in the temperature range 300–400 K have been observed in a number of works [1–10]. Kamentsev *et al.* [1] found that the $LiNbO_3$ crystals have a domain structure with domains of two types, which coexist in the temperature range ~290–350 K and sequentially disappear with an increase in the temperature at $T \sim 350$ K and $T > 400$ K. The anomalies in the Barkhausen thermal effect, dielectric properties, and the conductivity with an appreciable temperature hysteresis and changes in the character of the anomalies upon subsequent thermal cycles were also observed at these temperatures. Roĭtberg *et al.* [2] established that far from the ferroelectric phase transition temperature, there is a temperature range (~380–420 K) in which the domain structure of lithium niobate is unstable and the unipolarity of the samples changes in the absence of external field. At temperatures of 320–400 K in undoped and doped (Mn, Zn, Fe, Cr, and Ni) crystals with an applied conducting mask, Ped'ko *et al.* [3] observed the formation and evolution of the optical images whose geometry corresponded to that of the conducting mask.

In [4, 5], it was noted that the induced optical biaxiality of $LiNbO_3$ polydomain samples at $T \sim 370$ K and the residual luminous flux in the temperature range 310–350 K exhibit anomalous temperature behavior. Pronounced anomalies in the temperature dependences of the residual luminous flux in the temperature range 300–370 K were observed by Bagdasarov *et al.* [6] in doped $LiNbO_3$ single crystals and by Ped'ko and Lebedev [7] in undoped crystals of congruent and stoichiometric compositions. According to [5–7], these features are associated with the local electrooptical effect and the temperature behavior of the local electric fields responsible for this effect; moreover, they essentially depend on the type and the concentration of dopants and the conductivity of samples.

The temperature dependences of the anomalous birefringence of polydomain and single-domain undoped $LiNbO_3$ samples were studied by Belabaev *et al.* [8]. It was found that the dependence $\Delta n(T)$ along the optical axis for polydomain samples have maxima in the same temperature range, and the birefringence disappears at $T \sim 420$ K irrespective of the initial state of the domain structure. In [9], the anomalous temperature dependences of the refractive index were also observed in this temperature range for doped $LiNbO_3$ single crystals, which was related to the possible structural transformations upon doping. Furthermore, the anomalies of the electrooptical properties were revealed in crystals doped with Zn, Mn, and Ti [10].

Although the anomalous temperature behavior of different physical properties of undoped and strongly doped $LiNbO_3$ crystals was observed by many researchers, the absence of the quantitative reproducibility of the results that substantially depend on the

1063-7834/00/4208-1499$20.00 © 2000 MAIK "Nauka/Interperiodica"

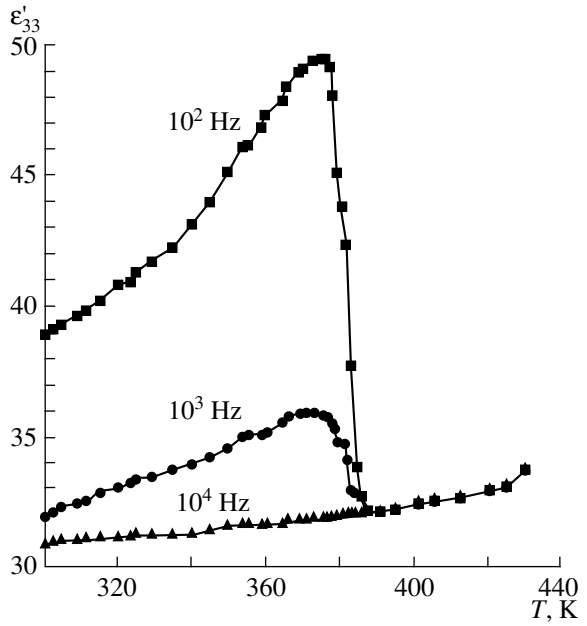

Fig. 1. Temperature dependences of the permittivity of the crystal $LiNbO_3$: Gd (0.44 wt %, *z* direction) at different frequencies.

thermal and field prehistory and real crystal structure is characteristic of the majority of the studies.

In order to obtain additional experimental evidence on the nature of the anomalies observed in the $LiNbO_3$ crystals, we grew single crystals doped with B, Zn, and Gd at a content of 0.002–0.44 wt % and studied their domain structure, static and dynamic piezoelectric properties, dielectric properties, and the conductivity in the above temperature range over a wide range of frequencies.

2. EXPERIMENTAL TECHNIQUE

The $LiNbO_3$ single crystals were grown by the Czochralski method in air on a Kristall-2 setup equipped with an automatic weight control system.

The synthesis of the batch and the growth procedure were described in [11]. The crystals were grown from the melt of congruent composition in Pt crucibles by using an undoped $LiNbO_3$ seed oriented along the *z* axis. Dopants in the form of oxides (high-purity grade) were introduced into the batch at the stage of melting in the crucible. The dopant concentration in the single crystals grown was checked by x-ray spectrum microanalysis and x-ray fluorescence, optical spectrum, and atomic absorption analyses.

The lithium niobate single crystals doped with B, Zn, and Gd exhibited a high optical quality (low residual luminous flux and the absence of light scattering centers). The resistance of these crystals to laser radiation damage was higher than that of the undoped crystals with the congruent composition. The grown crystals were not subjected to the procedure of the stimulated formation of single-domain structure.

With the aim of visualizing the domain structure, the *z*-oriented plates were etched in an $HF–HNO_3$ mixture at a temperature of 70°C for 4 h (hot etching) or at room temperature for 24 h (cold etching). The domain structure was examined by optical and atomic-force microscopy [an SMM-2000 atomic-force microscope (KPD)].

Samples of the studied crystals in the form of plane-parallel plates $5 \times 5 \times (0.6–1)$ mm in size were oriented normally to the *z* axis. Platinum electrodes were deposited onto plane-parallel faces of the samples by magnetron sputtering in an argon atmosphere at a pressure of $\sim 10^{-3}$ torr with the preliminary ionic cleaning.

The dielectric properties were studied by the amplitude–phase–frequency detection technique in the frequency range from 0.5 Hz to 1 MHz. The temperature dependences of the static piezoelectric modulus d_{33} were obtained under uniaxial mechanical loading of the *z*-oriented samples, and the induced charge was measured with an electrometric voltmeter. The piezoelectric resonance spectrum of the crystal was recorded on an SK4-58 spectrum analyzer.

3. RESULTS AND DISCUSSION

Figure 1 shows the temperature dependences of the real part of the permittivity $\varepsilon'_{33}(T)$ for the $LiNbO_3$ crystal doped by gadolinium at a content of 0.44 wt % at different frequencies. It can be seen that the dependence $\varepsilon'_{33}(T)$ in the temperature range ~330–380 K has a considerable anomaly, which decreases in magnitude with an increase in the frequency *f* and virtually disappears at $f \geq 10$ kHz. In the same temperature range, an anomaly in the form of a sharp jump is also observed in the temperature dependence of the conductivity (Fig. 2). These dependences are obtained with an increase in the temperature, and, what is more important, both anomalies decrease by more than one order of magnitude upon subsequent heating–cooling cycles. It should be noted that the dependence $\varepsilon'_{33}(T)$ measured at a frequency of 10 kHz for the doped $LiNbO_3$ crystal (Fig. 1) completely coincides with similar dependences for the *z*-cut plate of the undoped crystal over the entire studied ranges of temperatures and frequencies.

The data obtained suggest the relaxation character of the dielectric anomalies observed; hence, the frequency dependences of the complex permittivity were studied for the $LiNbO_3$ samples with the above doping. The experimental results in the form of the Cole–Cole diagrams for the studied crystal at different temperatures are displayed in Fig. 3 (frequencies are given in Hz, and numerals near the Cole–Cole curves indicate the heat treatment time (in hours) for the sample at $T =$

344 K). As follows from the diagrams, the dielectric dispersion of $LiNbO_3$: Gd in the frequency range from 1 Hz to 1 MHz is governed by the sole Debye-type relaxation process with the characteristic relaxation time $\tau \sim 2.5 \times 10^{-2}$ s at room temperature. No considerable changes in the depth of dispersion and the permittivity are observed upon heating the samples up to temperatures no higher than ~340 K. At the same time, it is found that the temperature dependence of the dielectric relaxation time obeys the Arrhenius law

$$\tau(T) = \tau_0 \exp(U_a/kT), \quad (1)$$

where U_a = 0.23 eV is the activation energy, and $\tau_0 \sim 2.0 \times 10^{-6}$ s is the preexponential factor.

An increase in the temperature ($T > 340$ K) leads to a sharp decrease in the depth of dispersion and an increase in the relaxation time (Figs. 3, 4). These changes in the dielectric properties are jumpwise in character and evolve with time in the range of temperature $T = T_0 = 340$–350 K, whereas the dynamic permittivity ε'_∞ remains unchanged. Heat treatment of the sample at $T_0 \approx 340$–350 K for 4 h results in the complete disappearance of the Debye dispersion. In this case, the frequency and temperature dependences of the permittivity become similar to those for the undoped lithium niobate crystals [12]. Note that this effect is reproduced with a small spread in the temperatures and τ_0 for all studied $LiNbO_3$: Gd samples with the given dopant concentration.

The temperature dependence of the bulk static conductivity σ_s was obtained from analysis of the diagrams for the complex conductivity (Fig. 4). At $T < T_0$, this dependence, like the dependence $\tau(T)$, exhibits a thermally activated behavior and satisfies the Arrhenius law

$$\sigma_s T = A_0 \exp(-H_a/kT) \quad (2)$$

with the activation enthalpy H_a = 0.22 eV and $A_0 \sim$ 0.19 K/(Ω m). In the vicinity of the T_0 temperature, the static conductivity jumpwise decreases (by more than two orders of magnitude) down to the values characteristic of undoped $LiNbO_3$ crystals at the same temperature.

A common feature of all the studied samples is the irreversibility of changes in the dielectric properties and the conductivity upon thermal cycles with a duration shorter than one day. The characteristic time required to recover the original state of different samples at room temperature varies from several days to several weeks and even months.

The experimental investigations into the dielectric relaxation in bias electric fields (the results obtained are shown in Fig. 5) demonstrate that an increase in the bias field strength E from 0 to 20 kV/cm even at room temperature decreases the depth of the dispersion but leaves its Debye behavior unchanged. In a bias electric field, the depth of dispersion regains its original value, as in the above case, over a long period.

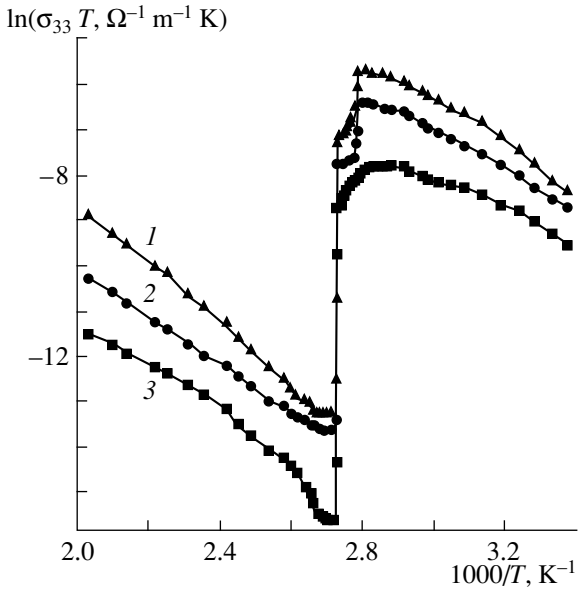

Fig. 2. Temperature dependences of the conductivity of the crystal $LiNbO_3$: Gd (0.44 wt %, *z* direction) at different frequencies (Hz): (*1*) 10^4, (*2*) 10^3, and (*3*) 10^2.

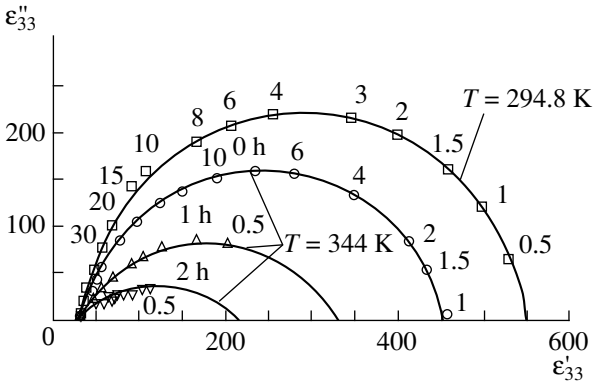

Fig. 3. Cole–Cole diagrams for the crystal $LiNbO_3$: Gd (0.44 wt %, *z* direction) at different temperatures. 0 h, 1 h, and 2 h indicate the heat treatment times at T = 344 K.

The examination of the etch patterns permits the conclusion that the regular domain structure based on rotational growth bands (Fig. 6) is formed in the $LiNbO_3$: Gd crystals, as was observed by Naumova [13] in lithium niobate crystals doped with Y^{3+}, Dy^{3+}, and Nd^{3+}. Doping with gadolinium, like the yttrium, dysprosium, and neodymium dopants, brings about the formation of a regular domain structure, because these dopants have noncompensated charges, large ionic radii (for Gd^{3+}, Y^{3+}, Dy^{3+}, and Nd^{3+}, the radii are equal to 0.94, 0.97, 0.88, and 0.99 Å, respectively), and the efficient distribution coefficients $K_{eff} < 1$.

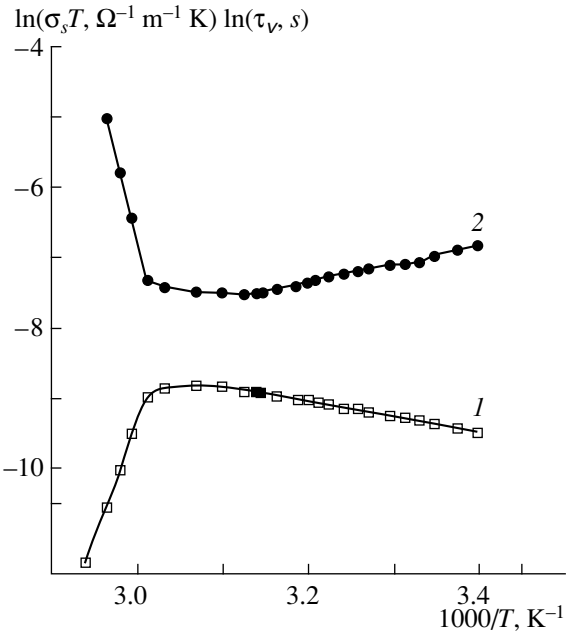

Fig. 4. Temperature dependences of the static conductivity and the dielectric relaxation time for the crystal $LiNbO_3$: Gd (0.44 wt %, *z* direction): (*1*) $\ln(\sigma_s T)$ and (*2*) $\ln\tau_v$.

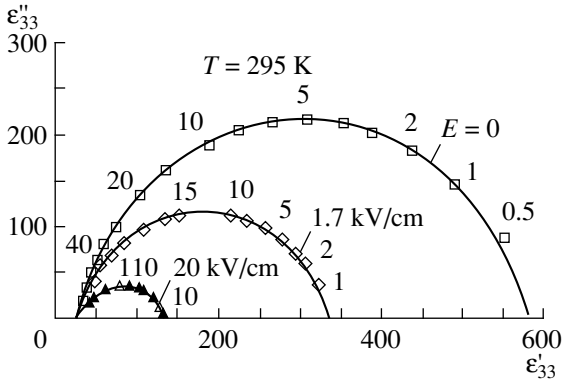

Fig. 5. Cole–Cole diagrams for the crystal $LiNbO_3$: Gd (0.44 wt %, *z* direction) in bias electric fields (T = 295 K).

Ming *et al.* [14] studied the distribution of the Y^{3+} dopant in the rotational growth bands of $LiNbO_3$: Y single crystals. The dopant distribution was measured along the normal to the domain boundaries. It was found that domains are formed near maxima and minima of the yttrium concentration. A sharp change in the concentration (at a minimum) corresponds to the smooth domain boundary, and a gradual change (at a maximum), to the rough boundary [14]. Apparently, a similar pattern should be observed in the case of Gd^{3+}, because yttrium and gadolinium belong to the same subgroup of Group III of the Periodic table and have identical charges and close values of atomic and ionic radii. Figure 6 shows the etch patterns of the $LiNbO_3$: Gd single crystal (*z* orientation), which are represented by the growth bands and the related ferroelectric domains. Indeed, it is clearly seen (Fig. 6b) that domains in the regular domain structure in the $LiNbO_3$: Gd single crystal can have both smooth and rough boundaries. Upon phase transition, the charge of the Gd^{3+} dopant in the crystal is incompletely shielded. Consequently, the nonuniform dopant distribution is equivalent to the nonuniform charge distribution and, correspondingly, to the nonuniform internal field and leads to the formation of domains with opposite polarization.

The observed anomalies in the temperature behavior of the dielectric properties and their specific slow evolution, the character of the dielectric dispersion, the relaxation times and activation energies (at least, in the temperature range in which the conductivity and the relaxation time are described by the Arrhenius law), and the domain structure type enable us to assume that the low-frequency dielectric dispersion is due to the relaxation of point defects (associated with the gadolinium dopant) interacting with the domain boundaries in the initial polydomain crystal.

However, an increase in the relaxation time with an increase in the temperature is quite unusual and can be caused by the transformation of the domain structure, which is attended by a considerable increase in the domain size and, correspondingly, by changes in the character of interaction between point defects and domains.

In order to verify the hypothesis that the $LiNbO_3$: Gd crystals have a labile domain structure, we studied the temperature dependences of the static and dynamic piezoelectric effects in the samples of this crystal. By ignoring a weak natural unipolarity, it can be assumed that the macroscopic piezoelectric effect is absent in the polydomain samples. According to different authors [12], the macroscopic piezoelectric modulus is maximum in the single-domain state far away from the Curie point. The piezoelectric moduli determined experimentally can serve as a measure of the unipolarity for particular samples of the crystal under study. From the above reasoning, we directly measured the static macroscopic piezoelectric modulus d_{33} and obtained its temperature dependence depicted in Fig. 7. The spread of the values in the "transition" temperature range (Fig. 7) is connected with the time drift of the measured moduli at T = const (toward an increase in d_{33} upon heating). As follows from the experimental data, upon heating the samples at $T < 340$ K, the piezoelectric modulus d_{33} is small and, most likely, is determined by a weak natural unipolarity. In the temperature range that corresponds to the anomalies observed in the dielectric properties and the conductivity, the piezoelectric modulus d_{33} jumpwise increases up to values close to those reported in [12] for undoped single-domain crystals. Figure 7 also demonstrates the normalized frequency dependences of the piezoelectric resonance signal for the thickness vibrations of the

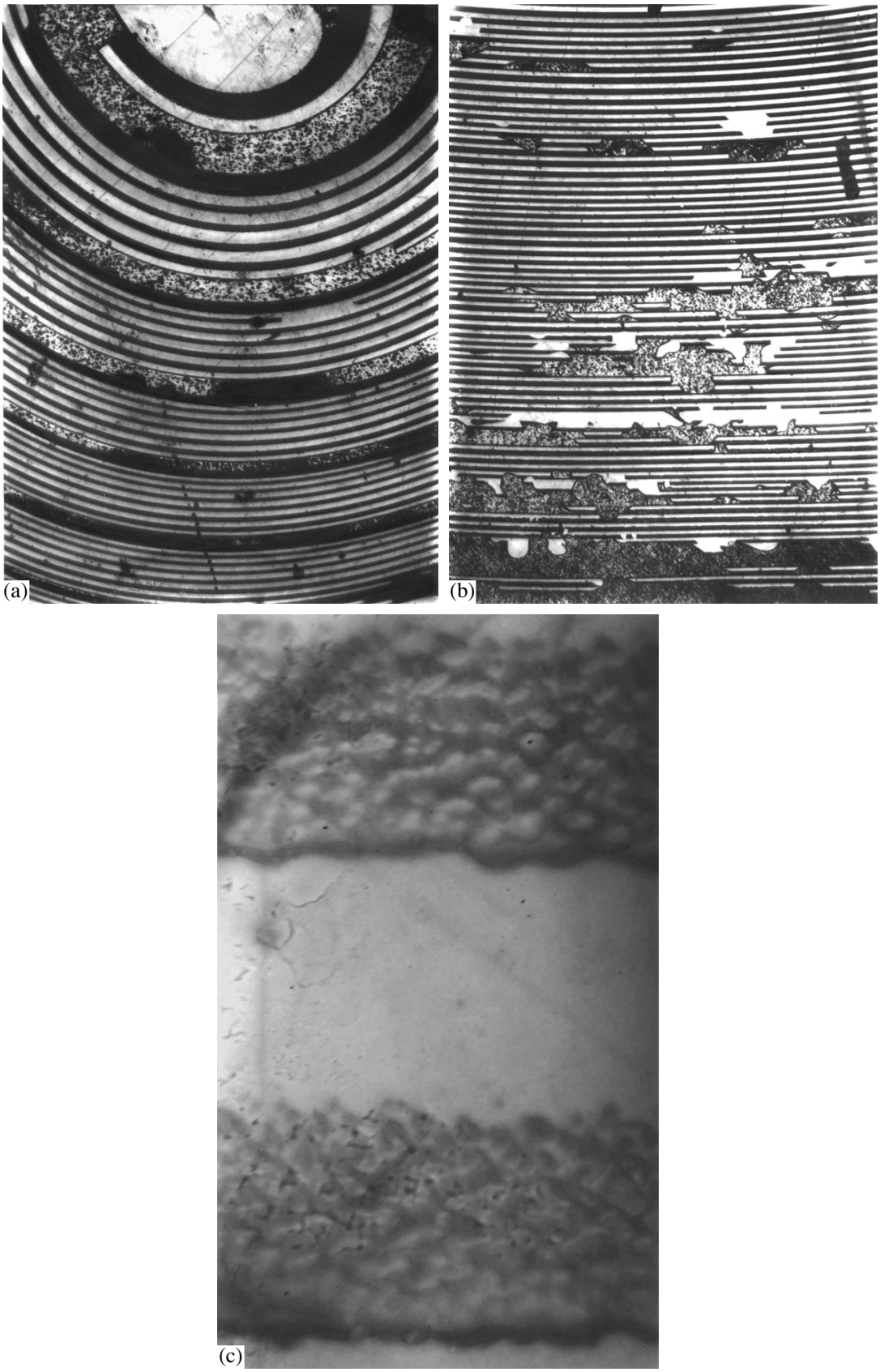

Fig. 6. Etch patterns of the $LiNbO_3$: Gd single crystal (0.44 wt %, *z*-cut). Magnification: (a) ×50, (b) ×120, and (c) ×2000. Etching of the samples at (a, b) 70°C and (c) room temperature.

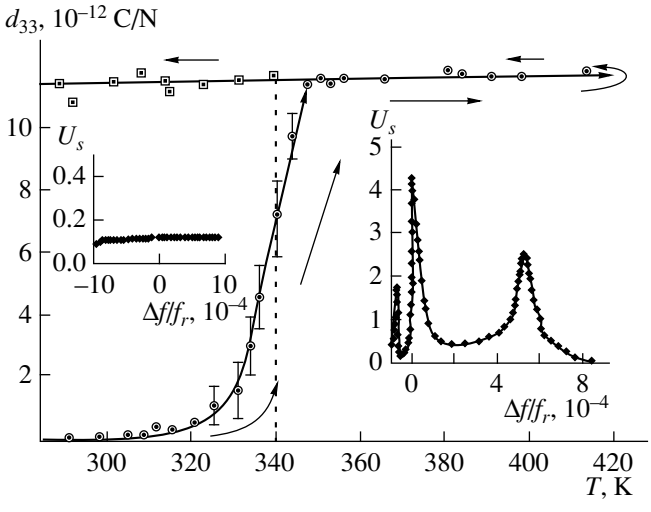

Fig. 7. Temperature dependences of the static piezoelectric modulus d_{33} for the crystal $LiNbO_3$: Gd (0.44 wt %, *z* direction). Insets show frequency dependences of the piezoelectric resonance signal at temperatures $T < T_0$ and $T > T_0$.

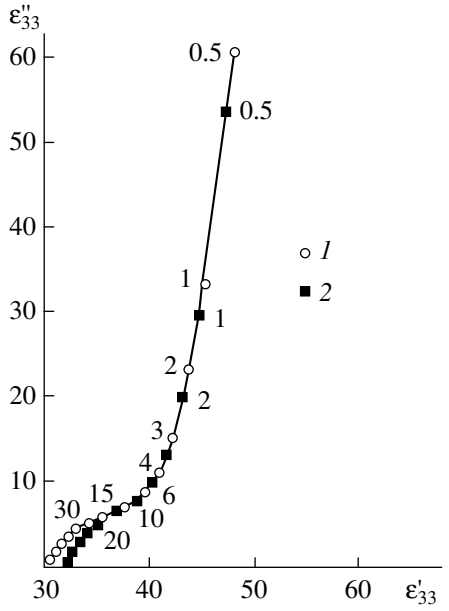

Fig. 8. Cole–Cole diagrams for crystals (*1*) $LiNbO_3$: B (0.09 wt %, *z* direction) and (*2*) $LiNbO_3$: Zn (0.1 wt %, *z* direction).

studied samples (*z* direction; thickness, 0.6–0.8 mm) in two temperature ranges, which likely correspond to two different states of the domain structure in the crystal. Similar to the static measurements, in these experiments, intense maxima of the signal at resonance frequencies also jumpwise arise at temperatures near $T_0 \sim$ 340 K upon heating the samples and irreversibly persist in the subsequent thermal cycles. Upon prolonged (up to several weeks) exposure of the samples in the state with an open circuit at room temperature, the macroscopic static piezoelectric moduli regain their initial low values, and the piezoelectric resonance virtually disappears (at a level of the signal-to-noise ratio of instrumentation).

Similar dependences are also observed for the $LiNbO_3$ crystals doped with Zn (0.1 wt %) and B (0.09 wt %). However, the above effects in these crystals are substantially less pronounced and cannot be reliably reproduced. In particular, although the dispersion of the complex permittivity in these crystals involves the Debye component, its value is not nearly so large as in the crystals $LiNbO_3$: Gd ([Gd] = 0.44 wt %). In the Cole–Cole diagrams (Fig. 8), the inclined line portion is determined by the bulk conductivity, and the arc with a small depth of dispersion, as in gadolinium-doped lithium niobate, corresponds to the relaxation of point defects. The arc in the diagram almost completely disappears at a field strength ≥5 kV/cm. These crystals possess a considerable piezoelectric effect ($d_{33} \sim 8 \times 10^{-12}$ C/N), but without substantial anomalies in the temperature dependence.

In this respect, the lithium niobate single crystal doped with gadolinium at a content of 0.44 wt % has been studied in detail in the present work. Especially as the crystals with a lower Gd content (0.002, 0.08, and 0.26 wt %) exhibit no anomalous temperature behavior of the dielectric and piezoelectric properties and the conductivity in the temperature range up to 600 K, and their characteristics are quantitatively similar to those of the undoped crystal.

A drastic increase in the piezoelectric modulus d_{33} for the $LiNbO_3$: Gd crystals is accompanied by a substantial change in the near-surface etch microrelief associated with the regular domain structure. Actually, the examination of the sample with a weak natural unipolarity under an SMM-2000 atomic-force microscope (KPD) prior to the measurements of temperature dependences revealed the microrelief with a clearly defined direction and a fine regular domain structure (Fig. 9a). In the figure, the sizes (*x* and *y*) of the scanning region are given in microns, and the scanning depth, in nanometers. The microrelief is virtually absent for the sample etched immediately after the dielectric measurements at $T > 340$ K (the piezoelectric modulus $d_{33} \approx (11–12) \times 10^{-12}$ C/N) (Fig. 9b). This experiment serves as direct evidence that the domain structure in the $LiNbO_3$: Gd single crystals undergoes transformations at temperatures close to T_0.

Thus, the experimental results corroborate the assumption that the initial polydomain $LiNbO_3$ crystals doped by gadolinium at a content of 0.44 wt % exhibit a very labile domain structure associated with point defects whose dynamics in low-frequency measuring fields contributes considerably to the static permittivity $\varepsilon_{s33}(T)$ of the polydomain samples (Fig. 3). With an increase in the temperature up to $T_0 \sim$ 340 K, the crys-

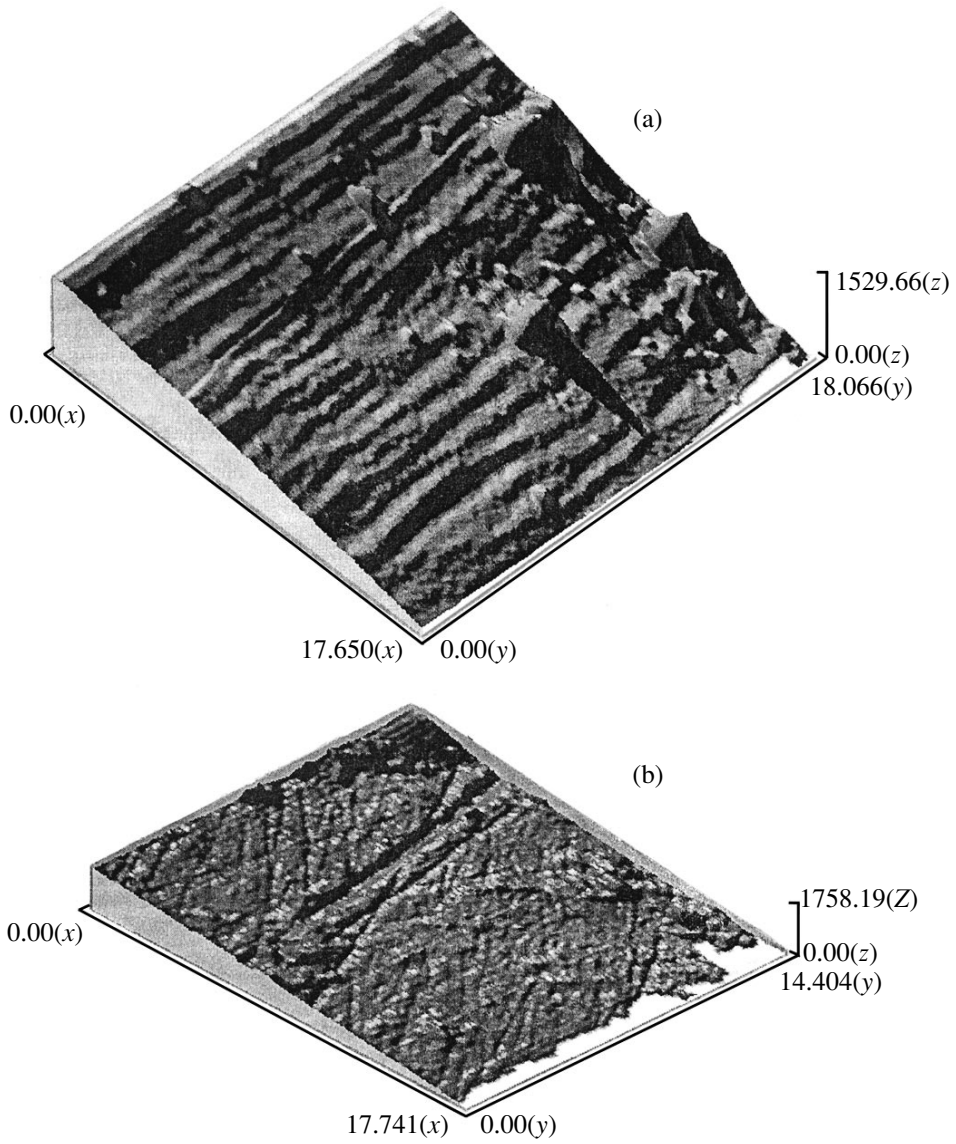

Fig. 9. Near-surface etch relief [obtained with a SMM-2000 atomic-force microscope (KPD)] of the crystal $LiNbO_3$: Gd (0.44 wt %, *z* direction): (a) prior to heating ($d_{33} \approx 0.2 \times 10^{-12}$ C/N) and (b) after electrical measurements ($d_{33} \approx (10–12) \times 10^{-12}$ C/N). Etching at room temperature.

tals under consideration are characterized by the anomalous temperature behavior, which indicates the transition of the domain structure to the strongly unipolar state close in properties to the single-domain state. This state is likely to be stable at temperatures $T > T_0$ and metastable at lower temperatures. Note that the spread in the T_0 temperatures for different sample does not exceed ~15 K. The kinetics of relaxation of the samples to the initial macroscopically nonpolar state depends, to a large measure, on their temperature–field prehistory. At room temperature, the relaxation times are as long as several weeks and even months, which is responsible for a substantial temperature hysteresis observed for the anomalies in shorter thermal cycles.

The conclusion that the strongly unipolar state of the domain structure is formed in the crystals with the above doping is in good agreement with the data on the photovoltaic effect in the undoped and doped crystals [15]. Upon scanning of the surface with a laser beam, the inertialess contribution to the photoresponse of the polydomain undoped crystal changes the sign, whereas the sign of photoresponse in $LiNbO_3$: Gd remains unaltered, which indicates a high degree of its unipolarity. Since the $LiNbO_3$: Gd samples used in [15] were obtained from the initially polydomain single crystal, it

should be supposed that the domain structure unipolarity revealed in the study of the photovoltaic effect is caused by photoinduced processes in the electronic subsystem of the crystal.

Pashkov *et al.* [16] investigated the photoconductivity in $LiNbO_3$ crystals and demonstrated that the external electric field in the crystal is shielded as a result of the thermally activated transition of electrons from shallow trapping centers with an activation energy of 0.2 eV to the conduction band. According to [17], this activation energy corresponds to the photoinduced optical inhomogeneity in the temperature range 300–360 K, where Δn_{st} = const. At temperatures $T > 370$ K, the effect is determined by deep trapping levels with an activation energy of ~1 eV.

In the $LiNbO_3$: Gd samples, the temperature dependence of the bulk static conductivity at temperatures of 300–340 K satisfies the Arrhenius equation with an activation enthalpy of ~0.22 eV (Fig. 4). Note that the conductivity is anomalously high (i.e., it exceeds the conductivity of the undoped $LiNbO_3$ crystals by more than two orders of magnitude). It can be assumed that the conductivity in the $LiNbO_3$: Gd crystals in the temperature range 300–340 K is also governed by the shallow trapping centers located near the bottom of conduction band.

Blistanov *et al.* [18] found that "nonphotorefractive" impurities (Mg) in $LiNbO_3$ can form shallow electron traps, for example, the "Mg^+ complex", which represents the Mg^+ ion occupying the Li^+ site with an electron delocalized on a number of surrounding ions [19]. In this case, the photorefractive effect considerably weakens at the expense of an increase in the efficiency of the recombination of photoexcited carriers without their capture into deep levels. In the study of thermostimulated luminescence [18], it was shown that these electron trapping centers can be thermolized at rather low temperatures ($T < 370$ K); i.e., their depth is relatively small. The energy levels of the local centers were calculated from the thermostimulated luminescence curves. The found values lie in the range 0.18–0.23 eV. The highest-temperature peak of the thermostimulated luminescence is located at 340–380 K, which closely coincides with the temperature range of the dielectric anomalies [18].

In our earlier works [15, 20–22], it was established that, upon doping of lithium niobate by cations (Mg, Zn, B, and Gd) whose charges and ionic radii are intermediate with respect to the host cations Li^+ and Nb^{5+} and leave the oxygen sublattice of the crystal undistorted, the degree of structural perfection of single crystals increases in a certain range of dopant concentrations. Moreover, the photorefractive effect is substantially suppressed [11, 23], which, apparently (by analogy with [18]), indicates an increase in the density of states near the bottom of the conduction band, i.e., the formation of shallow levels of electron trapping by the nonphotorefractive gadolinium impurity. This should result in an increase in both the dark conductivity and the photoconductivity, which is probably responsible for the anomalously high conductivity of the $LiNbO_3$: Gd crystals with an activation energy of ~0.2 eV in the temperature range 300–340 K.

It seems likely that the state of shallow trapping centers becomes unstable, and their population sharply decreases at temperatures $T > 340$ K. In this case, the electrons drift from regions with an increased content of the Gd^{3+} nonphotorefractive impurity (which corresponds to the domain boundaries) toward the positive pole of the spontaneous polarization and can be trapped into deep traps in the energy gap. These traps appear to be the niobium ions occupying the lithium sites, i.e., Nb_{Li} (antisite defects). According to Schirmer *et al.* [24], the Nb_{Li} defects are the deep electron traps, which form polarons and bipolarons upon electron trapping. This assumption agrees with the data obtained by Pashkov *et al.* [17], who established that the activation energy changes from ~0.2 to 1 eV in the temperature range covered. Furthermore, the results obtained by Akhmadullin *et al.* [25] indicate that the polaron mechanism of the conductivity in undoped lithium niobate crystals is predominant at temperatures above room temperature. Therefore, in the temperature range $T > T_0$, the static conductivity in the $LiNbO_3$: Gd single crystals decreases down to the conductivity characteristic of the undoped $LiNbO_3$ crystal at the same temperatures.

The loss of electrons from shallow electron traps based on the Gd^{3+} cationic complexes, which are predominantly localized at the domain boundaries, leads to a further polarization of the crystal environment by the field of charged centers. Kovalevich *et al.* [26] found that, as the temperature increases from room temperature to ~400 K, the polarization field in lithium niobate decreases by two orders of magnitude. In this case (under conditions of additional polarization), the sizes of domains in ferroelectrics can increase with a rise in the temperature due to an easier polarizability. At a sufficient concentration of impurity ions, the quasicooperative effect can arise with the formation of macroscopic domains whose sizes are comparable with the sample sizes [25]. This evidently explains why the unipolarity of the $LiNbO_3$: Gd crystal at the aforementioned Gd content drastically increases near the temperature ~340 K.

Most likely, the anomalies observed in the temperature range 300–400 K by different authors in various physical properties of doped and undoped lithium niobate crystals irrespective of the initial state of domain structure, to a certain degree, are associated with the change in the mechanism of electron conductivity. Particular magnitudes of the observed anomalies and the kinetics of related processes are presumably determined by the ratio between the densities of states of the

deep and shallow trapping centers and also by the real structure of samples.

ACKNOWLEDGMENTS

This work was supported by the Russian Foundation for Basic Research, project no. 97-03-33601a.

REFERENCES

1. V. P. Kamentsev, A. V. Nekrasov, B. B. Ped'ko, and V. M. Rudyak, Izv. Akad. Nauk SSSR, Ser. Fiz. **47** (4), 791 (1983).
2. M. B. Roĭtberg, V. K. Novik, and N. D. Gavrilova, Kristallografiya **14**, 938 (1969) [Sov. Phys. Crystallogr. **14**, 814 (1969)].
3. B. B. Ped'ko, É. V. Lebedev, I. L. Kislova, and T. R. Volk, Fiz. Tverd. Tela (S.-Peterburg) **40** (2), 337 (1998) [Phys. Solid State **40**, 308 (1998)].
4. Yu. S. Kuz'minov, *Electrooptical and Nonlinear Optical Lithium Niobate Crystal* (Nauka, Moscow, 1987).
5. A. A. Blistanov, E. V. Makarevskaya, V. V. Geras'kin, *et al.*, Fiz. Tverd. Tela (Leningrad) **20**, 2575 (1978) [Sov. Phys. Solid State **20**, 1489 (1978)].
6. Kh. S. Bagdasarov, M. Ya. Bogdanov, E. M. Uyukin, and M. N. Filippov, Fiz. Tverd. Tela (Leningrad) **29**, 2380 (1987) [Sov. Phys. Solid State **29**, 1370 (1987)].
7. B. B. Ped'ko and É. V. Lebedev, Izv. Akad. Nauk, Ser. Fiz. **61** (2), 321 (1997).
8. K. G. Belabaev, V. T. Gabrielyan, and V. Kh. Sarkisov, Kristallografiya **18** (1), 198 (1973) [Sov. Phys. Crystallogr. **18**, 123 (1973)].
9. B. B. Ped'ko, V. M. Rudyak, and A. L. Shabalin, Izv. Akad. Nauk SSSR, Ser. Fiz. **54**, 1154 (1990).
10. B. B. Ped'ko and V. M. Rudyak, Fiz. Tverd. Tela (Leningrad) **27**, 2815 (1985) [Sov. Phys. Solid State **27**, 1695 (1985)].
11. N. V. Sidorov and Yu. A. Serebryakov, in *Proceedings of the Second International Conference "Real Structure and Properties of Acentric Crystals," Aleksandrov, Russia, 1995*, p. 327.
12. *Acoustical Crystals*, Ed. by M. P. Shaskol'skaya (Nauka, Moscow, 1982).
13. I. I. Naumova, Kristallografiya **39**, 1119 (1994) [Crystallogr. Rep. **39**, 1029 (1994)].
14. N. Ming, J. Hong, and D. Feng, J. Mater. Sci. **17**, 1633 (1982).
15. N. V. Sidorov, M. N. Palatnikov, Yu. A. Serebryakov, *et al.*, Neorg. Mater. **33** (3), 1 (1997).
16. V. A. Pashkov, N. M. Solov'ev, and E. M. Uyukin, Fiz. Tverd. Tela (Leningrad) **21**, 1879 (1979) [Sov. Phys. Solid State **21**, 1079 (1979)].
17. V. A. Pashkov, N. M. Solov'ev, and N. B. Angert, Fiz. Tverd. Tela (Leningrad) **21** (1), 92 (1979) [Sov. Phys. Solid State **21**, 43 (1979)].
18. A. A. Blistanov, V. M. Lyubchenko, and A. N. Goryunova, Kristallografiya **43** (1), 86 (1998) [Crystallogr. Rep. **43**, 78 (1998)].
19. K. L. Sweeney, L. E. Halliburton, and D. A. Bryan, J. Appl. Phys. **57**, 1036 (1985).
20. N. V. Sidorov and Yu. A. Serebryakov, Vib. Spectrosc. **6**, 215 (1994).
21. Yu. Serebryakov, N. Sidorov, M. Palatnikov, *et al.*, Ferroelectrics **167**, 181 (1995).
22. N. V. Sidorov and Yu. A. Serebryakov, in *Proceedings of the Second International Conference "Real Structure and Properties of Acentric Crystals," Aleksandrov, Russia, 1995*, p. 338.
23. N. V. Sidorov and Yu. A. Serebryakov, Ferroelectrics **160**, 105 (1994).
24. O. F. Schirmer, O. Thieman, and M. Wohlecke, J. Phys. Chem. Solids **52**, 185 (1991).
25. I. Sh. Akhmadullin, V. A. Golenishchev-Kutuzov, S. A. Migachev, and S. P. Mironov, Fiz. Tverd. Tela (S.-Peterburg) **40**, 1307 (1998) [Phys. Solid State **40**, 1190 (1998)].
26. V. Kovalevich, L. Shuvalov, and T. Volk, Phys. Status Solidi **45** (1), 249 (1978).

Translated by O. Borovik-Romanova

Physics of the Solid State, Vol. 42, No. 8, 2000, pp. 1508–1511. Translated from Fizika Tverdogo Tela, Vol. 42, No. 8, 2000, pp. 1465–1468.

LATTICE DYNAMICS AND PHASE TRANSITIONS

Investigation of Superionic Phase Transition in the $CuCr_{1-x}V_xS_2$ System by X-ray Diffraction and Magnetic Methods

R. F. Al'mukhametov, R. A. Yakshibaev, É. V. Gabitov, and A. R. Abdullin

Bashkortostan State University, ul. Frunze 32, Ufa, 450074 Bashkortostan, Russia

e-mail: AlmukhametovRF@ic.bashedu.ru

Received November 2, 1999

Abstract—The unit cell parameters and the distribution of copper atoms over different crystallographic sites in the $CuCr_{1-x}V_xS_2$ superionic conductors have been determined by x-ray diffraction. It is demonstrated that a jumpwise change in the copper occupancy of different crystallographic sites for the compositions with $x = 0$, 0.05, 0.1, and 0.15 is associated with the transition to the superionic phase. The two-dimensional character of the ion transfer in the studied compounds is confirmed. No considerable anomalies in the temperature dependences of the paramagnetic susceptibility are revealed at temperatures of the superionic transition. © *2000 MAIK "Nauka/Interperiodica"*.

1. INTRODUCTION

The transition metal dichalcogenides YMX_2 (Y is the univalent metal, M is the transition metal, and X is chalcogen) have a layered structure [1–4] and represent the mixed ionic–electronic conductors [4–7]. The structure of these compounds is formed by alternating the X–M–X triple atomic layers aligned perpendicular to the hexagonal axis c with univalent metal atoms in between. In the triple X–M–X layers, the transition metal and chalcogen atoms are bound by strong ion-covalent bonds. Since the adjacent triple layers are linked together through weak van der Waals interactions, the univalent metal atoms possess a high mobility in the cavities between these layers. Owing to the relatively simple structure, these compounds serve as convenient model objects in studies of ion transfer. In practice, similar compounds can be used as electrode materials. In the present work, we carried out the structural and magnetic investigations of the $CuCr_{1-x}V_xS_2$ system.

2. RESULTS AND DISCUSSION

The synthesis of $CuCr_{1-x}V_xS_2$ compounds and some experimental results were reported in our earlier work [8]. It was found that the $CuCr_{1-x}V_xS_2$ compounds are the Cu^+ cationic conductors, and the interatomic bonds are essentially ionic in character. In the studied system, chromium is isomorphously replaced by vanadium; however, the valences of vanadium and chromium differ (V^{3+} and Cr^{2}+). As a result, the number of dangling bonds of sulfur atoms decreases, and the Cu^+ cationic conductivity increases. It is of interest to elucidate how this process affects the superionic phase transition.

2.1. Structural investigations. Figure 1 demonstrates a structural fragment of the initial compound $CuCrS_2$ [1, 2, 4]. In the interior of the S–Cr–S triple layers, the sulfur atoms form a close packing whose octahedral sites are occupied by the chromium atoms. Two nonequivalent tetrahedral sites (α' and β') are not filled by atoms. The sulfur atoms also form tetrahedral sites of two types (α and β) between triple layers. The α-type sites at room temperature are occupied by the copper atoms. In the superionic phase, the copper atoms are distributed over the α and β sites with equal probability [1, 2, 4, 6].

The table lists the unit cell parameters a and c at room temperature, which were determined from the (110) and (018) lines. These parameters were determined with Cr_2O_3 as a reference sample. Our results are in good agreement with the available data for $CuCrS_2$. It can be seen from the table that the unit cell parameters only slightly change for the compositions with $x = 0$, 0.05, 0.1, and 0.15. A jumpwise decrease in the lattice parameters is observed for the compositions with $x = 0.20$, 0.25, and 0.30. With allowance made for fact that the ionic radii of chromium and vanadium (accord-

Unit cell parameters of the $CuCr_{1-x}V_xS_2$ compounds at room temperature ($\Delta a = 0.002$ Å and $\Delta c = 0.004$ Å)

Composition, x	a, Å	c, Å
0.00	3.480	18.694
0.05	3.479	18.696
0.10	3.480	18.690
0.15	3.479	18.690
0.20	3.476	18.679
0.25	3.472	18.681
0.30	3.475	18.680

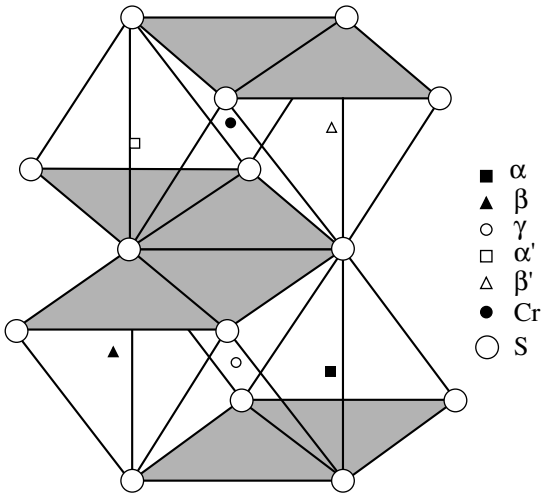

Fig. 1. A structural fragment of the $CuCrS_2$ compound.

ing to Belov and Bokiĭ) are R_V^{2+} = 0.72 Å, R_{Cr}^{2+} = 0.83 Å, R_V^{3+} = 0.67 Å, and R_{Cr}^{3+} = 0.64 Å [9], the observed decrease in the unit cell sizes can be explained by the replacement of the Cr^{2+} ions by the V^{3+} ions. This agrees with our earlier results obtained in the study of paramagnetic susceptibility.

In order to gain a better insight into the nature of the jump dependence of the unit cell parameters on the vanadium content, we investigated the distribution of copper atoms over different crystallographic sites. The site occupation probabilities were calculated from the experimental and calculated integrated intensities of reflections in the x-ray powder diffraction patterns by way of minimizing the discrepancy factor

$$R = \frac{\sum_j \left| I_{exp}^j - I_{calc}^i \right|}{\sum_j I_{exp}^j}.$$

The calculations were performed with due regard for the occupancies of all tetrahedral (α, β, α', and β') and octahedral sites, with variations in the coordinates of mobile copper atoms, and with inclusion of the temperature factor.

The results of calculations demonstrate that the octahedral sites in the compounds with x = 0, 0.05, 0.1, and 0.15 are virtually not occupied by copper atoms at room temperatures (Fig. 2). As the temperature increases, the occupancy of these sites jumpwise increases. For the compositions with x = 0.2, 0.25, and 0.30, the octahedral sites are occupied by the copper atoms even at room temperature, and their occupancies change only slightly with temperature. It is worth noting that the temperature at which the occupancy of the octahedral sites exhibits a jumpwise change is close to the temperature of the superionic phase transition in the $CuCrS_2$ compound (402°C) [10, 11]. Hence, we believe that the transition to the superionic phase in the studied compounds is associated with a partial occupation of

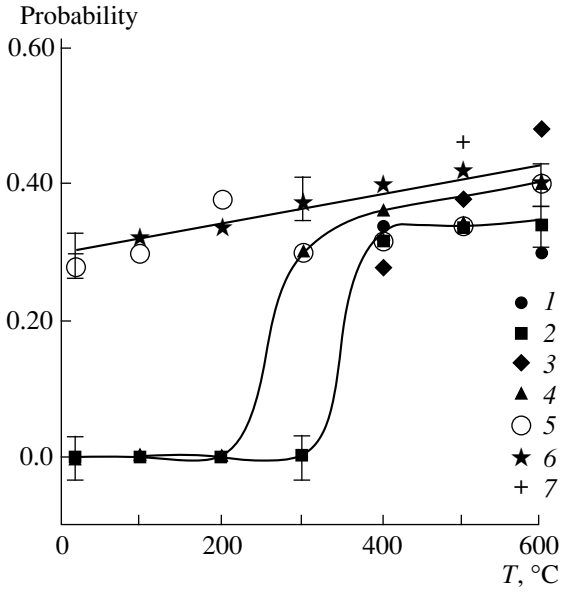

Fig. 2. Probability of copper occupation of the octahedral sites as a function of temperature for the $CuCr_{1-x}V_xS_2$ compounds with x = (*1*) 0, (*2*) 0.05, (*3*) 0.10, (*4*) 0.15, (*5*) 0.20, (*6*) 0.25, and (*7*) 0.30.

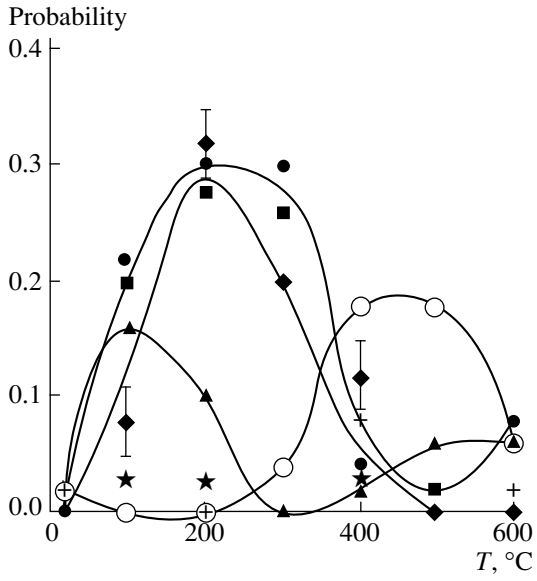

Fig. 3. Probability of copper occupation of the β sites as a function of temperature for the $CuCr_{1-x}V_xS_2$ compounds (designations are the same as in Fig. 2).

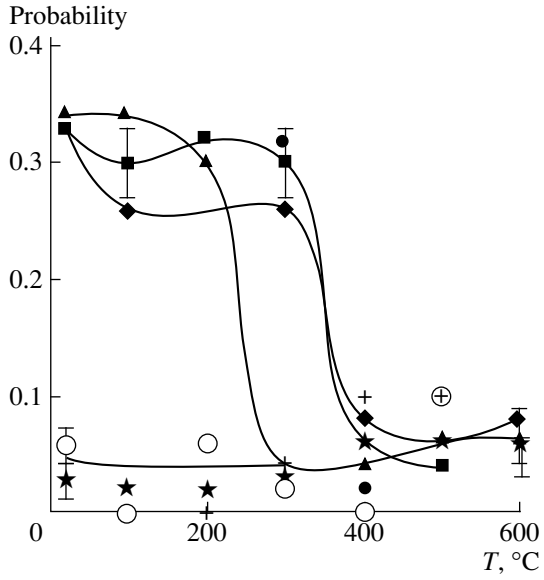

Fig. 4. Probability of copper occupation of the α'-type tetrahedral sites as a function of temperature for the $CuCr_{1-x}V_xS_2$ compounds (designations are the same as in Figs. 2, 3).

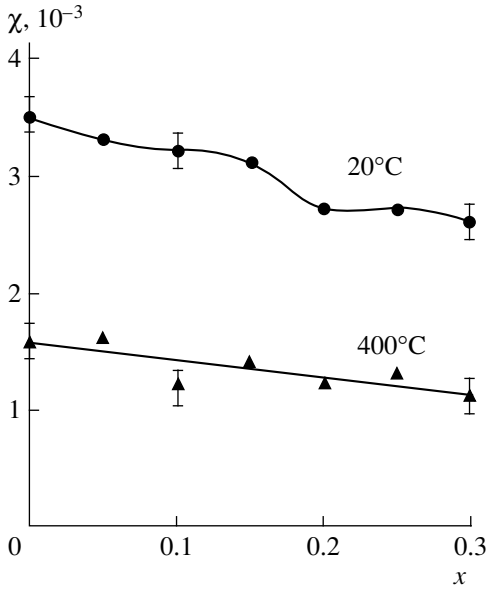

Fig. 5. Dependences of the paramagnetic susceptibility on the vanadium content for the $CuCr_{1-x}V_xS_2$ compounds.

the octahedral sites by copper atoms. On this basis, it can be assumed that the compositions with $x = 0.2$, 0.25, and 0.30, most likely, represent the ionic conductors even at room temperature. This assumption requires the experimental verification by measuring the ionic conductivity at these temperatures with the use of low-temperature ionic filters.

Earlier [10], it was shown that the occupancy of the β sites in $CuCrS_2$ is insignificant at room temperature, whereas the mobile atoms in similar structures at temperatures above the superionic phase transition point are distributed over the α and β sites with equal probability. The data obtained in the present work are displayed in Fig. 3. It can be seen that the occupancy of the β sites does not exceed 0.3. Upon transition to the superionic phase, the occupancy of the β sites decreases in the compounds with $x = 0$, 0.05, 0.1, and 0.15 and weakly increases in the compounds with $x = 0.2$, 0.25, and 0.30. These results are inconsistent with the data available in the literature and our previous results. This discrepancy likely stems from the fact that the occupation of two tetrahedral sites by the copper atoms inside the triple layers was ignored earlier. According to the data obtained, the occupancy of the β'-type tetrahedral sites is small and virtually does not depend on temperature. Figure 4 depicts the temperature dependences of the copper occupancy of the α'-type tetrahedral sites. A substantial occupancy of these sites at temperatures below the superionic phase transition point is observed for the compositions with $x = 0$, 0.05, 0.1, and 0.15. The transition to the superionic phase in these compounds is accompanied by a considerable decrease in the occupancy of the β' sites. All the foregoing suggests that the transfer of copper ions is primarily realized in the cavities between the layers linked by the van der Waals forces, has the two-dimensional character, and occurs through sequential jumps between the α and octahedral sites. This conclusion somewhat differs from the data available in the literature for similar systems, according to which the transfer occurs through sequential jumps between the α and β sites, while the octahedral sites are intermediate [9].

2.2. Paramagnetic susceptibility. As follows from the results obtained, the temperature dependences of the paramagnetic susceptibility obey the Curie–Weiss law and show no substantial anomalies (within the limits of experimental error) in the temperature range of the superionic phase transition. The latter fact indicates the absence of jumpwise changes in the character of chemical bonding. Figure 5 displays the dependences of the paramagnetic susceptibility on the vanadium content for the $CuCr_{1-x}V_xS_2$ compounds at room temperature and 400°C. It can be seen that the paramagnetic susceptibility at room temperature jumpwise changes in the range of $x = 0.2$. This jump is not observed at temperatures above the phase transition point and agrees well with the jumps in the dependences of the site occupancy and the unit cell parameters on the vanadium content. Consequently, the occupation of the octahedral sites by the copper ions is attended by a decrease in the paramagnetic susceptibility. Of particular interest is the absence of any anomalies in the dependences $\chi(T)$ in the temperature range of the superionic phase transition.

In our opinion, this can be explained by both a decrease in the accuracy of the paramagnetic suscepti-

bility measurements at high temperatures and a possible strong effect of the magnetic field on the superionic transition temperature. This problem calls for further investigation. For the compositions with $x = 0.2$, 0.25, and 0.30, a decrease in the paramagnetic susceptibility upon occupation of the octahedral sites by copper atoms is possibly brought about by the formation of a noncollinear magnetic structure, because no changes in the oxidation state of atoms is observed in this case.

Thus, it was shown that the superionic phase transition in the $CuCr_{1-x}V_xS_2$ system is accompanied by a jumpwise change in the occupancy of different crystallographic sites. Moreover, we established that the transfer of copper ions predominantly occurs through jumps between the α and octahedral sites. The two-dimensional character of the ion transfer was confirmed for the studied compounds. It was revealed that the paramagnetic susceptibility exhibits no considerable anomalies in the temperature range of the superionic transition.

REFERENCES

1. P. F. Bongers, C. F. van Bruggen, J. Koopstra, *et al.*, J. Phys. Chem. Solids **29**, 977 (1968).
2. F. M. R. Engelsman, G. A. Wiegers, F. Jellinek, and B. van Laar, J. Solid State Chem. **6**, 574 (1973).
3. A. G. Gerards, B. A. Boukamp, and G. A. Wiegers, Solid State Ionics **9** (10), 471 (1983).
4. N. Le. Nagard, G. Gollin, and O. Gorochov, Mater. Res. Bull. **14**, 1411 (1979).
5. R. A. Yakshibaev, V. N. Zabolotskiĭ, R. F. Al'mukhametov, and R. R. Galiullin, Fiz. Tverd. Tela (Leningrad) **29**, 1220 (1987) [Sov. Phys. Solid State **29**, 696 (1987)].
6. R. A. Yakshibayev, V. N. Zabolotski, and R. F. Almukhametov, Solid State Ionics **31**, 1 (1988).
7. R. A. Yakshibaev, A. F. Nadezhdina, and V. N. Zabolotskiĭ, Izv. Akad. Nauk SSSR, Neorg. Mater. **25**, 1390 (1989).
8. R. F. Al'mukhametov, R. A. Yakshibaev, and É. V. Gabitov, Fiz. Tverd. Tela (S.-Peterburg) **41**, 1450 (1999) [Phys. Solid State **41**, 1327 (1999)].
9. I. T. Goronovskiĭ, Yu. P. Nazarenko, and E. F. Nekryach, *A Brief Handbook on Chemistry* (Naukova Dumka, Kiev, 1987).
10. R. A. Yakshibayev, G. R. Akmanova, R. F. Almukhametov, and V. N. Konev, Phys. Status Solidi A **124**, 417 (1991).
11. V. M. Antropov, V. G. Pleshchev, V. N. Konev, and S. M. Kiskin, Fiz. Tverd. Tela (Leningrad) **26**, 2767 (1983) [Sov. Phys. Solid State **26**, 1593 (1983)].

Translated by O. Borovik-Romanova

Physics of the Solid State, Vol. 42, No. 8, 2000, pp. 1512–1516. Translated from Fizika Tverdogo Tela, Vol. 42, No. 8, 2000, pp. 1469–1473.

LATTICE DYNAMICS AND PHASE TRANSITIONS

Synergetics of Martensitic Structures in Shape Memory Crystals

G. A. Malygin

Ioffe Physicotechnical Institute, Russian Academy of Sciences, Politekhnicheskaya ul. 26, St. Petersburg, 194021 Russia
e-mail: malygin.ga@pop.ioffe.rssi.ru

Received January 20, 2000

Abstract—The kinetic mechanism of the formation of spatially inhomogeneous martensitic structures in shape memory alloys is discussed theoretically. In terms of synergetics, the formation of these structures is the result of the self-organization of elementary transforming volumes associated with the motion of transformation dislocations along interphase boundaries. In contrast to the pure thermodynamic approach based on the Ginzburg–Landau theory of phase transformations, the kinetic method allows one to determine the proper physical scale of the phenomenon and to elucidate the effect of structural factors on the transformation parameters. © *2000 MAIK "Nauka/Interperiodica"*.

INTRODUCTION

Numerous experimental studies [1–5] have revealed that spatially inhomogeneous ordered structures consisting of martensitic lamellae are formed in shape memory alloys during a thermoelastic structural transformation. As the temperature is lowered, the lamellae change in size and number until the entire crystal becomes transformed into the martensitic state.

By now, several attempts have been made to describe the formation of spatially inhomogeneous martensitic structures in terms of the Ginzburg–Landau (GL) theory of phase transitions [6–10]. In [6], for example, the structures that precede the appearance of martensite ("tweed" structures) were considered. Papers [7–10] are concerned with the formation of martensite structures.

The formation of "tweed" structures above the critical temperature (at which a full-size martensite structure arises) is due to heterophase fluctuations, which create nuclei of martensite. This is suggested by the small-scale (5–20 nm [11]) spatial modulation of lattice deformations and the reasonable agreement between the calculations [6] based on the GL theory and the experimental data.

The attempts to apply the GL theory to analyze the formation of spatially inhomogeneous martensitic structures during full-size martensitic transformation have not been successful. Both the size (thickness) of martensitic lamellae (1–10 μm) and the heterogeneous mechanism of their formation, as well as the strong effect of various structural factors on the transition parameters, have not been explained in terms of the pure thermodynamic approach.

The reason for the failure of this approach to account for the properties of martensitic structures is that these structures are nonequilibrium heterophase ones, because they are formed during a transition of the crystal lattice from one structural state to another. Such a transition does not occur uniformly over the crystal; there appear a great number of interphase boundaries, which interact with various defects of the crystal. This interaction limits the mobility of the interfaces and leads to diffuseness of the phase transition with temperature [12, 13]. The resulting martensitic structures are kinetic ones; they are in quasi-static equilibrium with the thermodynamic force acting on the interfaces and with the interaction force between the interfaces and lattice defects. The fact that the formation of martensitic structures proceeds through a nonclassical mechanism during the thermoelastic martensitic transformation was pointed out in [14].

In this paper, a kinetic theory of the formation of martensitic structures in real crystals is developed. In the first section, we derive a kinetic equation for the volume fraction of the martensitic phase. Using this equation, the evolution of spatially inhomogeneous martensitic structures in the process of the phase transformation with decreasing temperature is analyzed in Section 2. A quantitative comparison of the kinetic mechanism and the experimental data is made in Section 3. We have not attempted to solve all problems associated with the formation of martensitic structures. The aim of this paper is to formulate some of these problems and point out possible way of tackling them.

1. KINETIC EQUATION

In terms of the kinetic approach, the formation of martensitic structures is the process of self-organization of elementary transforming volumes. Because the transformation proceeds through the motion of transformation dislocations (atomic-scale martensite steps at interphase boundaries [15, 16]), one can write the

1063-7834/00/4208-1512$20.00

relative volume of the martensite phase as $\varphi = h\rho\lambda$ where ρ is the density of transformation dislocations (per unit area), h is the height of a step, and λ is the mean free path of a transformation dislocation between two successive obstacles. Therefore, the elementary transforming volume per unit dislocation length is $ah\lambda$, where a is the lattice parameter.

The transformation dislocations, like the usual lattice dislocations [17, 18], are generated by sources which are located in the bulk or on the surface of the crystal. The dislocations can multiply, annihilate, and diffuse. We will not consider these processes at the microscopic level; instead, we write the following phenomenological equation describing the evolution of the density of transformation dislocations:

$$\frac{\partial \rho_1}{\partial t} = n_0 w v + \frac{v}{\lambda_m}\rho_1 - h_a v \rho_1 \rho_2 + \lambda_D^2 v \frac{\partial^2 \rho_1}{\partial x^2}, \quad (1)$$

where v is the velocity of dislocations; n_0 is the volume density of sources (sinks) of transformation dislocations; h_a, λ_m, and λ_D are the characteristic lengths of the annihilation of martensite and austenite steps, dislocation multiplication, and diffusion of dislocations in the process of their interaction with lattice defects, respectively; t is the time; x is the coordinate along the normal to the habit plane of martensite; and ρ_1 and ρ_2 are the densities of transformation dislocations (steps) of martensite and austenite at interphase boundaries, respectively.

The thermodynamic probability (intensity) of the dislocation generation ($n_0 > 0$) or of their disappearance at sinks ($n_0 < 0$) is given by the expression [12, 13]

$$w(T) = [1 + \exp(\Delta U_{12}/kT)]^{-1}, \quad (2a)$$

where $\Delta U_{12} = \omega \Delta u$, $\omega = h\lambda^2$ is the elementary transforming volume; T is the temperature;

$$\Delta u = q\frac{T - T_c}{T_c} - \xi\sigma \quad (2b)$$

is the change in the internal energy per unit volume on the structural transformation; q is the specific heat of the phase transition; ξ is the spontaneous lattice shear due to the transition; σ is the shear stress on uniaxial crystal loading; and k is the Boltzmann constant.

Putting $\varphi_1 = \varphi = h\rho_1\lambda$ and $\varphi_2 = 1 - \varphi = h\rho_2\lambda$ in (1) and rearranging gives a kinetic equation for the volume density of the martensite phase

$$\tau\frac{\partial \varphi}{\partial t} = k_0 w + k_m \varphi - k_a \varphi(1 - \varphi) + \lambda_D^2 \frac{\partial^2 \varphi}{\partial x^2}, \quad (3)$$

where $k_0 = n\lambda^2 n_0$; $k_m = \lambda/\lambda_m$; and $k_a = h_a/h$ are coefficients determining the intensity of the corresponding processes and $\tau = \lambda/v$ is a characteristic time.

It is of interest to analyze static ($\partial\varphi/\partial t = 0$) solutions to equation (3). For this purpose, we write this equation in a dimensional form

$$2\frac{d^2\varphi}{dX^2} = -(\psi_0 + 2\psi_m\varphi + 3\varphi^2), \quad (4a)$$

where the following notation has been introduced:

$$X = \frac{x}{\Lambda_0}, \quad \Lambda_0 = \left(\frac{3\lambda_D^2}{2k_a}\right)^{1/2},$$
$$\psi_0(T) = \frac{3k_0}{k_a}w(T), \quad \psi_m = \frac{3}{2}\left(\frac{k_m}{k_a} - 1\right). \quad (4b)$$

Integrating (4a) and using the boundary condition for an extended crystal

$$\left.\frac{d\varphi}{dX}\right|_{\varphi = 1} = 0, \quad (5)$$

which implies the appearance of a homogeneous martensitic structure after the transformation comes to a close, we arrive at the equation

$$\left(\frac{d\varphi}{dX}\right)^2 = \Phi(\varphi) = (1 - \varphi) \times [(1 + \psi_0 + \psi_m) + (1 + \psi_m)\varphi + \varphi^2]. \quad (6)$$

Its solutions define the martensitic structures that are formed during the phase transition.

2. MARTENSITIC STRUCTURES

The general solution of equation (6) is the elliptic integral of the first kind

$$\mu^{-1}F(\theta, k) = \int_{\varphi}^{\varphi_n} \frac{d\varphi}{\sqrt{\Phi(\varphi)}} = \frac{x}{\Lambda_0}. \quad (7)$$

The form of partial solutions of integral (7) depends on the values of the parameters ψ_0 and ψ_m in (4b); these parameters determine the coefficient μ and the modulus k of the elliptic integral, as well as the value and sign of the roots φ_n of the cubic equation $\Phi(\varphi) = 0$

$$\varphi_1 = 1,$$
$$\varphi_{2,3} = \frac{1}{2}[-(1 + \psi_m) \pm \sqrt{(1 - \psi_m)^2 - 4(1 + \psi_0)}]. \quad (8)$$

According to (4b), the parameters ψ_0 and ψ_m depend on the relative values of the coefficients k_0, k_m, and k_a and the temperature.

Figure 1 shows the ranges of parameters (A, B, C) in which different solutions of integral (7) exist. Analysis reveals that the equation $\Phi(\varphi) = 0$ has a single root $\varphi_1 = 1$ if $(1 - \psi_m)^2 < 4(1 + \psi_0)$ (curve *1–1*). In this case, inte-

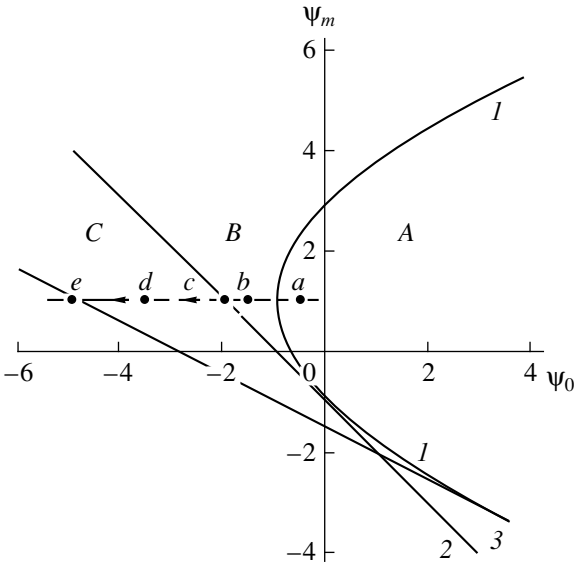

Fig. 1. Regions *A*, *B*, and *C* of the parameters ψ_0 and ψ_m, in which different martensitic structures exist.

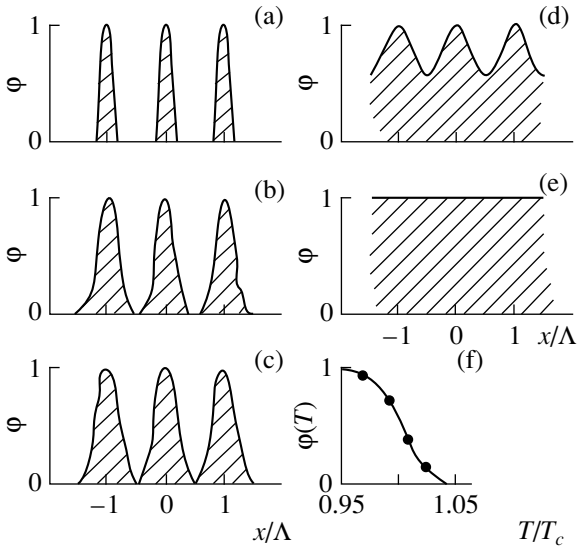

Fig. 2. Types of martensitic structures occurring at different temperatures T/T_c: (a) 1.022, (b) 1.008, (c) 1.004, (d) 0.992, and (e) 0.96; and (f) the temperature dependence of the volume fraction of martensite.

gral (7) describes a spatially periodic martensitic structure

$$\frac{x}{\Lambda} = \frac{1}{4}\frac{F(\theta, k)}{F(\pi/2, k)}, \quad \Lambda = 4\mu^{-1}F\left(\frac{\pi}{2}, k\right)\Lambda_0 \qquad (9a)$$

with a period Λ and with the martensitic lamella width (Fig. 2a) equal to

$$\Delta\Lambda_M = \frac{\Lambda}{2}\frac{F(\theta_M, k)}{F(\pi/2, k)}, \qquad (9b)$$

where $\cos\theta_M = \cos\theta|_{\varphi = 0}$,

$$\cos\theta = \frac{\mu^2 - 1 + \varphi}{\mu^2 + 1 - \varphi}, \quad k^2 = \frac{1}{2} + \frac{1}{4}\frac{3 + \psi_m}{\mu^2}, \qquad (9c)$$
$$\mu^2 = (3 + 2\psi_m + \psi_0)^{1/2}.$$

In region *A* in Fig. 1, the width of martensitic lamellae varies from zero to $\Lambda/2$.

Outside region *A*, the equation $\Phi(\varphi) = 0$ has three real roots $\psi_3 < \psi_2 < \psi_1$. In this case, integral (7) defines the martensitic structure

$$\frac{x}{\Lambda} = \frac{1}{2}\frac{F(\theta, k)}{F(\pi/2, k)}, \quad \Lambda = \frac{4\Lambda_0}{\sqrt{1 - \varphi_3}}F\left(\frac{\pi}{2}, k\right),$$
$$\sin\theta = \left(\frac{1 - \varphi}{1 - \varphi_2}\right)^{1/2}, \quad k = \left(\frac{1 - \varphi_2}{1 - \varphi_3}\right)^{1/2}. \qquad (10a)$$

When $\psi_m > -(1 + \psi_0)$ (straight line *2* in Fig. 1), both roots φ_2 and φ_3 are negative. Straight line *2* is the boundary of region *B* in which the width of martensitic lamellae

$$\Delta\Lambda_M = \Lambda\frac{F(\theta_M, k)}{F(\pi/2, k)}, \quad \sin\theta_M = \frac{1}{\sqrt{\varphi_2}} \qquad (10b)$$

varies from $\Lambda/2$ to Λ(Fig. 2b). The intersection point *c* of the dashed horizontal line (see below) and straight line *2* in Fig. 1 corresponds to a heterophase structure being half martensite and half austenite (Fig. 2c). Finally, when $\psi_m > -(3 + \psi_0)/2$, (straight line *3* in Fig. 1), there appears region *C*, in which the martensitic structure is nearly homogeneous (Fig. 2d). At points on straight line *3*, the martensitic structure is homogeneous (Fig. 2e).

The dashed line in Fig. 1 corresponds to the variation of parameters ψ_0 and ψ_m (4b) for $k_0/k_a = -3$ and $k_m/k_a = 5/3$. The arrows indicate the direction of their variation with decreasing temperature. Points *a*, *b*, *c*, *d*, and *e* of this line correspond to the martensitic structures presented in Figs. 2a to 2e, respectively. For these structures, the volume fraction of martensite $\varphi(T)$ equals the ratio of the hatched area to the total area of one period of the structure in Fig. 2, $\varphi(T) = \Delta\Lambda_M(T)/2\Lambda(T)$. Figure 2f shows the temperature dependence of $w(T) \equiv \varphi(T)$ for $\sigma = 0$ as given by the theory of diffuse martensitic transformations and described by formulas (2). Specified points in this figure correspond to $\varphi(T)$ for the martensitic structures in Figs. 2a to 2e. These points are seen to fit the curve fairly well.

Concluding this section, we estimate the size of martensitic lamellae $\Delta\Lambda_M$ and the average spacing between them Λ. According to (4b), their size is characterized by the scale $\Lambda_0 \approx \lambda_D$, where $\lambda_D \approx (h\lambda)^{1/2}$ is the mean diffusion distance for martensite steps of a height *h*, moving along an interphase boundary, with λ being their mean free path between obstacles. At $h = 10$ nm

and $\lambda = 100$ μm, we have $\lambda_D = 1$ μm and $\Delta\Lambda_M \approx \Lambda \approx 1$–10 μm, which is close to the experimental values.

3. COMPARISON WITH EXPERIMENT

For a diffuse martensitic transformation described by equations (2) [12, 13], the characteristic temperature T_c corresponds to the situation where the heterophase structure is half martensite and half austenite, i.e., $\Delta u = 0$. This is the case when the second root of the equation $\Phi(\varphi) = 0$ vanishes, that is, when the straight line *2* (Fig. 1) intersects the dashed line. At the intersection point, we have $|\psi_0(T_c(s))| = 1 + \psi_m(s)$, where the characteristic temperature $T_c(s)$ depends on the structure factor s. Taking into account (4b) and the temperature dependence $w(T)$ given by (2) at $\sigma = 0$, where T_{c0} is the critical temperature in the case where the structure factor has no effect, we obtain

$$T_c(s) = T_{c0}\left[1 + B^{-1}\ln\left(\frac{3|k_0|}{(1+\psi_m(s))k_a} - 1\right)\right], \qquad B = \frac{\omega q}{kT_c}. \tag{11}$$

As an example, we consider the effect of the grain size on the value of T_c in polycrystalline samples. In [19], it was found that, as the grain size increases, the characteristic temperature grows roughly logarithmically for small grain sizes, but it becomes constant for large ones.

The dependence of the characteristic temperature on the grain size may be due to the fact that the grain boundaries are obstacles for transformation dislocations and restrict their mean free path. As a consequence, the parameter ψ_m in (4b) becomes dependent on the grain size d,

$$\psi_m(d) = \frac{3}{2}\left(\frac{\lambda}{\lambda_m} + \frac{\lambda}{d} - \frac{1}{3}k_a\right). \tag{12}$$

Inserting this expression in (11) yields the characteristic temperature as a function of the grain size, which is similar to that observed for an Fe–31Ni alloy [19],

$$T_c(d) = T_{c0}\left[1 + B^{-1}\ln\left(\frac{A}{1+d_m/d} - 1\right)\right], \qquad A = \frac{6|k_0|}{3\lambda/\lambda_m - k_a}, \quad d_m = \frac{3\lambda}{3\lambda/\lambda_m - k_a}. \tag{13}$$

For a quantitative comparison of (13) and the experimental data [19], it is convenient to consider the relative variation of the characteristic temperature with the grain size

$$\frac{T_{c0} - T_c(d)}{T_{c0}} = -B^{-1}\ln\left(\frac{1}{A-1}\left(\frac{A}{1+d_m/d} - 1\right)\right) \approx B^{-1}\left(\ln\frac{A-1}{A} - \ln\frac{d}{d_m}\right). \tag{14}$$

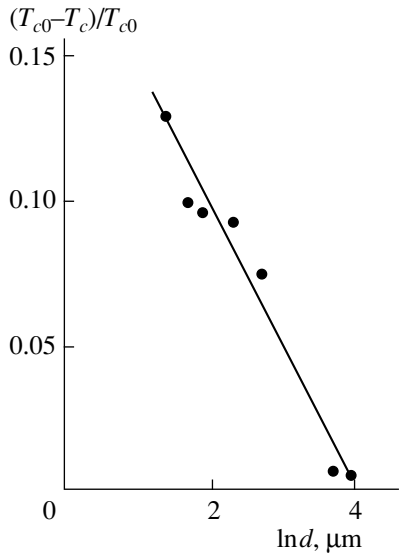

Fig. 3. Relative variation of the characteristic temperature of the martensitic transformation with grain size in an Fe–31Ni alloy [19].

The second equality in (14) is true if $Ad_m/d \gg 1$. From Fig. 3, it is seen that dependence (14) fits the experimental dots [19] rather well, which allows the unknown parameters to be found: $B \approx 20$, $d_m \approx 47$ μm, and $A \approx 20$.

In [20], it was found that the thermoelastic martensitic transformation in a TiNi alloy shows a size effect: a decrease in the thickness D of a titanium nickelide film caused the characteristic temperature to increase. Two reasons can be pointed out for this effect. In a thin crystal film, the mean free path of transformation dislocations is $\lambda = D$. According to (1a), we have $\psi_m \sim D$ and, therefore, this parameter decreases, which produces an increase in the characteristic temperature (11).

The other possible reason for the effect of the thickness of a crystal film on T_c is the more dramatic influence of the crystal surface (which is a sink for transformation dislocations) for smaller thicknesses. The increase in importance of the surface as a sink for lattice dislocations is evident from the relation $k_0 \sim D^{-1}$ [18]. This relation should also be true for transformation dislocations. Hence, according to (11), the characteristic temperature will increase with decreasing thickness of the crystalline film.

A dependence of the martensite elastic limit σ_M on the sample thickness and grain size was observed in [21] in a polycrystalline Cu–Zn–Sn alloy; as the ratio d/D was increased, the elastic limit was reduced, but it became independent of this ratio for $d/D \geq 1$.

Putting $\Delta u = 0$ in (2b), we obtain the Clausius–Clapeyron equation, according to which, the martensite

elastic limit at a temperature T is

$$\sigma_M = \sigma_m\left(\frac{T}{T_c} - 1\right) \sim T_c^{-1}, \quad \sigma_m = \frac{q}{\xi}. \tag{15}$$

The elastic limit is seen to vary inversely with the critical temperature. From the above discussion, it follows that we can write

$$T_c \approx T_{c0}\left(1 + B^{-1}\ln\frac{d}{D}\right), \tag{16}$$

hence, an increase in the ratio d/D produces a decrease in the critical temperature, thereby reducing the martensite elastic limit.

Thus, the synergetic approach to the problem of the formation of martensitic structures allows one to elucidate their morphological features and to determine the proper physical scale of the phenomenon, as well as to explain the influence (unusual from the thermodynamic standpoint) of the grain size on the critical temperature of the transformation.

REFERENCES

1. T. A. Schroeder and C. M. Wayman, Acta Metall. **27**, 405 (1979).
2. L. G. Khandros and I. A. Arbuzova, *Metals, Electrons, Lattice* (Naukova Dumka, Kiev, 1979), p. 109.
3. K. Shimizu and K. Otsuka, *Shape Memory Effects in Alloys* (Nauka, Moscow, 1979), p. 60.
4. J. W. Cristian, Metall. Trans. A **13**, 509 (1982).
5. H. Inagaki, Z. Metallkd. **83** (2), 97 (1992).
6. G. R. Barsch and J. A. Krumhansl, Metall. Trans. A **19**, 761 (1988).
7. F. Falk, J. Phys. (Paris) **43** (C-4), 3 (1982); **43** (C-4), 203 (1982).
8. F. Falk, Z. Phys. B **51**, 177 (1983).
9. S. K. Chan, in *Proceedings of the ICOMAT-89*, Mater. Sci. Forum **56**/**58**, 101 (1990).
10. S. Dorfman, D. Fuks, and A. Gordon, in *Proceedings of the ICOMAT-95*, J. Phys. IV **6** (C1), 35 (1996).
11. R. Oshima, M. Sugiyama, and F. E. Fujita, Metall. Trans. A **19**, 803 (1988).
12. G. A. Malygin, Fiz. Tverd. Tela (St. Petersburg) **36**, 1489 (1994) [Phys. Solid State **36**, 815 (1994)].
13. G. A. Malygin, Zh. Tekh. Fiz. **66** (11), 112 (1996) [Tech. Phys. **41**, 1145 (1996)].
14. G. B. Olson and M. Cohen, J. Phys. (Paris) **43** (C-4), 75 (1982).
15. G. B. Olson, Acta Metall. **29**, 1475 (1981).
16. D. Schrivers, J. Phys. IV **7** (C-5), 109 (1997).
17. G. A. Malygin, Fiz. Tverd. Tela (St. Petersburg) **35**, 3 (1993) [Phys. Solid State **35**, 1 (1993)].
18. G. A. Malygin, Usp. Fiz. Nauk **169**, 979 (1999).
19. M. Unemoto and W. S. Owen, Metall. Trans. **5**, 2041 (1974).
20. T. Kuninori, E. Sukeda, and H. Hashimoto, Mater. Trans., JIM **37** (1), 1404 (1996).
21. I. Dworak and E. B. Hawbolt, Metall. Trans. A **6**, 95 (1975).

Translated by Yu. Epifanov

Physics of the Solid State, Vol. 42, No. 8, 2000, pp. 1517–1521. Translated from Fizika Tverdogo Tela, Vol. 42, No. 8, 2000, pp. 1474–1478.

LATTICE DYNAMICS AND PHASE TRANSITIONS

Quasi-Reversible Superprotonic Phase Transition in $K_9H_7(SO_4)_8 \cdot H_2O$ Crystals

E. D. Yakushkin and A. I. Baranov

Shubnikov Institute of Crystallography, Russian Academy of Sciences, Leninskiĭ pr. 59, Moscow, 117333 Russia

Received February 7, 2000

Abstract—The heat capacity and the bulk conductivity have been measured in the $K_9H_7(SO_4)_8 \cdot H_2O$ crystal. The hysteresis phenomena have been studied upon superprotonic phase transition. It is revealed that the phase transition is reversible upon thermocycling only for the monohydrate form of the crystal. The exponential temperature dependence of the heat capacity in the supercooled disordered phase exhibits a thermally activated behavior and is determined by the defects responsible for the high conductivity of the crystal. © *2000 MAIK "Nauka/Interperiodica".*

1. INTRODUCTION

A high protonic conductivity in a series of crystals of acid alkali salts with the general formula $A_mH_n(XO_4)_p$ (A = K, Rb, NH_4, or Cs; and X = S, Se, P, or As) is determined by a specific structural disordering upon phase transition when the number of mobile protons becomes less than the number of their structurally equivalent sites and the energy barriers between these sites are relatively low (less than 0.5 eV) [1]. We pioneered in synthesizing a new superprotonic conductor of this type—the potassium hydrogen sulfate monohydrate crystal $K_9H_7(SO_4)_8 \cdot H_2O$. However, the preliminary investigations revealed that, unlike the aforementioned family of anhydrous salts, the high-conductivity phase formed in the $K_9H_7(SO_4)_8 \cdot H_2O$ crystal upon structural phase transition is readily supercooled down to low temperatures, and the superprotonic phase transition appears to be reversible only under certain conditions. In our opinion, the key role in this case is played by water molecules in the crystal and the dehydration–hydration processes.

The $K_9H_7(SO_4)_8 \cdot H_2O$ crystal at room temperature has a pseudohexagonal lattice with a monoclinic distortion (space group $P2/c$). (The x-ray structure investigations were carried out by Dilanyan at the Institute of Solid-State Physics, Russian Academy of Sciences.) The phase transition to the superprotonic state occurs at temperature T_{sp} = 398 K and leads to a change in the conductivity by three or four orders of magnitude (to 10^{-3} Ω^{-1} cm^{-1}) [2]. In accordance with the presumed hexagonal symmetry of the high-temperature phase, the network of acid hydrogen bonds and the molecular layers of crystallization water likely undergo a dynamic disordering at the phase transition point. The measurements of the conductivity revealed specific hystereses dependent on the time and thermal cycle. The thermogravimetric and IR spectroscopic data indicate the loss of crystallization water in the superprotonic phase [2]. It was found that the crystal under vacuum is partly dehydrated even at temperatures below the phase transition point. It is worth noting that the single-crystal state is retained in this case.

In the present work, we investigated the high-temperature heat capacity and the bulk conductivity of the $K_9H_7(SO_4)_8 \cdot H_2O$ crystal upon thermocycling in order to elucidate the nature of temperature hystereses and metastable states arising in the course of dehydration.

2. EXPERIMENTAL TECHNIQUE

Single crystals of $K_9H_7(SO_4)_8 \cdot H_2O$ in the form of colorless plates were grown from an aqueous solution by evaporation. The heat capacity was measured by the modulation calorimetry. The modulation frequency of thermal flux was equal to 1 Hz. Actually, we measured the relative change in the heat capacity. The samples were plates 2×2 mm in size and about 150 μm in thickness. In order to increase the absorption of modulated heat, the samples were blackened with soot. The chosen modulation frequency at the given sample sizes provided the quasi-adiabaticity of measurements over the entire temperature range. The fulfillment of this important condition was checked by the preliminary measurements of the frequency dependence of the heat wave amplitude according to the procedure described in detail in [3]. All the experiments were performed upon stabilization of the mean temperature of samples.

The bulk conductivity was measured with an alternating-current bridge at a frequency of 1 MHz. The thermocycling rate was varied in different experiments. Electrodes were applied by thermal evaporation of silver or with the use of a Degussa silver paste.

1063-7834/00/4208-1517$20.00

3. RESULTS AND DISCUSSION

Figure 1 demonstrates the temperature dependence of the heat capacity for the as-grown $K_9H_7(SO_4)_8 \cdot H_2O$ crystal in the first heating–cooling cycle. The jump in the heat capacity corresponds to the first-order phase transition to the superprotonic state (T_{sp} = 398 K). It is quite reasonable that the above condition for quasi-adiabaticity of measurements does not necessarily meet immediately at the phase transition point. However, this can affect only the magnitude of the jump in the heat capacity, but not the character of the $C_p(T)$ dependences above and below the phase transition point, which is of chief interest in our case. The heat capacity exhibits a jump only upon heating and monotonically decreases upon cooling. As is clearly seen from Fig. 1, the temperature dependences of the heat capacity upon heating and cooling coincide above the phase transition temperature and considerably differ below this temperature.

The temperature dependences of the conductivity for the $K_9H_7(SO_4)_8 \cdot H_2O$ crystal in two heating–cooling cycles are displayed in Fig. 2. It can be seen that the conductivity is described by the dependence $\sigma(T) \sim (1/T)\exp[-H/kT]$. According to the results obtained, the activation enthalpy H for conduction in the disordered phase is approximately equal to 0.47 eV, which is typical of protonic conductors. Moreover, it is seen that these curves, as for the heat capacity, substantially differ below T_{sp} for both thermal cycles.

It is essential that the differences in the dependences $C_p(T)$ and $\sigma(T)$ upon heating and cooling are not associated with the hysteresis characteristic of first-order phase transitions; i.e., no phase transition to the ordered phase is observed during the measurements (over a period of several hours) upon cooling the crystal. The absence of anomalies in the heat capacity and the conductivity upon cooling down to low temperatures, and the high conductivity (by several orders of magnitude higher than that upon heating), indicate the stabilization of the high-conductivity disordered phase. Furthermore, the $C_p(T)$ and $\sigma(T)$ dependences below T_{sp} are similar to those in the high-temperature disordered phase.

It should be noted that the temperature dependence of the heat capacity upon cooling in the first thermal cycle considerably deviates from linear behavior. The high-temperature heat capacity is most adequately described by the expression with the exponential term

$$C_p = A + BT + C(1/T^2)\exp[-H/kT]. \qquad (1)$$

Here, the last term follows from the known relationships for the thermally activated change in the concen-

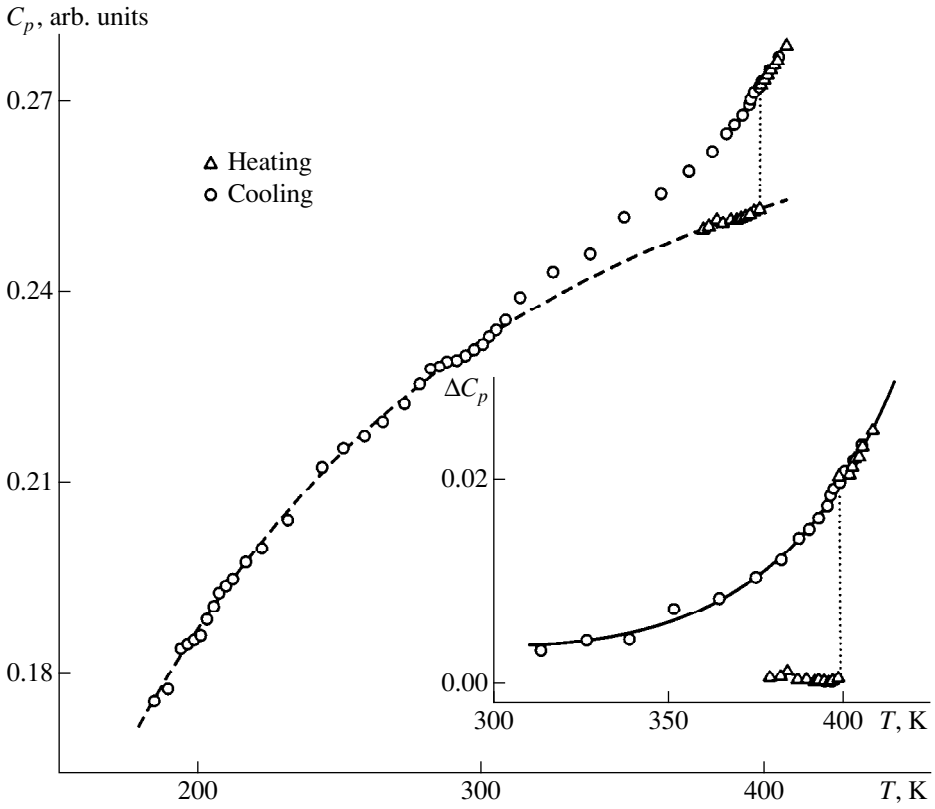

Fig. 1. Temperature dependences of the heat capacity for the $K_9H_7(SO_4)_8 \cdot H_2O$ crystal in the first heating–cooling cycle (dashed line, see text). The inset shows the exponential dependence of the excess heat capacity (solid line).

tration of defects $N \sim \exp[-H/kT]$ the enthalpy change caused by defects $\Delta H \sim N$, and the corresponding excess heat capacity $\Delta C_p \sim d/dT(\Delta H)$. The first term in formula (1) describes the phonon contribution. This contribution was evaluated from the low-temperature experimental points by extrapolating the sum of the Einstein and Debye model functions (the accuracy of these estimates is not very high, because the low-temperature heat capacity exhibit features associated with the specific relaxation phenomena considered in part earlier in [4]). The term linear in temperature accounts for the anharmonicity. The phonon contribution [the first and second terms in the right-hand side of relationship (1)] is shown in Fig. 1 by the dashed line.

The excess heat capacity ΔC_p was calculated by subtracting the approximating dependence of the phonon contribution from the experimental values of heat capacity. The temperature dependence of the excess heat capacity is depicted in the inset in Fig. 1, in which the solid line corresponds to the third term in relationship (1). It can be seen that the excess heat capacity of the $K_9H_7(SO_4)_8 \cdot H_2O$ crystal is sufficiently well described by the exponential temperature dependence. The least-squares approximation gives an activation enthalpy of 0.50 ± 0.03 eV. Within the limits of error, this value coincides with the activation enthalpy H found from the experimental dependence of the conductivity. The same value of H was obtained from the slope of the straight line on the $\ln(\Delta C_p T^2)$–$1/T$ coordinates. It is reasonable that the experimental data are more adequately described by the exponential function in the high-temperature range. As the temperature decreases, the errors in the approximation of the phonon contribution become more significant. For this reason, the error in determination of the activation enthalpy can increase.

The question arises now as to the origin of the exponential temperature dependence of the heat capacity observed upon cooling. It is clear that the time it takes for a thermal equilibrium to be attained in the phonon system is considerably shorter than the time of the experiment, and the anharmonicity contribution cannot be large at moderate temperatures (the melting temperature of the $K_9H_7(SO_4)_8 \cdot H_2O$ crystal is equal to ~500 K). This is supported by the fact that no pronounced nonlinearity is observed in the $C_p(T)$ dependence in the ordered phase upon heating. According to the available data on the dehydration of the $K_9H_7(SO_4)_8 \cdot H_2O$ crystal and the structural data for similar compounds, it can be inferred that the exponential nonlinear temperature dependence of the heat capacity is determined by the thermally activated change in the concentration of mobile defects formed as a result of the phase transition and dehydration in the disordered phase. This is also evidenced by the same (within the limits of error) activation enthalpies determined from the experimental data on the heat capacity and the conductivity. However, it can be assumed that

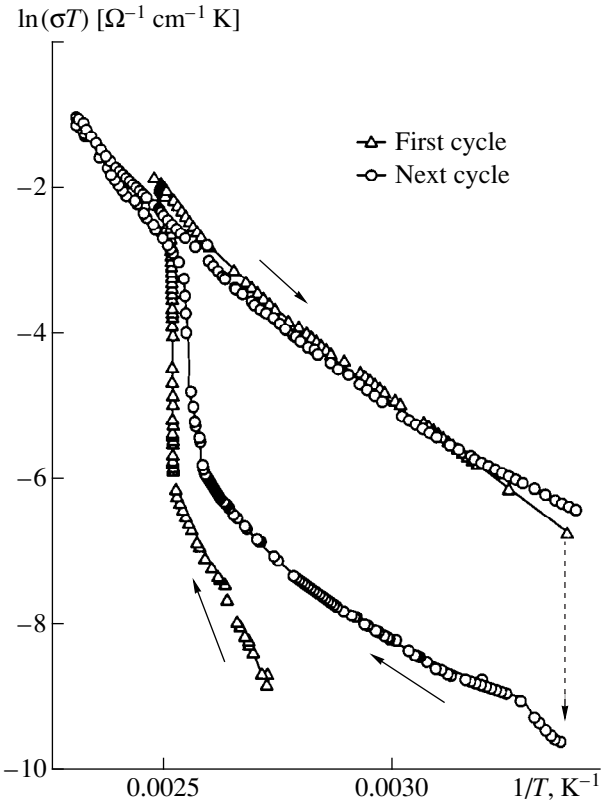

Fig. 2. Temperature dependences of the conductivity for the $K_9H_7(SO_4)_8 \cdot H_2O$ crystal in the first two heating–cooling cycles. The dashed arrow indicates the change in the conductivity at room temperature for 4 days after the first thermal cycle.

both mobile "acid" protons and other related structural defects contribute to the temperature dependence of the heat capacity. Indeed, the acid protons in the superprotonic phase are disordered over regular lattice sites and, in the strict sense, are not the structural defects. However, such a disordering of the acid protons results not only in the high conductivity of the crystal, but also in the high probability of the exchange between protons and crystallization water molecules. In turn, this stimulates the crystal dehydration process, which is governed by the diffusion of electroneutral water molecules toward the crystal surface and also by the formation and dissociation of oxonium ions H_3O^+. The contribution of the thermally activated defects to the conductivity of the disordered phase is either negligibly small (H_3O^+) or absent at all (H_2O). At the same time, these defects can contribute significantly to the heat capacity of the crystal at sufficiently high temperatures. Note that the exponential temperature dependence of the heat capacity was observed for metals in the premelting range due to the thermally activated formation of vacancies [5] and also for superionic conductors at high concentrations of mobile ions [6].

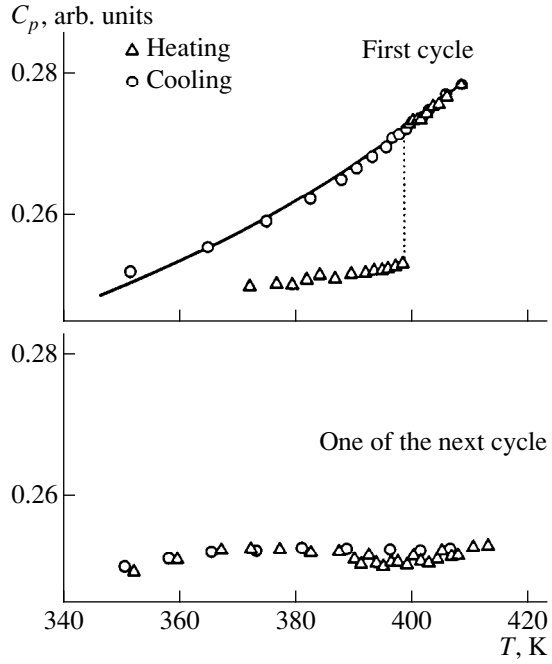

Fig. 3. Variation in the high temperature heat capacity of the $K_9H_7(SO_4)_8 \cdot H_2O$ crystal in two heating–cooling cycles. The solid line represents the approximation according to relationship (1).

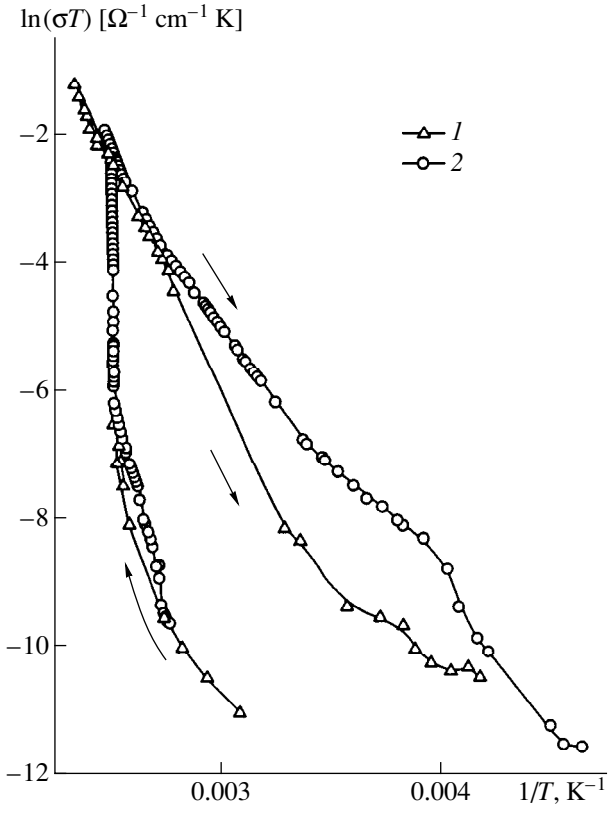

Fig. 4. Temperature dependences of the conductivity for the $K_9H_7(SO_4)_8 \cdot H_2O$ crystal samples in the first heating–cooling cycle under different conditions (see text).

The metastable state formed upon the phase transition is retained after the cooling of the crystal. The exponential decrease in the heat capacity with a decrease in the temperature is observed only for real times of measurements (over a period of several hours) and at real rates of change in the temperature from one experimental point to the next point (~1 K/min). After the cooling of the crystal and its holding, e.g., for a day at room temperature, the heat capacity in the subsequent cycles of measurements does not show exponential temperature behavior but follows the heating curve obtained in the first cycle of measurements (Fig. 3). Moreover, at this stage, neither phase transition nor temperature hysteresis are observed. This implies that the dehydration of the crystal has already been completed by the time of the onset of the second thermal cycle and the structural defects responsible for the diffusion of H_2O and H_3O^+ are absent. It is significant that the crystal after the cooling is in the disordered state even at room temperature, and the dehydration rate is considerably higher than that in the as-prepared sample, which initially was in the ordered state.

It seems likely that such behavior of the crystal is due to rather complex multistage solid-phase reactions, among which the dehydration–hydration processes play the key role. This is clearly seen from the changes observed in the IR absorption spectra with a change in the temperature [2]. In the cooled crystal, the dehydration can bring about the formation of a new phase (or a mixture of two phases) with the content of crystallization water ($x \cdot H_2O$) $x \ll 1$ and the structure differing from the initial monohydrate structure (note that the single-crystal state is retained). The structural phase transition is observed only in the equilibrium monohydrate structure. The formed state is metastable, because the inverse process of hydration becomes possible, the crystal recovers its original structure, and the phase transition occurs as before, etc. This solid-phase reaction proceeds rather slowly, and the monohydrate has no time to recover its initial state during the measurements of the heat capacity on the given time scale. However, this becomes possible in the cycles of the bulk conductivity measurements. After the first thermal cycle and treatment of the crystal at a moderate moisture (60%) for several days, the temperature dependences are reproduced; i.e., the superprotonic phase transition appears to be quasi-reversible (Fig. 2). As can be seen from Fig. 2, the conductivity at a fixed temperature decreases with time down to the value shown by the dashed arrow; upon the subsequent heating, the anomaly in the dependence $\sigma(T)$ at the phase transition point is reproduced, even though its magnitude is less than that in the first cycle. Certainly, the apparent disagreement of two experiments stems from different experimental conditions. A higher reaction rate in the case of conductivity measurements is caused by the presence of metallic electrodes on the studied sample. In this case, the initial monohydrate can rather rapidly recover its initial state according to the electrochemical

reaction $2e + 2H^+ + 1/2O_2 \longrightarrow H_2O$ and the subsequent diffusion of water molecules into the bulk. In this reaction, the electrodes play the role of catalysts. The kinetics of the above processes is a separate problem.

The interesting results were obtained in the conductivity measurements in the $K_9H_7(SO_4)_8 \cdot H_2O$ crystal under different conditions: the 30-min stabilization of temperature for the sample with thermally evaporated silver electrodes (the total duration of the thermal cycle was 40 h) (Fig. 4, curve *1*) and a continuous change in the temperature of the sample with Degussa silver paste electrodes at a rate of 0.1 K/min (the total duration of the thermal cycle was 8 h) (Fig. 4, curve *2*). It is seen that the curves for these samples upon the first heating virtually coincide both below and above the T_{sp} temperature. However, in the disordered phase upon cooling below ~350 K, the conductivity of the first sample becomes less than that of the second sample. This can be explained by different degrees of dehydration achieved in these samples upon cooling. A weak anomaly in the conductivity at $T \approx 250$ K for the second sample and a similar, but smeared, anomaly at a considerably higher temperature (≈350 K) for the first sample suggest that, under conditions of conductivity measurements, the kinetics of the reverse transition to the ordered low-conductivity phase is determined by the recovery rate of the initial hydrated crystal, which depends on the conditions of electrical measurements and the rate of change in the temperature. Below the temperatures of these anomalies, the crystal is in the two-phase state. This is confirmed by a lower conductivity as compared to the conductivity in the supercooled disordered phase at the same enthalpies and the constant T_{sp} temperature upon thermocycling.

Therefore, it was demonstrated that, unlike the known anhydrous alkali hydrosulfate salts, the superprotonic phase transition in the $K_9H_7(SO_4)_8 \cdot H_2O$ crystal is quasi-reversible, and the high-conductivity phase arising upon the structural phase transition is readily supercooled down to very low temperatures. These unusual properties of the crystal are explained by the partial or complete loss of structural crystallization water upon phase transition and thermocycling, which is governed by the experimental conditions. It was found that the temperature dependence of the heat capacity in the supercooled disordered phase exhibits exponential behavior due to the presence of mobile defects of the thermally activated nature. The explanation was provided for the agreement and disagreement between the obtained data on the heat capacity and the conductivity in the cases under consideration.

ACKNOWLEDGMENTS

This work was supported by the Russian Foundation for Basic Research, project no. 99-02-17443.

REFERENCES

1. A. I. Baranov, B. V. Merinov, A. V. Tregubchenko, *et al.*, Solid State Ionics **36**, 279 (1989).
2. A. I. Baranov, V. V. Sinitsyn, V. Y. Vinnichenko, *et al.*, Solid State Ionics **97**, 153 (1998).
3. E. D. Yakushkin and V. N. Anisimova, Prib. Tekh. Éksp., No. 3, 228 (1993).
4. A. I. Baranov, E. D. Yakushkin, D. J. Jones, and J. Roziere, Solid State Ionics **125**, 99 (1999).
5. Y. Kraftmakher, Eur. J. Phys. **15**, 329 (1994).
6. E. Gmelin, Thermochim. Acta **29**, 1 (1979).

Translated by O. Borovik-Romanova

Physics of the Solid State, Vol. 42, No. 8, 2000, pp. 1522–1528. Translated from Fizika Tverdogo Tela, Vol. 42, No. 8, 2000, pp. 1479–1485.

LOW-DIMENSIONAL SYSTEMS AND SURFACE PHYSICS

Effect of Quantizing Magnetic Field on the Spectrum and Damping of Polaritons in Double Two-Dimensional Electronic Systems

N. N. Beletskiĭ and S. A. Borisenko

Institute of Radiophysics and Electronics, Ukrainian Academy of Sciences, Kharkov, 310085 Ukraine
e-mail: beletski@ire.kharkov.ua

Received in final form January 11, 2000

Abstract—Nonradiative (surface and bulk) polaritons in a semiconductor structure composed of two heterojunctions GaAs/$Al_xGa_{1-x}As$ are investigated under the integer quantum Hall effect (IQHE) conditions. The dispersive, polarization, and energy characteristics of these polaritons are determined including energy dissipation in the two-dimensional electron semiconductor layers. The phase and group velocities of surface and bulk polaritons are shown to be quantized under the IQHE conditions. It is found that resonance coupling of two surface polariton modes may occur in double GaAs/$Al_xGa_{1-x}As$ heterojunctions. Possible experimental observation of nonradiative polaritons is discussed. © *2000 MAIK "Nauka/Interperiodica".*

1. Collective electromagnetic excitations in two-dimensional electron systems (2DESs) [1–5] attract considerable interest because of a significant advance having been made in the technology of GaAs/$Al_xGa_{1-x}As$ heterojunctions. Particular attention has been given to nonradiative (surface and bulk) polaritons, whose electromagnetic field is localized near the 2DES. These polaritons possess unusual and various properties, which are of practical and fundamental importance. Of particular interest are nonradiative polaritons in strong magnetic fields under the integer quantum Hall effect (IQHE) conditions [6–9]. In this case, the components of the 2DES conductivity tensor are quantized, i.e., they undergo abrupt changes in magnitude with magnetic field. As a result, the damping constants and phase and group velocities of nonradiative polaritons are also quantized.

The effect of a quantizing magnetic field B on the spectrum and damping of surface polaritons (SPs) in a single 2DES placed in a homogeneous dielectric medium was first treated in [6] and it was shown that the SP group velocity changes stepwise with magnetic field in the vicinity of cyclotron resonance. The magnitude of the steps was found to be proportional to the fine structure constant $\alpha = e^2/c\hbar$, where e is the electron charge and c is the velocity of light.

However, it should be noted that the model of a 2DES considered in [6] is oversimplified. An actual GaAs/$Al_xGa_{1-x}As$ heterojunction forming a 2DES has a more complex structure; the doped $Al_xGa_{1-x}As$ layer is of a finite thickness and is contiguous with air or vacuum, and the dielectric constants of GaAs and $Al_xGa_{1-x}As$ are different [10, 11]. For this reason, in a real GaAs/$Al_xGa_{1-x}As$ heterojunction, the magnitude of abrupt changes in the SP group velocity in the vicinity of cyclotron resonance depends not only on the thickness of the $Al_xGa_{1-x}As$ layer, but also on the relative values of the dielectric constants of GaAs and $Al_xGa_{1-x}As$ [7]. Furthermore, energy dissipation is shown [8] to be of importance in an actual GaAs/$Al_xGa_{1-x}As$ heterojunction; it leads to quantitative changes in the SP spectra and gives rise to new types of both surface and bulk nonradiative polaritons.

The properties of surface polaritons in a double 2DES were investigated in [9] and it was shown that, in this case, there are two SP modes, with the phase and group velocities of one of them being lower than the corresponding values for surface polaritons in a single 2DES. However, the SP dispersion and damping were considered in [9] under the assumption that the double 2DES was placed in a homogeneous dielectric medium. One may expect that the properties of surface polaritons are essentially different in a real double 2DES because of the appearance of new types of nonradiative polaritons and their possible interconvertion.

In this paper, we construct a theory of nonradiative surface and bulk polaritons in a double 2DES consisting of two real GaAs/$Al_xGa_{1-x}As$ heterojunctions and show that all characteristics of surface and bulk polaritons are quantized under the IQHE conditions. The effect of the geometrical sizes of a double 2DES on the spectrum, damping, and energy characteristics of nonradiative polaritons is investigated. Surface polaritons of the Brewster mode type and bulk polaritons of different orders are found to arise in a double 2DES with damping. It is shown that surface and bulk polaritons can transform into each other continuously.

1063-7834/00/4208-1522$20.00 © 2000 MAIK "Nauka/Interperiodica"

2. As a model of a double 2DES, we consider the structure depicted in Fig. 1. Semi-infinite medium *1* in the $z < 0$ half-space (substrate) is assumed to be semiconductor GaAs with permittivity $\varepsilon_3 = 12.9$. The layers $0 < z < d$ (region *2*) and $d < z < d + d'$ (overlayer, region *3*) are semiconductors $Al_xGa_{1-x}As$ ($\varepsilon_2 = 12.0$) and GaAs ($\varepsilon_3 = 12.9$), respectively. Semi-infinite medium *4* ($z > d + d'$) is air (or vacuum) with permittivity $\varepsilon_1 = 1$. Therefore, there are two GaAs/$Al_xGa_{1-x}As$ heterojunctions, located in the $z = 0$ and $z = d$ planes and forming 2DESs in these planes. An external quantizing magnetic field B is applied along the z axis normal to the two 2DESs. Surface and bulk polaritons in the double 2DES are assumed to be nonradiative; that is, their electromagnetic fields exponentially decrease to zero in media *1* and *4* with the distance from the boundaries of these media. Without loss of generality, we assume that polaritons propagate along the x axis. The dependences of all electromagnetic fields on the coordinate x and time t are taken to be $\exp[i(kx - \omega t)]$, where k is the wavenumber and ω is the frequency of polaritons.

In order to find the dispersion relation describing the propagation of polaritons in the double 2DES, we should consider waves of the TE and TM types [12] because of the presence of surface currents in the interfaces $z = 0$ and $z = d$, which affect both TE and TM waves. The tangential components of the electric field E of polaritons are continuous across all boundaries of the double 2DES, while the tangential components of their magnetic field H are continuous only across the $z = d + d'$ plane, but they suffer a discontinuity at the planes $z = 0$ and $z = d$.

Let $\sigma_{ij}^{(p)}(\omega)$ be the components of the conductivity tensor of the two 2DESs, where $p = 1$ and 2 for the 2DESs in the planes $z = 0$ and $z = d$, respectively. Then, the jump in the tangential components of the magnetic field of polaritons at the $z = 0$ plane is

$$H_{x,2}(0) - H_{x,1}(0) = \frac{4\pi}{c}(\sigma_{xx}^{(1)}E_y(0) - \sigma_{xy}^{(1)}E_x(0)), \quad (1a)$$

$$H_{y,2}(0) - H_{y,1}(0) = -\frac{4\pi}{c}(\sigma_{xx}^{(1)}E_x(0) - \sigma_{xy}^{(1)}E_y(0)). \quad (1b)$$

Similar expressions can also be written for the jump in the tangential components of the magnetic field of polaritons at the $z = d$ plane.

Spatial dispersion of the 2DES conductivity tensors is assumed to be negligible, which takes place under the condition $kl \ll 1$, where $l = (c\hbar/eB)^{1/2}$ is the magnetic length. In this case, the nonzero components of the 2DES conductivity tensor have the form [6–9]

$$\sigma_{xx}^{(p)} = \frac{2e^2}{h}\frac{N_p\gamma}{1+\gamma^2}, \quad (2a)$$

$$\sigma_{xy}^{(p)} = \frac{2e^2}{h}\frac{N_p}{1+\gamma^2}. \quad (2b)$$

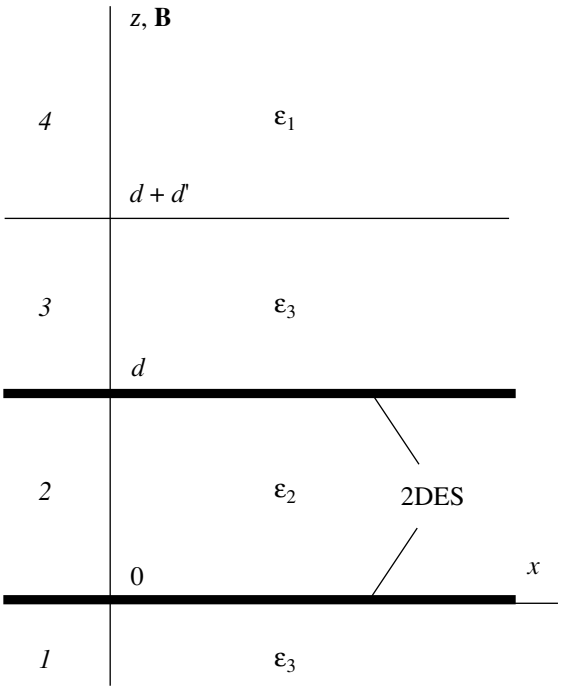

Fig. 1. Geometry of the double 2DES. The semi-infinite medium *1* (substrate) is a GaAs semiconductor with $\varepsilon_3 = 12.9$; medium *2* is an $Al_xGa_{1-x}As$ semiconductor layer with a thickness d and $\varepsilon_2 = 12.0$; medium *3* (overlayer) is a GaAs semiconductor layer with a thickness d' and $\varepsilon_3 = 12.9$; and the semi-infinite medium *4* is vacuum (air) with $\varepsilon_1 = 1$.

Here, $h = 2\pi\hbar$; $\gamma = (\nu - i\omega)/\Omega$; $\Omega = eB/mc$ is the cyclotron frequency of electrons; ν is the momentum relaxation rate of electrons, and $N_p = \pi l^2 n_p$ is the degree of the Landau level filling, which takes integral values ($N_p = 1, 2, \ldots$) equal to the number of completely filled Landau levels, lying below the Fermi level (n_p is the electron density in the corresponding 2DES).

Using the boundary conditions indicated above, we obtain the following dispersion equation for propagating nonradiative polaritons in the double 2DES under study:

$$\begin{aligned}&[A_1\exp(p_2d) + rA_2\exp(-p_2d)]\\ &\times[A_3\exp(-p_2d) + rA_4\exp(p_2d)]\\ &= (B_1 - rB_2)(B_3 - rB_4),\end{aligned} \quad (3)$$

where

$$r = N_1/N_2,$$

$$A_1 = LF + (4\pi\sigma_{xy}^{(1)}/c)^2 p_2 p_3,$$

$$A_2 = PR/(AB) + (4\pi\sigma_{xy}^{(2)}/c)^2 p_2 p_3,$$

$$A_3 = KD + (4\pi\sigma_{xy}^{(1)}/c)^2 p_2 p_3,$$

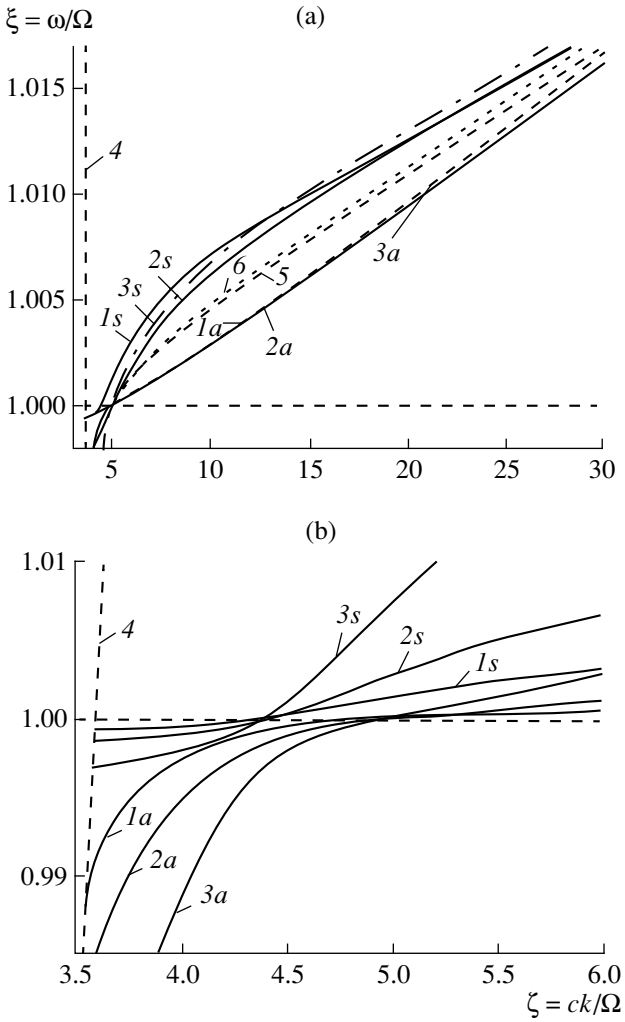

Fig. 2. Spectrum $\xi(\zeta)$ of low-frequency (index *a*) and high-frequency (index *s*) surface polaritons in a double 2DES with $N_1 = N_2 = N$, $\Gamma = 0$, and $\delta = 0.1$ for different values of N and δ': (a) $N = 1$ and δ' being equal to 0.1 (*1*) and 1.0 (*2*); and (b) $\delta = 0.1$, $\delta' = 0.1$, and N being equal to 1 (*1*), 2 (*2*), and 5 (*3*). The dotted line *4* is a dispersion curve of light for GaAs ($\xi = \zeta/\sqrt{\varepsilon_3}$). The dispersion curves *5* ($\varepsilon_2 = 12.0$, $\varepsilon_3 = 12.9$) and *6* ($\varepsilon_2 = \varepsilon_3 = 12.0$) correspond to a single 2DES being contiguous with two dielectric media with permittivities ε_2 and ε_3.

$$A_4 = QM/(AB) + (4\pi\sigma_{xy}^{(2)}/c)^2 p_2 p_3,$$

$$B_1 = KF - (4\pi\sigma_{xy}^{(1)}/c)^2 p_2 p_3,$$

$$B_2 = PQ/(AB) + (4\pi\sigma_{xy}^{(2)}/c)^2 p_2 p_3,$$

$$B_3 = LD - (4\pi\sigma_{xy}^{(1)}/c)^2 p_2 p_3,$$

$$B_4 = RM/(AB) + (4\pi\sigma_{xy}^{(2)}/c)^2 p_2 p_3,$$

$$A = \varepsilon_1 p_3 - \varepsilon_3 p_1 - (\varepsilon_1 p_3 + \varepsilon_3 p_1)\exp(2p_3 d'),$$

$$B = p_3 - p_1 + (p_3 + p_1)\exp(2p_3 d'),$$

$$C = \varepsilon_1 p_3 - \varepsilon_3 p_1 + (\varepsilon_1 p_3 + \varepsilon_3 p_1)\exp(2p_3 d'),$$

$$D = \varepsilon_2 p_3 - \varepsilon_3 p_2 - i4\pi\sigma_{xx}^{(1)} p_2 p_3/\omega,$$

$$F = \varepsilon_2 p_3 + \varepsilon_3 p_2 + i4\pi\sigma_{xx}^{(1)} p_2 p_3/\omega,$$

$$G = p_3 - p_1 - (p_3 + p_1)\exp(2p_3 d'),$$

$$K = p_2 - p_3 + i4\pi\omega\sigma_{xx}^{(1)}/c^2,$$

$$L = p_2 + p_3 - i4\pi\omega\sigma_{xx}^{(1)}/c^2,$$

$$M = \varepsilon_3 p_2[C - i4\pi p_3\sigma_{xx}^{(2)} A/(\omega\varepsilon_3)] - A\varepsilon_2 p_3,$$

$$P = \varepsilon_3 p_2[C - i4\pi p_3\sigma_{xx}^{(2)} A/(\omega\varepsilon_3)] + A\varepsilon_2 p_3,$$

$$Q = p_3 G - p_2 B + i4\pi\omega\sigma_{xx}^{(2)} B/c^2,$$

$$R = p_3 G + p_2 B + i4\pi\omega\sigma_{xx}^{(2)} B/c^2.$$

Here, the quantities

$$p_i = \sqrt{k^2 - \frac{\omega^2}{c^2}\varepsilon_i}, \quad i = 1, 2, 3 \qquad (4)$$

are the transverse wavenumbers characterizing the z dependence of the electromagnetic field of polaritons. For nonradiative polaritons, the conditions $\mathrm{Re}\,p_1 > 0$ and $\mathrm{Re}\,p_3 > 0$ should be fulfilled.

It is easily seen that equation (3) also describes the limiting cases of a single 2DES [6–8] and the double 2DES considered in [9].

3. We solved the dispersion equation (3) numerically by introducing the dimensionless quantities $\xi = \omega/\Omega$, $\zeta = ck/\Omega$, $\Gamma = \nu/\Omega$, $\delta = d\Omega/c$, and $\delta' = d'\Omega/c$. Let us first discuss the case of $\Gamma = 0$, where one can ignore energy dissipation in the double 2DES. From the condition $\mathrm{Re}\,p_3 > 0$, it follows that (for $\varepsilon_3 > \varepsilon_2$) only surface polaritons can exist in the double 2DES without energy dissipation.

Let the Landau level filling be the same in both 2DESs, $N_1 = N_2 = N$. Figure 2a shows the SP spectrum in the double 2DES with $N = 1$, $\Gamma = 0$, and $\delta = 0.1$ for two values of δ': 0.1 (solid lines *1*) and 1.0 (solid lines *2*). Because there exist two polariton modes in the double 2DES, we refer to one of them (with a lower frequency) as the low-frequency mode and to the other (with a higher frequency) as the high-frequency mode. The former mode is designated by the index *a* and the latter, by the index *s*. For comparison, Fig. 2a also shows dispersion curves (dashed lines 3*a* and 3*s*) for the double 2DES considered in [9] ($N = 1$, $\delta = 0.1$, $\delta' = 0.0$, $\varepsilon_1 = \varepsilon_2 = \varepsilon_3 = 12.0$) and two dispersion curves (dotted lines *5* and *6*) for a single 2DES. Curve *6* corresponds to the case of a single 2DES embedded in a homogeneous medium with a permittivity $\varepsilon = 12.0$ [6], while curve *5*, to the case where a single 2DES is contiguous, on its

one side, with a medium of a permittivity $\varepsilon_2 = 12.0$ and, on the other side, with a medium of a permittivity $\varepsilon_3 = 12.9$ [7]. The dashed line *4* is a dispersion curve of light for GaAs ($\xi = \zeta/\sqrt{\varepsilon_3}$). In the limit $\zeta \longrightarrow \infty$, where the penetration depths of the SP electromagnetic field into the surrounding media vanish, the dispersion curves *1a*, *1s*, *2a*, and *2s* asymptotically tend to the dispersion curve *5*, whereas the dispersion curves *3a* and *3s* tend to the dispersion curve *6*.

From Fig. 2a, it is seen that the quantity δ' affects the low-frequency SP modes only slightly. The point is that, in these modes, the surface charges of the two 2DESs oscillate in counterphase, i.e., they are opposite in sign. In this case, the electromagnetic field of low-frequency SP modes is localized between the 2DESs in the layer $0 < z < d$, i.e., in the $Al_xGa_{1-x}As$ layer. Hence, virtually all energy of low-frequency SP modes is transferred in the region between the 2DESs. In high-frequency SP modes, in contrast, oscillations of the surface charges of the two 2DESs are in phase and, hence, the electromagnetic field of these modes is concentrated predominantly outside the region $0 < z < d$. As a result, a high proportion of the energy of high-frequency SP modes is transferred in medium *3* and, hence, the spectrum of these modes depends heavily on the value of δ'.

Low- and high-frequency SP modes are coupled near cyclotron resonance ($\xi \approx 1$), which leads to their transformation into each other and to the repulsion between their dispersion curves. From Fig. 2a, it is seen that the position of the mode–mode coupling region depends on the value of δ' and this region can lie to the right ($\delta' = 1.0$), as well as to the left ($\delta' = 0.1$), of the mode–mode coupling region for the double 2DES considered in [9]. The repulsion between dispersion curves of the modes is the strongest at $\delta' = 0.1$. The reason is that, as δ' decreases, the mode–mode coupling region shifts towards the long-wavelength part of the spectrum. Hence, the penetration depth of the SP electromagnetic field into the $Al_xGa_{1-x}As$ layer increases and the coupling of the low- and high-frequency SP modes becomes stronger.

It should be noted that the surface polaritons have essentially different properties in the actual double 2DES under study and the double 2DES considered in [9]. The most important distinction is that, in the actual double 2DES, both SP modes can be slower than in the case treated in [9] in the high-frequency region $\xi > 1$. For instance, high-frequency SP modes (dispersion curves *1s* and *2s*) can lie above, as well as below, the dispersion curve *3s*, depending on the value of δ'. At large δ' values ($\delta' = 1.0$), the dispersion curve *2s* lies completely below the dispersion curve *3s*. Therefore, in this case, the phase velocity of high-frequency SP modes in the actual 2DES is lower than in the double 2DES dealt with in [9]. At the same time, at small δ' values ($\delta' = 0.1$), the dispersion curve *1s* first runs above

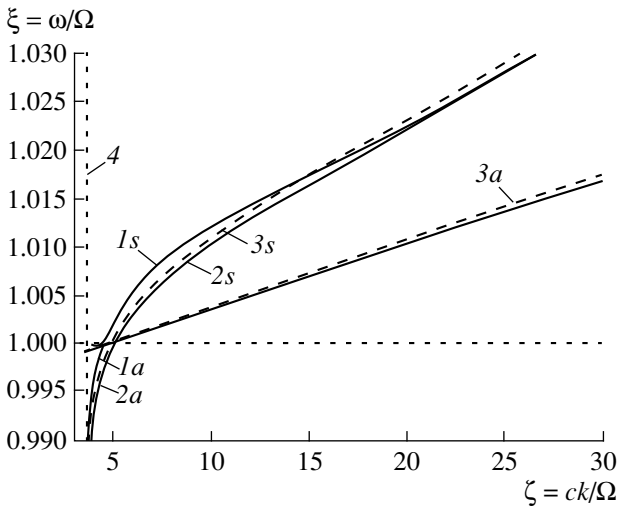

Fig. 3. Spectrum $\xi(\zeta)$ of low-frequency (index *a*) and high-frequency (index *s*) surface polaritons in a double 2DES with $N_1 = 1$, $N_2 = 2$, $\delta = 0.1$, $\Gamma = 0$, and different values of δ': 0.1 (*1*) and 1.0 (*2*); the dashed curves *3a* and *3s* are the spectrum of polaritons in the double 2DES considered in [9]; the dotted line *4* is a dispersion curve of light for GaAs ($\xi = \zeta/\sqrt{\varepsilon_3}$).

the dispersion curve *3s*, but then drops below it and asymptotically approaches the dispersion curve *2s* with increasing ζ. Therefore, in the double 2DES under study, high-frequency SP modes are faster in the long-wavelength spectral region but slower in the short-wavelength region than in the case considered in [9]. A similar situation also takes place for low-frequency SP modes (dispersion curves *1a* and *2a*), but δ' has only a marginal effect on them. Therefore, the phase velocity of high-frequency SP modes can be varied in the long-wavelength spectral region by varying δ'.

Now, we consider the effect of the Landau level filling *N* on the dispersive properties of surface polaritons. Figure 2b shows SP dispersion curves for double 2DESs with $\delta = 0.1$, $\delta' = 0.1$, and three different values of $N_1 = N_2 = N = 1$, 2, and 5 (solid curves *1*, *2*, *3*, respectively). It is seen from this figure that, near cyclotron resonance, the high-frequency (index *s*) and low-frequency (index *a*) SP modes resonantly interact and transform into each other. As ζ increases, the low-frequency SP modes change over from fast waves to slow ones. For the high-frequency SP modes, the reverse situation is observed: slow modes continuously transform into fast ones. It is significant that the group velocity of both high- and low-frequency SP modes undergoes abrupt changes near cyclotron resonance, because the Hall conductivity of the 2DES is quantized. We note that the initial points of SP dispersion curves, lying on the light dispersion curve *4* ($\xi = \zeta/\sqrt{\varepsilon_3}$) shift to higher frequencies with decreasing *N*. It is also significant that, in the $\xi > 1$ region, the properties of high-fre-

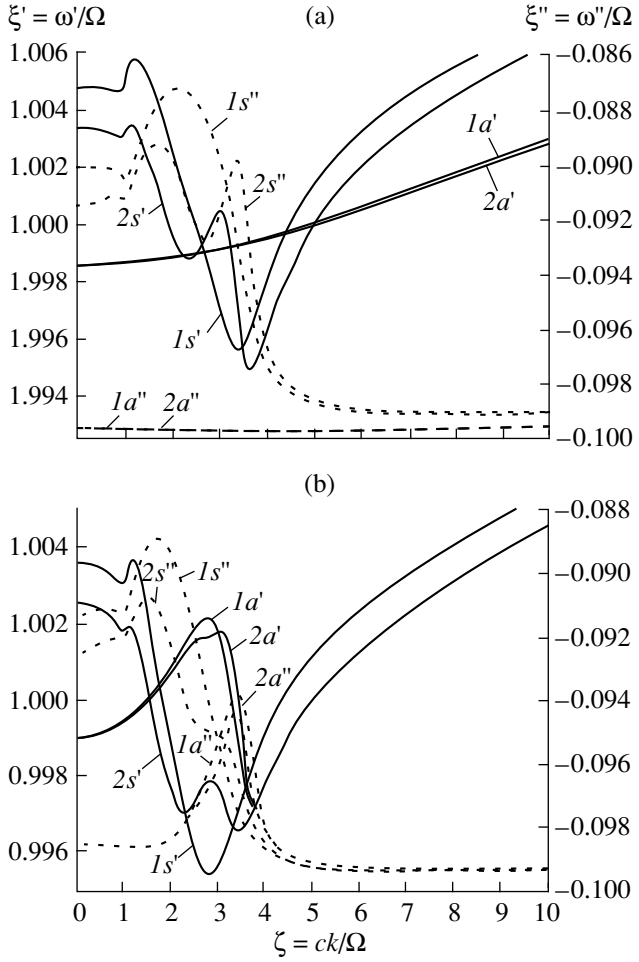

Fig. 4. Spectrum ξ'(ζ) (solid lines labeled by letters with a prime) and damping ξ''(ζ) (dotted curves labeled by letters with a double prime) for low-frequency (index *a*) and high-frequency (index *s*) nonradiative polaritons in a double 2DES with $N_1 = N_2 = 1$, Γ = 0.1, and δ' being equal to 0.1 (curves *1*) and 1.0 (curves *2*) for two values of δ: (a) 0.1 and (b) 1.0.

quency SP modes are similar to the properties of surface polaritons in a single 2DES with the Landau level filling twice as high: $N = N_1 + N_2$. This is further proof that the electromagnetic field of a high-frequency SP mode is concentrated predominantly outside the $0 < z < d$ layer.

Let us now consider the case of two 2DESs having different Landau level filling, $N_1 \neq N_2$. Figure 3 shows the SP spectrum of a double 2DES with $N_1 = 1$, $N_2 = 2$, δ = 0.1, and Γ = 0 for two different values of δ': 0.1 (solid lines *1a* and *1s*) and 1.0 (solid lines *2a* and *2s*). The dashed lines *3a* and *3s* depict the SP spectrum of the double 2DES considered in [9] ($N_1 = 1$, $N_2 = 2$, δ = 0.1, δ' = 0.0, $\varepsilon_1 = \varepsilon_2 = \varepsilon_3 = 12.0$). From Fig. 3, it is seen that, in the actual double 2DES, the SP modes in the short-wavelength spectral range are slower than in the case treated in [9]. In the long-wavelength range, the SP phase velocity depends crucially on δ' and can be lower (δ' = 1.0), as well as higher (δ' = 0.1), than the SP phase velocity in the double 2DES dealt with in [9]. Near cyclotron resonance, the position of the region where the low- and high-frequency SP modes resonantly interact with each other is sensitive to the value of δ'. As δ' increases, this region moves away from the dispersion curve *4* for light in GaAs ($\xi = \zeta/\sqrt{\varepsilon_3}$).

It should be noted that the double 2DES under consideration is asymmetrical. For this reason, in a double 2DES with $N_1 \neq N_2$, the dispersive properties of surface polaritons depend not only on the Landau level filling N_1 and N_2, but also on the mutual disposition of the 2DESs.

4. Now, we consider the effect of energy dissipation (Γ ≠ 0) on the properties of nonradiative polaritons in a double 2DES. The wavenumber *k* is assumed to be real, while the frequency $\omega = \omega' + i\omega''$ is complex, and the notation $\xi' = \omega'/\Omega$, $\xi'' = \omega''/\Omega$ is introduced.

In Fig. 4a, the solid curves labeled by letters with a prime represent the spectrum ξ'(ζ) (the ordinate axis on the left), while the dotted curves labeled by letters with a double prime represent damping ξ''(ζ) (the ordinate axis on the right) of low-frequency (letter *a*) and high-frequency (letter *s*) nonradiative polariton modes in a double 2DES with $N_1 = N_2 = 1$, δ = 0.1, and Γ = 0.1 for two values of δ': 0.1 (*1*) and 1.0 (*2*). From the figure, it is seen that nonradiative polaritons exist in the double 2DES with energy dissipation for all values of ζ. It is significant that the ξ'(ζ) dependences are nonmonotonic. For example, the dispersion curve *1s*' has two sections on which the derivative $\partial\xi'/\partial\zeta$ is positive, while curve *2s*' has three such sections. We note that each section with a positive $\partial\xi'/\partial\zeta$ corresponds to a certain type of nonradiative (surface or bulk) polaritons. In the dispersion curve *1s*', the first section with $\partial\xi'/\partial\zeta > 0$ corresponds to Brewster-type SP modes, which arise on the boundary $z = d + d'$. The Brewster modes of a TM polarization were predicted [2, 4] to arise on the interface between two dissipative media in which the real part of the permittivity is positive. A peculiarity of our case is that the Brewster-type SP modes in question have a mixed polarization and they are "bound" to the $z = d + d'$ interface because of energy dissipation in the two 2DESs situated at the boundaries $z = 0$ and $z = d$. From Fig. 4a, it is seen that the Brewster modes are formed at the $z = d + d'$ interface if $\zeta \approx \sqrt{\varepsilon_1} = 1$. Near this value of ζ, the component of the average energy flux $S(z) = (c/8\pi)\mathrm{Re}[\mathbf{EH}^*]$ along the *x* axis has a maximum in air (vacuum) in the vicinity of the boundary $z = d + d'$.

The dependence of $S_x(\chi)/S_x(+0)$ on the dimensionless coordinate $\chi = z\Omega/c$ along the *z* direction [$S_x(+0)$ is the *x* component of the average energy flux at the point $z = +0$] is presented in Fig. 5 for a double 2DES with $N_1 = N_2 = 1$, Γ = 0.1, δ = 0.1, and δ' = 0.1 for three points of the dispersion curves *1a*' and *1s*' (Fig. 4a) hav-

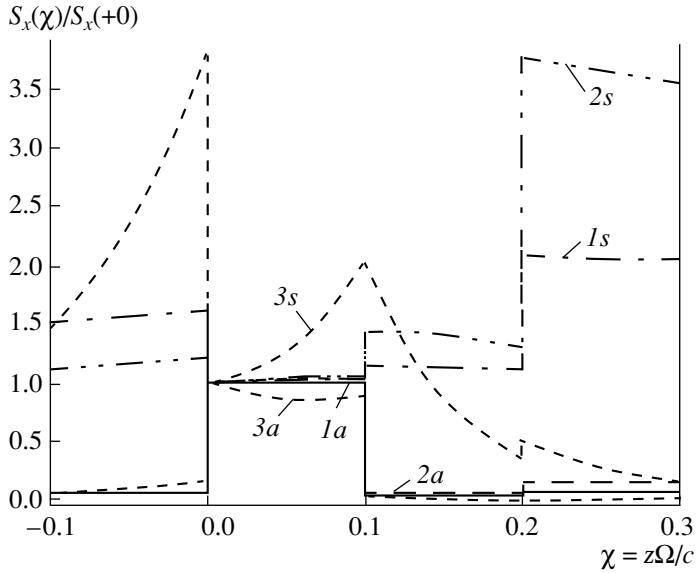

Fig. 5. $S_x(\chi)/S_x(+0)$ dependences for low-frequency (index *a*) and high-frequency (index *s*) nonradiative polaritons in a double 2DES with $N_1 = N_2 = 1$, $\Gamma = 0.1$, and $\delta = \delta' = 0.1$ for different values of ζ: 0.1 (*1*), 1.0 (*2*), and 6.0 (*3*).

ing the following ζ coordinates: 0.1 (*1*), 1.0 (*2*), and 6.0 (*3*). From Fig. 5, it is seen that, at all these points, the *x* component of the energy flux of low-frequency modes of nonradiative polaritons (curves *1a*, *2a*, *3a* in Fig. 5) is maximum in the layer $0 < z < d$ and is virtually constant with ζ. At the same time, the $S_x(\chi)/S_x(+0)$ distribution of high-frequency modes of nonradiative polaritons is heavily dependent on ζ in the double 2DES. For example, at the point of the dispersion curve *1s*' (Fig. 4a) with $\zeta = 0.1$ (curve *1s* in Fig. 5), the energy is transferred along the *x* axis predominantly outside the double 2DES, in the regions $z < 0$ and $z > d + d'$. At the point with $\zeta = 1.0$, the energy flux $S_x(\chi)/S_x(+0)$ increases sharply near the boundary $z = d + d'$ (curve *2s* in Fig. 5), which is associated with the formation of the Brewster mode near this boundary. Finally, at the point with $\zeta = 6.0$ (belonging to the second section with $\partial\xi'/\partial\zeta > 0$ of the dispersion curve *1s*'), the energy is transferred near the $z = 0$ and $z = d$ boundaries of the 2DESs. This energy distribution corresponds to the formation of surface polaritons in the double 2DES.

As δ' increases, the properties of high-frequency polariton modes change qualitatively in the long-wavelength spectral range. For instance, between the abovementioned two sections with $\partial\xi'/\partial\zeta > 0$ of the dispersion curve *2s*' (Fig. 4a), there appears another section, which corresponds to the formation of a first-order bulk polariton in the layer of the thickness δ'. For a bulk polariton of this type, the $S_x(\chi)/S_x(+0)$ dependence has one more maximum in the layer of the thickness δ'. We note that the damping of nonradiative polaritons is higher in the regions where surface and bulk modes exist.

Now, let us discuss the effect of δ on the properties of polaritons in the double 2DES. Figure 4b shows the spectrum and damping of low-frequency (index *a*) and high-frequency (index *s*) polariton modes in the double 2DES with $N_1 = N_2 = 1$, $\delta = 0.1$, and $\Gamma = 0.1$ for two values of δ': 0.1 (*1*) and 1.0 (*2*). From the figure, it is seen that the dispersion curves *1s*' and *2s*' (Fig. 4a) do not change qualitatively with increasing δ. The dispersion curves *1a*' and *2a*', on the contrary, are heavily affected. For example, there appears one more section with $\partial\xi'/\partial\zeta > 0$ in these curves, which corresponds to the formation of a first order bulk polariton in the layer of the thickness δ. For this polariton, the energy flux along the *x* direction has a maximum in the $0 < z < d$ layer. We note that, at $\delta' = 1.0$, one more maximum of the energy flux arises in the layer $d < z < d + d'$, which leads to the appearance of an inflection point in the dispersion curve *2a*' (Fig. 4b).

In closing, it is worthy of note that a large number of different types of surface and bulk polaritons can exist in the double 2DES of two GaAs/Al_xGa_{1-x}As heterojunctions under the integer quantum Hall effect conditions. Their properties depend critically on both the geometrical sizes of the double 2DES and the strength of the quantizing magnetic field. This allows one to use nonradiative polaritons for contactless diagnostics of the parameters of double GaAs/Al_xGa_{1-x}As heterojunctions. One can use these polaritons for determining the geometrical sizes of double 2DESs, the momentum relaxation rate of electrons in them, and the degree of Landau level filling. Furthermore, the nonradiative polaritons have the potential to be used in various devices of modern semiconductor nanoelectronics

because of their phase and group velocities being small and their properties being quantized.

Experimentally, the nonradiative polaritons in a double 2DES can be investigated using the method of frustrated total internal reflection [1, 2] or inelastic light scattering [13]. The latter method allows one to excite nonradiative polaritons with large values of k ($k \sim 2 \times 10^5$ cm^{-1}); slow surface polaritons in 2DESs with $N = 1$ under the IQHE conditions have been discovered by this method.

REFERENCES

1. *Surface Polaritons*, Ed. by V. M. Agranovich and D. L. Mills (North-Holland, Amsterdam, 1982; Mir, Moscow, 1985).
2. *Electromagnetic Surface Modes*, Ed. by A. D. Boardman (Wiley, New York, 1982).
3. T. Ando, B. Fowler, and F. Stern, Rev. Mod. Phys. **54**, 437 (1982).
4. R. S. Brazis, Litov. Fiz. Sb. **21** (4), 73 (1981).
5. Yu. A. Kosevich, A. M. Kosevich, and J. C. Granada, Phys. Lett. A **127**, 52 (1988).
6. I. E. Aronov and N. N. Beletskii, J. Phys.: Condens. Matter **8**, 4919 (1996).
7. N. N. Beletskii, G. P. Berman, A. R. Bishop, and S. A. Borisenko, J. Phys.: Condens. Matter **10**, 5781 (1998).
8. N. N. Beletskiĭ and S. A. Borisenko, Fiz. Tverd. Tela (St. Petersburg) **41**, 705 (1999) [Phys. Solid State **41**, 636 (1999)].
9. I. E. Aronov, N. N. Beletskii, G. P. Berman, and A. R. Bishop, Phys. Rev. B **56**, 10 392 (1997).
10. N. C. Constantinou and M. G. Cottam, J. Phys.: Condens. Matter **19**, 739 (1986).
11. R. F. Wallis and J. J. Quinn, Phys. Rev. B **38**, 4205 (1988).
12. M. Nakayama, J. Phys. Soc. Jpn. **36**, 393 (1974).
13. L. L. Sohn, A. Pinczuk, B. S. Dennis, *et al.*, Solid State Commun. **93** (11), 897 (1995).

Translated by Yu. Epifanov

Physics of the Solid State, Vol. 42, No. 8, 2000, pp. 1529–1534. Translated from Fizika Tverdogo Tela, Vol. 42, No. 8, 2000, pp. 1486–1491.

LOW-DIMENSIONAL SYSTEMS AND SURFACE PHYSICS

Effect of Localized-Exciton Energy Relaxation on the Emission Spectrum of ZnS–ZnSe Single Quantum Wells

N. V. Bondar'

Institute of Physics, National Academy of Sciences of Ukraine, pr. Nauki 144, Kiev, 258650 Ukraine

e-mail: vvti@iop.kiev.ua

Received January 24, 2000

Abstract—A study is reported on the dependence of exciton photoluminescence spectra of ZnS–ZnSe quantum wells with different localization-center concentrations on the excitation intensity and temperature. The shape of the experimental low-temperature photoluminescence band is shown to agree well with that calculated in a model of exciton hopping to the nearest localization center and in one that takes into account transitions of a localized exciton to all centers in its local environment. The parameters characterizing localized excitons in these quantum structures of a submonolayer thickness have been determined. *© 2000 MAIK "Nauka/Interperiodica".*

As follows from numerous experimental studies, the emission spectra of quantum structures of a submonolayer thickness are due to the recombination of the excitons localized in wells of the potential relief created by thickness fluctuations of semiconducting layers [1–11]. The fluctuations represent islands whose height does not exceed, as a rule, that of a monolayer (ML) and whose lateral dimensions (ξ) are of the order of the exciton Bohr radius. However, the formation of a low-temperature photoluminescence (PL) band in quantum-well (QW) structures is governed in most cases not only by the character of disordered interfaces but also by the kinetics of population of the density-of-states tail originating from thickness fluctuations, as a result of which the maximum of the PL band at low temperatures is shifted, as a rule, with respect to the minimum (maximum) of the exciton spectrum of reflectance (absorption) [1–4]. The nature of this shift is associated with the energy relaxation process, which assumes that excitons rapidly reach deep states in the density-of-states tail in times shorter than their radiative recombination time τ_0. Under steady-state excitation, the magnitude of the shift ε_m depends on the excitation intensity (i.e., on the *e–h* pair generation rate G) and the temperature T and can be readily observed experimentally. As T or G increases, the ensuing activation of states in the tail or its filling by excitons brings about a shift of the PL band maximum to shorter wavelengths, to the energy E_c corresponding to the mobility edge of localized excitons and, as the pump intensity or T continues to grow, the PL band starts to broaden toward shorter wavelengths as a result of a transition to emission from delocalized and free states [1, 12, 13].

A second case, observed to occur frequently in QWs, that is also interesting, is where neither the spectral position nor the shape of the PL band whose maximum underwent a large Stokes shift depends on pump density and T [11, 14]. As follows from a statistical topographic model of excitonic PL [11], such QWs exhibit a linear relation between ε_m and the full width at half maximum W of the absorption spectrum, namely, $\varepsilon_m = 0.553\ W$. In contrast to the first case, the shape of the PL band is symmetrical here and can be fitted by a Gaussian. Most of the theoretical and experimental studies concerning these issues consider primarily either the first [1–5, 8, 9, 12, 13] or the second case [6, 7, 10, 11, 14, 15] in QWs or superlattices with different nominal thicknesses L_z prepared by different technologies. It appeared, therefore, of interest to show that both cases can be observed in QWs having the same thickness L_z. If the latter condition is met, the binding energy, the Bohr radius (in both directions), the radiative lifetime, and other excitonic parameters, which depend on L_z and on which the Stokes shift ε_m depends in one way or another, will be identical and, therefore, the probability of observing the first or second situation in a QW will be determined by the structure of the disordered interfaces.

This work analyzes the emission spectra of single ZnS–ZnSe QWs in an attempt at establishing the effect exerted on their shape and spectral location by the relaxation of localized excitons in energy. Studies on QWs with equal nominal thicknesses under steady-state excitation revealed that the excitonic PL spectrum of each QW was shifted relative to the minimum in the reflectance spectrum by an amount varying from 6 to 13 meV, depending on the sample, in some of which the shift was found to be dependent on the pump intensity and temperature. We used the main results presented in [12, 13] to calculate two exciton energy distributions $n(\varepsilon)$ assuming the tail of the density-of-states function to have an exponential shape. It was shown that, within

a certain localization-center concentration region, the $n(\varepsilon)$ curves obtained by both models agree well with one another and with the experimental excitonic-PL band of one of the QWs chosen. The fitting parameters $N_0\alpha^2$, $\tau_0\nu_0$, and ε_0 were found to be similar in both models and to agree well in magnitude with those cited by other authors.

1. EXPERIMENTAL RESULTS AND SOME ESTIMATES

The single ZnS–ZnSe QWs grown on buffer-free GaAs substrates by photostimulated vapor-phase epitaxy and used in this study are strained because of a lattice mismatch among ZnS, ZnSe, and GaAs. The technology of fabrication of these structures and their optical spectra were discussed by us elsewhere [8, 16]. In this work, spectra of the ZnS–ZnSe QWs were obtained with a DFS-12 double-grating monochromator and an FÉU-79 PM tube operated in the photon-counting mode, with the electronics configured in the CAMAC system. The PL was excited by a He–Cd laser operating at λ= 325 nm with an average power ~10 mW, and a halogen lamp was used to obtain reflectance spectra.

Two QWs, 308 and 309, with practically coinciding spectral reflectance profiles, were selected for our study from one lot of QW samples with equal L_z = 11 and L_b = 60 Å. Figure 1 shows only one reflectance spectrum of QW 309 (E_{1S} = 2.997 eV) produced by heavy-hole (*hh*) excitons radiating from the first size-quantized level (n = 1), and exciton PL bands of QW 309 and 308 (labeled *1* and *2*, respectively). Band *1* has, besides the main peak, a short-wavelength one (E_{2S} = 3.031 eV), which coincides in position with a similar spectral reflectance feature. Calculations show that it is due to

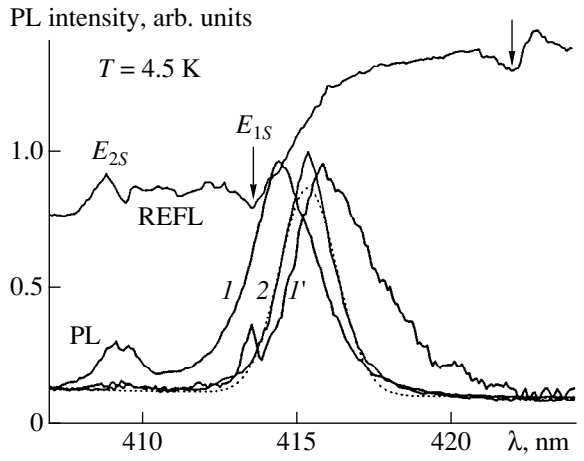

Fig. 1. Reflectance (QW 309) and photoluminescence spectra: (*1*, *1*') QW 309 for G_1 and G_{min}, respectively; (*2*) QW 308 for G_1; points are the Gaussian distribution approximating band *2*.

hh excitons in the 2*s* state [16]. It should be stressed that this peak is not elementary but has a doublet structure with the components spaced by ~3 meV, however, we have not established the nature of this splitting.

The shifts of bands *1* and *2* obtained at $G_1 \sim 1 \times 10^{21}$ cm^{-2} s^{-1} relative to E_{1S} are 6 and 13 meV, respectively, and they did not change with increasing pump density. The bands behaved differently with decreasing generation rate. As G decreased down to 10^{18} cm^{-2} s^{-1}, band *1* shifted toward longer wavelengths by ~11 meV, and as it was reduced monotonically still more to 10^{17} cm^{-2} s^{-1}, an additional minimum coinciding in position with a reflectance minimum appeared on the short-wavelength side of the main peak (now labeled *1*' in Fig. 1), the ratio of the integrated intensities of the two peaks being ~30. The change in the PL band shape observed to occur in QW 309 with decreasing G can be explained within a qualitative model taking into account the presence in a QW of regions differing in the character of disorder. If the generation rate does not exceed the level above which exciton–exciton collisions set in, the emission spectrum usually exhibits a single PL band due to recombination of localized excitons. When G is reduced by two to three orders of magnitude, one observes, besides the red-shifted main peak, a short-wavelength one corresponding to the emission of free excitons, which reside in QW regions of nominal thickness and which have not reached regions with disordered interfaces in the time τ_0. If one neglects free-exciton diffusion at $T \sim 0$ K, the integrated intensity of the short-wavelength peak is proportional, as a rule, to the total area of QW regions with L_z within the pump laser spot [15]. As for band *2*, no substantial change in its shape and position, except a decrease of its integrated intensity, was revealed within the same interval of G.

In order to study the temperature dependence of the PL bands of both QWs, we chose an exciton generation rate at which most of the shallow states in the density-of-states tail may be considered partially empty, a situation realizing in our case for $G < 10^{18}$ cm^{-2} s^{-1}. An increase of T to 40 K did not result in any noticeable change in the shape and position of band *2*. At the same time, band *1*' exhibited disappearance of the short-wavelength peak, a decrease in width from 22 to 12 meV, and a simultaneous monotonic shift to shorter wavelengths by 11 meV as T was increased to 30 K, while for T > 30 K, we observed only its broadening (Fig. 2). As follows from these results, the character of the band shift in QW 309 within a narrow interval of variation of G and T is caused by the filling or thermally induced activation of states in the density-of-states tail, while the energy E_c = 2.991 eV near which the maximum of the PL band of this QW stabilizes with increasing G and T corresponds apparently to the mobility edge of localized excitons, which is shifted by 6 meV relative to the free-state energy E_{1S}. On the other hand, despite QWs 309 and 308 having the same thickness,

the PL band of the latter did not exhibit any dependence on G and T, although its maximum is also shifted by a considerable amount (~13 meV) with respect to E_{1S} (Fig. 1). We note in this connection that a similar behavior of the exciton PL band was observed in an AlGaAs/GaAs QW [14]. A qualitative interpretation of this behavior will be put forward in the next section in terms of a model describing the population of tail states by excitons under steady-state excitation.

2. THE EMISSION BAND SHAPE OF SINGLE Zn–ZnSe QWs WITH IMPERFECT INTERFACES

1. As was shown in [3], the shape of the low-temperature exciton PL band of QWs with a submonolayer thickness is proportional to the energy distribution $n(\varepsilon)$ of localized excitons in the states in the density-of-states tail. The models of [12] and [13] were used to calculate two distribution curves $n(\varepsilon)$, which were compared subsequently with band *1'* (QW 309). Without going into a detailed analysis of both models, which have much in common, we note here only a few characteristic features. Both models permit one to calculate the average lifetime $\tau(r)$ and the population $f(\varepsilon, r)$ of a state with localization energy ε which is near a neighboring state with ε' at a distance r. The quantity $\tau(r)$ in the model of [12] was obtained in the approximation of exciton hopping to the nearest localization center, while in the model of [13], the exciton lifetime takes into account the possibility of exciton hopping to any center in the local environment, which becomes essential at high localization-center concentrations. A major approximation, common to both models, is the neglect of spatial correlation among the states that are successively occupied by the same exciton in the course of its relaxation. Prior to presenting the final expressions obtained in these models and permitting a calculation of $n(\varepsilon)$, we estimate the position of the PL band maximum with respect to E_c for small G, where the state into which an exciton hops may be considered empty. Let the density of localized states $g(\varepsilon)$ fall off into the band by an exponential law [2, 3]

$$g(\varepsilon) = \frac{N_0}{\varepsilon_0}\exp(-\varepsilon/\varepsilon_0), \tag{1}$$

where N_0 is the total density of states in the tail, and ε_0 is the energy characterizing the scale of their energy dependence. The density of states with an energy in excess of ε and the average exciton hop length $r(\varepsilon)$ are related through

$$\rho(\varepsilon) = \int_{\varepsilon}^{\infty} g(\varepsilon)d\varepsilon = N_0\exp(-\varepsilon/\varepsilon_0), \tag{2}$$

$$r(\varepsilon) = [\pi\rho(\varepsilon)]^{-1/2}. \tag{3}$$

Assuming a tunneling relaxation mechanism, the exciton hopping time between two localization centers with

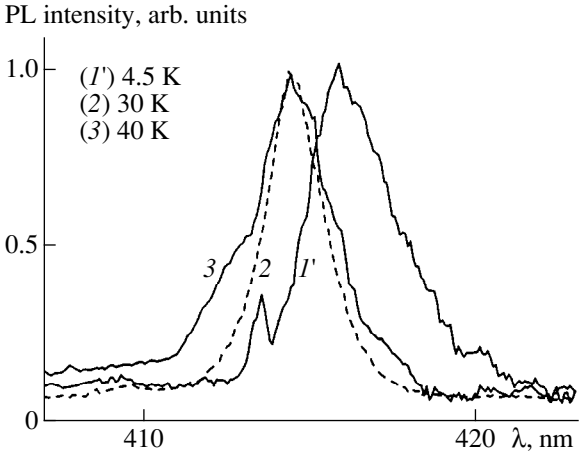

Fig. 2. Shape and position of band *1'* (QW 309) at different temperatures.

energies ε and ε' ($\varepsilon < \varepsilon'$) spaced by a distance r can be written as

$$\tau_h(r) = \nu_0^{-1}\exp\left(\frac{2r}{\alpha}\right), \tag{4}$$

where ν_0 is the exciton attempt frequency (which is of the order of the phonon one) and α is the decay length of the single-state wave function. Then the maximum of the PL band will lie at an energy ε_m satisfying the following condition [2, 3, 12]:

$$\tau_h[r(\varepsilon_m)] \approx \tau_0, \tag{5}$$

whence, using (1)–(5), we come to

$$\varepsilon_m = \varepsilon_0\ln\left[\frac{\pi N_0\alpha^2}{4}\ln^2(\tau_0\nu_0)\right]. \tag{6}$$

Thus, the position of the PL band maximum relative to the mobility edge for small G is determined by a set of universal parameters, namely, $N_0\alpha^2$, $\tau_0\nu_0$, and ε_0.

At $T \sim 0$, all states in the tail can be divided conventionally into hopping and radiative ones, whose density can be calculated using the Poisson distribution. It yields the following expression for the probability $p_k(r, \varepsilon)$ to observe a state with k neighbors within a circle of radius r near a given state of energy ε:

$$p_k(r\varepsilon) = \frac{[\pi r^2\rho(\varepsilon)]^k}{k!}\exp(-\pi r^2\rho(\varepsilon)). \tag{7}$$

The probability for a given state to have a kth neighbor at a distance from r to $r + dr$ is $P_k(r, \varepsilon)dr$, where [12, 13]

$$P_k(r, \varepsilon) = 2\pi r\rho(\varepsilon)\frac{[\pi r^2\rho(\varepsilon)]^{(k-1)}}{(k-1)!}\exp(-\pi r^2\rho(\varepsilon)), \tag{8}$$

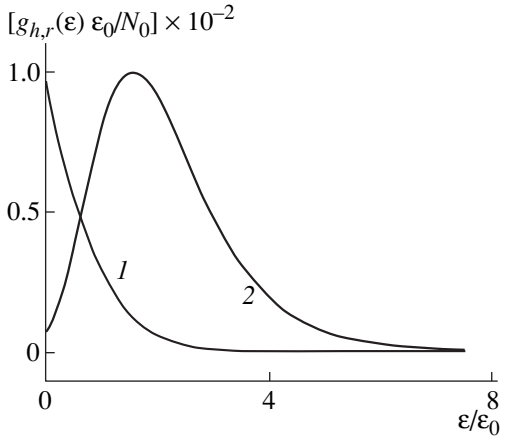

Fig. 3. Energy distribution of (*1*) hopping and (*2*) radiative states.

or, taking into account only the nearest ($k = 1$) empty state with $\varepsilon' > \varepsilon$,

$$P(r, \varepsilon) = 2\pi r\rho(\varepsilon)\exp(-\pi r^2\rho(\varepsilon)). \quad (9)$$

Then, for the energy density of the hopping states, we obtain

$$g_h(\varepsilon) = g(\varepsilon)\int_0^{r_m} P(r, \varepsilon)dr, \quad (10)$$

where the upper limit of integration is chosen taking into account that the maximum hopping length of an exciton is limited by its radiative relaxation time. The quantity r_m can be found from (4) by setting $\tau_h(r_m) \approx \tau_0$, namely, $r_m = (\alpha/2)\ln(\tau_0\nu_0)$. For the probability for a given state to have no ($k = 0$) neighbor within a circle of radius r_m, equation (7) yields

$$P(r_m, \varepsilon) = \exp\left[-\frac{\pi\alpha^2}{4}\rho(\varepsilon)\ln^2(\tau_0\nu_0)\right], \quad (11)$$

and, hence, for the energy density of radiative states one obtains

$$g_r(\varepsilon) = g(\varepsilon)P(r_m, \varepsilon). \quad (12)$$

Both calculated curves, $g_h(\varepsilon)$ and $g_r(\varepsilon)$, are shown in Fig. 3 (the parameters used for their calculation are presented below).

In the case of a random distribution of localization centers, the energy distribution function of localized excitons $n(\varepsilon)$ is related to $P(r, \varepsilon)$ through the equation [12]

$$n(\varepsilon) = g(\varepsilon)\int_0^{\infty} f(\varepsilon, r)P(\varepsilon, r)dr, \quad (13)$$

where $f(\varepsilon, r)$ is the population of the (ε, r) state obeying the rate equation

$$\frac{f(\varepsilon, r)}{\tau(r)} = \Gamma(\varepsilon)[1 - f(\varepsilon, r)], \quad (14)$$

with $\Gamma(\varepsilon)$ being the exciton generation rate in the ε state. By the model of [12], the lifetime $\tau(r)$ of a given state has the form

$$\tau(r) = \frac{\tau_0\tau_h(r)}{\tau_0 + \tau_h(r)}, \quad (15)$$

which, taking into account that the exciton hopping length does not exceed r_m, can be recast in the form of the approximation

$$\tau(r) = \begin{cases}\tau_0, & r > r_m\\ \tau_h(r), & r < r_m.\end{cases} \quad (16)$$

As a result, $n(\varepsilon)$ breaks down into two terms, $n(\varepsilon) = n_1(\varepsilon) + n_2(\varepsilon)$, where [12]

$$n_1(\varepsilon) = g(\varepsilon)\int_0^{r_m} P(r, \varepsilon)\Gamma(\varepsilon)\frac{\tau_h(r)}{1 + \Gamma(\varepsilon)\tau_h(r)}dr, \quad (17)$$

$$n_2(\varepsilon) = g(\varepsilon)P(r_m, \varepsilon)\Gamma(\varepsilon)\frac{\tau_0}{1 + \Gamma(\varepsilon)\tau_0}. \quad (18)$$

The energy distribution of localized excitons calculated by the second model [13] has a similar form

$$n(\varepsilon) = g(\varepsilon)\Gamma(\varepsilon)\tau(\varepsilon), \quad (19)$$

where the average lifetime $\tau(\varepsilon)$ of the state taking into account all possible intercenter transitions is

$$\tau(\varepsilon) = \int_0^{\infty}\exp\left[-\frac{t}{\tau_0} - 2\pi\rho(\varepsilon)\right.$$
$$\left.\times\int_0^{\infty} r\left(1 - \exp\left(\frac{t}{\tau_h(r)}\right)\right)dr\right]dt. \quad (20)$$

2. Figure 4 displays two calculated $n(\varepsilon)$ curves. The first was obtained using (17) and (18) and the following fitting parameters: $N_0 = 4.5 \times 10^{11}$ cm^{-2}; $\alpha = 40 \times 10^{-8}$ cm; $\tau_0 = 150$ ps; $\nu_0 = 5 \times 10^{13}$ s^{-1}; and $\varepsilon_0 = 8.4$ meV; while the second was calculated with (19) and (20) and $N_0 = 5 \times 10^{11}$ cm^{-2}; $\alpha = 40 \times 10^{-8}$ cm; $\tau_0 = 100$ ps; $\nu_0 = 7 \times 10^{13}$ s^{-1}; and $\varepsilon_0 = 6.5$ meV. One readily sees that both $n(\varepsilon)$ distributions agree well in shape and spectral position with the experimental band *1'* of the exciton PL of QW 309 measured at $T = 4.5$ K and $G \sim 1 \times 10^{17}$ cm^{-2}. Using (6) to estimate the Stokes shift ε_m and substituting the corresponding parameters from both models, we come to $\varepsilon_{m1} = 13$ and $\varepsilon_{m2} = 10.5$ meV. A comparison of these values with the experimental shift (11 meV) shows that the parameters of the second

model ($N_0\alpha^2 = 0.08$, $\tau_0\nu_0 = 7 \times 10^3$, and $\varepsilon_0 = 6.5$ meV) permit more accurate determination of the PL band position relative to the localized-exciton mobility edge in ZnS–ZnSe QWs with a thickness of 2–3 ML. Note that these parameters are close in magnitude to those obtained in a study [5] of $Zn_{0.8}Cd_{0.2}Se/ZnSe$ QWs similar to ours.

As follows from (6), or from (17)–(20), the shift of the PL band maximum increases with increasing concentration of states N_0, which is a consequence of increasing lateral overlap of the wave functions of neighboring states, and, therefore, it appears useful to estimate the concentration $N_0^{\max}$ at which the states start to delocalize. To do this, we find the minimum size ξ of the island capable of localizing an *hh* exciton of mass $M_{hh} = m_e + m_{hh}$, where m_e and m_{hh} are the effective masses of an electron and a heavy hole, respectively. Calculations show that an island 1 ML high (2.83 Å for ZnSe) in a QW with $L_z = 11$ Å creates a potential well for the *hh* exciton of depth $V_0 \approx 60$ meV. The existence of QW regions with thicknesses $L_z + 1$ ML is supported by an additional minimum in reflectance spectra (identified by an arrow) located at a distance of ~60 meV from E_{1S} (Fig. 1). For a bound state with a minimum localization energy to appear in such an island, the following relation must be obeyed: $\xi \equiv 2R = \pi\hbar/(2M_{hh}V_0)^{1/2}$, where R is the island radius [4], whence we obtain

$$R^2 = \pi^2\hbar^2/8M_{hh}V_0. \qquad (21)$$

Substituting the corresponding values in (21) yields $R = 14.2$ Å. When calculating the exciton energy and wave functions, one most frequently chooses a cylinder of radius R for the island shape. Such an island of height $\delta L = 2.83$ Å and volume $v = \pi R^2\delta L$ will accommodate 10 Se atoms; said in other words, in order for a localized state to split off the band edge in a QW with $L_z = 11$ Å, a cluster of 10 Se atoms has to form on its surface. Hence, for the cluster density, we obtain $N_0^{\max} \sim 1.5 \times 10^{13}$ cm^{-2}.

We estimate the minimum concentration of localization centers in a QW as a threshold value at which the tunneling hop time of an exciton from a given state will just exceed its radiative recombination time: $N_0^{\min} \approx [\pi r_m^2]^{-1} = [(\pi\alpha^2/4)\ln^2(\tau_0\nu_0)]^{-1}$. Using the corresponding parameters, we obtain $N_0^{\min} < 1 \times 10^{11}$ cm^{-2}. The condition of classical exciton localization in such a system can be written [11] in the form $r_m^2\delta L \gg L_z^3$. One immediately sees that this inequality holds well for the values of α and $\tau_0\nu_0$ obtained and $L_z = 11$ Å. In this case, the low-temperature exciton spectrum was also shown [11] to be Gaussian as a consequence of the Gaussian distribution of thickness fluctuations (localization centers) and of the absence of intercenter transitions. The above permits us to qualitatively understand the reason for the PL band of QW 308 to be independent of G and T (Fig. 1). As a result of the low center concentration ($N_0 \leq N_0^{\min}$), each localized state of this QW will be radiative, and the probability for the exciton to leave it in a hop will be practically zero, which is supported by the shape of band *2* as well, which is well fitted by a Gaussian (Fig. 1) [14]. But then an increase or decrease of the pump density should bring about only an increase or decrease of the integrated intensity of the PL band of QW 308 without affecting its position and shape, exactly what was observed in the experiment. The stability of band *2* to an increase of T up to 40 K is accounted for by the same reason, i.e., the time taken by an exciton to hop up in energy ($\varepsilon' \longrightarrow \varepsilon$) with absorption of an acoustic phonon also exceeds the exciton radiative lifetime in this state.

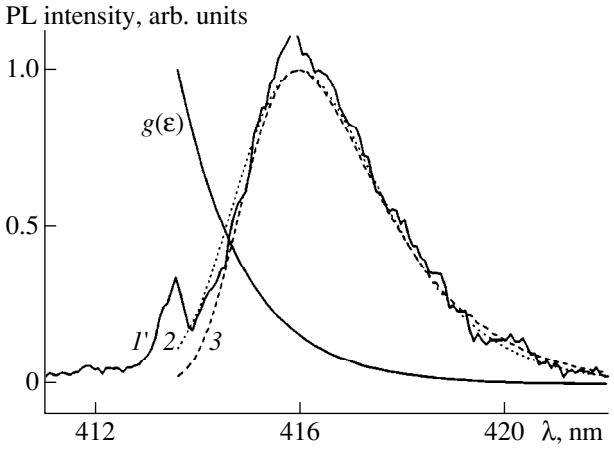

Fig. 4. Band *1'* is the same as in Fig. 1; (*2*, *3*) $n(\varepsilon)$distribution calculated from the first and second models, respectively; $g(\varepsilon)$ is the distribution of localized states.

Let us dwell on some conclusions following from these results. As pointed out in [13], the selection of the tunneling mechanism of exciton energy relaxation imposes certain constraints on the magnitude of N_0. Indeed, calculations show that the expression for $n(\varepsilon)$ from the first model diverges for $N_0 > 1 \times 10^{13}$ cm^{-2}. The reason for the divergence lies apparently in that excitons start to delocalize at such a center concentration because an exciton "feels" $\pi N_0\alpha^2 \approx 5$ localized states within a circle of radius α near the mobility edge [2]. This result follows also from the fact that the figure 1×10^{13} cm^{-2} is very close to $N_0^{\max}$, so that if the concentration of centers (microislands) becomes higher than $N_0^{\max}$, individual microislands merge to form conglomerates (macroislands) with lateral dimensions in excess of tens of microns, where exciton motion becomes free [15]. Thus, for concentrations $N_0 < N_0^{\max}$, both models yield identical results, and therefore, the

tunneling mechanism of exciton relaxation appears to be the most reasonable choice to describe the shape and position of the exciton PL band in ZnS–ZnSe QWs with thicknesses of a few monolayers in a model that assumes exponential decay of the density of localized states.

ACKNOWLEDGMENTS

Support of the Ukrainian Foundation for Basic Research (grant no. 2.4/86) is gratefully acknowledged.

REFERENCES

1. P. S. Kop'ev, I. N. Ural'tsev, Al. L. Éfros, *et al.*, Fiz. Tekh. Poluprovodn. (Leningrad) **22**, 424 (1988) [Sov. Phys. Solid State **22**, 259 (1988)].
2. H. Kalt, J. Collet, S. D. Baranovskii, *et al.*, Phys. Rev. B **45**, 4253 (1998).
3. S. D. Baranovskii, R. Eichmann, and P. Thomas, Phys. Rev. B **58**, 13081 (1998).
4. H. Castella and J. W. Wilkins, Phys. Rev. B **58**, 16186 (1998).
5. L. E. Golub, E. L. Ivchenko, S. V. Ivanov, *et al.*, Phys. Status Solidi B **205**, 203 (1998).
6. U. Jahn, S. W. Kwok, M. Ramsteiner, *et al.*, Phys. Rev. B **54**, 2733 (1996).
7. U. Jahn, S. W. Kwok, M. Ramsteiner, *et al.*, Phys. Rev. B **56**, R4387 (1977).
8. V. V. Tishchenko, N. V. Bondar, A. B. Kovalenko, *et al.*, Superlattices Microstruct. **24** (2), 143 (1998).
9. V. V. Tishchenko, N. V. Bondar', M. S. Brodin, and A. V. Kovalenko, Fiz. Tekh. Poluprovodn. (St. Petersburg) **31**, 1440 (1997) [Semiconductors **31**, 1244 (1997)].
10. E. Runge and R. Zimmermann, Phys. Status Solidi A **164**, 511 (1998); E. Runge, R. Zimmermann, and F. Henneberger, Phys. Status Solidi B **188**, 547 (1995).
11. F. Yang, M. Wilkinson, E. J. Austin, and K. P. O'Donnell, J. Phys.: Condens. Matter **4**, 8863 (1992); M. Hetterich, Ch. Markle, A. Dinger, *et al.*, Phys. Rev. B **59**, 10268 (1999).
12. A. G. Abdukadyrov, S. D. Baranovskiĭ, and E. L. Ivchenko, Fiz. Tekh. Poluprovodn. (Leningrad) **24**, 136 (1990) [Sov. Phys. Semicond. **24**, 82 (1990)]; A. G. Abdukadyrov, S. D. Baranovskiĭ, E. L. Ivchenko, *et al.*, Zh. Éksp. Teor. Fiz. **98**, 2056 (1990) [Sov. Phys. JETP **71**, 1155 (1990)].
13. A. A. Kiselev, Fiz. Tekh. Poluprovodn. (St. Petersburg) **32**, 546 (1998) [Semiconductors **32**, 488 (1998)].
14. G. Bastard, C. Delalande, M. H. Meynadier, *et al.*, Phys. Rev. B **29**, 7042 (1984).
15. M. A. Herman, D. Bimberg, and J. Christen, J. Appl. Phys. **70** (2), R1 (1991).
16. V. V. Tishchenko, N. V. Bondar, Y. E. Raptis, and E. Anastassakis, Solid State Commun. **96**, 793 (1995).

Translated by G. Skrebtsov

Physics of the Solid State, Vol. 42, No. 8, 2000, pp. 1535–1541. Translated from Fizika Tverdogo Tela, Vol. 42, No. 8, 2000, pp. 1492–1498.

LOW-DIMENSIONAL SYSTEMS AND SURFACE PHYSICS

Giant Burst of the Emission Line Intensity of Spatially Indirect Excitons in GaAs/AlGaAs Double Quantum Wells

E. S. Moskalenko, V. V. Krivolapchuk, and A. L. Zhmodikov

Ioffe Physicotechnical Institute, Russian Academy of Sciences, Politekhnicheskaya ul. 26, St. Petersburg, 194021 Russia

e-mail: Evgenii.Moskalenko@pop.ioffe.rssi.ru

Received December 29, 1999; in final form, February 20, 2000

Abstract—A study is reported on the low-temperature ($T \leq 30$ K) photoluminescence in the spatially indirect exciton line in GaAs/$Al_{0.33}Ga_{0.67}As$ double quantum wells as a function of optical pump power and applied electric field. We have revealed a giant (threefold) burst of luminescence intensity in a part of the spectral profile of the indirect-exciton line occurring at certain values of the external electric field, temperature, and optical pumping. We have also observed that this part of the indirect-exciton line profile varies in intensity (fluctuates) with time with a characteristic period of tens of seconds. The results obtained are discussed within a model of the Bose–Einstein condensation of a system of two-dimensional bosons that have, besides the free, a discrete energy spectrum lying below the bottom of the free-state band. *© 2000 MAIK "Nauka/Interperiodica".*

Investigation of the properties of double quantum wells (DQWs) has been attracting recently considerable attention from both a theoretical and an experimental viewpoint. This interest stems from the existence in DQWs of spatially indirect excitons (IX), which are formed of an electron (*e*) and a hole (*h*) localized in different quantum wells (QWs). Because the *e* and *h* in the IX are separated in real space, the IX possesses a substantially longer radiative lifetime than a direct exciton (DX) formed of an *e* and an *h* in the same QW. This permits one to obtain in practice an IX gas of a fairly high density, even at low optical-pump powers and, as a consequence, to expect a manifestation in an experiment of various collective properties in a high-density system of spatially separated electron–hole pairs (excitons). These properties were predicted theoretically in [1–3]. A comprehensive theoretical analysis of a system of spatially indirect excitons in a DQW [4] established the conditions for the onset of a stable liquid IX phase, whose formation at $T = 1.8$ K in GaAs/AlGaAs DQWs was experimentally shown in our preceding work [5].

One of the interesting collective properties of (quasi-)two-dimensional high-density bosons is the possibility of the onset in such a system, with certain conditions, of the Bose–Einstein condensation (BEC), i.e., a phase transition in which a macroscopic number of particles occupies the same quantum state lowest in energy of the system. It is well known [6] that the BEC cannot occur in a spatially homogeneous, purely two-dimensional system of free bosons at $T \neq 0$. However, as shown theoretically in [7], if a system of two-dimensional bosons also possesses, besides the free, a discrete spectrum of energies lying below the minimum of the free boson-state band, BEC can also set in this case at $T \neq 0$.

Indeed, the total number of free noninteracting particles (bosons) N with an energy spectrum $E = \hbar^2k^2/2m$ (where k is the wave vector and m is the particle mass), which reside in a volume V at temperature T, is equal to the sum of the occupation numbers of single-particle states $N_{\mathbf{k}}$

$$N = \sum_{\mathbf{k}} N_{\mathbf{k}} = \int_0^\infty \frac{\rho(E)dE}{e^{(E-\mu)/k_BT} - 1}, \qquad (1)$$

where $\rho(E)$ is the density of states, k_B is the Boltzmann constant, and μ is the chemical potential of the particle system; μ is negative and approaches zero (the $E = 0$ level) with increasing particle-gas density $n = N/V$. Einstein and Bose recognized in 1924 [8] that integral (1) assumes a finite value $n_c(T)$ for $\mu \longrightarrow 0$ for an ideal gas of noninteracting bosons in the three-dimensional case, where $\rho(E) \propto E^{1/2}$. This means that free states ($E > 0$) cannot hold a larger number of particles, so that, if the boson concentration in the system n exceeds n_c, all the extra particles $n - n_c$ will fall into the $E = 0$ state (BEC).

In the two-dimensional case, $\rho(E)$ is a constant, and integral (1) diverges for $\mu \longrightarrow 0$ and $T \neq 0$ because the denominator is zero at the lower integration limit, which implies that BEC is impossible in this case. The physical meaning of this is that the maximum occupation of free states ($E > 0$) is infinite. However, if the two-dimensional boson system has, besides the free, also discrete states (localized states, whose existence is made possible by potential fluctuations at the heterointerfaces [9], in our case, of GaAs/AlGaAs) ε_0, ε_1, etc. such that $\varepsilon_0 < \varepsilon_1 < E = 0$, then the situation changes radically. In these conditions, as the number of bosons in the system increases, the chemical potential cannot

arbitrarily closely approach the value $E = 0$ because of the requirement $N(\varepsilon_0) \geq 0$, therefore $(-\mu)_{\min} = |\varepsilon_0|$ and, hence, integral (1) is finite [7]:

$$n_c(T) = -\frac{mk_BT}{2\pi\hbar^2}\ln\left(1 - e^{-\frac{|\varepsilon_0|}{k_BT}}\right). \quad (2)$$

Therefore, as soon as n has become greater than $n_c(T)$, the localized states are filled by a macroscopic number of particles, $n - n_c(T) = n(\varepsilon_0) + n(\varepsilon_1)$. Thus, while the "classical" BEC (for free three-dimensional bosons) occurs into one quantum state $|\mathbf{k}\rangle = 0$ extending coherently over the whole gas volume, condensation into localized states takes place within a limited region of space. In this sense, the Bose–Einstein condensation in a system of two-dimensional bosons possessing, besides the continuous, a discrete energy spectrum reminds the BEC of alkali-metal atoms observed experimentally to occur in spatially confined traps created by a magnetic field [10].

Studies of the possibility of BEC realization in bulk semiconductors and quantum wells (for a comprehensive review of the relevant experimental and theoretical works see [11]), which have been pursued during the past few decades, have revealed a number of interesting properties; however, experimental evidence for the possible manifestation of BEC in these objects is ambiguous. For instance, the diffusion coefficient of indirect excitons in a GaAs/AlAs quantum well was found to increase sharply after reaching certain threshold conditions [12], an observation assigned to the onset of superfluidity, which the authors believed to indicate the onset of exciton condensation. However, the relation between the superfluidity and BEC phenomena is not unambiguous [13]. For instance, liquid helium has long been considered a classical object in which BEC is realized. At the same time, although the superfluidity of liquid helium discovered in 1938 [14] was proposed [15] to use as a criterion of BEC manifestation, experimental evidence for the existence of BEC in helium has only been demonstrated in a comparatively recent experimental study [16], where the momentum distribution of helium atoms was analyzed by neutron scattering.

Thus, the question of BEC realization in three- and, particularly, two-dimensional semiconductor crystals remains open and requires further investigation. An experimental measurement of the exciton distribution function in energy (momentum) would provide a convincing argument for the manifestation of the BEC phenomenon.

The present work studies the zero-phonon luminescence line of spatially indirect excitons in $GaAs/Al_{0.33}Ga_{0.67}As$ double quantum wells. Because this is a direct-band-gap material, radiative recombination does not involve of the free excitons present in the system (due to the exciton wave-vector conservation in the QW plane), but rather only a part of them located near the free-state band bottom (within the so-called radiative "belt," whose energy width Δ is determined to a considerable extent by exciton interaction with acoustic phonons [17]). Hence, the shape of the indirect-exciton emission line observed in an experiment cannot reflect the IX distribution function in the exciton band. At the same time, all the excitons occupying localized states take part in radiative recombination. This gives one grounds to expect that the experimentally measured radiation intensity (proportional to the particle occupation numbers) of the excitons in localized states and of free excitons in a DQW would indirectly reflect the distribution function of excitons over the free and localized states and permit one to observe, after reaching the critical conditions (2), the BEC effect predicted in [7] for a two-dimensional boson system.

An obvious advantage of the IX system in a DQW as a potential object for BEC observation over excitons in single quantum wells lies in the possibility of efficiently controlling the IX radiative lifetime τ_R by varying external factors. For instance, an external electric field applied to a DQW in the structure growth direction z substantially reduces the electron and hole overlap wave functions in the IX along z, which appreciably increases (up to three orders of magnitude [18]) τ_R. This allows the IX system to efficiently cool down to the lattice temperature, as well as offers the possibility of increasing the IX gas concentration without increasing the optical pump power, which is no less important. The latter circumstance is essential from the experimental viewpoint, because it makes possible a substantial reduction of sample heating by phonons, which are inevitably emitted in the relaxation of photoexcited carriers and excitons. It is sample heating that quite frequently places an obstacle to reaching the critical boson-gas temperature in experiments that use high optical-pump powers to create a critical density of bosons that have very short lifetimes.

The present work reports on a giant (threefold) increase in the luminescence intensity of a part of the IX spectral line profile in a $GaAs/Al_{0.33}Ga_{0.67}As$ DQW observed by varying the sample temperature and the external electric field applied to the DQW. Besides, the luminescence intensity of this part of the IX spectral profile fluctuates with a characteristic time of tens of seconds. Since the experimentally measured luminescence reflects the population by excitons of free and localized states, such unusual behavior of the IX line may indicate a substantial change in the exciton distribution over the free and localized states. We discuss this behavior of the IX line in terms of a possible onset of the BEC phenomenon in the system of two-dimensional bosons, which reside in a random potential created by the heterointerfaces of our sample.

1. EXPERIMENTAL RESULTS

The studies were carried out on samples with double quantum wells (see our previous publication for a detailed description of the samples [5]). We studied photoluminescence (PL) from a slightly asymmetric DQW, in which the thicknesses of the wide (WW) and narrow (NW) GaAs wells are 10.18 and 9.61 nm, respectively, and the thickness of the $Al_{0.33}Ga_{0.67}As$ barrier separating them is 3.82 nm. A dc electrical voltage V_{dc} was applied to two indium contacts deposited on the substrate and the sample side with the DQWs [5]. The PL excitation and measurement were effected through a small hole in the contact on the DQW side. The sample was studied either at the temperature of pumped liquid helium (T = 1.8 K) or in the temperature interval from 4.2 to 30 K. The excitation was done by light from a CW Ti–sapphire laser (wavelength λ = 765.2 nm, optical excitation power ≤1 mW, laser spot diameter on the sample 120 μm), which corresponds to the under-barrier excitation of DQWs. The DQW luminescence spectra were measured with a DFS-52 double-grating spectrometer operated in the time-correlated photon-counting regime.

Figure 1 presents DQW luminescence spectra measured at an optical-pump power density P = 5 W cm^{-2} for different V_{dc} at T = 1.8 K. At V_{dc} = 0 (Fig. 1, curve *a*), the emission spectrum is similar to the flat-band case and consists of two lines, DXW and DXN, corresponding to the luminescence of direct excitons from the wide and the narrow well, respectively. At a nonzero V_{dc} (Figs. 1, curves *b*–*e*) the indirect regime sets in (see inset to Fig. 1), in which the IX line occupies the lowest energy position in the PL spectra. As V_{dc} increases, the DXW and DXN lines, as well as the BDXW line corresponding to the radiative recombination of the impurity-bound DXW, do not change their spectral positions (Figs. 1, curves *b*–*e*), while the IX line shifts monotonically toward lower energies.

We note that within a certain V_{dc} interval part of the IX line profile undergoes a giant (up to threefold) intensity increase (burst) (Fig. 1, curve *d*). Significantly, there is no burst in the indirect exciton intensity throughout the covered spectral range of IX line positions, for any temperature 4.2 ≤ T ≤ 30 K and any optical-excitation density P ≤ 5 W cm^{-2}. In these experimental conditions, the integrated luminescence intensity I_{IX} of the total IX line only decreases monotonically while shifting toward lower energies. The dependence of the integrated intensity of the IX line on its spectral position measured at P = 5 W cm^{-2} and T = 10 K is presented in Fig. 2a. The decrease of I_{IX} observed to occur under the monotonic downshift of the IX line is caused by the increase in the IX radiative lifetime (and, hence, by the more important role of nonradiative recombination) as a result of the decreasing overlap of the *e* and *h* wave functions of which the IX is formed.

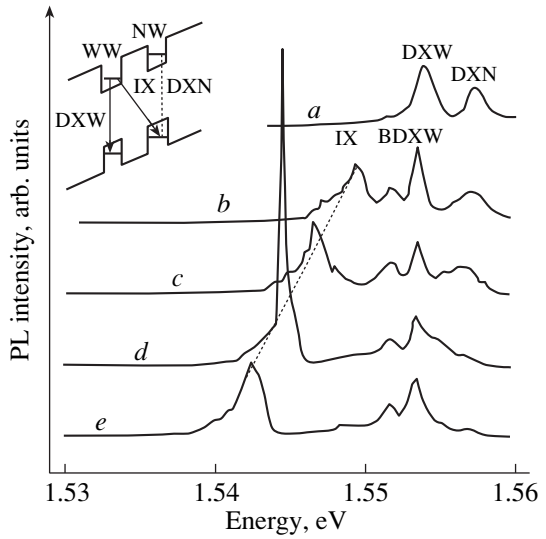

Fig. 1. Luminescence spectra measured at T = 1.8 K, P = 5 W cm^{-2}, and different $V_{dc}(V)$: (*a*) 0, (*b*) 0.5, (*c*) 1, (*d*) 2, and (*e*) 3.5. The inset schematically shows the indirect DQW regime.

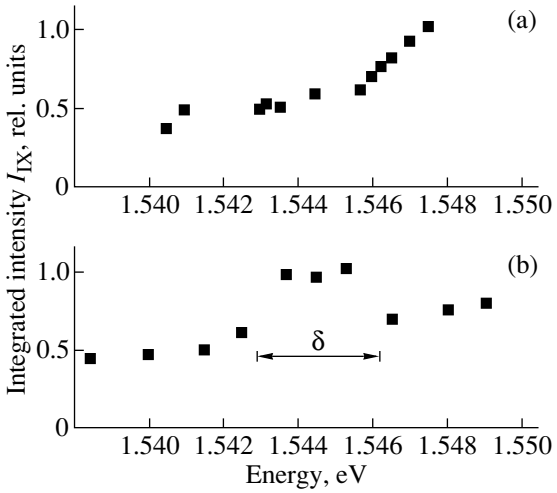

Fig. 2. Dependence of integrated luminescence intensity I_{IX} of the IX line on its spectral position obtained at P = 5 W cm^{-2} and different T(K): (a) 10 and (b) 1.8; δ identifies the spectral region of IX line positions where an IX intensity burst is observed to occur.

The dependence of the intensity I_{IX} of the IX line on its spectral position measured at P = 5 W cm^{-2} and T = 1.8 K is presented in Fig. 2b. Against a monotonic decrease in I_{IX} (with the IX shifting toward lower energies) one observes a growth of intensity within an energy interval δ (Fig. 2b) of the IX line positions. The dependence of I_{IX} on the spectral position of the IX line obtained at T = 1.8 K and substantially lower optical pump levels (P ≤ 1 W cm^{-2}) did not exhibit an intensity burst similar to that depicted in Fig. 2b and instead showed only a weak (within 15%) monotonic falloff of

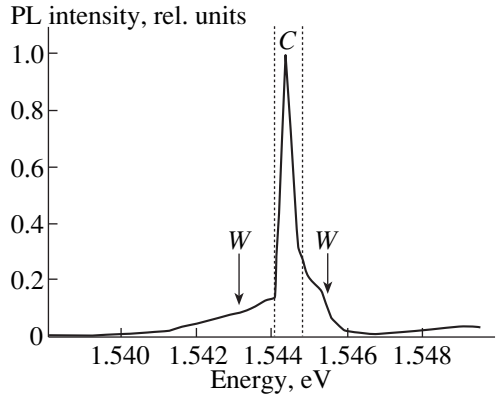

Fig. 3. The IX line from the spectrum presented in Fig. 1, *d*. The two dotted vertical lines separate different spectral regions of the IX line profile that exhibit (*C*) and do not exhibit (*W*) appreciable changes of the luminescence intensity in time.

I_{IX}, with the IX line shifting toward lower energies in the same spectral region.

The temperature dependence of the intensity of the IX line I_{IX} in the position corresponding to the case of Fig. 1, curve *c*, which was measured at $P = 5$ W cm^{-2}, revealed a substantial (by 15 times) monotonic decrease of I_{IX} with the temperature increasing from 1.8 to 30 K. While the dependence of I_{IX} on T obtained at considerably lower optical pump densities ($P <$ 1 W cm^{-2}) qualitatively retains the pattern seen in the $P = 5$ W cm^{-2} case, the rate of thermal quenching of I_{IX} is significantly lower (I_{IX} decreases to one eighth its value under variation of T from 1.8 to 30 K). Thermal quenching of I_{IX} was observed to behave similarly throughout the spectral range of variation of IX line positions for $P < 1$ W cm^{-2}, as well as for $P = 5$ W cm^{-2}, except the interval δ (in Fig. 2b, this interval is bounded by the values $1.543 < h\nu < 1.546$ eV).

The spectral profile of the IX line in Fig. 1, curve *d* is depicted in Fig. 3. It consists of a narrow strong line *C* and wings *W* of a substantially lower intensity. Measurements of the time evolution of the intensity of component *C* and of the wings *W* showed that the intensity of *C*, unlike that of *W*, fluctuates (varies by a factor three) with a characteristic time of tens of seconds.

2. DISCUSSION

The exciton emission line shape in a DQW is inhomogeneous and is determined by the emission of excitons from different spatial regions in the DQW plane, which differ from one another in QW layer thicknesses, DQW barrier composition fluctuations, as well as in the local impurity electric fields. The emission intensity within each spectral interval of the IX line is proportional to the exciton population of the corresponding spatial region in the quantum well plane.

Note that excitons in each spatial region may occupy both localized and free states. There is, however, an essential point, namely, not all free excitons can emit, but only those that are confined within an emitting belt Δ near the bottom of the exciton band, which follows from the conservation of momentum in a radiative recombination event. At the same time, all excitons occupying localized states participate in radiative recombination. Hence, in a general case, both localized excitons and free excitons from the emitting belt Δ contribute to the IX line intensity. As for the relative magnitude of the contributions due to localized and free excitons to the resultant IX luminescence intensity (the quantity measured in an experiment), it depends on the actual experimental conditions.

Our experimental results indicate that, for all spectral positions of the IX line, except the δ interval, the emission of free excitons provides a substantial contribution to the intensity of the indirect-exciton PL line at $P = 5$ W cm^{-2} and $T = 1.8$ K. This conclusion draws from the following considerations. The radiative lifetime of free excitons grows, whereas that of localized excitons does not change, with increasing temperature [19]. At the same time, as shown experimentally [20], the probability of nonradiative recombination of indirect excitons in localized states is substantially smaller than that of the free IXs, which is accounted for by the much more efficient transport of free IXs to nonradiative recombination centers.

The considerable (by a factor of 15) quenching of I_{IX}, which is observed experimentally at $P = 5$ W cm^{-2} with increasing temperature $1.8 \le T \le 30$ K for all spectral positions of the IX line, except the δ interval, and argues for the efficiency of nonradiative recombination processes, permits an assumption that free excitons provide a dominant contribution to the resultant PL intensity of the IX line. This assumption is corroborated by the substantially less efficient quenching of I_{IX} observed experimentally to occur at considerably lower optical pumping levels ($P < 1$ W cm^{-2}) in the same temperature region. The less efficient quenching is connected in the latter case with the larger contribution of localized states (because the localized states should be expected to saturate with increasing P) to the resultant PL intensity of the IX line.

The conclusion concerning the dominant contribution of free excitons to the experimentally observed PL intensity of the IX line measured outside the δ spectral region (Fig. 2b) at $P = 5$ W cm^{-2} and $T = 1.8$ K finds further support from a comparison of the dependences of I_{IX} on V_{dc} (on the spectral position of the IX line) obtained at $T = 1.8$ K and various P. As V_{dc} increases (and the IX line is downshifted), the IX radiative recombination time increases substantially due to the decreasing overlap of the *e* and *h* wave functions in the IX and, hence, if in the given experimental conditions the major contribution to the PL intensity of the IX line comes from free (localized) excitons, I_{IX} should

(should not) decrease noticeably. Indeed, as seen from Fig. 2b, I_{IX} measured at $P = 5$ W cm^{-2} and $T = 1.8$ K decreases to about one half its value as IX shifts from $h\nu = 1.549$ to 1.5385 eV. At the same time, similar measurements carried out at $T = 1.8$ K and $P < 1$ W cm^{-2} revealed only a slight (15%) decrease of I_{IX} for the same spectral shifts of the IX line. Thus, the totality of the experimental data obtained on the quenching of the integrated IX intensity as a function of external factors (V_{dc}, P, and T) permits a conclusion on a dominant contribution provided by free excitons to the resultant PL intensity of the IX line at $T = 1.8$ K and $P = 5$ W cm^{-2} throughout the region of the IX line positions covered, except the δ interval.

The considerable (threefold) increase in the luminescence intensity of a part of the IX spectral line profile (Fig. 1, curve *d*) and, consequently, the increase by a factor 1.5 of I_{IX}, which is observed within the energy interval δ of the IX line positions (Fig. 2b), is anomalous as compared to the monotonic falloff of I_{IX} (and, the most significant point, to no intensity burst) with increasing V_{dc} observed in other experimental conditions (at $T = 1.8$ K and $P < 1$ W cm^{-2}, as well as at $4.2 \leq T \leq 30$ K and any $P \leq 5$ W cm^{-2}). The anomalous behavior of the IX line suggests that the number of particles involved in the emission in the case of Fig. 1, curve *d* is substantially larger than that in Figs. 1, curves *b*, *c*, *e*; in other words, as the experimental conditions changed from the case of Fig. 1, curve *c* to that of Fig. 1, curve *d*, the population of radiating states changed noticeably.

In an attempt to interpret this observation, we propose to use the model of BEC developed for the two-dimensional case in [7]. As is well known, in a purely two-dimensional case, BEC is forbidden [6]. At the same time, if in a system of bosons (excitons) there is, besides the free states, a localized state ε_0 lying below the exciton band minimum, the exciton chemical potential involved in calculating the total number of particles n_c (2) that can be contained in the free-exciton band is captured by the localized state ε_0 and, as a consequence, n_c becomes finite. Therefore, as soon as the exciton concentration n in the system under study has become larger than n_c, the macroscopic number of particles $n - n_c$ turn out to occupy the lowest energy state of the total boson system (the free band plus the localized state), i.e., the localized state.

Because, as already mentioned, all localized excitons take part in radiative recombination, the substantial population of a radiative (localized) state may account for the pronounced increase in the IX line intensity. The phenomenon of the giant IX intensity burst is observed experimentally when downshifting the IX line (by varying V_{dc}, Fig. 1) as a result of an increase in the exciton radiative lifetime, which gives rise both to an increase in the concentration of excitons (under constant optical pumping) and to their efficient thermalization down to the lattice temperature. In our opinion, it is these two factors that bring about BEC condensation under the variation of the external electric field from the case of Fig. 1, curve *c* to that of Fig. 1, curve *d*.

Let us estimate the magnitude of the possible intensity increase in the IX line (part of the line) induced by varying the external field. We assume that, in the case of Fig. 1, curve *c*, the total exciton concentration $n_1 = n_1^{free} + n_1(\varepsilon_0) \approx n_1^{free}$ (where n_1^{free} is the free-exciton concentration) has practically reached n_c. The increase of the total exciton concentration n_2 estimated by us for the case of downshifting IX line (Fig. 1, curve *d*) is 30%, i.e., $n_2 = 1.3n_1$. Because the free-exciton band cannot accommodate more particles than n_c, in the case of Fig. 1, curve *d* one should expect the following exciton distribution over possible states (both free and localized): $n_2 = 1.3n_1 = n_2^{free} + n_2(\varepsilon_0)$, where $n_2^{free} = n_1^{free} = n_c$, and $n_2(\varepsilon_0) = n_2 - n_2^{free} = 1.3n_1 - n_1^{free} = 1.3n_1^{free} - n_1^{free} = 0.3n_1^{free}$.

As pointed out earlier, all localized excitons $n(\varepsilon_0)$ and only a part $n^{free}(\Delta)$ of the total number of free excitons n^{free} confined to the emitting belt Δ contribute to the radiation intensity. Therefore, while in the case of Fig. 1, curve *c* the luminescence intensity was proportional to $n_1^{free}(\Delta)$, in the case of Fig. 1, curve *d* the intensity became proportional to $n_1^{free}(\Delta) + 0.3n_1^{free}$. Thus, the intensity increase in the IX line (part of this line) α expected to be observed experimentally can be cast in the form

$$\alpha = \frac{n_1^{free}(\Delta) + 0.3n_1^{free}}{n_1^{free}(\Delta)} = 1 + \frac{0.3}{\beta}, \qquad (3)$$

where $\beta = n_1^{free}(\Delta)/n_1^{free}$. The energy distribution of n^{free} is described by the Bose–Einstein statistics, so that to estimate β, one has to know the values of $|\mu| = \varepsilon_0$ and Δ. The latter quantity can be estimated for GaAs from momentum conservation considerations for free-exciton emission, which yields $\Delta = 0.06$ meV. The value of $|\mu| = \varepsilon_0$ can be chosen from the following reasoning. We assume that a considerable contribution to the PL intensity of the IX line in our experiments is due, under BEC conditions, to a macroscopic number of excitons populating the localized state ε_0, and the typical values of ε_0 should thus be related to the spectral width (half-width) of the part of the IX line where the intensity burst is actually observed (region *C* of the IX line in Fig. 3). The half-width (full width) of the *C* part of the IX line is 0.4 meV (1 meV), and to estimate the value of β for $T = 1.8$ K we take $0.4 \text{ meV} < \varepsilon_0 < 1$ meV. The calculation shows that $\beta \approx 0.2$ and varies within narrow (5%) limits, with ε_0 varying from 0.4 to 1.0 meV. This yields $\alpha \approx 2.5$, which is in good agreement with the experi-

mentally observed integrated-intensity increase (threefold) of part *C* of the IX line profile (Fig. 3).

Besides, as was pointed out earlier, the part played by nonradiative recombination for localized excitons is much smaller than that for the free ones [20], and therefore the onset of the macroscopic population by excitons of a localized state should give rise to an additional increase in the resultant PL intensity of the IX line.

Note that, in contrast to β, n_c varies quite strongly as ε_0 changes from 0.4 to 1.0 meV. For instance, for GaAs at $T = 1.8$ K, equation (2) yields $n_c = 1.51 \times 10^9$ cm^{-2} at $\varepsilon_0 = 0.4$ meV, while for $\varepsilon_0 = 1$ meV we have $n_c = 0.34 \times 10^8$ cm^{-2}. Such relatively low concentrations, $n_c \sim 10^9$ cm^{-2}, can certainly appear at the excitation levels we use, $P = 5$ W cm^{-2}.

The absence of an intensity burst at $T = 1.8$ K and $P < 1$ W cm^{-2}, as well as at $|4.2| \le T \le 30$ K and for any $P \le 5$ W cm^{-2} implies that the critical conditions (critical particle concentration and critical temperature) for BEC observation are only realized in our experiments at the minimum temperature and maximum optical pumping of the range of *T* and *P* values used in this work.

It appears significant that the intensity burst is only observed within a certain part of the IX line profile. Because each part of the unhomogeneously broadened spectral profile corresponds to different spatial regions in the quantum-well plane differing from one another in the magnitude of the random potential of the heterointerfaces, the BEC only sets in within a part of the excitation spot on the quantum-well surface. A very important argument in support of the suggestion that processes that occur in various spatial regions of a DQW (within the excitation spot) are of a radically different nature comes from the observation of long-period (10 s) intensity fluctuations of a part of the IX line (spectral part *C* of the IX profile in Fig. 3) and from the absence of fluctuations in time within the other parts of the IX line (spectral parts *W* of the IX profile in Fig. 3).

The behavior of the IX line can be qualitatively understood by drawing an analogy between the BEC of excitons occupying localized states (traps) in DQWs and the BEC phenomenon in alkali-metal atoms confined in magnetic traps. Indeed, in both cases, condensation takes place in traps, i.e., spatially limited regions. Certain progress has recently been reached in understanding BEC of atoms in traps. For instance, [21] predicts the existence of metastability for condensate atoms, and [22] calculated the dynamics of the collapse and growth of the number of condensate atoms in a trap and showed the evolution of the number of particles in the condensate to be characterized by long-period (tens of seconds) oscillations. Because it is by the concentration of condensed particles (in our experiment, the particles condensed on traps due to localized states) that the burst in the IX line intensity is determined, the experimentally observed long-period fluctuations in part *C* of the IX line profile may imply a common nature of the reasons accounting for the dynamics of growth and collapse of the condensate of Bose particles in the cases of indirect excitons in DQWs and of alkali-metal atoms in magnetic traps.

Thus, the totality of the experimental data describing the evolution of the IX emission line (more specifically, the onset, at some values of V_{dc}, *T*, and *P*, of a large increase in intensity of a part of the IX spectral profile accompanied by long-period oscillations) may, in our opinion, indicate that, in an indirect-exciton system, a high-density Bose–Einstein condensate is formed in localized states (traps) of double quantum wells. A number of fundamental issues await further study, namely, to what extent spatially indirect excitons are "good" bosons, the shape of the trap potential, the conditions conducive to the formation and possible disappearance of exciton traps, and specific features of the emission mechanisms in the case of a substantial coherence length (or of a length limited by the spatial region of the trap) of radiating states (the role of superluminescence).

ACKNOWLEDGMENTS

The authors are indebted to T.S. Cheng and C.T. Foxon of the Physics Department, Nottingham University (Great Britain), for providing the samples used in this work.

Partial support of the Russian Foundation for Basic Research (grant no. 98-02-18296) is gratefully acknowledged.

REFERENCES

1. Yu. E. Lozovik and V. I. Yudson, Zh. Éksp. Teor. Fiz. **71**, 738 (1976) [Sov. Phys. JETP **44**, 389 (1976)].
2. I. V. Lerner and Yu. E. Lozovik, Zh. Éksp. Teor. Fiz. **80**, 1488 (1981) [Sov. Phys. JETP **53**, 763 (1981)].
3. D. Yoshioka and A. H. MacDonald, J. Phys. Soc. Jpn. **59**, 4211 (1990).
4. Yu. E. Lozovik and O. L. Berman, Zh. Éksp. Teor. Fiz. **111**, 1879 (1997) [JETP **84**, 1027 (1997)].
5. V. V. Krivolapchuk, E. S. Moskalenko, A. L. Zhmodikov, *et al.*, Fiz. Tverd. Tela (St. Petersburg) **41**, 325 (1999) [Phys. Solid State **41**, 291 (1999)].
6. P. C. Hohenberg, Phys. Rev. **158**, 3837 (1967).
7. J. F. Jan and Y. C. Lee, Phys. Rev. B **58**, R1714 (1998).
8. A. Einstein, Sitzungsber. K Preuss. Akad. Wiss., 261 (1924); S. N. Bose, Z. Phys. **26**, 178 (1924).
9. Y. C. Lee, C. S. Chu, and E. Castano, Phys. Rev. B **27**, 6137 (1983).
10. F. Dalfolo, S. Giorgini, L.P. Pitaevskii, and S. Stringari, Rev. Mod. Phys. **71**, 463 (1999).
11. S. A. Moskalenko and D.W. Snoke, *Bose–Einstein Condensation of Excitons and Biexcitons and Coherent Nonlinear Optics with Excitons* (Cambridge Univ. Press, Cambridge, 2000) (in press).

12. L. V. Butov, Z. Zrenner, G. Abstreiter, *et al.*, Phys. Rev. Lett. **73**, 304 (1994).
13. D. W. Snoke and G. Baym, in *Bose–Einstein Condensation*, Ed. by A. Griffin, D. W. Snoke, and S. Stringari (Cambridge Univ. Press, Cambridge, 1995), p.1.
14. P. Kapitza, Nature **141**, 74 (1938); J. F. Allen and A. D. Misener, Nature **141**, 75 (1938).
15. F. London, Nature **141**, 643 (1938).
16. P. E. Sokol, in *Bose–Einstein Condensation*, Ed. by A. Griffin, D. W. Snoke, and S. Stringari (Cambridge Univ. Press, Cambridge, 1995), p. 51.
17. L. Schultheis, A. Honold, J. Kuhl, and K. Kohler, Phys. Rev. B **34**, 9037 (1986).
18. A. Alexandrou, J. A. Kash, E. E. Méwndez, *et al.*, Phys. Rev. B **42**, 9225 (1990).
19. J. Feldman, G. Peter, E. O. Gobel, *et al.*, Phys. Rev. Lett. **59**, 2337 (1987).
20. G. D. Gilliland, A. Antonelli, D. J. Wolford, *et al.*, Phys. Rev. Lett. **71**, 3717 (1993).
21. Yu. Kagan, G. V. Shlyapnikov, and J. T. M. Walraven, Phys. Rev. Lett. **76**, 2670 (1996).
22. C. A. Sackett, H. T. C. Stoof, and R. G. Hulet, Phys. Rev. Lett. **80**, 2031 (1998).

Translated by G. Skrebtsov

Physics of the Solid State, Vol. 42, No. 8, 2000, pp. 1542–1547. Translated from Fizika Tverdogo Tela, Vol. 42, No. 8, 2000, pp. 1499–1504.

LOW-DIMENSIONAL SYSTEMS AND SURFACE PHYSICS

Electronic Structure of Cobalt Disilicide Film

S. I. Kurganskiĭ and N. S. Pereslavtseva

Voronezh State University, Universitetskaya pl. 1, Voronezh, 394693 Russia

e-mail: phssd18@main.vsu.ru

Received January 10, 2000

Abstract—The electronic structure of cobalt disilicide film has been investigated theoretically. The calculations are performed within the framework of the linearized augmented plane wave method. A combined analysis of the total and local partial densities of states and the photoelectron and x-ray emission spectra of different series for all the nonequivalent atoms of the film makes it possible to interpret the main features of the spectral characteristics of this material. © *2000 MAIK "Nauka/Interperiodica".*

1. INTRODUCTION

Transition metal silicides are of considerable interest as promising materials for microelectronics. As a rule, these compounds possess a high conductivity, and their electronic characteristics are stable over a wide range of temperatures. Since the unit cell dimensions in some transition metal silicides (for example, $NiSi_2$ and $CoSi_2$) match those in silicon—the main structural material of microelectronics [1] well, the possibility exists of growing high-quality epitaxial silicide films on the silicon surface and producing heterostructures. The extensive use of silicides in microelectronic devices required detailed investigations into the electrical properties of these materials. Modern theoretical methods, as applied to the study of the electronic structure of transition metal silicides in combination with empirical analysis, make adequate descriptions of their properties and characteristics possible.

The present paper reports the results of theoretical calculations for the spectral characteristics of a $CoSi_2$ film, namely, the total and local partial densities of states and the photoelectron and x-ray emission spectra of different series for all nonequivalent atoms. A comparison of our results with the available experimental data [2–6] permits a qualitative analysis of the structural features of the valence band in cobalt disilicide. For the most part, we used the approaches advanced in our earlier study [7] on the electronic structure of the $NiSi_2$ film, because both films have identical crystal structures of the fluorite type with close lattice parameters (a_0 = 5.362 Å for $CoSi_2$ and 5.4066 Å for $NiSi_2$ [8, 9]). The unit cell of the calculated cobalt disilicide film consists of two unit cells of the bulk crystal and two surface layers of silicon [7].

2. COMPUTATIONAL TECHNIQUE

The electronic structure of the film was calculated within the linearized augmented plane wave method, which was considered in detail in [10]. A brief scheme of calculating the aforementioned spectral characteristics was described earlier in [7].

3. RESULTS AND DISCUSSION

The local partial densities of states were calculated for all nonequivalent atoms in the $CoSi_2$ film (all the atomic designations were specified in [7]). The local partial densities of states for the central and surface Co atoms and the bulk and surface Si atoms are compared in Figs. 1 and 2. According to the calculations, the valence band width in $CoSi_2$ is equal to 13.51 eV, which is somewhat less than that in $NiSi_2$ (13.89 eV) [7]. This decrease in the valence band width can be explained as follows. The valence band width is determined by two factors: the interatomic distance and the number of valence electrons. The shorter the interatomic distance, the stronger the interaction between atoms, because the region of electron cloud overlap increases, and, hence, the splitting of levels increases as well. On the other hand, a decrease in the number of valence electrons results in a decrease in the filled part of the split subbands. It is seen from Table 1 that, compared to $NiSi_2$, the distance between silicon and metal atoms in $CoSi_2$ decreases by approximately 0.02 Å and the number of valence electrons per unit cell decreases by five electrons. The competition of these processes and the domination of the latter factor over the former lead to a decrease in the valence band width in $CoSi_2$ by approximately 0.38 eV as compared to $NiSi_2$.

The Co *d*, Si *s*, and Si *p* states make the main contribution to the formation of the valence band. The Co *d* states are localized about 2.3 eV below the Fermi level E_F. The Si *s* and Si *p* states are localized in two energy ranges: 5–11 and 0–1 eV below E_F. The Co *s* and Co *p* states are distributed throughout the valence band, and their contribution to the total density of states, like the contribution of the Si *d* states, is relatively small. As the

Table 1. Selected crystal and energy parameters of nickel and cobalt disilicides

Compound	a_0, Å	R^*_{MT}(Si), Å	R^*_{MT}(Me), Å	Number of valence electrons per unit cell	ΔE_V, eV
$NiSi_2$	5.4066	1.161	1.18	98	13.89
$CoSi_2$	5.362	1.151	1.17	93	13.51

*R_{MT} are the radii of the so-called "muffin-tin" spheres—nonoverlapping spheres surrounding each atom of the film.

surface is approached, the depth of potential well decreases, and the electronic states are shifted toward the Fermi level, which is clearly seen in Fig. 2. Simultaneously, the densities of the Si *s* and Si *p* states considerably increase in the near-Fermi region and immediately at the Fermi level. It should be noted that the distribution of states over the valence band for atoms of cobalt disilicide as a whole is similar to that of nickel disilicide [7].

The photoelectron spectra of the $CoSi_2$ film were calculated at different excitation energies $\hbar\omega$. A comparison of the calculated spectra with the experimental photoelectron spectra obtained by Weaver *et al.* [2] is given in Fig. 3. As follows from Figs. 1–3, the main peak in these spectra corresponds to the Co *d* state. The locations of this peak at different excitation energies are listed in Table 2. As the excitation energy increases from 25 to 120 eV, the peak shifts away from the Fermi level from 2.11 to 2.2 eV. At low excitation energies (up to 50 eV), the photoelectron spectra exhibit small "shoulders" in the energy ranges 0–1.25, 3.2–4.5, and 6–8 eV below E_F, which are associated primarily with the Si *s* and Si *p* states. An increase in the excitation energy leads to a decrease in the intensity of these fea-

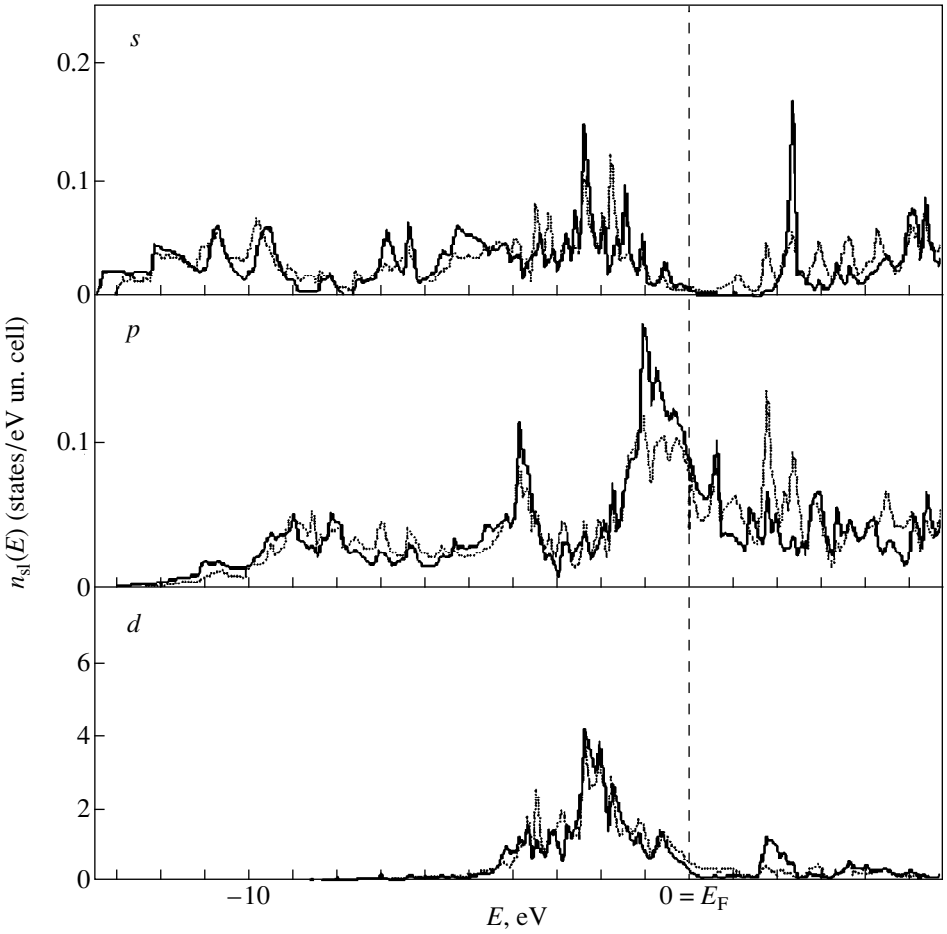

Fig. 1. Local partial densities of states for the central (solid line) and surface (dashed line) Co atoms.

Table 2. Location of the main peak in the photoelectron spectra of cobalt disilicide film (eV)

$\hbar\omega$	25	35	70	120
This work	2.11	2.16	2.16	2.20
[2]	1.30	1.30	1.40	1.40

tures. This is explained by the fact that, with an increase in the excitation energy, the photoionization cross-section for the Co *d* states increases more rapidly than that for the Si *s* and Si *p* states, and, hence, the contribution of the Co *d* states becomes substantially larger. It should be noted that, although the calculated and experimental photoelectron spectra virtually coincide, the locations of the main peak in these spectra of $CoSi_2$ differ considerably. In the calculated spectra, the main peak being attributed predominantly to the Co *d* states is shifted toward higher binding energies by approximately 0.8 eV with respect to the peak observed in the experiments [2]. As the same Co *d* states manifest themselves in the $M_{2,3}$ x-ray emission spectrum, we compared our calculations of this spectrum (see below) with the experimental data obtained by Jia *et al.* [3]. According to [3], the main feature in the Co $M_{2,3}$ x-ray spectrum is observed at a binding energy of an order of 2.4 eV below the Fermi energy E_F, which agrees well with our data (2.3 eV). A substantial difference between the locations of the main peak observed in [2] and [3] can result from inexact location of the Fermi level and differences in the techniques of measuring the spectra and the procedures of silicide preparation.

The calculated x-ray emission spectra of different series for all the atoms of the cobalt disilicide film and the experimental spectra taken from [3–6] are compared in Figs. 4 and 5.

According to the dipolar selection rules, the Si $L_{2,3}$ spectra (Fig. 4) reflect the distribution of the Si *s* and Si *d* states over the valence band. As follows from the calculations, the peaks at energies of ~7–10 and 0.5 eV below E_F are attributed to the *s* states, and the peak near 2.3 eV corresponds to the *d* states. The relative intensity

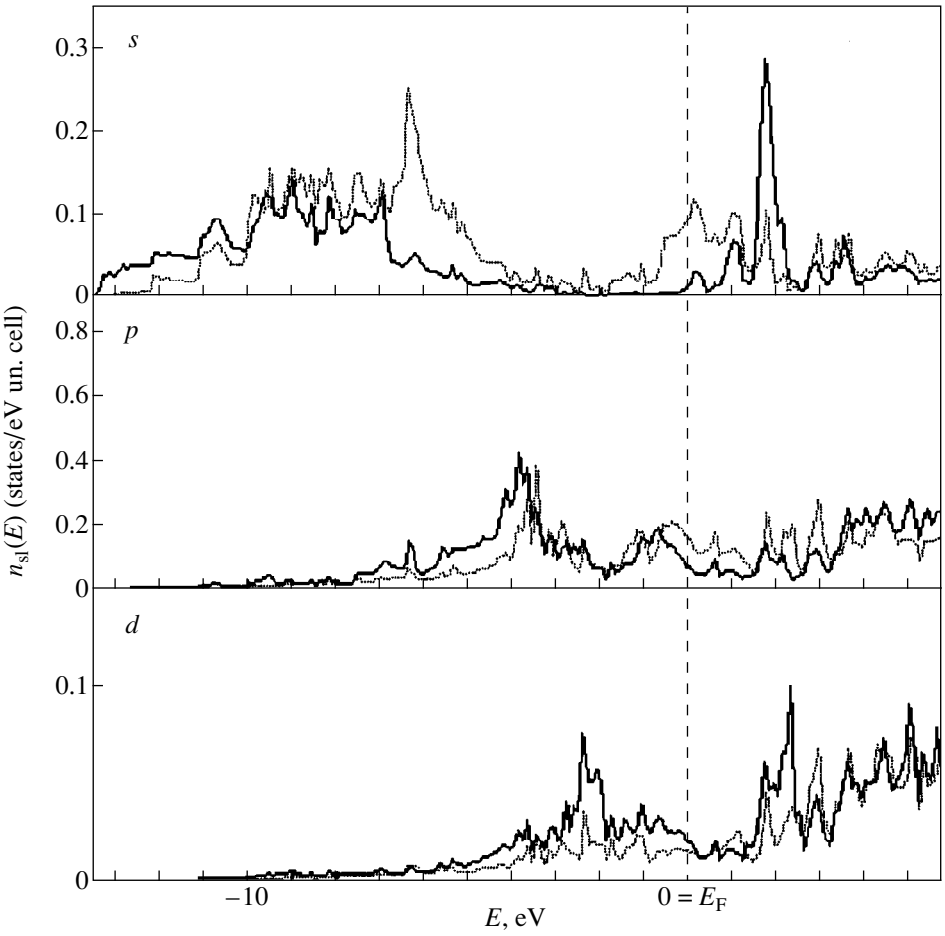

Fig. 2. Local partial densities of states for the bulk (solid line) and surface (dashed line) Si atoms.

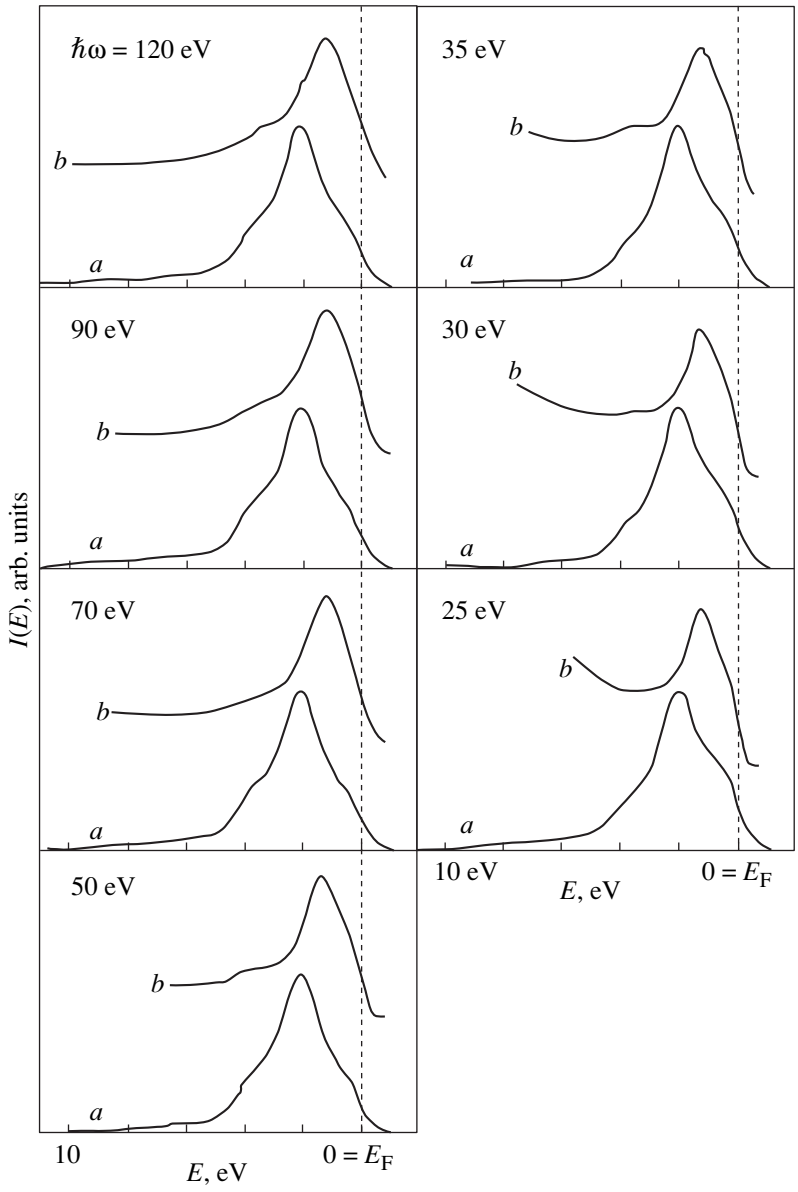

Fig. 3. (*a*) Calculated (this work) and (*b*) experimental (taken from [2]) photoelectron spectra of the $CoSi_2$ film at different excitation energies $\hbar\omega$.

of the last peak is small, because the matrix element of the transition probability for the *s* states is approximately one order of magnitude larger than that for the *d* states. Therefore, the Si $L_{2,3}$ spectra are predominantly determined by the *s* states. A comparison of these spectra with the Si *s* local partial densities of states indicates that the intensity of the peak near the Fermi level with respect to the intensity of the main feature in the range ~7–10 eV in the x-ray emission spectrum is higher than that for the corresponding *s* partial densities of states. This is caused by a monotonic increase in the matrix element of transition probability with an increase in the binding energy, and, as a result, the features in the x-ray emission spectrum near the Fermi level are more pronounced.

The evolution of the peak at an energy of ~0.5 eV is characteristic of the Si $L_{2,3}$ x-ray emission spectra of the film. As follows from the calculations (Fig. 4), the relative intensity of this peak increases as the surface is approached. This effect becomes all the more pronounced in the case of the nickel disilicide films studied earlier. The nature of this phenomenon is associated with the charge transfer from silicon atoms to metal atoms and has been explained in detail in [7]. The relative intensity and the width of this peak in the spectra of the $CoSi_2$ film are less than those in the spectra of the $NiSi_2$ film. This is due to the fact that the contribution of cobalt is one electron less than that of nickel, which leads to the shift in the Fermi level downward on the

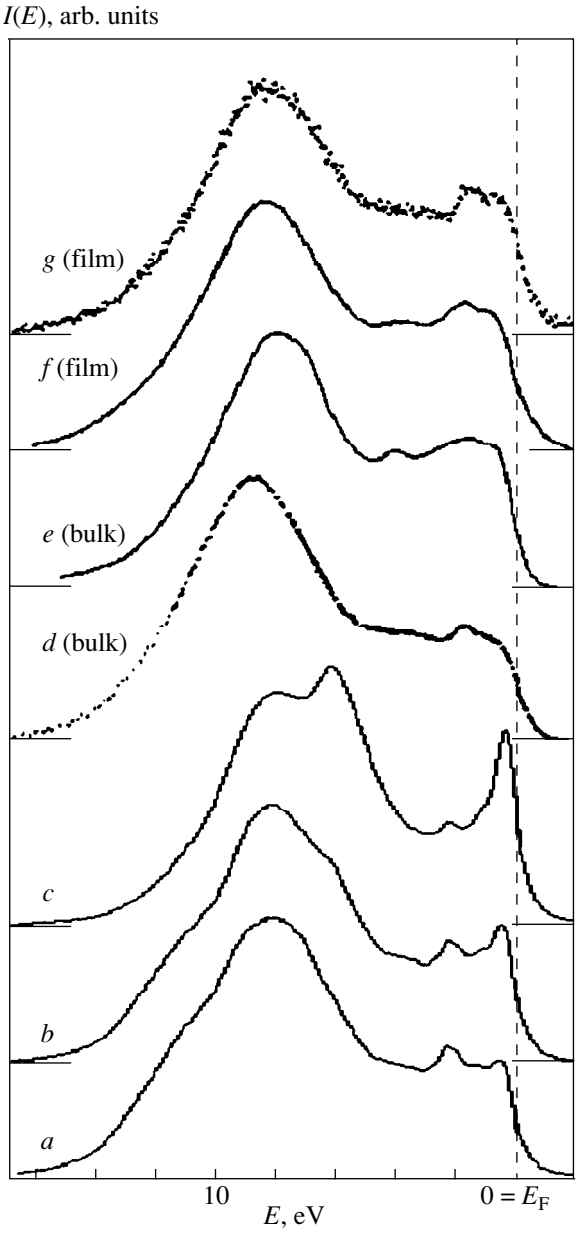

Fig. 4. Si $L_{1,2}$ x-ray emission spectra: the calculated spectra of atoms in (*a*) inner, (*b*) intermediate, and (*c*) surface layers of the film and the experimental spectra of (*d*, *e*) bulk [6, 4] and (*f*, *g*) film [5] samples.

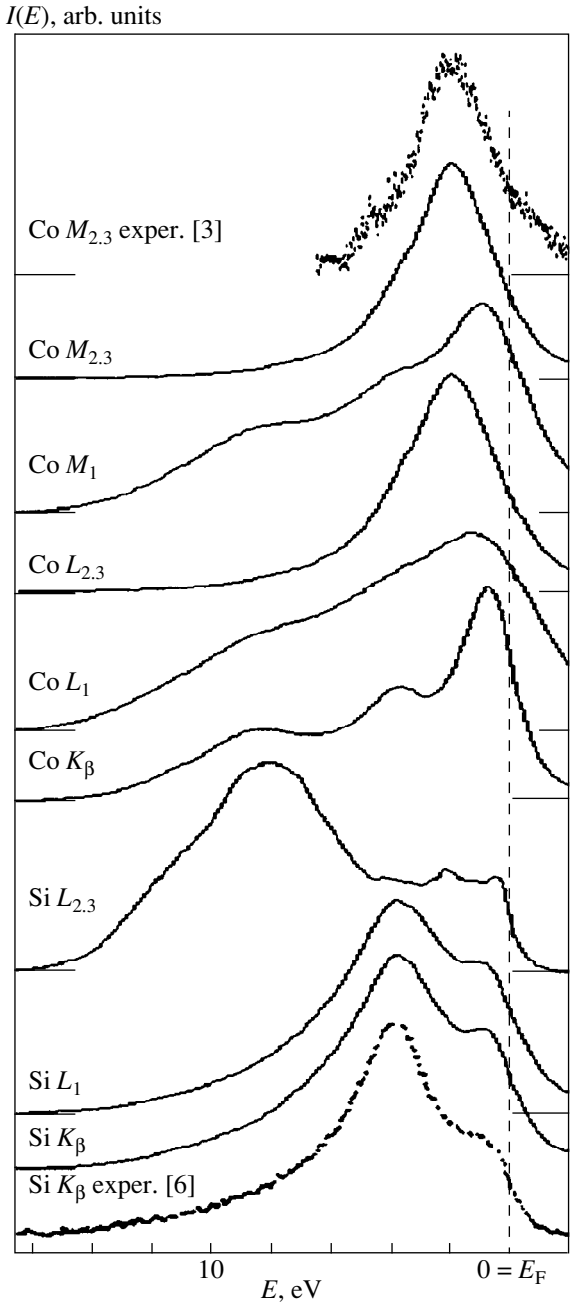

Fig. 5. X-ray emission spectra of different series for atoms of the $CoSi_2$ film.

energy scale. In turn, the shift of the Fermi level brings about a decrease in the number of filled Si *s* states below the Fermi level (Fig. 2) and, correspondingly, a decrease in the linewidth and the intensity of the Si $L_{2,3}$ x-ray emission spectrum in this range. However, as can be seen from Fig. 4, this peak in the experimental spectra of $CoSi_2$ film [4–6] appears to be less intense than that in the calculated spectra. This is explained by a higher content of superstoichiometric silicon in the calculated films as compared to the real films. To put it differently, the width of filled parts of the energy bands in the calculated films is larger than that in the real films.

Figure 5 displays the calculated x-ray emission spectra of all the series for atoms of the $CoSi_2$ film. According to the dipolar selection rules, the Si K_β and Si L_1 spectra shown in this figure reflect the distribution of the Si *p* states in the valence band. The differences in these spectra are caused by a decrease in the width of the 2*s* core level (1.8 eV [11]) as compared to the width of the 1*s* level (2.5 eV [11]). As a consequence, the Si

L_1 spectrum is somewhat narrower than the Si K_β spectrum with more pronounced features. The characteristic double-humped structure of these spectra is explained by the *d–s, p* resonance [12]. According to our calculations, the *d* states of transition metals interact with the Si *s* and Si *p* states and split them into two components with a minimum in the range in which the *d* states of transition metals are localized (see Figs. 1, 2).

The Co K_β, L_1, and M_1 spectra correspond to the same Co *p* states. The K_β spectrum exhibits three clearly defined features. The middle feature is virtually indistinguishable in the L_1 spectrum and again manifests itself in the M_1 spectrum but is not so pronounced as in the K_β spectrum. This is connected with a nonmonotonic change in the width Γ of the core level, into which the transition occurs: $\Gamma_K = 1.09$, $\Gamma_{L_1} = 4.2$, and $\Gamma_{M_1} = 2.6$ eV [11].

Thus, the results obtained in the present work allow us to make the following conclusions:

(1) The valence band of the films is predominantly formed by the Co *d* states localized at an energy of about 2.3 eV below E_F with impurities of the Co *s* and Co *p* states distributed throughout the band and also by the Si *s* and Si *p* states localized in two energy ranges (5–11 and 0–1 eV below E_F) with the impurity of the Si *d* states. The valence band width of cobalt disilicide is equal to 13.51 eV. As the surface is approached, the states shift toward the Fermi level.

(2) At low excitation energies (up to 50 eV), the photoelectron spectra of the film are associated with the Co *d*, Si *s*, and Si *p* states. At high energies of incident photons, the photoelectron spectra are formed only at the expense of the Co *d* states.

(3) The structure of the Si $L_{2,3}$ x-ray emission spectra is primarily determined by the *s* states. The *d* states manifest themselves in the form of a small peak at an energy of 2.3 eV below the Fermi level. As the surface is approached, the evolution of the peak at an energy of ~0.5 eV in the Si $L_{2,3}$ x-ray emission spectrum is brought about by the charge transfer from silicon to cobalt atoms.

(4) The characteristic double-humped shape of the Si K_β and Si L_1 spectra is explained by the *d–s, p* resonance [12].

REFERENCES

1. N. E. Christensen, Phys. Rev. B **42**, 7148 (1990).
2. J. H. Weaver, A. Franciosi, and V. L. Moruzzi, Phys. Rev. B **29**, 3293 (1984).
3. J. J. Jia, T. A. Callcott, W. L. O'Brien, *et al.*, Phys. Rev. B **43**, 4863 (1991).
4. E. P. Domashevskaya and Yu. A. Yurakov, J. Electron. Spectrosc. Relat. Phenom. **96**, 195 (1998).
5. H. Nakamura, M. Iwami, M. Hirai, *et al.*, Phys. Rev. B **41**, 12092 (1990).
6. P. J. W. Weijs, H. van Leuken, R. A. de Groot, *et al.*, Phys. Rev. B **44**, 8195 (1991).
7. N. S. Pereslavtseva and S. I. Kurganskiĭ, Fiz. Tverd. Tela (S.-Peterburg) **41**, 2075 (1999).
8. E. I. Gladyshevskiĭ, *Crystal Chemistry of Silicides and Germanides* (Metallurgiya, Moscow, 1971).
9. P. V. Gel'd and F. A. Sidorenko, *Transition Metal Silicides* (Metallurgiya, Moscow, 1972).
10. H. Krakauer, M. Posternak, and A. J. Freeman, Phys. Rev. B **19**, 1706 (1979).
11. M. A. Blokhin and I. G. Shveĭtser, *A Handbook on X-ray Spectroscopic Analysis* (Nauka, Moscow, 1982).
12. E. P. Domashevskaya and V. A. Terekhov, Phys. Status Solidi B **105**, 121 (1981).

Translated by O. Borovik-Romanova

Physics of the Solid State, Vol. 42, No. 8, 2000, pp. 1548–1553. Translated from Fizika Tverdogo Tela, Vol. 42, No. 8, 2000, pp. 1505–1510.

POLYMERS AND LIQUID CRYSTALS

Structural Defects in Carbazolyl-Containing Polymers with Polymethine Dye Impurities

Yu. A. Skryshevskiĭ, A. K. Kadashchuk, and N. I. Ostapenko

Institute of Physics, National Academy of Sciences of Ukraine, pr. Nauki 144, Kiev, 258650 Ukraine

e-mail: Kadash@iop.kiev.ua

Received November 10, 1999

Abstract—Photoluminescence spectra and thermoluminescence curves of pure and doped carbazolyl-containing polymers polyvinyl carbazole (PVC) and poly-*N*-epoxypropyl carbazole (PEPC) are investigated in the temperature range 5–300 K. The impurities are cationic indocarbocyanines with various lengths (n) of the polymethine chain: HIC (n = 1), HID (n = 2), HIT (n = 3) and squaryl dye HISq with the same polymethine chain length and the same structure of heterocyclic end groups as for the HID dye. It is found that solvation of dye molecules by polar groups of a polymer is accompanied by conformation changes in the polymer, which are considerably enhanced with increasing n, as well as upon a transition from a rigid-chain PVC macromolecule to a more flexible PEPC molecule. As a result, the concentration of structural defects, viz., excimer-forming sites playing the role of traps for singlet excitons and charge carriers, increases considerably in doped PEPC films. This leads to the emergence of a band with a peak at 460 nm in the luminescence spectra of PEPC films with HID and HIT and at 480 nm for films with the HISq impurity, while the thermoluminescence curve for PEPC with HISq acquires an additional band with a peak at 275 K. © *2000 MAIK "Nauka/Interperiodica".*

The wide application of amorphous organic photosemiconductors as electrophotoreceptors, optoelectronic devices, and media for optical recording of information stimulates the study of charge carrier transport and electron excitation spectra in these systems [1–4]. The spectra of excited states of molecules and the energy states of charge carriers in amorphous systems are broadened nonuniformly due to the energy-disordering effects and can be described by the density of states (DOS) function. For this reason, many properties of amorphous photosemiconductors can be explained on the basis of energy relaxation processes for electron excitations or photogenerated charge carriers in a system of disordered energy states [5, 6]. We demonstrated earlier [7–10] that the information of the DOS shape and the energy spectrum of charge carrier traps can be obtained by analyzing thermostimulated luminescence of an organic photosemiconductor.

Since carbazolyl-containing polymers based on polyvinyl carbazole (PVC) and poly-*N*-epoxypropyl carbazole (PEPC) absorbing the near UV range, special admixtures which usually serve as the centers of absorption, as well as photogeneration, are introduced for their sensitization to visible and IR radiation and for increasing the quantum yield of the photogeneration of charge carriers. The role of sensitizers is usually played either by acceptors forming intermolecular complexes with electron-donor carbazolyl group as a result of charge transport, or by dyes which form in many cases exciplexes with the above groups [1, 2].

We recently proved [11] that the introduction of some dyes into PEPC leads to the emergence of deep charge carrier traps whose origin is associated with conformation changes in the polymer. This work is a continuation of the study of structural reorganization of carbazolyl-containing polymers upon the introduction of polymethine dyes of various structures and of the origin of the emerging structural defects and their role in the migration of electron excitation energy and charge carrier transport. For the same purpose, we investigated the photoluminescence spectra and thermoluminescence (TL) curves of PVC and PEPC films with impurities of cationic and squaryl indocarbocyanines HIC, HID, HIT, and HISq at temperatures T = 5–300 K in the concentration range $10^{-3}\% \le C \le 2\%$. The structural formulas of the dyes under investigation are shown in Fig. 1.

1. EXPERIMENTAL TECHNIQUE

The PVC and PEPC polymers and dyes were purified by the reprecipitation of their solutions in methylene chloride or toluene. The molecular masses of PVC and PEPC were $M = 10^6$ and 10^3, respectively. Pure and doped polymer films of thickness 1–100 μm were prepared by pouring their solutions in methylene chloride or toluene on stainless steel substrates (for measuring the TL curves) or on quartz substrates (for optical measurements).

Low-temperature experiments (T = 5–300 K) were made by using a controllable optical helium cryostat with quartz windows and an automatic temperature-control system. The sample temperature was measured by a differential copper–constantan thermocouple.

1063-7834/00/4208-1548$20.00 © 2000 MAIK "Nauka/Interperiodica"

The luminescence spectra (T = 5–300 K) were recorded on a SDL-1 spectrometer. The source of excitation was a DRSh-250-2 mercury lamp equipped with a set of light-absorbing glass filters. The absorption spectra (T = 300 K) were measured on the spectro-compu-tional complex KSVU-23.

In order to obtain TL curves, we illuminated the samples in the helium cryostat with light emitted by a DRSh-500M mercury lamp in the range λ_{exc} = 365 nm during a time t = 60 s at T = 5 K, kept them in the dark until the quenching of phosphorescence and isothermal recombination luminescence, and then heated them at a constant rate of 0.15 K/s. The integrated signal of thermostimulated luminescence was measured on an automated setup with the help of the photoelectric multiplier FEU-106 operating in the photon counting mode. The energy spectrum of charge carrier traps was determined by the method of partial thermoluminescence, which is a temperature modulation of the linear heating of the sample [12].

2. DISCUSSION OF RESULTS

2.1. Luminescence Spectra of Pure PVC and PEPC Polymer Films

In a PVC macromolecule, carbazolyl groups are attached to every second carbon atom in the polymer chain, and their sequential position facilitates the formation of a high concentration of structural defects, viz., excimer-forming sites (C = 0.1% [13]), which have the form of predimer configurations of two carbazolyl groups with a partial overlapping of their π-electron systems. The luminescence spectrum of PVC at T = 5 K is a broad structureless band with a peak at λ_{max} = 378 nm (curve *1* in Fig. 2), which is attributed to the fluorescence of excimers with a partial overlapping of two carbazolyl chromophores [14–16]. The long-wave edge of this band has a weakly pronounced step at λ = 400 nm. As the temperature increases, the relative intensity of this step increases, and at T > 100 K, it is replaced by a band with λ_{max} = 415 nm attributed to the fluorescence of excimers with complete overlapping of carbazolyl groups [14–16].

In contrast to rigid-chain PVC, PEPC is a completely amorphous substance whose x-ray diffraction patterns do not reveal any features of ordering [17], and its polyester chains are distinguished by a high flexibility and consist of only three or four monomeric links [17]. The presence of excimers in a polymer remains disputable to this day.

The luminescence spectrum of pure PEPC (T = 5 K) for λ_{exc} = 313 nm contains bands for λ_{max} = 358 and 374 nm, which can be attributed unambiguously to the electron and electronic–vibrational transitions in monomeric carbazolyl chromophores [18], as well as low-intensity bands at 408, 433, 460, and 485 nm (curves *1* and *2* in Fig. 3). The spectral structure in the range λ = 400–500 nm is manifested more clearly for

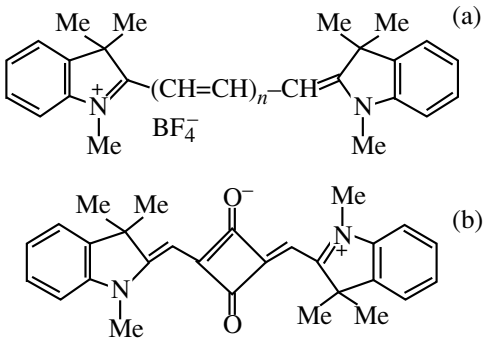

Fig. 1. Structural formulas (a) of ionic dyes HIC (n = 1), HID (n = 2), HIT (n = 3), and (b) of the squaryl dye HISq.

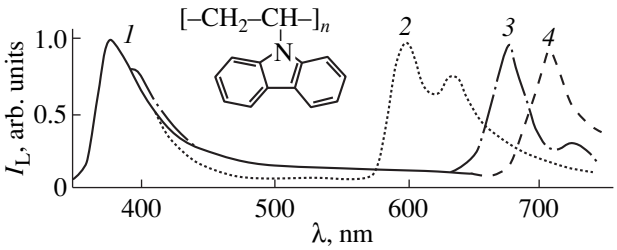

Fig. 2. Photoluminescence spectra of pure (*1*) PVC and with the dyes (C = 2%) (*2*) HIC, (*3*) HISq, and (*4*) HID, measured at T = 5 K and λ_{exc} = 313 nm. The inset shows the structural formula of PVC.

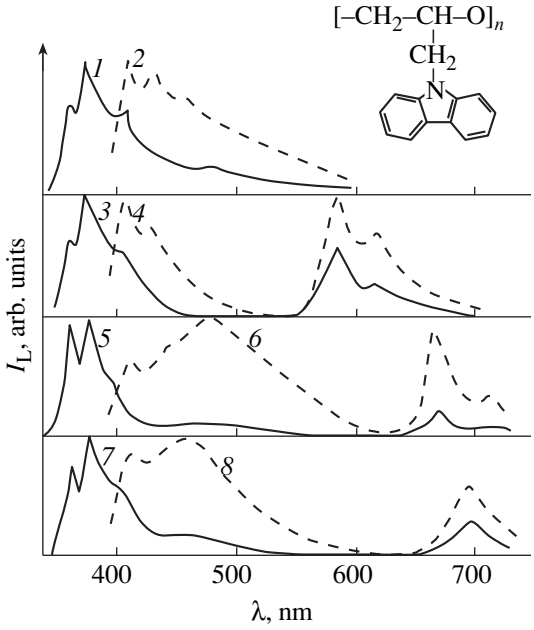

Fig. 3. Photoluminescence spectra of pure (*1*, *2*) PEPC and with the dyes (C = 0.1%) (*3*, *4*) HIC, (*5*, *6*) HISq, and (*7*, *8*) HID, measured at T = 5 K and λ_{exc} = 313 nm (*1*, *3*, *5*, *7*) and λ_{exc} = 365 nm (*2*, *4*, *6*, *8*). The inset shows the structural formula of PEPC.

the excitation in the range of weak absorption by the polymer (λ_{exc} = 365 nm), where the penetration depth for the exciting light is much larger than for λ_{exc} = 313 nm. Consequently, the concentration of the centers responsible for the structural emission in the range of λ = 400–500 nm is insignificant.

The origin of these centers was studied most thoroughly by Piryatinskiĭ *et al.* [18], who studied the luminescence spectra of solutions and films of PEPC and *N*-vinyl carbazole (NVC) in the temperature range T = 5–300 K by the time resolution technique. It was shown that the luminescence spectrum of PEPC contains four components: the fluorescence of monomer links (358, 374, and 389 nm), fluorescence of the anthracene impurity (392, 412, and 434 nm), the excimer–exciplex fluorescence (450–460, 485, and 525 nm), and the phosphorescence for $\lambda > 400$ nm. These components differ in the kinetics of buildup and decline of radiation intensity, in the energy position, and the temperature interval in which these are observed. For example, the phosphorescence intensity decreases upon heating above T = 5 K, while the intensity of excimer radiation decreases as a result of sample cooling below T = 300 K. It should be noted that the fluorescence band for λ_{max} = 460–465 nm was also observed in the spectra of NVC films [8] and crystals [19].

The PVC phosphorescence spectrum lies in the region of $\lambda > 400$ nm. At T = 5 K, it has a structure with λ_{max} = 425 and 460 nm. This structure disappears with increasing temperature, and the spectrum at T = 77 K consists of a wide structureless band with λ_{max} = 500 nm. The PEPC phosphorescence spectrum at T = 5–77 K is similar to the PVC spectrum at T = 77 K.

2.2. Luminescence Spectra of PVC and PEPC Films with HIC, HID, HIT, and HISq Dyes

Fluorescence bands of HIC, HID, and HISq dyes are observed in the spectra of impurity films for $C \geq (10^{-3}$–$10^{-2})$%, the positions of their peaks being displaced bathochromically upon an increase in the concentration up to C = 2% (Figs. 2 and 3). In particular, for the HIC dye in PVC and PEPC for C = 0.1%, one observes λ_{max} = 590 nm, while for C = 2%, λ_{max} = 600 nm. For the HID dyes in PVC and PEPC with C = 0.1%, one observes λ_{max} = 695 nm, while for C = 2%, λ_{max} = 700 and 715 nm, respectively. For the HISq dye with C = 0.1%, the peak position is λ_{max} = 670 nm in the PEPC matrix and λ_{max} = 676 nm in PVC. For C = 2%, λ_{max} = 676 nm for all polymer matrices (see Fig. 2).

An increase in the dye concentration in a polymer in the range $0.1\% \leq C \leq 2\%$, together with the intensification of sensitized luminescence, leads to a decrease in the intensity of radiation emitted by the matrix, which is pronounced most clearly for the HIC dye. This indicates an effective transfer of the electron excitation energy from the polymer matrix to the impurity. Let us consider the change in the luminescence spectra of polymer matrices as a result of introducing HIC, HID, HIT, and HISq dyes. It was found that these dyes with $C = (10^{-2}$–2)% do not affect the structure of the phosphorescence spectra of PVC and PEPC.

An increase in the HIC concentration in PVC and PEPC in the interval $C = (10^{-2}$–2)% causes barely any significant variation of the spectral structure (T = 5 K) in the excimer and monomer emission range (curve *2* in Fig. 2 and curves *3* and *4* in Fig. 3) and leads to a strong suppression of the intensity of phosphorescence in PVC and PEPC.

In contrast to HIC, the introduction of the HISq and HID dyes ($C = (10^{-2}$–2)%) practically does not affect the PVC phosphorescence intensity at T = 5 K and leads to a slight increase in the relative intensity of the fluorescence band for excimers with λ_{max} = 415 nm as compared to the band with λ_{max} = 378 nm (curves *3* and *4* in Fig. 2).

The fluorescence spectra of PEPC with HISq and HID dyes for $0.01\% \leq C \leq 0.5\%$ acquire new intense and wide bands with λ_{max} = 480 and 460 nm, respectively (curves *5*–*8* in Fig. 3). A further increase in the dye concentration leads to a decrease in the intensity of these bands, and for $C \geq 1\%$ they are suppressed altogether. The band with λ_{max} = 460 nm is also present in the fluorescence spectra of PEPC with the HIT dye ($10^{-2}\% \leq C \leq 1\%$).

The bands with λ_{max} = 480 and 460 nm do not belong to uncontrollable impurities in dyes, since the radiation emitted by uncontrollable impurities was not detected in the luminescence spectra of polyvinyl butyral films with HISq and HID dyes. It should be noted that polyvinyl butyral does not contain aromatic groups, and the pure polymer does not exhibit luminescence in this spectral region.

The bands with λ_{max} = 480 and 460 nm are not associated with the radiation from the complexes formed among electron-donor carbazolyl groups and electron-acceptor dye molecules or uncontrollable impurities in them, either, since their intensity must increase with the dye concentration, which is not observed in experiments. Besides, these bands are absent in the spectra of PVC impurity films (curves *3* and *4* in Fig. 2) whose molecules contain carbazolyl groups like PEPC molecules. Consequently, the emergence of these bands in the spectra of PEPC impurity films is associated with the emergence of structural defects of the conformation origin in the polymer.

2.3. Association of HISq and HID Dyes in Polymer Matrices

In order to establish the factors leading to conformational changes in PEPC upon the introduction of HISq and HID dyes, we studied the association processes of these dyes in various polymers [20]. For this purpose, we measured the absorption and luminescence spectra

of HISq and HID dyes in polystyrene (PS), PEPC, and PVC with $C = (10^{-3}–2)\%$.

The cationic dye HID is a saltlike compound (see Fig. 1). For this reason, it can dissociate into an anion and a cation in polar solvents for low concentrations and may exist in the form of solvated ions. With increasing concentration, contact (or solvate- separated) ionic pairs are the first to be formed, followed by their associates [21].

A molecule of the squaryl dye HISq has the same length of polymethine chain and the same structure of heterocyclic end groups as the cation HID, but unlike this cation, it is a chemically coupled undissociated ionic pair (see Fig. 1). The associate HISq consists of two monomer molecules and is formed as a result of the electrostatic interaction between unlike charges localized at the nitrous heterocycle and the squaryl group of each molecule.

It was found that the association processes of HID and HISq dyes in various polymeric matrices differ significantly. For example, the HID dye exists in the form of solvated ions in the polar PEPC and in the form of contact ionic pairs in the low-polarity PS (the refractive indices of PEPC and PS are 1.80 and 1.59, respectively). This conclusion is based on the different dependences of the absorption and luminescence spectra on the impurity concentration in PEPC and PS. An increase in the HID concentration in PEPC leads to a bathochromic displacement of the peaks of the impurity absorption and luminescence bands. On the contrary, these peaks in PS experience a hypsochromic shift, and the intensity of the short-wave edge of the absorption band increases.

In both polymers, the HISq dye with $C \geq 10^{-3}\%$ exists only in the associated form. However, for low concentrations ($C < 1\%$) at which the structure of associates is formed, their intermediate forms were detected in PEPC, which are manifested in the form of additional absorption and luminescence bands. These extra bands vanish for $C \geq 1\%$, when the structure of associates is completely formed (in this case, the positions of the peaks of the absorption, as well as luminescence bands, in PEPC and PS coincide since they are determined only by the interaction of HISq monomeric molecules). In contrast to PEPC and PS, intermediate forms of associates of HISq molecules were not detected.

These results lead to the conclusion that the weaker association of HISq and HID dyes in PEPC as compared to PS is due to the electrostatic interaction of its polar groups with the charged centers of HISq and HID molecules, i.e., as a result of their solvation [20]. As we go over from the PEPC to the PVC matrix, the association of HISq and HID dyes is enhanced. This follows from a comparison of the concentration dependences of the positions of the absorption and luminescence bands of dyes in these polymers. It was mentioned in the previous subsection that the displacements of the luminescence bands of the dyes as a result of a change in their concentration C from 0.1 to 2% decrease as we go over from PEPC to PVC. In contrast to PEPC, the structure of associates of HISq molecules in PVC is completely formed even for $C = 0.1\%$, and a further increase in the concentration to $C = 2\%$ does not change the position of the emission band for associates (the fluorescence band of the HISq dye in the PVC matrix corresponds to $\lambda_{max} = 676$ nm for $C = 0.1–2\%$).

2.4. Origin of Structural Defects in PEPC Films with HISq and HID Dyes

The above results suggest that new wide bands with $\lambda_{max} = 480$ and 460 nm in the luminescence spectra of doped PEPC films appear as a result of the solvation of dye molecules by the polar groups of the polymer and can be associated with conformational changes in the polymer.

Figure 3 shows that the band with $\lambda_{max} = 460$ nm is not present in the luminescence spectrum of PEPC with HIC, but appears in the spectrum of PEPC with HID. This band was also observed in the spectrum of PEPC with HIT. It is well known [21] that the solvation of these dyes occurs through the electrostatic interaction of the distributed charge of cations with the dipoles of solvent molecules and is enhanced upon an increase in the length (n) of the polymethine chain of the cation. The maximum change in the interaction energy occurs upon a transition from $n = 1$ (HIC) to $n = 2$ (HID) and, to a smaller extent, upon a transition from $n = 2$ to $n = 3$ (HIT) [21], which correlates with the emergence of a band with $\lambda_{max} = 460$ nm in the fluorescence spectra of PEPC with HID and HIT dyes. Considering that PEPC is a low-molecular polymer [17] and that its chains are quite flexible, we can assume that the long-range electrostatic interaction of the distributed charge of HISq and HID molecules with the polar groups of the polymers leads to the ordering of the orientation of carbazolyl chromophores, their convergence, and the enhancement of the interaction between their electron systems. As a result, the carbazolyl chromophores of PEPC form a set of predimer configurations in the vicinity of a dye molecule, which leads to an increase in the concentration of an excimer-forming site in impurity films and to the emergence of bands with $\lambda_{max} = 480$ and 460 nm in their luminescence spectra (Fig. 3). It should be noted that these bands, though with a much lower intensity, are also present in the luminescence spectra of pure PEPC [18].

In contrast to PEPC with flexible polymer chains, PVC is a rigid-structure polymer with an ordered arrangement of carbazolyl chromophores. Consequently, HISq and HID molecules in the high-molecular PVC form aggregates much more intensely than in PEPC, and the luminescence spectra of doped PVC films do not acquire any new bands associated with conformational changes in the polymer. The introduc-

tion of the above impurities leads only to an insignificant increase in the relative intensity of the fluorescence of excimers with λ_{max} = 415 nm as compared to excimers with λ_{max} = 378 nm (see Fig. 2).

2.5. Thermostimulated Luminescence of Pure and Doped PVC and PEPC Films

An analysis of luminescence spectra of carbazolyl-containing polymers proved that the introduction of HISq and HID dyes leads to their solvation by the polar groups of the polymer and is accompanied by an enhancement of the interaction between carbazolyl chromophores, which becomes much stronger as we go over from PVC to PEPC. According to Andreev *et al.* [22], this should lead to a local increase in the electron polarization energy of the matrix in the vicinity of a dye molecule and to the formation of charge carrier traps of a structural origin, whose depth increases upon a transition from PVC to PEPC. Charge carrier traps in pure and doped polymers are studied by the thermostimulated luminescence technique.

The TL curves for PVC and PEPC are qualitatively similar and consist of a wide asymmetric band in the temperature range T = 5–200 K with peaks at T_{max} = 110 and 130 K in PVC and PEPC, respectively (curves *1* and *2* in Fig. 4), and a sharp high-temperature edge. The low-temperature wing of TL curves has an additional peak at T_{max} = 30–40 K, whose relative intensity is different for different samples. We proved earlier [23] that this peak is associated with thermally activated tunnel recombination of closely spaced hymenal electron–hole pairs.

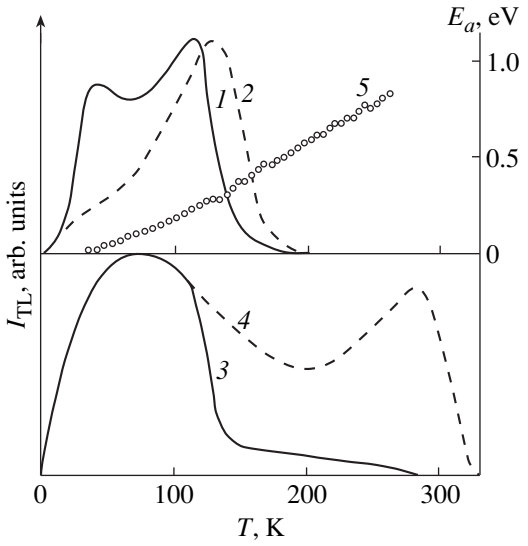

Fig. 4. TL curves for PVC (*1*, *3*) and PEPC (*2*, *4*) films: pure (*1*, *2*) and with HISq dye (*3*, *4*); curve *5* corresponds to the dependence $E_a(T)$.

The fractional thermoluminescence method was used to measure the temperature dependences of the activation energy E_a of thermal liberation of charge carriers along the TL curves for PVC and PEPC. These dependences for both polymers coincide and have the form of a monotonically increasing continuous function (curve *5* in Fig. 4). The introduction of HISq and HID dyes (C = 2%) into a polymer does not affect the $E_a(T)$ dependence.

We proved earlier [7–10] that the role of traps for charge carriers in pure amorphous polymers is played by the lowest energy states in the DOS. The temperature T_{max} on the TL curve corresponds to the depth E_{max} of traps for which the density of occupied states in the DOS has the maximum value. Thus, the value of E_{max} = 0.24 eV for PVC and 0.33 eV for PEPC (Fig. 4).

Let us consider the TL curves for PVC and PEPC with the HISq dye (C = 2%). The introduction of a dye into PVC leads to only an insignificant pulling of the high-temperature edge of the TL curve and to the emergence of a weakly pronounced plateau in the temperature range T = 150–250 K (curve *3* in Fig. 4), which corresponds to the emergence of new charge carrier traps having a depth E = 0.41–0.80 eV. This effect is considerably enhanced as we go over from PVC to PEPC. The TL curve for PEPC with HISq acquires a new high-intensity band in the region of T = 200–300 K (E = 0.51–1.12 eV) with a peak at T_{max} = 275 K (E_{max} = 0.91 eV) (curve *4* in Fig. 4).

We can assume that new traps are formed in doped polymers as a result of capture of charge carriers (holes), either directly at dye molecules or at structural defects of the conformation origin. According to [13, 22], the depth of an impurity trap for holes is determined by the difference in the ionization potentials of the matrix molecules (I_H) and impurity molecules (I_G). Since the values of I_H for PVC and PEPC molecules virtually coincide (7.32 and 7.34 eV, respectively [24]), the depths of impurity traps in these matrices must also coincide.

Figure 4 shows that the depths of the traps formed as a result of introducting HISq dyes increase as we go over from PVC to PEPC. Consequently, their origin can be associated with structural defects formed as a result of enhancement of interaction between chromophores in doped polymers.

Thus, we have established that the introduction of cationic and squaryl indocarbocyanines into carbazolyl-containing polymers is accompanied by their solvation, leading to conformational changes and to an enhancement of the interaction between chromophores in a doped polymer. The conformational changes are considerably enhanced with the increasing length of the polymethine chain of the dye cation, as well as upon a transition from the rigid-chain PVC with an ordered structure of the polymer chain to the completely amorphous atactic PEPC. As a result, doped polymers

acquire deep traps for singlet excitons and charge carriers of the conformational origin, which emerge in the photo- and thermostimulated luminescence.

ACKNOWLEDGMENT

This research was partially supported by the CRDF grant no. UE1-326.

REFERENCES

1. A. V. Vannikov and A. D. Grishina, *Photochemistry of Polymer Donor–Acceptor Complexes* (Nauka, Moscow, 1984).
2. P. M. Borsenberger and D. S. Weiss, *Organic Photoreceptors for Xerography* (Marcel Dekker, New York, 1998).
3. C. Adachi, K. Nagai, and N. Tamoto, Appl. Phys. Lett. **66**, 2679 (1995).
4. W. E. Moemer and S. M. Silence, Chem. Rev. **94**, 127 (1994).
5. H. Bassler, Phys. Status Solidi B **175** (1), 15 (1993).
6. H. Bassler, in *Disordered Effect on Relaxational Processes* (Springer, Berlin, 1994), p. 585.
7. A. Kadashchuk, N. Ostapenko, V. Zaika, and S. Nespurek, Chem. Phys. **234**, 285 (1998).
8. S. Nespurek, A. Kadashchuk, N. Ostapenko, and V. Zaika, Mol. Cryst. Liq. Cryst. **324**, 95 (1998).
9. A. Kadashchuk, N. Ostapenko, V. Zaika, and P. M. Borsenberger, J. Imaging Sci. Technol. **43** (3), 213 (1999).
10. A. Kadashchuk, D. S. Weiss, P. M. Borsenberger, *et al.*, Chem. Phys. **247**, 307 (1999).
11. N. A. Davidenko, A. A. Ishchenko, A. K. Kadashchuk, *et al.*, Fiz. Tverd. Tela (St. Petersburg) **41** (2), 203 (1999) [Phys. Solid State **41**, 179 (1999)].
12. I. A. Tale, Phys. Status Solidi A **66**, 65 (1981).
13. M. Pope and S. E. Swenberg, *Electronic Processes in Organic Crystals* (Clarendon, Oxford, 1982).
14. S. Tagawa, M. Washio, and Y. Tabata, Chem. Phys. Lett. **68**, 276 (1979).
15. G. Peter, H. Bassler, W. Schrof, and H. Port, Chem. Phys. **94**, 445 (1985).
16. G. Giro, P. G.Di Marco, M. Pizzoli, and G. Ceccorulli, Chem. Phys. Lett. **150** (1–2), 159 (1988).
17. A. I. Undzenas and E.V. Gert, Vysokomol. Soed., Ser. A **25**, 984 (1983).
18. Yu. P. Piryatinskiĭ, V. N. Yashchuk, Yu. A. Cherkasov, *et al.*, Zh. Prikl. Spektrosk. **53** (1), 41 (1990).
19. R. Sano and S. Matsuda, J. Chem. Phys. **64**, 4523 (1976).
20. Yu. A. Skryshevskiĭ, N. A. Davidenko, A. A. Ishchenko, *et al.*, Opt. Spektrosk. **88**, 399 (2000) [Opt. Spectrosc. **88**, 352 (2000)].
21. A. A. Ishchenko, *Structure and Spectral Luminescence Properties of Polymethine Dyes* (Naukova Dumka, Kiev, 1994).
22. V. A. Andreev, M. V. Kurik, S. Neshpurek, É. A. Silin'sh, V. I. Sugakov, L. F. Taure, E. L. Frankevich, and V. Chapek, *Electronic Processes in Organic Molecular Crystals: Transport, Capture, and Spin Effects* (Zinatne, Riga, 1992).
23. A. K. Kadashchuk, N. I. Ostapenko, Yu. A. Skryshevskiĭ, *et al.*, Fiz. Tverd. Tela (Leningrad) **31** (7), 203 (1989) [Sov. Phys. Solid State **31**, 1212 (1989)].
24. R. I. Blyumbergas and A.I. Undzenas, Zh. Nauchn. Prikl. Fotogr. Kinematogr. **29** (3), 219 (1984).

Translated by N. Wadhwa

Physics of the Solid State, Vol. 42, No. 8, 2000, pp. 1554–1560. Translated from Fizika Tverdogo Tela, Vol. 42, No. 8, 2000, pp. 1511–1517.

POLYMERS AND LIQUID CRYSTALS

X-ray Scattering from Freely Suspended Smectic-A Films

L. V. Mirantsev

Institute of Problems in Machine Science, Russian Academy of Sciences, Vasil'evskiĭ Ostrov, Bol'shoĭ pr. 61, St. Petersburg, 199178 Russia

e-mail: miran@microm.ipme.ru

Received December 7, 1999; in final form, February 11, 2000

Abstract—This work is devoted to a theoretical analysis of specular reflection and diffuse scattering of x-rays from a freely suspended smectic-A film, taking into account its spatial inhomogeneity and deviations of orientational and position ordering in smectic layers from ideal ordering. The results of the calculations are compared with the experimental data on small-angle scattering of x-rays from freely suspended films of 7 AB liquid crystals. It is found that the theoretical results agree with the experimental data. © *2000 MAIK "Nauka/Interperiodica".*

Liquid crystals (LC) are organic compounds formed in most cases by elongated molecules [1, 2]. The simplest LC phase is a nematic LC (NLC) distinguished from an ordinary isotropic liquid by the presence of a long-range orientational order, such that the long axes of its molecules are directed predominantly along a certain direction **n** known as a director. In more ordered smectic phases (SLC), a periodicity in a certain direction (position ordering) is observed apart from the long-range orientational order. In the simplest smectic phase referred to as the smectic-A (Sm A) phase, the molecules form equidistant layers perpendicular to the direction of **n**. In this case, there is no ordering in the arrangement of the centers of mass of molecules in the plane of the layers themselves. The layered structure of SLC makes it possible to create freely suspended films that cannot be formed by isotropic liquids or NLC. The area of such films can be as large as of the order of 1 cm^2 [3], while their thickness varies from several hundreds of layers to two or even one smectic layer [4, 5]. This makes freely suspended smectic films the perfect objects for studying the crossover from the behavior of three-dimensional physical systems to the behavior of 2*D* systems and explains the considerable interest of experimenters [3–21], as well as theorists [22–30], in these objects in the last 10–20 years.

The most comprehensive information on the structure of freely suspended smectic films can be obtained from the experiments on small-angle x-ray scattering. These experiments make it possible to determine the film thickness, the thickness of smectic layers contained in it [9, 10], and the amplitudes of thermal fluctuations in the film, as well as the correlation between them [18–21]. However, such information can be obtained only with the help of a theoretical model of a freely suspended smectic film of any preset thickness, which would correctly describe its equilibrium properties and thermal fluctuations in it. Holyst [22, 23] proposed a simple discrete model for describing such fluctuations of the displacement of smectic layers in a freely suspended smectic-A film, which takes into account the compression and transverse bend of smectic layers, as well as the surface tension of the film. Later [24, 25], a more convenient continual version of this theory for describing experimental data was developed. This model makes it possible to easily calculate the fluctuation profile for the displacement of smectic layers of the film, as well as the correlation between the layers, and to evaluate the angular dependences of the specular reflection coefficients and diffuse scattering of x-rays. The model can be used to correctly describe the results of experiments on small-angle scattering of x-rays from freely suspended films of certain LC compounds [18, 19].

In Holyst's model, a freely suspended smectic-A film is assumed to be spatially homogeneous and is characterized by the number N of smectic layers, the surface tension γ, and elastic moduli of transverse bending K and extension (compression) B of smectic layers. These moduli are assumed to be identical for all layers of the film, irrespective of their position, and are equated to the corresponding elastic moduli in the bulk of the Sm A phase. It was shown in [30] that this assumption is physically justified only at much lower temperatures than those of the phase transitions Sm A $\longrightarrow$ nematic (Sm A $\longrightarrow$ N) or Sm A $\longrightarrow$ isotropic phase (Sm A $\longrightarrow$ I) in the bulk of a LC. However, recent experiments showed [13, 15–17, 21] that freely suspended smectic-A films of some LC compounds can also exist at temperatures much higher than the temperatures of Sm A $\longrightarrow$ N or Sm A $\longrightarrow$ I phase transitions. According to the model developed in [26, 27, 29] and correctly describing the behavior of freely suspended Sm A films during their heating above the temperature corresponding to the disappearance of smectic order in the bulk of mesogenic materials, the inner layers of the

1063-7834/00/4208-1554$20.00

film can be less ordered than the layers near the free surfaces confining them. The moduli K and B for such films must decrease with increasing distance to the free surface and attain their minimum values at the center of the film. Since the spatial inhomogeneity of the elastic parameters for smectic layers are completely disregarded in the model [22, 23] and its continual modifications [24, 25], these models cannot adequately describe fluctuation profiles for smectic layer displacements and the correlations between these fluctuations.

Another considerable drawback of Holyst's model is that the Sm A structure is simulated in it by a set of equidistant planes containing the centers of mass of LC molecules, so that the temperature-dependent center-of-mass distribution of molecules in each layer along its normal is completely disregarded. Besides, all molecules are assumed to be oriented perpendicularly to the plane of smectic layers, i.e., the orientational order in the film is assumed to be perfect. Thus, the model [22, 23] completely disregards the temperature-dependent "intrinsic disorder" in smectic layers, and the deviation of one-dimensional position ordering in the film from the ideal ordering is associated solely with hydrodynamic fluctuations of smectic layer displacements from their equilibrium positions. For this reason, the coefficients of specular reflection and diffuse scattering of x-rays from freely suspended smectic-A films calculated by using Holyst's model turn out to be almost independent of temperature, which completely contradicts the experimental results [21]. In order to match the results of experiments on small-angle scattering of x-rays from freely suspended smectic-A films to the theoretical results [22–25], the mean square of the total amplitude σ_{tot}^2 of thermal fluctuations in the film in [18– 21] is assumed to be the sum of two components:

$$\sigma_{tot}^2 = \sigma^2 + \sigma_{loc}^2, \quad (1)$$

where σ^2 is the mean square amplitude of the layer displacement fluctuations, which is determined by using the model of [22, 23] or its continual modification [25], and σ_{loc}^2 is the mean square amplitude of fluctuations describing the local disorder in smectic layers. The latter quantity is introduced *ad hoc*; the results on specular reflection of x-rays at temperatures much higher than the Sm A $\longrightarrow$ N phase transition point in the bulk of the LC can be satisfactorily described by assuming that the local disorder is minimal in the vicinity of the free surfaces of the film and maximal at its center. However, the elastic moduli K and B in this case are assumed to be identical for all the layers in the film. Mol *et al.* [20, 21] admit the intrinsic contradiction of such a description and the necessity of improving Holyst's model for taking into account the spatial inhomogeneity of a freely suspended smectic-A film, as well as the intrinsic disorder in its layers.

A simple generalization of Holyst's discrete model [22, 23] proposed in [30] makes it possible to calculate the amplitudes of displacement fluctuations for layers in a freely suspended smectic-A film, as well as the correlations between these fluctuations, taking into account the dependence of the elastic moduli K and B on the distance to the confining surfaces of the film. In turn, these dependences are determined by using a microscopic model of a freely suspended smectic-A film [26, 27, 29], which is a generalization of the well-known McMillan model [31] for the Sm A phase in the bulk of LC. This model takes into account the center-of-mass distribution of molecules in smectic layers along their normal, as well as the deviation of the orientational ordering in the system from the ideal, ordering. In the present work, we present the results of calculations of the coefficients of specular reflection and diffuse scattering of x-rays from a freely suspended smectic-A film in the entire temperature range of its existence on the basis of the models developed in [26, 27, 29, 30]. The results match the experimental data on small-angle scattering of x-rays from freely suspended smectic-A films of 7 AB LC (4,4'-diheptylazoxybenzene) [20, 21].

1. SPECULAR REFLECTION AND DIFFUSE SCATTERING OF X-RAYS FROM FREELY SUSPENDED SMECTIC-A FILMS

The intensity of x-ray diffraction from a system is proportional to the Fourier transform $S(\mathbf{Q})$ of the correlation function of the electron density in the system, which is defined by the equation [22, 23]

$$S(\mathbf{Q}) = \int d\mathbf{r} \int \langle \hat{\rho}(\mathbf{r}) \hat{\rho}(\mathbf{r}') \rangle \exp[i\mathbf{Q}(\mathbf{r} - \mathbf{r}')] d\mathbf{r}', \quad (2)$$

where $\hat{\rho}(\mathbf{r})$ is the electron density operator of the system, $\mathbf{Q}$ is the recoil momentum for scattering of x-rays at the electrons, and the symbol $\langle \ldots \rangle$ indicates statistical averaging over thermal fluctuations in the system. In turn, the electron density operator $\hat{\rho}(\mathbf{r})$ for an N-layer freely suspended smectic-A film can be written in the form

$$\hat{\rho}(z) = \rho_0 \sum_{k=1}^{N} \int_{-L/2\cos\vartheta}^{L/2\cos\vartheta} f_k(z - z', \vartheta) \times \Omega_k(z - z') \rho_e(z') dz' d\cos\vartheta. \quad (3)$$

Here, ρ_0 is the number density of molecules in the LC, $\rho_e(z')$ is the component of the electron density in a molecule along the z axis perpendicular to the plane of the film, $f_k(z - z', \vartheta)$ is the one-particle distribution function of molecules in the kth layer of the film, ϑ is the polar angle between the z axis and the long axis of a molecule, L is the length of a molecule, and $\Omega_k(z - z')$ is the step function equal to 1 for $z_k^{(1)} \le (z - z') \le z_k^{(2)}$ and 0 for values of $z - z'$ outside this interval. In the absence of displacement fluctuations in smectic layers of the

film, the coordinates $z_k^{(1)}$ and $z_k^{(2)}$ defining the position of the upper and lower boundary planes of the kth layer of the film can be written as $(k - 1/2)d$ and $(k + 1/2)d$, respectively, where d is the smectic-layer thickness. If the kth layer is displaced from its equilibrium position by $u_k(\mathbf{r}_\perp)$ along the z axis, these coordinates assume the form $(k - 1/2)d + u_k(\mathbf{r}_\perp)$ and $(k + 1/2)d + u_k(\mathbf{r}_\perp)$. In this case, equation (2) can be written in the form

$$S(\mathbf{Q}) = \rho_0^2 \int d\mathbf{r}_\perp \int \exp[i\mathbf{Q}_\perp(\mathbf{r}_\perp - \mathbf{r}'_\perp)]d\mathbf{r}'_\perp$$
$$\times \left\langle \sum_{k=1}^{N} \int_{(k-1/2)d + u_k(\mathbf{r}_\perp)}^{(k+1/2)d + u_k(\mathbf{r}_\perp)} f_k(z - z'', \vartheta)\exp[iQ_z(z - z'')] \right\rangle$$
$$\times d(z - z'')d\cos\vartheta \int_{-L/2\cos\vartheta}^{L/2\cos\vartheta} \rho_e(z'')\exp(iQ_z z'')dz'' \quad (4)$$
$$\times \sum_{n=1}^{N} \int_{(n-1/2)d + u_n(\mathbf{r}'_\perp)}^{(n+1/2)d + u_n(\mathbf{r}'_\perp)} f_n(z' - z''', \vartheta')\exp[iQ_z(z' - z''')]$$
$$\times d(z' - z''')d\cos\vartheta' \int_{-L/2\cos\vartheta'}^{L/2\cos\vartheta'} \rho_e(z''')\exp(-iQ_z z''')dz''' \Big\rangle.$$

The calculations made in [22–25] and [30] show that the amplitudes $\sigma_k = \langle u_k(\mathbf{r}_\perp)^2\rangle^{1/2}$ of displacement fluctuations of the layers of freely suspended smectic-A films are much smaller than the layer thickness d, and their profile is quite smooth. In this case, it can be easily proven that equation (4) can be reduced to the form

$$S(\mathbf{Q}) = \rho_0^2 \int d\mathbf{r}_\perp \int \exp[i\mathbf{Q}_\perp(\mathbf{r}_\perp - \mathbf{r}'_\perp)]d\mathbf{r}'_\perp$$
$$\times \sum_{k=1}^{N}\sum_{n=1}^{N} \langle \exp[iQ_z(u_k(\mathbf{r}_\perp) - u_n(\mathbf{r}'_\perp))]\rangle$$
$$\times \exp[iQ_z(k-n)d] \int_{-d/2}^{+d/2} \exp(iQ_z z_1)dz_1 \int_0^1 f_k(z_1, \vartheta) \quad (5)$$
$$\times S_{M1}(Q_z, \vartheta)d\cos\vartheta \int_{-d/2}^{+d/2} \exp(-iQ_z z_2)dz_2$$
$$\times \int_0^1 f_n(z_2, \vartheta')S_{M2}(Q_z, \vartheta')d\cos\vartheta',$$

where

$$S_{M1}(Q_z, \vartheta) = \int_{-L/2\cos\vartheta}^{L/2\cos\vartheta} \rho_e(z)\exp(iQ_z z)dz, \quad (6)$$

$$S_{M2}(Q_z, \vartheta) = \int_{-L/2\cos\vartheta}^{L/2\cos\vartheta} \rho_e(z)\exp(-iQ_z z)dz. \quad (7)$$

If we also assume that the electron distribution in a molecule is symmetric relative to its center of mass, and one-particle distribution functions are even functions of the coordinate z, we can write

$$S(\mathbf{Q}) = 4\rho_0^2 \int d\mathbf{r}_\perp \int \exp[i\mathbf{Q}_\perp(\mathbf{r}_\perp - \mathbf{r}'_\perp)]d\mathbf{r}'_\perp$$
$$\times \sum_{k=1}^{N}\sum_{n=1}^{N} \langle \exp[iQ_z(u_k(\mathbf{r}_\perp) - u_n(\mathbf{r}'_\perp))]\rangle \quad (8)$$
$$\times \cos[(k-n)dQ_z]\tau_k(Q_z)\tau_m(Q_z),$$

where

$$\tau_k(Q_z) = \int_{-d/2}^{+d/2} \cos(Q_z z)dz \times \int_0^1 f_k(z, \vartheta)S_M(Q_z, \vartheta)d\cos\vartheta, \quad (9)$$

$$S_M(Q_z, \vartheta) = \int_0^{L/2\cos\vartheta} \rho_e(z)\cos(Q_z z)dz. \quad (10)$$

Taking into account that

$$\int d\mathbf{r}_\perp \int d\mathbf{r}'_\perp \exp[i\mathbf{Q}_\perp(\mathbf{r}_\perp - \mathbf{r}'_\perp)]$$
$$\times \langle \exp[iQ_z(u_k(\mathbf{r}_\perp) - u_n(\mathbf{r}'_\perp))]\rangle$$
$$= S_0 \int d\mathbf{r}_\perp \exp(i\mathbf{Q}_\perp\mathbf{r}_\perp) \quad (11)$$
$$\times \exp[-(1/2)Q_z^2(\sigma_k^2 + \sigma_n^2 - 2\langle u_k(\mathbf{r}_\perp)u_n(0)\rangle)],$$

where S_0 is the surface area of the film, the expression for $S(\mathbf{Q})$ can be written in the following compact form:

$$S(\mathbf{Q}) = 4\rho_0^2 S_0 \sum_{k=1}^{N}\sum_{n=1}^{N} \int d\mathbf{r}_\perp \exp(iQ_\perp\mathbf{r}_\perp) \quad (12)$$
$$\times \cos[(k-n)dQ_z]\tau_k(Q_z)\tau_n(Q_z)F_{kn}(Q_z)C_{kn}(Q_z, \mathbf{r}_\perp),$$

where

$$F_{kn}(Q_z) = \exp[-(1/2)Q_z^2(\sigma_k^2 + \sigma_n^2)], \quad (13)$$

$$C_{kn}(Q_z, \mathbf{r}_\perp) = \exp[Q_z^2\langle u_k(\mathbf{r}_\perp)u_n(0)\rangle]. \quad (14)$$

Formula (12) differs from the analogous expression for $S(\mathbf{Q})$ in [23] only in the values of the coefficients $\tau_k(Q_z)$. In Holyst's theory presuming the existence of perfect orientational and one-dimensional position ordering in the layers of a freely suspended smectic-A film, these coefficients are just equal to the molecular

form factor (10) for $\vartheta = 0$. The expressions for one-particle distribution functions in each layer of the film are given in [26, 27]. As regards the form factor $S_M(Q_z, \vartheta)$, its form depends on the specific model describing the electron distribution in a molecule of the LC. For example, if we assume, following [18–21], that the molecules consist of a core with the electron density ρ_{core} and two identical alkyl tails with the density ρ_{tail}, the form factor $S_M(Q_z, \vartheta)$ is given by

$$S_M(Q_z, \vartheta) = (\rho_{core}/Q_z)\{(\rho_{tail}/\rho_{core})\sin(Q_z L\cos\vartheta/2) - (\rho_{tail}/\rho_{core} - 1)\sin[Q_z(L/2 - d_{tail})\cos\vartheta]\}, \quad (15)$$

where d_{tail} is the length of the alkyl tail.

Equation (12) describes both the specular reflection of x-rays from a freely suspended smectic-A film, for which $\mathbf{Q}_\perp = 0$, and the diffuse scattering from the film for $\mathbf{Q}_\perp \neq 0$. However, these two particular cases should be considered separately for the sake of a further simplification of this expression. Let us first consider the specular reflection. It can easily be shown that, in this case, the factor $C_{kn}(Q_k, \mathbf{r}_\perp)$ in (12) can be simply equated to unity with a high degree of accuracy. Indeed, for x-ray scattering from freely suspended films with transverse dimensions ~1 cm (such films were studied in real experiments [18–21]), the main contribution to the intensity of scattered radiation comes from the values of this factor with the exponent in (14) that are much smaller than 0.1. In this case, we can write the following expression for the specular reflection of x-rays:

$$S(Q_z) \approx 4\rho_0^2 S_0^2 \times \sum_{k=1}^{N}\sum_{n=1}^{N}\cos[(k-n)dQ_z]\tau_k(Q_z)\tau_n(Q_z)F_{kn}(Q_z). \quad (16)$$

Let us now consider the diffuse scattering of x-rays ($\mathbf{Q}_\perp \neq 0$). In this case, we can expand the factor $C_{kn}(Q_z, \mathbf{r}_\perp)$ in (12) into a power series in $Q_z^2\langle u_k(\mathbf{r}_\perp)u_n(0)\rangle$ and confine the expansion to the first two terms. Since

$$\int \exp(i\mathbf{Q}_\perp\mathbf{r}_\perp)d\mathbf{r}_\perp = 0$$

for films with macroscopic transverse dimensions if $\mathbf{Q}_\perp \neq 0$, the contribution to the intensity of diffuse scattering comes only from the second term of the expansion, and

$$S(Q_z, \mathbf{Q}_\perp) \approx 4\rho_0^2 S_0 \sum_{k=1}^{N}\sum_{n=1}^{N}\cos[(k-n)dQ_z]\tau_k(Q_z) \times \tau_n(Q_z)F_{kn}(Q_z)Q_z^2\int\langle u_k(\mathbf{r}_\perp)u_n(0)\rangle\exp(i\mathbf{Q}_\perp\mathbf{r}_\perp)d\mathbf{r}_\perp. \quad (17)$$

According to Holyst and Tweet [22, 23], the correlator $\langle u_k(\mathbf{r}_\perp)u_n(0)\rangle$ is given by

$$\langle u_k(\mathbf{r}_\perp)u_n(0)\rangle = \frac{k_B T}{(2\pi)^2} \times \int M_{kn}^{-1}(\mathbf{q}_\perp)\exp(-i\mathbf{q}_\perp\mathbf{r}_\perp)d\mathbf{q}_\perp, \quad (18)$$

where $M_{kn}^{-1}(\mathbf{q}_\perp)$ is an element of the matrix inverse of the matrix $M_{kn}(\mathbf{q}_\perp)$ given in [30], k_B is the Boltzmann constant, and T is the absolute temperature of the system. Substituting (18) into (17) and considering that

$$\frac{1}{(2\pi)^2}\int\exp[i(\mathbf{Q}_\perp - \mathbf{q}_\perp)\mathbf{r}_\perp]d\mathbf{r}_\perp = \delta(\mathbf{Q}_\perp - \mathbf{q}_\perp), \quad (19)$$

where $\delta(\mathbf{x})$ is the Dirac delta function, we obtain

$$S(Q_z, \mathbf{Q}_\perp) \approx 4\rho_0^2 S_0 k_B T \sum_{k=1}^{N}\sum_{n=1}^{N}\cos[(k-n)dQ_z] \times \tau_k(Q_z)\tau_n(Q_z)F_{kn}(Q_z)Q_z^2 M_{kn}^{-1}(\mathbf{Q}_\perp). \quad (20)$$

Equations (16) and (20) make it possible to calculate the coefficients of specular reflection and diffuse scattering of x-rays from a freely suspended N-layered smectic-A film for any temperature at which it exists. The entire information on the orientational and position molecular ordering is contained in the coefficients $\tau_k(Q_z)$; the coefficients $F_{kn}(Q_n)$ determine the dependences of these intensities on the amplitudes σ_k and σ_n of displacement fluctuations in the film layers, while the matrix elements $M_{kn}^{-1}(\mathbf{Q}_\perp)$ determine the dependence of the diffuse scattering intensity on the correlations between these fluctuations. It should also be noted that the fluctuation amplitudes σ_k, as well as the matrix elements $M_{kn}^{-1}(\mathbf{Q}_\perp)$, are also determined in the long run by temperature-dependent profiles of the orientational and positional order parameters of the film [30]. Thus, the obtained relations allow us to consistently calculate the coefficients of specular reflection and diffuse scattering of x-ray radiation from a freely suspended smectic-A film, taking into account its spatially inhomogeneous and temperature-dependent structure.

2. RESULTS OF NUMERICAL CALCULATIONS AND DISCUSSION

The coefficients of specular reflection and diffuse scattering of x-rays were calculated numerically for a freely suspended smectic-A film consisting of N = 24 layers. We assumed that the film was prepared from an LC exhibiting a weak first-order phase transition Sm A ⟶ N. Such films were studied in experiments on small-angle scattering of x-rays [20, 21]. The values of the model parameters used in the calculations were the same as in our previous publication [30]. The molecular form factor $S_M(Q_z, \vartheta)$ was taken in the form (15), the values of the parameters $(\rho_{tail}/\rho_{core})$ = 1/1.5 and $d_{tail} = 0.23L$ being the same as in [20, 21]. The cal-

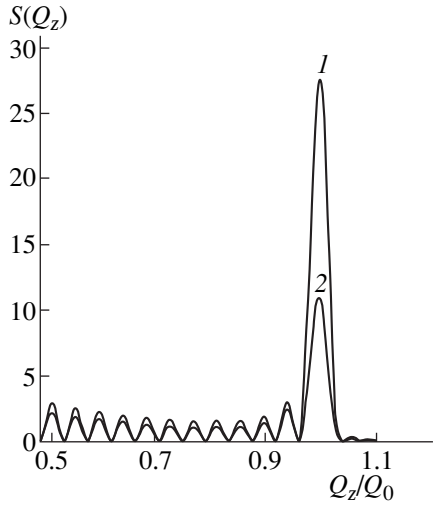

Fig. 1. Dependence of x-ray specular reflection coefficient (in arbitrary units) on the transferred momentum component Q_z for a 24-layer freely suspended smectic-A film: $T = T_1$ (curve *1*) and T_2 (curve *2*).

culations were made for temperatures much lower than the temperature corresponding to the Sm A ⟶ N phase transition in the bulk of the LC, as well as for limiting high temperatures for the existence of a freely suspended smectic-A film of a given thickness.

Figure 1 shows the dependences of the x-ray specular reflection coefficient on the transferred momentum component Q_z calculated by using formula (16). Curve *1* corresponds to a temperature $T = T_1$ lower than that of the Sm A ⟶ N transition, while curve *2* describes the results of calculations for a temperature $T = T_2$ close to the limiting high temperature at which the film can exist.

The values of these temperatures are given in [30]. According to the model of [26, 27, 29], for the chosen values of the model parameters, the heating of the 24-layer freely suspended smectic-A film above the limiting temperature $T = T_2$ must lead to an abrupt decrease in the film thickness by an integral number of smectic layers. Such an effect was observed in the experiments [20, 21]. Both curves in Fig. 1 demonstrate principal Bragg peaks for $Q_z = Q_0 = 2\pi/d$, which appear due to the interference between x-rays reflected from all film layers, as well as subordinate peaks, which appear due to the interference between the rays reflected from the two surface layers [18–21]. It can be seen from the figure that an increase in the film temperature only slightly affects the intensity of the subordinate peaks, while the intensity of the Bragg peak is approximately 2.5 times less at $T = T_2$ than at $T = T_1$. Precisely, such behavior of the specular reflection coefficient was observed in the experiments on small-angle scattering of x-rays from freely suspended smectic-A films of a 7 AB LC [21]. The obtained result has a simple physical interpretation. The model of [26, 27, 29] predicts an insignificant decrease in the orientational and positional orders in the surface layers of the film as a result of its heating. At the same time, according to this model, the orientational and positional orderings in the inner layers of the film in the vicinity of the limiting temperature $T = T_2$ of its existence must be much lower than at $T = T_1$. However, the interference between x-rays reflected from the inner layers of the film contributes only to the principal

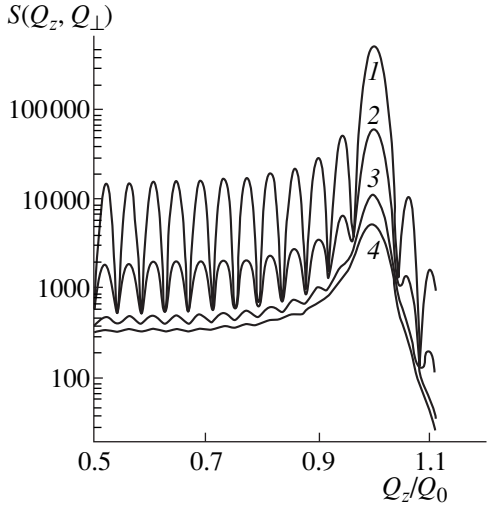

Fig. 2. Dependence of x-ray diffuse scattering coefficient (in arbitrary units) on the transferred momentum component Q_z for a 24-layer freely suspended smectic-A film for various values of the transferred momentum component $Q_\perp$ at $T = T_1$: $Q_\perp/Q_1 = 0.001$ (curve *1*), 0.003 (curve *2*), 0.007 (curve *3*), and 0.01 (curve *4*).

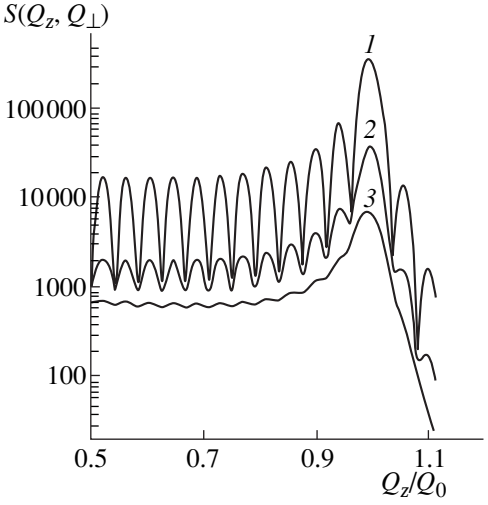

Fig. 3. The same dependences as in Fig. 2 at $T = T_2$: $Q_\perp/Q_1 = 0.001$ (curve *1*), 0.003 (curve *2*), and 0.007 (curve *3*).

Bragg peak and does not affect the intensities of subordinate peaks in any way. Thus, the experimentally observed, considerable decrease in intensity of the principal Bragg peak and the slight decrease in the height of the subordinate peaks can be regarded as facts confirming the validity of the model of [26, 27, 29]. There is no need to introduce any quantity in the theory *ad hoc*, as required in Holyst's theory [22, 23] for describing the experimental results [20, 21].

The results of calculations of the coefficient of diffuse x-ray scattering from a 24-layer freely suspended smectic-A film at temperatures $T = T_1$ and T_2 are presented in Figs. 2 and 3, respectively. The figures show the dependences of the diffuse scattering coefficients on the recoil momentum component Q_z along the normal to the film for several values of the recoil momentum component $Q_\perp$ parallel to the plane of the film. As in the case of specular reflection (see Fig. 1), these dependences display principal Bragg peaks for $Q_z = Q_0 = 2\pi/d$, as well as subordinate peaks that appear as a result of the interference of x-ray radiation scattered from the surface layers of the film. It was noted in [18–21] that the presence of such peaks indicates the conformity of the displacement fluctuations in different layers of the film. In other words, smectic layers fluctuate not independently, but in unison. Besides, these figures show that, as the transferred momentum component $Q_\perp$ increases, the height of diffuse scattering peaks decreases, with the height of the subordinate peaks decreasing more rapidly. Finally, for a certain value of $Q_\perp$, the subordinate peaks vanish altogether, while the Bragg peak can still be observed (although its height is considerably less). This indicates the loss of conformity of displacement fluctuations in different layers of the film with increasing $Q_\perp$, i.e., with decreasing wavelengths of undulation displacement modes [18–21]. The more rapid decrease in the height of subordinate peaks indicates that the conformity of fluctuations in surface layers of the film separated by largest distances is the first to be lost. These results are in complete accordance with the experimental data [18–21] and can be described in Holyst's model [22, 23]. However, Figs. 2 and 3 demonstrate an important feature in the behavior of the intensity of x-rays undergoing diffuse scattering, which, in principle, cannot be obtained with the help of the model of [22, 23] and its continual generalizations [24, 25]. It follows from the figures that, in the vicinity of the limiting temperature $T = T_2$ for the existence of a freely suspended smectic-A film, the displacement fluctuations in its layers must lose conformity with increasing $Q_\perp$ at lower values of these parameter than in the case of a lower temperature $T = T_1$. For example, according to Fig. 2 ($T = T_1$), subordinate peaks (although very weak) still exist for $Q_\perp = 0.007Q_1$, where $Q_1 = 2\pi/a$, $a \approx 4$ Å being the molecular diameter. At the same time, according to Fig. 3, subordinate peaks are completely suppressed for the same value of $Q_\perp$ at $T = T_2$. This means that displacement fluctuations in the surface layers at the limiting high temperature of the existence of the film become independent for lower values of $Q_\perp$, i.e., for larger wavelengths of undulation displacement modes as compared to the case of lower temperatures. In accordance with equation (17), the intensity of diffuse scattering of x-rays from a freely suspended smectic-A film is proportional to the correlation between displacement fluctuations of its layers. It was proven in [30] that the heating of the film weakens these correlations, the correlations between the surface layers of the film separated by the longest distances being suppressed most strongly. Such a suppression of the correlations is due to a considerable decrease in the elastic moduli K and B in the central part of the film during its heating, which is completely disregarded in Holyst's theory [22, 23]. Unfortunately, the diffuse scattering of x-rays from freely suspended smectic-A films was only studied in [20, 21] at one value of temperature below the Sm A $\longrightarrow$ N phase transition point in the bulk of the LC, and we are not in a position to compare the above theoretical result with the experimental data. In this connection, the experimental investigation of diffuse scattering of x-rays from freely suspended LC films in the region of limiting high temperatures of their existence must be of considerable interest.

ACKNOWLEDGMENT

This research was supported by the Russian Foundation for Basic Research (grant no. 98-03-32448).

REFERENCES

1. P. de Genes, *The Physics of Liquid Crystals* (Clarendon, Oxford, 1974; Mir, Moscow, 1977).
2. S. Chandrasekhar, *Liquid Crystals* (Cambridge University, Cambridge, 1977; Mir, Moscow, 1980).
3. P. Pieranski, L. Beliard, J. P. Tournellec, *et al.*, Physica A (Amsterdam) **194** (1–4), 364 (1993).
4. C. Rosenblatt, R. Pindak, N. A. Clark, and R. B. Meyer, Phys. Rev. Lett. **42**, 1220 (1979).
5. M. Veum, C. C. Huang, C. F. Chou, and V. Surendranath, Phys. Rev. E **56**, 2298 (1997).
6. C. Y. Young, R. Pindak. N. A. Clark, and R. B. Meyer, Phys. Rev. Lett. **40** (12), 773 (1978).
7. C. Rosenblatt and N. M. Amer, Appl. Phys. Lett. **36** (6), 432 (1980).
8. S. Heinekamp, R. A. Pelcovits, E. Fontes, *et al.*, Phys. Rev. Lett. **52**, 1017 (1984).
9. E. B. Sirota, P. S. Pershan, S. Amador, and L. B. Sorensen, Phys. Rev. A **35**, 2283 (1987).
10. P. Lambooy, S. Gierlotka, and W. H. de Jeu, Europhys. Lett. **12** (4), 341 (1990).
11. C. Bahr and D. Fliegner, Phys. Rev. A **46**, 7657 (1992).
12. I. Kraus, P. Pieranski, E. Demikhov, *et al.*, Phys. Rev. E **48**, 1916 (1993).

13. T. Stoebe, P. Mach, and C. C. Huang, Phys. Rev. Lett. **73**, 1384 (1994).
14. P. Mach, S. Grantz, D. A. Debe, *et al.*, J. Phys. II (Paris) **5** (2), 217 (1995).
15. E. I. Demikhov, V. K. Dolganov, and K. P. Meletov, Phys. Rev. E **52**, R1285 (1995).
16. V. K. Dolganov, E. I. Demikhov, R. Fouret, and C. Gors, Phys. Lett. A **220**, 242 (1996).
17. P. Johnson, P. Mach, E. D. Wedell, *et al.*, Phys. Rev. E **55**, 4386 (1997).
18. J. D. Shindler, E. A. L. Mol, A. Shalaginov, and W. H. de Jeu, Phys. Rev. Lett. **74**, 722 (1995).
19. J. D. Shindler, E. A. L. Mol, A. Shalaginov, and W. H. de Jeu, Phys. Rev. E **54** (1), 536 (1996).
20. E. A. L. Mol, G. C. L. Wong, J. M. Petit, *et al.*, Phys. Rev. Lett. **78**, 3157 (1997).
21. E. A. L. Mol, G. C. L. Wong, J. M. Petit, *et al.*, Physica B (Amsterdam) **248**, 191 (1998).
22. R. Holyst and D. J. Tweet, Phys. Rev. Lett. **65**, 2153 (1990).
23. R. Holyst, Phys. Rev. A **44**, 3692 (1991).
24. A. Poniewerski and R. Holyst, Phys. Rev. B **47**, 9840 (1993).
25. A. N. Shalaginov and V. P. Romanov, Phys. Rev. E **48**, 1073 (1993).
26. L. V. Mirantsev, Phys. Lett. A **205**, 412 (1995).
27. L. V. Mirantsev, Liq. Cryst. **20** (4), 417 (1996).
28. Y. Martínez-Raton, A. M. Somoza, L. Mederos, and D. E. Sullivan, Phys. Rev. E **55**, 2030 (1997).
29. L. V. Mirantsev, Phys. Rev. E **55**, 4816 (1997).
30. L. V. Mirantsev, Fiz. Tverd. Tela (St. Petersburg) **41**, 1882 (1999) [Phys. Solid State **41**, 1729 (1999)].
31. W. L. McMillan, Phys. Rev. A **4** (3), 1238 (1971).

Translated by N. Wadhwa

Physics of the Solid State, Vol. 42, No. 8, 2000, pp. 1561–1568. Translated from Fizika Tverdogo Tela, Vol. 42, No. 8, 2000, pp. 1518–1524.

FULLERENES AND ATOMIC CLUSTERS

Collective Electron Excitations in 3*D* Graphite Clusters

S. S. Moliver

Ul'yanovsk State University, ul. L. Tolstogo 42, Ul'yanovsk, 432700 Russia

Received August 9, 1999

Abstract—Group-theoretical analysis and subsequent quantum-chemical calculations based on the molecular orbital method applied to a cyclic model of 3*D* semimetallic graphite lead to a multiplet of spectroscopic combinations of Slater determinants. The transition energies ΔE between terms of the multiplet are interpreted as the energies of collective electron mesoscopic excitations $\hbar\omega$ in the entire set of electron states characterizing the metal-type conductivity of a cluster. The estimate $\hbar\omega \sim 0.2\Delta E(N_0/1000)^{2/3}$ is obtained for a cluster consisting of N_0 primitive cells. Depending on the thermal processing, $N_0 = (0.3–20) \times 10^6$ in pyrolytic graphite, and accordingly $\hbar\omega \sim$ (10–150) eV. In the case when the energy cannot be determined accurately, methods permitting the variation of an excitation over a wide range (such as the spectroscopy of synchrotron radiation absorption and the characteristic energy losses of charged particles) appear to be the most promising. © *2000 MAIK "Nauka/Interperiodica".*

The electron structure of crystalline 3*D* graphite is studied in detail experimentally and described theoretically by using empirical band methods [1]. The structure is characterized by metallic filling, and the Fermi surface is formed by chains of electron and hole pockets aligned along the lateral edges of the Brillouin zone (BZ) having the shape of a regular hexagonal prism. Since the Fermi surface embraces a small phase volume (3*D* graphite is a semimetal), the electron structure is adequately described by a cyclic model in which a slight extension of a unit cell of the crystal allows one to calculate the wave functions at several high-symmetry points $\mathbf{k}_i$ of the BZ, including those close to the Fermi surface (e.g., in electron pockets). Having formed an open electron shell populated by n electrons from n_b wave functions degenerate in energy and characterized by the wave vectors $\mathbf{k}_i$ of the star, we obtain a quantum-chemical model of the Fermi surface (n_b is the product of the number of vectors in the star and the degeneracy of the band energy level). The difference between such an open crystal shell from an atomic or a molecular one lies in it containing subshells that correspond to different wave vectors of the star. As a result, the dimensionality of an irreducible representation of the point group of the extended cell increases on account of the cyclic conditions, and the states should be selected according to the wave vector and point symmetry. Besides, only states with zero total spin have a physical meaning for a defect-free crystal.

Like other models, the cyclic model of a crystal can be calculated by various methods [2, 3]. In this work, the analysis is performed in terms of molecular orbitals (MOs). The group-theoretical analysis of an open shell in the model gives a multiplet a multi-electron structure formed by spectroscopic combinations of Slater determinants from MOs, which form the basis of irreducible representations. The multiplet structure of the model serves as the basis for conclusions concerning the properties of the crystal. For example, the ground state of a multiplet can be used to predict many-electron properties of the ground state of the crystal, such as the peculiarities of the pair correlation function of charge carriers.

In this connection, the physical meaning of the terms of the multiplet that do not correspond to the ground state should be clarified. Let us consider a finite electron system belonging, for example, to an atom or a molecule. It contains quasiparticle excitations for which a filled Hartree–Fock state becomes empty (hole), while an unfilled state is populated. In the presence of an open electron shell, collective excitations of a special type (transitions between multiplet terms of the ground electron configuration) appear, for which the number of electrons in the open shell does not change, and no holes appear. Such an excitation involves not only the (valence) electrons from the open shell, but also, to a lesser extent, all the remaining electrons (through the self-consistent field). The excitation energy for such a collective mode is determined by direct and exchange Coulomb integrals involving the MO of the open shell, as well as by the electron number in the open shell.

Suppose we have a finite cluster of the crystal being modeled, which consists of a sufficiently large (mesoscopic) number of atoms, so that its electron structure and properties are almost the same as for an unbounded crystal. In particular, the wave functions of states at the Fermi surface of the crystal are close to the wave functions of those electron states of the cluster through which the metal-type conduction is realized. In this case, the cyclic model of the crystal also describes the cluster properties, i.e., the transition energies ΔE between multiplet terms of the cyclic model correspond

to collective mesoscopic excitations of all N_F electrons in the states corresponding to the metal-type conduction of the cluster. Owing to the finite size of the cluster, the number of electrons participating in such a collective excitation is not very large:

$$N_F = \frac{1}{4\pi^2} S_F (N_0 V_0)^{2/3}, \quad (1)$$

where S_F is the area of the Fermi surface of crystalline graphite (in reciprocal length units), $V_0 = 35.2 \times 10^{-24}$ cm^3 is the volume of its primitive cell, and N_0 is the number of cells in the cluster.

The open shell in the cyclic model formed by n_b orbitals contains n electrons, and its excitation corresponds to the energy ΔE. In the states corresponding to the metal-type conduction of the cluster, N_F electrons are grouped to form open subshells consisting of the stars of corresponding wave vectors, each containing n_F electrons on the average. Assuming that the excitation energy of each such subshell is approximately equal to ΔE, we arrive at the following estimate for the collective excitation energy:

$$\hbar\omega \sim \Delta E \frac{N_F}{n_F}. \quad (2)$$

These excitations can be experimentally observed and used in the spectroscopy of growth processes, as well as for studying many-electron features of 3*D* graphite.

1. SELECTION OF AN EXTENDED CELL

The computation of the multiplet structure in the cyclic model involves the group-theoretical analysis of the open electron shell in the cyclic model of the crystal, as in the case of divacancy in silicon [4]. In quantum chemistry, the cyclic model is known as a quasimolecular extended unit cell (QEUC) [3]. The MO wave vectors of the QEUC model form a set of points $\{\mathbf{k}_i\}$ covered by the centers of contracted BZ of the model, which fill the actual BZ of the crystal.

In Herring's notation [5], the Brillouin zone of 3*D* graphite having the form of a regular hexagonal prism can be presented as follows. The center of the Brillouim zone Γ, the center of a lateral edge K, and the center of a lateral face M form a triangle, which is the irreducible 1/12 part of the central regular hexagonal BZ cross section with a side equal to $\frac{4\pi}{3\sqrt{3}d}$, where $d = 1.42$ Å is the separation between the nearest atoms in the basal plane, and an area $S_{BZ} = 7.54 \times 10^{16}$ cm^{-2}. The sides of the triangle ΓKM contain the high-symmetry points Σ (on ΓM) and (T on ΓK). The regular hexagonal bases of the BZ contain points that are projections of the points belonging to the central cross section (which are given in parentheses): $A(\Gamma)$ (the center of the base), $H(K)$ (ends of lateral edges of the BZ), as well as $L(M)$ and $S(T)$. The BZ height is $2KH = \frac{2\pi}{2c}$, where $2c = 6.71$ Å is the double separation between graphite layers, i.e., the Bravais lattice period. The Fermi surface of crystalline graphite embraces the high-symmetry boundary points K and H of the BZ, and hence the **k**-set of the sought QEUC must contain at least one such point (low-symmetry **k** can only be described by very large QEUC).

The smallest QEUC contains atoms from two graphite layers (graphite has four atoms in the primitive cell formed by two atoms each from adjacent layers). In order to include points H in our analysis, we must take atoms from four or more layers, while the inclusion of points K requires the extension of the primitive cell in the plane of the layer. The simulation of the Fermi surface must be combined with the reproduction of the chemical bonds between graphite layers. Since the highest bonding states lie just near K, an open shell should be formed from MOs with these wave vectors.

By gradually extending the primitive cell of graphite, we obtain the following sequence of the cell numbers in the QEUC whose **k**-sets contain point K of the BZ (the numbers of points in the vector stars in the BZ are indicated):

$$N_0 = \begin{cases} 3,\ \{\Gamma + 2K\}\ \ 12 \text{ atoms;} \\ 9,\ \{\Gamma + 6\Sigma + 2K\}\ \ 36 \text{ atoms, } \Sigma = 2/3\Gamma M; \\ 12,\ \{\Gamma + 6T + 3M + 2K\}\ \ 48 \text{ atoms,} \\ T = 1/2\Gamma K; \\ 24,\ \{\Gamma + 6T + 3M + 2K \\ + A + 6S + 3L + 2H\}\ \ 96 \text{ atoms.} \end{cases} \quad (3)$$

The first three QEUC in (3) consist of atoms from two adjacent graphite layers, while the last cell is formed by atoms from four layers. A direct quantum-chemical analysis carried out by the author (using a technique similar to that employed for other crystal systems composed of C and Si atoms [4, 6]) revealed that the chemical bonding of graphite layers is described only by the last two QEUC in (3) (with 48 and 96 atoms). This is due to the fact that **k**-sets of smaller QEUC do not contain point M of the BZ, at which a local maximum of the valence band is attained, i.e., one more bonding state is formed in the graphite crystal apart from K and Γ [1].

It is appropriate to estimate here the area S_F of the Fermi surface, which is a scale factor for the collective excitation energy (2). If we disregard minor features of the connection between pockets, whose contribution to the total area is insignificant, the Fermi surface of graphite [1] can be divided into two identical electron pockets with centers at points K' and K'' and four identical hole pockets with centers near points H' and H''.

The areas of maximum cross sections of the pockets perpendicular to [001] have been measured and amount to a small fraction of the BZ cross-sectional area: $\hbar^2 S_e = (6.52 \pm 0.06) \times 10^{-42}$ g^2 cm^2 s^{-2} and $\hbar^2 S_e = (4.80 \pm 0.05) \times 10^{-42}$ g^2 cm^2 s^{-2} [7]; this allows us to estimate the minor semiaxes of the pockets. Disregarding trigonal corrugation, i.e., assuming that the pockets are ellipsoids of revolution with semimajor axes along [001] approximately equal to $1/2KH$ for an electron pocket and $\approx 1/4KH$ for a hole pocket [1], we obtain

$$S_F \approx 2 \times 4\pi \frac{1}{2}\frac{2\pi}{2c}\sqrt{\frac{S_e}{\pi}} + 4 \times 4\pi \frac{1}{4}\frac{2\pi}{2c}\sqrt{\frac{S_h}{\pi}} \approx 1.5 \times 10^{15} \text{ cm}^{-2}. \quad (4)$$

This estimate obtained from the geometrical parameters of the Fermi surface agrees with that obtained from the density of states (the calculated value of $g_F \sim 2.5 \times 10^{20}$ eV^{-1} cm^{-3} [1]) and the average electron velocity on the Fermi surface ($v_F \sim 10^8$ cm s^{-1}):

$$S_F \sim 8\pi^3 g_F \hbar v_F \sim 4 \times 10^{15} \text{ cm}^{-2}.$$

2. CONFIGURATIONS AND THEIR MULTIPLET STRUCTURES

The band state of graphite at point *K* closest to the Fermi surface is of the π type, i.e., is formed by p_z atomic orbitals (AOs) and is doubly degenerate [1]. The BZ for graphite has two points *K* that cannot be transformed into each other by translation through a reciprocal lattice vector; henceforth, these points will be denoted by *K*' and *K*''. The open shell of the cyclic model formed by these states includes four degenerate MOs ($n_b = 4$) grouped into two subshells with different wave vectors. Each subshell is a spatial MO doublet transformed according to one of the 2*D* representations *E*' or *E*'' of the QEUC point group D_{3h} [8]. Four π-type MOs, which are degenerate in energy and belong to different subshells, can be easily distinguished during calculations. The MO coefficients of the LCAO doublet of a subshell are transformed through one another under point group operations which do not take atoms of one layer into atoms of the adjacent layer. Consequently, of the four degenerate MOs, the pair characterized by larger AO coefficients of one layer and smaller AO coefficients of the adjacent layer obviously belongs to the same doublet. The remaining two MOs form a doublet of the other subshell, and their AOs are characterized by the inverse ratio between the AO coefficients of the layers. In order to transform one subshell into another, improper crystal symmetry operations are required for transforming *K*' into *K*'', e.g., a rotation through 60° about [001] plus a partial translation along this axis (in this case, one layer is transformed into another).

Three spinless $(2K)^n$-type configurations with an even number of electrons $n = 2, 4, 6$ can be formed from the MOs of the open shell. It should be emphasized once again that this small number of electrons simulates a macroscopic number of electrons on the Fermi surface of an unbounded crystal and a mesoscopic number N_F of states with metal-type conduction in clusters. For each configuration, we must form terms with a definite wave vector (Γ or *K*), which can be obtained by summing up the wave vectors of *n* electrons distributed over the four MOs of the open shell. The terms are spectroscopic combinations of Slater determinants with definite wave vectors classified into three different types, depending on the population of MOs of the open shell:

χ, pairing determinant; open shell contains only doubly filled MOs;

ψ, exchange determinant; open shell contains only singly filled MOs;

φ, mixed determinant.

The terms are selected in accordance with the $\boldsymbol{D}_{3h}$ representations as shown in Tables 1–3. The notation of the terms reflects all the selection stages; α and β denote the basis spin functions, K_i are the spatial components of wave functions ($i = 1, 2$ labels the partners in each subshell), and *n*-electron functions are obtained by composing symmetrized two-electron functions (as *n* is even) that are transformed according to the irreducible representations A_1', A_2', and (E', i). A 2*D* determinant representation corresponds to two types of compositions with different notations:

$$E_i' = A_1' \times (E', i) = A_2' \times (E', i),$$

$$(E', 1) = (E', 1) \times (E', 1) - (E', 2) \times (E', 2),$$

$$(E', 2) = (E', 1) \times (E', 2) + (E', 2) \times (E', 1).$$

All that has been said above concerning configurations and their multiplet structure is also applicable to a model open shell constructed on doubly degenerate π states [1] with two wave vectors of the star at point *H*. The corresponding calculations can only be carried out for the 96-atom model (3) and can be used to find the configuration [$(2K)^n$ or $(2H)^n$] that corresponds to the ground state and to determine the excitation energies ΔE in the multiplet.

3. SELF-CONSISTENT ANALYSIS OF AN OPEN SHELL

The Hartree–Fock–Roothaan (ROHF) self-consistent finite method of molecular orbitals for an open shell based on the universal technique of projecting by the density matrices of electron shells [2] was realized

Table 1. Multiplet structure of the $(2K)^4$ configuration, $f = 1/2$

$(K')^2(K'')^2(\Gamma)$		A_J	A_K	A_I	B_J	B_K
$A'_\chi(\Gamma)$	$\frac{1}{\sqrt{4}}(\chi_{11}+\chi_{12}+\chi_{21}+\chi_{22})\alpha\beta\alpha\beta$	0	–2	0	2	6
$2E'_{1\chi}(\Gamma)$	$\frac{1}{\sqrt{4}}(\chi_{11}\pm\chi_{12}\mp\chi_{21}-\chi_{22})\alpha\beta\alpha\beta$	0	0	2	2	2
$A'_{1\psi}(\Gamma)$	$\frac{1}{\sqrt{12}}\psi\theta''$	1	2	0	0	–6
$2E'_{2\varphi}(\Gamma)$	$\frac{1}{\sqrt{4}}(\varphi_{11}+\varphi_{21})\theta,\ \frac{1}{\sqrt{4}}(\varphi_{12}+\varphi_{22})\theta$	$\frac{1}{2}$	–2	–2	1	6
	$\frac{1}{4}[A'_{1\chi\psi}+E'_{1\chi\psi}+A'_{2\varphi}+E'_{2\varphi}](\Gamma)$	$\frac{1}{2}$	0	0	1	2
$A'_{1\chi\psi}(\Gamma)$	$\frac{1}{\sqrt{8}}[(\chi_{11}-\chi_{12}-\chi_{21}+\chi_{22})\alpha\beta\alpha\beta+\psi\theta']$	$+J_{21}-K_{21}$				
$E'_{1\chi\psi}(\Gamma)$	$\frac{1}{\sqrt{8}}[(\chi_{11}-\chi_{12}-\chi_{21}+\chi_{22})\alpha\beta\alpha\beta-\psi\theta']$	$-J_{21}+K_{21}$				
$A'_{2\varphi}(\Gamma)$	$\frac{1}{\sqrt{8}}[(\varphi_{11}-\varphi_{21})-(\varphi_{12}-\varphi_{22})]\theta$	$+J_{21}-K_{21}$				
$E'_{2\varphi}(\Gamma)$	$\frac{1}{\sqrt{8}}[(\varphi_{11}-\varphi_{21})+(\varphi_{12}-\varphi_{22})]\theta$	$-J_{21}+K_{21}$				
$2(K')^3(K'')^1(K)$		A_J	A_K	A_I	B_J	B_K
	$\frac{1}{4}[A'_{1\varphi}+(E',2)_\varphi+A'_{2\varphi}+(E',1)_\varphi](K)$	1	1	0	$-\frac{1}{2}$	–4
$2A'_{1\varphi}(K)$	$\frac{1}{\sqrt{4}}(\varphi_{12}+\varphi_{21})\theta$	$+2J_{21}-K_{12}$				
$2(E',2)_\varphi(K)$	$\frac{1}{\sqrt{4}}(\varphi_{12}-\varphi_{21})\theta$	$-2J_{21}+K_{12}$				
$2A'_{2\varphi}(K)$	$\frac{1}{\sqrt{4}}(\varphi_{11}-\varphi_{22})\theta$	$-2K_{21}+K_{12}$				
$2(E',1)_\varphi(K)$	$\frac{1}{\sqrt{4}}(\varphi_{11}+\varphi_{22})\theta$	$+2K_{21}-K_{12}$				
$2(K')^4(K'')^0(K)$		A_J	A_K	A_I	B_J	B_K
$2A'_{1\chi}(K)$	$K'_1K'_1K'_2K'_2\alpha\beta\alpha\beta$	2	2	0	–4	–4
$(2K)^4(\Gamma+K)$	Diagonal Slater sum	0.8	0.4	0	0	0

Notes: (1) Spatial functions. $(K')^2(K'')^2$: $\chi_{ij} = K'_iK'_iK''_jK''_j$; $\psi = K'_1K'_2K''_1K''_2$; $\varphi_{i1} = K'_iK'_iK''_1K''_2$; $\varphi_{i2} = K'_1K'_2K''_iK''_i$; $(K')^3(K'')^1$: $\varphi_{i1} = K'_1K'_1K'_2K''_i$; $\varphi_{2i} = K'_1K'_2K'_2K''_i$.

(2) Spin functions. $\theta = \alpha\beta\alpha\beta - \beta\alpha\beta\alpha$; $\theta' = \alpha\beta\alpha\beta - \alpha\beta\beta\alpha - \beta\alpha\alpha\beta + \beta\alpha\beta\alpha$; $\theta'' = 2\alpha\alpha\beta\beta + 2\beta\beta\alpha\alpha - \alpha\beta\alpha\beta - \alpha\beta\beta\alpha - \beta\alpha\alpha\beta - \beta\alpha\beta\alpha$.

and described by the author earlier [4]. Since computation details are immaterial for the given analysis, we will only clarify the meaning of ROHF coefficients required for calculations, which, like the multiplet of the open shell, can be obtained with the help of the group-theoretical analysis.

The N_e electrons of the model are distributed between a closed shell formed by n_a molecular orbitals

Table 2. Multiplet structure of the $(2K)^2$ configuration, $f = 1/4$

$(K')^1(K'')^1(\Gamma)$		A_J	A_K	A_I	B_J	B_K
	$\frac{1}{4}[A'_{1\psi} + A'_{2\psi} + 2E'_{\psi}](\Gamma)$	0	0	0	2	−4
$A'_{1\psi}(\Gamma)$	$\frac{1}{\sqrt{4}}(\psi_{11} + \psi_{22})(\alpha\beta - \beta\alpha)$	$+K_{21} + K_{12}$				
$A'_{2\psi}(\Gamma)$	$\frac{1}{\sqrt{4}}(\psi_{12} - \psi_{21})(\alpha\beta - \beta\alpha)$	$-J_{21} - K_{12}$				
$2E'_{\psi}(\Gamma)$	$\frac{1}{\sqrt{8}}[(\psi_{11} - \psi_{22}) \pm (\psi_{12} + \psi_{21})](\alpha\beta - \beta\alpha)$	$\frac{1}{2}(+J_{21} - K_{21})$				
$2(K')^2(K'')^0(K)$		A_J	A_K	A_I	B_J	B_K
$2A'_{1\chi}(K)$	$\frac{1}{\sqrt{2}}(\chi_1 + \chi_2)\alpha\beta$	0	−4	0	0	8
$2(E', 1)_{\chi}(K)$	$\frac{1}{\sqrt{2}}(\chi_1 - \chi_2)\alpha\beta$	0	−4	8	0	−8
$2(E', 2)_{\psi}(K)$	$\frac{1}{\sqrt{2}}(K'_1K'_2)(\alpha\beta - \beta\alpha)$	2	−4	−8	−4	8
$(2K)^2(\Gamma + K)$	Diagonal Slater sum	0.4	−0.8	0	0	0

Note: $\psi_{ij} = K'_iK''_j$; $\chi_i = K'_iK'_i$.

denoted by a' and an open shell consisting of n_b MOs denoted by b', so that the Roothaan occupation number for the open shell with the given configuration is

$$f = \frac{n}{2n_b} = \frac{N_e - 2n_a}{2n_b} < 1.$$

The ROHF method can be used for self-consistent calculations of the energy of a term or the diagonal Slater sum of terms [9, 10]. This energy can be divided into two components formed, in accordance with the Slater rules, from the matrix elements of one-electron (h) and two-electron (g) components of the Hamiltonian.

The first addend in the expression for the total energy is independent of the electron distribution over the open shell; it can be written in the same form for all terms and diagonal sums of a given configuration and is equal to the energy of the closed shell plus the one-electron energy of the open shell and the energy of interaction between all MOs of the closed shell and all MOs of the open shell, which are proportional to the occupation number f.

The second addend in the expression for the total energy, viz., the energy of interaction in the open shell, depends on the type of electron distribution over MOs of the open shell in the determinants selected for the spectroscopic sum (term):

$$g^{(b)} = \sum_{b'}^{n_b}\sum_{b''}^{n_b}[2A_J\langle b'b''|g|b'b''\rangle - A_K\langle b'b''|g|b''b'\rangle] + \sum_{b'}^{n_b}A_I\langle b'b'|g|b'b'\rangle. \quad (5)$$

The essence of the ROHF method lies in a self-consistent analysis being possible only if the energy of interaction (5) has a form similar to that of the component corresponding to the closed shell; in this case, the coefficient A_I must be equal to zero. Thus, carrying out a symmetry selection of the determinants for a term, we must find the energy of interaction (5) for this term according to the Slater rules, and calculate the ROHF coefficients A_I, A_J, and A_K. If $A_I = 0$ for the given term, its energy can be calculated self-consistently. Otherwise, the term must be included in the Slater diagonal sum for which $A_I = 0$ (the number of such sums can be greater than one). The energy of each term appearing in the diagonal sum can be derived by using the MO of the diagonal sum and the ROHF coefficients for the given term.

In the presence of an open shell, the variational principle requires, in each self-consistency cycle, the calculation of two electron density matrices constructed on the LCAO coefficients of the electron shells (closed and open). The Fock matrix is calculated in each self-con-

Table 3. Multiplet structure of the $(2K)^6$ configuration, $f = 3/4$

$(K')^3(K'')^3(\Gamma)$		A_J	A_K	A_I	B_J	B_K
	$\frac{1}{4}[A'_{1\varphi} + A'_{2\varphi} + 2E'_{\varphi}]$	$\frac{8}{9}$	$\frac{8}{9}$	0	$\frac{2}{9}$	$-\frac{4}{9}$
$A'_{\varphi}(\Gamma)$	$\frac{1}{\sqrt{4}}(\varphi_{11} + \varphi_{22})\theta$	$+K_{21} + K_{12}$				
$A'_{2\varphi}(\Gamma)$	$\frac{1}{\sqrt{4}}(\varphi_{12} - \varphi_{21})\theta$	$-J_{21} - K_{12}$				
$2E'_{\varphi}(\Gamma)$	$\frac{1}{\sqrt{8}}[(\varphi_{11} - \varphi_{22}) \pm (\varphi_{12} + \varphi_{21})]\theta$	$\frac{1}{2}(+J_{21} - K_{21})$				
$2(K')^4(K'')^2(K)$		A_J	A_K	A_I	B_J	B_K
$2A'_{1\chi}(K)$	$\frac{1}{\sqrt{2}}(\chi_1 + \chi_2)\alpha\beta\alpha\beta\alpha\beta$	$\frac{8}{9}$	$\frac{4}{9}$	0	0	$\frac{8}{9}$
$2(E', 1)_{\chi}(K)$	$\frac{1}{\sqrt{2}}(\chi_1 - \chi_2)\alpha\beta\alpha\beta\alpha\beta$	$\frac{8}{9}$	$\frac{4}{3}$	$\frac{8}{9}$	0	$-\frac{8}{9}$
$2(E', 2)_{\varphi}(K)$	$\frac{1}{\sqrt{4}}(K'_1K'_1K'_2K'_2K''_1K''_2)\theta$	$\frac{10}{9}$	$\frac{4}{9}$	$-\frac{8}{9}$	$-\frac{4}{9}$	$\frac{8}{9}$
$(2K)^6(\Gamma + K)$	Diagonal Slater sum	$\frac{14}{15}$	$\frac{4}{5}$	0	0	0

Notes: (1) Spatial functions ($\dot{i}$ denotes the partner of i in the subshell) $\varphi_{ij} = K'_iK'_iK'_iK''_jK''_j$; $\chi_i = K'_1K'_1K'_2K'_2K''_iK''_i$.

(2) Spin function $\theta = \alpha\beta\alpha\beta(\alpha\beta - \beta\alpha)$.

sistency cycle by projecting by density matrices, taking into account the ROHF coefficients that have been determined for the term being calculated or for the diagonal sum [4]. The eigenvalue problem for the Fock matrix is solved in each self-consistency cycle, and the total energy of the term or the Slater diagonal sum can be determined as soon as the preset convergence level is reached.

It should be noted that the fundamental difference from the case of a closed shell is not a modification of energy (5) with the help of ROHF coefficients, but the projecting of the Fock matrix, which ensures the orthogonality of the MO set of all the shells [2]. The projecting procedure consumes most of the computer time and considerably extends the counting time as compared to that for a closed shell. However, the computational procedures for an open shell that do not involve projecting give a nonorthogonal set of MOs, which complicates the computation of observables and requires the development of a special approach for obtaining a multiplet structure.

An open shell of crystalline graphite consists of subshells with different wave vectors. In this case, energy (5) contains additional direct and exchange components associated with the subshells, for which the ROHF coefficients are introduced in accordance with the equality

$$\Delta g^{(b)} = \sum_{b'}^{\{K'\}}\sum_{b''}^{\{K''\}}[2B_J\langle b'b''|g|b'b''\rangle - B_K\langle b'b''|g|b''b'\rangle]. \quad (6)$$

The ROHF coefficients of all the terms and diagonal sums calculated by us are presented in Tables 1–3.

Some terms contain electron–electron interaction integrals of a non-Hartree–Fock type (defined on four different MOs):

$$K_{12} = \langle K'_1K''_2|g|K'_2K''_1\rangle, \quad K_{21} = \langle K'_1K'_2|g|K''_2K''_1\rangle, \quad J_{21} = \langle K'_1K'_2|g|K''_1K''_2\rangle, \quad (7)$$

which are cancelled out during the formation of the sums. For the groups of terms with such addends in the columns for Slater determinants in Tables 1–3, the sums of the terms and the ROHF coefficients for these sums are indicated, and the corrections to the energy of the corresponding sum of the terms are given for the terms themselves.

4. RESULTS OF CALCULATIONS AND CONCLUSIONS

Using the coefficients from Tables 1–3, we carried out self-consistent numerical calculations, whose details associated with the evaluation of equilibrium atomic spacings, the choice of the summation radii for direct and exchange integrals of electron–electron interaction, etc. (see the author's previous publications on systems of C and Si atoms with open shells [4, 6]) are immaterial for drawing a general conclusion on collective excitations.

According to the results of quantum-chemical analysis of a 48-atom QEUC (3), the configuration $(K')^2(K'')^2$ of crystalline 3*D* graphite with equilibrium atomic spacings corresponds to the ground state. At present, it is impossible to perform the entire set of computations involving the variation of atomic spacings for a 96-atom QEUC (3) (the computer time increases in proportion to the third power of the number of AOs of the model). Self-consistent analysis has not revealed any fundamental differences in the case of a 48-atom model with respect to properties of the $(K')^2(K'')^2$ configuration. It was found that the ground term is

$$A'_{1\psi}(\Gamma) = \frac{1}{\sqrt{12}}K'_1K'_2K''_1K''_2(2\alpha\alpha\beta\beta + 2\beta\beta\alpha\alpha - \alpha\beta\alpha\beta - \alpha\beta\beta\alpha - \beta\alpha\alpha\beta - \beta\alpha\beta\alpha). \quad (8)$$

Being the combination of eight Slater determinants, this term (8) describes the electron correlation on the Fermi surface of crystalline graphite. This can be used for calculating the observables, for example, a pair correlation function.

Semiquantitative conclusions concerning the ground and excited states of multiplets can also be drawn without self-consistency by using the same tables and estimates for the electron–electron interaction integrals on MOs of an open shell. The main contribution to energy comes from the Hartree–Fock integrals appearing in (5) and (6), whose estimated values are 7–8 eV for the coefficient A_I, 5–6 eV for A_J and B_J, and 0.1–0.2 eV for A_K and B_K. The non-Hartree–Fock integrals (7) are an order of magnitude smaller than these values, and the terms containing them are almost degenerate.

Low-lying excitations of the ground state (8) (Table 1) are most interesting from the viewpoint of experimental observation. These are the four almost degenerate transitions to non-Hartree–Fock states of the model multiplet without a change in the quasi-momentum:

$$A'_{1\psi}(\Gamma) \longrightarrow \{A'_{1\chi\psi}(\Gamma), E'_{1\chi\psi}(\Gamma), A'_{2\varphi}(\Gamma), E'_{2\varphi}(\Gamma)\}, \quad \Delta E \sim 1 \text{ eV}. \quad (9)$$

In order to estimate the collective excitation energy (2), we require not only ΔE, but also the scale factor n_F, viz., the average number of electrons in the states with the metal-type conductivity of a cluster, which are grouped to form an open subshell (i.e., a subshell whose wave vectors belong to the same star and whose energies are identical). The following numbers of one-electron states combined in the open subshell are possible on the Fermi surface: $n_b = 8$ at the four points $P \approx 1/2KH$ lying on the BZ edges, where the electron and hole pockets are connected and where the electron energy band intersecting the Fermi level is doubly degenerate [1]. In the remaining cases, band states are not degenerate, and the presence of 3, 4, 6, 12, or 24 vectors in the star are due to the trigonal symmetry of the Fermi surface. Since $n_b = 24$ at the overwhelming majority of points that do not lie on high-symmetry lines, it is these open shells that give the average value of n_F. Assuming that the main configuration in all cases is that for which the open shell is half-filled ($n = n_b$), as in the case of the basic configuration $(K')^2(K'')^2$ or $(H')^2(H'')^2$ of the cyclic model, we obtain $n_F = 24$. On the basis of (1), (2), (4), and (9), we find that the excitation energy for the collective mode can be estimated as

$$\hbar\omega \sim 0.2\Delta E\left(\frac{N_0}{1000}\right)^{2/3}. \quad (10)$$

The approximate nature of this relation is due not only to inaccuracy of the method, but also to the approximate nature of the cyclic model, the incorrectness of the cluster boundaries, etc. For this reason, we have introduced in (10) a scale factor in the form of one thousand of unit cells. Let us numerically estimate relation (10) for crystallites of pyrolythic graphite. Depending on the thermal treatment, the average diameter of a crystallite is 260–1000 Å and its height is 200–830 Å [11]. This gives an estimate $(0.3–20) \times 10^6$ for the number of cells N_0 and, accordingly, the limits 10–150 eV for the collective excitation quantum $\hbar\omega$. When the energy is determined inaccurately, the most promising methods are those that make it possible to vary the excitation energy over a wide range (e.g., the spectroscopy of synchrotron radiation absorption and the characteristic energy losses of charged particles).

Before concluding this section, we propose the following hypothesis on the experimental observation of collective electron excitations in 3*D* graphite clusters. If we visualize a system of growing graphite clusters or a "graphitizing" surface of a diamond, the clusters must grow in the form of hexagons, in view of the strong coupling in the layers, and the number of primitive cells varies from cluster to cluster with a discreteness $\Delta N_0 = 3m/4, 2m/4, 4m/4$, where m is the number of the layers; the discreteness $3m/4$ must be encountered most frequently. Thus, according to (10), each transition ΔE of the multiplet structure in the cyclic model in the high-energy excitation spectrum of a hypothetical system of clusters must correspond to a "comb" of peaks with a characteristic discreteness.

ACKNOWLEDGMENTS

The author is grateful to I. V. Stankevich and his colleagues from Quantum Chemistry Laboratory at the Institute of Hetero-organic Compounds, Russian Academy of Sciences, for fruitful discussions. The encouragement provided by S. V. Bulyarskiĭ in the course of this research is gratefully acknowledged.

This research was supported by the Russian Foundation for Basic Research (project no. 98-02-03327).

REFERENCES

1. M. S. Dresselhaus, G. Dresselhaus, K. Sugihara, I. L. Spain, and H. A. Goldberg, *Graphite Fibers and Filaments* (Springer, Berlin–New York, 1988), Vol. X.
2. R. McWeeny, *Methods of Molecular Quantum Mechanics* (Academic, London, 1989), Vol. XV.
3. R.A. Évarestov, *Quantum-Chemical Methods in Solid State Theory* (Leningrad. Gos. Univ., Leningrad, 1982).
4. S. S. Moliver, Fiz. Tverd. Tela (St. Petersburg) **41** (3), 404 (1999) [Phys. Solid State **41**, 362 (1999)].
5. C. Herring, J. Franklin Inst. **233**, 525 (1942); in R. S. Knox and A. Gold, *Symmetry in the Solid State* (Benjamin, New York, 1964; Nauka, Moscow, 1970), Vol. XII.
6. S. S. Moliver, Fiz. Tverd. Tela (St. Petersburg) **38**, 2029 (1996) [Phys. Solid State **38**, 362 (1999)].
7. N. B. Brandt, A. S. Kotosonov, S. V. Kuvshinnikov, and M. V. Semenov, Zh. Éksp. Teor. Fiz. **79** (9), 937 (1980) [Sov. Phys. JETP **52**, 476 (1980)].
8. L. D. Landau and E. M. Lifshitz, *Quantum Mechanics: Non-Relativistic Theory* (Nauka, Moscow, 1989, 4th ed.; Pergamon, Oxford, 1977, 3rd ed.).
9. J. C. Slater, Phys. Rev. **34**, 1293 (1929).
10. D. R. Hartree, *The Calculation of Atomic Structures* (Wiley, New York, 1957).
11. S. E. Vyatkin, A. N. Deev, V. G. Nagornyĭ, V. S. Ostrovskiĭ, A. M. Sigarev, and G. A. Sokker, *Nuclear Graphite* (Atomizdat, Moscow, 1967).

Translated by N. Wadhwa

Physics of the Solid State, Vol. 42, No. 8, 2000, pp. 1569–1574. Translated from Fizika Tverdogo Tela, Vol. 42, No. 8, 2000, pp. 1525–1530.

FULLERENES AND ATOMIC CLUSTERS

Energy of Deformed and Defective Carbon Clusters

A. E. Romanov[1] and A. G. Sheĭnerman[2]

[1] *Ioffe Physicotechnical Institute, Russian Academy of Sciences, ul. Politekhnicheskaya 26, St. Petersburg, 194021 Russia*
e-mail: alexei@romanov.ioffe.rssi.ru

[2] *Institute of Problems in Machine Science, Russian Academy of Sciences, Vasil'evskiĭ Ostrov, Bol'shoi pr. 61, St. Petersburg, 199178 Russia*

Received February 1, 2000

Abstract—A method is proposed for calculating the energy of deformed spherical and cylindrical carbon clusters of nanometer size. The application of the method is demonstrated by calculating the elastic energy of a spherical cluster deformed as a result of the introduction of two types of defects (disclination or dilatation center). It is proven that the energy of a defect in the cluster shell is determined by the curvature of its surface and that the spherical shape of the defect-free shell is stable. *© 2000 MAIK "Nauka/Interperiodica".*

Quantum-chemical and molecular-dynamics simulation [1–4] of carbon clusters are among the most widespread methods for calculating their energy and for determining their equilibrium configurations. An analytic method proposed recently [5, 6] for calculating the cluster energy presumes that clusters are formed from fragments of a graphite monolayer by bending their surface without deforming it, i.e., without changing the lengths of the bonds between the atoms of these fragments. The introduction of defects (e.g. vacancy pileups) into the clusters, as well as external mechanical action, can lead to bending of the clusters, their deformation, and the formation of new stable cluster configurations.

The idea of studying defects in carbon clusters by the methods of continuum mechanics was first put forward in [7], where it was proposed that the theory of thin shells can be used for calculating the energy of defective clusters. However, the thin-shell theory was found to be inapplicable for describing carbon clusters, since it describes a three-dimensional isotropic elastic medium, while the clusters are formed by one or several two-dimensional monolayer shells. In the present work, we propose a continual model of large (monolayer or multilayer) carbon clusters in which each layer (shell) includes at least several thousand atoms. Examples of such clusters are carbon nanotubes and multilayer spherical carbon clusters ("onion shells"). We propose that the energy of the shells be calculated by using a combination of the linear theory of elasticity (taking into account the deformation of the shells) and the method [5, 6] taking into account their curvature. In the framework of this model, each cluster shell is presented as a continuous two-dimensional isotropic elastic medium characterized by four parameters: the shear modulus G, the Poisson coefficient ν, and the two principal curvatures K_1 and K_2. The interaction between adjacent shells is described by elastic forces depending on the separation between these shells. Such a representation is most suitable for the shells of idealized open carbon nanotubes, viz., two-dimensional crystals formed by regular hexagons. In contrast to the surfaces of open shells, the surfaces of closed layers of carbon clusters are formed by hexagons, as well as pentagons, which can be treated as surface regions with elastic parameters differing from the elastic characteristics of the main (hexagonal) layer of the material. We assume that, in the larger shells that we studied, the fraction of the surface occupied by pentagons is small as compared to the total area of the surface. For this reason, while calculating the energy of a deformed shell, we assume that the elastic constants characterizing pentagons are equal to the corresponding constants of the hexagonal layer.

By way of illustrating the proposed general method, we carry out an analysis of the elastic energy associated with the formation of a dilatation center or disclination in a spherical monolayer carbon cluster. By a disclination in the shell of a spherical cluster, we mean a defect associated either with the removal of a sector of this shell, followed by joining of the cut edges, or with the introduction of a sector into the shell. In other publications [7–10], a disclination is associated with the presence of five-link rings. The number of such five-link rings in closed shells of carbon clusters is equal to 12, and the five-link rings themselves are defects inherent in carbon clusters. In the present case, we introduce a disclination into an already formed carbon clusters.

1. METHOD OF CALCULATION OF THE ELASTIC ENERGY OF DEFORMED CLUSTERS

In order to calculate the energy of deformed carbon clusters, we present the additional elastic energy stored as a result of deformation as the sum of two terms. The

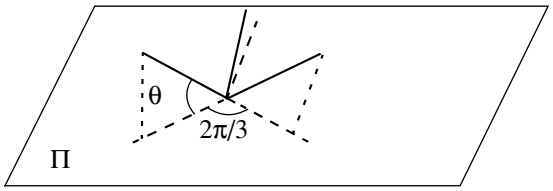

Fig. 1. Bending of atomic bonds in a carbon cluster. The directions of three interatomic bonds formed by an atom *A* on a curved surface are shown by solid lines, and the dashed lines show the projections of these bonds on the plane Π in which all the angles between the projections are equal.

first term, which is associated with extension–compression of the shells and involving a change in their separation, will be calculated by using the linear theory of elasticity. The second term associated with a change in values of the principal curvatures will be calculated by using the analytic method proposed by Rotkin and Suris [5, 6].

Rotkin and Suris [5, 6] assumed that the energy $E_{\text{curv}}^{\text{bond}}$ associated with the curvature of the bond between the atoms in hexagons on the surface of a bent graphite monolayer is proportional to the square of the angle θ between the direction of the bond and the direction that the bond would have in the plane (Fig. 1):

$$E_{\text{curv}}^{\text{bond}} = E_c\theta^2, \tag{1}$$

where E_c = 0.9 eV is a phenomenological parameter determined by matching it to the results of independent computer simulation. For the case $b/R \ll 1$, corresponding to a small normal curvature $1/R$ of the shell surface of a carbon cluster in the direction connecting two atoms of a hexagon with the atomic spacing b = 0.14 nm, the approximate equality $\theta \approx b/R$ is satisfied.

The bond curvature energy per atom of a hexagon is given by [5, 6]

$$E_{\text{at}}^{\text{curv}} = 1/2E_cb^2[3/4(K_1 + K_2)^2 + 3/8(K_1 - K_2)^2], \tag{2}$$

where K_1 and K_2 are the principal curvatures of the surface. Using this expression and assuming that the cluster shell is formed only by hexagons, we go over to a continuous distribution of the energy associated with curvature over the shell surface. The expression for the surface curvature energy density has the form

$$w^{\text{curv}} = \frac{E_{\text{at}}^{\text{curv}}}{S_{\text{at}}} = 3/8D[2(K_1 + K_2)^2 + (K_1 - K_2)^2], \tag{3}$$

where $S_{\text{at}} = 3\sqrt{3}\,b^2/4$ is the area per atom in a graphite monolayer and $D = (2/(3\sqrt{3}))E_c$.

We apply the Gauss–Bonnet theorem [11] to a defect-free shell, i.e., a shell with a closed and smooth surface:

$$\int_S K_1K_2d\sigma = 2\pi\chi. \tag{4}$$

Here, S is the shell surface area, σ is the integration variable, and χ is the Euler characteristic of the surface; χ = 2 for any surface that can be deformed into a sphere. In combination with formula (3), this theorem makes it possible to present the curvature energy E^0 of the shell of a defect-free cluster in the form

$$\begin{aligned} E^0 &= \int_S w^{\text{curv}}d\sigma \\ &= 3/8D\left(3\int_S (K_1 - K_2)^2 d\sigma + 16\pi\chi\right). \end{aligned} \tag{5}$$

According to this equality, the surface with identically equal main curvatures ($K_1 = K_2$) possesses a minimum energy among all the surfaces that can be deformed into a sphere. The normal curvatures of such a surface have the same value in all directions, which means that the surface is a sphere.

An expression for the surface density w^s of the extension–compression energy of the shell in the linear theory of elasticity has the form [12]

$$w^s = \frac{Gh}{1-\nu}[(\varepsilon_1)^2 + (\varepsilon_2)^2 + 2\nu\varepsilon_1\varepsilon_2 + 2(1-\nu)\varepsilon_{12}^2], \tag{6}$$

where G and ν are the shear modulus and the Poisson ratio for the basal planes of graphite, h = 0.34 nm is the separation between its basal planes, and ε_1, ε_2, and ε_{12} are the strains of these planes.

The elastic energy of interaction of the given shell with other shells can be calculated by the formula

$$w^{\text{int}} = p(\varepsilon)\varepsilon, \tag{7}$$

where $\varepsilon = (\Delta h_i + \Delta h_{i-1})/(2h)$ is the shear strain; Δh_i and Δh_{i-1} are the changes in the distance between the ith and $(i-1)$th and between the ith and $(i+1)$th shells, respectively, as a result of deformation; h = 0.34 nm is the separation between the shells prior to the deformation, which coincides with the separation between the basal planes in graphite; and $p(\varepsilon)$ is the external pressure normal to the basal planes of the graphite single crystal, which is responsible for the shear strain ε in this single crystal.

The total elastic energy of the deformed state is calculated as the sum of the curvature energy, the energy of deformation, and also the energy of interaction of the given shell with other shells (in the case of a multilayer cluster):

$$E = \int_s (w^{\text{curv}} + w^s + w^{\text{int}})d\sigma. \tag{8}$$

In order determine the additional elastic energy stored as a result of deformation of the shell, we must

subtract the energy E^0 of the shell prior to the deformation from the elastic energy of the shell with a defect:

$$E^{\text{extra}} = E - E^0. \quad (9)$$

The elastic energy of the deformed shell of a carbon cluster can be calculated as follows. We first express the shell strains and the changes in the curvatures of its surface in terms of displacements and their derivatives. Substituting the obtained expressions for longitudinal strains ε_1, ε_2, and ε_{12} into formula (6), the expression for the transverse strain ε into formula (7), the expressions for the main curvatures K_1 and K_2 into formula (3), and taking into account formula (8), we present the energy as a functional depending on the displacements and their derivatives. The equilibrium position of the deformed shell corresponds to a minimum of this functional. If the deformation of the shell is due to the introduction of defects into it, the defects can be introduced into the shell by using the boundary conditions imposed on their displacements.

2. ELASTIC ENERGY OF A DISCLINATION AND A DILATATION CENTER IN A SPHERICAL MONOLAYER CARBON CLUSTER

By way of an example, let us determine the elastic energy of a disclination and a dilatation center in a monolayer spherical carbon cluster. For this purpose, we introduce the spherical and cylindrical reference frames with origins coinciding with the center of the sphere (Fig. 2).

We will henceforth refer to the curves on the sphere specified by the equation φ = const as meridians and the contours with θ = const as parallel circles.

We will introduce a disclination into the sphere as follows (Fig. 3a). We assume that the disclination line coincides with the axis of the sphere. A positive disclination of intensity $\omega > 0$ is obtained by removing from the sphere a sector confined by the meridians $\varphi = 2\pi - \omega$ and $\varphi = 2\pi$ and by subsequently joining the cut banks. A negative disclination of intensity $\omega < 0$ is obtained by cutting the sphere along the meridian $\varphi = 2\pi$, compressing it along the coordinate line φ (which leads to a rotation of the cut banks through an angle ω), filling the formed gap with the material and joining it with the shell. A similar disclination in an elastic sphere was investigated in [13]. Mathematically, a disclination in the shell of a spherical carbon cluster will be defined by the following boundary conditions:

(a) the definition of the disclination

$$u_\varphi = \frac{\omega}{2\pi}(R\sin\theta)\varphi; \quad (10)$$

(b) continuity conditions for the sphere at the poles

$$u_\theta(\theta = 0) = 0, \quad u_\theta(\theta = \pi) = 0; \quad (11)$$

(c) fixation conditions that rule out the motion of the sphere as a perfectly rigid body parallel to its axis, i.e.,

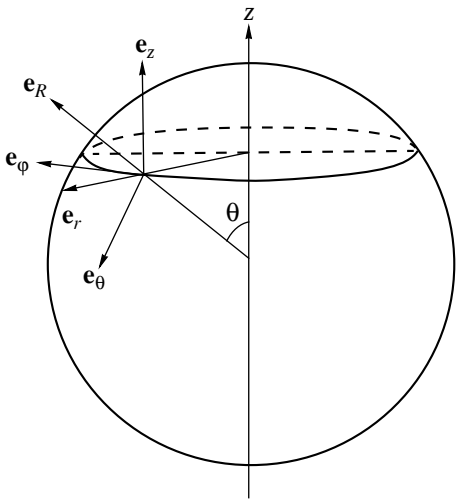

Fig. 2. Spherical and cylindrical reference frames used for calculating the energy of defects in a spherical shell. The spherical reference frame is determined by the triple of basis vectors ($\mathbf{e}_R$, $\mathbf{e}_\theta$, $\mathbf{e}_\varphi$), while the cylindrical reference frame is determined by the triple of the basis vectors ($\mathbf{e}_r$, $\mathbf{e}_\varphi$, $\mathbf{e}_z$).

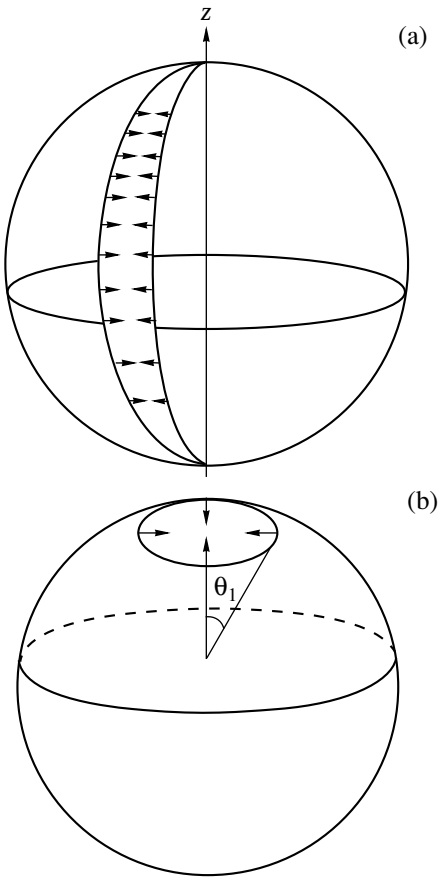

Fig. 3. Disclination and a dilatation center in a spherical shell. (a) The method of introducing a positive disclination: a sector is cut from the sphere, the banks of the cut are joined, and then all the applied external forces are removed; (b) the method of introducing a dilatation center. A region bounded by a parallel circle $\theta = \theta_1$ is cut out of the sphere, and then this parallel circle is compressed or extended.

defining the displacement u_z at a point of the sphere. The last condition is imposed for the convenience of calculations. Since the deformation of a spherical shell with a disclination is symmetric relative to the equator of the sphere, it is convenient to choose this condition in the form $u_z(z = 0) = 0$, or, in the spherical reference frame,

$$u_\theta(\theta = \pi/2) = 0. \tag{12}$$

For such a choice of the fixation conditions for a sphere, the displacements of a spherical shell with a disclination must satisfy the following condition, in view of the symmetry of the problem:

$$\begin{aligned} u_\theta(\theta, \varphi) &= -u_\theta(\pi - \theta, \varphi), \\ u_R(\theta, \varphi) &= u_R(\pi - \theta, \varphi). \end{aligned} \tag{13}$$

Let us now consider the method of introducing a dilatation sphere into a spherical shell (Fig. 3b). We assume that this defect is located at one of the poles of the sphere ($\theta = 0$). In order to introduce the dilatation center, we cut from the sphere a spherical segment including this pole and bounded by the contour $\theta = \theta_1$, where θ_1 is the dimensionless radius of the defect. We assume that the introduction of the defect into the segregated region can be reduced to a change in the radius of the parallel circle $\theta = \theta_1$, i.e., to the definition of constant displacements u_r for points of this parallel circuit.

The following boundary conditions must hold for a dilatation center in the shell of a spherical carbon cluster:

(a) the definition of the dilatation center $u_r(\theta = \theta_1) = R\delta\sin\theta_1$ or, in the spherical reference frame,

$$u_\theta(\theta = \theta_1)\cos\theta_1 + u_R(\theta = \theta_1)\sin\theta_1 = R\delta\sin\theta_1, \tag{14}$$

where δ is the intensity of the defect;

(b) the continuity condition for the surface at the pole $\theta = \pi$:

$$u_\theta(\theta = \pi) = 0; \tag{15}$$

(c) the condition of smoothness of the deformed surface at the same pole:

$$\frac{\partial u_R}{\partial u_\theta}(\theta = \pi) = 0. \tag{16}$$

Expressions for strains in terms of displacements in a spherical shell containing a disclination or a dilatation center follow from the general formulas [14] and the symmetry of defects presuming the absence of a shear:

$$\begin{aligned} \varepsilon_\theta &= \frac{1}{R}\left(\frac{\partial u_\theta}{\partial\theta} + u_R\right), \\ \varepsilon_\varphi &= \frac{1}{R}\left(\frac{\omega R}{2\pi} + u_\theta\cot\theta + u_R\right), \\ \varepsilon_{\theta\varphi} &= 0. \end{aligned} \tag{17}$$

In the second formula in (17), the quantity ω for the disclination corresponds to its intensity, while $\omega = 0$ for the center of dilatation.

We obtain the dependences of variations of the principal curvatures on displacements from the general formulas [14] describing the variations of the curvatures in the direction of meridians and parallel circles and Meusnier's formula [15]

$$K_n = k\cos\theta. \tag{18}$$

In this expression, K_n is the normal curvature of the surface in a certain direction, k is the curvature of an inclined section of the surface in the same direction, and θ is the angle between the planes of the corresponding sections. The expressions for the variations of the principal curvature have the form

$$\begin{aligned} \Delta K_1 &= -\frac{1}{R^2}\left(\frac{\partial^2 u_R}{\partial\theta^2} + u_R\right), \\ \Delta K_2 &= -\frac{1}{R^2} \\ &\times\left(\frac{1}{\sin^2\theta}\frac{\partial^2 u_R}{\partial\varphi^2} + \frac{\partial u_R}{\partial\theta}\cos\theta + u_R\sin\theta - u_\theta\cos\theta\right). \end{aligned} \tag{19}$$

The principal curvatures K_1 and K_2 of a spherical shell of radius R with a defect can then be expressed in terms of displacements by substituting (19) into the formulas

$$K_1 = 1/R + \Delta K_1, \quad K_2 = 1/R + \Delta K_2. \tag{20}$$

In order to find a minimum of the energy functional E defined by (8), we will use the Ritz method. For the sake of simplicity, we confine our analysis to the deformation of a sphere symmetric relative to its axis. For a disclination with a line passing through the poles of the sphere, we present the displacements u_θ and u_R in the form of the following expressions satisfying the boundary conditions (10)–(12):

$$\begin{aligned} u_\theta &= (\pi/2 - \theta)\sum_{k=1}^{N} a_k\theta^k(\pi - \theta)^k, \\ u_R &= \sum_{m=0}^{N} b_m\theta^m(\pi - \theta)^m. \end{aligned} \tag{21}$$

After this, we use the condition for the energy minimum

$$\begin{aligned} \frac{\partial E^{\text{extra}}}{\partial a_k} &= 0 \quad (k = 1\ldots N), \\ \frac{\partial E^{\text{extra}}}{\partial b_m} &= 0 \quad (m = 1\ldots N) \end{aligned} \tag{22}$$

to obtain a set of $2N$ linear equations in a_k and b_m. Solving these equations, we find the displacements of the

surface of a shell with a disclination and its elastic energy.

For a dilatation center located at the pole $\theta = 0$, we present the displacements u_θ and u_R in the form of the following expressions satisfying two boundary conditions, (15) and (16), out of three:

$$u_\theta = \sum_{k=1}^{N} a_k(\pi - \theta)^k, \quad u_R = b_1 + \sum_{m=2}^{N} b_m(\pi - \theta)^m. \quad (23)$$

In order to determine a minimum of the energy functional E under the third boundary condition (14), we introduce the function

$$F = E^{\text{extra}} + \lambda[u_\theta(\theta_1)\cos\theta_1 + u_R(\theta_1)\sin\theta_1 - R\delta\sin\theta_1], \quad (24)$$

whose minimum corresponds to the conditional minimum E^{extra}. Solving now the set of $2N + 1$ linear equations

$$\frac{\partial F}{\partial \lambda} = 0, \quad \frac{\partial F}{\partial a_k} = 0 \quad (k = 1\ldots N), \quad \frac{\partial F}{\partial b_m} = 0 \quad (m = 1\ldots N) \quad (25)$$

for a_k, b_m, and λ, we find the displacements of the shell with the dilatation center and the elastic energy of this defect.

3. DISCUSSION OF RESULTS

Our numerical calculations made for a spherical shell with the parameters $G = 380$ GPa, $\nu = 0.3$, and $R = 2$ nm led to the following results. The value of elastic energy of a disclination of intensity $+\pi/3$ was found to be –1.50 eV. The negative value of the energy of a positive disclination defined as the change in the energy of a cluster relative to the energy of the initial spherical cluster is apparently due to the violation of the smoothness of the surface at the poles of the sphere.

After the introduction of a disclination into the shell (Figs. 4a and 4b), both hexagons surrounding the poles of the sphere are transformed into pentagons. The angles between the bonds formed by the atoms of these pentagons differ considerably from the angles between the bonds formed by the atoms of hexagons. As a result, the surface of the sphere near the poles ceases to be locally flat, i.e., smooth, and is transformed into a surface close to a conical surface with a negative value of K_1 (which is one of the principal curvatures) (Fig. 4c). The formation of regions with a negative curvature in the shell is apparently responsible for the decrease in its energy, since the energy associated with the curvature of the formed shell is smaller than that of the sphere [see formula (3)], while deformations caused by the introduction of a disclination are small (and hence, the corresponding energy of deformation is also small).

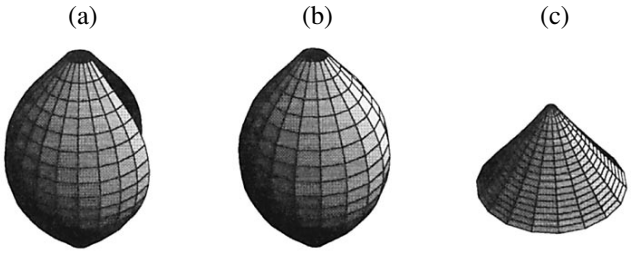

Fig. 4. The surface of a spherical shell containing a disclination of intensity $+\pi/3$. (a) The shell after the removal of the sector, (b) the shell after the removal of all the applied forces, and (c) the same in the vicinity of a pole. The indicated neighborhood is bounded by the contour $\theta = 0.3$.

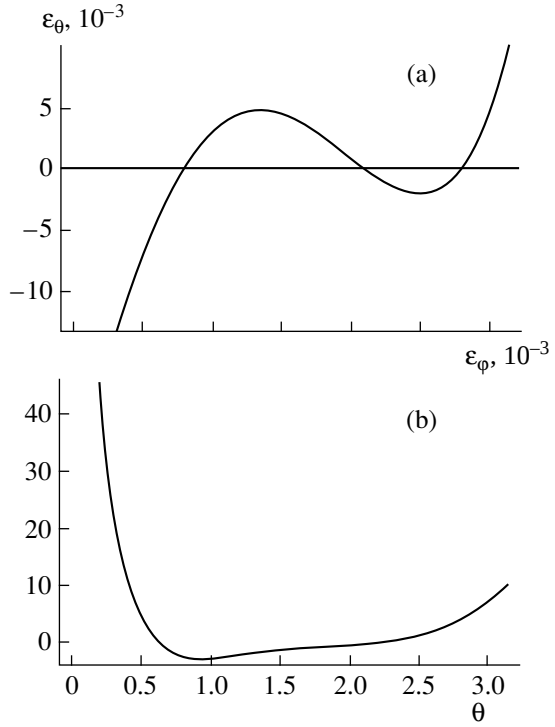

Fig. 5. Deformations (a) $\varepsilon_\theta(\theta)$ and (b) $\varepsilon_\varphi(\theta)$ created by a dilatation center in a spherical shell. The parameters of the dilatation center: dilatation intensity $\delta = -0.2$ and dimensionless radius $\theta_1 = 0.07$.

Since the introduction of a disclination of intensity $+\pi/3$ into the spherical shell leads to considerable distortions of its surface (see Figs. 4a and 4b), the formulas used for calculating the disclination energy are not quite accurate.

The calculations of displacements and strains (Fig. 5) made for a shell with dilatation centers proved that considerable strains can appear in the shell only in small neighborhoods of the centers of these defects, i.e., at their cores. Consequently, the computation formulas are correct for dilatational centers. The results of all calculations given below correspond to dilatation

Table 1. Elastic energy of a dilatation center in a spherical shell of a carbon cluster

Intensity of defect δ	−0.4	−0.2	0.2	0.4
Elastic energy E^{extra}, eV	11.96	3.11	2.68	10.99

Note: The parameters of the dilatation center are $\theta_1 = 0.07$ and $\theta_c = 0.14$.

Table 2. Energy of elastic interaction between identical centers of dilatation in the spherical shell of a carbon cluster

Intensity of defects δ	Relative distance between defects θ_1/θ_0	Interaction energy E^{int}, eV
−0.2	4	1.73
0.2	4	2.13
−0.2	8	0.99
0.2	8	1.56

Note: The parameters of the dilatation center are $\theta_1 = 0.07$ and $\theta_c = 0.14$.

centers with a dimensionless radius $\theta_1 = b/R$ and a dimensionless radius of the core $\theta_c = 2\theta_1$. The results of calculations of the elastic energy of dilatation centers with various values of the parameter δ are given in Table 1. The high values of elastic energy (of the order of several electronvolts) are due to large displacements specifying defects, i.e., due to large chosen values of the parameter δ.

The results presented above show that the values of energy of dilatation centers with opposite values of intensity are different, the larger energy corresponding to a dilatation center with $\delta < 0$. This circumstance is associated with the difference in the curvatures of the shells containing a dilatation center with a positive or negative value of δ. Indeed, the introduction of a dilatation center of intensity $\delta < 0$ into a spherical shell increases the values of its principal curvatures. The introduction of a dilatation center with $\delta > 0$ decreases these curvatures; hence, the additional curvature energy E_{curv}^{extra}, which is a monotonically increasing function of the curvatures.

The results of calculating the interaction energy between two identical dilatation centers as a function of their intensity δ and the angular separation θ_0 between them are presented in Table 2. The results compiled in this table indicate that identical dilatation centers repel each other, the energy of their interaction being a function of the parameter δ.

Thus, the obtained results show that the spherical shell possesses the least energy among all the shells of clusters with a preset area that can be deformed into a sphere. The centers of dilatation with opposite intensities (i.e., vacancies and introduced atoms or their pileups) in a spherical shell possess different elastic energies. The energy of a defect in the shell of a cluster depends on the curvature of its surface, the introduction of a defect into the shell leading to a change in its curvature.

It should be noted, in conclusion, that the method for calculating the energy of deformed carbon clusters proposed in the present work is only applicable to clusters with large shells (consisting of 10^3 and more atoms) that can be regarded in the continual approximation.

ACKNOWLEDGMENTS

The authors are grateful to M. Yu. Gutkin for reading the manuscript and suggesting improvements.

This work was carried out in the framework of the scientific program “Fullerenes and Atomic Clusters” (project “Klaster” no. 98065) under partial support of the Russian Scientific Council “Physics of Solid Nanostructures” (project no. 97-3006).

REFERENCES

1. C. T. White, J. W. Mintmire, R. C. Mowrey, D. W. Brenner, D. H. Robertson, J. A. Harrison, and B. I. Dunlap, in *Buckminsterfullerenes*, Ed. by W. Edward Billups, and Marco A. Ciufolini (VCH, New York, 1993), p. 125.
2. T. G. Schmalz and D. J. Klein, in *Buckminsterfullerenes*, Ed. by W. Edward Billups and Marco A. Ciufolini (VCH, New York, 1993), p. 83.
3. G. E. Scuseria, in *Buckminsterfullerenes*, Ed. by W. Edward Billups and Marco A. Ciufolini (VCH, New York, 1993), p. 103.
4. H. Terrans and A. L. Mackay, Prog. Cryst. Growth Charact. **34** (1), 25 (1997).
5. V. V. Rotkin and R. A. Suris, Proc. Electrochem. Soc. **95**, 1263 (1995).
6. V. V. Rotkin and R. A. Suris, in *Proceedings of 4th International Conference on Advanced Materials, Cancun, Mexico, 1995*, S3–P34.
7. A. L. Kolesnikova and A. E. Romanov, Fiz. Tverd. Tela (St. Petersburg) **40**, 1178 (1998) [Phys. Solid State **40**, 1075 (1998)].
8. Lewis T. Chadderton and Eugene G. Gamaly, Nucl. Instrum. Methods Phys. Res. B **117** (1–4), 375 (1996).
9. A. Krishnan, E. Dujardin, M. M. J. Treacy, *et al.*, Nature **388** (6641), 451 (1997).
10. V. V. Rotkin and R. A. Suris, Fiz. Tverd. Tela (St. Petersburg) **41** (5), 809 (1999) [Phys. Solid State **41**, 729 (1999)].
11. J. Thorpe, *Elementary Topics in Differention Geometry* (Springer, New York, 1979; Mir, Moscow, 1982).
12. V. V. Novozhilov, *Theory of Elasticity* (Sudpromgiz, Leningrad, 1958).
13. I. A. Polonsky, A. E. Romanov, V. G. Gryaznov, and A. M. Kaprelov, Philos. Mag. A **64** (2), 281 (1991).
14. V. V. Novozhilov, *Theory of Thin Shells* (Sudpromgiz, Leningrad, 1962).
15. É. G. Poznyak and E.V. Shikin, *Differential Geometry* (Mosk. Gos. Univ., Moscow, 1990).

Translated by N. Wadhwa

Physics of the Solid State, Vol. 42, No. 8, 2000, pp. 1575–1578. Translated from Fizika Tverdogo Tela, Vol. 42, No. 8, 2000, pp. 1531–1534.

FULLERENES AND ATOMIC CLUSTERS

Effect of Hydrogen on the Structure of Ultradisperse Diamond

A. E. Aleksenskiĭ, M. V. Baĭdakova, A. Ya. Vul', A. T. Dideĭkin, V. I. Siklitskiĭ, and S. P. Vul'

Ioffe Physicotechnical Institute, Russian Academy of Sciences, Politekhnicheskaya ul. 26, St. Petersburg, 194021 Russia

Received January 20, 2000; in final form, February 18, 2000

Abstract—The paper reports on a study of the effect of annealing in hydrogen on the structural phase transition in clusters of ultradisperse diamond (UDD) obtained by the detonation method. The samples studied were of two types, namely, prepared by the "dry" and "wet" techniques, which differ in the cooling rate of the detonation products and, accordingly, in the structure of the diamond nanocluster shell. It is shown that, irrespective of the type of synthesis, the relative content of the diamond (*sp*3) phase increases within the anneal temperature range of 450 to 750°C, the increase being more pronounced in the samples prepared by "dry" synthesis. A model accounting for the observed structural transformation processes is discussed. A hypothesis of the possibility of compacting UDD clusters into bulk single crystals is put forward. © *2000 MAIK "Nauka/Interperiodica".*

Ultradisperse diamond (UDD) represents a carbon cluster material with clusters typically about 50 Å in size. UDD forms in a detonation wave of an exploding mixture of trinitrotoluene with hexogen at the temperature and pressure corresponding to the region of thermodynamic stability of diamond [1–5]. The cluster structure of the material is determined by the short (tens of microseconds) detonation time.

Recent studies [6] present an elementary UDD cluster as a diamond-lattice core 40–50 Å in size enclosed inside a shell of an essentially different structure. The shell thickness varies from 4 to 10 Å and depends on the actual technological parameters of the synthesis. The structure of the shell consisting of *sp*2-hybridized carbon is determined by the UDD synthesis conditions, more specifically, by the cooling rate of the detonation products and the technique used to subsequently extract the diamond phase. The model proposed in [6] suggests, in particular, that the shell is nonuniform in the degree of ordering of structural fragments, starting with the continuous onionlike carbon sheets directly coating the cluster diamond core to small (a few tens of atoms) fragments of graphene monolayers located primarily in the peripheral layers of the shell. The suggestion that, in the case of small carbon clusters, it is the diamond rather than graphite that is the thermodynamically stable phase [7, 8] permits one to expect an increase of the *sp*3/*sp*2 ratio during the phase transition under some conditions as a result of the shell atoms transferring to the cluster core. As shown by earlier studies [3], however, the converse is true; namely, when UDD is heated in vacuum or in an inert atmosphere, the destruction of the diamond core forces the diamond–graphite phase transition, and it occurs at lower temperatures than it does in bulk crystals.

On the other hand, there are well-known methods of diamond synthesis by carbon deposition from the vapor phase at low temperatures and pressures (CVD) methods. In this case, the synthesis is run in a hydrogen atmosphere, which stabilizes the forming diamond (*sp*3) phase by precluding structurization of the graphite (*sp*2) phase, and, possibly, plays the part of an intermediate stage in the formation of the diamond lattice [9]. It appeared, therefore, of interest to investigate the changes in the cluster shell structure during the phase transition in UDD incurred by annealing in a hydrogen environment.

1. SAMPLES AND EXPERIMENTAL TECHNIQUES

The samples used were obtained from carbon produced by the detonation method, with the detonation products cooled in different ways, more specifically, by gas (CO_2) (the so-called dry technique) and by water (the wet technique). Thus, the starting materials differed in the cooling rate of the detonation products and, accordingly, in the cluster shell structure [10].

The cleaning (extraction of UDD from the detonation products) was achieved by treatment in a 50% water solution of nitric acid at a temperature of 240–260°C. Following repeated rinsing in water, the UDD was dried in air at 200°C to become a powder with grains 10–100 μm in size, a characteristic figure for UDD cluster aggregates [1].

Figure 1 presents an electron micrograph of a sample of the wet-synthesis UDD made in transmission. One readily sees a part of the aggregate consisting of separate clusters. They have a close-to-spherical shape and practically the same characteristic dimensions. The parts filled by parallel dark lines correspond to the cluster diamond core pattern in the (111) plane. The characteristic network structure forms a superposition of

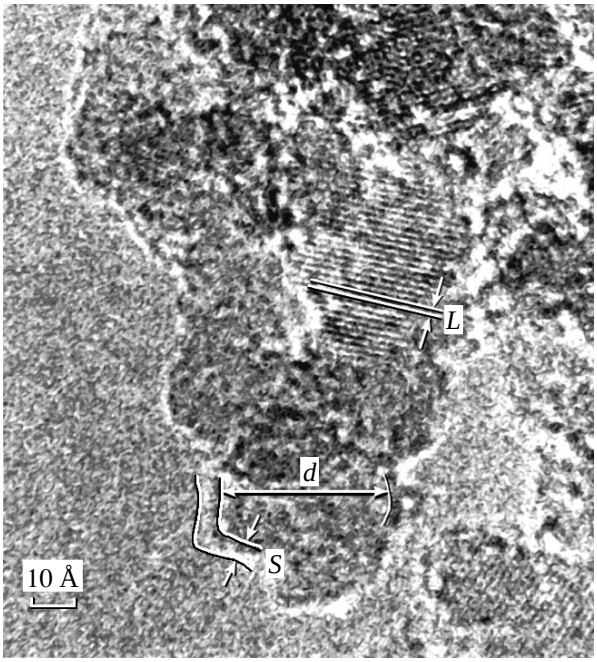

Fig. 1. Electron micrograph of an UDD sample prepared by wet technology before annealing.

two or more clusters with differently oriented lattices. The observed interplanar distance (L = 2.05 Å) can be used as a reference scale for the image and permits direct determination of the cluster size d = 52 Å.[1] This aggregate has a dense structure (note the characteristic absence of visible voids between the cluster boundaries) and there are no isolated clusters, which is in accordance with the current concepts of the UDD structure [2, 6]. The thickness of the clusters observed in this image S = 4–7 Å; the shell has a relatively smooth surface and, as assumed above, does not exhibit a clearly pronounced ordered structure.

In order to study the structural changes in UDD cluster shells induced by annealing in hydrogen, identical amounts of uncompressed material were subjected to annealing in hydrogen. The annealing was performed in an externally heated quartz reactor vessel at atmospheric pressure in a flow of hydrogen passed preliminarily through a palladium filter. The samples were loaded in a cold reactor and heated to the preset temperature, then maintained in isothermal conditions for three hours and cooled subsequently with the heater turned off. The time taken by heating to the desired temperature did not exceed 20 min, and the cooling time equaled two hours.

[1] The image presented in Fig. 1 was obtained by scanning the print with its subsequent computer processing to improve the contrast. The electron micrograph was taken with a high-resolution transmission electron microscope operated by the group of V. L. Kuznetsov (Sib. Div. RAS).

The structure was studied by the traditional method of analyzing the intensity of x-ray scattering and diffraction (λ = 1.542 Å) as a function of wave vector in the angular range $10° < 2\theta_{Br} < 80°$.

2. EXPERIMENTAL RESULTS AND DISCUSSION

Figure 2a presents the angular dependences of x-ray diffraction measured on dry-synthesis UDD samples before and after annealing in hydrogen at different temperatures. The corresponding results for UDD samples obtained by wet synthesis are depicted in Fig. 2b. To avoid superposition, the curves plotting the scattered x-ray intensity are displaced with respect to one another.

The strong symmetric maxima observed at the angles $2\theta_{Br}$ = 43.9° and 75.3° are produced by the (111) and (220) reflections from the diamond lattice, respectively. The halfwidths of these maxima correspond to a size of the coherent scattering region of about 45 Å in the spherical particle approximation (for both wet and dry synthesis material). This is in accordance with the known size of UDD cluster cores [2, 6] and that derived from electron micrographs. The maxima retain their shape (the intensity ratio and symmetry) up to the anneal temperature T = 900°C. According to the concepts developed in [6], this indicates that the structure and size of the cluster diamond cores do not change. All the relations exhibit strong diffuse scattering (halo) with a maximum around $2\theta_{Br}$ = 17°. This halo is associated with scattering on structural elements of the cluster shell [10]. Its shape and location on the scattering curve are determined by the form-factor of the structural element of the UDD shell. This element is a group of six *sp*2-hybridized carbon atoms arranged in a flat ring (the so-called carbon hexagon) with characteristic dimensions of the diagonals of 2.46 and 2.84 Å (the corresponding wave vectors are 1.28 and 1.11 Å^{-1}). The carbon hexagon is a component part of both the solid inner layers of the diamond core shell (the onion-like carbon) and the small graphite-sheet fragments ("aromatic clusters" in the terminology of [6]) making up the outer shell layers. The halo intensity is determined both by the total number of the carbon hexagons and by the extent of their ordering in the cluster shells. Because, as pointed out above, the diamond phase (*sp*3) retains its state in the sample unchanged up to T = 900°C, it becomes possible to use the intensity of any diffraction maximum (for instance, q = 3.05 Å^{-1} of the (111) diamond plane) as a scale size to follow the halo intensity for q = 1.20–1.25 Å^{-1}, associated with the *sp*2 phase, as a function of the anneal temperature.

Figure 3a plots the inverse relative intensity of this halo ($I_{3.05}/I_{1.20}$) vs. the temperature of annealing in hydrogen of UDD samples prepared by the dry and wet techniques. The plots were fitted by a second-order polynomial. For comparison, Fig. 3b presents similar curves for the dry- and wet-prepared UDD samples obtained after annealing under similar conditions in a

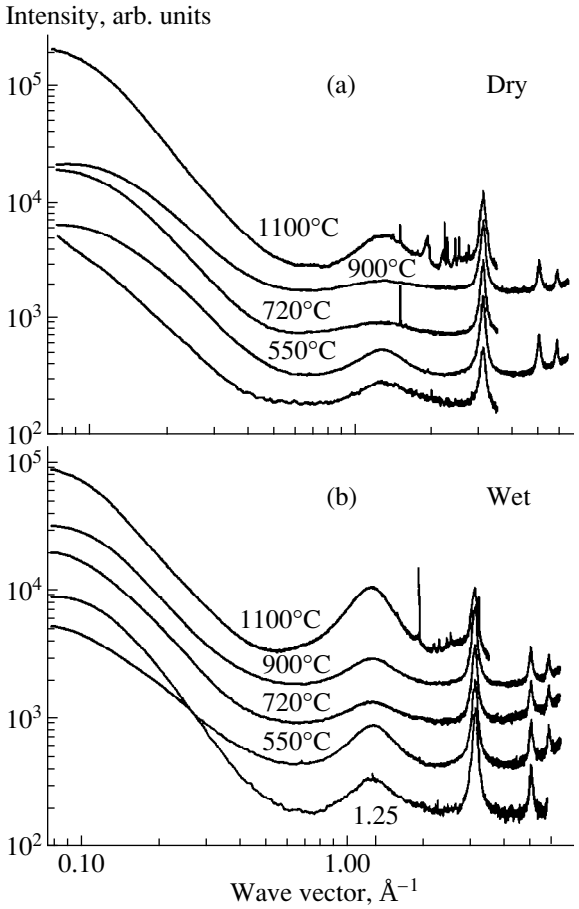

Fig. 2. X-ray scattering and diffraction intensity vs. wave vector plots obtained on UDD samples prepared by (a) dry and (b) wet technology after their annealing in hydrogen at different temperatures. The distinct narrow maxima on the curves measured at anneal temperature T = 1100°C are due to diffraction from crystallized impurities.

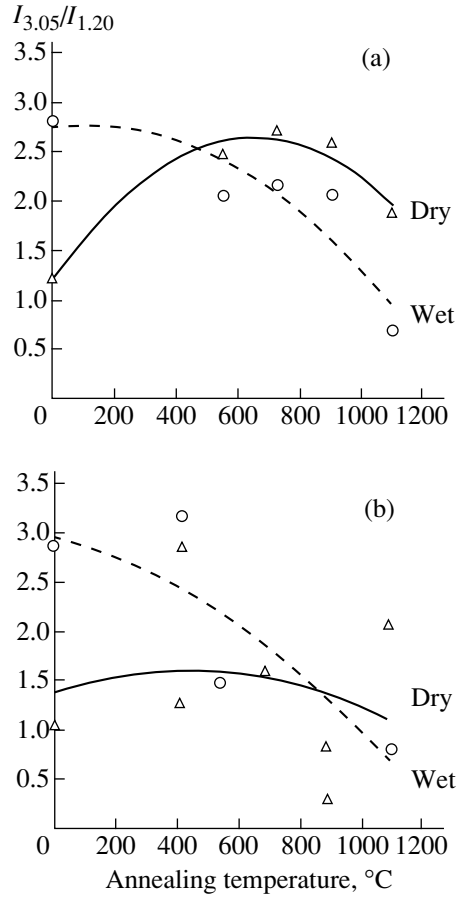

Fig. 3. Relative intensities of the halo due to scattering from elements of the aromatic cluster obtained on UDD samples after annealing at different temperatures in (a) hydrogen and (b) argon.

neutral (argon) atmosphere, which were constructed from the data of [2].

As follows from the above graphs, the $I_{3.05}/I_{1.20}$ ratio of wet-prepared UDD samples falls off (i.e., the halo brightness increases) monotonically with increasing temperature of anneal in the neutral atmosphere and in hydrogen. UDD samples obtained by dry synthesis and annealed in hydrogen exhibit a characteristic maximum in the temperature region from 600 to 800°C.

The monotonic increase of the brightness of this halo at a constant diamond phase fraction observed for wet-prepared samples under annealing near T = 900°C can be attributed to ordering of the *sp*2 cluster shell structure in the course of annealing. The reason for this is that the *sp*2 diamond cluster shell of wet-prepared UDD has no time to acquire an ordered structure because of the fast cooling of the detonation products accepted in this technology. This is also supported by the observation that the $I_{3.05}/I_{1.20}$ ratio for unannealed samples is considerably higher for the UDD prepared by the wet technology. A comparison of the anneals made in hydrogen and argon suggests no noticeable effect of atmosphere composition on changes in the shell structure in wet-prepared UDD samples. This observation is corroborated by the fact that the Raman spectrum obtained on a wet-prepared sample after annealing at T = 720°C (Fig. 4) exhibits, besides the strong line of nanocrystalline diamond at 1322 cm^{-1}, a clear signature of an ordered *sp*2 phase (the strong bands at 1350 and 1580 cm^{-1}).

The above relations permit a conclusion that the cluster shell of UDD prepared by the dry technology differs substantially from that of the wet-prepared UDD. This is apparently due to the cluster shell of dry-prepared UDD having enough time to acquire an ordered structure because of slow cooling. This is supported by the weak dependence of the $I_{3.05}/I_{1.20}$ relative intensity on the temperature of annealing in an inert atmosphere (Fig. 3b). When annealed in hydrogen, the relative halo intensity is seen to decrease noticeably (the $I_{3.05}/I_{1.20}$ ratio passes through a clearly pronounced

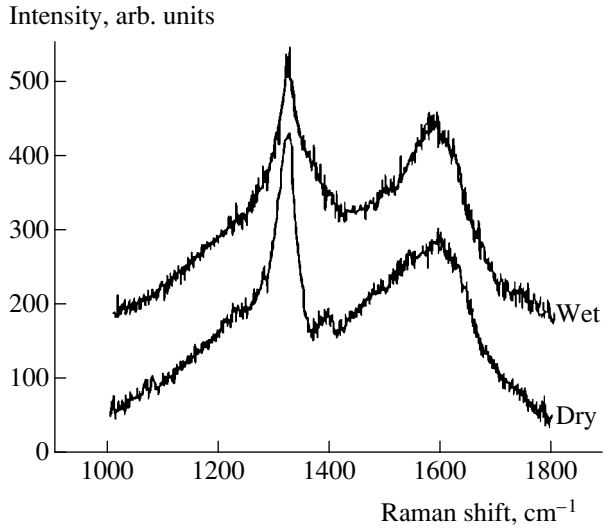

Fig. 4. Raman scattering spectra of UDD samples obtained after annealing in hydrogen at $T = 720$°C.

maximum at $T = 700$–800°C). At higher temperatures, the halo intensity rises again. It may be conjectured that hydrogen favors destruction of the *sp*2 structure of the UDD cluster shell at temperatures $T = 700$–800°C. This may entail a decrease in the absolute shell mass as a result of CH_4 formation, as this occurs in diamond film deposition by CVD (although in this case the hydrogen is in the atomic state) [9]. One cannot also rule out a partial transfer of carbon from the shell to the core with an intermediate formation of hydrocarbons (similar to the CVD process). The destruction of the *sp*2 phase is also indicated by the shape of the Raman spectrum of a dry-prepared sample obtained after annealing in hydrogen. As seen from Fig. 4, the 1350 cm^{-1} band associated with the *sp*2 ordered phase is practically absent here.

The increase in halo intensity for $T > 900$°C is obviously associated with the onset of the formation of the *sp*2 phase in the form of onionlike sheets on the surface of diamond cores undergoing destruction [11].

The decrease in the content of the *sp*2 phase and/or its disordering in UDD observed by us to occur at annealing temperatures of 600–800°C in hydrogen, which is accompanied by a rearrangement of the cluster shell structure, suggests a possibility of formation of appreciable amounts (in volume) of polycrystalline and single-crystal diamond through transformation of the cluster shell carbon from the *sp*2 to *sp*3 phase. This process was directly observed in irradiation of UDD by electrons [12]. We also detected formation of crystals of up to 0.1 mm in size in UDD annealed in hydrogen. This effect is apparently connected with direct transformation of UDD clusters into bulk single crystals. A similar observation was reported in [13]. On the other hand, at elevated temperatures, UDD undergoes a reverse transition, *sp*3–*sp*2 (graphitization), in some cases [3], while the formation of crystals in UDD was found to be poorly reproducible. This means that the equilibrium between the *sp*2 and *sp*3 phases in UDD clusters may also be governed by other factors, in particular, by metal impurities, which can act as catalysts to initiate the formation of the *sp*3 phase.

ACKNOWLEDGMENTS

The authors are indebted to V. L. Kuznetsov for obtaining electron microscope images of UDD samples and to V. Yu. Davydov for Raman spectral measurements and fruitful discussions.

This work was supported by the Russian State Program "Fullerenes and Atomic Clusters" (project "Plenka-2"). The work of one of authors (V.I. Siklitskiĭ) was supported by the Russian Foundation for Basic Research (project no. 98-07-90336) and the Russian State Program "Physics of Solid Nanostructures" (project no. 97-0003).

REFERENCES

1. A. I. Lyamkin, E. A. Petrov, A. P. Ershov, *et al.*, Dokl. Akad. Nauk SSSR **302**, 611 (1988) [Sov. Phys. Dokl. **33**, 705 (1988)].
2. A. E. Aleksenskiĭ, M. V. Baĭdakova, A. Ya. Vul', *et al.*, Fiz. Tverd. Tela (St. Petersburg) **39**, 1125 (1997) [Phys. Solid State **39**, 1007 (1997)].
3. V. L. Kuznetsov, A. L. Chuvilin, Yu. V. Butenko, *et al.*, Chem. Phys. Lett. **222**, 343 (1994).
4. N. R. Greiner, D. S. Phillips, J. D. Johnson, and F. Volk, Nature **333**, 440 (1988).
5. Odd E. Andersson, B. L. V. Prasad, Hirohiko Sato, *et al.*, Phys. Rev. B **58**, 16388 (1998).
6. A. E. Aleksenskiĭ, M. V. Baĭdakova, A. Ya. Vul', and V. I. Siklitskiĭ, Fiz. Tverd. Tela (St. Petersburg) **41**, 740 (1999) [Phys. Solid State **41**, 668 (1999)].
7. P. Badziak, W. S. Verwoerd, W. P. Ellis, and N. R. Greiner, Nature **343**, 244 (1990).
8. M. Y. Gamarnik, Phys. Rev. B **54**, 2150 (1996).
9. *Synthetic Diamond: Emerging CVD Science and Technology*, Ed. by Karl E. Spear and John P. Dismukes (Wiley, New York, 1993).
10. M. V. Baĭdakova, A. Ya. Vul', V. I. Siklitskiĭ, and N. N. Faleev, Fiz. Tverd. Tela (St. Petersburg) **40**, 776 (1998) [Phys. Solid State **40**, 715 (1998)].
11. V. L. Kuznetsov, I. L. Ziberberg, V. U. Butenko, and A. L. Chuvilin, J. Appl. Phys. **86**, 863 (1999).
12. Y. Lytovich and F. Banhart, Appl. Phys. Lett. **74**, 659 (1999).
13. R. Roy, H. S. Dewan, and P. Rawindranathan, J. Mater. Chem. **3**, 685 (1993).

Translated by G. Skrebtsov